THE UNIVERSITY *of* EDINBURGH

Development of *In Vitro* and *In Vivo* Models to Underpin Advances in Human Radiotherapy

THE UNIVERSITY *of* EDINBURGH

Edmund Mark Gray

Presented for Doctor of Philosophy

The University of Edinburgh

2019

Declaration

I declare that this thesis has been composed by me and the work contained within it has been performed by myself, except where otherwise stated. The work presented in this thesis has not been submitted for any other degree or professional qualification.

Edmund Mark Gray

Acknowledgements

I would like to take this opportunity to thank my supervisors Professor David Argyle, Dr Carol Ward, Dr Lisa Pang and Professor Ian Kunkler for their help, support and guidance throughout my PhD. Although not officially my supervisor, Dr Simon Langdon has also been a great support throughout my studies. My thanks go to all members of the Argyle Group in the Roslin Institute, those in the Division of Pathology in the IGMM and those in the IMPACT project for their help and advice.

I consider myself extremely lucky to have been given the opportunity to work in such a fantastic multidisciplinary project as IMPACT. The project has brought together experts in the fields of engineering, chemistry, medicine, veterinary medicine and social science and being part of such a big and friendly team has made my studies and research ever more exciting.

I would like to thank the College of Medicine and Veterinary Medicine for providing the opportunity for me to undertake my PhD at the University of Edinburgh. Similarly, I would like to give my appreciation to the BBSRC and EPSRC for their funding of the IMPACT project. The following people also deserve a specific thank you for their contributions in this study:

- Contributions to bioinformatic data analysis - Dr Arran Turnbull
- Tissue processing and sectioning - Helen Caldwell and Elaine Mclay
- IGMM mass spectrometry – Dr Jimi Wills
- IGMM imaging facility - Matthew Pearson and Dr Laura Murphy
- Veterinary pathology - Dr Linda Morrison
- OPA case identification – Dr Chris Cousens, Dr David Griffiths and Dr Phil Scott
- Dryden farm – James Nixon, Peter Tennant and Adrian Ritchie
- LARIF – Professor Eddie Clutton, Dr Rachael Gregson, Dr Stephen Greenhalgh and Lynne Grant
- University College London – Professor Mervyn Singer and Dr Alex Dyson
- IMPACT engineers – Dr Jamie Marland, Dr Paul Sullivan, Dr Ewen Blair and Dr Andreas Tsiamis

A big thank you goes to my parents Margaret and Malcolm for their support not only during my post graduate studies but my entire life and to my brother Richard who is always willing to proofread my work.

I would also like to thank James for his support and friendship for the last few years since I started my studies and Arran, Carlos and Maria for being great friends.

Abstract (scientific)

Radiotherapy (RT) is commonly used for the local control of many cancer types. Unfortunately, not all patients will achieve a therapeutic benefit, and some will develop loco-regional recurrences and/or metastatic disease. The hypoxic nature of the tumour microenvironment and the development of radioresistant cancer cells can contribute to these treatment failures. Understanding the mechanisms involved in acquired radioresistance and the development of techniques to identify and target hypoxic tumour areas has the potential to improve RT response rates.

The first aim of this project was to investigate the development of acquired radioresistance and identify radiation-induced secreted biomarkers which could be used as indicators of a radiation response or radiosensitivity. Human radioresistant (RR) breast cancer cell lines were developed from parental MCF-7, ZR-751 and MDA-MB-231 cells. Parental and RR cells underwent genotypic, phenotypic and functional characterisation. RR cells exhibited enhanced migration and invasion, with evidence of epithelial-to-mesenchymal transition. MCF-7 RR and ZR-751 RR cell lines exhibited significant phenotypic changes, including loss of ERα and PgR expression and increased EGFR expression, which were associated with the down-regulation of ER signalling genes and up-regulation of genes associated with PI3K, MAPK and WNT pathway activation. A change in subtype classification from luminal A to HER2-overexpressing (MCF-7 RR) and normal-like (ZR-751 RR) subtypes was also observed, consistent with radiation and endocrine therapy resistance and a more aggressive phenotype.

To identify biomarkers secreted in response to radiation, human and canine breast and ovine lung cancer cell lines were radiated. Secretome samples were analysed by liquid chromatography-mass spectrometry. Using results from the MCF-7 cell line, 33 radiation-induced secreted biomarkers were identified which had higher (up to 12-fold) secretion levels compared to untreated controls. Based on secretion profiles and functional analysis 9 candidate biomarkers were selected (YBX3, TK1, SEC24C, EIF3G, EIF4EBP2, NAP1L4, VPS29, GNPNAT1 and DKK1) of which the first 4 underwent in-lab validation. To identify biomarkers related to radiosensitivity transcriptomic analysis identified higher expression of genes encoding 7 of the candidate biomarkers in the MCF-7 cell line compared to its

radioresistant derivative. WB analysis identified increased levels of the 4 biomarkers in the conditioned media of parental cells 24 h post-radiation which was not seen in the RR cell lines. These biomarkers, which had differential gene expression and secretion profiles between parental and RR cell lines, may be useful for both predicting and monitoring a tumour's response to RT.

A further aim was to investigate the biocompatibility and functionality of an implantable electrochemical sensor, developed within the Engineering and Physical Sciences Research Council funded IMPACT project. This sensor was designed to measure tissue O_2 tension (ptO_2) within a tumour, enabling the identification and monitoring of radioresistant hypoxic tumour areas. This study developed a novel *in vivo* tumour xenograft model to evaluate the potential of 6 materials (silicon dioxide, silicon nitride, Parylene-C, Nafion, biocompatible EPOTEK epoxy resin and platinum) used in the construction of the sensor, to trigger a foreign body response (FBR) when implanted into a solid tumour. Following implantation none of the materials affected tumour growth and all mice remained healthy. Immunohistochemistry performed on the tumour showed no significant changes in necrosis, hypoxic cell number, proliferation, apoptosis, immune cell infiltration or collagen deposition around the implant site. The absence of a FBR supports their use in the construction of implantable medical devices.

In vivo validation of the O_2 sensor to provide real-time measurements on intra-tumoural ptO_2 was performed using a novel large animal ovine model. To achieve this aim, we developed a novel computed tomography (CT) guided trans-thoracic percutaneous implantation technique for the delivery of sensors into naturally occurring ovine pulmonary adenocarcinoma (OPA) tumours. This model successfully integrated techniques such as ultrasound, general anaesthesia, CT and surgery into the OPA model, all of which are techniques commonly used in the treatment of human lung cancer patients. This methodology resulted in the accurate implantation of sensors into OPA tumours with minimal complications and demonstrated the sensor's ability to detect changes in intra-tumoural ptO_2 following manipulation of the inspired fractional O_2 concentration (FiO_2).

To investigate other possible clinical applications, sensors were validated for measuring intestinal ptO_2 using a novel rat model. These experiments assessed the

potential of the sensor to monitor intestinal perfusion following an intestinal resection and anastomosis. The sensor was placed onto the serosal surface of the small intestine of anaesthetised rats that were subsequently exposed to ischaemic, hypoxaemic and haemorrhagic insults. Decreases in intestinal ptO_2 were observed following superior mesenteric artery occlusion and reductions in FiO_2; these changes were reversible after reinstating blood flow or increasing FiO_2. These results provided evidence that the sensors could detect changes in intestinal perfusion which could be utilised in a clinical setting to monitor peri-anastomotic intestinal ptO_2.

Overall this PhD project has conducted both *in vitro* and *in vivo* work aimed at the investigation of mechanisms of radioresistance, identifying secreted biomarkers of radiosensitivity and validating the ability of an implantable sensor to measure real-time intra-tumoural and visceral surface O_2 tension. Identification of factors contributing to poor RT responses, such as radioresistance development and hypoxic tumour areas could provide a means by which RT could become personalised. Patients identified as having radioresistant tumours or those not responding to RT based on radiation-induced secreted biomarkers, could be given higher dose of radiation or radiosensitising agents to improve patient outcomes.

Abstract (lay)

Cancer is a disease characterised by the abnormal growth of cells within the body. The disease can cause patients to die either from cancer cells destroying the organ from which they started growing in or from spreading throughout the body. Radiotherapy (RT) is a commonly used cancer treatment that causes cancer cell death through irreparable DNA damage. Unfortunately, this treatment does not always work. Low O_2 levels (hypoxia) within the tumour and the presence of radioresistant (RR) cancer cells can decrease the effectiveness of RT.

Breast cancer is the most commonly diagnosed female cancer in the world, with 2 million cases and 0.7 million deaths occurring per year. Breast tumours can develop resistance to radiation, which leads to the development of aggressive cancer cells and disease recurrence. One of the aims of this project was to model the development of breast cancer radioresistance in the lab so that we can study changes in the cells which could warn doctors of the emergence of treatment resistant cancer cells. To do this, we treated breast cancer cells with high doses of radiation. While many cells died, some survived and were able to grow. These are the RR cells that would kick-start tumour growth after treatment. By developing these cells, in the laboratory setting, we can compare them to the original cells and determine how they are different. The main differences we observed were that the RR cells became more aggressive, with an increased ability to migrate and invade. These cells also showed resistance to endocrine therapy, meaning they had developed resistance to multiple treatment strategies. Differences in the proteins that were released from the original and RR cells in response to radiation were also seen. The main differences we identified were the increased release of EIF3G, SEC24C, YBX3 and TK1 from the original cells, which did not occur in the RR cells. We propose that monitoring the level of these proteins may help doctors monitor a patient's response to RT and help them to alter the treatment plan accordingly.

Using a sensor that can be implanted into a tumour to measure tissue O_2 concentrations could improve a patient's treatment through the identification of RR hypoxic tumour areas. Unfortunately, when a foreign material is placed within the body a reaction can occur to isolate it from the surrounding tissues. This foreign body response (FBR) may limit the devices ability to function correctly. The

potential of materials used in the construction of an implantable miniaturised O_2 sensor to trigger this tissue reaction was assessed by implanting them into human tumours grown in mice. None of the materials tested had any effect on tumour growth or mice body weight, with the mice remaining healthy throughout the implantation period. Tumour analysis showed no significant tissue reactions, which supports the use of these materials for devices designed for implantation within tumours. To assess the ability of working sensors to measure O_2 levels within a tumour, we implanted them into sheep lung tumours. In order to improve the model's clinical usefulness, we used techniques commonly used in the treatment of human lung cancer patients (ultrasound, general anaesthesia, computed tomography and surgery). The method resulted in accurate implantation of sensors into lung tumours with minimal complications and demonstrated the sensor's ability to detect changes in O_2 levels within the tumour.

The use of these O_2 sensors is not only restricted to cancer patients. One alternative clinical use is for monitoring intestinal O_2 levels as a means of assessing intestinal healing following surgery. To investigate this application sensors were placed onto the surface of the small intestine of anaesthetised rats. These sensors were able to detect lower intestinal O_2 levels following ligation of the blood supply to the intestine and reduction in blood O_2 levels. These results provided evidence that the sensors could detect changes in intestinal oxygenation which could be utilised in clinical settings following surgery.

This PhD project has conducted both *in vitro* and *in vivo* work aimed at investigating mechanisms of radioresistance, identifying proteins released from cancer cells in response to radiation and testing the ability of an implantable sensor to measure O_2 levels within a tumour. In the future, these techniques could be used to help personalise RT, whereby patients identified as having RR tumours could be given higher dose of radiation or drugs to improve treatment responses. We have also shown that these sensors could have multiple applications where the measurement of tissue O_2 levels is clinically important.

Abbreviations

ABE	Arterial base excess
ACPGBI	Association of Coloproctology of Great Britain and Ireland
AKT	Protein kinase B
AL	Anastomotic leak
ALCAM	Activated leukocyte cell adhesion molecule
ANOVA	Analysis of variance
AP1	Activating protein 1
ARCON	Accelerated radiotherapy with carbogen with nicotinamide
ATF	Activating transcription factor
BAC	Bronchioloalveolar carcinoma
BCA	Bicinchoninic acid
BiP	Binding proteins
BOLD	Blood oxygen level-dependent
BSA	Bovine serum albumin
BTV	Biologic target volume
CA	Carbonic anhydrase
CA 15-3	Carbohydrate antigen 15-3
CAM	Chorioallantoic membrane
CDH1	E-cadherin
CDH2	N-cadherin
CE	Counter electrode
CEA	Carcinoembryonic antigen
CF	Colony formation
CHOP	C/EBP homologues protein
CM	Conditioned media
CMT	Canine mammary tumour
CO_2	Carbon dioxide
COPII	Coat protein complex II
CRP	C-reactive protein
CT	Computed tomography
CT	Core temperature
CTF	Computed tomography combined with fluoroscopy
Cu	Copper
Cu-ATSM	Copper-complexed dithiosemicarbazone
D	Day
DAB	3,3′-Diaminobenzidine
DCE-MRI	Dynamic contrast-enhanced magnetic resonance imaging
dH_2O	Distilled water
DMEM	Dulbecco's modified Eagle's Media
DMSO	Dimethyl sulfoxide
DPBN	Dose painting by numbers
DTP	Developmental Therapeutics Program
DVS	Dose verification system
enJSRV	Endogenous JSRV
EDTA	Ethylenediaminetetraacetic acid
EGFR	Epidermal growth factor receptor 1
eIF	Eukaryotic initiation factor
EIF3G	Eukaryotic Translation Initiation Factor 3 Subunit G
EMT	Epithelial-to-mesenchymal transition
ER	Oestrogen receptor
ERE	Oestrogen response elements
ERS	European Respiratory Society
ET	Endocrine therapy

exJSRV	Exogenous JSRV
FBGC	Foreign body giant cells
FBR	Foreign body response
FCS	Foetal calf serum
FDA	Food and drug administration
FIJI	Fiji is just ImageJ
FiO_2	Inspired fractional oxygen concentration
FMISO-PET	18F-fluoromisonidazole–positron emission tomography
G-CSF	Granulocyte-colony stimulating factor
GLUT	Glucose transporter
GM-CSF	Granulocyte macrophage colony stimulating factor
GTV	Gross tumour volume
Gy	Gray
H	Hour
H&E	Haematoxylin and eosin
Hb	Haemoglobin
HER2	Human epidermal growth factor receptor tyrosine-protein kinase erbB-2
hcG-β	β subunit of human chorionic gonadotrophin
hPTH(1-34)	Human parathyroid hormone fragment (1-34)
HIF	Hypoxia-inducible factor
HIF-1	Hypoxia inducible factor-1
HNSCC	Head and neck squamous cell carcinoma
HR	Heart rate
IASLC	International Association for the Study of Lung Cancer
IC_{50}	Drug/radiation dose required to reduce proliferation by 50%
ICC	Immunocytochemistry
IGMM	Institute of Genetics and Molecular Medicine
IGRT	Image guided radiotherapy
IF	Immunofluorescence
IHC	Immunohistochemistry
IL	Interleukin
IVL	Intralumenal vesicles
IMPACT	Implantable Microsystems for Personalised Anti-Cancer Therapy
IMRT	Intensity-modulated radiotherapy
IRE1	Inositol-requiring enzyme 1
ISO	International Standards Agency
LARIF	Large animal research and imaging facility
LC-MS	Liquid chromatography–mass spectrometry
JSRV	Jaagsiekte sheep retrovirus
KRAS	Kirsten rat sarcoma
MAP	Mean arterial blood pressure
MAPK	Mitogen-activated protein kinase
MEMS	Micro-electro-mechanical system
Min	Minute
MISS	Membrane-initiated steroid signalling
MRI	Magnetic resonance imaging
MRSw	Magnetic relaxation switches
MTOR	Mammalian target of rapamycin
MTS	Multicellular tumour spheroid
MVB	Multivesicular body
n	Number
NCI	National Cancer Institute
NF-ƙB	Nuclear factor- ƙB
NISS	Nuclear-initiated steroid signalling
NK	Natural killer cells

NKT	Natural killer cells T cells
NOD SCID	Non-obese diabetic severe combined immune deficiency
NSCLC	Non-small cell lung cancer
NT	Needle tract
O_2	Oxygen
OD	Optical density
OE-MRI	Oxygen-enhanced magnetic resonance imaging
OPA	Ovine pulmonary adenocarcinoma
P53	Tumour protein 53
PaO_2	Arterial oxygen partial pressure
$PaCO_2$	Arterial carbon dioxide partial pressure
PBS	Phosphate buffered saline
PBS-T	Phosphate buffered saline-tween20
PDX	Patient derived xenograft
PE	Plating efficiency
PERK	PKR-like endoplasmic reticulum kinase
PET	Positron emission tomography
PEU	Polyether polyurethane
PgR	Progesterone receptor
PI3K	Phosphoinositide 3-kinases
PMN	Polymorphonuclear
PO_2	Partial pressure of oxygen
Pt	Platinum
PTEN	Phosphatase and tensin homolog
PtO_2	Tissue oxygen tension
PTV	Planned target volume
RBCs	Red blood cells
RE	Reference electrode
ROS	Reactive oxygen species
Rpm	Revolutions per minute
RR	Radioresistant
RR	Respiratory rate
RT	Radiotherapy
SaO_2	Haemoglobin oxygen saturation
SDS-PAGE	Sodium dodecyl sulphate-polyacrylamide gel electrophoresis
SCID	Severe combined immune deficiency
SCLC	Small cell lung cancer
SDS	Sodium dodecyl sulphate
Sec	Second
SEM	Standard error of the mean
SERD	Selective oestrogen receptor down-regulators or degraders
SERM	Selective oestrogen receptor modulators
SF	Survival fraction
SFM	Serum-free media
SiO_2	Silicon dioxide
SIRS	Systemic inflammatory response syndrome
Si_3N_3	Silicon nitride
SMA	Superior mesenteric artery
SRB	Sulforhodamine B
TAM	Tumour-associated macrophage
TCA	Trichloroacetic acid
Ti	Titanium
TK	Thymidine kinase
TME	Tumour microenvironment
TNF-α	Tumour necrosis factor- α

TNBC	Triple negative breast cancer
TTNB	Trans-thoracic needle biopsy
UPR	Unfolded protein response
VEGF	Vascular endothelial growth factor
VIM	Vimentin
VHL	von Hippel-Lindau
WB	Western blot
WE	Working electrode
WNT	Wingless/Integrated
XBP	X-box-binding protein
YBX	Y-box binding protein

List of Figures

List of Tables

Table of Contents

1 Introduction

This introduction chapter is an expanded version of 2 published review articles: 1) Gray M, Meehan J, Ward C, Langdon SP, Kunkler IH, Murray A, Argyle D. Implantable biosensors and their contribution to the future of precision medicine. The Veterinary Journal 2018; 239: 21-29. 2) Gray M, Meehan J, Sullivan P, Marland JRK, Greenhalgh SN, Gregson R, Clutton RE, Ward C, Cousens C, Griffiths D, Murray A, Argyle D. Ovine Pulmonary Adenocarcinoma: A Unique Model to Improve Lung Cancer Research. Frontiers in Oncology - Molecular and Cellular Oncology 2019; 9(335): 1-11. These articles are open access with the authors retaining copyright to their work with permission to use published figures in this thesis. Sections of text and figures used from these articles have been referenced accordingly.

1.1 The hallmarks of cancer

Cancer (also referred to as a malignant tumour or neoplasm) is a term used to describe a large group of heterogenous diseases characterised by aberrant growth of abnormal cells with a potential to spread from the primary site of origin throughout the body (metastasis). Genetic and environmental factors (lifestyle, pathogens or carcinogens) can influence cancer development (carcinogenesis) and progression; however, carcinogenesis is likely due to a multistep process beginning with the accumulation of somatic mutations that eventually leads to an altered genome resulting in the transformation of normal cells into malignant ones[1-3].

Carcinogenesis can potentially occur in any cell in the human body that has replicative capabilities, because of this more than 100 different cancer types have been identified, each of which can have multiple subtypes[4]. Tumours originating from different tissues will be composed of specific cell types and stromal components; these factors in combination with malignant cells possessing unique genetic alterations make trying to understand cancer as a single disease entity very difficult. To overcome these issues Hanahan and Weinberg originally described 6 essential cell physiology capabilities applicable to all cancer types that can cause malignant transformation. These ‘hallmarks’ are: growth signal self-sufficiency,

insensitivity to growth suppressors, resisting apoptosis, replicative immortality, increased angiogenesis and tissue invasion and metastasis[3]. With advances in understanding tumour biology, 2 further 'hallmarks' were subsequently described as energy metabolism reprogramming and avoiding immune system destruction[5].

These 8 functional capabilities are likely to develop in different tumour types through various mechanisms and at different stages in the process of carcinogenesis, these factors ultimately influence how cancer cells survive, proliferate, invade and metastasise. The development of these malignant capabilities requires certain cellular enabling characteristics, among which genomic instability and tumour promoting inflammation are considered important. Hanahan and Weinberg proposed that the study of tumour biology should not simply focus on cancer cells but should also include the investigation of recruited normal cells that make up the tumour-associated stroma and the tumour microenvironment (TME), as these factors can also play roles in carcinogenesis and the development of hallmark capabilities[5].

1.2 Worldwide cancer incidence and mortality

Cancer is a disease that occurs throughout the world, creating social and economic burdens for both developed and developing countries alike. Although advances in pre-clinical and clinical research are improving cancer diagnosis and treatment, the disease remains the most common cause of death throughout the world. It is estimated that 18.1 million new cancer cases and 9.6 million cancer-related deaths occurred in 2018; combined data for both sexes showed that lung, breast, prostate and colon cancers account for approximately 40% of all newly diagnosed cases[6]. In males, lung cancer is the most frequently diagnosed cancer and leading cause of cancer-related deaths, whereas in females, breast cancer is the most common. Overall, the top 10 cancer types account for over 65% of newly diagnosed cases and deaths (Figure 1.1). If current trends in global population growth combined with the effects of an aging population continue, these figures could increase to 20.3 million new cancer cases and 12.7 million deaths by 2030[7].

1.3 United Kingdom cancer incidence and mortality

Cancer incidence and mortality rates can vary between countries and continents. In the United Kingdom, approximately 360,000 new cancer cases and

165,000 cancer-related deaths occurred in 2015[4]. Approximately 36% of these new cases were diagnosed in people above 75 years of age, giving an indication of the effect that the aging population can have on cancer incidence rates. In line with global incidences, the 4 most common cancer types in the UK are breast, prostate, lung and bowel, which account for approximately 53% of all new cancer cases and approximately 45% of all cancer-related deaths. Lung cancer is a major contributor to this mortality rate accounting alone for approximately 20% of deaths. The scale of the health problem that cancer creates is highlighted by the estimate that in 2016 cancer accounted for 28% of all UK deaths; these figures are only likely to increase as UK cancer incidence rates are expected to rise by 2% by 2035[4].

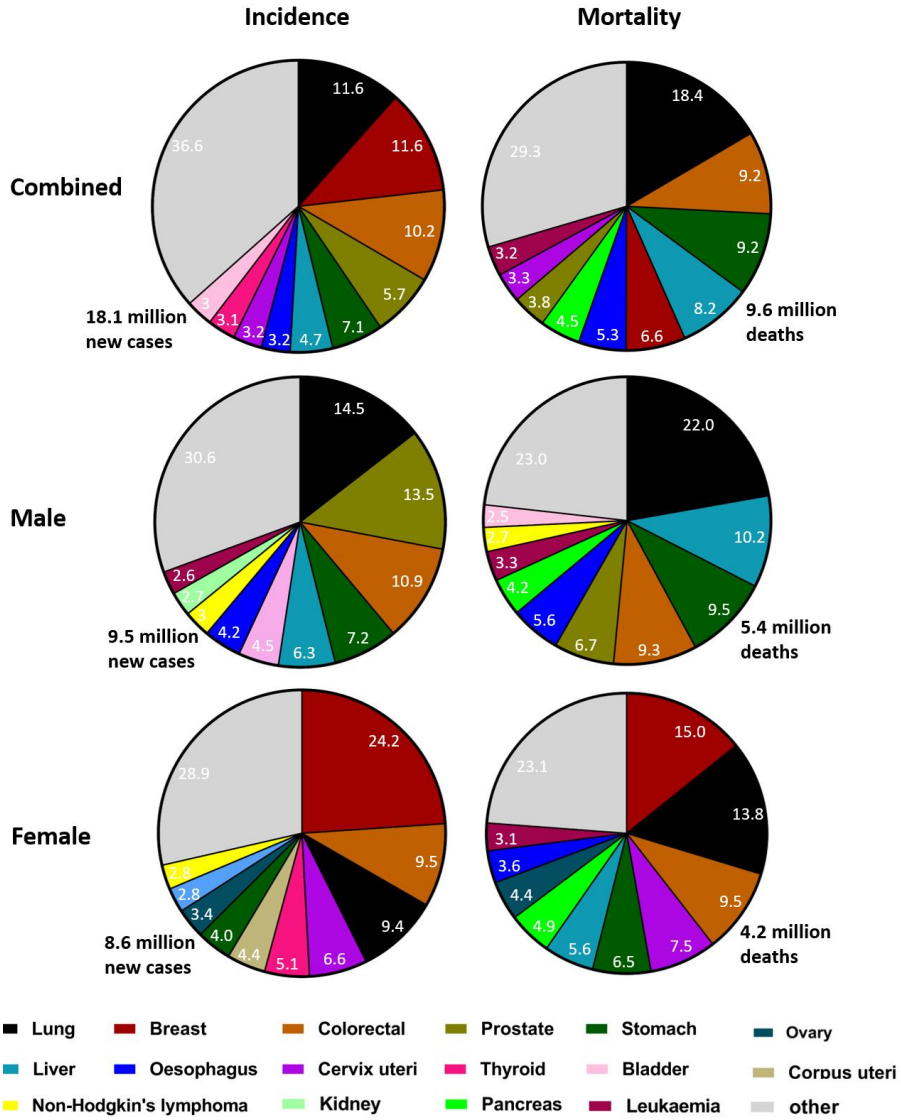

Figure 1.1. Pie charts representing the distribution of cancer cases and deaths for the 10 most common cancer types in the world in 2018. For each sex, the area of the pie chart reflects the percentage of the total number of cases or deaths[6].

1.4 Precision medicine

The terms precision and personalised medicine are interchangeable; however, concerns amongst clinicians that the term 'personalised' could be interpreted as treatments/drugs being developed specifically for individual patients has led to the term precision medicine being favoured[8,9]. Precision medicine is defined as the incorporation of disease biomarkers, phenotype, molecular signatures, lifestyle and environment into the prevention, investigation and treatment of diseases[10]. Patients can be classified according to their differences in disease susceptibility, treatment response and prognosis, information which can be used to select patients that are most likely to benefit from specific treatments to improve clinical outcome[11]. Precision medicine has gained increased awareness in recent years aided by world leaders such as the former President of the United States Barack Obama. His 'Precision Medicine Initiative', announced in 2015 aimed 'to bring us closer to curing diseases like cancer and diabetes – and to give us all access to the personalised information we need to keep ourselves and our families healthier'[12].

Dedicated centres such as The Personalised Medicine Coalition in the USA and The Centre for Personalised Medicine in the UK will help to improve the use of precision medicine into healthcare practices[13]; however, for precision medicine to be integrated into the field of oncology we will need to understand and map tumour heterogeneity at genomic, epigenomic and microenvironmental levels[14,15].

1.5 Breast cancer

Breast cancer is the most common female cancer in the world, with approximately 2 million new cases and 0.7 million cancer-related deaths occurring per year[6]. Following a diagnosis of breast cancer, immunohistochemistry (IHC) is used to classify the tumour based on the expression of certain cellular receptors. These receptors typically include human epidermal growth factor receptor 2 (HER2), oestrogen receptor α (ERα), progesterone receptor (PgR) and epidermal growth factor receptor (EGFR) which can classify the tumour as hormone dependant or independent[16]. ERα is the most important predictive biomarker, with approximately 85% of breast cancers expressing this receptor. PgR is expressed in approximately 67% of breast cancers and is known to regulate epithelial proliferation[17] and can alter

which genes are stimulated by ER binding[18,19]. PgR expression is strongly dependent on the presence of ER, so the majority of ER^+ cancers are also PgR^{+}[20]. ER^+ breast cancers are hormone dependent which rely on oestrogen for both carcinogenesis and tumour progression.

1.5.1 Oestrogen signalling

Oestrogen can modulate gene expression and promote cancer progression either directly through the genomic signalling pathway termed nuclear-initiated steroid signalling (NISS)[21] or indirectly through the non-genomic signalling pathway termed membrane-initiated steroid signalling (MISS)[22]. In NISS oestrogen binds directly to ERα causing the formation of an oestrogen-ERα complex. This complex translocates to the nucleus where it interacts with co-activators and binds specific DNA regions called oestrogen response elements (EREs). These ERS regulate transcription of oestrogen responsive genes involved in angiogenesis, apoptosis, proliferation and invasion[21]. In MISS, following ligand binding, the oestrogen-ERα complex can interact with and activate other transcription factors and signal transduction pathways, such as nuclear factor-κB (NF-κB), activating protein 1 (AP1), p53, PI3K/AKT and ERK/MAPK. Following their recruitment and activation transcription of their target genes can occur[22-24]. Both the genomic and non-genomic pathways can also be activated through cross talk with other oncogenic pathways such as those involving the EGFR and HER tyrosine kinases[23,25,26]. Such interactions can lead to ERα signalling activation even in the absence of oestrogen.

1.5.2 Endocrine therapy

Typically, early and locally advanced breast cancer is treated with surgery followed by adjuvant radiotherapy (RT), chemotherapy and/or endocrine therapy (ET). ET plays an important role in the treatment of patients with ER^+ breast cancers and can be used either to stop oestrogen synthesis or reduce its effect by preventing its binding to ER. Although there are various ET strategies, treatment selection is usually based on menopausal status, clinicopathological factors and the presence of co-morbidities[27,28]. In pre-menopausal women, as the ovaries are the main source of oestrogen production, oestrogen synthesis blockade can be achieved either through removal of the ovaries (oophorectomy) or by chemical suppression (luteinising

hormone releasing hormone agonists, such as goserilin)[16]. In post-menopausal women the ovaries cease to be the main source of oestrogen production with oestrogen instead being synthesised from androgens in bone, fat, and breast tissue through a reaction catalysed by the enzyme aromatase[29,30]. Oestrogen synthesis can therefore be blocked through the administration of aromatase inhibitors such as anastrazole, letrozole, or exemestane. These inhibitors work either by competing with substrates binding to aromatase or by mimicking the substrates of aromatase and inactivating the enzyme. The overall result is to reduce the amount of oestrogen produced, thus inhibiting tumour growth[31]. To reduce the effect that oestrogen has on cancer cells ER function can also be chemically blocked in both pre- and post-menopausal women using anti-oestrogens. These drugs include selective ER modulators (SERMs) and selective ER down-regulators or degraders (SERDs). Tamoxifen is an example of a SERM that acts as a partial oestrogen agonist which blocks the ER and removes the growth-promoting effects that oestrogen has on the tumour. Fulvestrant is an example of a SERD that acts as a full oestrogen antagonist, that both inhibits the ER and accelerates its degradation[16].

Overall, both ER and PgR have been used as diagnostic and predictive markers for response to ET treatment since the 1970s[32,33] and their assessment by IHC is now a mandatory requirement in all breast cancer patients to assist treatment selection[34].

1.6 Radiotherapy

RT remains a commonly used treatment modality for many different cancer types with approximately 50% of cancer patients receiving radiation either as a sole means of treatment or combined with surgery, ET or chemotherapy[35]. RT can be given as a neoadjuvant treatment with curative intent, such as in prostate[36] or laryngeal cancers[37], or to shrink a tumour before definitive surgery in cases such as locally advanced rectal cancer and various forms of head and neck cancers[38]. RT can also be given after surgery as an adjuvant treatment to improve patient outcome[39]. Unfortunately, not all patients obtain a therapeutic benefit from RT; factors such as innate[40] and acquired radioresistance[41] can contribute to treatment failures, resulting in local recurrences or metastatic disease. RT is also not a benign procedure; for example, in breast cancer known radiation-associated side effects include cardiac and

skin toxicities, lymphedema, secondary cancers, rib fractures and brachial plexopathy[42]. The use of RT in a patient's treatment plan must therefore consider the potential therapeutic benefits against the potential patient risks.

1.6.1 Breast cancer and radiotherapy

RT with curative intent or as a palliative treatment is estimated to benefit up to 83% of breast cancer patients[43]. Multiple studies have also shown that whole breast RT following breast conserving surgery provides local control and survival rates equivalent to mastectomy[39,44,45], with added advantages of improved cosmetic outcomes and reduced side effects. Although overall 5-year survival rates after RT are approximately 80%, it is estimated that 30% of these patients will develop loco-regional recurrences or metastatic disease, the majority of which will die within 5 years[46]. RT treatment plans typically involve the delivery of radiation to the tumour in multiple fractions over a period of several weeks; the standard adjuvant RT fractionation regime following breast conservation surgery is 25 fractions of 2 Gy over a 5 week period, or hypofractionated regimes consisting of a total of 40 Gy delivered in 15 fractions over 3 weeks[47].

Regardless of whether RT is given as a neoadjuvant or adjuvant treatment, the clinical effects of RT are only seen towards the end or even after the treatment course has finished, therefore patients who fail to respond to RT will initially go undetected. This delay in identifying non-responding tumours will expose patients to the risk of developing RT-induced side effects for no therapeutic gain, allow tumour progression, impact on long-term survival and delay the provision of alternative treatments[48]. One method being used in the management of cancer patients is the measurement of tumour-related biomarkers in serum and plasma.

1.6.2 Using tumour biomarkers for precision radiotherapy

Biomarkers can be defined as a characteristic which can be objectively measured and evaluated as indicators of normal biological processes, pathogenesis, or responses to therapy[49]. Biomarkers can be diagnostic and prognostic (estimating the likelihood of disease recurrence) but can also be used for predicting (identifying patients likely respond to a specific treatment) and monitoring treatment responses[50]. Post-operative reductions in the levels of the serum biomarkers carcinoembryonic

antigen (CEA) and carbohydrate antigen 15-3 (CA 15-3) have been shown to be prognostic for disease-free and overall survival in breast cancer patients[51] and can improve the detection of recurrent/metastatic disease by 5–6 months[52]. However, these biomarker assays have limitations. For example, low biomarker concentrations in the presence of high abundance proteins (albumin and immunoglobulins) can make their detection difficult. Typically, biomarkers are also not specific for one cancer type and their levels can be altered in various disease conditions. The assays can also have low sensitivity and/or specificity and may not reflect a tumour's response to therapy whilst a patient is on treatment.

The ability of a biomarker to provide information on a tumour's response to radiation could represent an important tool to help tailor a patient's treatment plan; patients not responding to traditional RT regimens could be given alternative therapies at an earlier stage of the treatment process. This would help direct health services resources, ease the burden on RT machines and ultimately reduce the economic cost of cancer treatment. More importantly, this could potentially improve patient outcomes and survival rates. Unfortunately, at present, no robust or validated secreted biomarkers for monitoring a tumours response to RT whilst a patient is on treatment are available. To address this unmet clinical issue, research using the secretome of cancer cells/tissue is becoming more popular for the discovery of novel, clinically relevant biomarkers.

1.6.3 Secretome analysis for biomarker discovery

The term secretome was first used to describe both secretory pathways and secreted substances[53], but has since been refined to include only the latter[54]. Approximately 10-15% of proteins encoded by the human genome are secreted, which play important roles in various cellular functions including immune responses, cell signaling and extra-cellular matrix remodeling. As research into the secretome of normal cells has increased, it has become clear that cancer cells have their own unique set of secreted substances. The term cancer secretome was first used in 2006 in a study comparing the secretome of pancreatic cancer cells with that of non-neoplastic pancreatic ductal cells[55]. Substances within the cancer secretome are now known to play roles in cancer pathogenesis including angiogenesis, differentiation, invasion and metastasis[56]. For proteins to be secreted into the extra-cellular space

they must pass through either the classical or non-classical secretory pathways. To undergo classical secretion, proteins are synthesised as precursors containing N-terminus signal peptides that direct them to the translocation apparatus of the rough endoplasmic reticulum. Subsequent transfer to the Golgi apparatus allows the proteins to be released into the extracellular environment through fusion of Golgi-derived secretory vesicles with the plasma membrane[57]. In contrast to this, at least 4 non-classical secretory pathways have been identified for the release of proteins that lack the signal peptide for endoplasmic reticulum/Golgi-dependent secretion. Examples of non-classical secretion include intra-cellular vesicles undergoing endosomal recycling, direct translocation across the plasma membrane using transporter systems, membrane-anchored flip-flop mechanisms or exosomal secretion[58]. Exosomes are intralumenal vesicles (IVL) formed from inward budding of the membrane of multivesicular bodies (MVB). During their formation, cytosolic proteins and substances such as lipids, microRNAs and mRNA may be incorporated into the invaginating membrane and become contained within the ILV. As a result, when the MVB fuse with the plasma membrane, both ILV and their cytosolic contents are released into the extra-cellular space[54].

1.7 The tumour microenvironment

Tumour physiology differs from normal tissue physiology in that tumours typically have areas of varying O_2 tension, glucose and energy deprivation, extra-cellular acidosis and high lactate levels. This TME, influenced by the tumours abnormal vasculature and heterogeneous microcirculation[59], can affect a tumour's response to RT and chemotherapy. The concepts of precision medicine are applicable to the idea of monitoring the TME. If TME parameters such as biomarkers, cancer metabolites, chemotherapeutic drug concentrations or intra-tumoural pH and O_2 could be safely and continuously measured throughout therapy without any or with minimal intervention from the patient or clinician, then this information could influence the management of a patient's treatment[60].

1.7.1 Tumour hypoxia

Tissue oxygenation is a balance between O_2 supply and its use through cellular metabolic demands. Most normal mammalian tissues function in O_2

concentrations of 2-9%, whereas hypoxic and severely hypoxic conditions are defined as $\leq 2\%$ O_2 and $\leq 0.02\%$ O_2 respectively[61]. Intra-tumoural hypoxia is an important and common component of many cancers[59], with up to 60% of solid tumours containing heterogeneously distributed areas of hypoxic tissue. Multiple pathogenic mechanisms can influence the formation of these hypoxic regions, largely due to the abnormal tumour vasculature. The first to be described in the literature was diffusion-limited hypoxia, when a connection between increasing distance from blood vessels and the development of necrotic tumour tissue was identified[62]. Diffusion-limited hypoxia largely influences the development of chronic hypoxia and occurs as a result of viable aerobic tumour cells near blood vessels utilising the available O_2 carried in red blood cells (RBCs). O_2 concentrations decrease as the distance from blood vessels increase, resulting in hypoxia[63]. Although the diffusion distance of O_2 from a blood vessel is approximately 150-180 μm, the point at which hypoxia develops will depend upon the O_2 carrying capacity of RBCs and the metabolic demands from cells closest to the blood vessel[64]. The second hypoxic mechanism is perfusion-limited or cycling hypoxia caused by interruptions to blood flow[65,66]. These interruptions can be acute and transient in nature and relate to the structural and functional abnormalities of tumour micro-vessels and collapse/blockade of these vessels by tumour cells[67]. Anaemic hypoxia is caused by tumour-associated and/or therapy-induced anaemia, leading to a reduced RBC O_2 transport capacity[63,68]. Macroscopic regional hypoxia is a recent term used to describe the situation where hypoxic cancer cells are found situated near a blood vessel[69,70]. This occurs due to the production of an O_2 gradient along the length of a blood vessel contained within the tumour. Blood at the arterial end of a vessel will contain the highest O_2 concentration which will be readily used by cells present in this region. As the distance from the arterial end of the blood vessel increases the O_2 concentration of blood will decrease, so cells situated at the distal end of the vessel, even if near it, may still be hypoxic.

1.7.2 Hypoxia and its effect on treatment responses

The abnormal tumour blood supply leading to hypoxia can affect the response of a tumour to RT and chemotherapy. The irregular tumour vasculature can reduce the effective delivery of systemic drugs such as chemotherapeutic, hormone or

targeted therapies, leading to heterogeneous drug distribution within the tumour[71]. Hypoxic conditions can also reduce cancer cells proliferation rates[72] which can reduce the effectiveness of cytotoxic agents that predominantly target rapidly dividing cells[73]. Tissue O_2 concentrations at the time of radiation can also influence the degree of cellular radiosensitivity; studies have demonstrated that radiated anoxic cells are less sensitive to the effects of radiation than those which are well oxygenated[74]. When exposed to a given dose of radiation, cancer cells in low O_2 conditions can withstand a dose 2-3 times higher than aerobic cells. This phenomenon is known as the O_2 enhancement effect. The pivotal role of O_2 in the effectiveness of RT is described through the O_2 fixation hypothesis[61,75]. The clinical effects from RT arise largely through its DNA damaging ability which occurs via the indirect route due to the production of free radicals or through the direct route due to DNA ionisation. O_2 present at the time of radiation can react with radiation-induced DNA radicals producing chemically irreparable peroxy radicals; however, in the absence of O_2 this reaction cannot occur, and DNA damage can be repaired by radical scavengers such as endogenous thiols[76] giving these hypoxic cells a significant survival advantage.

1.7.3 Cellular response to hypoxia

Although it seems intuitive that hypoxia would generate an unfavourable environment for cellular survival, cancer cells can produce a hypoxic response through changes in gene expression, which protect them against cell death[77]. Those cancer cells not able to adapt to hypoxia will die, leading to the selection of cancer cells with genetically-fixed features of this 'hypoxic phenotype'[78]. This process, termed hypoxia-driven malignant progression, can cause cancer cells to become more invasive, metastatic and treatment resistant[79].

Key transcription factors involved in the hypoxic response are the hypoxia-inducible factors (HIF). The most extensively studied is hypoxia inducible factor-1 (HIF-1), composed of a constitutively expressed HIF-1β subunit and a regulated HIF-1α subunit. In normoxic conditions HIF-1α is degraded by the von Hippel-Lindau (VHL)-mediated ubiquitin-proteasome pathway; however, in hypoxic conditions VHL cannot bind to HIF-1α, preventing its degradation. Accumulation and nuclear translocation of HIF-1α leads to heterodimerisation with HIF-1β and

binding to specific DNA sequences within hypoxia-response elements to promote target gene transcription. Approximately 40 HIF-1 regulated genes have been identified[80]. In combination with other inducible transcription factors[81-83] it is estimated that approximately 1.5% of the genome is transcriptionally responsive to hypoxia[84]. These hypoxia-regulated genes are involved in processes such as angiogenesis, erythropoiesis, iron homeostasis, cell survival, proliferation, apoptosis, glucose metabolism and invasion; it is these adaptive changes that improve a cancer cell's ability to survive in the hostile hypoxic TME[85].

1.7.4 Endoplasmic reticulum stress and the unfolded protein response

The unfolded protein response (UPR) consists of signalling pathways that attempt to protect a cell from the accumulation of misfolded or unfolded proteins within the endoplasmic reticulum[86]. Accumulation of these proteins can occur as a result of cellular stress from hypoxia, alterations in pH and nutrient deprivation[87]. The UPR can also be activated by radiation[88,89] and can promote cancer cell survival in hypoxic conditions by regulating the translation of angiogenic factors[87]. The UPR is mediated through protein kinase RNA (PKR)-like ER kinase (PERK), inositol-requiring enzyme 1α (IRE1α) and activating transcription factor 6 (ATF6)[90] signalling pathways. These endoplasmic reticulum membrane-bound transducer proteins are inactive under non-stressed states through binding of their luminal domains with chaperone immunoglobulin heavy-chain binding proteins (BiP). However, during endoplasmic reticulum stress unfolded proteins bind directly to the transducer proteins or to BiP (causing their sequestration) leading to transducer activation (Figure 1.2).

PERK homodimerises and autophosphorylates when activated, which mediates the phosphorylation of the eukaryotic initiation factor 2α (eIF2α), leading to translation suppression and reduced protein transport into the endoplasmic reticulum[91]. PERK activation can also induce the translation of activating transcription factor 4 (ATF4) which controls the transcription of endoplasmic reticulum chaperone proteins, along with those involved in amino acid production and transport. IRE1α activation splices X-box-binding protein 1 (XBP1) mRNA, leading to the transcription of endoplasmic reticulum stress genes that promote

misfolded protein degradation, correct protein folding and secretion[92]. Activated ATF6 functions as a transcription factor; following its transport to the Golgi apparatus in COPII vesicles[93] it is cleaved by proteases before translocating to the nucleus and inducing the transcription of endoplasmic reticulum stress genes[94-96].

The combined function of these pathways is to reduce endoplasmic reticulum protein translocation, increase misfolded protein degradation and improve endoplasmic reticulum protein folding and secretion. However, prolonged stress with insurmountable accumulation of misfolded proteins can overwhelm these responses, causing a switch of UPR signalling to initiate apoptosis. Typically, endoplasmic reticulum stress-induced apoptosis is mediated by the PERK/eIF2α /ATF4 UPR pathway[90,97]. ATF4 can induce expression of the transcription factor C/EBP homologues protein (CHOP)[98,99], which increases the expression of Bim, (pro-apoptotic member of the Bcl-2 family)[100] and decreases the expression of Bcl-2 (an anti-apoptotic protein)[101]. Radiation-induced PERK activation can also cause cell death through autophagy in caspase 3/7-deficient cells[102].

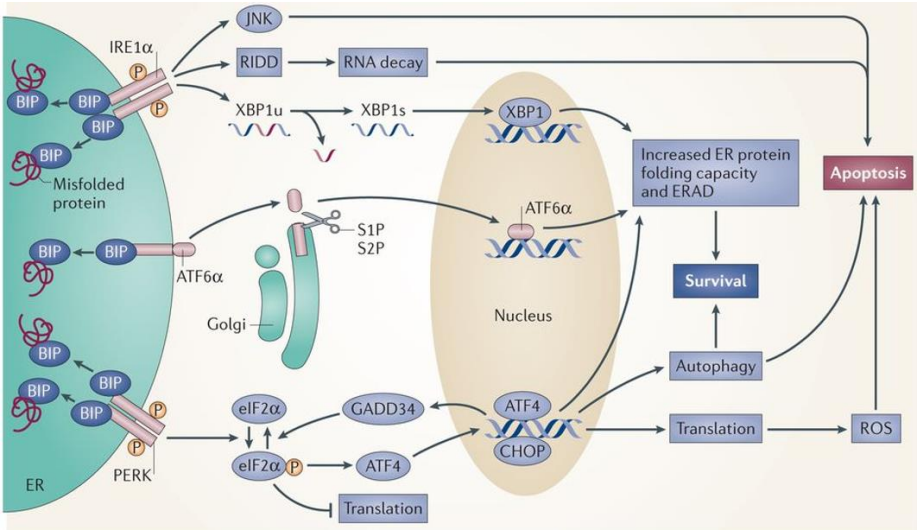

Figure 1.2. PERK, IRE1 and ATF6 pathways of the unfolded protein response. The UPR is comprised of 3 signalling pathways: protein kinase RNA (PKR)-like ER kinase (PERK), inositol-requiring enzyme 1α (IRE1α), X-box binding protein 1 (XBP1) and activating transcription factor 6 (ATF6) (GADD34, growth arrest and DNA damage-inducible protein 34; CHOP, C/EBP homologous protein; JNK, JUN N-terminal kinase; RIDD, regulated IRE1-dependent decay; XBP1s transcriptionally active XBP1, XBP1u; P, phosphorylation)[103].

1.7.5 Clinical relevance of tumour hypoxia

Tumour hypoxia has been shown to influence tumour progression and prognosis in a range of tumour types. One large international study demonstrated that

pre-treatment tumour O_2 status for head and neck cancer patients was prognostic for survival after RT (+/- surgery, chemotherapy, or radiosensitiser)[104]. Another study showed that low O_2 levels measured in squamous cell carcinoma lymph node metastasis was associated with poor or no response to RT; this study concluded that O_2 levels could be used to identify patients who would benefit most from additional treatments[105]. The prognostic significance of tumour hypoxia has also been shown in cervical cancer[106] where patients with hypoxic tumours had worse disease-free and overall survival rates compared to patients with non-hypoxic tumours[107]. Similar results have been observed in patients with soft tissue sarcomas[108].

1.7.6 Tumour hypoxia functional imaging

To target hypoxic, treatment-resistant tumour areas, clinicians need to be able to detect them. Multiple direct or indirect methods are available to detect hypoxic areas within tumours, but none are used routinely either due to their invasive nature or difficulties in incorporating them into clinical practice (Table 1.1). One of the first approaches for direct measuring of intra-tumoural O_2 levels used polarographic electrodes, such as the Eppendorf O_2 electrode[109]. This technique showed associations between hypoxia and treatment responses in numerous cancer types[105,107,110-113] and that O_2 concentrations within breast cancer tissue can be lower than that of normal breast tissue[109]. However, this technique is invasive and only applicable to readily accessible tumours and is not used routinely in the clinic.

Indirect methods for assessing tumour hypoxia include the use of molecular reporters of O_2 such as pimonidazole, which forms adducts with intra-cellular macromolecules at low O_2 levels[114]. Pimonidazole has been used in trials for hypoxia assessment to determine the use of hypoxia modifying drugs with accelerated RT; results demonstrated that patients with hypoxic laryngeal tumours benefited from additional treatments[115]. Other indirect assessment methods include the evaluation of genes and proteins whose levels are regulated by O_2 (HIF-1, CA9 and GLUT1)[116,117]. Hypoxic gene signatures have also been identified which can be prognostic[118] and predictive of response to radiosensitising agents[119]. All these indirect methods require a biopsy sample which can be challenging or impossible to obtain; recurrent measurements using repeat biopsies are also difficult to perform and justify clinically. Blood samples assessing biomarkers of hypoxia, such as osteopontin, can

be used to circumvent the issue of repeat biopsy sampling. These 'liquid biopsies' have been used to assess head and neck patients undergoing RT. Results showed that high osteopontin plasma concentrations were associated with a poor prognosis which could be improved with O_2 mimetic drugs[120]. However, hypoxia assessment through biopsy samples only allows the analysis of specific tumour areas at specific times and hypoxia assessment through blood samples does not analyse the tumour at all. These limitations mean that the hypoxic heterogeneity of the entire tumour and the changing distribution of O_2 that occurs during treatment are not evaluated.

Advanced imaging techniques provide a non-invasive way of assessing hypoxia throughout the whole tumour volume and a means by which serial measurements can be obtained. The most common methods used are positron emission tomography (PET) and magnetic resonance imaging (MRI). PET hypoxia imaging uses tracers such as nitroimidazoles, copper-complexed dithiosemicarbazone (Cu-ATSM) derivatives, fluorodeoxyglucose or endogenous markers such as CA9 labelled with radioisotopes that allow images depicting hypoxia to be obtained. Each tracer has its own specific disadvantages; for example, the expression of CA9 can be induced by factors other than hypoxia and at reduced O_2 levels that are not low enough to have a radiobiological effect. Nitroimidazole-based tracers also require cells to be hypoxic for significant periods of time, meaning levels of acute hypoxia may be underestimated. Resolution may also be a problem; voxel size (3D representation of a pixel – determined by slice thickness and pixel size) tends to be much larger than potential hypoxic areas, so areas of low hypoxia that contain hypoxic hotspots could be classified as negative if the average value for that region falls below a cut-off point. Therefore, the actual PET image may not accurately reflect tumoural hypoxic heterogeneity at the microregional level.

Most MRI-based techniques use either dynamic contrast-enhanced MRI (DCE-MRI) or blood O_2 level-dependent (BOLD) imaging. In DCE-MRI, a gadolinium-based contrast agent is injected into a vein and its passage is tracked through the tumour vasculature; signal changes identified by MRI give an estimation of perfusion. BOLD techniques detect signal differences induced by regional changes in deoxygenated haemoglobin levels and are carried out with dynamic challenges to alter oxygenated and deoxygenated haemoglobin ratios to map hypoxic regions[121].

Table 1.1. Methods used for measuring tumour hypoxia. Advantages and disadvantages of each method used to measure tumour hypoxia[121].

Microelectrode **Method:** An O_2 electrode is placed directly into a solid tumour. **Advantages:** Direct measurement of ptO_2. Easy to use. Real-time measurements can be obtained. **Disadvantages:** Invasive. Can only be used in accessible tumours. Inability to distinguish tumour areas with viable hypoxic cells from regions of necrosis.
Tissue based biomarkers **Method:** Nitroimidazole compounds (pimonidazole) are administered systemically which are converted into protein adducts in hypoxic cells. Proteins are detected by IHC using biopsy samples. **Advantages:** IHC can estimate hypoxia heterogeneity within different tumour areas. **Disadvantages:** Indirect measurement of ptO_2. Invasive as requires a biopsy. Compounds may not be sensitive enough to detect intermediate hypoxic phenotypes as HIF-1 is stabilised at higher ptO_2 than those at which nitroimidazole adducts are formed. Does not provide real-time measurements.
Tissue based biomarkers **Method:** Evaluating the expression levels of hypoxia-induced proteins (CA9, GLUT1). **Advantages:** IHC can identify the location of protein expression and provide information on functional status. IHC can estimate hypoxia heterogeneity within different tumour areas. **Disadvantages:** Indirect measurement of ptO_2. Invasive as requires a biopsy. Protein expression can be influenced by other factors not just hypoxia. Antibody specificity and sensitivity can limit the technique to a small number of biomarkers. Does not provide real-time measurements.
Tissue based biomarkers **Method:** Evaluating gene expression signatures (HIF-1α, CA9). **Advantages:** Prognostic and predictive of responses to agents that radiosensitise hypoxic cells. **Disadvantages:** Indirect measurement of ptO_2. Invasive as requires a biopsy. Genes can be up/down-regulated by other factors not just hypoxia. Does not provide real-time measurements.
Serological based biomarkers **Method:** Measurement of serum biomarkers (osteopontin, hepatocyte growth factor, IL-8). **Advantages:** Non-invasive. Real-time measurements can be obtained. **Disadvantages:** Indirect measurement of ptO_2. Biomarker expression can be influenced by other factors not just hypoxia. Does not give information about hypoxia heterogeneity within different areas of a tumour.
Positron emission tomography **Method:** Nitroimidazole or copper-complexed dithiosemicarbazone compounds are administered systemically which are taken up by hypoxic cells. Compounds are labelled with radiotracers (F-fluoromisonidazole used for nitroimidazole compounds) which can be detected using PET imaging. **Advantages:** Non-invasive. Real-time measurements can be obtained. PET imaging can give an estimation of hypoxia heterogeneity within different areas of a tumour. **Disadvantages:** Indirect measurement of ptO_2. Compounds may not be sensitive enough to detect intermediate hypoxic phenotypes as HIF-1 is stabilised at higher ptO_2 than those at which nitroimidazole adducts are formed. Safety concerns over using radioisotopes.
Magnetic resonance imaging **Method:** Most MRI studies either use dynamic contrast-enhanced MRI (DCE-MRI), blood oxygen level-dependent (BOLD) imaging or oxygen-enhanced MRI (OE-MRI). **Advantages:** Non-invasive. Real-time measurements can be obtained. MRI can give an estimation of hypoxia heterogeneity within different areas of a tumour. Avoids radiation exposure. **Disadvantages:** Potential for artefacts. The biological meaning of the parameters used to reflect hypoxia and the link with the hypoxic phenotype has yet to be established.

1.7.7 Using hypoxic imaging for precision radiotherapy

Identification of tumours containing significant levels of hypoxia would enable patient selection for additional treatments to overcome hypoxia-related radioresistance. Options include increasing tumour oxygenation through patients

breathing O_2 at higher than normal partial pressures (hyperbaric O_2 treatment), improving haemoglobin levels with blood transfusions, erythropoietin, and erythropoiesis-stimulating agents and administering hypoxia targeting drugs. Hyperbaric O_2 treatment, largely from studies conducted in the 1970s, has been shown to have a therapeutic benefit in patients with head and neck squamous cell carcinomas (HNSCC)[122]; however, inconsistent clinical trial data for other cancer types and logistical issues have impeded its widespread use. Another approach to increasing tumoural oxygenation is by administering carbogen with nicotinamide. Carbogen, a mixture of O_2 and CO_2 gas, can reduce diffusion-limited hypoxia, whereas nicotinamide, an amide derivative of vitamin B6, is a vasoactive agent which counteracts perfusion-related acute hypoxia. Accelerated RT with carbogen and nicotinamide (ARCON) has been evaluated in numerous clinical trials with studies showing improved loco-regional control and disease-free survival rates[115,123]. Similarly, clinical trials of nitroimidazole derivatives that act as O_2 mimetics such as doranidazole and nimorazole have yielded survival benefits when used in combination with chemoradiotherapy in HNSCC patients[124] and non-small cell lung cancer (NSCLC) patients[125] or with RT alone[126,127]. Nimorazole in combination with RT is a standard of care treatment in Denmark for head and neck cancers[128]. Pro-drugs have been developed that are given to patients in an inactive form and are converted to their pharmacologically active form within hypoxic cells, thus enabling the selective killing of hypoxic cells. Numerous pro-drugs are undergoing pre-clinical or clinical trials[129]. Although studies involving the pro-drug tirapazamine have shown disappointing results in terms of improving progression-free or overall survival[130,131]; these studies failed to identify patients with hypoxic tumours that may gain the most benefit from this treatment. Another hypoxia-activated prodrug, TH-302, is showing promise in improving progression-free survival in phase II trials in combination with chemotherapy for pancreatic cancer[132] and soft tissue sarcomas[133], providing evidence for further evaluation in phase III trials.

An important aspect of clinical trials evaluating the potential benefit of hypoxia-modifying therapies is case selection. Most historical studies failed to specifically identify hypoxic tumours and so treatments would inevitably be given to patients who were unlikely to benefit from hypoxic modification. A hypoxic tumour

classifier based on a hypoxic gene signature has been used in a large cohort of HNSCC patients; tumours classified as hypoxic were associated with a significantly poorer outcome; however, outcomes were improved for patients with hypoxic tumours who received nimorazole[134]. These results are also supported by studies that specifically identified hypoxic tumours in HNSCC patients through methods such as 18F-fluoromisonidazole–positron emission tomography (FMISO-PET) imaging[135], osteopontin[120] or immunohistochemical analysis of pimonidazole labelling[115,123]; with their results showing better tumour responses to nimorazole, tirapazamine, or ARCON, compared with standard treatments emphasising the need for accurate assessment of tumour hypoxia before treatment. One large meta-analysis study looked at the results of 64 clinical trials from HNSCC patients who received RT with curative intent and found that the addition of hypoxic modification improved loco-regional control, disease-free and overall survival[136].

Hypoxic imaging can also be used to enable more effective delivery of radiation to a tumour. Tumours identified as having large areas of hypoxia could be treated with increased radiation doses across the entire gross tumour volume (GTV); however, this technique could increase the risk of damage to the surrounding tissues. A more refined approach would be to determine a biological target volume (BTV) based on hypoxia. In this situation, the total radiation dose delivered to the GTV would remain the same, but the dose redistributed; raising the dose received by the hypoxic regions while reducing that received by the higher oxygenated regions. Alternatively, the BTV could receive boost doses of radiation either uniformly spread throughout the hypoxic sub-volume or varied according to the regional levels of hypoxia. Advancements in radiation-delivery machines, such as image-guided RT (IGRT) and intensity-modulated RT (IMRT), that allow highly conformal and accurate radiation delivery have meant that dose painting by numbers (DPBN) or sculpturing techniques are becoming more attainable[137]. These techniques also have the advantage of limiting the radiation dose received by the nearby normal tissues.

If GTV or BTV dose escalation is to be used clinically, then determining how much additional radiation is required to obtain an increase in the benefit-to-risk ratio will need to be determined. Modelling studies have begun to investigate this question. One study combined PET imaging with IMRT planning as a means of

delivering a boost dose of 10 Gy to the hypoxic sub-volume of patients with HNSCC for those prescribed 70 Gy to the planned target volume (PTV). This study reported that this boost dose would provide a tumour control probability (TCP) increase of 17% without increasing complication risks within the surrounding normal tissues[138]. Another study has shown that dose escalation using DPBN to the BTV would provide improved TCP compared with uniform dose escalation (both methods used the same mean dose). This study also showed that DPBN may be especially beneficial in cases with tumour regions of chronic hypoxia[139]. Uniform BTV dose escalations of 10% have also been compared with DPBN in 13 scans from patients with HNSCC. DPBN again showed significantly improved TCP (70.2%) compared to conventional IMRT (55.9%) and uniform BTV (57.7%) dose escalation[140]. These improved TCP rates are comparable with that seen using ARCON.

Although these results are promising, they are only radiobiological modelling studies and validation in clinical trials is needed. A potential significant limitation to using dose escalation plans based on functional imaging such as PET or MRI is that they fail to account for the dynamic nature of tumour hypoxia and the spatial and temporal changes that occur to the hypoxic volume during treatment. Serial images before and during treatment may provide an indication of changes but they still only provide a static indication of hypoxia at the time of image capture. Real-time data acquisition is currently not possible, and these techniques do not provide information on acute versus chronic hypoxia. Therefore, despite advances, approaches that give an accurate 3D map of hypoxic areas within the entire tumour volume in real-time are still not available. A potential solution to this unmet clinical need is the use of an implantable sensor that is designed to measure intra-tumoural O_2 tension at the time of treatment, which would also be able to provide information on the spatial and temporal changes that can occur during a patient's treatment course.

1.7.8 Electrochemical oxygen sensors

The electrochemical reduction of O_2 was first demonstrated at the end of the 19th century by Danneel and Nerst[141]. However, in 1965 Clark was the first to be credited with the development of the amperometric 'Clark electrode' O_2 sensor capable of detecting O_2 at a platinum electrode[142]. Here, at the electrode, O_2 undergoes electrochemical reduction which generates a measurable electric current

proportional to the partial pressure of O_2 contained in the environment surrounding the sensor. This sensor used a gas permeable membrane to separate the electrodes and the liquid electrolyte in which they worked from the external environment. This technique prevented environmental proteins and electrolytes interfering with O_2 detection and reduction thus improving the sensor's function in biological media[141]. Unfortunately, these conventional Clark electrodes are unsuitable as implantable medical devices due to their large size and use of liquid electrolytes.

The Implantable Microsystems for Personalised Anti-Cancer Therapy (IMPACT) project is developing a miniaturised implantable solid-state Clark O_2 sensor to overcome limitations with conventional Clark-type electrodes[143]. The project's primary aim is to develop an implantable sensor that can monitor intra-tumoural O_2. However, the ability of a sensor to continually measure tissue O_2 tension could prove to be a valuable monitoring tool for clinicians in a wide range of pathological and traumatic conditions where the measurement of organ perfusion is required. The IMPACT sensor is a 3-electrode cell composed of a platinum working electrode (WE), a Ag/AgCl reference electrode (RE) and a platinum counter electrode (CE), all microfabricated on silicon wafers[143]. Oxygen reduction occurs at the WE against a fixed electrochemical potential provided by the RE. The function of the CE is to supply current to balance the WE reactions[144]. A potential of -0.5 V (measured against the RE) is typically required to cause O_2 reduction at the WE. Nafion, a perfluorinated ion exchange resin, is O_2 permeable and can conduct protons between the electrodes and is used to coat the sensor surface, acting as both a gas permeable membrane and as a replacement for the traditional liquid electrolyte; this solid polymer membrane also helps prevents rapid electrode deterioration, increasing the sensors longevity[145,146]. The silicon wafers are diced into 2.0 mm x 3.0 mm chips which each carry a single sensor. Individual chips are then bonded to a 1.7 mm x 200 mm long flexible printed circuit board (lead wire) and the chips are sealed in epoxy resin, resulting in an overall sensor size of approximately 2.6 mm x 5.0 mm x 1.4 mm (width x length x height). A window clear of epoxy resin over the central active sensor area permits interaction with the tissue environment (Figure 1.3).

Although several previous studies have designed microfabricated electrochemical O_2 sensors[147-150], IMPACT's use of silicon-based microfabrication

techniques is currently unique. As well as having reproducibility and reduced manufacturing costs, silicon-based systems allow the integration of built-in complementary metal oxide semiconductor instrumentation electronics. This can create a fully autonomous 'smart sensor' eliminating the requirement of bulky external equipment, both of which are desirable characteristics for its use as an implantable medical device[143].

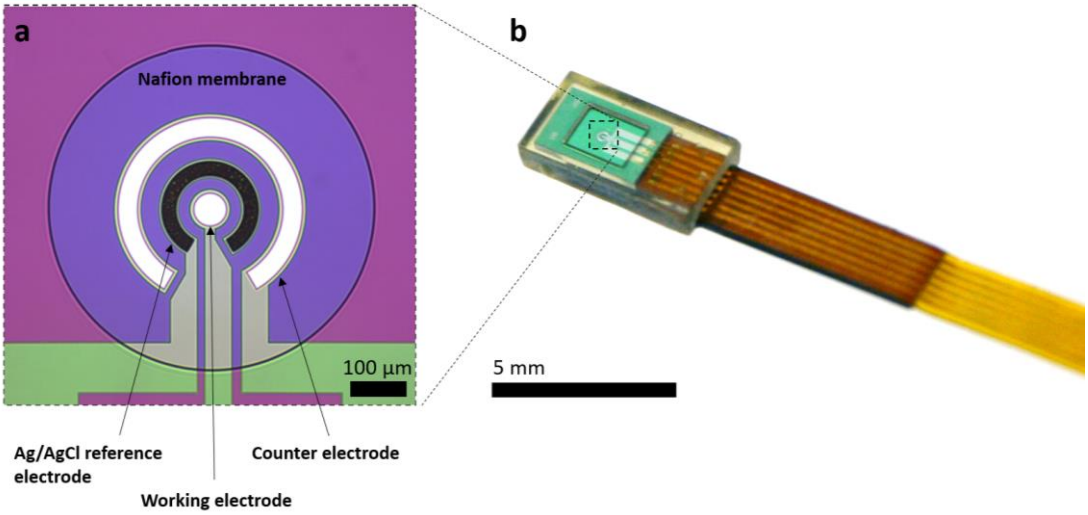

Figure 1.3. Microscopic and macroscopic images of the IMPACT O_2 sensor. (a) High magnification image documenting the position of the working, reference and counter electrodes covered by the Nafion membrane. **(b)** Macroscopic image documenting the chip covered in epoxy resin and bonded to the lead wire (images kindly provided by Dr J. Marland).

1.7.9 Cancer treatment and implantable technology

The concept of integrating implantable medical devices into cancer diagnosis, treatment and disease monitoring is becoming attainable due to advances in electronics and microfabrication techniques. Although most cancer studies using implantable devices are experimental or pre-clinical, promising results highlight their potential use in the field of precision medicine.

Pre-clinical studies have investigated the use of short-term implantable devices for high-throughput drug sensitivity testing within tumours. One study used a device containing multiple reservoirs which were capable of releasing drugs into distinct tumour regions at systemically achievable concentrations. Removal of tumour tissue surrounding the device 24 h after implantation allowed assessment of the anti-neoplastic effect of each drug through immunohistochemical analysis[151]. This type of device could be employed to improve the identification of optimal drug

treatment before definitive systemic treatment commences. Releasing drugs directly within the TME could also reduce the severity of side effects seen with systemically administered drugs, whilst still achieving effective therapeutic doses. A tumour type that would benefit from a localised drug delivery system would be malignant brain tumours. The presence of the blood-brain barrier is a limitation to the development of effective brain tumour therapies, as it prevents the transfer of substances larger than 500 KDa and non-lipid soluble molecules into the brain[152]. Because of this, chemotherapeutic systemic toxicity is often reached before obtaining effective therapeutic concentrations in the brain. The use of an implanted intra-cranial micro-electro-mechanical system (MEMS) to deliver the chemotherapy drug temozolomide to gliosarcoma brain tumours in rats has shown that implantation was safe and that drug delivery from the MEMS improved survival times. This silicon microchip was composed of 3 separate temozolomide containing reservoirs; each reservoir was covered by a membrane that could be independently opened by applying an electrical current. This study provided evidence that drugs can be locally administered to brain tumours at specific time points, allowing for active control over drug release rates. This concept could have applications for a range of tumours that require additional local treatments[153].

This MEMS type of implantable drug delivery systems also has potential for use in a wide range of diseases in which treatment regimens are difficult to implement. The first-in-human testing of a wirelessly-controlled drug delivery silicon microchip was used in the treatment of osteoporosis as a means of overcoming long-term daily injections of human parathyroid hormone fragment 1-34 (hPTH(1-34))[154]. The device consisted of multiple individual reservoirs filled with concentrated hPTH(1-34) solution. Even though a fibrous capsule developed around the device following implantation, pharmacokinetic evaluation showed similar bone formation results as compared to repeated daily hPTH(1-34) injections. This study provided evidence of an implantable device being utilised to overcome difficult treatment regimens and poor patient compliance[15].

Implantable devices are not restricted to chemotherapeutic applications; they also have potential to be used in combination with RT. As previously mentioned, newer external beam RT techniques, such as 3D conformal RT can accurately

conform and deliver radiation to the shape of the PTV. As the clinical success of RT will depend upon the accuracy of delivering the calculated dose to the target area, it is important to be able to verify that the planned radiation dose is accurately delivered to the tumour. This has traditionally been achieved through regular calibration of the radiation source, using predictive algorithms and through placing diodes, thermo-luminescence dosimeters or metal oxide semiconductor field-effect transistor (MOSFET) dosimeters on the patient's skin surface[155,156]. However, a novel and potentially more accurate way to achieve dose monitoring has been achieved using an implantable dosimeter. This dose verification system (DVS) has undergone clinical testing and received Food and Drug Administration (FDA) approval for use in breast and prostate cancer. This device can verify the radiation dose received by the PTV for each fraction[157] and provides the ability for radiation oncologists to verify and optimise radiation treatment on an individual basis.

As well as influencing a patient's treatment, implantable sensors are suited for sampling the local tissue environment. Placed within a tumour or in surrounding tissue at the time of surgery or biopsy, sensors could play a role in monitoring the response of a tumour to treatment or in detection of recurrence or metastasis by measuring specific biomarkers. This would be especially useful in areas where imaging (MRI/CT) makes it difficult to distinguish between tumour recurrence, fibrosis, necrosis or benign lesions from previous surgery or chemoradiotherapy (gliomas)[158]. The first *in vivo* description of such a device was used to detect the β subunit of human chorionic gonadotrophin (hcG-β)[159], a known soluble cancer biomarker, which shows elevated secretion levels in testicular and ovarian cancers. This study used an implantable device containing nanoparticle magnetic relaxation switches (MRSw) conjugated with antibodies for hcG-β. The device was implanted in tissue near hcG-β producing JEG-3 (human choriocarcinoma) xenografts. Aggregation of these MRSw through hcG-β antibody binding was detected through MRI, showing that the device was able to detect the biomarker in peri-tumoural tissue. MRSw can be functionalised to detect a variety of molecules, providing opportunities for their use in a variety of monitoring purposes[160].

1.7.10 Regulations governing implantable medical devices

In 1992, Canada, the USA and Great Britain formed the International Standards Agency (ISO), which developed and published international standards on the Biological Evaluation of Medical Devices: ISO 10993. These standards classify implantable sensors as devices that are in contact with body tissues for geater than 30 days and describes pre-clinical *in vitro* and *in vivo* biocompatibility testing. *In vitro* tests include those for genotoxicity, cytotoxicity, carcinogenicity, developmental and reproductive toxicity, haemocompatibility, degradation assessment and biofunctionality (cellular adhesion and spreading); whereas *in vivo* tests focus on evaluating ethylene oxide residues, material degredation, sensitisation and irritation, local tissue effects and systemic toxicity[161].

The Active Implantable Medical Devices Directive 90/385/ECC, developed by the Medicines and Healthcare products Regulatory Agency, aims to protect patient safety by ensuring manufacturers provide evidence of device safety and performance. This is essential for devices to gain market approval but also continues through post-market surveillance so adverse incidents can be identified by clinicians and patients. For a device to gain market approval manufactures can use 'equivalence data' and published clinical work of similar devices. This can decrease costs and the time required to get a product to market but can potentially lead to safety concerns, as each device is not fully evaluated; even high risk medical devices have been certified as safe without any supporting evidence in human trials[162].

1.8 Biocompatibility and the foreign body response

During the development of implantable medical devices they must undergo biocompatibility evaluation to assess the device in terms of its biofunctionality (performance) and biosafety (local and systemic tissue responses and the absence of carcinogenesis, mutagenesis and cytotoxicity)[15,163-165]. Following implantation medical devices can lose functionality, this failure is largely due to biofouling (non-specific protein adsorption) that occurs around the device. This process results in a tissue reaction known as the foreign body response (FBR)[165-167] and represents a clinical challenge in implantable technology design and development. It is the surface properties of the device that will influence the extent of the FBR that occurs

during the initial weeks following implantation, although the reaction at the tissue/surface interface will be present for the *in vivo* lifetime of the device.

1.8.1 Acute inflammatory response

Acute inflammation starts immediately after the implantation of a medical device within the body and typically resolves within 5 days[168]. The magnitude of this initial response is related to the trauma caused by the insertion device, whereas the subsequent chronic inflammatory responses and fibrous encapsulation are largely affected by sensor size[169]. Tissue injury at the implantation site will activate the intrinsic and extrinsic coagulation systems, complement and fibrinolytic system, kinin-generating system and platelets, causing the formation of a provisional matrix around the device[170]. The device surface characteristics will affect the extent and type of proteins, such as albumin, fibrinogen, complement, fibronectin, vitronectin, and γ globulin that adhere to it[167,171-173]. These proteins at the tissue/device interface provide structural, biochemical and cellular components that contribute to the ongoing inflammation through cytokine, chemoattractant and growth factor release[174]. These substances can further regulate activation of the coagulation cascade, complement system, platelets and the subsequent immune responses through interacting with adhesion receptors present on inflammatory cells. Mast cell degranulation, with histamine release and fibrinogen adsorption, is also important during this stage for the recruitment of inflammatory cells[175,176].

Polymorphonuclear (PMN) leukocytes (neutrophils, granulocytes) are the predominant inflammatory cell type present for up to 2 days post-implantation[167]. These cells play roles in microorganism phagocytosis and pathogen killing through the secretion of proteolytic enzymes and reactive O_2 species. However, these enzymes may also be damaging to implanted materials and increase the duration of the acute inflammatory response. Prolonged PMN activation, due to the continual presence of the implanted medical device, can lead to metabolic exhaustion and depletion of oxidative resources. This situation can reduce their microbial killing ability and can contribute to the development of implant-related infections[177]. PMNs secrete immunoregulatory signals such as IL-8[178,179], monocyte chemoattractant protein-1 and macrophage inflammatory protein-1β, which recruit further PMNs, monocytes, macrophages, lymphocytes and immature dendritic cells into the

area[180,181]. Continued chemokine release leads to suppression of PMN infiltration and their numbers begin to fall as they are engulfed by macrophages or become apoptotic[182].

1.8.2 Chronic inflammatory response

The continued presence of an implanted medical device within the body leads to the development of chronic inflammation; this phase is characterised by the presence of monocytes, macrophages, fibroblasts, neovascularisation and the production of granulation and fibrous tissue around the implanted device[167]. Macrophages are the predominant cell type present for up to 3 weeks following resolution of acute inflammation and will drive the ongoing immune response, enhancing the propagation of chemoattractive signals through the production of factors such as: PDGF, fibroblast growth factor, tumour necrosis factor-α (TNF-α), IL-1, IL-6, granulocyte-colony stimulating factor (G-CSF), transforming growth factor-β, transforming growth factor-α, chemokine (C-C motif) ligand 2 (CCL2) and granulocyte macrophage colony stimulating factor (GM-CSF)[174,183]. Macrophages are only capable of phagocytosing particles up to 5 μm in size; as a consequence of this, macrophages, in an attempt to deal with large implanted materials, fuse together to form foreign body giant cells (FBGCs) which spread over the material's surface through integrin binding[184,185].

In vitro and *in vivo* studies have shown that FBGC formation can be induced by the cytokines IL-4 and IL-13[186-188]; although, the exact source of these cytokines is under debate, natural killer cells (NK), natural killer-T cells (NKT) cells[189,190], mast cells, eosinophils, and basophils are all potential sources[191]. However, the functions of these cell types in FBGC formation is unknown, as mouse models deficient in NK or NKT lymphocytes, mast cells or IL-4 receptor-α can still form FBGC in response to implanted materials[192]. Activated T lymphocytes ($CD4^+$ cells), transiently present at the implant site during chronic inflammation[167], are another possible source of these cytokines. *In vivo* lymphocyte/macrophage co-cultures have shown the ability of lymphocytes to increase macrophage adhesion to material surfaces and enhance FBGC formation, while macrophages can stimulate lymphocytes to proliferate[193]. However, as the FBR has been shown to occur in the absence of T cells, the role of lymphocytes in FBGC formation remains unclear[194].

1.8.3 Consequences of foreign body giant cell formation

A unique environment exists between the device surface and the FBGC/macrophage cell membranes. Following failed attempts of classically activated macrophages and FBGC to phagocytose the material, they release degradative substances such as reactive O_2 intermediates, free radicals, enzymes and acids into the microenvironment; this process is termed 'frustrated phagocytosis'[195-197]. The slow rate at which buffers and inhibitors of these substances gain access to this environment results in the surface of the device being exposed to high concentrations of these degradative agents[198]. It is these reactions that can lead to material degradation and device failure[167].

1.8.4 Extracellular matrix remodelling

Macrophages are involved in angiogenesis, fibroproliferation and tissue remodelling through the secretion of growth and angiogenic factors and matrix metalloproteinases[167,199]. Alternatively activated macrophages produce profibrogenic factors leading to fibrogenesis by fibroblasts[200], which can lead to the deposition of a collagenous and vascular fibrous capsule around the device. This capsule is the end stage of the FBR[201] and can be 50–200 μm thick[165]. It is this capsule, in combination with FBGC on the device surface, that can contribute to loss of device function through the creation of a barrier that confines and prevents the implant from interacting with the surrounding tissues (Figure 1.4).

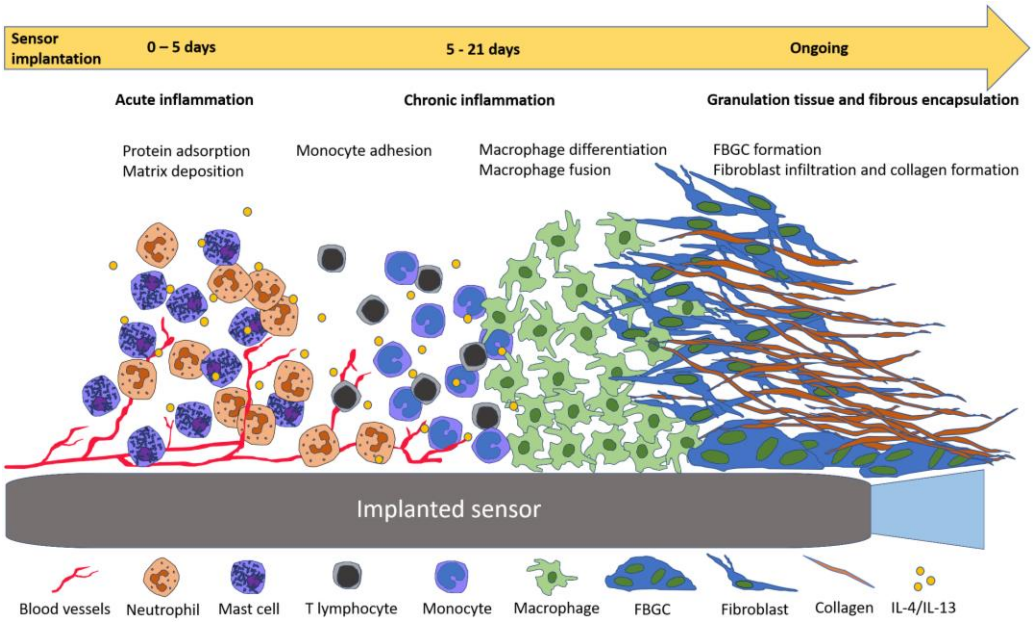

Figure 1.4. Sequence of inflammatory responses leading to FBGC formation and fibroblast infiltration. The result of the FBR is the production of granulation tissue with subsequent fibrous capsule formation. This reaction causes 'walling-off' of the sensor from its immediate surrounding area. This reaction combined with the degradative chemicals released from the FBGC can lead to loss of sensor function[15].

1.9 Pre-clinical *in vitro* models used in the development of cancer therapeutics

The development and assessment of anti-cancer agents follow a stepwise process from *in vitro* and *in vivo* testing through to phase 0, I, II, III and IV clinical trials. A typical development plan would involve the assessment of compounds through *in vitro* cell-based assays investigating cell survival, proliferation, death, migration and invasion. Compounds would then progress onto *in vivo* studies assessing anti-tumour activity and pharmacological studies to define drug absorption, distribution, metabolism and elimination before progressing into clinical trials. This process is expensive and time consuming; from concept to completion of phase III trials, may take over 10 years and several hundred million pounds[202]. Time and expense are not the only issues with cancer drug development; attrition rates for new cancer therapeutics are very high, with only 5% of agents that show pre-clinical promise gain a license to be used in patients[203].

Most pre-clinical studies assessing the efficacy of cancer agents rely on cancer cells grown in 2D cultures. Unfortunately, these models lack tumour heterogeneity and extended culturing may select for clones which survive and grow best in these

conditions. Using large panels of cell lines, such as the National Cancer Institute-60 panel (NCI-60)[204], or the expansion of cell lines derived directly from tumour tissue may partially overcome this problem[205]. However, 2D cultures cannot replicate complex stromal components, interactions with immune cells/inflammatory mediators/growth factors or the acidic/hypoxic TME[206]. The development of 3D cell culture and co-culture systems such as multicellular tumour spheroids (MTS) and organoids aim to better mimic the structural and functional properties of normal and tumour tissue and to bridge the gap between cell-based assays and animal studies[207]. High-throughput assays have also been developed using MTS cultured in microwells with non-adherent hydrogels[208,209]. MTS from cervical, breast and HNSCC cells form within 3-6 days, allowing high-throughput drug assays to be performed[210].

The National Cancer Institute's (NCI) Developmental Therapeutics Program has developed *in vivo* rodent screening models to select agents for evaluation as clinical candidates. Common *in vivo* models include the hollow fibre assay[211], human tumour xenograft models, carcinogen-induced models, genetically-engineered models and inbred strains with high rates of spontaneous tumour development[212]. Murine models have historically dominated medical research due to ease of breeding and housing and the availability of a large number of genetically identical strains and genetically-engineered models.

Subcutaneous and orthotopic xenograft murine tumour models can be established by inoculating human tumour cells grown *in vitro* or by implantation of patient tumour tissue into immunodeficient mice (athymic, severe combined immunodeficient (SCID), or non-obese diabetic/SCID); these models allow *in vivo* monitoring of tumour growth, drug toxicity, efficacy and pharmacokinetic studies, and reflect the O_2 and pH gradients found in solid tumours[213]. These models have increased our molecular understanding of cancer and have been used successfully in pre-clinical cancer drug development; their use as predictors of clinical activity has also been validated for numerous cytotoxic agents[214,215]. A retrospective analysis of 39 compounds using data from both xenograft testing and phase II clinical trials was performed by the NCI. This study showed that 15/33 agents with activity in more than one-third of cell line derived xenografts showed clinical activity. However, with the exception of NSCLC, activity within a particular xenograft histological type did

not predict for clinical activity in the same tumour type in patients[216]. A further study using patient-derived xenografts (PDX) showed similar results[217].

Unfortunately, these murine models have limitations and reliance on them has contributed to high attrition rates in cancer drug development. Subcutaneous xenografts, particularly those established from cell lines, do not represent the primary tumour from which they are derived in terms of heterogeneity, tumourigenesis and metastasis[218,219]. Orthotopic transplantation models are thought to be more representative of clinical tumours in terms of the development of metastatic disease[220]. However, stromal tumour components in both models will be murine in origin and therefore the effects of drugs on the TME may not be representative of human tumours. This limitation may be minimised by using PDX, although even in this model human stromal elements are progressively lost over time. Other limitations include poor uptake of PDX and difficulties in obtaining patient material[221]. Importantly, the growth rates of human xenografts are higher than that of primary tumours, as a result of this, they are much more likely to respond to anti-proliferative agents and so might provide a false indication of drug efficacy[219]. The use of immunocompromised models hinders the testing of immunomodulatory agents; although immunocompetent genetically-engineered murine models, carcinogen-induced models or strains that have spontaneously-occurring tumours can overcome some of these limitations they still suffer from having murine-derived stroma. It can also be difficult to extrapolate drug doses to human trials as maximum tolerated murine doses may be far higher than those used in human patients[222].

Rodents also differ considerably from humans in size, physiology, anatomy, lifespan and immunology, all of which can reduce their usefulness[215]. Their small size precludes their use for the development of human surgical procedures[223]. It is also difficult to scale down equipment such as imaging technologies or surgical instrumentation. Samples can also only be collected in small quantities, which can be insufficient for detailed analyses. Modelling treatment protocols commonly used in human patients such as RT is hampered in rodents by uncertainties regarding the scaling of energy doses. An approach to overcome these limitations would be to combine murine studies with comparative cancer studies in other species to optimise the development of the most effective cancer therapies.

1.10 Comparative oncology

Comparative oncology is a field of research that uses naturally occurring cancers in animals as a means of investigating similar cancers in human patients. This approach can include all aspects of cancer research including pathogenesis and the evaluation of cancer treatments. Dogs, cats and large animals with naturally-occurring tumours that have incidence rates, clinicopathological features and risk factors similar to specific human cancers are regarded as excellent translational models of human disease[224-226]. These models are particularly important as these cancers develop in the presence of an intact immune system where tumour, TME and host have developed together[227].

Dogs and sheep have many features that make them suitable for a range of comparative studies. The shorter lifespan of these species compared to humans enables tumours that develop after a few years instead of decades to be studied more readily; this can allow clinical trials to be performed rapidly whilst still providing a sufficient time course to allow comparison of treatment responses. Similarities in anatomy, size, physiology, immunology and metabolism to humans allow procedures or drugs that are commonly used in human medicine to be used in translational studies. Recent canine genome sequencing[228] has also shown significant similarities between dog and human genetic sequences; which is far greater than that seen between human and mice sequences[229]. Dogs have also been shown to be a highly predictive model for human drug development[224,226,230]. As a result of these factors various canine and ovine translational models have become popular in pre-clinical trials as they can overcome the limitations associated with murine models.

1.11 Comparative human and canine breast cancer

Mammary tumours are the most commonly diagnosed cancer in female dogs with the disease accounting for approximately 50% of all canine neoplasms[231]. The peak incidence age for dogs to develop mammary tumours is between 8-11 years old which is comparable to that seen in humans (50-58 years)[232-236]. Canine mammary tumours (CMT) are known to have a hormonal aetiology with one study showing that the disease developed in approximately 0.5% of female dogs that were spayed before their first season compared with 8% and 26% of dogs spayed after their first or

second season[237]. Other risk factors for disease development include diet and obesity[238,239]. In humans, obesity has been suggested to increase the risk breast cancer by raising circulating oestrogen levels and increasing local oestrogen production by aromatases[240,241].

Approximately 50% of canine mammary carcinomas will metastasise to regional lymph nodes, lungs and bone[242,243]. This clinical course is similar to that seen in humans where approximately 37% of women will either present with or develop metastatic disease[244]. In both human and canine patients tumour size, age, clinical stage, the presence of local/distant metastases and histological subtype can be used as prognostic markers that can identify patients at higher risk of recurrence or mortality[245,246]. Studies have also shown that there are significant similarities in the transcriptome[247] and proteome[248] of metastatic canine and human mammary carcinomas. These results suggest that similar mechanisms of mammary carcinogenesis may occur between the 2 species and that metastatic canine carcinomas are a suitable model for human breast tumours in order to identify prognostic molecular signatures and potential therapeutic targets.

1.11.1 Molecular markers and signalling pathways

The assessment of hormone or signalling receptor expression in human breast cancer has been shown to provide prognostic information and predict which patients will most likely respond to certain treatments. Although these markers are not routinely used in veterinary medicine, increasing evidence suggests that these human-derived molecular markers might be similarly useful for CMT evaluation.

ER and PgR expression occur in approximately 70% of benign and 60% of malignant CMT[249-251], this is similar to that seen in human breast cancer where approximately 85% express ER and 67% express PgR[17]. Several studies have now shown that ER and PgR expression can be prognostic and predictive of disease-free and overall survival, with a decrease in hormonal dependency commonly seen in canine malignant mammary tumours and metastatic disease[250,252-254]. One recent study showed that dogs with ER^+/PgR^+ tumours had better survival rates compared with ER^-/PgR^+ tumours and that ER^-/PgR^- tumours had the worst prognosis of all[255].

HER2 expression occurs in approximately 30% of all human breast cancers and is associated with high metastatic rates and poor prognosis[256]. Several studies

have identified HER2 expression in approximately 35% of malignant CMT[257-259]; however, the use of HER2 as a marker of CMT malignancy is unclear. Although some studies have shown HER2 expression is associated with high proliferation rates, histological grade, tumour size and poor prognosis[257,259-261] others have shown no difference in HER2 expression between benign and malignant tumours[258,262,263].

EGFR has been suggested as a prognostic marker in human triple negative breast cancer ($ER^-/PgR^-/HER2^-$)[264]. In CMT high EGFR expression has been associated with tumour size, angiogenesis, proliferation rate, tumour necrosis, histological grade and clinical stage[265-267]. However, its role in carcinogenesis or prognosis is unclear. Although a tendency toward shorter disease-free survival and overall survival has been identified in dogs with CMT expressing EGFR, these associations failed to reach statistical significance[266]. EGFR downstream signalling pathways have also been implicated in human breast cancer pathogenesis; results from the first genome-wide comparative analysis of canine and human mammary cancers demonstrated that tumours from both species had up-regulation of pathways related to proliferation, whereas pathways related to cell development, cell matrix adhesion and cell communication were down-regulated. Furthermore, this study demonstrated a great degree of homology between human and canine mammary tumours with respect to many cancer-related pathways including PI3K/AKT, KRAS, PTEN, WNT-β-catenin, and MAPK[268]. Other molecular markers which have been investigated for similarities between human and canine mammary tumours include insulin-like growth factor, growth hormone, mucins, heat shock proteins, P53, CEA, CA 15-3, VEGF and cyclooxygenases[261,269-272].

The similarities in aetiology, histopathology, pathogenesis, oncogenic drivers, target genes and molecular signalling pathways observed between canine and human mammary cancers supports the use of spontaneously occurring canine mammary tumours as a model for human disease. This model has great potential to not only advance the molecular understanding of breast cancer, but also improve pre-clinical research and treatment of canine and human breast cancer patients.

1.12 Comparative human and ovine lung anatomy and physiology

Sheep are excellent models for investigating human lung function and disease largely due to their similarities in terms of lung physiology and anatomy[273]. Both species have 2 lungs, in humans the left is divided into superior and inferior lobes and the right is divided into superior, inferior and middle lobes; whereas, in sheep the left divided is into cranial and caudal lobes and the right is divided into cranial, caudal, middle and accessory lobes[274] (Figure 1.5). Although the right cranial lobe bronchus originates proximal to the tracheal bifurcation[275] and bronchioles are less well developed in sheep[274], the remaining tracheobronchial anatomy is very similar to humans. Both species show an irregular dichotomous tracheobronchial branching pattern with similar distribution of differentiated respiratory epithelial cells[276], mast cells[277] and airway smooth muscle[278]. Although fewer intra-vascular pulmonary macrophages are seen in human lungs, increased numbers can be induced after endotoxic insults[279]. Lung development between the species is also comparable, with lamb and human infant lungs showing prenatal alveologenesis and the same tracheobronchial branching pattern. Type II alveolar epithelial cell (pneumocytes) development and number of bronchiolar club cells and airway submucosal glands is also similar[280]. Similarities in lung size also allow sheep to be used in ways not achievable using rodent models. Techniques used in the treatment of human patients such as endoscopy, advanced imaging[281], ultrasound[282] and surgery can be performed in sheep, providing the model with excellent translational potential[283]. Repeated blood and tissue collection are easier in sheep and their increased lifespan compared to rodents allows chronic conditions to be modelled whilst enabling long-term treatments to be evaluated. These factors have made sheep excellent models for human respiratory diseases[275] such as asthma[284], cystic fibrosis, chronic obstructive respiratory disease[285], respiratory syncytial virus infection[286] and now cancer[287].

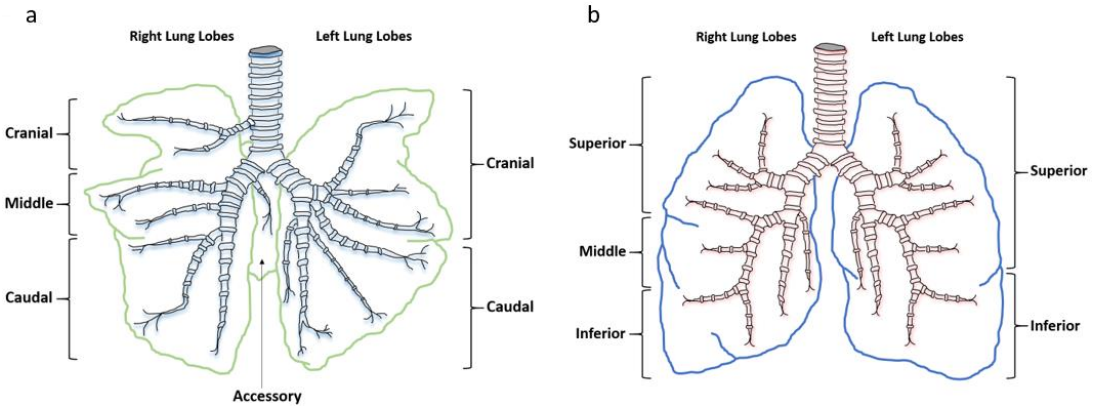

Figure 1.5. Human and ovine comparative gross anatomy. (a) Ovine lower respiratory tract. **(b)** Human lower respiratory tract[273].

1.12.1 Human lung cancer

Global estimates indicate that lung cancer accounts for approximately 2 million new cases and 1.8 million cancer-related deaths per year, making it the most commonly diagnosed cancer in the world[6]. Unfortunately, 5-year survival rates are only 15%; this low rate is largely due to patients being diagnosed with advanced disease, when poor responses to chemotherapy and RT are seen. Lung cancer is a highly heterogenous disease and is divided into multiple subtypes[273]. These subtypes undergo periodic review and in 2011 a multidisciplinary classification system was suggested by the European Respiratory Society (ERS) and International Association for the Study of Lung Cancer (IASLC)[288]. Based on pathogenesis, biology and histopathology, this system rendered previous terms such as bronchioloalveolar carcinoma (BAC), including its non-mucinous and mucinous forms redundant. Lung cancer is broadly classified into non-small cell lung cancer (NSCLC), originating from epithelial lung cells and small-cell lung cancer (SCLC), originating from neuroendocrine bronchial cells. NSCLC accounts for 80% of lung cancer cases and is further subtyped into adenocarcinomas, squamous cell carcinomas, large-cell carcinomas, undifferentiated and mixed tumours[289]. Adenocarcinomas are the most common form of lung cancer, accounting for 40% of all cases.

Adenocarcinoma tumourigenesis is complex but is thought to begin with cellular changes occurring through hyperplasia of lung epithelial cells. The cells making up these pre-malignant lesions, known as ‘atypical adenomatous hyperplasia’[290], accumulate genetic abnormalities causing them to become pleomorphic resulting in a lepidic, non-invasive, growth pattern along alveolar walls.

Lesions less than 30 mm in diameter are known as adenocarcinoma-in-situ; if treated at this stage by complete surgical resection, almost 100% of cases will achieve 5-year disease-free survival. Untreated/undiagnosed lesions will continue to grow and develop into invasive adenocarcinomas. Minimally invasive adenocarcinoma is a term used to describe lesions less than 30 mm in diameter with an invasive component of less than 5 mm; lesion resection is still likely to give excellent disease-free survival rates. Invasive adenocarcinomas greater than 30 mm in diameter are classified on the predominant cellular growth pattern present within the lesion (lepidic, acinar, papillary or solid); it is these invasive subtypes that are most commonly diagnosed in patients. Lepidic-predominant adenocarcinoma describes an invasive adenocarcinoma subtype that has a predominant lepidic growth pattern with an invasive component greater than 5 mm; these subtypes can be non-mucinous or mucinous (previously termed non-mucinous and mucinous BAC). The mucinous form can be non-invasive, minimally-invasive or invasive and is often bilateral and multifocal with extensive mucous production. Patients suffering from this subtype present with a cough and extensive mucous production which can lead to death from respiratory failure without any evidence of invasive disease[288].

1.12.2 Models of human lung cancer

Although numerous animal models are available for lung cancer research (hamsters, mice, dogs, primates)[291,292], mice have been considered the model of choice due to their ease of genetic manipulation and cost-effectiveness[293]. These factors have led to numerous mouse models being developed. Inbred strains with high rates of spontaneous lung tumour development are commonly used in chemoprevention studies[294-296]. Chemical[297], carcinogen[291] and environmental-induced lung cancer models allow for the study of tumourigenesis and progression[298], whereas orthotopic xenograft models are used to investigate both primary and metastatic disease[299-302]. Transgenic mouse strains incorporating genetic mutations that occur in human lung cancers such as tumour suppressor gene inactivation (p53, retinoblastoma and p16), oncogene activation (K-ras), altered growth factor expression[303] and amplification of specific chromosomal regions[304,305] will produce tumours with greater similarity to those seen in humans and can be used to identify genes that drive lung cancer development and progression[304]. Mouse

models using fluorescent or bioluminescent reporters have also been described[306,307] which can be used for the identification of oncogenes involved in tumourigenesis and determination of tumour cell type origin[308].

Despite their uses, these mouse models do not accurately represent advanced stages of human lung cancer and suffer from the same general limitations as mouse models for other cancer types, as described in section 1.9. The perceived advantages of having numerous models available can also be a significant limitation, as no one single model can be used to investigate all stages of the disease.

1.12.3 Ovine pulmonary adenocarcinoma

Ovine pulmonary adenocarcinoma (OPA) is becoming regarded as a valuable translational model for studying human lung cancer[309]. OPA is a naturally occurring neoplastic lung disease caused by the jaagsiekte sheep retrovirus (JSRV)[310-313]; the disease was first described in the 19th century in sheep flocks in South Africa[314]. Since then, JSRV infection has been identified throughout the world in numerous sheep breeds and small ruminants (including goats) but has never been identified in humans[315,316]. Endemic within the UK, OPA is an economic and animal welfare concern[317]. Although within-flock disease incidence can be as high as 30%, levels of 2-5% are more common[309]. Mortality rates tend to reduce from 50%, following initial disease diagnosis within the flock[318], to approximately 1-5% as it becomes endemic[314,319]. Apart from increased mortality, production losses occur through decreased weight gain and reduced fertility[312]. Disease transmission occurs most commonly through the aerosol route[314,318,320], although the virus has also been isolated from the milk and colostrum of infected ewes[321].

1.12.4 JSRV biology

JSRV is the only known betaretrovirus capable of lung adenocarcinoma tumourigenesis. Each JSRV particle contains 2 single-stranded positive sense RNA copies containing a genome of approximately 7,460 nucleotides. Four genes encode viral proteins[312], *gag* (encoding structural proteins), *pro* (encoding aspartic protease), *pol* (encoding reverse transcriptase and integrase enzymes) and *env* (encoding surface and transmembrane envelope glycoproteins)[322,323]. Although an additional open reading frame, known as *orfX*, has also been identified, its function remains

unclear as it is not required for cellular transformation[324] or oncogenesis[325-327]. The cellular mechanism underlying neoplastic transformation following JSRV infection involves the Env glycoprotein acting as a viral oncoprotein; this transforming ability has been shown using *in vitro* systems[324,328] and *in vivo* mice[327] and sheep[326] models. It is thought that plasma membrane localised Env glycoprotein may interact with protein kinases, adapter proteins and signalling molecules that are capable of triggering cellular proliferation and survival pathways[329]. The Ras-MEK-ERK and PI3K-AKT-mTOR[287] pathways are commonly activated in OPA and human lung adenocarcinomas but others may include RON-HYAL2, EGFR and heat shock proteins[330]. Further mutations such as telomerase activation[331], inactivation of tumour-suppressor genes or activation of additional oncogenes[287] are likely to be required if tumours are to develop following initial pathway activation[273].

1.12.5 Endogenous retrovirus and immune responses

Endogenous retroviruses are viruses that have become integrated into host germ-line DNA and are passed to subsequent generations. Numerous endogenous JSRV (enJSRV) have been found in the sheep genome which have over 90% sequence homology to exogenous JSRV (exJSRV)[332,333]. Although enJSRV are non-oncogenic[310,322,334,335], viral RNA and proteins have been identified in the female reproductive tract and in foetal tissues, providing evidence of their transcriptional potential[335,336]. Viral proteins may protect from exJSRV infection by receptor competition or through the prevention of exJSRV transport and cellular exit[336,337].

Although JSRV infection can induce the production of neutralising antibodies[338,339], cellular or humoral adaptive immune responses typically do not occur. This is likely the result of immunological tolerance to JSRV antigens due to enJSRV protein expression in the foetal thymus during T lymphocyte development. Ineffective immune responses are also thought to occur through overproduction of surfactant proteins combined with tumour cells down-regulating major histocompatibility complex class I antigens preventing cellular recognition by $CD8^+$ T lymphocytes. Alveolar macrophages can also produce large amounts of interferon gamma, which can inhibit T cell activation and JSRV-specific immune responses[340].

1.12.6 OPA diagnosis

OPA cases are typically diagnosed in sheep aged 2-4 years of age. Diagnosis of clinical cases can be obtained from a physical examination; common clinical signs include weight loss, pneumonia, tachypnoea and dyspnoea[341]. Thoracic auscultation may identify adventitious lung sounds[342]; however, a pathognomonic sign of OPA is copious amounts of fluid draining from the nostrils[343] which typically occurs when tumours occupy more than 30% of the lung volume[341]. Although these advanced stage tumours may develop over many months or years[341], new evidence indicates that some tumours can develop quickly[344]. Pre-clinical antemortem OPA diagnosis is important for removing infectious sheep from flocks but also for identifying cases for research. Unfortunately, this pre-clinical diagnosis is difficult to achieve, as many sheep never develop clinical signs during their commercial lifespan[345]. Diagnostic serological assays are not useful, as JSRV-infected sheep fail to produce humoral immune responses[346]. Virus detection in the blood is possible through PCR technology[347] but due to low numbers of virally infected blood cells (monocytes, T and B lymphocytes) high false negative results are seen[348]. Despite this, PCR testing is useful for identifying infected flocks rather than individual animals. The same PCR technique has been used successfully to detect JSRV-infected cells in bronchoalveolar[343] and lung fluid[349] samples. This PCR test offers better sensitivity compared to blood samples; although, early cases can be missed as the procedure only samples a small region of the lung. The procedure also requires sedation and so is not practical for routine large-scale on-farm testing. Because of these factors, the standard diagnostic test for pre-clinical and clinical OPA cases is gross pathology and histology performed at the post-mortem examination.

1.12.7 OPA histology and comparison with human lung adenocarcinomas

Histological examination of OPA lesions reveal non-encapsulated tumours originating from JSRV-transformed alveolar and bronchiolar epithelial cells[273,350,351]. Lesions are composed predominantly of type II pneumocytes, involved with alveolar surfactant production, with smaller numbers of undifferentiated cells and bronchiolar club cells that are involved with producing proteins that line bronchioles[352]. Tumours can be highly heterogenous, with typical areas composed of columnar or cuboidal

cells with a low mitotic rate, whereas other areas show higher degrees of malignancy with high mitotic rates and necrosis[352,353]. Tumour cells become surrounded by fibrovascular connective tissue which aids the influx of inflammatory cells. Although large numbers of macrophages are seen[340], neutrophil numbers can be variable, which is largely determined by whether a bacterial infection is present. Cancer cells spread along alveolar septa (lepidic growth) before forming acinar or papillary proliferations within bronchioles. JSRV virions, released from infected cells, cause the formation of new foci of infection throughout the lung[354] and as neighbouring neoplastic foci enlarge, they coalesce to form a single large tumour. Although not common, intra-thoracic and extra-thoracic metastasis has been identified in approximately 10% of cases[355-358]. Initial histological classification systems described OPA as having similarity to human BAC; however, under the revised lung classification system early OPA lesions closely resemble those of minimally invasive adenocarcinoma or lepidic-predominant adenocarcinoma, whereas advanced disease would fit a description of adenocarcinoma with an acinar or papillary growth pattern with or without mucinous features. An important consideration is that OPA has significant similarities to the rare non-invasive, multifocal subtypes of human lung adenocarcinoma (such as the mucinous forms), where clinical samples are difficult to obtain, and is less similar to the more common metastatic forms of the disease[287].

1.13 Hypothesis and aims

The radiation response of a tumour depends not only on innate radiosensitivity but also on the TME and the development of acquired radioresistance. For RT to become integrated into the concept of precision medicine we require a detailed understanding of the mechanisms that contribute to cancer cells gaining radioresistance, as well as the development of novel methods by which tumour hypoxia can be monitored in real-time. This would provide a means by which these treatment resistant areas can be targeted. Monitoring patients during therapy would allow assessment of response to treatment and would assist the early identification of non-responding patients; more effective therapies could then be instigated sooner whilst sparing the patient from RT-induced side effects. With these currently unmet clinical issues in mind, the following hypothesis was devised and specific research aims identified.

1.13.1 Hypothesis

The overriding hypothesis that forms the basis for the body of work within this thesis is that complementary *in vitro* and *in vivo* research is required to advance the understanding of radioresistance and investigate means by which RT can become tailored to individual patients.

We hypothesise that developed *in vitro* radioresistant (RR) cell lines will undergo phenotypic and genotypic changes with respect to their original parental cell lines. Alterations in signalling pathways are hypothesised to identify therapeutic targets to reverse radioresistance; whereas changes in secretion profiles can be used to identify biomarkers related to radiation response and radioresistance. These biomarkers, when validated, could provide a means by which the radiation response of a tumour can be monitored either through blood samples or more locally using a sensor implanted into the tumour itself.

For medical devices to be implanted into tumours the *in vivo* biocompatibility of sensor components must be assessed. We hypothesise that a murine xenograft model can be developed to obtain intra-tumoural biocompatibility data for materials being consideration for use in the IMPACT O_2 sensor. Previous studies have suggested that these materials, commonly used in medical devices, have good biocompatibility when implanted into healthy tissues. We therefore hypothesise that these materials when implanted into xenografted tumours will be biocompatible and produce a minimal FBR. These results could be used in conjunction with previous studies to justify the use of these materials in the construction of implantable devices for a range of medical conditions. For validation of ability of the IMPACT O_2 sensor to be able to be implanted into a tumour and provide real-time intra-tumoural O_2 measurements we hypothesise that an ovine lung cancer model would not only answer these questions but would also be an excellent novel translational model of human lung cancer.

Our final hypothesis is that although the IMPACT O_2 sensor was originally designed for intra-tumoural use, this sensor could also be utilised for real-time monitoring of visceral surface O_2 levels in a range of medical conditions. One such application would be monitoring post-operative intestinal perfusion following an intestinal resection and anastomosis. The use of the sensor in this way could detect

peri-anastomotic tissue hypoxia and enable goal-directed treatments to be provided to restore intestinal oxygenation and prevent anastomotic dehiscence. We hypothesis that a developed murine model will provide proof-of-concept for this application.

1.13.2 Aims

1. **To develop and characterise radioresistant breast cancer cell lines**
    - Develop novel RR breast cancer cell lines using ER^+ and ER^- cell lines representing different molecular breast cancer subtypes.
    - Undertake genotypic, phenotypic and functional characterisation of parental and RR cell lines to demonstrate cellular differences at gene, protein and functional levels.
    - Identify differential phenotypic and signalling pathways between parental and RR cell lines to highlight potential mechanisms of radioresistance.
2. **To develop a method to identify and validate radiation-induced cancer cell secreted biomarkers**
    - Obtain secretome samples from cancer cells up to 24 h post-radiation treatment from a variety of species and cancer types.
    - Use liquid chromatography-mass spectrometry to characterise the MCF-7 secretome in both untreated and radiation-treated samples.
    - Select candidate radiation-induced secreted biomarkers for further validation and examine their secretion patterns in other human and canine breast and ovine lung cancer cell lines.
    - Combine secretomic results with whole-transcriptome gene expression data from both radiation-treated parental and RR cell lines to identify biomarkers of radiosensitivity and validate them through western blot, immunofluorescence and immunohistochemistry.
3. **To develop a method to investigate the biocompatibility of implantable sensor materials in a tumour model**
    - Assess the intra-tumoural biocompatibility of materials under consideration for use in the IMPACT O_2 sensor.
    - Develop a novel *in vivo* murine biocompatibility model whereby materials are implanted into human breast cancer xenograft tumours and their effects

assessed through tumour immunohistochemistry (necrosis, proliferation, apoptosis, hypoxic markers, innate immune responses and fibrosis).

- Provide evidence to justify the use of these materials in the IMPACT O_2 sensor.

4. **To validate functionality of the IMPACT O_2 sensor to measure tissue O_2 tension for clinical applications**
    - Develop an *in vivo* murine model for validation of the IMPACT O_2 sensor to provide real-time measurements of intestinal and muscular ptO_2.
    - Investigate the sensor's ability to detect changes in intestinal ptO_2 following ischaemic, hypoxic and haemorrhagic challenges and its ability to detect changes in muscular ptO_2 following hypoxic challenges.
    - Provide evidence to justify further development of the IMPACT O_2 sensor towards clinical applications in man.
5. **To develop a pre-clinical translation large animal model of human lung cancer and validate functionality of the IMPACT O_2 sensor to measure tissue O_2 tension within a solid tumour**
    - Develop a novel *in vivo* ovine pulmonary adenocarcinoma model for the surgical implantation and validation of the IMPACT O_2 sensor.
    - Develop a novel CT-guided trans-thoracic percutaneous implantation procedure with integration of techniques such as ultrasound, general anaesthesia, CT and surgery into the model.
    - Assess the sensor's ability to detect changes in intra-tumoural ptO_2 following hypoxic challenges.
    - Provide evidence to justify further development of the IMPACT O_2 sensor towards clinical applications in man.

2 Materials and Methods: *In Vitro* Experiments

2.1 Introduction

All cell tissue culture and laboratory experiments were performed in the Division of Pathology Laboratories, Western General Hospital (University of Edinburgh).

2.2 Cell tissue culture

2.2.1 Cell lines

A panel of 4 human breast cancer cell lines, MCF-7, ZR-751, MDA-MB-231 and HBL-100, were chosen for this study due to their differing molecular classifications and phenotypic traits. For comparative studies involving different species and cancer cell types, 1 canine breast cancer cell line, REM-134, and 1 ovine lung cancer cell line, JS7, were chosen. The characteristics of these cell lines are outlined in Table 2.1.

All human breast cancer cell lines were obtained from the American Type Culture Collection (LGC Standards, Teddington, UK) and were authenticated by short tandem repeat (STR) profiling performed at Health England (Porton Down, Salisbury, UK). All cell line DNA samples matched 9 of 9 tested core alleles in DNA from known cell line samples confirming their identity. The canine breast cancer cell line was a kind gift from Professor R.W. Else (College of Veterinary Medicine, University of Edinburgh) and the ovine lung cancer cell line was a kind gift from Dr D. Griffiths (Moredun Research Institute, Pentlands Science Park, UK). All cells were maintained at a low passage number from frozen stocks with mycoplasma testing performed at 6 monthly intervals.

Table 2.1. Human, canine and ovine cell lines used in this study. (ER, oestrogen receptor; wt, wild type; PgR, progesterone receptor; HER2, human epidermal growth factor receptor 2; TNBC, triple negative breast cancer; SV40, Simian Virus 40).

Cell line	Origin	Classification	Description
MCF-7	**Human breast cancer:** pleural effusion from a 69-year-old female suffering from metastatic disease originating from a luminal mammary adenocarcinoma[359].	Luminal A	ER^+ (wt and variants)/ PgR^+/$HER2^-$[360]
ZR-751	**Human breast cancer:** ascitic effusion from a 63-year-old female suffering from metastatic disease originating from a ductal mammary adenocarcinoma[361].	Luminal A	ER^+/ PgR^+/$HER2^-$
MDA-MB-231	**Human breast cancer:** pleural effusion from a 51-year-old female suffering from metastatic disease originating from a basal mammary adenocarcinoma[362].	Basal B	ER^-/PgR^-/$HER2^-$ (TNBC)
HBL-100	**Human breast cancer:** primary cultures of epithelial cells from an early lactation sample of human milk[363].	Basal B	ER^-/PgR^-/$HER2^-$ (TNBC) HBL-100 harbours the SV40 genome and exhibits characteristics of transformation including the ability to form colonies in soft agar, an aneuploid chromosome complement and continuous replication in culture
REM-134	**Canine breast cancer:** primary cultures of a mammary carcinoma[364].	Unknown	ER^-/PgR^-/$HER2^-$ (TNBC)
JS7	**Ovine lung cancer:** primary cultures of a pulmonary adenocarcinoma[365].	Retrovirally induced	Known activated pathways: Ras-MEK-ERK and PI3K-AKT-mTOR[287]

2.2.2 Cell culture

Cell culture procedures were performed inside a category II biological safety hood using aseptic techniques. Media was stored at 4°C and was used or discarded within 4 weeks of the addition of supplements. Foetal calf serum (FCS) used for cell culture was inactivated by heating for 15 min at 37°C, then for 30 min at 56°C. For routine cell culture, all cell lines were grown using the appropriate media (Table 2.2) in an incubator at 37°C in a humidified atmosphere at 21% O_2 with 5% CO_2. Media was changed every 48-72 h. Cells were used for no more than 15 passages, after which new cells were obtained from frozen stocks. Periodic recording of morphology and doubling times was undertaken to ensure maintenance of phenotype. Phase

contrast images of cells were captured with a monochrome digital Axiocam camera fitted to a Zeiss Axiovert S100 (Carl Zeiss Ltd, UK) microscope.

Table 2.2. Growth media and supplements required for each cell line.

Cell line	Media	Supplements
MCF-7 ZR-751 MDA-MB-231 HBL-100	Dulbecco's Modified Eagle Media (Gibco Life Technologies, Invitrogen, UK)	10% heat-inactivated FCS 1% Penicillin/Streptomycin (100 IU/ml)
REM-134	Dulbecco's Modified Eagle Media-high glucose (Gibco Life Technologies, Invitrogen, UK)	10% heat-inactivated FCS 1% Penicillin/Streptomycin (100 IU/ml)
JS7	Iscove's Modified Dulbecco's Media (Sigma-Aldrich, UK)	10% heat-inactivated FCS 1% Penicillin/Streptomycin (100 IU/ml) 4mM L-glutamine

2.2.3 Recovery of cells from liquid nitrogen storage

Cell stocks were stored in freezing mix media (90% FCS, 10% DMSO) within cryovials in liquid nitrogen storage tanks at -196^{o}C. To recover cells from storage, cryovials were defrosted as rapidly as possible in a water bath at 37^{o}C. Cells were transferred into 10 ml of warmed media and centrifuged at 1000 x g for 5 min. The supernatant containing DMSO was removed and the cell pellet re-suspended in 8 ml of media and transferred to a T25 flask. Cells were used in experiments after a minimum period of 2 weeks after recovery from liquid nitrogen storage.

2.2.4 Cell passage

Cells were passaged when they reached 75-85% confluency. Media was removed and cells were washed twice with sterile phosphate-buffered saline (PBS). An appropriate volume of 0.05% trypsin ethylenediaminetetraacetic acid (EDTA) (Table 2.3) was added and the cells incubated for 3-5 min at 37^{o}C until they detached from the flask surface. FCS-containing media was then added to neutralise the trypsin. Cells were centrifuged at 1000 x g for 5 min and the supernatant removed. Cells were then re-suspended in media and seeded into new culture vessels (Table 2.3) or counted as required. All experiments were performed using sub-confluent cultures in the log-phase of growth.

Table 2.3. Summary of culture vessels used. Data includes volumes of media and trypsin EDTA required for each culture vessel.

Culture container	Surface area (mm^2)	Cell number seeded	Trypsin EDTA (ml)	Media used to curtail trypsinisation (ml)	Total vol. of media (ml)	Approx. cell number at 100% confluency
Flasks						
T25	2,500	0.1-$1x10^6$	1	5	3-5	$2.5x10^6$
T75	7,500	1-$3x10^6$	2	7	8-15	$8x10^6$
T175	16,200	$4x10^6$	3	7	15-30	$18x10^6$
Plates						
75 mm	2,100	$1x10^5$	2	5	5-10	$3x10^6$
150 mm	15,200	1-$2x10^6$	3	7	15-30	$20x10^6$
6 well	900	0.23-$1x10^6$	1	3	2-5	$1x10^6$
96 well	320	1.5-$10x10^2$	N/A	N/A	0.2	N/A
Spinner Flasks						
100 ml	N/A	1.5-$3x10^6$	N/A	N/A	90	N/A
250 ml	N/A	3-$6x10^6$	N/A	N/A	150	N/A

2.2.5 Cell counting and determination of cell viability

Following trypsinisation and the addition of FCS-containing media the cell suspension was transferred to a Falcon tube and centrifuged at 1000 x g for 5 min. The supernatant was removed, and the cell pellet re-suspended in media. A single cell suspension was created by passing the cell suspension 3 times through a 21G needle attached to a 10 ml syringe. 10 µl of this cell suspension was added to 10 µl of 0.4% trypan blue (Sigma-Aldrich, UK) and incubated for 2 min. 10 µl of this trypan blue cell suspension was then added to a haemocytometer. The total number and the number of dead cells were then counted (Table 2.4).

Table 2.4. Formulas used for cell counting and viability assessment. (*0.1 µl is the volume contained within the haemocytometer counting chamber).

Dilution factor = (volume of cell suspension + volume of trypan blue)/volume of new cell suspension
Cell density (cells/ml) = total cell count/0.1 µl* x dilution factor $x10^3$
Total number of cells = cells/ml x volume of cell suspension
Percentage cell viability = total number of live cells/total cell count x100

2.2.6 Cryopreservation of cells and storage into liquid nitrogen

Surplus cells were allowed to reach 80-90% confluency in a T175 flask before undergoing routine trypsinisation and counting as described in sections 2.2.4

and 2.2.5. Cells were re-centrifuged at 1000 x g for 5 min and the supernatant removed. Cells were then re-suspended in freezing media at a density of 2-5x10^6 cells per 0.5 ml freezing media, transferred into separate cryovials and placed into a freezing container (Nalgene Mr. Frosty, Sigma-Aldrich, UK) containing 100% isopropyl alcohol and stored overnight at -70^{o}C. Cryovials were then transferred to a liquid nitrogen tank for long term storage (Institute of Genetics and Molecular Medicine, University of Edinburgh).

2.2.7 Irradiation of cells

Cells were irradiated using a Faxitron cabinet X-ray system 43855D (Faxitron X-ray Corporation, IL, USA). Dosimetry and dose-rate [mGy/s] checks were conducted at least once a year (NHS Medical Physics Department, Western General Hospital, Edinburgh, UK) using an Innovision Dosimeter 35050A and 150cc ion chamber 96020C. The Faxitron cabinet used no extra filtration, with x-rays passing through a 1.6 mm beryllium window. Culture vessels were placed in the centre of the glass shelf which rotates at 2 rpm to ensure uniform dosing. The distance from the focal spot of the x-ray tube to the culture vessels was 40.6 cm and when operated at 130 kV it produces a central dose of 1 Gy/min. For all experiments that involved radiation treatment, control cells were included that consisted of cells undergoing mock radiation treatment being placed within the Faxitron cabinet for the desired length of time without undergoing radiation treatment.

2.2.8 Development of radioresistant cell lines

Radioresistant cell lines (MCF-7 RR, ZR-751 RR, MDA-MB-231 RR, REM-134 RR and JS7 RR) were developed from their respective parental cell lines by weekly exposure to single fractions of radiation. An initial dose of 2 Gy was followed by weekly incremental doses of 0.5 Gy for 12 weeks. During this period cells received a total radiation dose of 57 Gy. Cells were subsequently maintained with further weekly doses of 5 Gy. Radioresistant cell lines were maintained in routine media. Following exposure to radiation, cells were left at least 24 h before undergoing trypsinisation and passage.

2.2.9 Generation of multicellular tumour spheroids

Numerous cancer cell line models are available to increase the complexity of cell culture systems that more accurately replicate the *in vivo* TME. The use of multicellular tumour spheroids (MTS) represents one such commonly used model[366].

A single cell suspension from a T175 flask (approximately $15x10^6$ cells) was created and transferred into a spinner flask (Cellcontrol Spinner Flask, Integra, Switzerland) containing 100 ml of media and incubated routinely on a magnetic stirrer platform (Cellspin, Integra, Switzerland) to provide convective mixing of the culture media and cell suspension to generate MTS. Flasks were checked daily for MTS formation, the media was changed as required. When MTS had reached a sufficient size (generally 7-14 d) they were removed from the spinner flask using a 25 mL serological pipette.

2.3 Cellular assays

2.3.1 Sulforhodamine B proliferation (SRB) assay

The SRB assay was originally described in 1990 as a new technique for anti-cancer drug screening[367]. The SRB assay measures cellular proliferation based on the ability of the SRB dye to bind the basic amino acids of fixed proteins in a pH-dependent manner[367-369]; colorimetric evaluation provides an estimate of total protein, which is related to cell number[369].

Due to differences in proliferation rates between cell lines, initial optimisation experiments were conducted to identify cell seeding numbers to ensure optical density (OD) saturation did not occur over the time course of the experiments. If the OD values produced by the assay are below 3.5, the relationship between OD and cell number is linear. However, if the OD values are greater than 3.5 there is a risk saturation may be occurring with values becoming inaccurate. Seeding densities used for each cell line gave a confluency of approximately 10-30% at 24 h post-seeding and produced OD values less than 3.5 up to 144 h post seeding.

Cells were seeded into flat-bottom 96 well plates and incubated for 24 h before treatment with drugs or radiation in a final volume of 200 µl in each well. Controls included untreated and drug vehicle (DMSO or ethanol) treated cells. Drug vehicle controls were treated corresponding to the highest drug concentration used in

each experiment (final concentration of DMSO/ethanol was not greater than 1%). Media only controls were also included to allow background readings to be assessed. Six replicates of each treatment group were performed in each experiment. Cellular proliferation was assessed at 0, 24, 48, 72, 96, 120 and 144 h following drug or radiation treatment. To perform the SRB assay, cells were fixed with 50 µl/well of cold 25% trichloracetic acid (TCA) (Sigma-Aldrich, UK) for 60 min at 4ºC and subsequently washed 10 times with water to remove the TCA, media, metabolites and serum proteins. Plates were dried, and the fixed cells stained with 50 µl of 0.4% SRB dye solution (Sigma-Aldrich, UK) dissolved in 1% acetic acid (VWR International) for 30 min at room temperature. The SRB solution was removed and the plates washed in 1% glacial acetic acid 4 times to remove unbound dye. Once the plates were dry, the protein-bound SRB was solubilised with 150 µl of 10 mM Tris-NaOH buffer (pH 10.5) for 60 min at room temperature before measuring the OD of each well at 540 nm using a Biohit BP800 spectrophotometer (Biohit Ltd, UK) and Wallac 1420 Manager. OD values were corrected by subtracting average values of blanks and normalising to vehicle controls. Mean values and standard deviations were calculated from the technical replicates. IC_{50} values were generated through sigmoidal concentration response curves fitted using Prism 7 (GraphPad Software, San Diego, CA, USA).

2.3.2 Colony formation assay

Cells were seeded into 75 mm plates ($1x10^3$ cells/plate) and incubated for 24 h before radiation treatment. Untreated cells were used as controls; once visible colonies (approximately 50 cells/colony) had formed in the untreated control group (approximately 10-14 d post-seeding) the cells were fixed and stained for counting. The media was discarded, and the cells washed twice in PBS. Clonogenic reagent (1,9-dimethyl-methylene blue zinc chloride double salt, Sigma Aldrich, UK; 0.5 g methylene blue dissolved in 100 ml ethanol and 100 ml H_2O) was added to the plates, which were then left to incubate for 45 min at room temperature. The plates were washed twice in H_2O then left to dry before manually counting the colonies; only colonies greater than 50 cells were counted. Analysis was performed by calculating plating efficiencies (PE) and survival fractions (SF) for untreated and radiation treated cells. PE, which indicates the proportion of cells seeded into the

plate that grew to form a colony, was calculated by dividing the number of colonies counted by the initial number of cells seeded. Following determination of PE, the fraction of cells surviving a given radiation treatment was calculated; this SF was calculated by dividing the PE of the treated cells by that of the PE of the untreated control cells.

2.3.3 Scratch (migratory) assays

The migratory capabilities of parental and RR cell lines were investigated through 2D scratch assays. Cells were seeded into 6 well plates to achieve 100% confluence after 24 h. Scratch assays were performed as described by Liang *et al*,. 2007[370]. A scratch was made in the monolayer of cells using a p1000 pipette tip. Media was discarded and the cells were washed in PBS until all floating cells were removed and a clean, sharp edged scratch could be identified by phase contrast light microscopy. 0.1% FCS-supplemented media was then added (lower percentage FCS-supplemented media was used to minimise cell proliferation while preventing apoptosis and/or cell detachment). Controls included untreated and drug vehicle (DMSO or ethanol) treated cells. For drug assays, the drug or drug vehicle was added to the 0.1% FCS-supplemented media. Photographs were taken using the 2.5x objective lens at regular intervals until the cells had migrated across the scratch (or up to a maximum of 48 h post-scratch). At each time point the area remaining of the scratch was calculated using FIJIJ software and expressed as a percentage of the scratch area at 0 h, giving a final relative migratory distance at each time point.

2.3.4 MTS invasion assays

The invasive capabilities of parental and RR cell lines were investigated through 3D invasion assays as the movement of cells through a 3D matrix more closely mimics *in vivo* invasion[371]. A collagen gel solution was made by mixing 0.1% filtered acetic acid, cell matrix type 1-A (an acid soluble type 1 collagen solution produced from porcine tendon, pH 3, 3 mg/ml, Alphalabs, UK), 0.22 M NaOH (Sigma-Aldrich, UK), FCS and 10x DMEM (Sigma-Aldrich, UK) at concentrations of 45%, 25%, 10%, 10% and 10% respectively. All solutions were kept on ice to prevent collagen polymerisation. A single MTS was added with 500 ul of collagen mix into a well of a 24 well plate and incubated for 1 h at 37^{o}C to allow

the collagen to polymerise. Following polymerisation, a p200 pipette tip was used to release the collagen gel from the edges of the well and a further 500 ul of DMEM was added to each well. Controls included untreated and drug vehicle (DMSO or ethanol) treated cells. For drug assays, the drug or drug vehicle was added to both the collagen mix and the media. Photographs were taken using a 2.5x objective lens at regular intervals up to 120 h post-seeding. MTS invasion was measured using a macro programme developed by Matthew Pearson (Light Microscopy Application Specialist, IGMM, University of Edinburgh). This macro processes the image to find the edges of the MTS and highlights the cells using morphological filters and intensity thresholding. This macro programme provided 3 readings after analysis; the total area, the MTS area and the invasive area. To assess invasion the total MTS area at each time point was expressed as a percentage of the MTS area at 0 h (Figure 2.1).

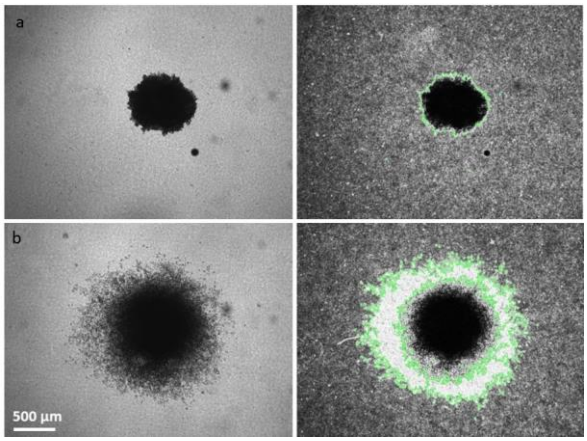

Figure 2.1. MTS invasion measurement. MCF-7 RR MTS are shown at **(a)** 0 h and **(b)** 96 h post-seeding into collagen. Images are shown pre- and post-macro analysis using FIJI software. The green lines outline the MTS and the invasive front.

2.4 Protein recovery and detection

2.4.1 Whole cell protein extraction from adherent cells

Protein extraction was carried out on ice to minimise protein degradation. Cells were washed twice in ice cold PBS before the addition of ice-cold isotonic lysis buffer (Table 2.5). Using a cell scraper, the cells were scraped off the surface of the culture vessel and mixed with the lysis buffer. The cells were left on ice for 10-15 min to allow lysis to occur. The lysate was collected and transferred to a cold 1.5 ml Eppendorf tube then centrifuged at 13,000 x g for 6 min at 4^{o}C. The supernatant (lysate) was removed and transferred to a new Eppendorf tube, which was then either frozen and stored at -70^{o}C or placed on ice for immediate use.

Table 2.5. Lysis buffer. Volumes of lysis buffer used were dependent on the size of culture vessel: 400 µls per T175 flask or 150 mm petri dish; 200 µl per T75 flask or 75 mm petri dish; 100 µl per well in a 6 well plate.

Lysis buffer	Lysis buffer additives per 10 ml lysis buffer
50 mM Tris (pH 7.5), 5 mM EGTA (pH 8.5), 150 mM NaCl	• 1 complete 'protease inhibitor tablet' (Roche, UK) • 100 µl phosphatase inhibitor cocktail 2 (Sigma-Aldrich, UK) • 100 µl phosphatase inhibitor cocktail 3 (Sigma-Aldrich, UK) • 50 µl aprotinin (Sigma-Aldrich, UK) • 100 µl Triton-X (Sigma-Aldrich, UK)

2.4.2 Protein quantification using the bicinchoninic acid assay

Protein concentrations from cellular lysates were determined using the bicinchoninic acid (BCA) assay. A 1 mg/ml bovine serum albumin (BSA) (Sigma-Aldrich, UK) standard was used to create an 8-point standard curve. Known BSA protein standards were made up to a final volume of 50 µl. The standard curve was produced using the same plate on which the samples were assayed. 5 µl of each protein sample was diluted into 45 µl of distilled water in borosilicate glass tubes. Fresh BCA solution was made by adding 1 ml of copper (II) sulphate (Sigma-Aldrich, UK) into 49 ml of BCA (Sigma-Aldrich, UK). 1 ml of this BCA solution was added to each 50 µl aliquot of sample or BSA standard. The samples were briefly vortexed and incubated for 15 min at 60^{o}C then allowed to cool. In a 96 well plate, 200 µl of each solution (sample or known BSA protein standard) was added to a designated well. All samples were performed in duplicate. OD values were measured at 540 nm using a Biohit BP800 spectrophotometer (Biohit Ltd, UK) and Wallac 1420 Manager program (PerkinElmer, UK). Protein concentrations were determined from the standard curve generated using the known BSA concentrations.

2.4.3 Sodium dodecyl sulphate-polyacrylamide gel electrophoresis (SDS-PAGE)

Protein samples were resolved in sodium dodecyl sulphate-polyacrylamide gels using electrophoresis. Different percentage SDS-polyacrylamide gels (5-15%) were used according to the size of the protein of interest. Lower percentage gels were used to separate high molecular weight proteins and higher percentage gels were used for lower molecular weight proteins. All SDS-polyacrylamide gels were prepared using the Bio-Rad Protean II mini-gel system (Bio-Rad Laboratories, UK). The resolving gel was prepared (Table 2.6) and approximately 8 ml was poured

between the plates; this was overlaid with isopropanol to remove air bubbles. The gel was allowed to set at room temperature, the isopropanol was discarded, and the top of the gel was washed with dH_2O. The stacking gel (Table 2.6) was prepared and approximately 1.5 ml was poured on top of the resolving gel. A loading comb was then inserted into the stacking gel and allowed to set at room temperature. Once set, the comb was removed, and the wells were washed with dH_2O. The gel was placed into a running module which was then immersed in SDS-PAGE running buffer (Table 2.6). Protein samples were prepared into 40 µg aliquots by adding the appropriate volume of 4x Laemmli sample buffer (Bio-Rad Laboratories, UK) and lysis buffer to cell lysates as determined by the BCA assay. Samples were heated for 5 min at 95^{o}C to denature the proteins, which were then loaded into the wells in the stacking gel. A pre-stained protein marker (broad range ladder, 11-190 KDa, Cell Signalling Technology, UK) was run in parallel to allow identification of the protein bands by size. The gel was subjected to electrophoresis at 80 V for 15 min (which allows the samples to move through the stacking gel), then at 150 V until the dye front had run off the bottom of the resolving gel (approximately 45 min).

2.4.4 Immunoblotting

Resolved proteins were electrophoretically transferred onto methanol-activated polyvinylidene difluoride nitrocellulose membranes (Immobilon-P PVDF, 0.45 µm, Merck Millipore, UK) in ice-cold transfer buffer (Table 2.6) using the Protean Transfer Cell equipment (Bio-Rad laboratories, UK). Transfer was performed at 100 V for 90 min at 4^{o}C. Nitrocellulose membranes were stained with Revert total protein stain for 5 min, then washed twice in Revert wash solution for 30 s each time to allow visualisation of protein bands and confirm equal loading (Li-COR Biotechnology, UK). Membranes were visualised using the LI-COR Odyssey Infrared Imager (LI-COR, Bioscience, UK) using the 700 nm channel (as described below). Membranes were then washed with Revert reversal solution (Li-COR Biotechnology, UK) for 10 min until the stain was no longer visible. Non-specific antibody binding was blocked by incubating membranes in Li-COR Odyssey blocking buffer solution (Li-COR Biotechnology, UK) for 1 h at room temperature. Primary antibodies (targeting the protein of interest and loading control) were diluted

in Li-COR Odyssey blocking buffer solution (Table 2.7). The membranes were subsequently probed with primary antibodies and incubated overnight at 4^{o}C.

Table 2.6. Gels and solutions required for SDS-PAGE and immunoblotting.

Reagent	Composition
Resolving gel	5-15% acrylamide gels were made according to the size of protein of interest. 390mM Tris-HCL (pH 8.8), 0.1% SDS. Polymerisation was initiated by the addition of 0.1% ammonium persulphate and 0.08% TEMED immediately prior to pouring the gel
SDS-PAGE running buffer	25mM Tris, 190mM glycine, 0.1% (v/w) SDS
Stacking gel	5% acrylamide, 123mM Tris-HCL (pH 6.8), 0.1% SDS. Polymerisation was initiated by the addition of 0.1% ammonium persulphate and 0.1% TEMED immediately prior to pouring the gel
Transfer buffer	25mM Tris, 190mM glycine, 20% (v/v) methanol

Following overnight incubation, the primary antibodies were removed, and the membrane washed 3 times in phosphate-buffered saline-Tween 20 (PBST, 1:1000 solution of Tween20) 5 min per wash. Fluorescently labelled secondary antibodies IRDye 800CW and IRDye 680LT (LI-COR, Bioscience, UK) were diluted in Li-COR Odyssey blocking buffer solution (1:10,000) with the addition of 0.01% SDS. These fluorescently labelled secondary antibodies are susceptible to photo-bleaching, therefore subsequent steps were performed in the dark. The membranes were probed with the secondary antibodies and incubated for 45 min at room temperature. Following incubation, the secondary antibody was removed, and the membrane washed 3 times in PBST, followed by a further 3 washes with PBS (5 min per wash). Membranes were visualised using the LI-COR Odyssey Infrared Imager (LI-COR, Bioscience, UK) using the 700 and 800 nm channels to detect the loading control and protein of interest bands respectively. Images were saved as TIFF files for quantification. For storage, membranes were washed in PBST for 10 min and frozen at -20^{o}C. Membranes required the following day were covered in PBS and stored at 4^{o}C.

2.4.5 Protein quantification using infra-red radiation

Relative protein intensities were measured by quantifying infra-red radiation emitted from labelled antibodies using Odyssey software (Image Studio Lite, Li-COR Biosciences, UK). Protein intensities were normalised to loading controls.

Table 2.7. Primary antibodies. Primary antibodies used for western blotting (WB), immunocytochemistry (ICC) and immunohistochemistry (IHC).

Primary antibody target antigen	Antibody details	Dilutions and applications	Antigen retrieval
Anti-α tubulin	Mouse mAb; Abcam; ab7291	1:10,000 (WB)	N/A
Anti-β actin	Rabbit pAb; Abcam; ab8227	1:10,000 (WB)	N/A
Anti-GAPDH	Mouse mAb; Abcam; ab8245	1:5000 (WB)	N/A
Anti-ERα	Mouse mAb; Dako; M7047	1:50 (WB, ICC, IHC)	Sodium citrate
Anti-EGFR	Rabbit mAb; Cell Signaling Technology; 4267	1:1000 (WB); 1:50 (ICC, IHC)	EDTA
Anti-Phospho EGFR	Mouse mAb; Abcam; ab24918	1: 1000 (WB)	N/A
Anti-HER2	Rabbit mAb; Cell signaling Technology; 2242	1:1000 (WB); 1:50 (ICC, IHC)	Sodium citrate
Anti-PgR (A/B)	Rabbit mAb; Cell Signaling Technology; 8757	1:1000 (WB)	N/A
Anti-PgR	Mouse mAb; DAKO; M3569	1:150 (ICC, IHC)	EDTA
Anti-AKT	Mouse mAb; Cell Signaling technology; 2920	1:1000 (WB)	N/A
Anti-Phospho AKT	Rabbit pAb; Cell Signaling technology; 9271	1:1000 (WB)	N/A
Anti-ERK	Rabbit pAb; Cell Signaling Technology; 9102	1:1000 (WB)	N/A
Anti-Phospho ERK	Mouse mAb; Cell Signaling Technology; 9106	1:1000 (WB)	N/A
Anti-Ki67	Mouse mAb; DAKO; M7240	1:150 (ICC, IHC)	Sodium citrate
Anti-E-cadherin	Mouse mAb; BD Transduction; 610182	1:50 (ICC, IHC)	Sodium citrate
Anti-N-cadherin	Mouse mAb; BD Transduction; 610921	1:150 (ICC, IHC)	Sodium citrate
Anti-vimentin	Mouse mAb; Abcam; ab8069	1:50 (ICC, IHC)	Sodium citrate
Anti-SNAIL	Rabbit pAb; Abcam; ab128530	1:250 (ICC, IHC)	Sodium citrate
Anti-SEC24C	Rabbit pAb; Atlas Antibodies; HPA040196	1:500 (WB); 1:500 (IHC)	Sodium citrate
Anti YBX3	Mouse mAb; Novus biologicals; H00008531-MO6	1:500 (WB); 1:100 (IHC)	Sodium citrate
Anti-EIF3G	Rabbit pAb; Atlas Antibodies; HPA041997	1:1000 (WB); 1:250 (IHC)	Sodium citrate
Anti-TK1	Rabbit mAb; Abcam; ab76495	1:500 (WB); 1:500 (IHC)	Sodium citrate
Anti-PERK	Rabbit mab; Cell Signaling Technology; 5683	1:500 (WB)	N/A
Anti-Phospho PERK	Rabbit pAb; Thermo Scientific; PA5-30294	1:500 (WB)	N/A
Anti-PhosphoEIF2α	Rabbit pAb; Cell Signaling Technology; 9721	1:500 (WB)	N/A
Anti-Phospho IRE1	Rabbit pAb; Thermo Scientific; PA1-16927	1:500 (WB)	N/A
Anti-WNT5a	Mouse mAb; Thermo Scientific; MA5-15502	1:500 (WB, ICC)	Sodium citrate

2.4.6 Membrane Stripping

Membranes required for re-probing were stripped using NewBlot PVDF Stripping Buffer (LI-COR Biosciences, UK). Membranes were first washed in PBST then covered in stripping buffer (diluted 1:5 with dH_2O) for 20 min at room temperature. The membranes were visualised using the LI-COR Odyssey Infrared Imager to ensure the secondary antibodies had been removed. Blots were then re-probed with secondary antibodies for 45 min at room temperature and re-visualised to ensure the primary antibody had also been removed. Blots were washed in PBS then blocked and probed as previously described in section 2.4.4.

2.4.7 Assessment of the effects of radiation on pathway activation

Cells were seeded into 75 mm plates at a density of $1x10^6$ cells per plate and incubated for 24 h. Cells were washed twice with PBS before 7 ml of FCS-free media was added into the wells. The cells were serum starved for 2 h then exposed to 2 Gy radiation (control cells were not treated with radiation). All cells underwent routine harvesting and lysis collection at 0, 5, 10- and 30-min post-radiation. The lysate was snap frozen on dry ice and stored at -70^{o}C for subsequent western blot (WB) analysis.

2.5 Immunohistochemistry

2.5.1 Fixation and sectioning of MTS and tissue for immunohistochemistry

MTS were fixed for 24 h in 4% formaldehyde (Genta Medical, UK). After fixation, the formaldehyde was removed and 100-200 µl of molten 2% agarose was added. A 1 ml pipette tip was then used to gently stir the agarose and MTS, being careful to conserve the integrity of the MTS. The suspension was allowed to set at room temperature before being processed. Harvested xenograft tumours and OPA tissue were fixed for at least 24 h (depending on tissue thickness) in 4% formaldehyde before being processed. Processing of MTS and tissue for IHC was performed using the Thermo Scientific Excelsior AS Tissue Processor (Thermo Scientific, UK). Once processed, MTS and tissue were embedded in paraffin blocks and stored at room temperature. Sectioning of samples was performed using the Leica RM2235 rotary microtome (Leica Microsystems Ltd, UK). Microtome sections

of 4 µm were placed on SuperFrost Plus glass slides (Thermo Scientific, UK) and allowed to dry for a minimum of 4 h at 53^{o}C for H&E and Masons trichrome staining or overnight at 37^{o}C for IHC. Sections cut for IHC were stored at 4^{o}C.

2.5.2 Haematoxylin and eosin staining

Sections were deparaffinised by 3 changes in 100% xylene for 5 min each time, then rehydrated by placing into decreasing concentrations of alcohol; 2 changes in 100% ethanol, followed by 80% then 50% for 2 min each time. The slides were then washed in running water for 2 min, before placing in haematoxylin (Shandon Harris Haematoxylin, Thermo Scientific, UK) for a maximum of 10 min. Slides were washed in running water for 2 min before being placed into Scott's tap water substitute for a maximum of 10 min until the tissue sections turned blue. Sections were counterstained by placing them into Eosin Y (Shandon Eosin Y Cytoplasmic Counterstain, Thermo Scientific, UK) for 5 min. The slides were dehydrated by placing them into increasing concentrations of alcohol; 50% ethanol for 30 s, 80% ethanol for 30 s, then 2 changes in 100% ethanol for 2 min each time. The slides were placed in xylene for 10 min before being mounted with coverslips using DXP mountant (Sigma-Aldrich, UK). Mounted slides were given a brief wash in 100% xylene before being left to dry at room temperature.

2.5.3 Masson's trichrome staining

All solutions for Masson's Trichrome staining were obtained from TCS Biosciences Ltd, UK. Sections were routinely deparaffinised and rehydrated then washed in running water for 2 min. Slides were mordanted with Bouin solution for 24 h at room temperature, before washing in running water for 60 s or until free of yellow colouration. Slides were then stained in Weigert iron haematoxylin for 5 min, washed for 5 min in running water and rinsed in distilled water. Slides were stained with Masson's Trichrome for 5 min, rinsed in distilled water and then treated with phosphotungstic/phosphomolybdic acid solution for 5 min. Slides were counter stained in aniline blue for 5 min, immersed in 1% acetic acid, then routinely dehydrated and mounted.

2.5.4 Vertical immunohistochemistry for paraffin embedded MTS and tissue samples

Sections were routinely deparaffinised and rehydrated. The slides were washed in running water for 10 s before being placed into a pressure cooker and covered with pre-warmed antigen retrieval solution. The pressure cooker was placed into a microwave and heated on maximum power for 5 min. Following heating, the slides were left to cool for 20 min, then washed twice in PBST for 5 min. Cover plates were added and the slides placed into a Sequenza rack (Thermo Scientific, UK) before washing in PBST for 5 min. Following this wash endogenous peroxidase activity was blocked by the addition of 120 µl of 3% H_2O_2 (Dako, UK) for 10 min, followed by 2 washes in PBST for 5 min each time. Non-specific staining was blocked by the addition of Total Protein Block (Dako, UK) for 10 min at room temperature. Primary antibodies were diluted in Dako antibody diluent (Dako, UK), added to the slides and incubated for 1 h at room temperature. Negative controls consisted of adding antibody diluent containing no primary antibodies. Following incubation, the slides were washed twice in PBST for 5 min each time and then incubated with Dako Envision labelled polymer or IgG specific secondary antibody for 30 min at room temperature. Following incubation, the slides were washed twice in PBST for 5 min followed by the addition of Dako chromophore/substrate solution (1:50) to the slides, which were incubated for 10 min at room temperature. The slides were then removed from the Sequenza rack and cover plates and placed into a slide rack submerged in water. The slides were counterstained in haematoxylin for 60 s, rinsed in water for 60 s until the purple colour had washed away then placed in Scott's tap water substitute for 30 s before rinsing in water. The slides were then routinely dehydrated and mounted.

2.5.5 Horizontal immunocytochemistry and immunofluorescence using chamber slides

Cells were seeded into 2-well chamber slides (Lab-Tek II, Scientific Laboratory Supplies, UK) to achieve confluences of approximately 80% at 24 h (total of 2 ml media/chamber). Following incubation, the media was discarded, and the cells washed twice in cold PBS. The cells were fixed in cold acetone (500 µl/chamber) for 10 min at 4^{o}C and then washed twice in PBS for 10 min each time.

For immunocytochemistry the slides underwent the same protocol as described for paraffin embedded MTS/tissue starting with the addition of the H_2O_2 solution. To perform immunofluorescence the slides also underwent the same protocol as described for paraffin embedded MTS/tissue starting with the addition of the H_2O_2 solution, continuing up to the addition of the labelled polymer. At this point secondary antibodies conjugated with fluorescent dyes (AlexaFluro 568, IgG. Life Technologies, UK), diluted to 1:300 in Dako antibody diluent (Dako, UK), were added to the chambers and incubated in the dark for 1 h at room temperature. Following incubation, the slides were washed 3 times in PBST for 5 min each time. Slides were then mounted using anti-fade mounting media containing DAPI (Vetorshield, Vector Laboratories Inc, Burlingame, CA, USA).

2.5.6 Image acquisition

High resolution digital scans of the entire microscope slide were obtained using the NanoZoomer ER slide scanner (Hamamatsu Photonics, UK) and viewed using NanoZoomer Digital Pathology software. All mounted slides were stored at room temperature.

2.6 RNA interference

2.6.1 ERα knockdown using siRNA

An individual pre-designed ERα siRNA (J-003401-12; ESR1), a combined mixture of 4 siRNAs (L-003401-00-0005; Smart pool ESR1) and a non-targeting siRNA (D-001810-01) were purchased from the ON-TARGET *plus* series (GE Healthcare Dharmacon, UK). siRNAs were re-suspended to create 20 µM stock solutions using siRNA buffer (Dharmacon, UK) and RNase-free water. The solutions were mixed by pipetting and placed on an orbital shaker for 30 min at room temperature. The concentration of the reconstituted siRNA was then verified using the NanoDrop Spectrophotometer ND1000 (Thermo Fischer Scientific, UK) at 260 nm (for siRNAs 1 µM = 13.3 ng/µl). Aliquots of the stock solution were made and stored at -20^{o}C. Freeze-thaw events were limited to no more than 5 for each stored siRNA.

2.6.2 Liposome-mediated transfection optimisation

MCF-7 cells were seeded into either 96 or 6 well plates at a density of 1.5x 10^3 or 2.3x 10^5 respectively using antibiotic-free, 10% FCS-supplemented DMEM. Cells were seeded to achieve confluences of approximately 20-30% by 24 h. Transfections were performed using the manufacturer's transfection protocol; briefly, 24 h post-seeding the media was removed, and the cells washed in PBS. Antibiotic-free DMEM was then added to the wells (1 ml for 6 well plate, 100 µl for 96 well plate). The transfection protocol consisted of diluting DharamaEFECT 1 transfection reagent (GE Healthcare Dharmacon,UK) into serum and antibiotic-free DMEM and incubating the solution for 5 min at room temperature. Required amounts of siRNA were also diluted into serum and antibiotic-free DMEM which was also incubated for 5 min at room temperature. siRNA was diluted to achieve the desired concentration in the wells (Table 2.8). The 2 solutions were combined and incubated for 20 min at room temperature. The solution was diluted with antibiotic-free 10% FCS-supplemented DMEM then added drop wise to the appropriate wells. Cells were incubated routinely with the media changed to routine DMEM (containing antibiotics and FCS) 24 h post-transfection.

For each experiment controls included; untreated cells, mock transfected cells (cells treated only with transfection reagent but no siRNA) and non-targeted transfected cells (cells transfected with a non-targeting siRNA sequence). Lysates of transfected samples were collected, and efficiency of knockdown was assessed at protein level through western blotting. The expression of the targeted protein in the transfected cells was compared to the expression in the mock and non-targeted treated cells. All transfection reactions were optimised for individual experiments to achieve the maximum knockdown while preserving cell viability.

Table 2.8. siRNA transfection concentrations and volumes required for 96 and 6 well plate formats. Data provided is to achieve siRNA end concentrations of 25 nM.

Reagent	Concentration/volume per well	
	96 Well Plate	**6 Well Plate**
siRNA	0.25 µl	2.5 µl
Volume of FCS and antibiotic-free DMEM used for siRNA dilution	9.75 µl	197.5 µl
Total volume of diluted RNA	10 µl	200 µl
DharmaFECT 1 transfection reagent	0.1 µl	4 µl
Volume of FCS and antibiotic-free DMEM used for DharmaFECT 1 transfection reagent dilution	9.9 µl	196 µl
Total volume of diluted transfection reagent	10 µl	200 µl
Volume of antibiotic-free 10% FCS DMEM added to the combined transfection mixture	80 µl	600 µl
Total end volume of media, transfection reagent and siRNA solution per well	200 µl	2 ml

2.7 Nucleic acid isolation and quantification

2.7.1 RNA extraction and assessment of nucleic acid purity

The RNeasy Mini Kit using QIAshredder technology (Qiagen, UK) was used to extract total RNA from cells following the manufacturer's protocol for the purification of RNA from cells using spin technology. The protocol included the addition of a genomic DNA (gDNA) eliminator column for the removal of gDNA.

Cells were seeded into 75 mm plates at a density of $3x10^6$ cells per plate and incubated for 24 h. Cells were washed twice with PBS before 7 ml of FCS-free media was added. The cells were serum starved for 2 h after which the treatment groups were exposed to 2 Gy radiation. The cells underwent routine trypsinisation at 0, 2 and 8 h post-radiation. A cell suspension containing up to $1x10^7$ cells (the maximum number of cells recommended for each spin column) was centrifuged at 1000 x g for 5 min. The supernatant was removed, and the cell pellet was snap frozen on dry ice and stored at -70^{o}C for subsequent RNA extraction.

For RNA extraction the cell pellet was defrosted on ice and re-suspended in 350-600 µl (depending on cell number) of RLT lysis buffer. The lysate was transferred into a QIAshredder placed into a 2 ml collection tube; the assembled QIAshredder was centrifuged for 2 min at full speed. To eliminate gDNA contamination the homogenised lysate was then transferred to a gDNA eliminator

spin column placed into a 2 ml collection tube and centrifuged for 30 s at 13000 x g. The spin column was discarded but the flow through was saved.

Depending on cell number, 350 or 600 µl of 70% ethanol was added to the homogenised and gDNA-removed lysate before the solution was transferred to a RNeasy spin column placed in a 2 ml collection tube and centrifuged for 15 s at 13000 x g. The flow through was discarded and 700 µl of buffer RW1 was added to the RNeasy spin column and centrifuged for 15 s at 13000 x g to wash the spin column membrane. The flow through was discarded and care was taken to ensure the RNeasy spin column collection tube did not contact the flow through. Two further washes using 500 µl of buffer RPE containing 80% ethanol with centrifugation steps of 15 s and 2 min at 13000 x g were performed to wash the spin column membrane. The RPE buffer dissolves RNA salts but nucleic acids are left behind. After each wash the flow through was discarded. To ensure that no RPE buffer was carried over, the RNeasy spin column was placed in a new 1.5 ml collection tube and centrifuged at full speed for 1 min. The RNeasy spin column was then placed in a new 1.5 ml collection tube and 30-50 µl of RNase-free water was added directly to the spin column membrane, the RNA was eluted by centrifugation for 1 min at 13000 x g. The eluted RNA was used immediately or stored at -20^{o}C.

Extracted RNA samples were assessed for quality and quantified using the NanoDrop Spectrophotometer ND1000 (Thermo Fischer Scientific). Nucleic acid purity was assessed using the A_{260}:A_{280} and A_{260}:A_{230} ratios. An A_{260}:A_{280} ratio value of approximately 2.0 is accepted as pure for RNA. Only good quality RNA with acceptable A_{260}:A_{280} ratios were used in subsequent experiments.

2.7.2 Whole-transcriptome gene expression analysis

Gene expression analysis was performed using Lexogen QuantSeq sequencing (Edinburgh Clinical Research Facility, University of Edinburgh). Analysis was performed by Dr A. K. Turnbull (Cancer Research UK, University of Edinburgh). Full genome expression read-counts were generated using Lexogen QuantSeq 3’ FWD sequencing technology on an Illumina flow cell which was scanned using an Illumina HiScanSQ system. NGS reads were generated towards the poly(A) tail and read 1 directly reflects the mRNA sequence. RNA integrity number (RIN) was generated for each sample to assess RNA quality (Agilent Bioanalyzer);

all samples had RIN values above 9.7. FASTQ files of raw read-count data were pre-processed using the Lexogen recommended BlueBee high-performance NGS analysis software which implemented poly(A) tail trimming and alignment to the Genome Reference Consortium Human genome build 38 reference genome using the Spliced Transcripts Alignment to a Reference (STAR) algorithm[372]. Prior to analysis, data were log2 transformed and quantile normalised in R (Bioconductor) software and packages[373]. Differentially expressed genes were identified using a log2 fold-change increase or decrease cut-off of greater than 1. Gene enrichment and multi-dimensional scaling analysis were performed using R (Bioconductor) software and packages[373]. Pathway-focused analyses, heatmap and cluster analysis were performed using TM4 MeV (multiple experiment viewer) software[374]. Heatmap clustering was carried out using Pearson correlation with average linkage. For integration of gene expression data with public datasets, correction for integration batch effects was performed in R using ComBat[375,376]. Hierarchical clustering of parental and RR cell lines was performed using a published list of genes whose expression profile denotes the breast cancer intrinsic subtypes (basal, normal-like, HER2, luminal A and luminal B)[377]. Assignment of individual samples to intrinsic subtypes was performed using the *genefu* R package[378]. *Genefu* implements a Single Sample Predictor algorithm which is a nearest-centroid classifier. The centroids representing the breast cancer molecular subtypes were identified through hierarchical clustering using the same intrinsic gene list that were used for cluster analysis. Venn diagrams were generated using jvenn[379]. All datasets generated and/or analysed during the study are available in the NCBI's Gene Expression Omnibus[380] and are accessible through GEO Series accession number GSE120798.

2.8 Cancer cell secretome analysis

2.8.1 Assessment of the effects of radiation on secretome profiles of cancer cells

Cells were seeded into 6 well plates to achieve approximately 40–50% confluency at 24 h. Cells were washed 3 times with PBS before 2 ml of FCS-free media was added. The cells were serum starved for 2 h. Cells were then exposed to radiation (0, 2, 4, 6, 8 or 10 Gy) and the conditioned media (CM) was harvested at 1, 2, 4, 8 and 24 h post-radiation for each radiation dose. Secretome samples underwent

processing for liquid chromatography-mass spectrometry (LC-MS) or WB analysis immediately following collection. Following CM harvesting cells were routinely trypsinised and counted using a haemocytometer with trypan blue exclusion (Sigma-Aldrich, UK). Secretome samples were stored at -80^{o}C.

2.8.2 Secretome sample preparation

CM samples were centrifuged at 1000 x g for 5 min at 4^{o}C to remove dead cells and large debris then passed through a 0.22 µm filter (Millex, Merck Millipore, UK). The samples were further centrifuged at 100,000 x g for 60 min at 4^{o}C (Beckman Coulter Optima L-90K Ultracentrifuge with SW 55 Ti rotor); the supernatant was removed and placed into a new universal container. Proteins were concentrated from the supernatant using the Amicon Ultra-0.5 Centrifugal Filter Unit with Ultracel-3 membrane (Merck Millipore, UK) as per the manufacturer's protocol. Briefly, 500 µl of the CM was added to the Amicon Ultra filter device and the sample was centrifuged at 14,000 x g for 30 min at 4^{o}C. The filter was removed and placed upside down into a new 1.5 ml microcentrifuge tube. The sample was centrifuged at 1000 x g for 2 min at 4^{o}C to elute the concentrated protein. Protein concentrations were determined using the BCA assay. The ultrafiltrate was then stored at -80^{o}C prior to undergoing LC-MS or WB analysis.

2.8.3 Liquid chromatography-mass spectrometry (LC-MS) and sample analysis

Secretomic samples underwent in-solution digests for LC-MS analysis, which was performed by Dr J. Wills (Mass Spectrometry Facility, IGMM, University of Edinburgh). Using 96 well plates with silicon lids, 50 µg of protein was added to 2 M urea/100 mM tris/10 mM DTT and heated for 30 min at 50^{o}C. 55 mM iodoacetamide was then added and incubated in the dark for 30 min at room temperature. Trypsin at 1:100 was then added and incubated overnight at room temperature. 10 µg of the resulting peptide solution was loaded onto an activated (20 µl methanol) and equilibrated (100 µl 0.1% trifluoroacetic acid (TFA)) C18 StAGE tip, and washed with 100 µl of 0.1% TFA. Bound peptides were eluted into Protein LoBind tubes with 20 µl of 80% acetonitrile (ACN) and 0.1% TFA solution and concentrated to less than 4 µl in a vacuum concentrator. The final volume was adjusted to 6 µl with

0.1% TFA. Online LC was performed using a Dionex RSLC Nano. Following the C18 clean-up, 5 µg of the peptide solution was injected onto a C18 packed emitter and eluted over a gradient of 2-80% ACN for 120 min with 0.1% TFA. Eluted peptides were ionised at +2 kV before data-dependent analysis on a Thermo Q-Exactive Plus. MS1 was acquired with mz range 300-1650 and resolution 70,000, and the top 12 ions were selected for fragmentation with normalised collision energy of 26, and an exclusion window of 30 s. MS2 were collected with resolution 17,500. The AGC targets for MS1 and MS2 were $3x\ 10^6$ and $5x\ 10^4$ respectively, and all spectra were acquired with 1 microscan without lockmass.

Pre-processing and analysis of data was performed by Dr A. K. Turnbull (Cancer Research UK, University of Edinburgh). Data were analysed using MaxQuant in conjunction with uniport fasta database with match between runs. Prior to analysis all data were log2 transformed. For fold change analysis, data were normalised to untreated controls at each time point using R (Bioconductor) software and packages[373]. Venn diagrams were generated using jvenn[379]. Heatmap and cluster analysis were performed using TM4 MeV (multiple experiment viewer) software[374]. Heatmap clustering was carried out using Pearson correlation with average linkage For integration of gene expression data with public datasets, correction for integration batch effects was performed in R using ComBat[375,376]. Protein interaction networks of candidate biomarkers were generated using the STRING protein interaction database[381] and Markvo clustering algorithms[382].

2.9 Immunohistochemistry and statistical analysis

Image analysis software QuPath[383] version 0.1.2 was used to analyse Ki67, ERα and WNT5a target protein expression. Two-way ANOVA with Holm-Šídák multiple comparisons test was used to test for differences between 2 groups in CF, SRB, invasion and migration assays and WB experiments. Unpaired two-sample t-test was used to test for differences between 2 groups in IHC analysis. p values <0.05 were deemed statistically significant. Data are shown as mean ± SEM with all statistical analysis and graphs generated using Prism 7 (GraphPad Software, San Diego, CA, USA).

3 Materials and Methods: *In Vivo* Experiments

3.1 Introduction

The murine and ovine experiments were performed in accordance with a UK Home Office Project Licence. The murine study was carried out in the BRF facility (University of Edinburgh), with the ovine study performed at the Large Animal Research and Imaging Facility (LARIF) at Dryden Farm (University of Edinburgh) and at the Royal (Dick) School of Veterinary Studies (University of Edinburgh). The rat experiments were conducted at the Institute for Biomedical Research (University College London). All studies were performed using my own personal licence gained through the Scottish Accreditation Board in accordance with the Animals (Scientific Procedures) Act 1986. All projects were approved by either the University of Edinburgh or University College London Animal Ethics Committee. The recommended guidelines for welfare and use of animals in research were followed.

The following materials and methods sections will cover general procedures relating to each animal model. The development of specific novel techniques will be described in-depth in the relevant result chapters.

3.2 Biocompatibility assessment of common implantable sensor materials in a tumour xenograft model

3.2.1 Background

CD-1 female nude mice (Charles River Laboratories, Tranent, UK) were used in all experiments. The mice were allowed a period of adaptation of at least 7 days before use in experiments and were housed in cages of 6 on an alternating 12 h light cycle in a sterile and specific pathogen-free environment, with ad libitum access to food and water. As nude mice are immunocompromised, they were housed in individually ventilated cages in a barrier environment.

3.2.2 Generation of MDA-MB-231 stock xenograft tumours

MDA-MB-231 cells were grown routinely, trypsinised and counted as previously described in sections 2.2.4 and 2.2.5. Approximately $2x\ 10^9$ cells were re-suspended in 1 ml of FCS-free DMEM. Using a 21G needle, 0.1 ml of this cell suspension was injected bilaterally into subcutaneous tissue of the flanks of 5 mice.

Mice were monitored for the development of xenograft tumours which occurred within 6-8 weeks post-injection.

3.2.3 Generation of MDA-MB-231 xenograft tumours for biomaterial implantation

Once stock tumours had grown to an adequate size (approximately 0.7-1.2 cm in length), mice were euthanised by cervical dislocation. In a sterile cabinet, xenograft tumours were harvested and placed into DMEM with no additives and sectioned into small fragments, approximately 1-2 mm in length. Implantation of tumour fragments into experimental mice was performed under local anaesthetic (ethyl chloride) using a 12G trocar. Each mouse received 1 tumour fragment injected bilaterally into subcutaneous tissue of the flanks. Mice were monitored for the development of xenograft tumours which occurred within 6-8 weeks post-implantation. The tumour uptake success rate was approximately 90%.

3.2.4 General anaesthesia for biomaterial implantation procedures

Mice underwent general anaesthesia using 5% isoflurane (IsoFlo, Abbot Animal Health, Maidenhead, UK) gaseous anaesthesia delivered in room air. Animals were positioned onto a heat mat to maintain rectal temperature between 36.5–37.5^{o}C and adequate depth of anaesthesia was maintained using end-tidal concentrations of 1.5-2.0% isoflurane. All animals were euthanised when required by cervical dislocation.

3.2.5 Biomaterial fabrication

The outward-facing materials of the IMPACT sensor were selected for testing; the materials chosen were silicon dioxide (SiO_2), silicon nitride (Si_3N_4), Parylene-C, Nafion, OG116-31 resin (Epoxy Technology) and platinum (Pt). Materials were prepared in the Scottish Microelectronics Centre Class 10 cleanroom facility (Kings Buildings, University of Edinburgh) and comprised of 3–7 mm long pieces of titanium (Ti) wire, diameter 0.4 mm, coated with the material to be tested. Copper (Cu) wire (99.999% purity; Sigma Aldrich, UK) was used for positive control samples.

3.2.6 Biomaterial manufacture

Manufacture of materials for xenograft implantation was performed by Dr E. Blair and Dr J. Marland (School of Engineering, University of Edinburgh). For all coated materials Ti wire was first cleaned in isopropyl alcohol at 50°C with ultrasonic agitation for 15 min, followed by the same treatment in deionised water, then dried using an N_2 gun; Cu wire was also cleaned using the same protocol. Parylene-C samples were produced using a vapour deposition system SCS (Speciality Coating Systems 2010 Labcoater), ensuring a conformal coating of 5 μm of Parylene-C. SiO_2 and Si_3N_4 samples were prepared using Plasma Enhanced Chemical Vapour Deposition (PECVD); a 1 μm layer of each material was deposited. Pt samples were produced using electron-beam evaporation in an ANS Cluster tool which deposited a 50 nm thick Pt film onto the wire. Nafion samples were created by dipping Ti wire in a solution of 5% by weight Nafion in lower aliphatic alcohols and water, before air curing for 5 min; the process was repeated 5 times before curing for 1 h at 120°C[145]. Resin samples were produced by dip coating the Ti wire in OG116-31 resin which were then cured for 800 s under ultraviolet light. After completion of each coating process wires were optically inspected to ensure uniformity. All wires were sterilised prior to implantation. Nafion coated wires were sterilised by routine autoclaving; all other biomaterials were sterilised in 100% ethanol for 10 min, rinsed in deionised water and stored in penicillin and streptomycin. All wires were washed in sterile distilled water immediately before implantation.

3.2.7 Immunohistochemistry

Sections for IHC underwent routine vertical IHC and counterstaining in haematoxylin as described in section 2.5.4. Primary antibodies used in the murine study are described in Table 3.1. Appropriate positive and negative controls were included in all IHC staining protocols (Figure 3.1). The staining pattern of each antibody was verified by a board-certified veterinary pathologist (Dr L. Morrison, The Royal (Dick) School of Veterinary Studies, University of Edinburgh). Additional sections were also routinely stained with haematoxylin and eosin (H&E) or Masson's Trichrome as described in sections 2.5.2 & 2.5.3.

Table 3.1. Primary antibodies used in the murine experiments.

Primary antibody target antigen	Histological marker/cited publications	Antibody details and antigen retrieval solution	Manufacturer	Dilution
Anti-Ki67	Proliferation[384-387]	Rabbit mAb Sodium citrate	Abcam; ab92742	1:1000
Anti-carbonic anhydrase 9	Hypoxia[117,388,389]	Rabbit pAb Sodium citrate	Abcam: ab15086	1:750
Anti-cleaved caspase 3	Apoptosis[390-393]	Rabbit pAb Sodium citrate	Cell Signaling Technology; 9661	1:150
Anti-Ly-6G	Neutrophil[394-397]	Rat mAb EDTA	Abcam; ab25377	1:50
Anti-F4/80	Macrophage[398-401]	Rat mAb Enzymatic	Biolegend; 123101	1:100
Anti-ER-TR7	Fibroblast[402-405]	Rat mAb Enzymatic	Novus Biologicals; NB100-64932	1:50

3.2.8 Immunohistochemical analysis

QuPath version 0.1.2[383] was used to analyse target protein expression and the percentage area of tumour necrosis using the entire tumour area contained within whole slide images. The image analysis pipeline was comprised of several steps. The initial step required, for both target protein expression and percentage area of tumour necrosis analysis, was to isolate the diagnostically relevant areas within the tissue in each whole slide image. Extraneous tissue such as subcutaneous fat and skin was excluded from image analysis and all areas of necrosis were identified. H&E stained sections were used to calculate the percentage area of tumour necrosis; the area of necrosis was divided by the total tumour area (tumour tissue and necrotic area) and then multiplied by 100 (Figure 3.2 & Figure 3.3). Further steps were required for target protein expression analysis. Intensity thresholds and detection parameters for positive and negatively stained cells for each antibody were optimised (Table 3.2). DAB-positive cells were detected using positive cell detection and negative cells were detected by haematoxylin staining. These antibody specific parameters were then applied to every section stained using that antibody. All results were visually assessed for accuracy in all tumour sections following analysis. Examples of this method of cell detection are shown for each antibody in Figure 3.4-Figure 3.15. To calculate the percentage of positively stained cells, the number of positively stained cells was divided by the total number of cells and then multiplied by 100.

Table 3.2. QuPath parameters for cell detection. Intensity threshold values were optimised for each specific antibody other values remained as default settings.

Parameter	Setting	Parameter	Setting
Scan magnification	20x	Max. background intensity	2
Stain vectors	QuPath default	Split by shape	on
Detection image	Haematoxylin OD	Exclude DAB	off
Pixel size	0.5 µm	Cell expansion	5
Background radius	8 µm	Include cell nucleus	on
Median filter radius	0 µm	Smooth boundaries	on
Sigma	1.5 µm	Make measurements	on
Minimum area	10 µm	Score compartment	Nucleus DAB OD mean
Maximum area	400 µm	Threshold 1+	**Antibody specific**
Intensity threshold	0.1	single threshold	on

Threshold 1+	
Ki67, CA9, Ly-6C, F4/80	0.2
Caspase 3	0.1
ER-TR7	0.45

Image J (NIH, Bethesda, MD, USA) was used to analyse the percentage area of collagen using the entire tumour area contained within whole slide images. A colour deconvolution macro programme developed by Dr L. Murphy (IGMM, University of Edinburgh) was used in conjunction with Image J for this purpose. Following the isolation of the diagnostically relevant areas (as was performed with the QuPath analysis) and colour deconvolution, thresholds were set to detect collagen appearing as red on a white background. This stain specific threshold was then applied to every section. All results were visually checked for accuracy in all tumour sections following analysis. Examples for collagen detection using whole slide images are shown in Figure 3.16 & Figure 3.17. To calculate the percentage area of collagen, the stained area was divided by the total area and then multiplied by 100.

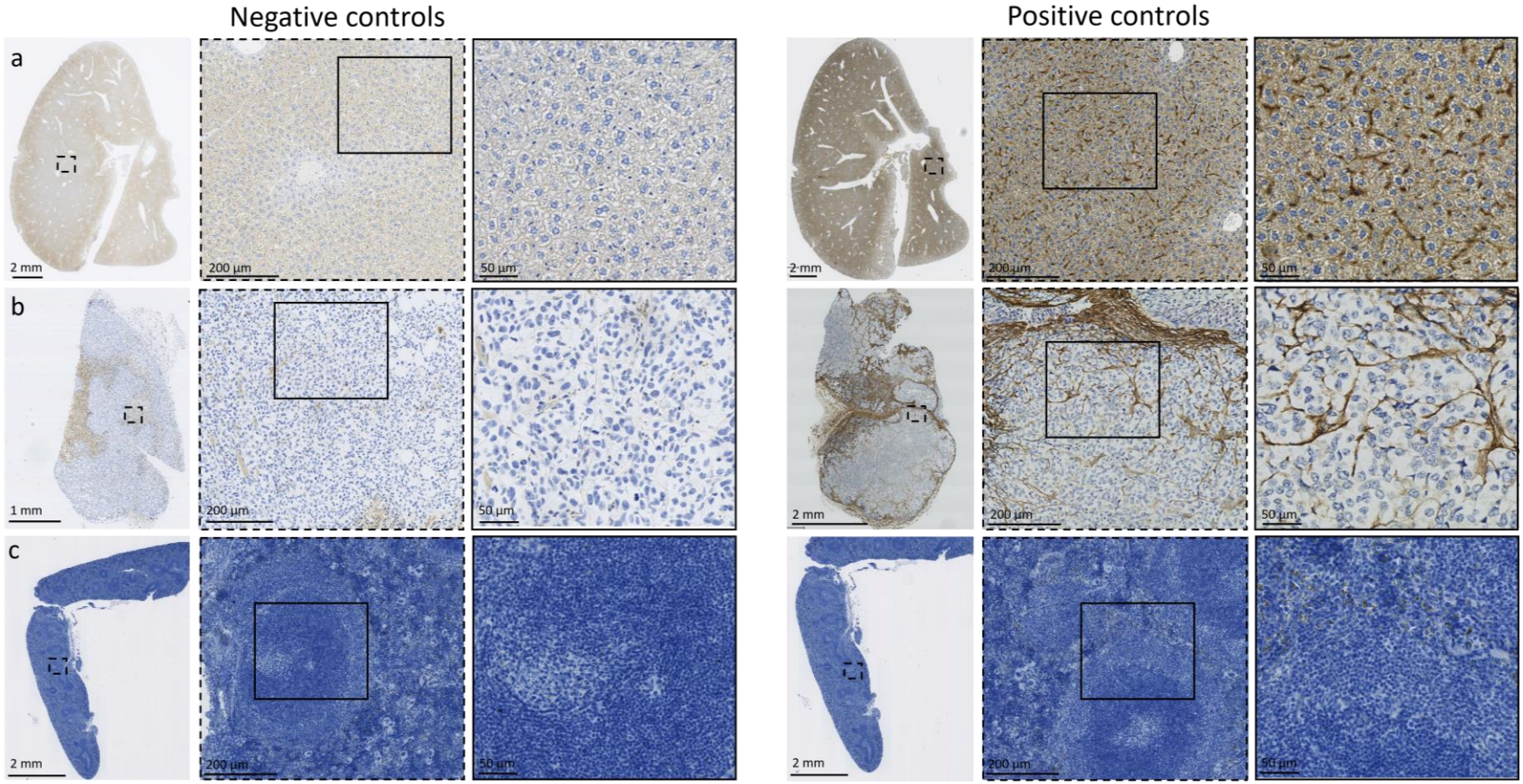

Figure 3.1. Positive controls used for verifying murine immune antibodies. (**a)** Liver used for F4/80 (macrophage), **(b)** SKOV xenograft tumour used for ER-TR7 (fibroblast), **(c)** Spleen used for Ly-6G (neutrophil). Negative controls underwent the same IHC procedure as for positive controls, with the exception that antibody diluent containing no primary antibodies was added to the slides. Positive DAB staining is seen for each antibody at the expected cellular localisation region and in the correct cell type: positive F4/80 staining is seen predominately at the cell membrane in hepatic macrophages, ER-TR7 staining is seen predominantly in the cytoplasm in fibroblasts, Ly-6G staining is seen in the cytoplasm of neutrophils.

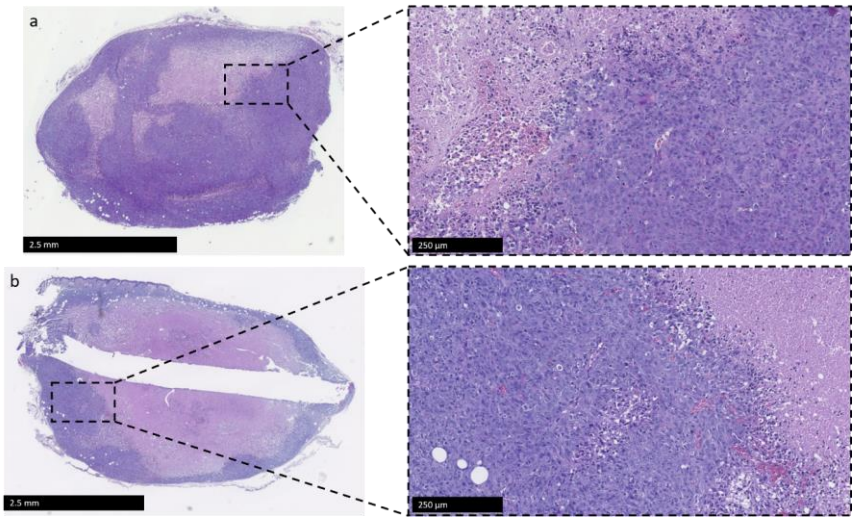

Figure 3.2. Representative H&E stained sections from tumours harvested at day 7. (**a)** Untreated, **(b)** Parylene-C implanted.

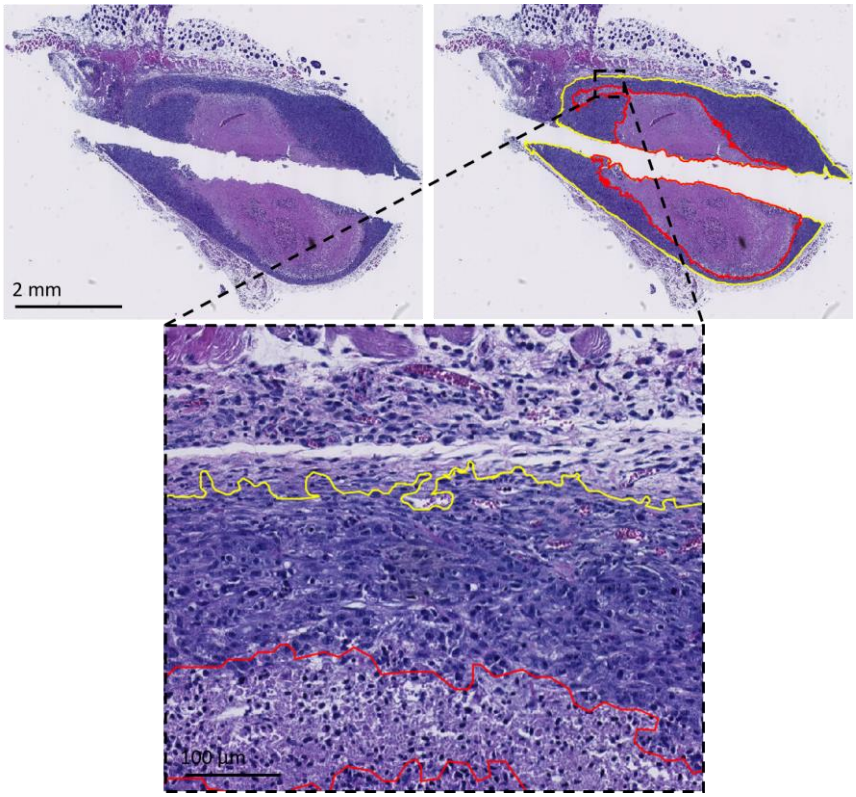

Figure 3.3. Representative H&E stained sections for QuPath analysis of the area of necrosis. Yellow line is outlining the total tumour area including the necrotic area, but with the removal of skin and subcutaneous tissue. Red line is outlining the area of necrosis.

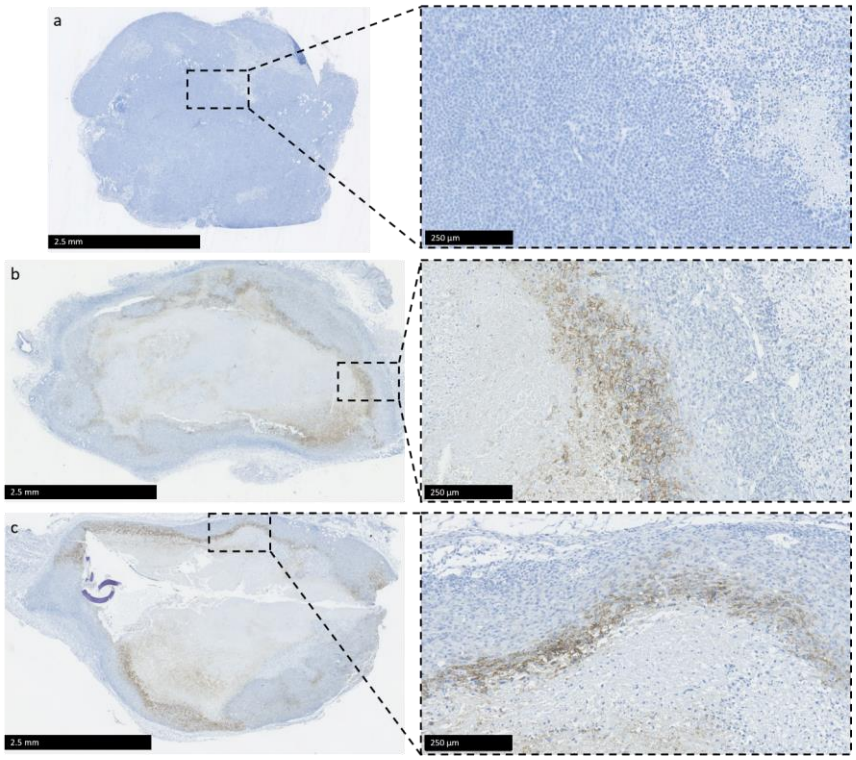

Figure 3.4. Representative CA9 stained sections from tumours harvested at day 7. (**a)** Negative control, **(b)** Untreated, **(c)** Nafion implanted.

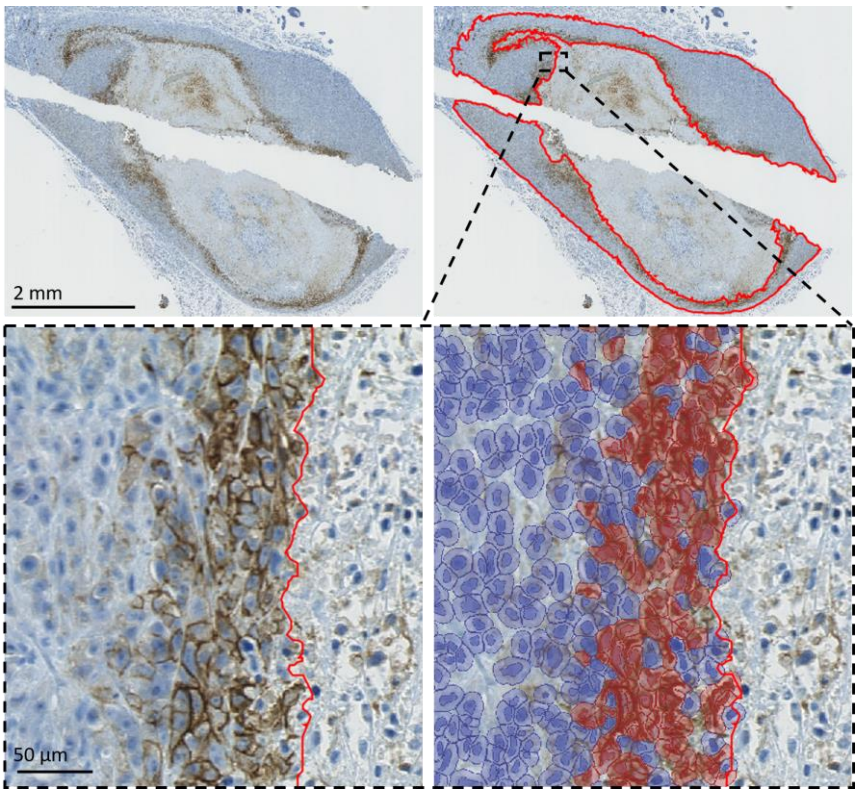

Figure 3.5. Representative CA9 stained sections for QuPath analysis of hypoxia. CA9 staining, as expected, is predominantly localised to the cell membrane.

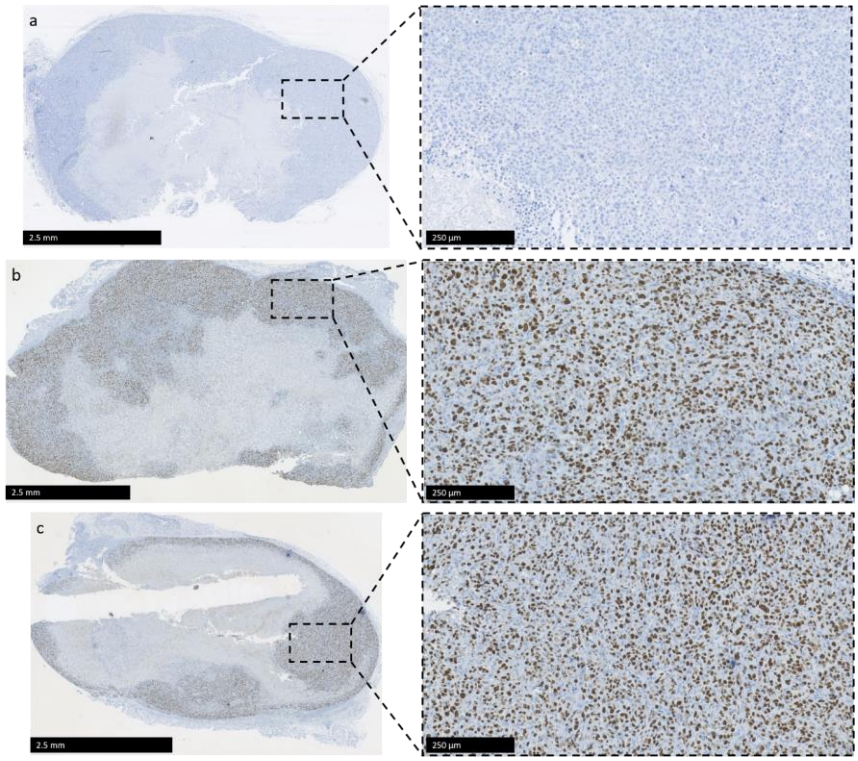

Figure 3.6. Representative Ki67 stained sections from tumours harvested at day 7. (a) Negative control, **(b)** Untreated, **(c)** Silicon dioxide implanted.

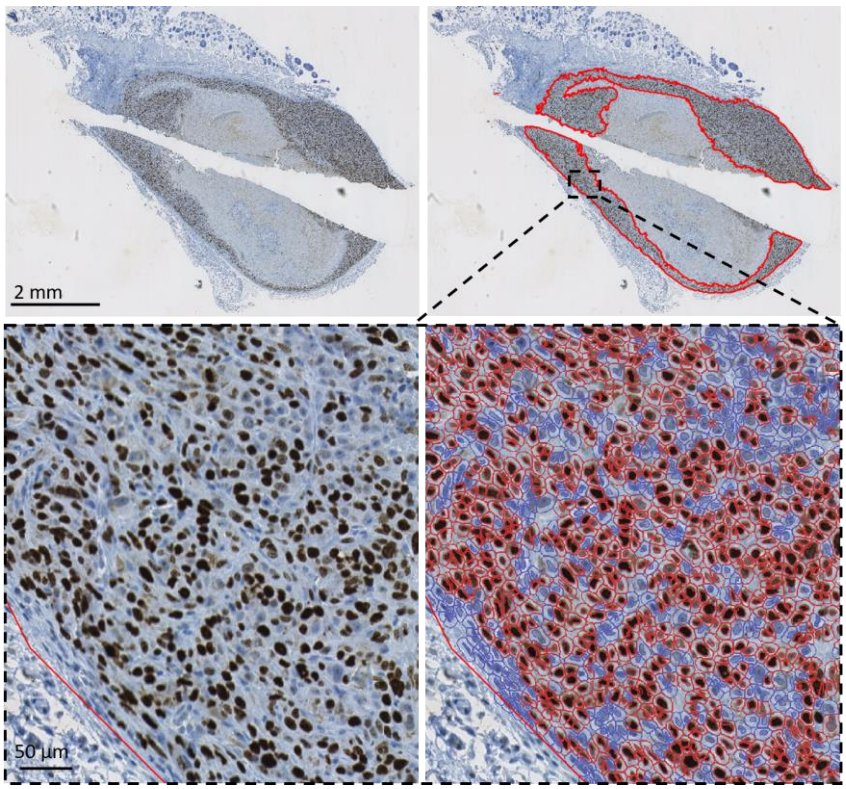

Figure 3.7. Representative Ki67 stained sections for QuPath analysis of proliferation. Ki67 staining, as expected, is localised to the cell nucleus.

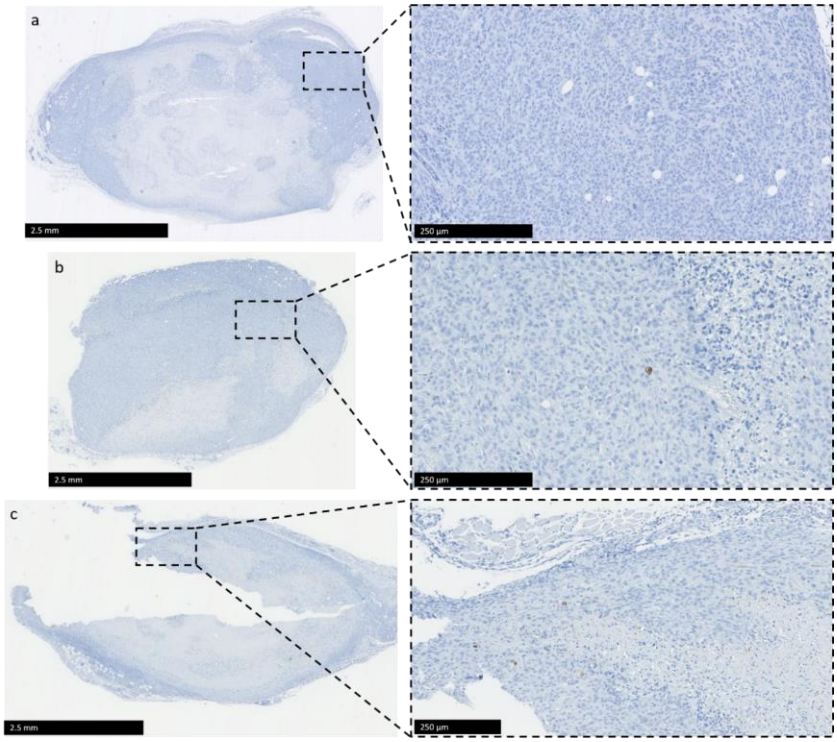

Figure 3.8. Representative caspase 3 stained sections from tumours harvested at day 7. (a) Negative control, **(b)** Untreated, **(c)** Copper implanted.

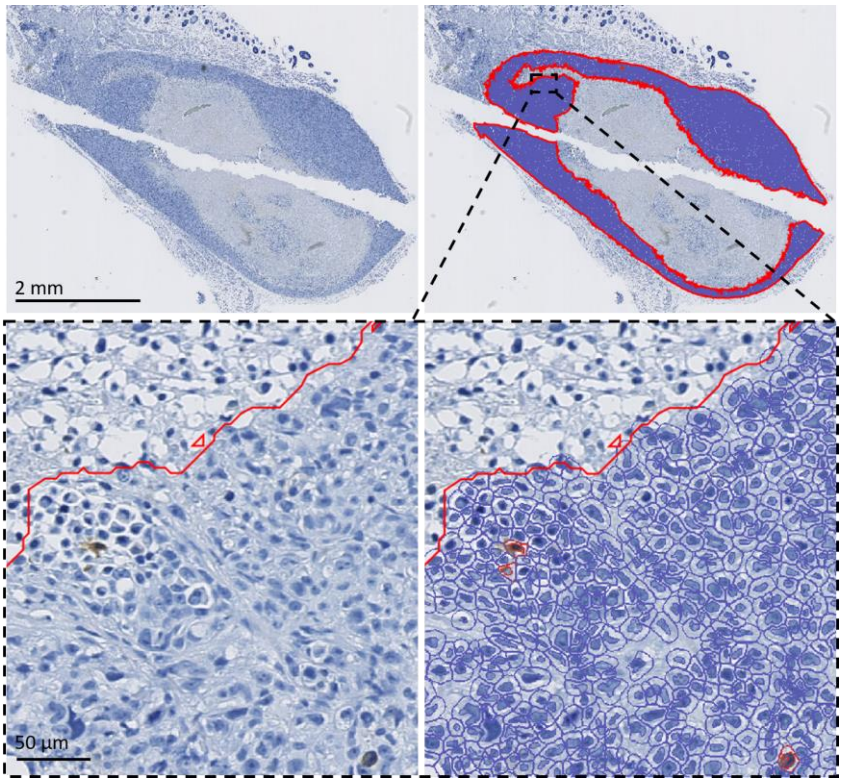

Figure 3.9. Representative caspase 3 stained sections for QuPath analysis of apoptosis. Caspase 3 staining, as expected, is predominantly localised to the cytoplasm.

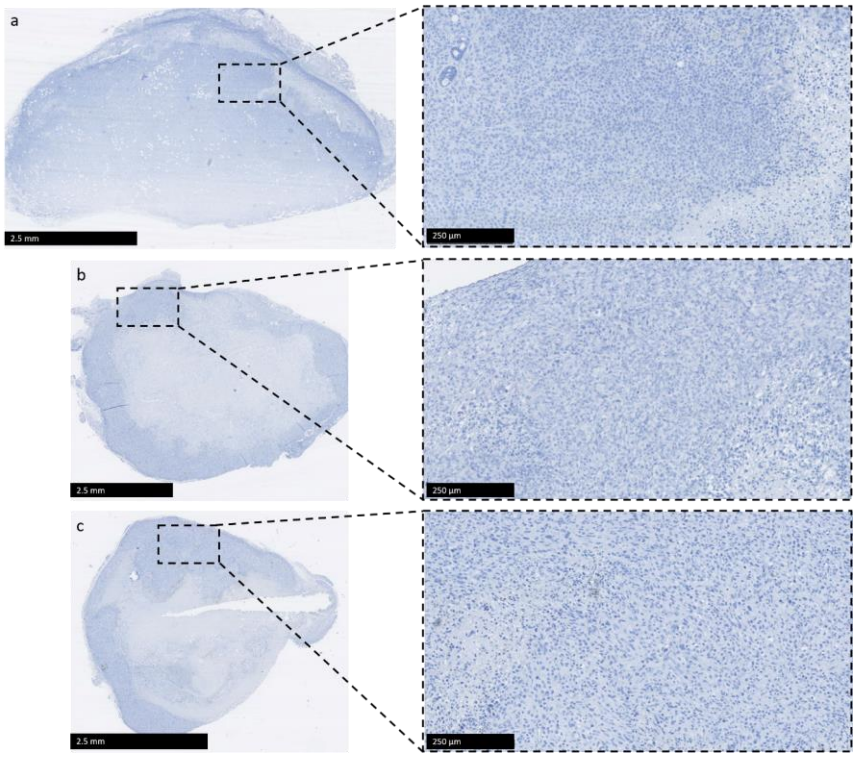

Figure 3.10. Representative Ly-6G stained sections from tumours harvested at day 7. (a) Negative control, **(b)** Untreated, **(c)** Silicon nitride implanted.

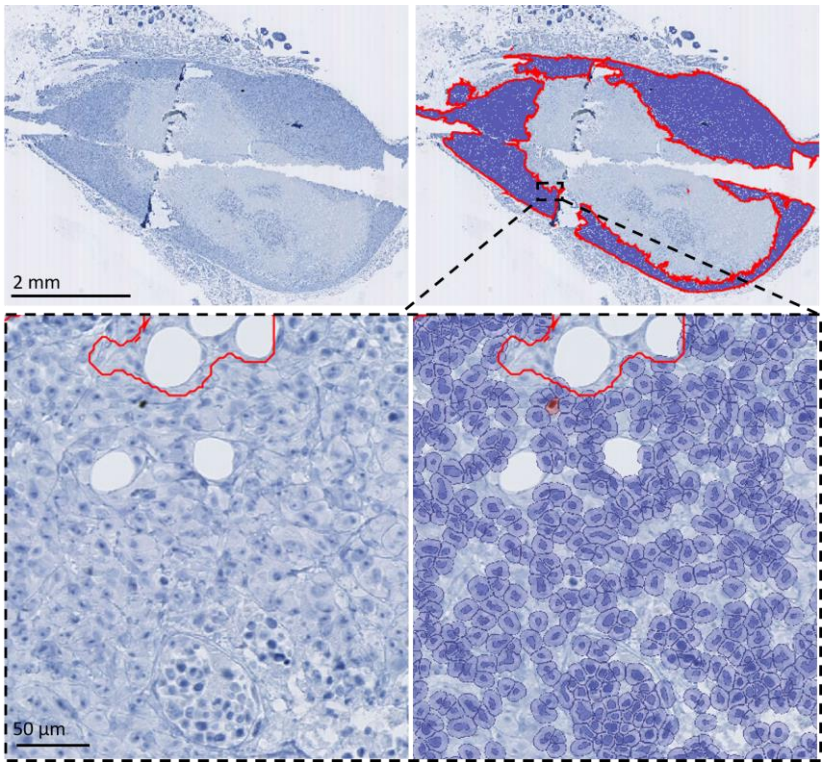

Figure 3.11. Representative Ly-6G stained sections for QuPath analysis of neutrophil numbers. Ly-6G staining, as expected, is predominantly localised to the cytoplasm.

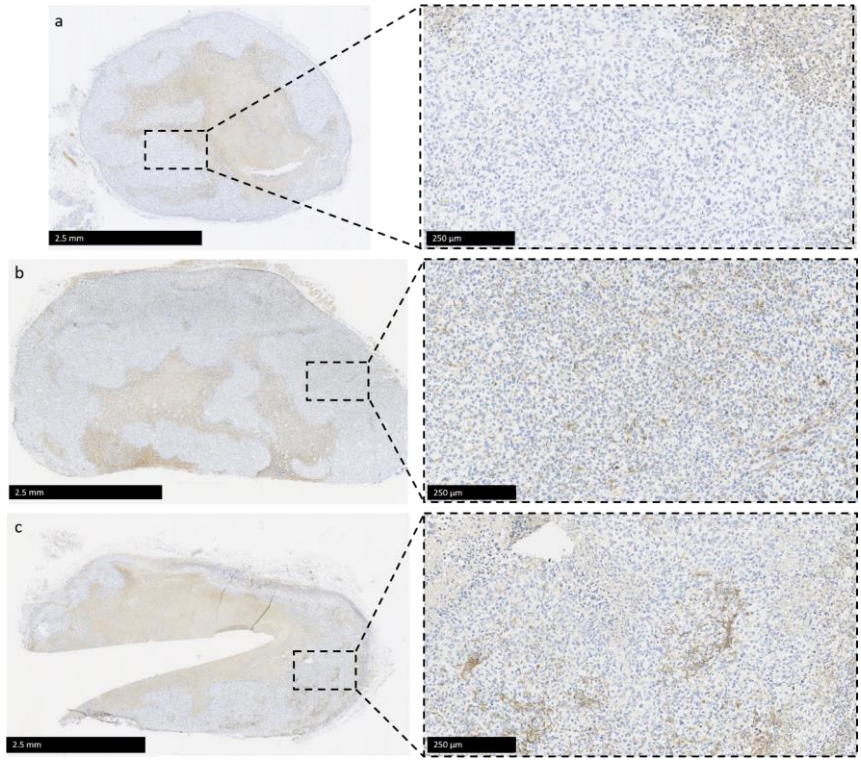

Figure 3.12. Representative F4/80 stained sections from tumours harvested at day 7. (a) Negative control, **(b)** Untreated, **(c)** Parylene-C implanted.

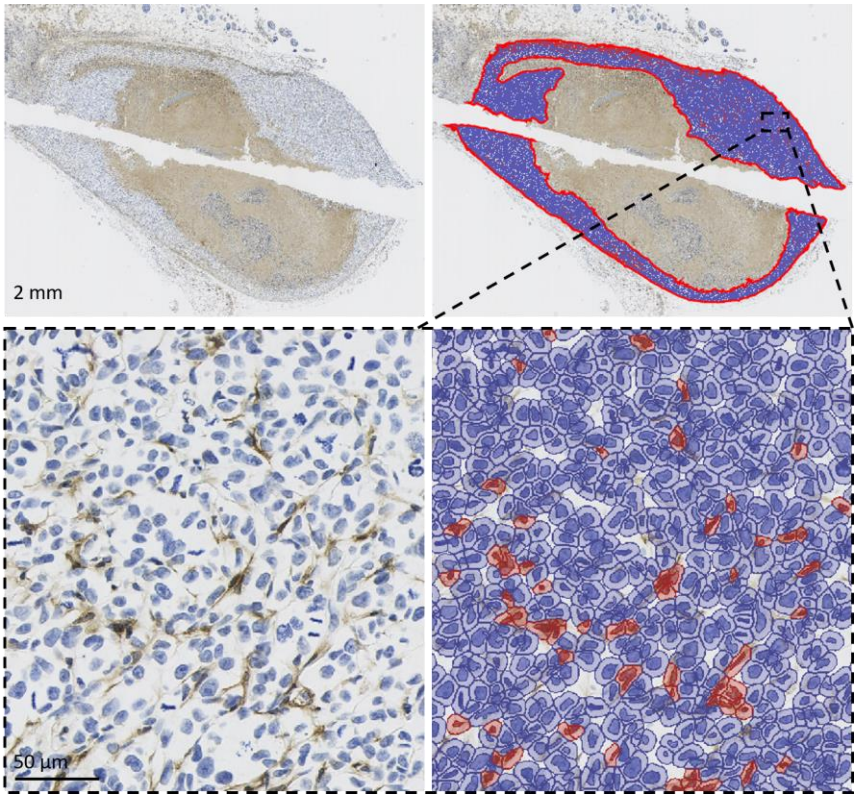

Figure 3.13. Representative F4/80 stained sections for QuPath analysis of macrophage numbers. F4/80 staining, as expected, is predominantly localised to the cell membrane.

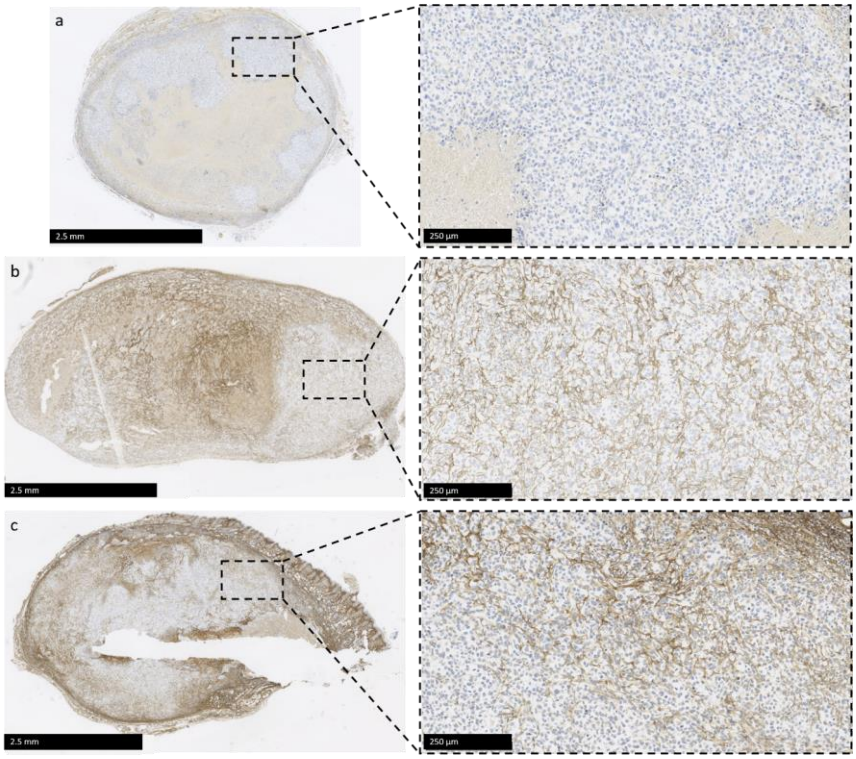

Figure 3.14. Representative ER-TR7 stained sections from tumours harvested at day 7. (a) Negative control, **(b)** Untreated, **(c)** Platinum implanted.

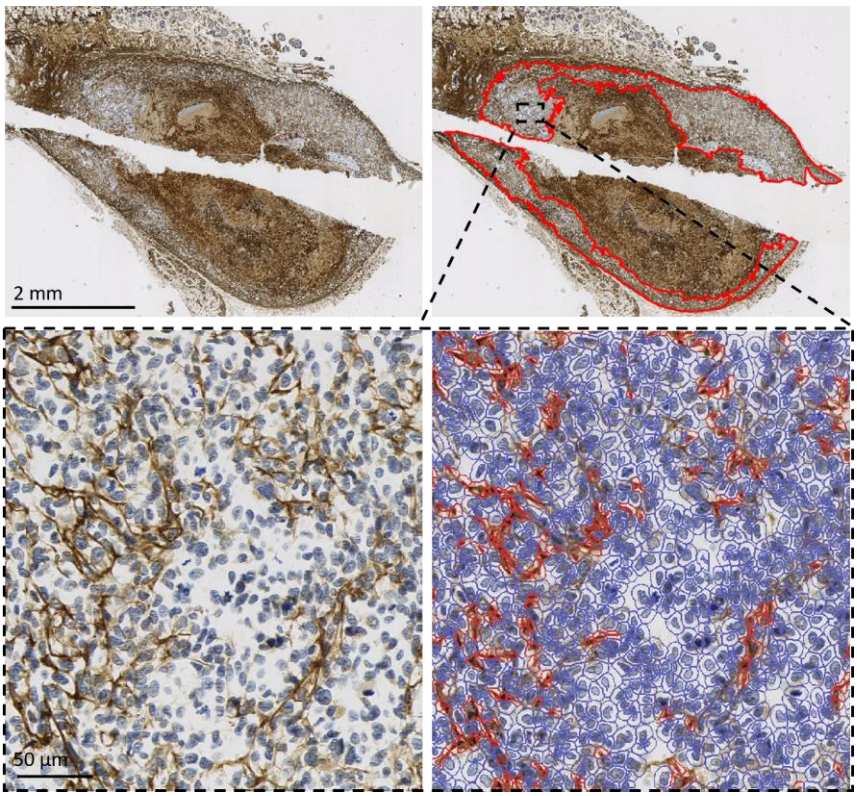

Figure 3.15. Representative ER-TR7 stained sections for QuPath analysis of fibroblast numbers. ER-TR7 staining, as expected, is predominantly localised to the cytoplasm.

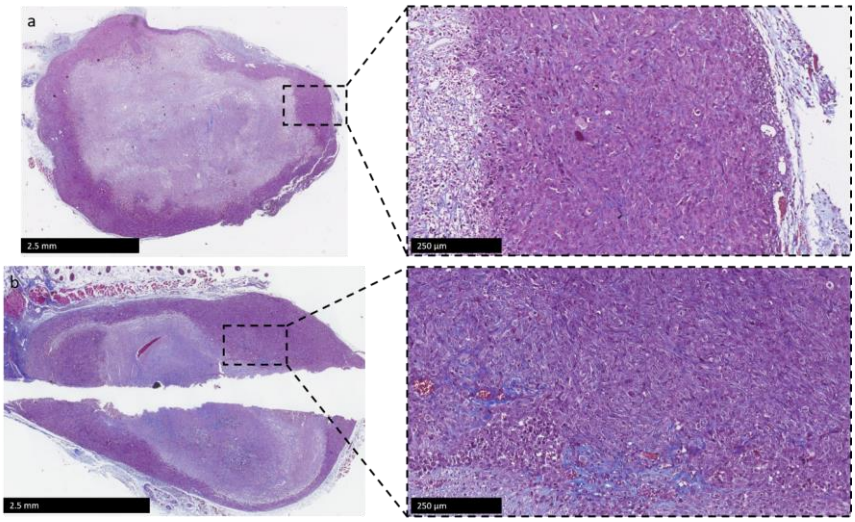

Figure 3.16. Representative Masson's trichrome stained sections from tumours harvested at day 7. (a) Untreated, **(b)** Silicon dioxide implanted.

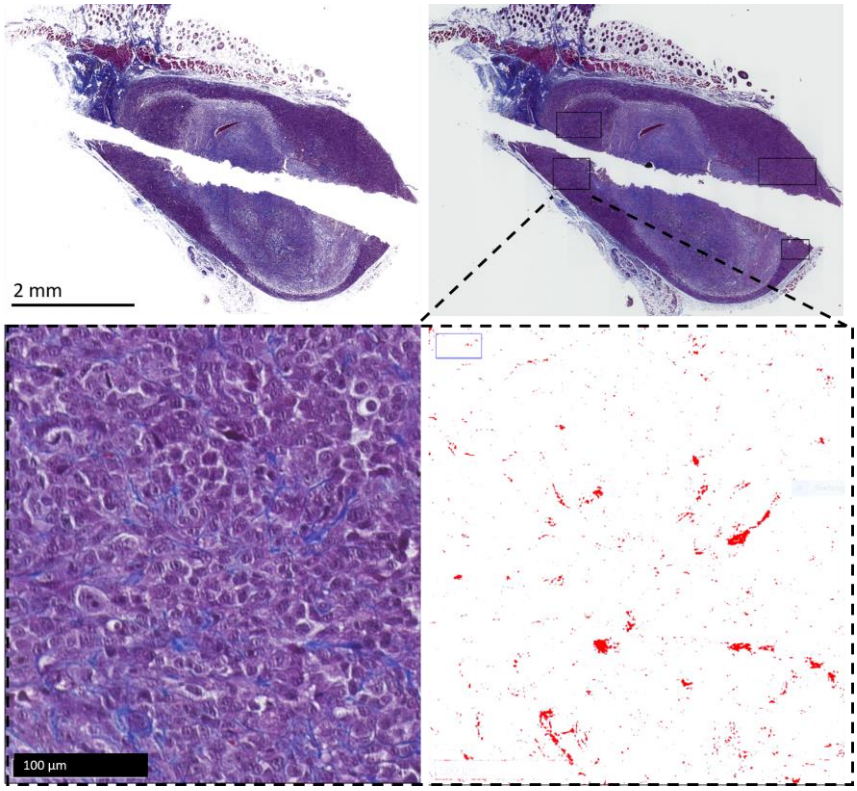

Figure 3.17. Representative Masson's trichrome stained sections for Image J analysis of collagen deposition. Following colour devolution, the collagen is highlighted in red against a white background.

3.3 Validation of functionality of the IMPACT oxygen sensor to measure tissue oxygen tension for clinical applications

3.3.1 Background

Male Wistar rats (Charles River Laboratories, Margate, UK) of approximately 400 g body weight were used in all experiments. Prior to instrumentation, the rats were allowed a period of adaptation of at least 7 days and were housed in cages of 4 on an alternating 12 h light cycle in a specific pathogen-free environment, with ad libitum access to food and water.

3.3.2 Anaesthesia, arterial and venous cannulation and tracheostomy tube placement

Rats underwent general anaesthesia using 5% isoflurane (IsoFlo, Abbot Animal Health, Maidenhead, UK) gaseous anaesthesia delivered in room air and were positioned onto a heat mat to maintain rectal temperature between 36.5–37.5^{o}C, which was continuously recorded using a temperature sensor (Harvard Apparatus, Cambridge, UK). Adequate depth of anaesthesia was maintained using end-tidal concentrations of 1.5-2.0% isoflurane. Placement of arterial and venous cannulas was performed in accordance with a previous study[406]. A 2 cm ventral midline cervical incision was made with cervical dissection to identify the right internal jugular vein and left common carotid artery. Both vessels were cannulated using 0.96 mm external diameter PVC catheters (Scientific Commodities Inc., Lake Havasu City, AZ, USA) (Figure 3.18 & Figure 3.19) and secured in place with 1 metric braided silk (Ethicon, UK). The arterial line was subsequently connected to a pressure transducer (Powerlab, AD Instruments, Chalgrove, UK) for continuous monitoring and recording of mean arterial blood pressure and heart rate; this was performed by connecting the transducer to a computer using a 16-channel Powerlab system and Chart 5 acquisition software (AD Instruments, Charlgrove, UK). The arterial line was also used for intermittent blood sampling; when required, 0.1 ml of arterial blood was taken into heparinised capillary tubes for immediate blood-gas (pH, pCO_2, pO_2, HCO_3^-, arterial base deficits and paO_2), biochemical (glucose, lactate, Na^+, K^+, Cl^-, Ca^{2+}) and haematological (tCO_2, Hct, Hgb) analysis (ABL90 Analyser; Radiometer, Copenhagen, Denmark). The venous line was used for the

administration of fluids; all animals received surgical doses of crystalloid fluids throughout the procedures, which consisted of a continuous infusion of 10-20/ml/kg/h compound sodium lactate (Aqupharm No 11, Animalcare, York, UK) to sustain cardiac preload and replace lost fluids and electrolytes. Mean arterial blood pressure was maintained at approximately 100 mmHg. A tracheostomy was created using 2.08 mm external diameter polythene tubing (Portex Ltd, Hythe, UK); this was attached to a T-piece breathing circuit to secure the airway, maintain anaesthesia and allow changes in the inspired fractional oxygen concentration (FiO_2) to be delivered (Figure 3.20). All animals were euthanised with intravenous sodium pentobarbitone (Pentoject; Animalcare, York, UK).

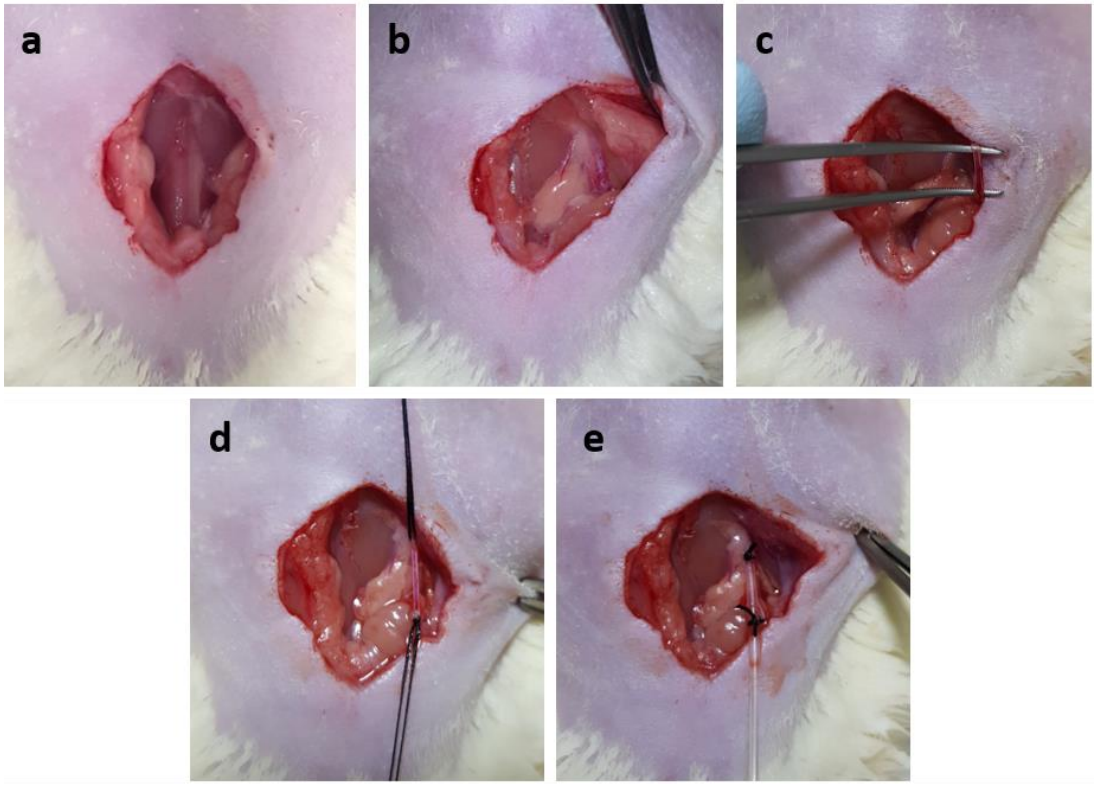

Figure 3.18 Intra-operative photographs depicting cannulation of the right jugular vein. (a) A 2 cm ventral cervical skin incision is made. **(b&c)** Cervical dissection is performed to allow identification and mobilisation of the right jugular vein. **(d)** One untied suture is placed distally around the jugular vein and a second is placed proximally and tied securely, leaving about 1 cm of vein between the 2 sutures. **(e)** A venotomy is created just distal to the proximal suture; the cannula is inserted and advanced 2-3 cm into the vein before tying the distal suture around the vein and cannula.

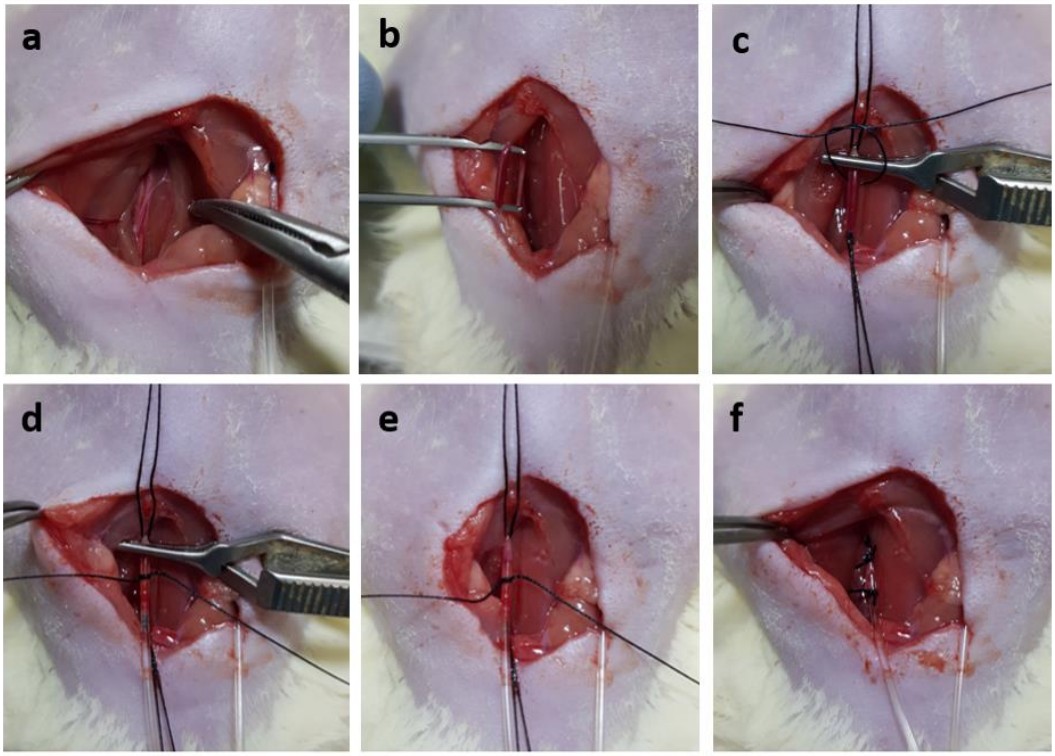

Figure 3.19. Intra-operative photographs depicting cannulation of the left carotid artery. (a) Cervical dissection is performed to allow identification of the left carotid artery. **(b)** The carotid artery is dissected from the vagus nerve. **(c)** One untied suture is placed distally around the carotid artery and a second is placed proximally and tied securely leaving about 1.5 cm of artery between the 2 sutures. A clamp is added just proximal to the distal suture before placing a third untied suture. **(d)** An arteriotomy is created between the 2 sutures and the cannula is inserted and advanced up to the clamp. **(e)** The third suture is tied loosely over the cannula and the clamp is removed. **(f)** The cannula is advanced a further 2 cm before tying the distal suture around the artery and cannula.

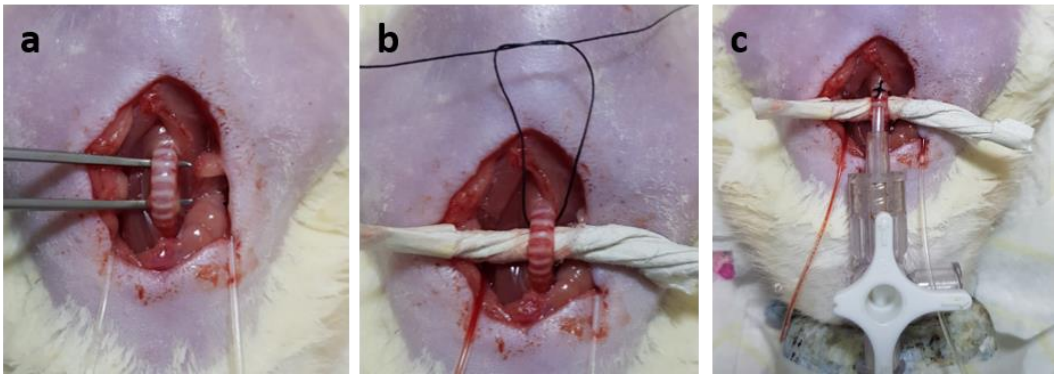

Figure 3.20. Intra-operative photographs depicting placement of a tracheostomy tube. (a) Cervical dissection is performed to allow identification of the trachea. **(b)** The trachea is elevated and maintained in position with a piece of sterile paper and an untied suture is placed distally. **(c)** An incision is made between tracheal cartilage rings through which the tracheostomy tube is inserted. The tubing is advanced 1 cm before tying the distal suture around the trachea and tracheostomy tube. The tubing is attached to a 3-way tap connected to the inflow of anaesthetic gases.

3.4 Development of a pre-clinical ovine pulmonary adenocarcinoma model for human lung cancer and validation of intra-tumoural functionality of the IMPACT oxygen sensor

3.4.1 Background

For initial protocol development, post-mortem carcasses were obtained through the Royal (Dick) School of Veterinary Studies Large Animal Practice (University of Edinburgh). All experimental OPA sheep were obtained in collaboration with Dr C. Cousens at the Moredun Institute (Pentland Science Park, UK) through an on-farm ultrasound eradication programme run by Dr P. Scot.

Eight post-mortem carcases were used for initial protocol development. A total of 12 adult female sheep diagnosed with OPA were used in the study. Of these cases, 3 were used to refine the model and 9 were used in experimental procedures. All sheep weighed between 39-76 kg and were transported direct from the farm of origin to Dryden farm. Sheep were bedded on straw, with ad libitum access to food and water in groups of at least 2 animals and were allowed a period of adaptation of at least 24 h before undergoing anaesthesia. Anaesthesia, CT imaging, sensor placement and post-mortem examinations were carried out at the Large Animal Research and Imaging Facility (LARIF) at Dryden Farm (University of Edinburgh).

3.4.2 General anaesthesia for CT imaging and sensor implantations

All sheep underwent pre-anaesthetic assessment, which included distant observation of demeanour and breathing, followed by physical examination. Only animals that passed veterinary assessment underwent anaesthesia and surgery. Food was withheld for 12 h before anaesthesia, but access to water was permitted until pre-anaesthetic medication was administered. Anaesthesia was managed by a specialist team of anaesthetists at the LARIF.

All sheep received pre-anaesthetic sedation to reduce stress, facilitate the induction of anaesthesia and decrease induction agent dose requirements. To limit the risk of sedation-induced respiratory decompensation, intravenous sedative administration was followed by induction of general anaesthesia within 10 min. This pre-anaesthetic sedation was achieved by the intravenous injection of medetomidine in combination with midazolam. Following sedation, the head was elevated to limit

respiratory secretions and rumen contents entering the upper airway. Once sedative effects were evident, generally within 5 min, intravenous propofol was given to effect to allow endotracheal intubation. Intubation was assisted by a laryngoscope with a long (350 mm) blade and a rigid atraumatic stylet; suction was also used when required to aid larynx visualisation; once intubated, the endotracheal tube cuff was inflated and secured in place. Generally, a 10 mm internal diameter endotracheal tube was required for a 30-60 kg sheep. Oropharyngeal and tracheobronchial suction was used as required. Morphine in combination with flunixin was given pre-emptively, either at the time of sedation or immediately post-induction, to provide analgesia for the duration of anaesthesia (Table 3.3).

Anaesthesia was maintained with isoflurane (IsoFlo, Abbot Animal Health, Maidenhead, UK) vaporised in an O_2/air mixture administered via a Bain or circle breathing system connected to the endotracheal tube; end-tidal concentrations of 1.5-2.0% isoflurane were used to maintain adequate depth of anaesthesia. After tracheal intubation, intermittent positive pressure, volume controlled, ventilation was provided using a mechanical ventilation system to achieve adequate tidal volumes of 8-10 ml/kg. Respiratory rate was adjusted to maintain normocapnia ($PaCO_2$ range 4.7–6 kPa). To aid ventilation sheep were positioned in sternal recumbency; however, animals were placed temporarily in lateral recumbency, with OPA lesion(s) uppermost, for CT imaging and sensor implantation (Figure 3.21).

Body temperature was monitored using rectal and oesophageal temperature sensors and maintained between 38.5–39.5ºC. A central (jugular) venous 14G cannula was placed which was used for the administration of drugs and crystalloid fluids. Animals received surgical doses of fluids throughout anaesthesia and surgery, which consisted of a continuous infusion of 5-10/ml/kg/hr compound sodium lactate (Aqupharm No 11, Animalcare, York, UK) to maintain cardiac preload and replace lost fluids and electrolytes. Mean arterial blood pressure was maintained at approximately 70-80 mmHg. An arterial cannula was placed in the central auricular artery which was used for intermittent blood sampling; when required, 1 ml of arterial blood was taken into heparinised syringes for immediate blood-gas (pH, pCO_2, pO_2, HCO_3^-, arterial base deficits and paO_2), biochemical (glucose, lactate, creatinine, Na^+, K^+, Cl^-, Ca^{2+}) and haematological (tCO_2, Hct, Hgb) analysis (Epoc

portable blood-gas electrolyte and critical care analyser; Woodley Equipment Company Ltd, Lancashire, UK). A multiparameter patient monitoring device (Datex-Ohmeda S/5, SOMA Technology, Madison, USA) was used to continuously monitor pulse rate and blood pressure along with pulse oximetry, capnography, temperature, spirometry, electrocardiography and inspired and expired gases (O_2, CO_2 and inhalant anaesthetic agent). All animals were euthanised with intravenous sodium pentobarbitone (Pentoject; Animalcare, York, UK).

Table 3.3. Anaesthesia and analgesia options in sheep diagnosed with OPA.
*Until conditions for endotracheal intubation are present (i.m., intramuscular; i.v., intravenous) (information provided by Professor E. Clutton and Dr S. Greenhalgh).

Phase	Drug	Manufacturer	Dose (mg/kg)	Route
Sedation	Medetomidine	'Sedator'; Dechra Veterinary Products, Shrewsbury, UK	0.003-0.01	i.v.
	in combination with			
	Midazolam	'Hypnovel'; Roche, Welwyn Garden City, UK	0.25-0.5	i.v.
Induction	Propofol	'Propofol'; Fresenius Kabi, Cheshire, UK	To effect* (e.g. 3-10)	i.v.
Maintenance	Isoflurane	'IsoFlo'; Abbot Animal Health, Maidenhead, UK		inhaled
Analgesia	Flunixin	'Flunixin Injection'; Norbrook, Newry, UK	2.2	i.v.
	Morphine	'Morphine Sulphate'; Martindale Pharmaceuticals, Essex, UK	0.1-0.3	i.v./i.m

Figure 3.21. Photographs of an anaesthetised sheep undergoing sensor readings.
Sheep are positioned in sternal recumbency with the head elevated above the thorax.

3.4.3 Computed tomography

CT imaging was performed by Mrs L. Grant (The Royal (Dick) School of Veterinary Studies, University of Edinburgh). A single-section SOMATOM Definition AS 64 slice helical CT machine (Siemens Healthcare Ltd, Camberley, UK) was used for all advanced imaging procedures. Imaging parameters of the scanner were 120 kVp, 35 mA, 3-5 mm collimation with 1 mm section thickness. The window width and level were approximately 2000 and -500 HU respectively, allowing simultaneous visualisation of the implantation needle, blood vessels, lesions, pneumothorax, bone, muscle and fat. All scans were obtained through the entire thoracic cavity from the first to the last rib using a section thickness of 1 mm to improve the visualisation of the needle tip and sensor in relation to the OPA lesion (Figure 3.22).

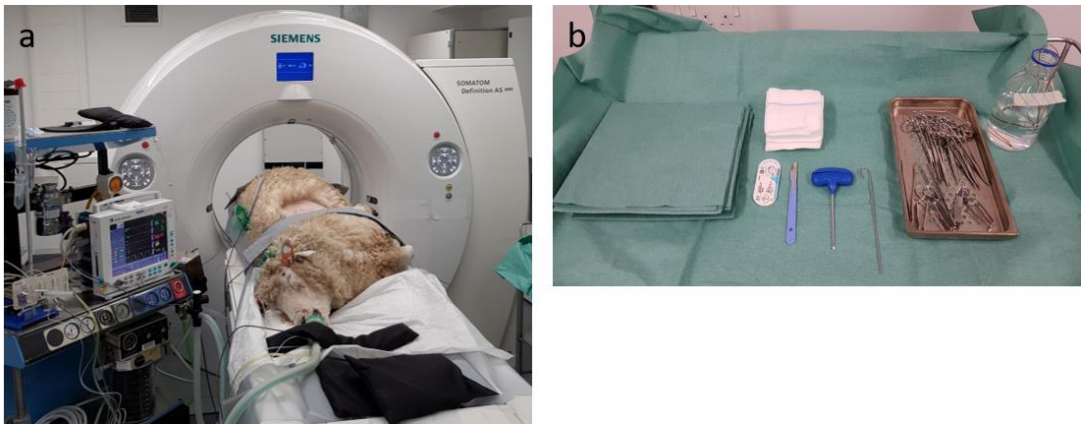

Figure 3.22. Photographs of imaging and surgical facilities. (a) The sheep is anaesthetised and positioned on the gantry, rump first, for CT scanning in lateral recumbency, with the OPA affected lungs uppermost. **(b)** Surgical equipment required for sensor implantation including a general surgical kit and Jamshidi insertion needle. An IMPACT O_2 sensor can be seen in a bottle of sterile saline at the top right-hand side of the image.

3.4.4 Oxygen sensor recordings

Oxygen sensor recordings in both the rat and ovine experiments were performed by Dr J. Marland (School of Engineering, University of Edinburgh). Following sensor implantation, the lead wire was connected to an EmStat3 Blue potentiostat (PalmSens BV, Netherlands). Periodic O_2 measurements were performed using chronoamperometry at -0.5 V (versus the on-chip Ag/AgCl reference electrode) for 20 s, followed by a rest period of 20 s. These cycles were repeated

continuously for the duration of the experiments. The working electrode current over the final 5 s of each 20 s chronoamperometry recording was analysed using MATLAB R2017a (MathWorks, Natick, MA, USA) to derive the mean current. The measured working electrode current is directly proportional to the ptO_2 at the sensor surface.

3.4.5 Statistical Analysis

Data for all murine and ovine experiments were analysed with either one-way or two-way ANOVA with Holm-Šídák multiple comparisons tests to test for differences between 2 groups; *p* values <0.05 were deemed statistically significant. Data are shown as mean ± SEM with all statistical analysis and graphs generated using Prism 7 (GraphPad Software, San Diego, CA, USA).

4 Development and Characterisation of Acquired Radioresistant Breast Cancer Cell Lines

This results chapter is an expanded version of a published research article: Gray M, Turnbull AK, Ward C, Meehan J, Martínez-Pérez C, Bonello M, Pang LP, Langdon SP, Kunkler IH, Murray A, Argyle D. Development and characterisation of acquired radioresistant breast cancer cell lines. Radiation Oncology 2019; 14(64): 1-19. This article is open access with the authors retaining copyright to their work with permission to use published figures in this thesis. Sections of text and figures used from this article have been referenced accordingly.

4.1 Abstract

Background: The response of a tumour to radiotherapy will be influenced by the tumour's innate radiosensitivity and the development of acquired radioresistance. Research into understanding and targeting the mechanisms involved in acquired radioresistance is required if patient outcomes are to be improved. **Methods:** Radioresistant breast cancer cell lines (RR) were established by treating ZR-751, MCF-7 and MDA-MB-231 parental cells with weekly fractions of radiation. Parental and radioresistant cell lines underwent phenotypic, functional and genotypic characterisation. Intrinsic differences between parental and RR cells were investigated by gene expression analysis to identify differentially expressed or activated signalling networks. **Results:** Radioresistance was confirmed through colony formation and proliferation assays. Radioresistant cells exhibited evidence of epithelial-to-mesenchymal-transition with enhanced invasion and migration. ZR-751 RR and MCF-7 RR cell lines demonstrated loss of ERα and PgR expression with an increase in EGFR expression. Based on gene analysis, these cell lines changed classification from luminal A (parental) to normal-like (ZR-751 RR) or HER2-overexpressing (MCF-7 RR) subtypes. Gene expression analysis identified that RR cell lines derived from ER^+ cells demonstrated down-regulation of ER signalling genes and up-regulation of genes associated with WNT, MAPK and PI3K pathway activation; this was confirmed by western blot. **Conclusions:** This study has successfully developed 3 novel radioresistant breast cancer cell lines which underwent phenotypic, functional and genotypic characterisation. Comparisons made

with their parental cells identified multiple differentially expressed or activated signalling networks which warrant further investigation as potential targets for overcoming acquired radioresistance.

4.2 Introduction

Tumour recurrence following RT can be due to the survival of a population of cells that have either greater intrinsic (innate) resistance to radiation (e.g. hypoxic or cancer stem cells) or acquire resistance. Ultimately, through clonal selection, it is these radioresistant cells that can repopulate the tumour site, leading to recurrence and treatment failure. Research into understanding and targeting the mechanisms involved in cancer cells acquiring radioresistance is therefore required to improve patient outcome. Previous studies have identified multiple factors which are likely to be involved in radioresistance development, including increased oncogenic miRNA production, epithelial-to-mesenchymal transition (EMT), signalling pathway activation (EGFR, PI3K/AKT, MAPK, NF-ƙB), improved DNA damage responses, cancer stem cell repopulation and changes in cancer cell metabolism. The TME (including hypoxia) can also influence the effectiveness of RT[407]. Unfortunately, these studies tend to focus on isolated pathways which fail to appreciate the complex and likely interconnected cellular changes that are required for cancer cells to become radioresistant. Hypoxia, for example, can cause cancer cells to adopt a more undifferentiated phenotype characterised by increased stem cell marker expression and can also affect the expression of genes and pathways controlling stemness, such as Oct4, Notch and EMT[408,409].

In comparison with studies investigating chemoresistance, research into understanding radioresistance is currently limited; this is partly due to a lack of radioresistant model systems. To overcome this, RR models are required that can be used with techniques capable of studying multiple pathways simultaneously. This research could provide an overview of complex interrelated biological systems and a detailed understanding of cellular changes involved in the development of radioresistance. This could ultimately lead to a more effective way of identifying pathways which could be targeted to overcome radioresistance[409,410].

This chapter describes the development of novel *in vitro* radioresistant ER positive (ER^+) and ER negative (ER^-) breast cancer cell lines. Analysis of gene

expression data was performed by Dr A. K. Turnbull (Cancer Research UK, University of Edinburgh). Parental cell lines were chosen to represent different molecular subtypes of breast cancer and included MCF-7 and ZR-751 cell lines (ER^+, PgR^+, $HER2^-$), which are hormone-dependent, and the MDA-MB-231 cell line, which is triple negative (ER^-, PgR^-, $HER2^-$) and consequently hormone-independent. Genotypic, phenotypic and functional characterisation of the RR model was undertaken, allowing validation of results at gene, protein and functional levels. This approach identified multiple differences between paired parental and RR cell lines and between the different breast cancer subtypes (ER^+ and ER^-), resulting in an in-depth characterisation of the RR model. To our knowledge, this is the first description of a developed ZR-751 RR cell line and the use of MTS derived from RR cells in IHC and functional assays.

4.3 Results

4.3.1 Development and confirmation of acquired radioresistance in human ER^+ and ER^- breast cancer cell lines

Parental cells (MCF-7, ZR-751 and MDA-MB-231) were used to develop radioresistant cell lines (MCF-7 RR, ZR-751 RR and MDA-MB-231 RR). Parental cells were exposed to weekly single fractionated doses of radiation, increasing by 0.5 Gy per week over a 12-week period; cells were subsequently maintained by weekly doses of 5 Gy. Although this maintenance radiation dose still caused cell death in all 3 RR cell lines, this was significantly less than the level seen during the 12-week development period and did not appear to change with chronic radiation exposure.

Following the 12-week development period, CF and SRB assays were used to confirm radioresistance. All RR cell lines had significantly higher CF ability than their parental cell lines when exposed to a single dose of radiation up to 6 Gy (Figure 4.1). Proliferation of the RR cell lines was inhibited less than that of their parental cell lines when exposed to a single dose of radiation up to 10 Gy (Figure 4.2, Figure 4.3 & Figure 4.4), with correspondingly higher IC_{50} values seen in the RR cell lines (Table 4.1). MCF-7 RR and MCF-7 rr cells (a MCF-7 RR cell line which had not received radiation for 6 months), showed comparable radioresistance when exposed to a single dose of radiation up to 6 Gy in CF assays and up to 4 Gy in SRB assays. Both cell lines showed significantly greater resistance to the effects of radiation in

terms of proliferation and CF ability compared to the parental MCF-7 cell line, suggesting maintenance of their acquired phenotype (Figure 4.5).

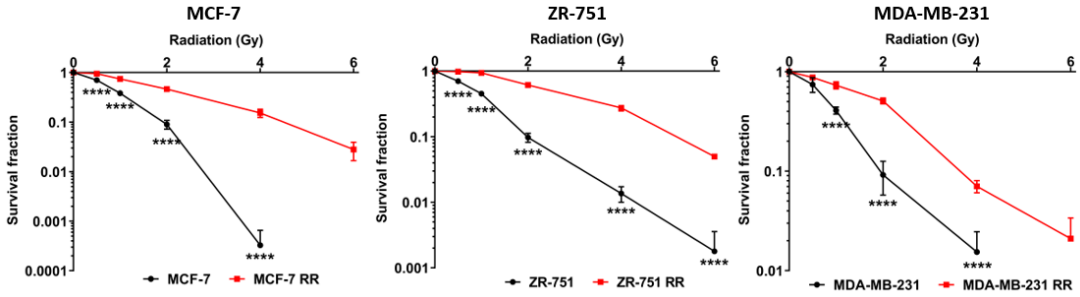

Figure 4.1. Radioresistant cell lines have increased colony formation ability. Colony formation assays at 10-14 d post-radiation comparing MCF-7 RR, ZR-751 RR and MDA-MB-231 RR cell lines with their respective parental cell lines (two-way ANOVA with Holm-Šídák multiple comparisons test; data expressed as mean ± SEM, n=3, ****$p \leq 0.0001$).

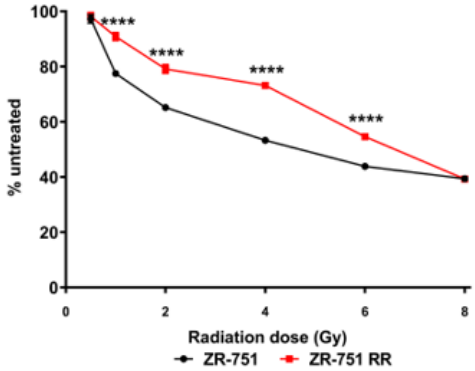

Figure 4.2. Proliferation of the ZR-751 RR cell line is inhibited less than its parental cell line following exposure to radiation. SRB proliferation assay comparing ZR-751 RR with its parental cell line at 144 h post-radiation (two-way ANOVA with Holm-Šídák multiple comparisons test; data expressed as mean ± SEM, n=3, ****$p \leq 0.0001$).

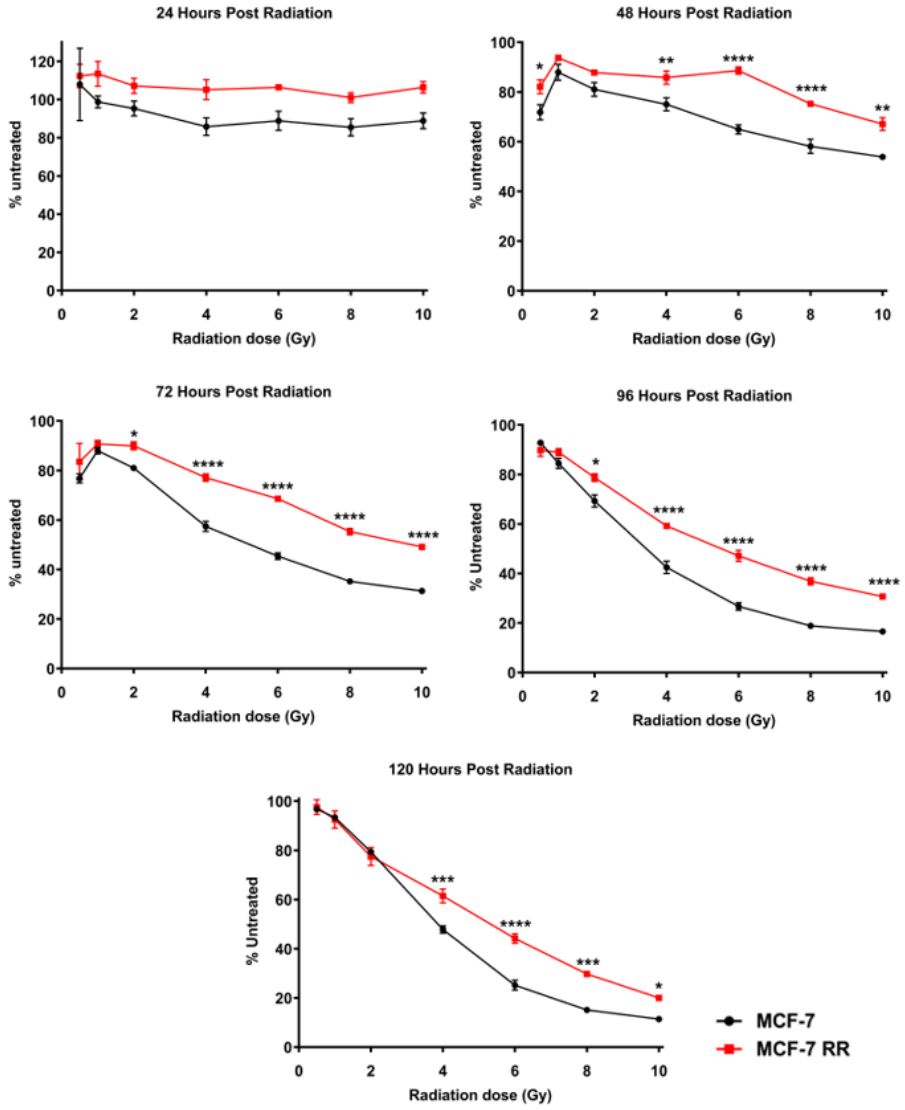

Figure 4.3. Proliferation of the MCF-7 RR cell line is inhibited less than its parental cell line following exposure to radiation. SRB proliferation assays comparing MCF-7 RR with its parental cell line up to 120 h post-radiation (two-way ANOVA with Holm-Šídák multiple comparisons test; data expressed as mean ± SEM, n=3, ****$p \leq 0.0001$; ***$p \leq 0.001$; **$p \leq 0.01$; *$p \leq 0.05$).

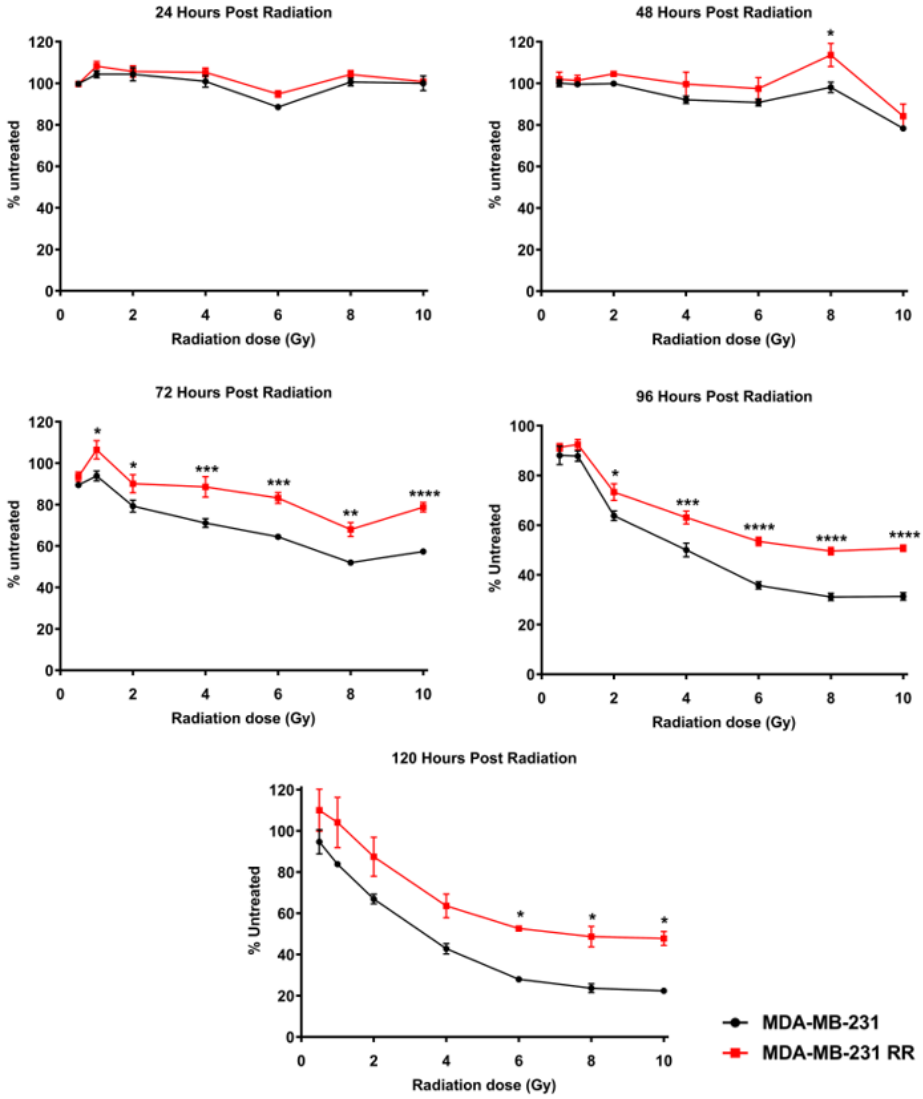

Figure 4.4. Proliferation of the MDA-MB-231 RR cell line is inhibited less than its parental cell line following exposure to radiation. SRB proliferation assays comparing MDA-MB-231 RR with its parental cell line up to 120 h post-radiation (two-way ANOVA with Holm-Šídák multiple comparisons test; data expressed as mean ± SEM, n=3, ****$p \leq 0.0001$; ***$p \leq 0.001$; **$p \leq 0.01$; *$p \leq 0.05$).

Table 4.1. IC_{50} values for each parental and RR cell line up to 144 h post-radiation. If no value is recorded this indicates that a reduction in proliferation by 50% had not occurred at that time point; MCF-7 and MDA-MB-231 cell lines were evaluated up to 120 h post-radiation, whereas the ZR-751 cell line was evaluated up to 144 h post-radiation.

Time post-radiation (h)	MCF-7	MCF-7 RR	ZR-751	ZR-751 RR	MDA-MB-231	MDA-MB-231 RR
24	-	-	-	-	-	-
48	-	-	-	-	-	-
72	4.98	9.64	-	-	-	-
96	3.27	5.36	-	-	3.53	9.71
120	3.74	5.22	-	-	3.13	7.11
144	N/A	N/A	4.38	6.91	N/A	N/A

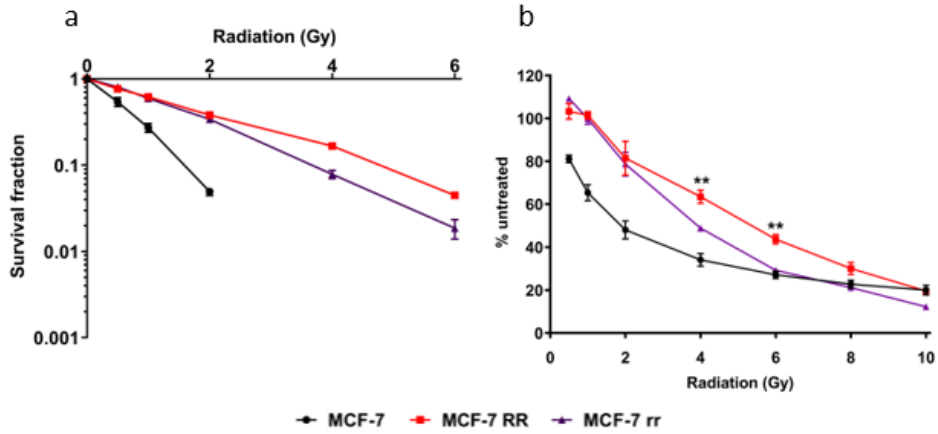

Figure 4.5. CF and SRB assays comparing MCF-7, MCF-7 RR and MCF-7 rr cell lines. MCF-7 rr is a radioresistant cell line not radiated for 6 months (24 passages). (**a)** Colony formation assay at 14 d post-radiation. (**b)** SRB assay at 120 h post-radiation (two-way ANOVA with Holm-Šídák multiple comparisons test; data expressed as mean ± SEM, n=3, $**p \leq 0.01$).

4.3.2 Development and confirmation of acquired radioresistance in a canine ER$^-$ breast cancer and an ovine lung cancer cell line

Parental cells (REM-134 and JS7) were used to develop radioresistant cell lines (REM-134 RR and JS7 RR). These cell lines were developed for use in the secretomic experiments (described in chapter 5). Following the 12-week radiation protocol, as previously described, SRB assays were used to confirm radioresistance (CF assays were not used, as both cell lines would not form colonies from single cells). Proliferation of the JS7 RR and REM-134 RR cell lines was inhibited less than that of their parental cell lines when exposed to a single dose of radiation up to 4 and 10 Gy respectively (Figure 4.6 & Figure 4.7), with corresponding higher IC_{50} values seen in the RR cell lines (Table 4.2). REM-134 RR and REM-134 rr cells (a REM-134 RR cell line which had not received radiation for 6 months), showed comparable radioresistance when exposed to radiation doses of up to 10 Gy in SRB assays. Both cell lines showed significantly greater resistance to the effects of radiation in terms of proliferation compared to the parental REM-134 cell line, suggesting maintenance of their acquired phenotype (Figure 4.8).

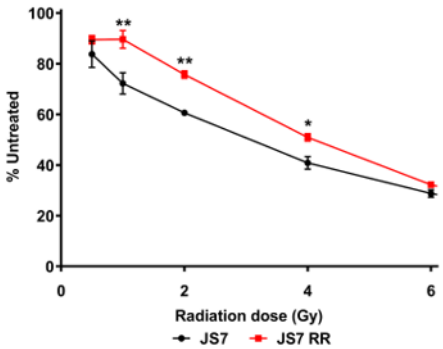

Figure 4.6.Proliferation of the JS7 RR cell line is inhibited less than its parental cell line following exposure to radiation. SRB proliferation assay comparing JS7 RR with its parental cell line at 144 h post-radiation (two-way ANOVA with Holm-Šídák multiple comparisons test; data expressed as mean ± SEM, n=3, $**p \leq 0.01$; $*p \leq 0.05$).

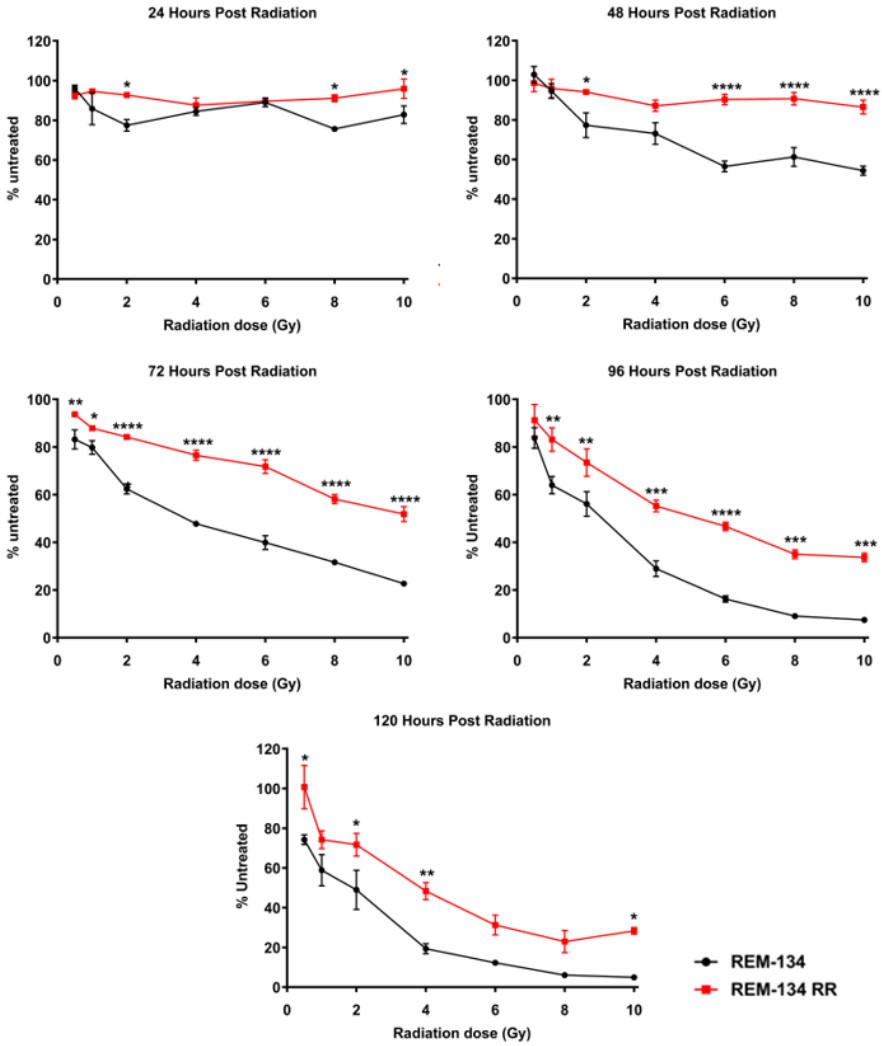

Figure 4.7. Proliferation of the REM-134 RR cell line is inhibited less than its parental cell line following exposure to radiation. SRB proliferation assays comparing REM-134 RR with its parental cell line up to 120 h post-radiation (two-way ANOVA with Holm-Šídák multiple comparisons test; data expressed as mean ± SEM, n=3, $****p \leq 0.0001$; $***p \leq 0.001$; $**p \leq 0.01$; $*p \leq 0.05$).

Table 4.2. IC_{50} values for each parental and RR cell line up to 144 h post-radiation. If no value is recorded this indicates that a reduction in proliferation by 50% at that time point had not occurred; REM-134 cell line was evaluated up to 120 h post-radiation whereas JS7 cell line was evaluated up to 144 h post-radiation.

Time post-radiation (h)	REM-134	REM-134 RR	JS7	JS7 RR
24	-	-	-	-
48	-	-	-	-
72	3.85	10.34	-	-
96	3.32	4.98	-	-
120	1.7	3.6	-	-
144	N/A	N/A	2.82	4.12

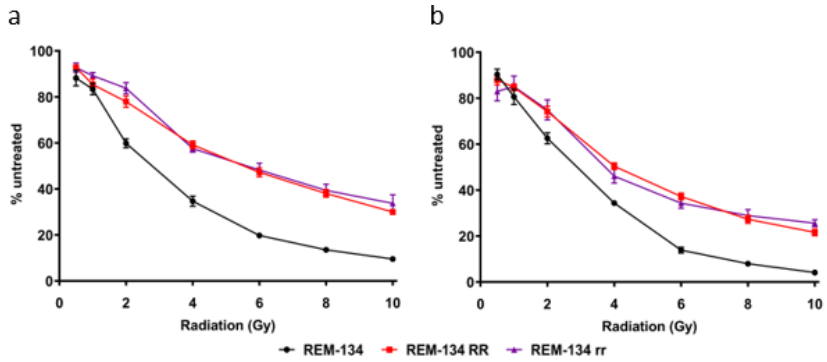

Figure 4.8. SRB assays comparing REM-134, REM-134 RR and REM-134 rr cell lines. REM-134 rr is a radioresistant cell line not radiated for 6 months (24 passages). (**a)** SRB assay at 96 h post-radiation. (**b)** SRB assay at 120 h post-radiation (two-way ANOVA with Holm-Šídák multiple comparisons test; data expressed as mean ± SEM, n=3).

4.3.3 Gene expression analysis identifies inherent similarities between radioresistant cell lines derived from ER^+ cells

A large number of genes were found to be inherently differentially expressed (using a log2 fold-change cut-off of 1) between ER^+ parental and RR cell lines. These changes were consistent between both MCF-7 RR and ZR-751 RR cell lines. Fewer differentially expressed genes were observed between the MDA-MB-231 parental and RR cell lines. Cluster analysis using differentially expressed genes (n=8796) identified that the MDA-MB-231 and RR cell lines clustered closely together, having similar expression patterns. Parental ZR-751 and MCF-7 cells also had a similar pattern of gene expression to the MDA-MB-231 cells except for 2 gene clusters, 1 enriched for focal adhesion and tight junctions and 1 enriched for glycan biosynthesis. MCF-7 RR and ZR-751 RR cell lines clustered together and separately from all the other cell lines, with lower expression of ribosomal genes and genes involved in proliferation, metabolism and DNA repair and higher expression of genes involved in WNT and MAPK signalling (Figure 4.9).

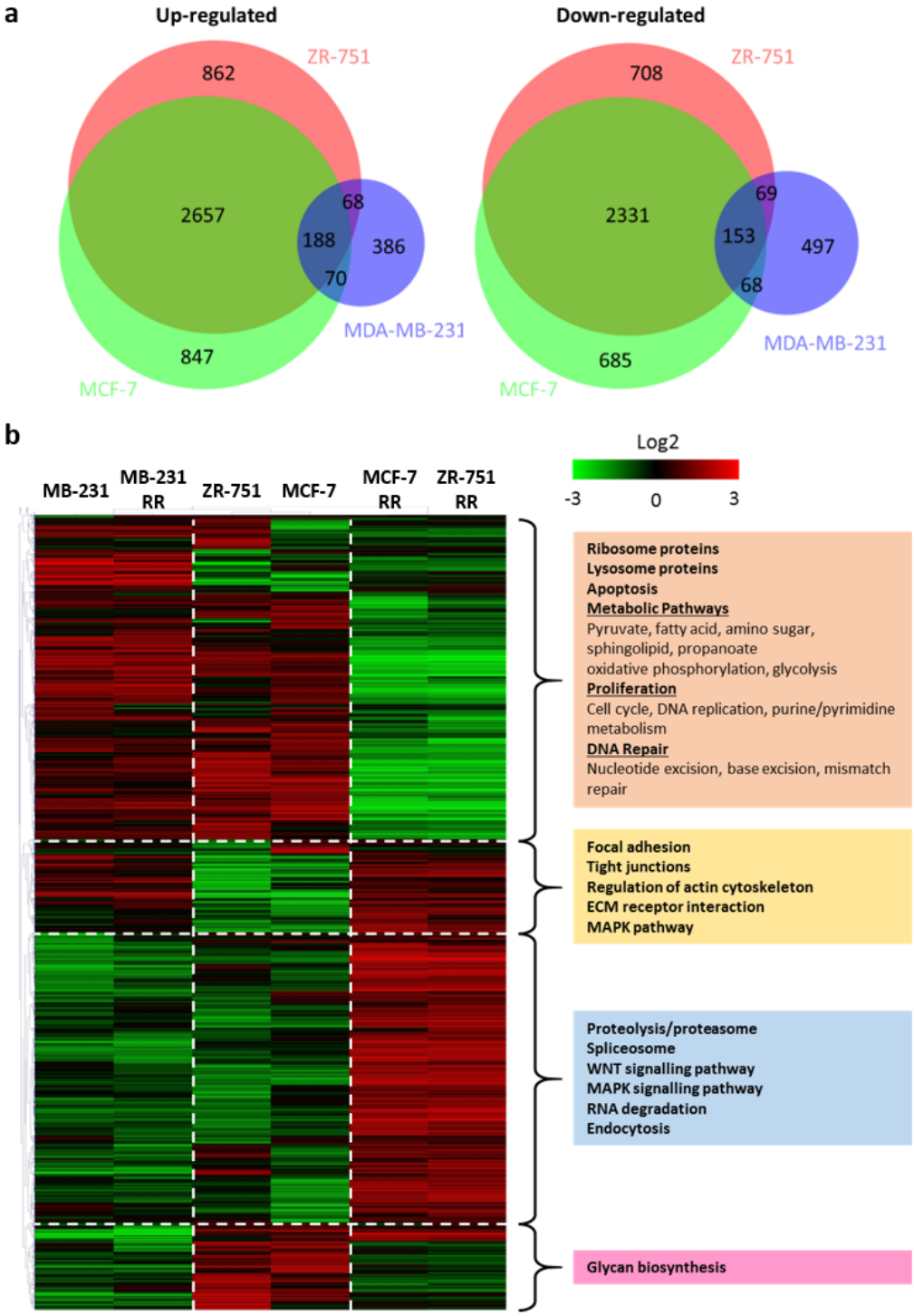

Figure 4.9. Global gene expression analysis identifies significant inherent similarities between RR cell lines derived from ER$^+$ cells. (a) Venn-diagrams comparing all 3 cell lines, showing the overlap of up-regulated (left) and down-regulated (right) genes with log2 fold changes >1 between paired parental and RR untreated cell lines. **(b)** Log2 mean-centered gene expression heatmap, labelled with cluster-enriched gene ontology, showing expression of the most differentially expressed genes, taken from the Venn-diagram analysis (red=higher expression, black=no change, green=lower expression, n=1). Heatmap clustering was carried out using Pearson correlation with average linkage.

4.3.4 Radioresistant cell lines have concurrent lower expression of cell cycle associated genes and modified basal proliferation rates

SRB assays using cells grown in 2D cultures showed lower proliferation rates in the MCF-7 RR and MDA-MB-231 RR cell lines and higher rates in the ZR-751 RR cell line in comparison to their respective parental cells (Figure 4.10a). Gene expression analysis from 2D cultures characterised the MCF-7 RR and ZR-751 RR cell lines as having lower expression of genes involved in DNA repair and replication and those related to G1/S-phase transition and cell cycle regulation, along with higher expression of cell cycle arrest genes. Changes were less marked in the MDA-MB-231 parental and RR cell lines, both of which clustered next to each other and to the MCF-7 and ZR-751 parental cell lines (Figure 4.10b). To investigate the apparent differences between the gene expression and SRB proliferation data in the ZR-751 RR cell line, Ki67 staining by IHC was performed using MCF-7 and ZR-751 parental and RR MTS (MDA-MB-231 cells failed to form MTS that could withstand IHC processing). Quantitative analysis showed that RR MTS contained lower percentages of positively stained Ki67 cells compared with parental MTS, suggesting lower basal proliferation rates (Figure 4.11).

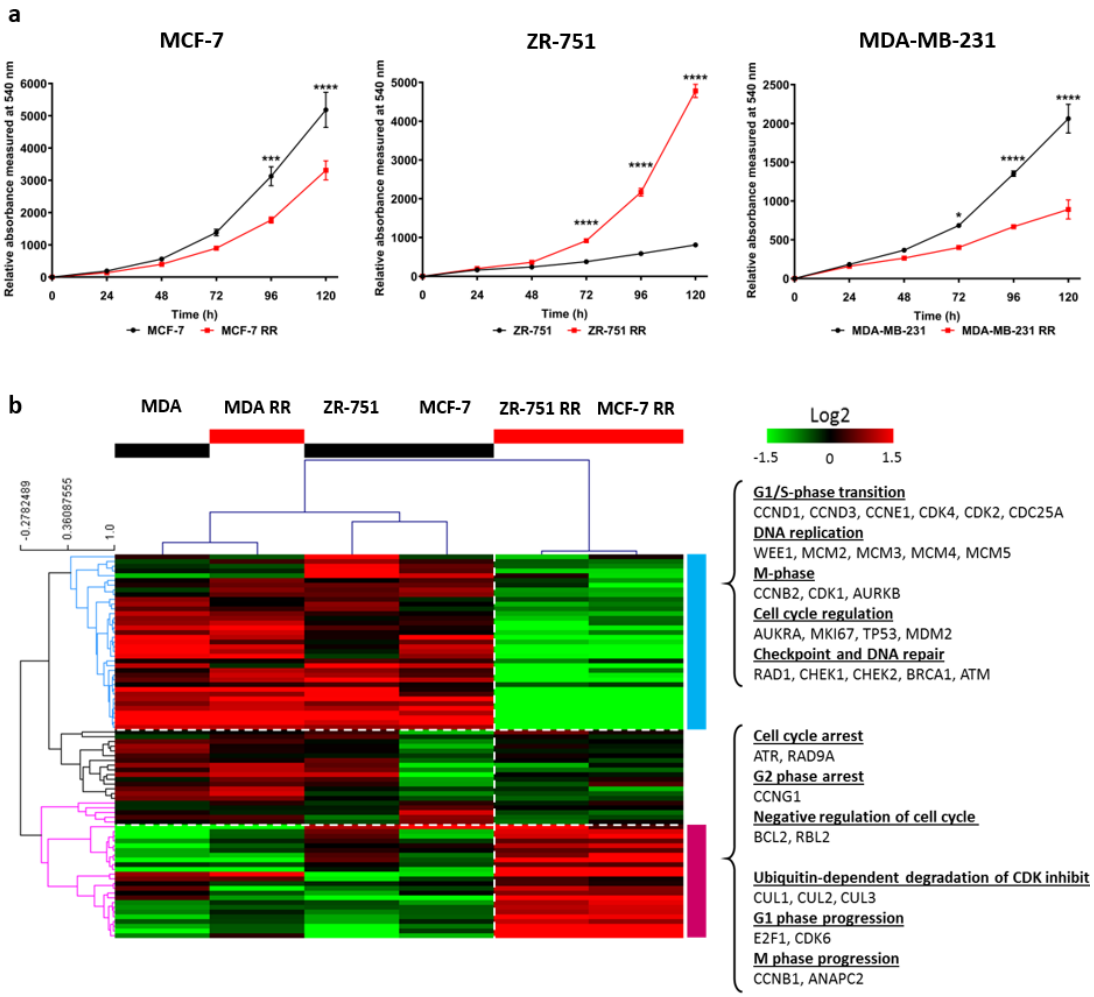

Figure 4.10. Radioresistant cell lines have modified proliferation rates relative to their parental cells. (a) SRB assays showing differences in proliferation rates between parental and RR cell lines grown in 2D cultures over 120 h (two-way ANOVA with Holm-Šídák multiple comparisons test; data expressed as mean ± SEM, n=3, ****$p \leq 0.0001$; ***$p \leq 0.001$; *$p \leq 0.05$). **(b)** Log2 mean-centered gene expression heatmap showing differences in expression between parental and RR cell lines in respect of proliferation genes taken from the KEGG database cell cycle pathway[411] (red=higher expression, black=no change, green=lower expression, n=1). Heatmap clustering was carried out using Pearson correlation with average linkage.

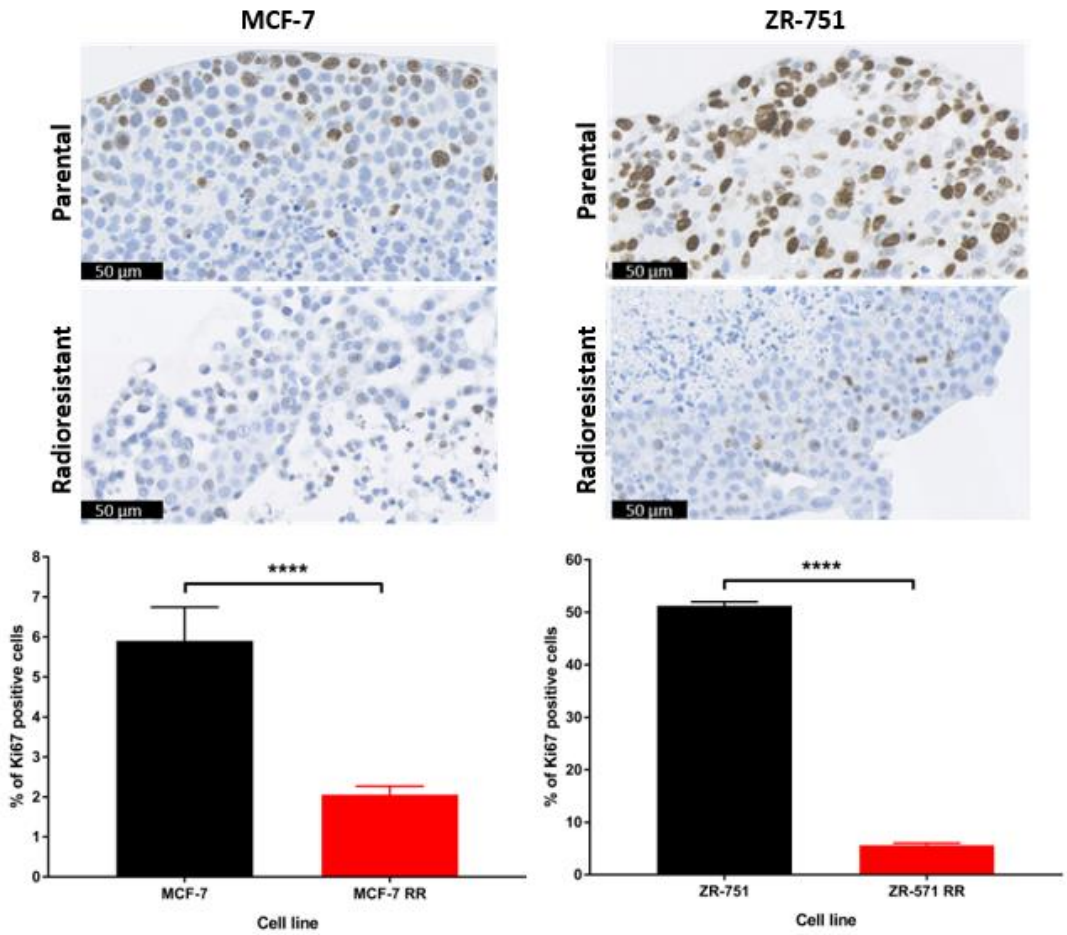

Figure 4.11. MCF-7 RR and ZR-751 RR MTS show decreased expression of Ki67. IHC of MTS stained for Ki67 using MCF-7 and ZR-751 parental and RR cell lines with quantitative analysis of the % of positively stained cells. Ki67 staining, as expected, is localised to the cell nucleus (unpaired two-sample t-test; data expressed as mean ± SEM, n=3, ****$p \leq 0.0001$).

4.3.5 Radioresistant cell lines have increased invasion and migration potential

Considered to be a normal feature of embryonic development, epithelial-to-mesenchymal transition (EMT) is a process involved in cellular movement and morphogenesis[412]. However, cancer cells can also undergo EMT, causing them to develop a more invasive and migratory phenotype[413]. Here, using a 3D collagen invasion assay, we showed a statistically significant increase in the invasive potential of MTS derived from MCF-7 RR and ZR-751 RR cells compared to parental MTS (which demonstrated no invasive capabilities); although at 72 h the MDA-MB-231 RR MTS showed a small increase in invasiveness, this was not statistically significant (Figure 4.12). However, results from 2D scratch assays demonstrated that

all 3 RR cell lines had significantly enhanced migratory ability compared to their parental cells (Figure 4.13, Figure 4.14 & Figure 4.15).

The morphology of parental ER^+ cell lines was typically epithelial-like, consisting of clumps of tightly packed cells forming cobblestone-like monolayers. The cells themselves consisted of a small amount of cytoplasm and a single large nucleus. However, following the initial 12 weeks of radiation exposure significant morphological changes were evident in the RR derivatives. Single cells or those within small clusters gained a spindle-shaped morphology with cellular contact between cells occurring via focal points rather than along their entire perimeter. Parental MDA-MB-231 cells originally exhibited a mesenchymal-like phenotype, therefore phenotypic changes in its RR derivate were not obvious (Figure 4.16).

These morphological changes that occurred with the acquisition of radioresistance were consistent with EMT and this process was initially investigated using IHC and ICC to examine the expression levels of EMT markers. Increased expression of vimentin, N-cadherin and SNAIL, along with the partial down-regulation of E-cadherin was identified in the MCF-7 RR and ZR-751 RR cell lines compared with their parental cells. No differences between the MDA-MB-231 parental and RR cell lines were identified, with these cell lines exhibiting high vimentin along with low N-cadherin and E-cadherin expression (Figure 4.17). The IHC results were mirrored in the gene expression data, firstly by investigating the expression of the vimentin, E- and N-cadherin genes (VIM, CDH1 and CDH2) (Figure 4.18a) and secondly by using a published EMT signature (Figure 4.18b)[414]. This pan-cancer EMT-associated gene expression signature was from a study that combined bioinformatic expression data from 7 tumour types using The Cancer Genome Atlas and Cancer Cell Line Encyclopaedia databases (the gene lists used are provided in the appendix). In our analysis, as expected, MCF-7 and ZR-751 parental cell lines had a gene expression pattern consistent with an epithelial genotype, whereas the MDA-MB-231 parental and RR cell lines had higher mesenchymal gene expression. A mixed pattern of gene expression was identified in the MCF-7 RR and ZR-751 RR cell lines, with higher expression of both epithelial and mesenchymal genes; this suggested a transition from an epithelial towards a more mesenchymal-like gene expression profile.

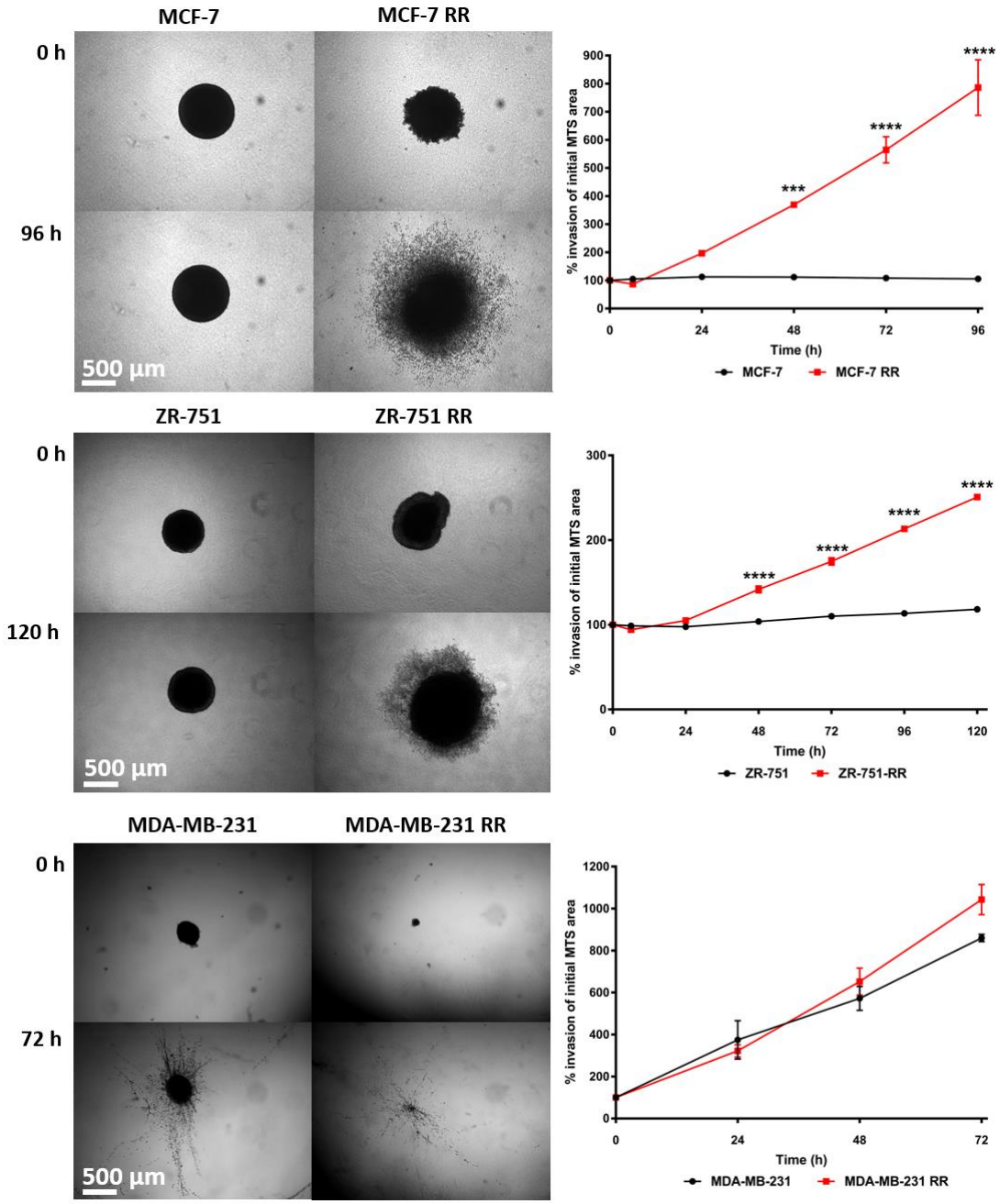

Figure 4.12. Radioresistant cell lines have increased invasion potential. 3D invasion assays comparing MCF-7 RR, ZR-751 RR and MDA-MB-231 RR MTS with their respective parental MTS. Following placement in collagen MTS invasion was assessed up to 120 h. Area of MTS at each time point was calculated and expressed as a % of the initial MTS area at day 0 (two-way ANOVA with Holm-Šídák multiple comparisons test; data expressed as mean ± SEM, n=3, ****$p \leq 0.0001$; ***$p \leq 0.001$).

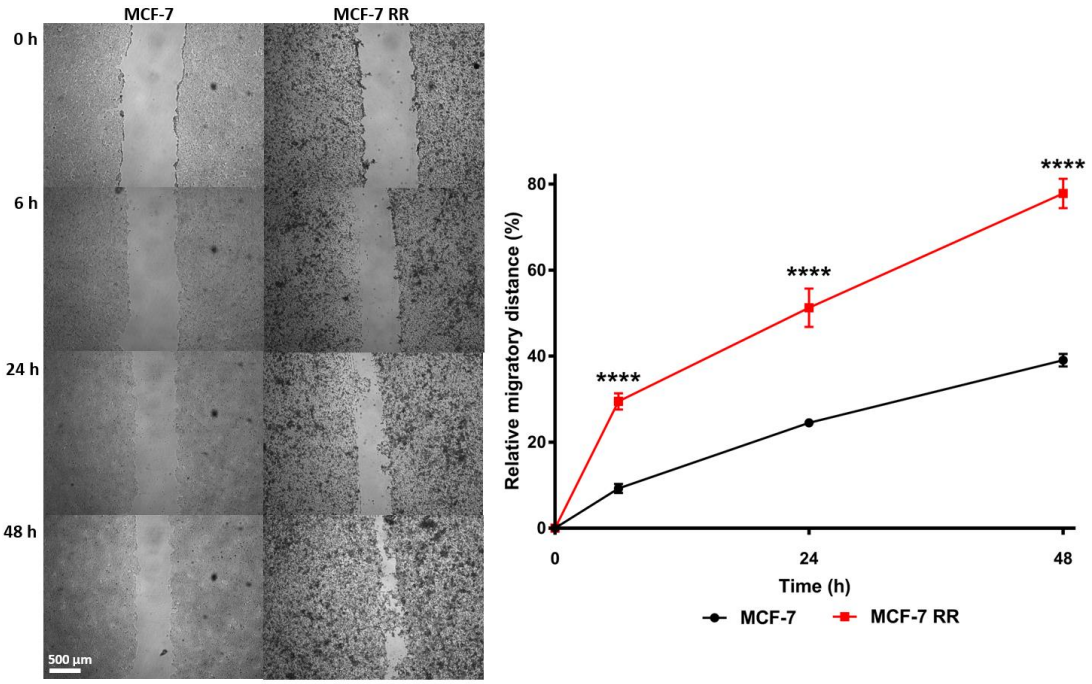

Figure 4.13. MCF-7 RR cell line has increased migration potential. 2D migration scratch assays comparing MCF-7 RR with its parental cell line. Relative migratory distance was calculated at each time point and expressed as a % area devoid of cells based on the initial scratch area at day 0 (two-way ANOVA with Holm-Šídák multiple comparisons test; data expressed as mean ± SEM, n=3, ****$p \leq 0.0001$).

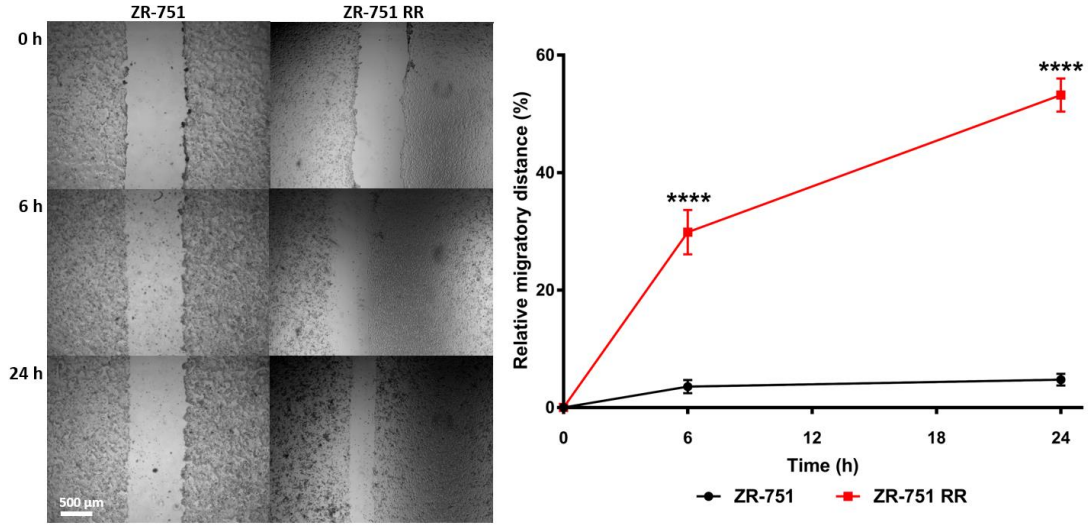

Figure 4.14. ZR-751 RR cell line has increased migration potential. 2D migration scratch assays comparing ZR-751 RR with its parental cell line. Relative migratory distance was calculated at each time point and expressed as a % area devoid of cells based on the initial scratch area at day 0 (two-way ANOVA with Holm-Šídák multiple comparisons test; data expressed as mean ± SEM, n=3, ****$p \leq 0.0001$).

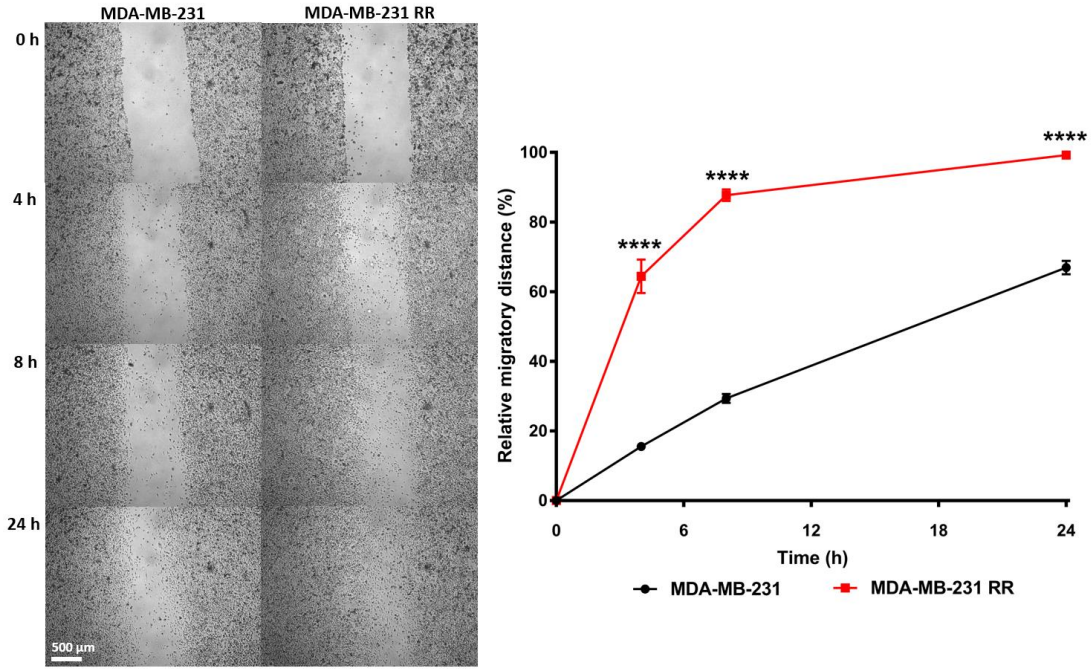

Figure 4.15. MDA-MB-231 RR cell line has increased migration potential. 2D migration scratch assays comparing MDA-MB-231 RR with its parental cell line. Relative migratory distance was calculated at each time point and expressed as a % area devoid of cells based on the initial scratch area at day 0 (two-way ANOVA with Holm-Šídák multiple comparisons test; data expressed as mean ± SEM, n=3, ****$p \leq 0.0001$).

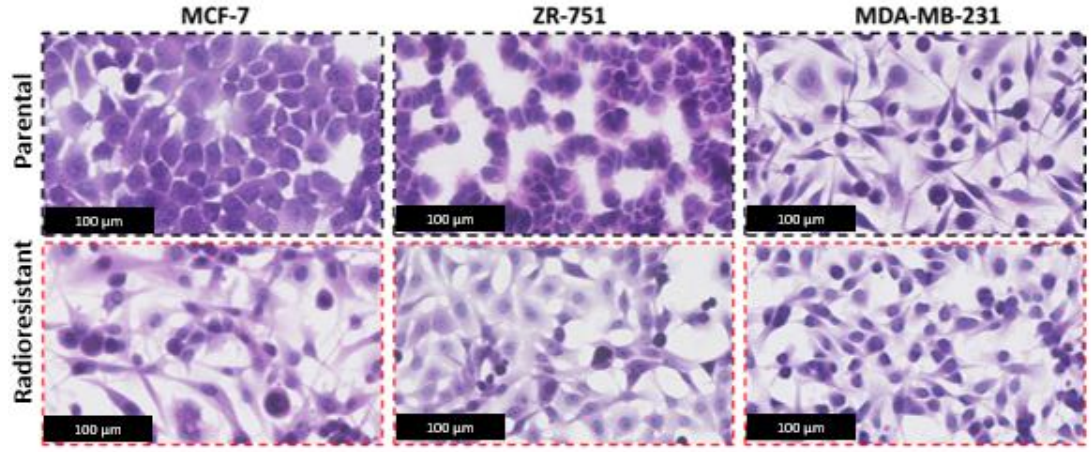

Figure 4.16. MCF-7 RR and ZR-751 RR cells show phenotypic changes consistent with EMT. H&E staining of parental and RR cell lines detailing their morphology (representative images, n=3).

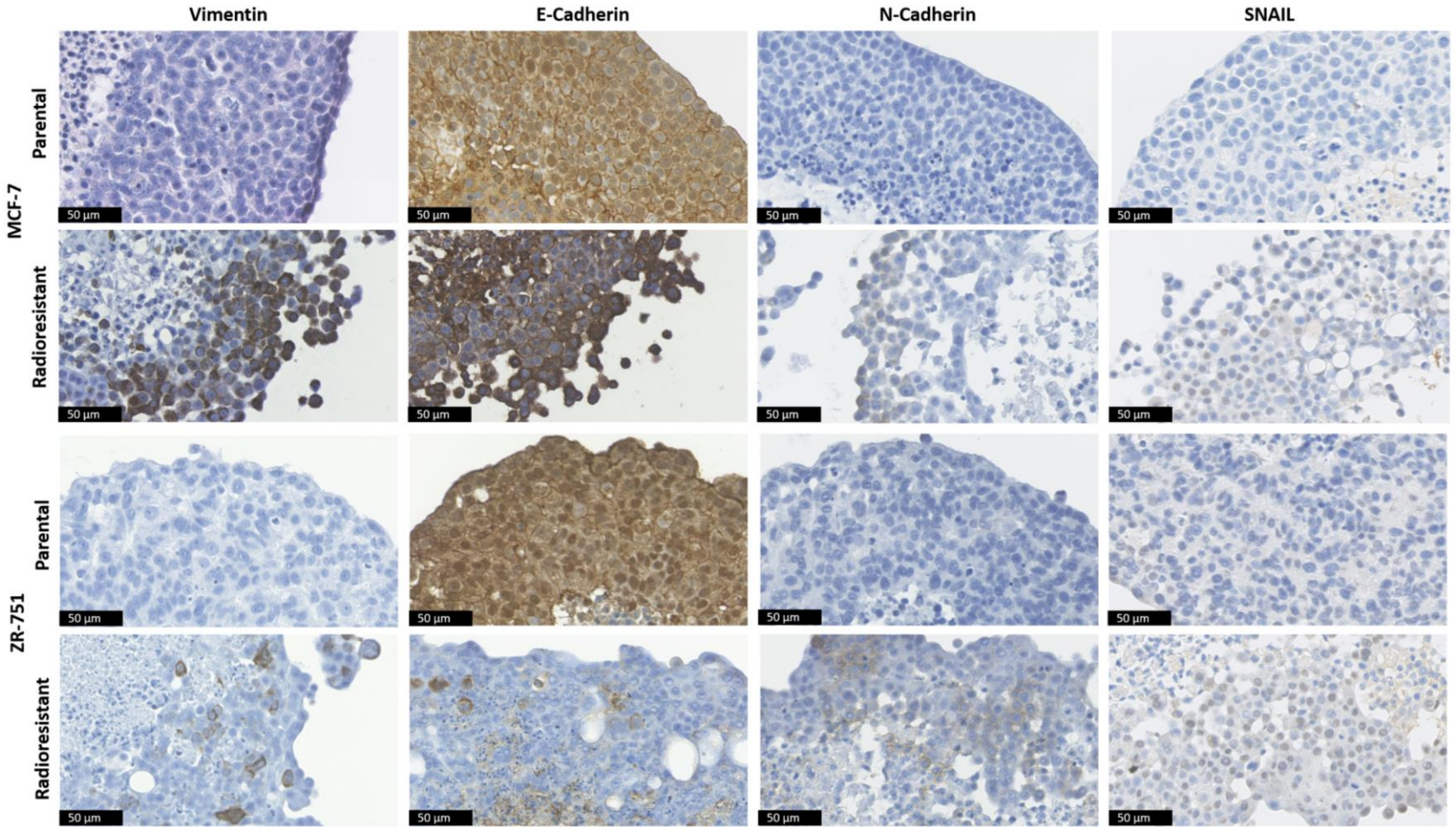

Figure legend on following page.

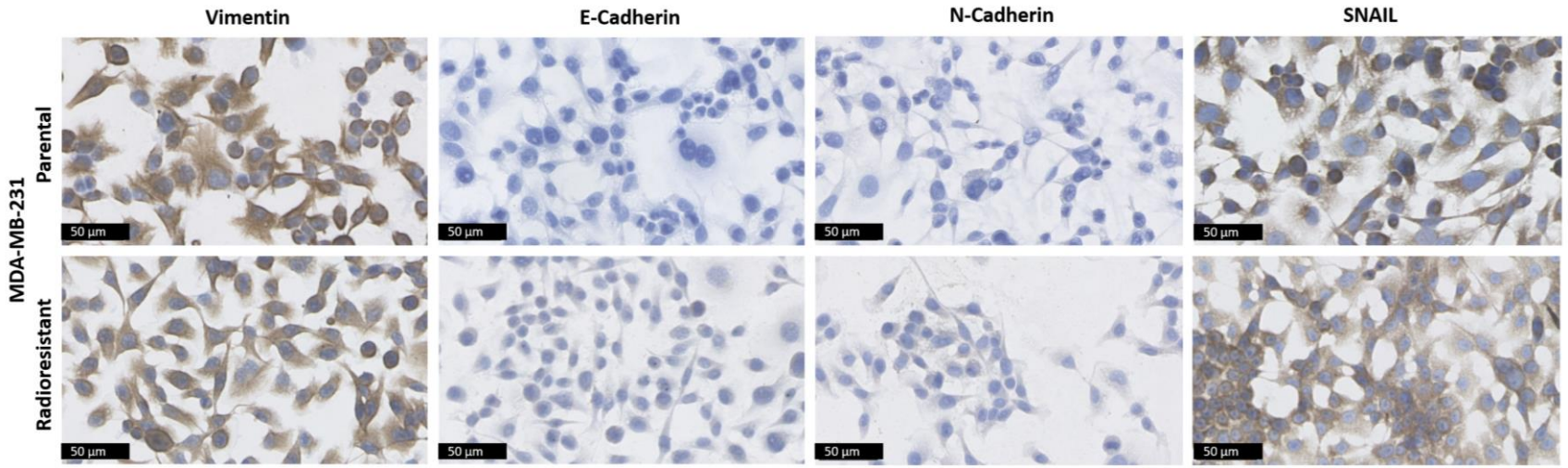

Figure 4.17. MCF-7 RR and ZR-751 RR cell lines show increased expression of vimentin, N-cadherin and SNAIL with partial down-regulation of E-cadherin. IHC staining for EMT markers (vimentin, N-cadherin, SNAIL and E-cadherin) in MCF-7, ZR-751 and MDA-MB-231 parental and RR cells. Positive DAB staining is seen for each antibody at the expected cellular localisation region: positive vimentin and SNAIL staining is seen predominately in the cytoplasm whereas E and N-cadherin staining is seen predominantly in the cell membrane and cytoplasm (representative images, n=3).

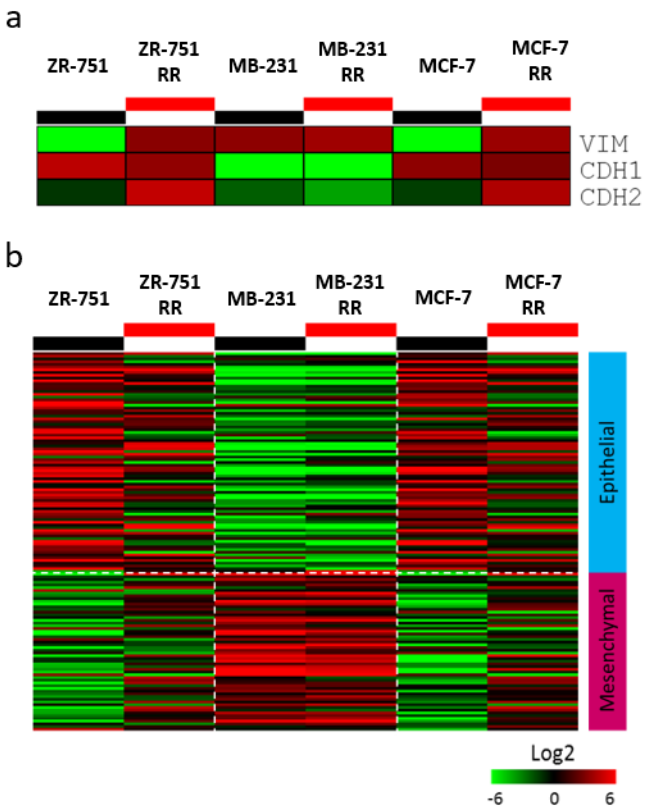

Figure 4.18. MCF-7 RR and ZR-751 RR cell lines show increased gene expression of vimentin and N-cadherin with the partial down-regulation of E-cadherin. (a) Log2 mean-centered gene expression heatmap showing relative inherent gene expression differences between parental and RR cell lines in respect of classical EMT markers; VIM=vimentin, CDH1=E-cadherin, CDH2=N-cadherin (red=higher expression, green=lower expression). **(b)** Log2 mean-centered gene expression heatmap showing expression differences in respect of a published cancer cell EMT-signature[414] (red=higher expression, black=no change, green=lower expression, n=1). Heatmap clustering was carried out using Pearson correlation with average linkage. The gene list and the order in which they appear in the heatmap is shown in the appendix.

4.3.6 WNT signalling is increased in radioresistant cell lines derived from ER$^+$ cells

WNT signalling has been reported to be involved in EMT and radioresistance[415]. To investigate this, the expression levels of WNT pathway-related genes was determined in the ER$^+$ parental and RR cell lines. To perform this analysis panels of WNT signalling pathway members and their down-stream targets were taken from the KEGG database[411] (the gene lists used are provided in the appendix). The majority of genes in these panels, including WNT5a, WNT5b and FRIZZLED family members 1/2/5/7/8, showed increased expression in the RR cell lines derived from ER$^+$ cells (Figure 4.19a & Figure 4.19b); WNT5a showed a log2 5-fold and 15-

fold increase in count-number in the ZR-751 RR and MCF-7 RR cell lines respectively when compared to their parental cell lines. IHC and quantitative analysis using MCF-7 and ZR-751 parental and RR MTS showed increased WNT5a expression in the RR cell lines (Figure 4.20a). Further validation through WB experiments using whole cell lysates from serum-starved cells (in accordance with conditions for the gene expression experiments) also showed increased WNT5a expression in the RR cell lines at 0 and 24 h post-serum starvation (Figure 4.20b).

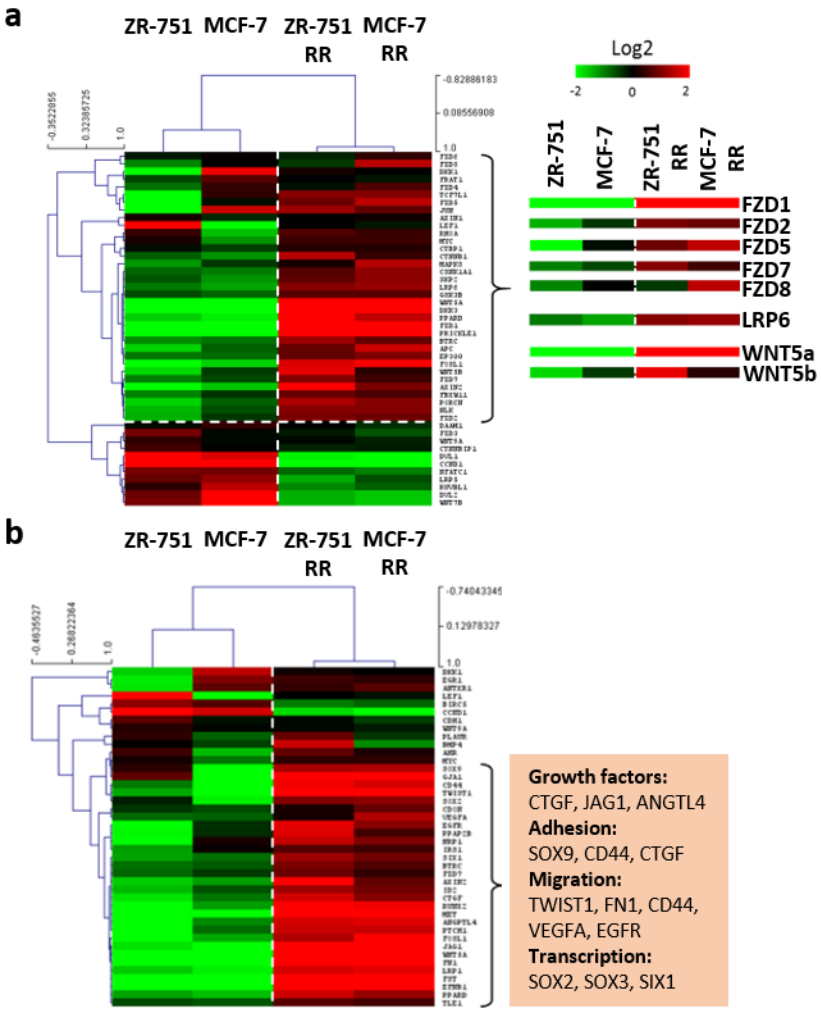

Figure 4.19. WNT signalling is increased in RR cell lines derived from ER$^+$ cells. Log2 mean-centered gene expression heatmaps showing differences between parental and RR cell lines. **(a)** WNT pathway-related genes with highlighted WNT and FRIZZLED genes. **(b)** WNT target genes, taken from the KEGG pathway database[411] (red=higher expression, black=no change, green=lower expression, n=1). Heatmap clustering was carried out using Pearson correlation with average linkage. The gene list and the order in which they appear in the heatmap is shown in the appendix.

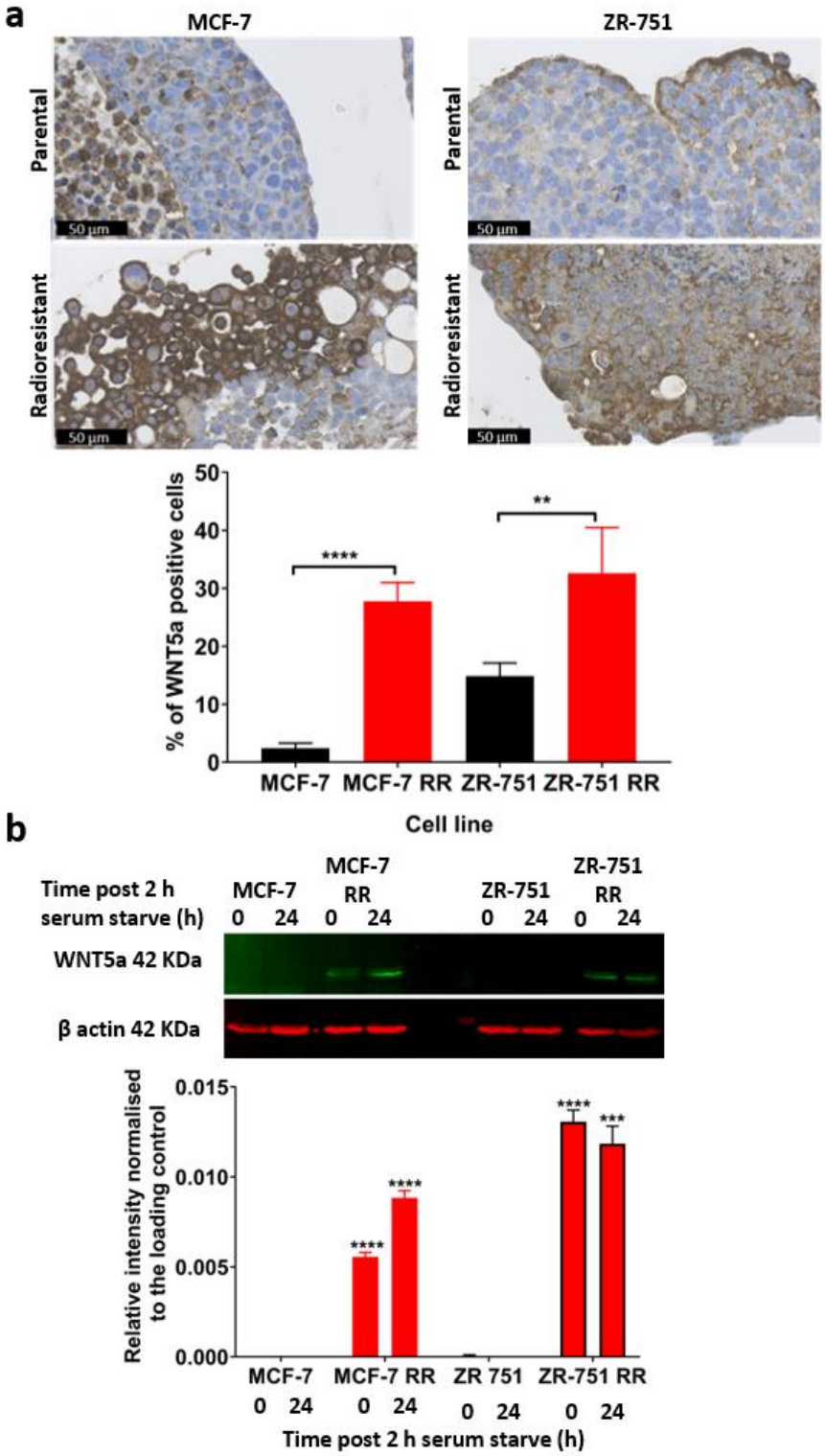

Figure 4.20. WNT signalling is increased in RR cell lines derived from ER$^+$ cells. **(a)** IHC of WNT5a expression using MCF-7 and ZR-751 parental and RR MTS; WNT5a staining, as expected, is predominantly localised to the cytoplasm. **(b)** WB analysis showing the levels of WNT5a in untreated MCF-7 and ZR-751 cell lines in comparison with their RR derivatives (samples were obtained at 0 and 24 h after 2 h serum starvation), (unpaired two-sample t-test; data expressed as mean ± SEM, n=3, ****$p \leq 0.0001$; ***$p \leq 0.001$, ** $p \leq 0.01$).

4.3.7 Radioresistant MCF-7 and ZR-751 cell lines show loss of ERα and PgR expression and gain in EGFR expression

Breast cancers can be characterised into subtypes by the expression of certain signalling receptors (ERα, PgR, HER2 and EGFR)[416-418]. IHC showed that the phenotype of the RR cell lines derived from ER^+ cells was characterised by ERα and PgR expression loss in combination with a gain in EGFR expression (Figure 4.21 & Figure 4.22). MDA-MB-231 parental and RR cells maintained their TNBC phenotype with no significant EGFR expression changes (Figure 4.23); these IHC results were confirmed by WB (Figure 4.24a). ICC with quantitative analysis confirmed reduction in the percentage of ERα positive staining cells in the MCF-7 RR cell line (0.27 ± 0.17%) compared with the parental MCF-7 cell line (81 ± 1.1%) and in the ZR-751 RR cell line (0.52 ± 0.36%) compared with the parental ZR-751 cell line (96.5 ± 1.8%). Loss of ERα in the MCF-7 RR cell line was associated with tamoxifen resistance; after 72 h of tamoxifen treatment a statistically significant increase in proliferation of the MCF-7 RR cell line was evident compared to the parental cells at concentrations ranging from 0.01–3 μM (Figure 4.24b). Tamoxifen at concentrations of 1 and 3 μM had no effect on migration in the MCF-7 RR cells, whereas an inhibition of migration was seen in the parental cell line (Figure 4.24c).

To investigate the cellular effects of increased EGFR expression on proliferation, invasion and migration, parental and RR cells were treated with the EGFR inhibitor, gefitinib (Selleckchem, Munich, Germany). A statistically significant decrease in MCF-7 RR proliferation was seen after 72 h of treatment with gefitinib at concentrations ranging from 0.1-15 μM compared to MCF-7 parental cells. A significant reduction in migration of the MCF-7 RR cells was also seen, with a concentration of 5 μM decreasing their migratory potential to that of the parental cells (Figure 4.25a & Figure 4.25b). Similar results were also seen in the ZR-751 parental and RR cell lines (Figure 4.25c & Figure 4.25d). Although only a small decrease in MDA-MB-231 RR proliferation was seen at higher gefitinib concentrations compared to the parental cells, a significant reduction in migration was seen, with a concentration of 5 μM decreasing the migratory potential of the RR cell line below that of the parental cells (Figure 4.25e & Figure 4.25f). IC_{50} values were reduced in all RR cell lines but were more pronounced in the MCF-7 RR and

ZR-751 RR cell lines (Table 4.3). The effects of gefitinib on invasion were also investigated in the ER^+ cell lines, with results showing a significant reduction in invasion of the MCF-7 RR and ZR-751 RR cell lines with a concentration of 5 μM (Figure 4.26).

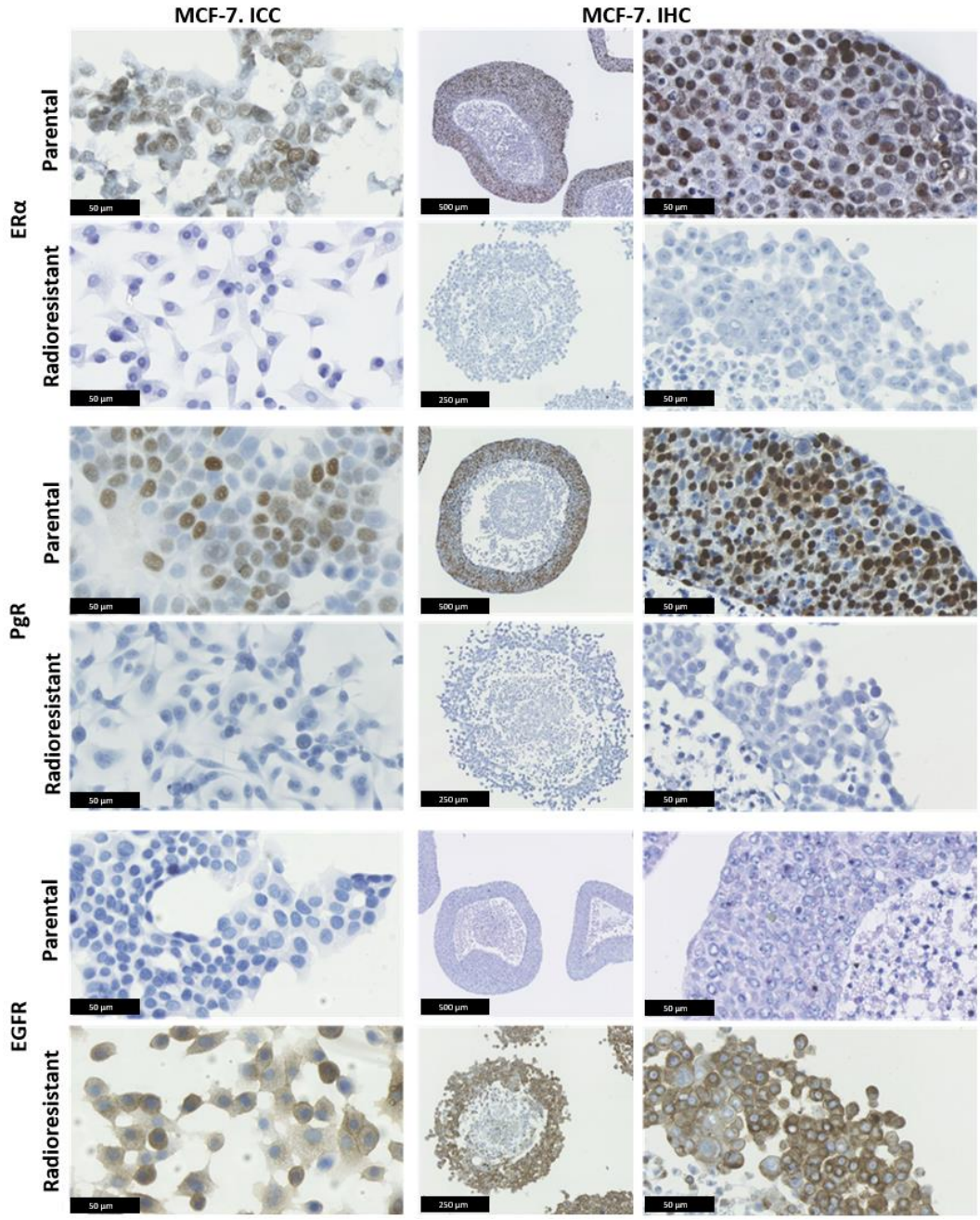

Figure 4.21. MCF-7 RR cells show loss of ERα and PgR and gain in EGFR expression. ICC and IHC expression profiles of signalling receptors, ERα, PgR and EGFR in MCF-7 and MCF-7 RR cell lines using 2D monolayer of cells and MTS. Positive DAB staining is seen for each antibody at the expected cellular localisation region: positive ERα and PgR staining is seen in the nucleus whereas EGFR is seen predominantly in the cell membrane (representative images, n=3).

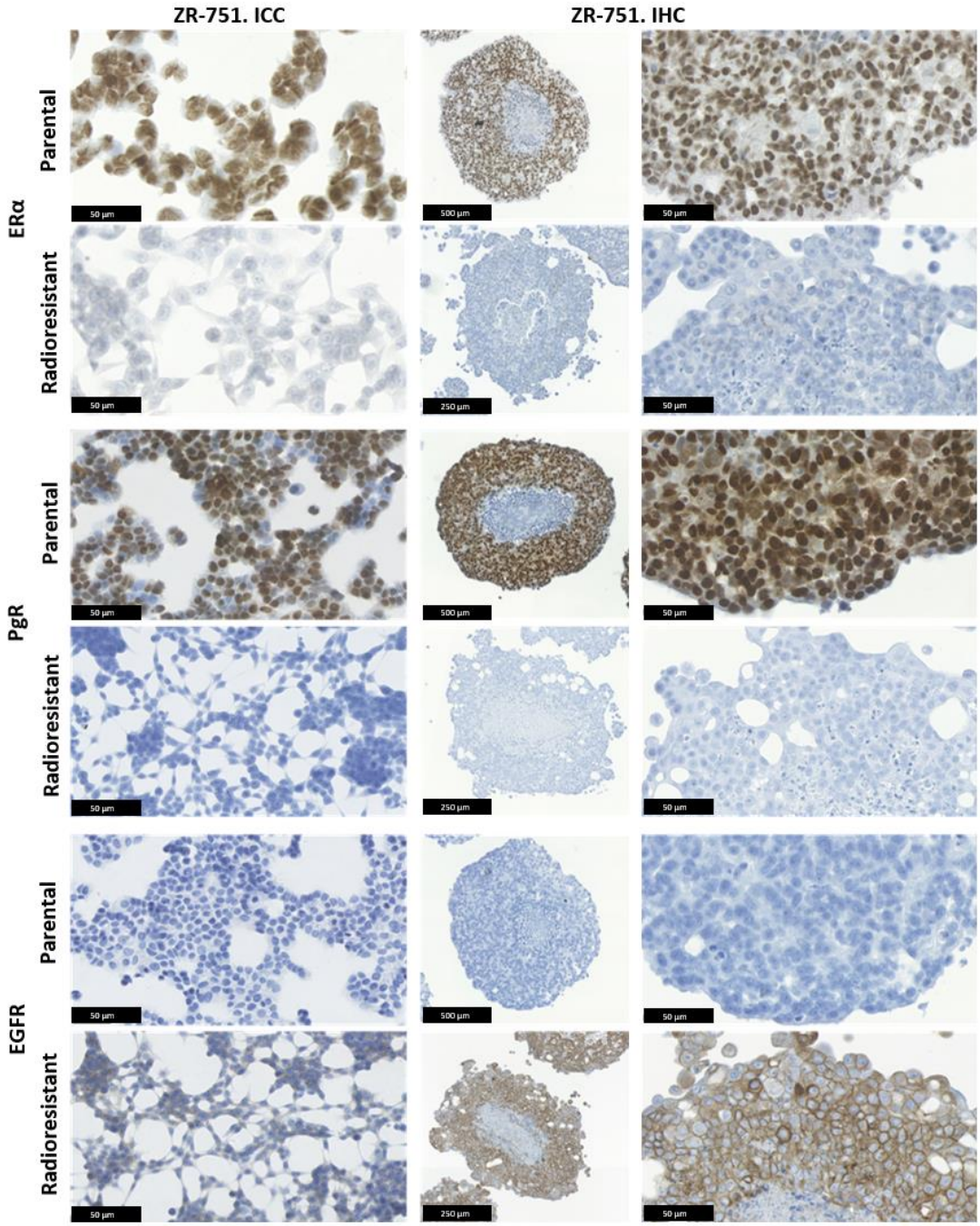

Figure 4.22. ZR-751 RR cells show loss of ERα and PgR and gain in EGFR expression. ICC and IHC expression profiles of signalling receptors, ERα, PgR and EGFR in ZR-751 and ZR-751 RR cell lines using 2D monolayer of cells and MTS. Positive DAB staining is seen for each antibody at the expected cellular localisation region: positive ERα and PgR staining is seen in the nucleus whereas EGFR is seen predominantly in the cell membrane (representative images, n=3).

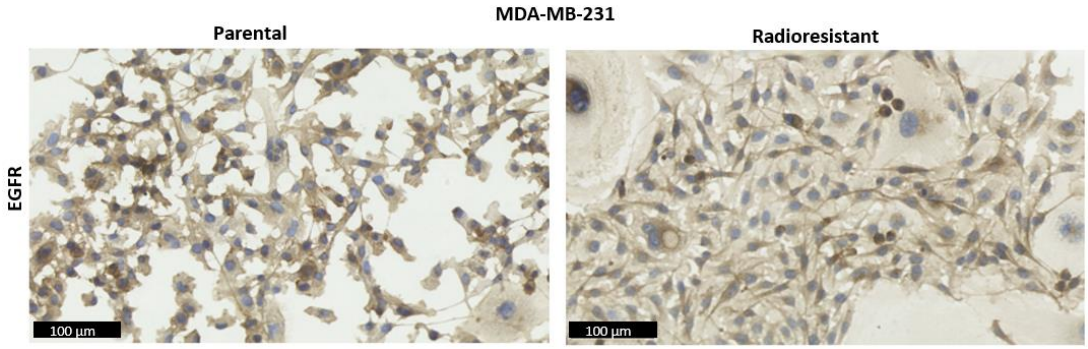

Figure 4.23. MDA-MB-231 parental and RR cells show similar EGFR expression. ICC expression profiles of EGFR in MDA-MB-231 and MDA-MB-231 RR cell lines using 2D monolayer of cells. Positive DAB staining is seen at the expected cellular localisation region: positive EGFR staining is seen predominantly in the cell membrane (representative images, n=3).

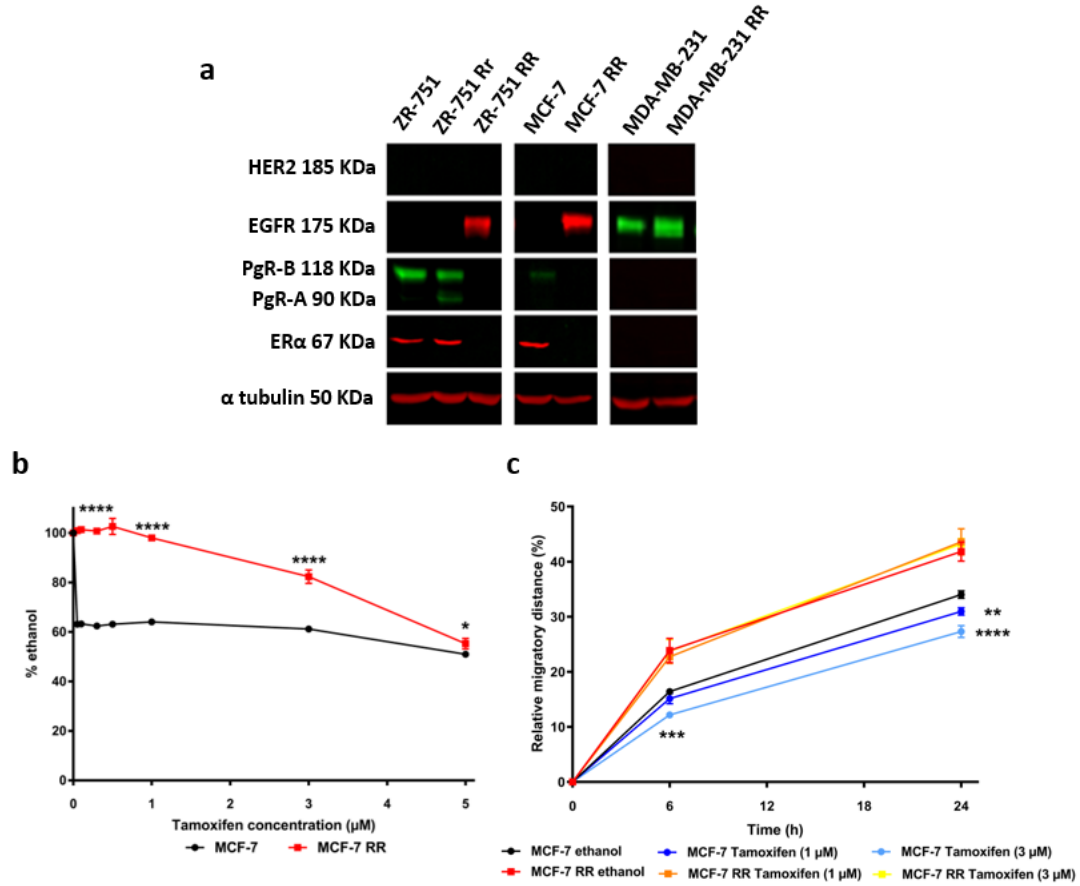

Figure 4.24. MCF-7 RR and ZR-751 RR cell lines show loss of ERα and PgR expression and gain in EGFR expression. (a) WB analysis showing parental and RR cell lines. The ZR-751 Rr cell line shows results from cells only receiving 6 weeks radiation as opposed to the 12 week course of radiation required for the development of confirmed radioresistance. **(b)** SRB at 72 h and **(c)** scratch assay up to 24 h showing the effects of tamoxifen in MCF-7 and MCF-7 RR cell lines (two-way ANOVA with Holm-Šídák multiple comparisons test; data expressed as mean ± SEM, n=3, ****$p \leq 0.0001$; ***$p \leq 0.001$; **$p \leq 0.01$; *$p \leq 0.05$).

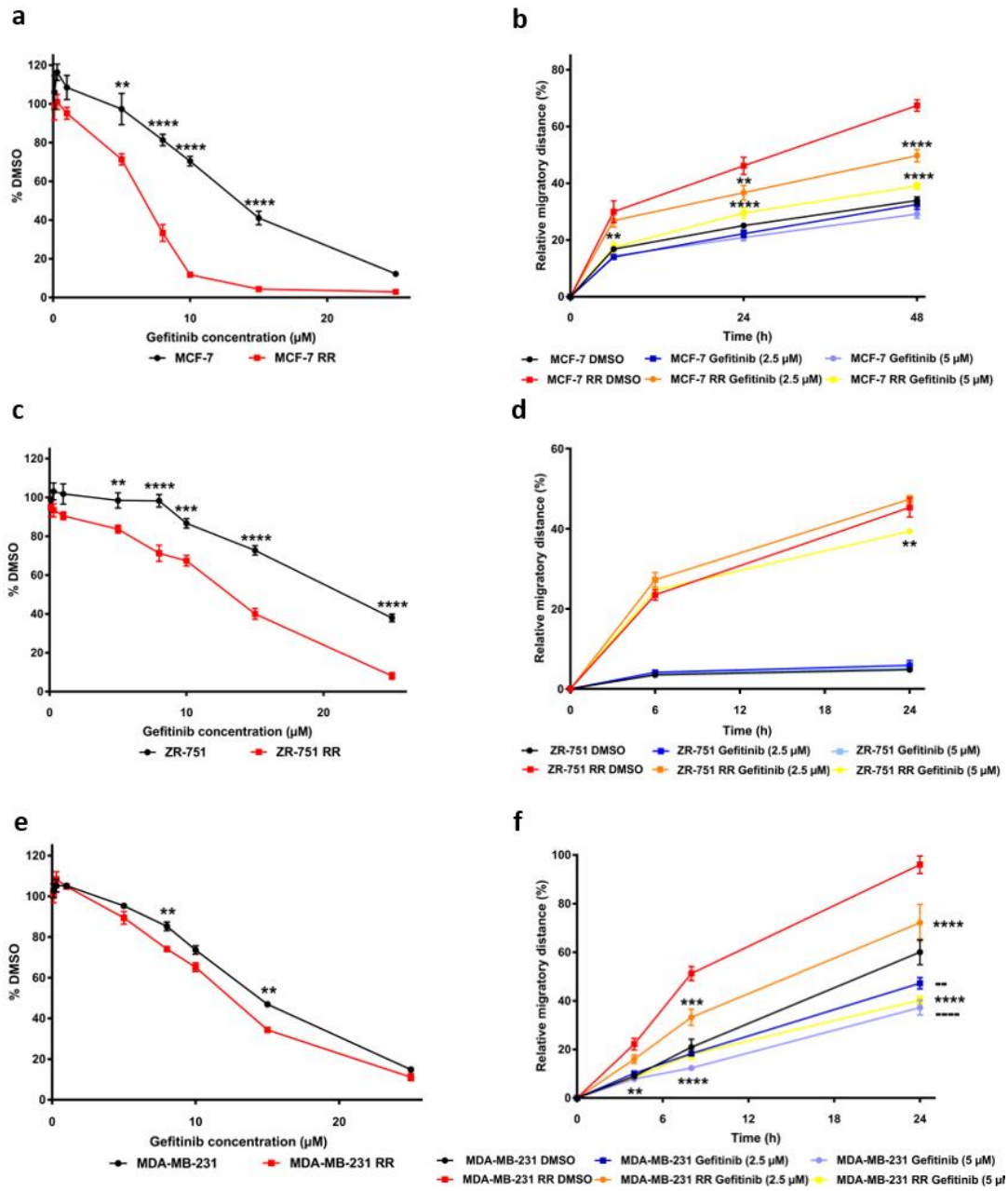

Figure 4.25. Radioresistant cell lines show increased sensitivity to gefitinib. (a) SRB at 72 h and **(b)** scratch assay up to 48 h showing the effects of gefitinib in MCF-7 and MCF-7 RR cell lines. **(c)** SRB at 72 h and **(d)** scratch assay up to 24 h showing the effects of gefitinib in ZR-751 and ZR-751 RR cell lines. **(e)** SRB at 72 h and **(f)** scratch assay up to 24 h showing the effects of gefitinib in MDA-MB-231 and MDA-MB-231 RR cell lines (two-way ANOVA with Holm-Šídák multiple comparisons test; data expressed as mean ± SEM, n=3, ****$p \leq 0.0001$; ***$p \leq 0.001$; **$p \leq 0.01$).

Table 4.3. IC_{50} values of gefitinib for each parental and RR cell line 72 h post-treatment.

Time post gefitinib treatment (h)	MCF-7	MCF-7 RR	ZR-751	ZR-751 RR	MDA-MB-231	MDA-MB-231 RR
72	13.37	6.43	22.02	13.12	14.45	12.16

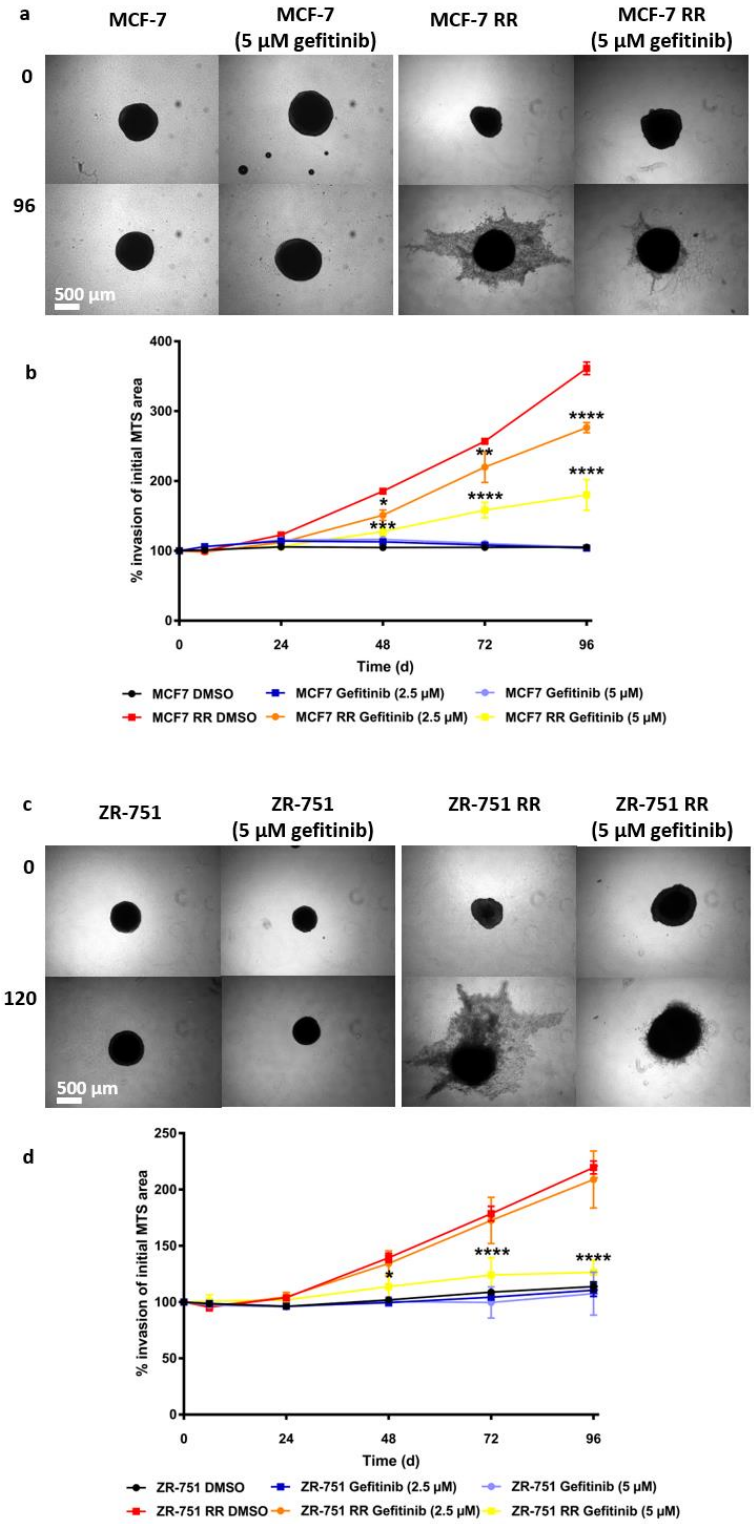

Figure 4.26. Gefitinib inhibits MCF-7 RR and ZR-751 RR invasion. 3D invasion assay showing the effects of gefitinib in **(a&b)** MCF-7 and MCF-7 RR MTS and **(c&d)** ZR-751 and ZR-751 RR MTS. MTS were placed in collagen and invasion was assessed up to 120 h post-seeding. Area of MTS at each time point was calculated and expressed as a % of the initial MTS area at day 0 (two-way ANOVA with Holm-Šídák multiple comparisons test; data expressed as mean ± SEM, n=3, ****$p \leq 0.0001$; ***$p \leq 0.001$; **$p \leq 0.01$; *$p \leq 0.05$).

4.3.8 Radioresistant MCF-7 and ZR-751 cell lines show activation of PI3K and MAPK pathways

Increased total EGFR expression was further investigated through the evaluation of downstream signal transduction pathways of the HER/ERBB tyrosine-kinase receptor family. WB analysis of time course experiments up to 30 min after 2 Gy radiation showed increased p-ERK levels in MCF-7 RR and ZR-751 RR cell lines 5 min post-radiation, whereas only smaller increases were seen in the parental cells at a much later time point (Figure 4.27). Although p-AKT did not show a response with radiation, the MCF-7 RR and ZR-751 RR cell lines had overall higher expression levels compared to those of their parental cell lines (Figure 4.28). No differences were seen in the MDA-MB-231 and RR cell lines.

MAPK pathway activity was investigated by integrating the transcriptomic data with a published gene expression signature[419], whereas PI3K activity was assessed using genes taken from the KEGG pathway database[411] in combination with FOXO-regulated genes (which have an inverse expression pattern to PI3K activity)[420]. Analysis suggested that active MAPK and inactive PI3K signalling were constitutive in the MDA-MB-231 parental and RR cell lines and expression of genes related to these pathways were not affected by radiation. Untreated ER^+ cell lines were characterised by inactive MAPK and PI3K pathway signalling, whereas their RR derivatives showed significant changes in gene expression patterns suggesting a switch to active MAPK and PI3K signalling (Figure 4.29 & Figure 4.30).

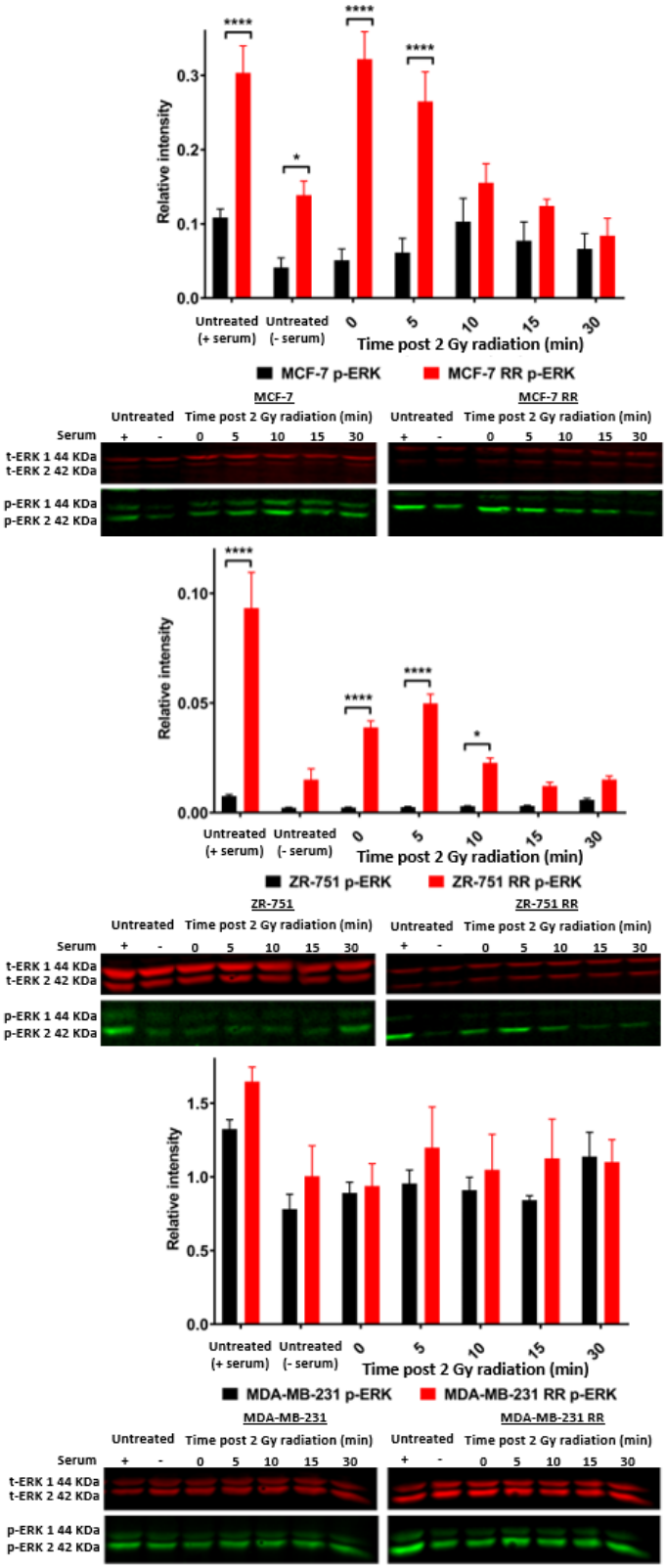

Figure 4.27. Western blot results showing activation of MAPK signalling in RR cell lines derived from ER$^+$ cells. WB analysis showing the levels of p-ERK in response to 2 Gy of radiation in MCF-7, ZR-751 and MDA-MB-231 cell lines in comparison with their RR derivatives (two-way ANOVA with Holm-Šídák multiple comparisons test; data expressed as mean ± SEM, n=3, ****$p \leq 0.0001$; *$p \leq 0.05$).

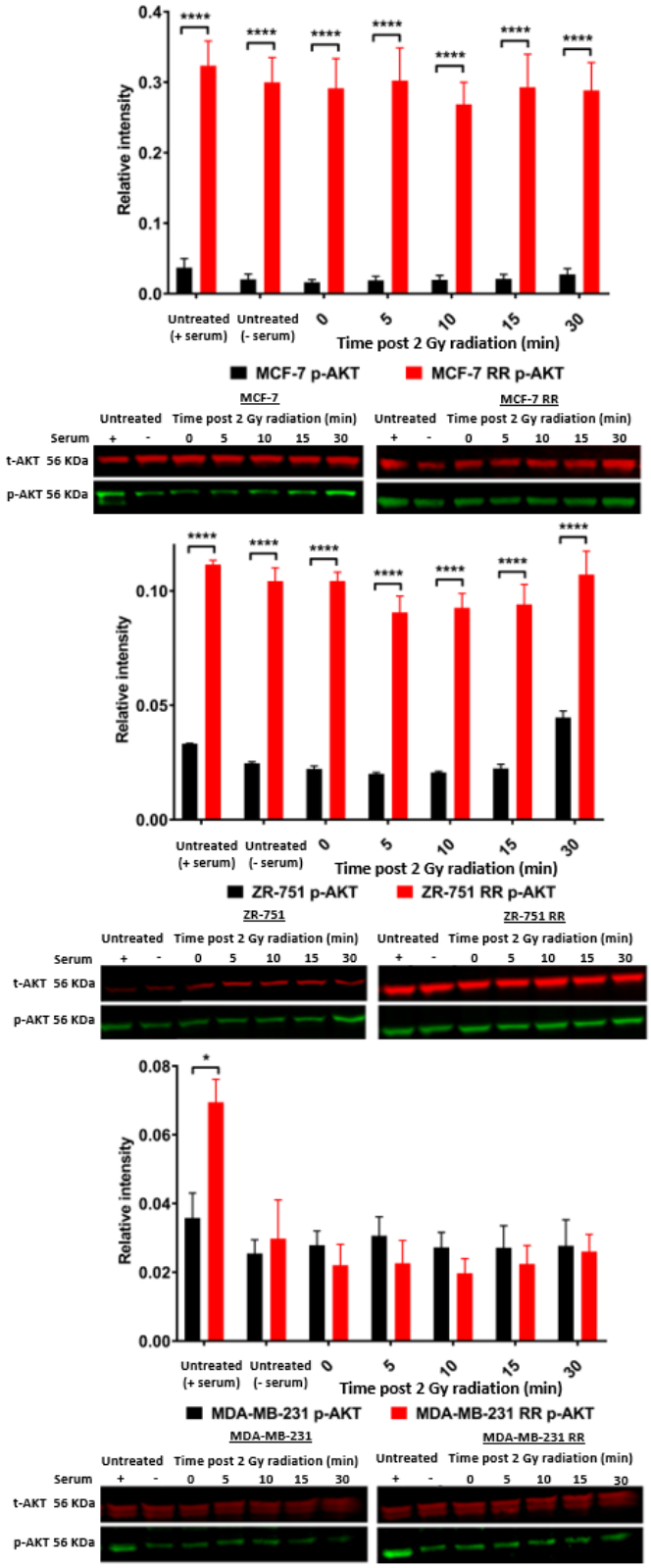

Figure 4.28. Western blot results showing activation of PI3K signalling in RR cell lines derived from ER$^+$ cells. WB analysis showing the levels of p-AKT in response to 2 Gy of radiation in MCF-7, ZR-751 and MDA-MB-231 cell lines in comparison with their RR derivatives (two-way ANOVA with Holm-Šídák multiple comparisons test; data expressed as mean ± SEM, n=3, ****$p \leq 0.0001$; *$p \leq 0.05$).

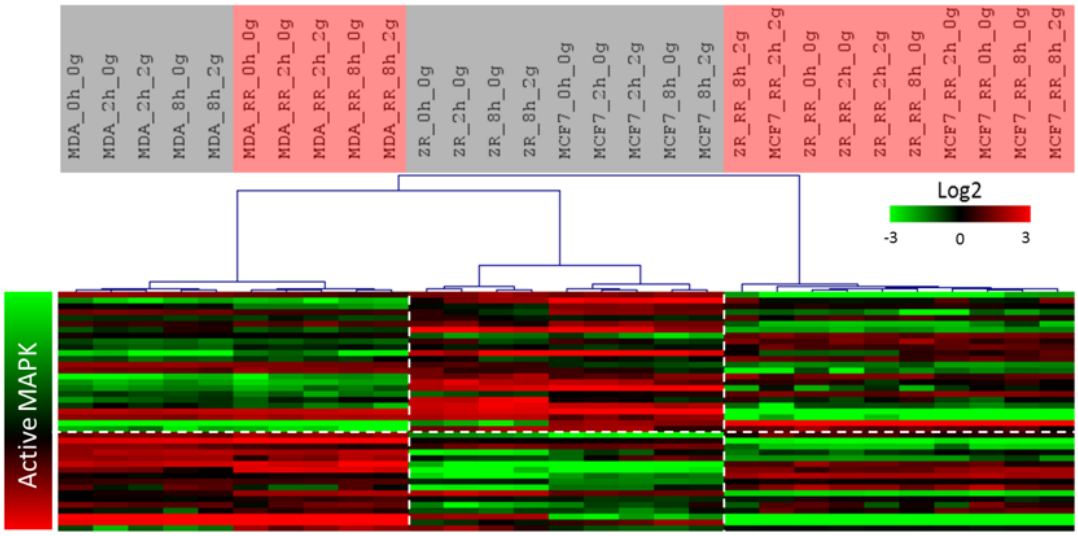

Figure 4.29. Gene analysis showing activation of MAPK signalling in RR cell lines derived from ER$^+$ cells. Log2 mean-centered gene expression heatmap showing differences between parental and RR cell lines in respect to a MAPK pathway activity gene signature[419] (red=higher expression, black=no change, green=lower expression, n=1). Heatmap clustering was carried out using Pearson correlation with average linkage.

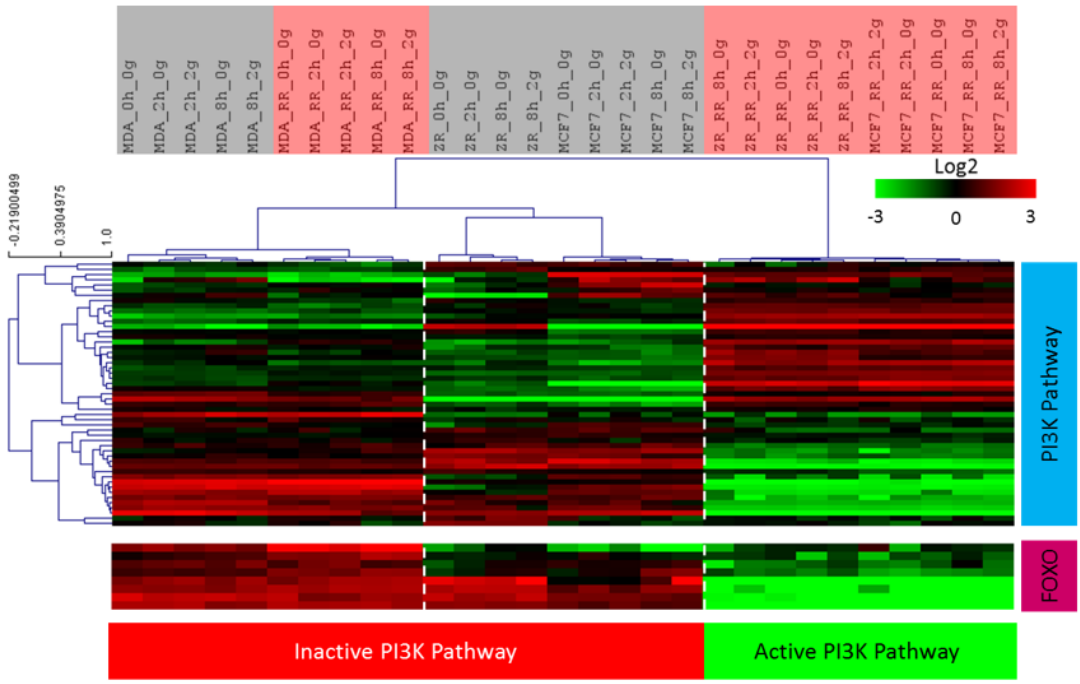

Figure 4.30. Gene analysis showing activation of PI3K signalling in RR cell lines derived from ER$^+$ cells. Log2 mean-centered gene expression heatmap showing differences between parental and RR cell lines in respect of the PI3K pathway; associated genes taken from the PI3K KEGG pathway[411] (upper heatmap) and FOXO-regulated genes[420] (lower heatmap) (red=higher expression, black=no change, green=lower expression, n=1). Heatmap clustering was carried out using Pearson correlation with average linkage.

4.3.9 ERα knockdown in MCF-7 cells results in EGFR expression, reduced proliferation and enhancement of radiosensitivity

siRNA optimisation was performed using SRB and WB analysis to select the appropriate transfection reagent concentration and the most efficient ERα siRNA to achieve maximum knockdown while preserving cell viability. Using the MCF-7 cell line, 0.1 µl of transfection reagent had no detrimental effect on proliferation up to 96 h post-transfection in mock and non-targeting transfected cells. This volume was sufficient to produce a significant reduction in proliferation when transfected with ERα siRNA (Figure 4.31). The J-003401-12, ESR1 siRNA was chosen for use in siRNA experiments over the Smart pool siRNA as lower concentrations could be used to achieve the same knockdown efficiency. WB results showed that ERα siRNA transfection lasted for 120 h, although at 120 h post-transfection ERα expression began to increase. No statistical difference in ERα expression was identified between the mock and non-targeting transfected cells, whereas ERα expression was statistically lower in the ERα siRNA transfected cells (Figure 4.32 & Table 4.4).

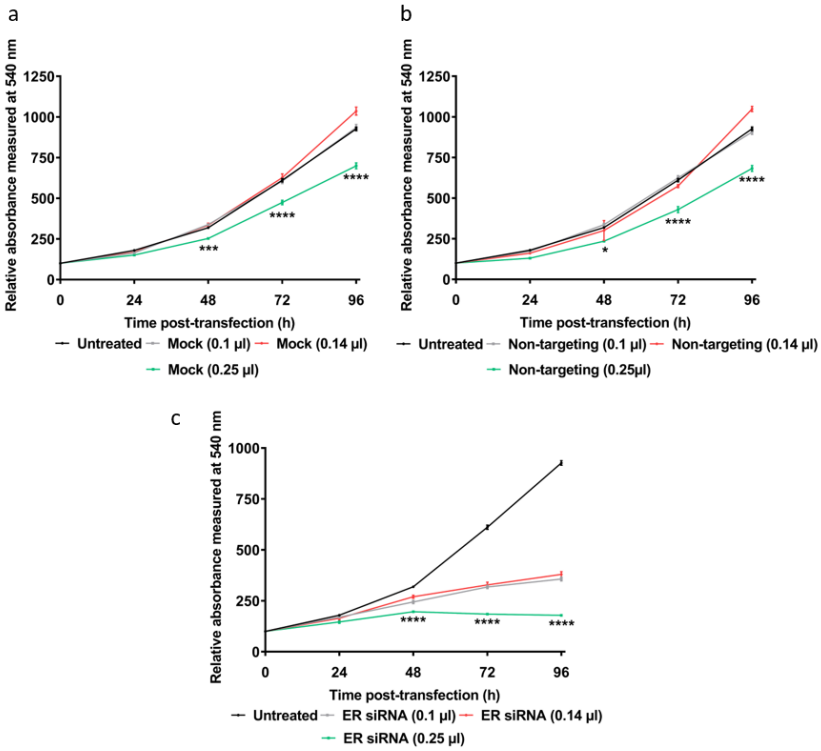

Figure 4.31. SRB assay showing proliferation of the MCF-7 cell line when exposed to different volumes of transfection reagent. Transfection volumes of 0.1, 0.14 and 0.25 µl were used in **(a)** Mock transfected, **(b)** Non-targeting transfected (25 nM) and **(c)** ERα siRNA transfected (25 nM) (two-way ANOVA with Holm-Šídák multiple comparisons test; data expressed as mean ± SEM, n=3, ****$p \leq 0.0001$; ***$p \leq 0.001$; *$p \leq 0.05$).

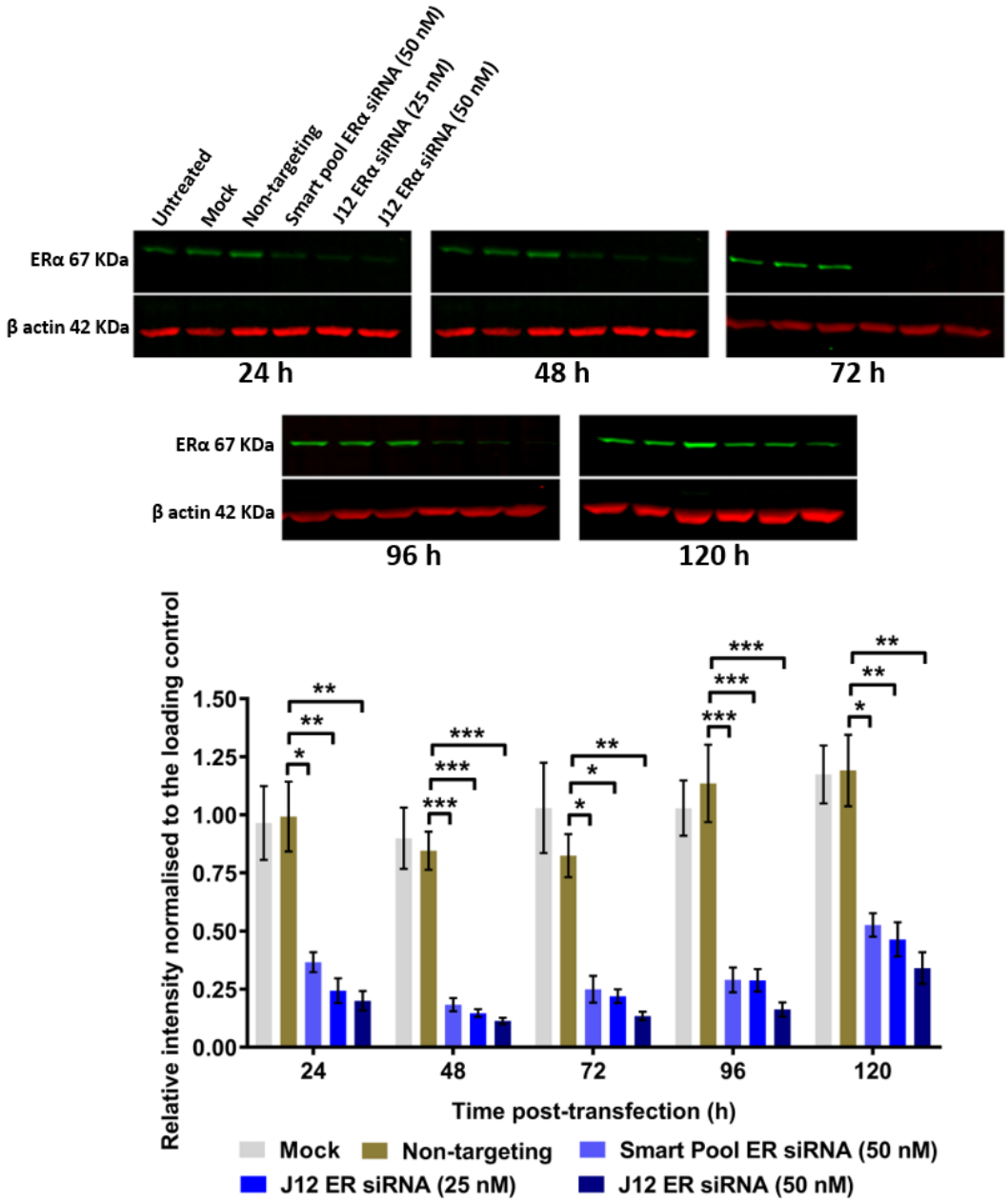

Figure 4.32. Validation of ERα siRNA knockdown in MCF-7 transfected cells. (two-way ANOVA with Holm-Šídák multiple comparisons test; data expressed as mean ± SEM, n=3, ***$p \leq 0.001$; **$p \leq 0.01$; *$p \leq 0.05$).

Table 4.4. ERα percentage knockdown compared to non-targeting transfected cells. Excellent reductions in ERα expression was seen using both the Smart pool and J12 ESR1 siRNAs based on WB analysis.

Time post-ERα siRNA transfection (h)	24	48	72	96	120
Smart pool ERα siRNA (50 nM)	62.51	78.45	70.55	74.55	40.64
J12 ERα siRNA (25 nM)	75.63	82.68	73.30	73.07	43.59
J12 ERα siRNA (50 nM)	79.45	86.70	83.71	85.83	63.08

ERα loss in the MCF-7 RR cell line was further investigated using ERα siRNA knockdown. At 72 h post ERα siRNA knockdown (25 nM) or tamoxifen treatment (0.05 µM) results showed significant reductions in MCF-7 proliferation, whereas no change was identified in the MCF-7 RR cell line (Figure 4.33). An additional reduction MCF-7 proliferation was observed when ERα knockdown or tamoxifen treatment was combined with radiation 24 h post-transfection/tamoxifen treatment, suggesting acute loss of ERα provides a radiosensitising rather than a radioprotective effect (Figure 4.34). WB analysis also showed increased EGFR expression at 96 and 120 h post-ERα knockdown (Figure 4.35).

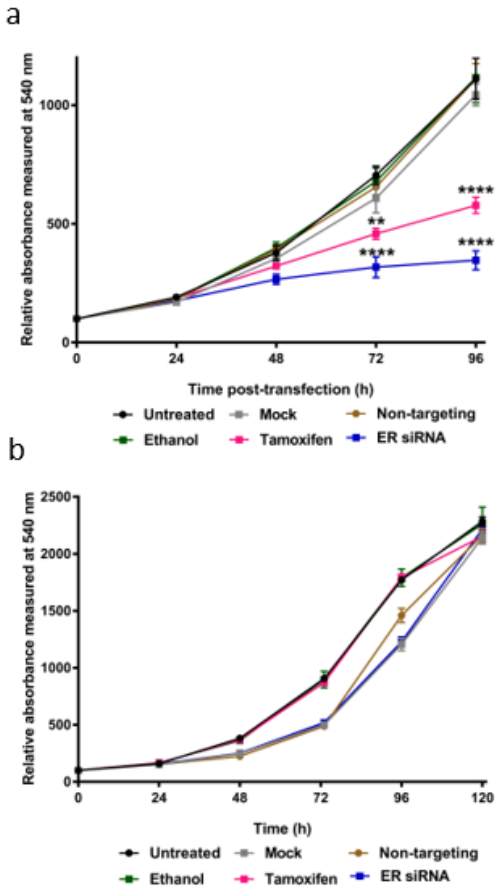

Figure 4.33. ERα siRNA transfection or tamoxifen treatment reduces MCF-7 proliferation. SRB assays showing the effect of ERα siRNA (25 nM) or tamoxifen (0.05 µM) on proliferation 72 h after treatment in **(a)** MCF-7 cells and **(b)** MCF-7 RR cells (two-way ANOVA with Holm-Šídák multiple comparisons test; data expressed as mean ± SEM, n=3, ****$p \leq 0.0001$; **$p \leq 0.01$).

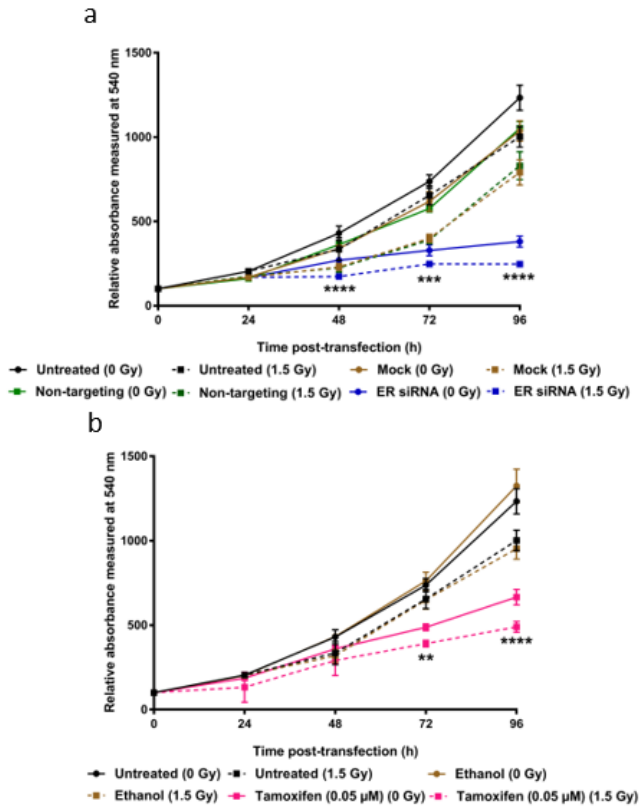

Figure 4.34. Radiation treatment combined with either ERα siRNA transfection or tamoxifen treatment results in an additional reduction in MCF-7 proliferation. Cells were exposed to 1.5 Gy radiation 24 h following either **(a)** ERα siRNA transfection or **(b)** tamoxifen treatment (two-way ANOVA with Holm-Šídák multiple comparisons test; data expressed as mean ± SEM, n=3, ****$p \leq 0.0001$; ***$p \leq 0.001$; **$p \leq 0.01$).

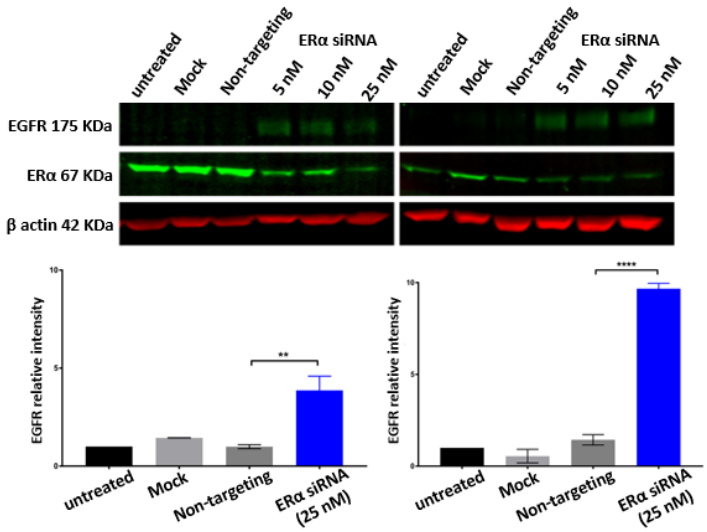

Figure 4.35. EGFR expression increases in MCF-7 cells following ERα siRNA transfection. WB results showing EGFR and ERα expression following ERα siRNA knockdown (5, 10 and 25 nM) with quantitative analysis at 96 and 120 h post-transfection (graphs document the relative intensity of EGFR normalised to the loading controls) (one-way ANOVA with Holm-Šídák multiple comparisons test; data expressed as mean ± SEM, n=3, ****$p \leq 0.0001$; **$p \leq 0.01$).

4.3.10 Radioresistant cell lines exhibit cellular plasticity within the context of intrinsic breast cancer subtyping

ER signalling was investigated further through the integration of a published ER signalling gene expression signature with the transcriptomic data[421]. As expected, both ER^+ parental cell lines were characterised by high expression of ER signalling genes in comparison to the ER^- parental and RR cell lines which had several-fold lower expression of the same genes. Interestingly, using hierarchical clustering analysis both MCF-7 RR and ZR-751 RR cell lines clustered closely with the ER^- cell lines, although they still maintained higher expression levels for a subset of these genes, similar to their parental cells. Radiation treatment did not affect the expression of these genes (Figure 4.36a).

Gene expression data was further integrated with a public gene expression dataset (GSE50811) of 67 breast cancer cell lines[422]. Untreated and radiation treated MDA-MB-231 parental and RR cell lines clustered tightly with each other in the dendrogram branch enriched for the basal breast cancer subtype. MCF-7 and ZR-751 parental cell lines obtained a luminal A classification whereas their RR derivates clustered independently and were enriched for HER2-overexpressing (MCF-7 RR) and normal-like (ZR-751 RR) intrinsic subtypes (Figure 4.36b).

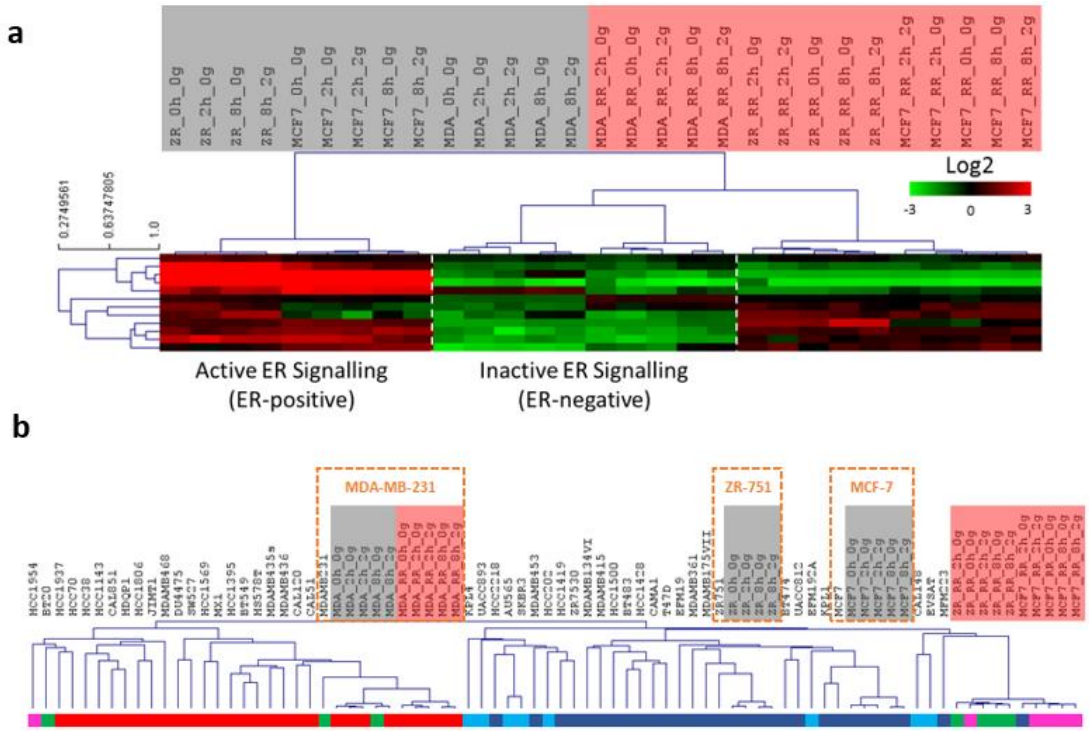

Figure 4.36. Radioresistant cell lines derived from ER$^+$ cells exhibited a change in oestrogen signalling associated genes and a change in intrinsic breast cancer subtype classification. (a) Log2 mean-centered gene expression heatmap showing differential expression of oestrogen-signalling associated genes[421] (red=higher expression, black=no change, green=lower expression). Heatmap clustering was carried out using Pearson correlation with average linkage. **(b)** Transcriptomic data integrated with a public gene expression dataset (GSE50811). Hierarchical clustering of parental and RR cell lines based on Pearson correlation to centroids of Sørlie 2003 intrinsic genes[377] (red=basal, dark blue=luminal A, light blue=luminal B, purple=HER2-overexpressing, green=normal-like, n=1).

4.3.11 Radioresistant cell lines derived from ER$^+$ cells show reduced activation of the PERK/eIF2α signalling pathway

Endoplasmic reticulum stress leading to the UPR has been shown to be implicated in radiation-induced cell death[88,89,102]. To investigate the 3 arms (PERK, IRE1, ATF6) of the UPR, gene and/or protein expression levels of UPR transducers and mediators were investigated, assessing both their inherent levels and changes in response to radiation between MCF-7 and ZR-751 parental and RR cell lines. Selected UPR components included: endoplasmic reticulum chaperone BIP, primary UPR transducer IRE1α and its target XBP1, UPR transducer ATF6, UPR transducer PERK and its target eIF2α and UPR mediators of the PERK/eIF2α pathway ATF4 and CHOP.

Gene analysis of endoplasmic reticulum stress markers identified inherently higher expression of genes encoding for BiP, ATF4, ATF6, XBP1 and PERK in MCF-7 cells compared to MCF-7 RR cells. Gene expression in both parental and RR cell lines was not altered by 2 Gy radiation at either 2 or 8 h post-treatment. Conversely, the expression of CHOP and IRE1 was inherently higher in the MCF-7 RR cells compared with their parental cells and again their expression levels did not change in response to radiation (Figure 4.37a). To investigate activation of components of the UPR, phosphorylated levels of IRE1, total PERK and its down-stream target EIF2α were examined through WB analysis in both MCF-7 and ZR-751 parental and RR cell lines. Results confirmed statistically higher levels of total PERK ($p \leq 0.0001$), p-PERK ($p \leq 0.0083$), and p-eIF2α ($p \leq 0.0068$) in the MCF-7 parental cells compared to the MCF-7 RR cell line. These results were mirrored in the ZR-751 parental and RR cell lines, with statistically higher levels of total PERK ($p \leq 0.0001$), p-PERK ($p \leq 0.0056$), and p-eIF2α ($p \leq 0.0469$) in the ZR-751 parental cell line. An almost complete loss of total and p-PERK was seen in both RR cell lines. MCF-7 parental cell lines also demonstrated increased p-PERK expression at 8 h post-radiation returning to baseline levels at 24 h; this radiation response did not occur in the MCF-7 RR cell line. Statistically lower levels of p-IRE1 were seen in MCF-7 ($p \leq 0.0009$) and ZR-751 ($p \leq 0.0114$) parental cells compared with their RR derivatives (Figure 4.37b & Figure 4.38).

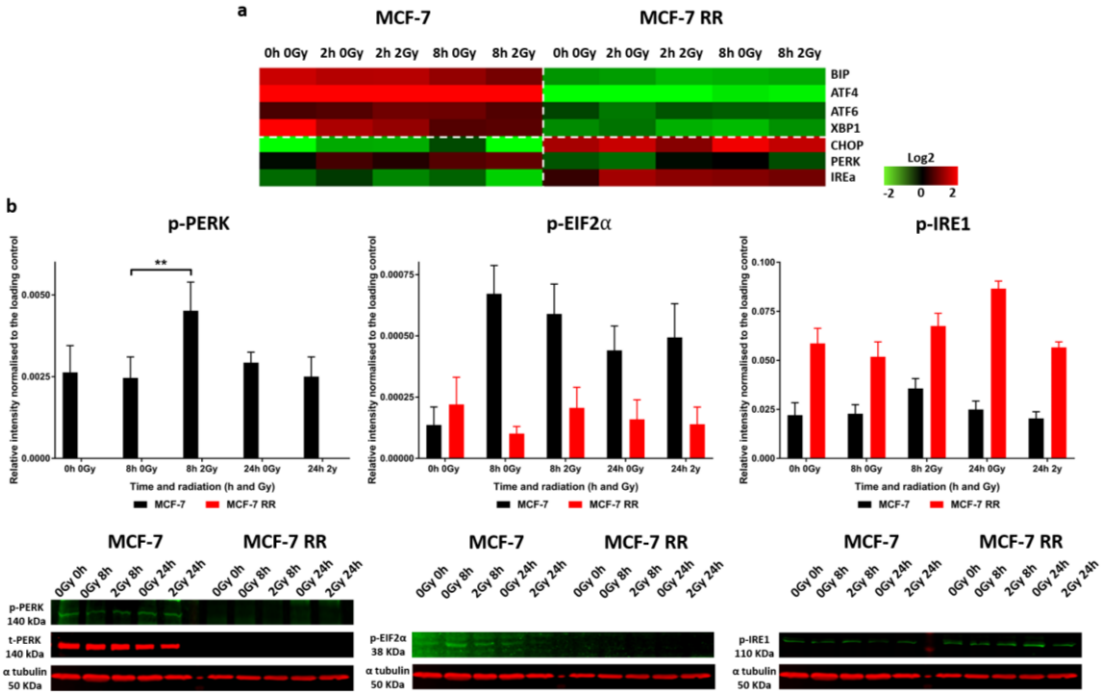

Figure 4.37. Gene expression and western blot analysis show inherent differences in UPR pathway activation between MCF-7 and MCF-7 RR cell lines. (a) Log2 mean-centered gene expression heatmap showing differences in respect of endoplasmic reticulum markers between untreated and radiation treated MCF-7 and MCF-7 RR cell lines (red=higher expression, black=no change, green=lower expression, n=1). Heatmap clustering was carried out using Pearson correlation with average linkage. **(b)** WB analysis showing the levels of p-PERK, p-eIF2α and p-IRE1 in untreated MCF-7 and MCF-7 RR cell lines in comparison to 2 Gy treated cells at 0, 8 and 24 h post-radiation (two-way ANOVA with Holm-Šídák multiple comparisons test; data expressed as mean ± SEM, n=3, $^{**}p \leq 0.01$).

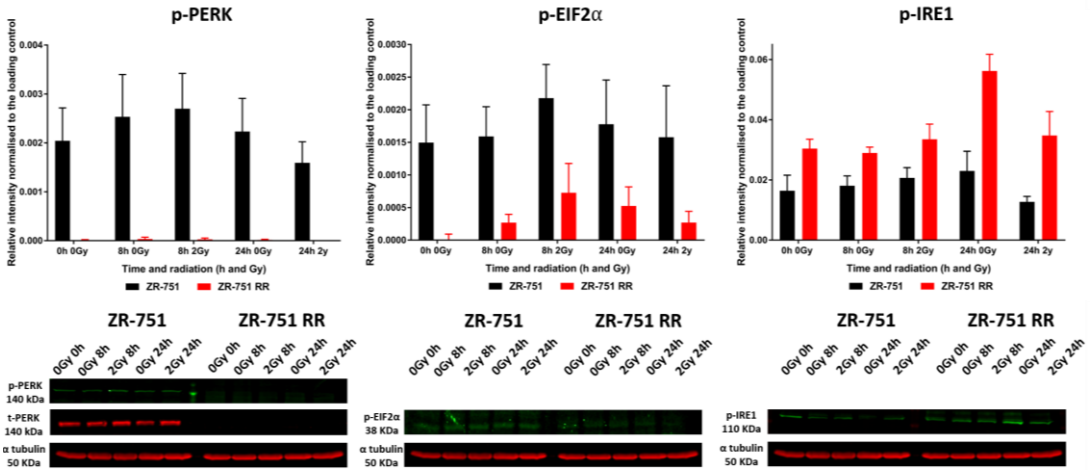

Figure 4.38. Western blot analysis shows inherent differences in UPR pathway activation between ZR-751 and ZR-751 RR cell lines. WB analysis showing the levels of p-PERK, p-eIF2α and p-IRE1 in untreated ZR-751 and ZR-751 RR cell lines in comparison to 2 Gy treated cells at 0, 8 and 24 h post-radiation (two-way ANOVA with Holm-Šídák multiple comparisons test; data expressed as mean ± SEM, n=3).

4.4 Discussion

Cancer cells that possess innate radioresistance or those that acquire it can contribute to treatment failures and poor patient outcomes. Treatment failures can occur through tumours not responding or only partially responding to RT or due to the development of recurrent loco-regional and/or metastatic disease. Through the identification of genes, proteins and signalling pathways that are related to the acquisition of radioresistance, targets can be identified, and therapeutic approaches developed to overcome the clinical issue of radioresistance. The generation of *in vitro* RR cancer cell line models can help study, and subsequently target, the mechanisms involved in the development of acquired radioresistance. However, only a small number of previous studies have developed RR cell lines to investigate acquired radioresistance and these focused on single specific pathways, which limited their ability to determine the complex interrelated systems that govern radioresistance development[410,423-427].

This chapter describes the development of novel RR breast cancer cell lines from both ER^+ hormone-responsive (MCF-7 and ZR-751) and ER^- hormone non-responsive (MDA-MB-231) molecular subtypes and the characterisation of their inherent differences and responses to radiation. Using genetic, molecular and functional assays, in 2D and 3D model systems, a more global characterisation of this RR model was achieved. 3D culture systems were incorporated into the experiments to increase the complexity of the RR model. These MTS models more accurately represent the TME within a solid tumour, as they develop O_2, nutrient and pH gradients, producing a central necrotic core with an outer mantle of proliferating cells[428]. The novel MTS derived from RR cells developed in this study have not been described before in the literature and serve as excellent *in vitro* RR tumour models which were used to investigate invasiveness and protein expression through IHC.

Following the 12-week development period, all RR cell lines were confirmed as radioresistant through proliferation and CF assays with respect to their sensitivity to a single, clinically relevant, dose of radiation. These initial experiments validated the use of these cell lines as *in vitro* models to characterise the radioresistant phenotype and investigate the mechanisms involved in its development. Using the same assays, the radioresistant phenotype was also shown to be maintained in MCF-

7 RR (and REM-134 RR) cells that had not been exposed to radiation for 6 months. This indicated RR models were generated in which the acquisition of radioresistance was not transient. This is in contrast to a previous study that showed that radioresistant MCF-7 cells lost their resistant phenotype 12 weeks after a final dose of radiation[424]. The difference in maintenance of the RR phenotype could be due to the fact that we developed our model by increasing weekly radiation doses by 0.5 Gy or due to cell lines being exposed to radiation over a longer period of time. These factors could contribute to the generation of a more stable phenotype. Varying results from different RR models highlights the importance of regular confirmation of maintained radioresistance through CF/SRB assays.

The cell cycle of a cancer cell can significantly influence the effects of radiation. Cells during the G2/M phase are most sensitive to radiation-induced DNA damage whereas those in late S-phase are most resistant. Fractionated RT treatment plans can help overcome this cell cycle-associated radioresistance by allowing radioresistant S-phase cells to progress into a more sensitive cell cycle phase in between the daily fractions of radiation. Quiescent cells or those that only progress slowly through the cell cycle are known to be more radioresistant, as they have more time to activate DNA damage response pathways and repair DNA damage before cellular division occurs. Results from our study suggested reduced proliferation in terms of cell cycle arrest genes and Ki67 staining in MTS, which is in accordance with other studies showing reduced proliferation rates of *in vitro* prostate cancer RR cell lines[429]. In clinical terms, reduced cancer cell proliferation rates as demonstrated by Ki67 staining has been associated with poor local control of HNSCC tumours[430].

Among breast cancer patients, metastatic disease accounts for more than 90% of cancer-related deaths[431], so understanding the processes involved in breast cancer metastasis and treatment failure is of clinical importance. Results obtained using functional assays identified that MCF-7 RR and ZR-751 RR cell lines had significantly increased migration and invasion ability compared with their parental cells, whereas the MDA-MB-231 RR cell line exhibited increased migration with only a marginal and non-significant increase in invasion compared to its parental cell line. These results suggested that the RR cell lines had developed a more aggressive phenotype, which was more evident in the RR cell lines derived from ER^+ cells.

Clinically these results could lead to a greater potential for local tissue invasion and metastasis. These functional changes are likely to be orchestrated by EMT. EMT is a critical process involved in malignant cellular transformation leading to reduced cell–cell contacts, increased cell motility and metastasis[432-434]. In addition, EMT can influence other cellular processes such as enhanced survival[435], genomic instability[436], cancer stem cells[425,437] and resistance to chemotherapy and RT[415,425,438]. The loss of epithelial morphology that occurs during EMT has been shown to be a prognostic indicator that correlates with poor prognosis[439]. We evaluated known biomarkers for breast cancer EMT[440] in our RR model and demonstrated, at both gene and protein levels, down-regulation of E-cadherin and up-regulation of vimentin, N-cadherin and SNAIL in the MCF-7 RR and ZR-751 RR cell lines. These results supported the morphological and functional changes identified in these RR cells, which developed a more mesenchymal-like phenotype with increased invasive and migratory potential. In contrast to the epithelial-like ER^+ cell lines, the MDA-MB-231 cell line has a much more mesenchymal-like phenotype with constitutively low E-cadherin and high vimentin expression; because of this, further development of EMT in its RR derivative was difficult to ascertain. Multiple signalling pathways can activate EMT in both normal and cancer cells, including receptor tyrosine kinase signalling, WNT-β-catenin and Notch signalling[441,442]. Radiation alone can also induce EMT through the expression of TGFβ[443,444]. Both EGFR downstream signalling pathways and WNT signalling were found to be activated in MCF-7 RR and ZR-751 RR cell lines suggesting possible mechanisms by which EMT may be activated. WNT signalling has been shown to play a role in EMT, with one study using MCF-7 cells showing that WNT signalling could inhibit Snail phosphorylation, causing an increase in Snail protein and activity levels resulting in the MCF-7 cells gaining a mesenchymal-like phenotype[441]. It is interesting to note that in our results the same population of cells, predominantly those around the periphery of the MTS formed from RR cells from ER^+ cell lines, showed increased co-expression of vimentin, Snail, N-cadherin and WNT5a[409].

Breast cancers can be characterised and subtyped using IHC and gene expression analysis. Expression of receptors such as HER2, ERα, PgR and EGFR can be assessed by IHC, whereas gene expression profiling can be used to identify

cancer cell molecular profiles and classify them into 5 specific tumour subtypes: basal, luminal A, luminal B, HER2-overexpressing and normal-like[416,445]. These subtypes exhibit differential sensitivities to radiation and have distinct clinical outcomes[417,418]. The clinical usefulness of breast cancer molecular subtyping is undeniable, as it can help influence a patient's treatment plan and give an indication of prognosis. However, its usefulness in subtyping *in vitro* cell lines remains controversial. This issue has been previously investigated by comparing genomic and transcriptional characteristics of primary breast tumours with those of cancer cell lines. One study showed that genome aberrations and transcriptional changes identified in 51 cancer cell lines (including MCF-7, ZR-751 and MDA-MB-231) were well preserved compared to those found in primary tumours of a similar subtype[446]. Although the cell lines carried more genome aberrations, possibly related to certain cell lines having been derived from pleural effusions or late stage tumours, the study concluded that cell lines can show stable genomic patterns which do not necessarily accumulate significant numbers of new mutations during extended culture. This study also reported that cell lines are well suited to assess the functional consequences of genome aberrations-mediated gene deregulation and are useful in the identification of molecular features that predict sensitivity/resistance to agents targeting these changes. However, it is important to understand that profiling cell lines does not consider the TME, which includes normal stromal tissue and epithelial cells, nor will it reflect intra-tumoural heterogeneity. With these caveats in mind, the purpose of subtyping the parental and RR cell lines in this study was to demonstrate that radioresistance development is consistent with a change in intrinsic subtype to a prognostically less favourable classification[409].

Transcriptional profiles of the parental and RR cell lines were used to assign each one to an intrinsic breast cancer subtype. Both parental and RR MDA-MB-231 cell lines were triple negative and transcriptional subtyping identified them both as basal[377,445,447,448]. Treatment of basal breast cancers mainly relies on chemotherapy, as targeted therapies are lacking. Unfortunately, basal breast cancer is associated with lower disease-specific survival rates and a higher risk of local and regional recurrence compared with luminal subtypes[445,447,448]. It is therefore not surprising that no significant changes were identified in the MDA-MB-231 RR cell line as the

parental MDA-MB-231 cell line is inherently aggressive in nature. A change in subtype classification was identified in both RR cell lines derived from ER^+ cells, with a shift from luminal A for both MCF-7 and ZR-751 cell lines towards a non-luminal classification. The MCF-7 RR cell line closely correlated with the HER2-overexpressing subtype while the ZR-751 RR cell line correlated with the normal-like subtype. Although the MCF-7 RR cell line did not express HER2 in IHC assessment, it is likely that it gained its HER2-overexpressing classification due to its gain in EGFR expression in combination with MAPK and PI3K activity, which are also found in HER2 positive breast cancers. Normal-like breast cancers resemble normal breast tissue with high expression of genes associated with adipocytes and non-epithelial cell types, and low expression of genes related to luminal epithelial cells. Both HER2-overexpressing and normal-like subtypes carry a worse prognosis compared to luminal A tumours, with HER2-overexpressing tumours having a higher risk of locoregional recurrence[377,445,447,448]. Luminal A tumours also respond well to hormone and radiation treatment[447], and so a shift away from this subtype would be consistent with endocrine therapy resistance, reduced radiosensitivity and a more aggressive phenotype. These results show that the acquisition of radioresistance can be linked with cellular plasticity through extensive alterations in gene expression resulting in a change in molecular subtype classification.

Investigation of common breast cancer signalling receptors demonstrated that MCF-7 RR and ZR-751 RR cell lines lost ERα and PgR expression and gained EGFR expression. Furthermore, when siRNA transfection was used in the MCF-7 cell line to knockdown ERα this resulted in increased EGFR expression, suggesting a direct relationship between ERα loss and EGFR expression. Gene analysis also corroborated ERα loss, with lower expression of ER driven genes in the RR cell lines derived from ER^+ cells. An inverse relationship between ER activity and EGFR and HER2 expression has been reported in clinical breast cancers and overexpression of these receptor tyrosine kinases is associated with reduced sensitivity to endocrine therapy and worse prognosis[449-451]. This apparent switch from ER signalling to EGFR-mediated signalling in the RR cell lines derived from ER^+ cells was investigated using the EGFR inhibitor gefitinib and the anti-oestrogen tamoxifen.

Gefitinib treatment produced greater concentration-dependent reductions in cell proliferation, migration and invasion in the MCF-7 RR and ZR-751 RR cell lines compared with their parental cells. The calculated IC_{50} values were 6.43 (MCF-7 RR) and 13.12 μM (ZR-751 RR); although these values were approximately half that of the parental cells (13.34 μM for the MCF-7 and 22.02 μM for the ZR-751), these concentrations are still relatively high compared to clinically relevant doses[452-454]. Therefore, these results suggest that, although the MCF-7 RR and ZR-751 RR cell lines are still relatively insensitive to the effects of gefitinib, a significant sensitisation was seen in comparison to their parental cell lines. Results also showed that the MCF-7 RR cells developed simultaneous resistance to tamoxifen at clinically relevant doses. In the clinic, patients with ER^+ breast cancer may be treated with tamoxifen for 5-10 years following surgery and RT. If radioresistant cells survive following completion of the RT course then, as our results suggest, these radioresistant cells may also gain tamoxifen resistance. Repopulation of the tumour site with endocrine therapy-resistant and radioresistant cancer cells could significantly limit treatment options and have a negative impact on patient outcome. Mechanisms for acquired tamoxifen resistance are complex, since resistant tumours do not usually lose ERα expression and the receptor remains functional[455]. This is demonstrated by patient cohorts with recurrent disease still being able to respond to second line endocrine therapy[456,457]. Studies have suggested that this form of resistance could work through ER function modification by growth factor pathways[458,459]. Another study investigated tamoxifen resistance in MCF-7 RR cells, showing resistance occurred without a change in the expression levels of ER but with enhanced AKT phosphorylation. This study suggested that sequential tamoxifen treatment post-radiation treatment could be more effective than providing the treatments concurrently[427]. Conversely, results from our study showed an additional inhibition of proliferation when radiation was delivered 24 h after tamoxifen treatment or ERα knockdown in the MCF-7 cells. Suggesting that the use of tamoxifen before and during a patient's RT treatment would be advantageous. Another study determined that tamoxifen-resistant MCF-7 cells showed increased EGF sensitivity, with oestradiol stimulating MAPK activation. Tamoxifen was able to elicit rapid MAPK phosphorylation in the MCF-7 resistant cells, whereas

inhibition of the EGFR/MAPK pathway caused a significant inhibition of proliferation. Although ERα was not lost in these tamoxifen-resistant cells, it became redistributed to extra-nuclear sites (cytoplasmic translocation). It was postulated that the enhanced function of ERα was due to cooperation with EGFR and is a possible mechanism for the development of acquired resistance to tamoxifen[460]. Similar results have also been shown in anti-oestrogen-resistant MCF-7 cell lines developed through continuous culture in fulvestrant. These resistant cells developed reduced ERα expression and loss of PgR with a shift towards dependence on EGFR/MAPK-mediated signalling[461]. Our RR model is the first to report a link between acquired radioresistance and the loss of ERα and PgR and resistance to tamoxifen. Therefore, this suggests that tamoxifen resistance secondary to acquired radioresistance may involve different pathways compared to the development of tamoxifen resistance from chronic drug exposure and that additional targeted therapy may be required in these cells to overcome both endocrine and radiation resistance.

Following the identification of increased EGFR expression in the RR cell lines, downstream signal transduction pathways of the HER tyrosine-kinase receptor family were investigated. Increased activation of the PI3K/AKT/mTOR cascade is frequently seen in a wide range of cancer types and can trigger downstream pathway responses related to cell survival, apoptosis, proliferation, migration, invasion, and metabolism[462,463]. This pathway can be activated by radiation and has been associated with resistance mechanisms, with constitutively activated AKT being linked to intrinsic radioresistance[464,465]. In this study we found that the gene expression signature in the MCF-7 RR and ZR-751 RR cell lines fitted with activation of the PI3K pathway. Although p-AKT did not increase in response to radiation, expression levels were statistically higher than in the parental cell lines, suggesting a constitutively activated PI3K/AKT/mTOR signalling pathway in these RR cell lines, which may play an important role in their radioresistant phenotype. These pathways have also been shown to be activated in RR prostate cancer cell lines (androgen responsive and non-responsive) in combination with enhanced EMT/cancer stem cell phenotypes and activation of checkpoint proteins[425].

In breast and other cancers, EGFR activation with stimulation of the downstream components of the MAPK cascade, including phospholipase-C, Ras, and

Raf-1, has been linked with radiation-induced cancer cell proliferation[466-469] and is considered to be a cytoprotective response[470] and a mechanism by which cancer cells can cause tumour repopulation during fractionated RT. Results at gene and protein level from this study suggest that MAPK signalling is activated in the MCF-7 RR and ZR-751 RR cell lines. Basal expression levels of p-ERK1 and p-ERK2 were significantly higher in MCF-7 RR and ZR-751 RR cell lines compared with their parental cells. Radiation-induced ERK1 and ERK2 phosphorylation also occurred more quickly and to a greater degree following a 2 Gy dose of radiation in these RR cell lines. These results suggest that EGFR signalling, and multiple components of its downstream pathways are activated in the MCF-7 RR and ZR-751 RR cell lines. This finding could have clinical implications, as multiple pathways may need to be targeted to improve therapeutic responses to radiation and overcome resistance[409].

The UPR is an important cellular process that enables cells to respond to endoplasmic reticulum stress, resulting in either restoration of normal cellular functions and endoplasmic reticulum homeostasis or cell death[471]. The UPR of ER^+ parental and RR cell lines was characterised because previous studies have shown that radiation can induce endoplasmic reticulum stress and UPR activation[88,89]. If differential pathway activation is occurring in the RR cell lines, then this may provide a radiation-induced pro-survival mechanism rather than activating endoplasmic reticulum-induced apoptotic or autophagic cell death pathways. The most striking finding from our results was an almost complete loss of total and p-PERK expression and significantly reduced expression of eIF2α in both RR cell lines derived from ER^+ cells. A previous study using MDA-MB-231 cells showed that, although endoplasmic reticulum stress markers and CHOP levels were not elevated following radiation, the PERK-eIF2α pathway did become activated; these results led the authors to conclude that PERK-dependent radiation-induced apoptosis was not CHOP mediated. Furthermore, PERK down-regulation using siRNA resulted in lower levels of radiation-induced apoptosis, leading to increased radioresistance[472]. Although this study used an ER^- cell line, it provides an important comparison with our results, as our RR cell lines derived from ER^+ cells have some ER^- phenotypic characteristics. As endoplasmic reticulum stress-induced apoptosis is primarily mediated by the PERK/eIF2α UPR pathway[90,97], these results support our findings

that a reduction in PERK-eIF2α pathway activation may be contributing to the RR phenotype.

Although apoptosis is considered the main mechanism by which irreversibly endoplasmic reticulum stressed cells are removed, typical apoptotic pathways may not occur in the MCF-7 cell line since, although it possesses caspase 6 and 7, it is deficient in functional caspase 3. One study showed that PERK and radiation-induced phosphorylation of eIF2α were essential for autophagy and radiosensitivity in caspase 3/7-deficient cells[102]. Although our study reported almost identical results for MCF-7 and ZR-751 cell lines, further work would be required to determine if they are undergoing similar caspase 3-independent autophagy or some other cell death mechanism. The increased gene and protein expression levels of IRE1 in the RR cell lines warrant further investigation, as this part of the UPR can be protective or lead to apoptosis. If the MCF-7 and MCF-7 RR cell lines are predominantly relying on PERK-mediated radiation-induced autophagy, then IRE1 activation may suggest the pathway is being used as a pro-survival mechanism, as this pathway has not been shown to be involved in cell death through autophagy. Although expression signatures of the major UPR genes differ among tissues and diseases, BiP, PERK, IRE1α and ATF6 have been shown to have increased expression in breast carcinomas[473]. Inherent expression of these markers could explain the base line gene and protein levels seen in our experiments, especially in the MCF-7 and ZR-751 parental cells.

4.5 Conclusion

This chapter has described the development of novel RR models which incorporated the use of both 2D and 3D culture systems. Characterisation of these RR breast cancer cell lines was performed using multiple different techniques including gene, protein and functional experiments. This in-depth characterisation allowed results to be validated through independent means and provided a more global approach to understanding the cellular changes that occur following the acquisition of radioresistance. The development of RR cells from both ER^+ and ER^- parental cell lines allowed for comparisons to be made between not only paired parental and RR cell lines but also between the different molecular breast cancer subtypes. The most striking cellular changes were identified in the RR cell lines

derived from ER^+ cells; these RR cells were characterised by a shift towards a more invasive mesenchymal phenotype, with changes in oestrogen-regulated signalling pathways, gain of EGFR signalling and a change in subtype classification. The ER^- cell line possessed these characteristics at the outset and hence its phenotype changed relatively little with radioresistance development.

Well characterised models of resistant disease, as developed and examined in this chapter, are needed if continued progress is to be made in understanding the mechanisms and signalling pathways involved in the development of radioresistance. Future studies using this RR model can now target the differentially activated pathways identified in the RR cell lines to focus on radioresistance reversal. The use of paired parental and RR cell lines can also be used to identify genetic and secretomic signatures to assess a tumour's response to radiation. This type of study will likely be instrumental in the development of new therapeutic strategies for patients who either fail to respond to treatment or develop recurrent disease.

5 Identification of Biomarkers Released from Cancer Cells in Response to Radiation – A Pilot Study

5.1 Abstract

Background: Identification of patients that fail to respond to radiotherapy during treatment could decrease the number of patients receiving radiation treatment for no therapeutic gain and allow the use of alternative therapies at an earlier stage. Monitoring radiation-induced secreted cancer biomarkers could assess a tumours response to radiotherapy, determine radiosensitivity and provide a means of identifying non-responding patients. **Methods:** To identify radiation-induced secreted biomarkers, cancer cells were exposed to radiation and liquid chromatography-mass spectroscopy was performed on conditioned media samples. To identify biomarkers related to radiosensitivity, gene expression analysis was performed using parental and radioresistant cell lines. **Results:** Using the MCF-7 cell line, 33 biomarkers were identified as having up to a 12-fold increase in secretion in response to radiation compared to controls at 24 h. Based on secretion profiles and functional analysis 9 candidate biomarkers were selected (YBX3, TK1, SEC24C, EIF3G, EIF4EBP2, NAP1L4, VPS29, GNPNAT1 and DKK1), of which the first 4 underwent in-lab validation. Gene analysis identified higher expression of genes encoding 7 of the candidate biomarkers in the MCF-7 cell line compared to its radioresistant derivative. Western blot identified increased levels of the 4 biomarkers in the conditioned media of parental cells 24 h post-radiation which was not seen in the RR cell lines. C**onclusions:** The identification of biomarkers that have differential gene expression and secretion profiles in response to radiation between sensitive and RR cell lines has provided initial evidence that these biomarkers may be useful for predicting and/or monitoring the response to radiotherapy.

5.1 Introduction

Monitoring a tumours response to radiation whilst a patient is undergoing RT could provide a means by which a patient's treatment could become tailored, with patients not responding to traditional RT given alternative therapies at an earlier stage of the treatment process. One method through which response could be

measured is through the detection of tumour secreted biomarkers, either in the blood or within the tumour itself using an implanted sensor. Research using the secretome of cancer cells is likely to aid the discovery of these clinically relevant biomarkers.

Although the term 'cancer secretome' should be used to describe all substances secreted by cancer cells and cancer-associated stromal cells through the classical or non-classical pathways it is more commonly applied to proteins identified by mass spectrometry in the conditioned media (CM) of cancer cell lines[474]. Although these types of experiments do not accurately re-create the complex TME, the CM obtained with these experiments is less complex than that of biological fluids, which increases the likelihood of identifying low abundance substances. Several secretomic studies have used CM from breast cancer cell lines as *in vitro* model systems[475-479]. Many of these studies are comparative, using non-tumourigenic and tumourigenic cell lines to investigate differentially secreted proteins related to malignant transformation, with the aim of identifying secreted biomarkers for early breast cancer diagnosis[475-477]. The MCF-10 isogenic cell line has been used in various secretomic studies to help identify differentially secreted proteins from cell lines representing different tumourigenic stages, ranging from the non-tumourigenic MCF-10A through to the tumourigenic/metastatic MCF-10CA cl. Differential secretome profiles between non-tumorigenic and malignant cell lines have been confirmed in numerous studies[475,477], providing evidence that secreted proteins within the cancer secretome can be used to predict the aggressiveness of breast cancer cells. Cancer cell line *in vitro* secretomic results have also been validated using clinical samples; following *in vitro* identification that activated leukocyte cell adhesion molecule (ALCAM) was secreted in higher levels in non-invasive and metastatic breast cancer cell lines compared with breast epithelial cells[480], a clinical study investigated its use as a serum biomarker for breast cancer diagnosis. This study showed ALCAM serum concentrations were statistically higher in breast cancer patients compared with normal women, with the test having higher diagnostic sensitivity compared to other serum biomarker assays currently used (CA15-3 and CEA)[481].

Secretomic studies have also been used for the investigation of predictive biomarkers of chemotherapy resistance. For example, one study characterised the secretomes from MCF-7 doxorubicin sensitive and resistant cell lines[478]; a total of

2084 proteins were identified in the 2 cell lines, of which 89 were differentially secreted. *In vitro* validation showed that doxorubicin resistance could be induced by IL-18, whereas doxorubicin sensitivity was restored upon IL-18 inhibition. *In vivo* validation using breast cancer lysates from patients resistant to neoadjuvant doxorubicin showed higher IL-18 levels compared to responding patient samples, demonstrating the functional role of IL-18 in doxorubicin resistance.

Although these secretomic studies have identified novel biomarkers of aggressive phenotypes or as therapeutic predictors, no study has investigated the immediate effects of radiation on the cancer secretome as a means of assessing a cancer cells response to RT and/or determining their radiosensitivity. This chapter describes the development of an *in vitro* secretomic screening and validation method to identify such biomarkers. Analysis of gene expression and secretomic data was performed by Dr A. K. Turnbull (Cancer Research UK, University of Edinburgh). Parental cell lines were used to investigate the secretome of cancer cells and characterise the changes that occur in response to radiation. These cell lines, unlike their RR derivatives, have not received any prior exposure to radiation and therefore could be considered a more appropriate model for monitoring a naive cellular response to radiation as would be the case in most tumours in patients receiving RT for the first time. Characterisation of the cancer secretome was performed using LC-MS on CM samples from untreated and radiation-treated parental cells up to 24 h post-treatment. Secretion patterns of candidate biomarkers were initially identified using the MCF-7 cell line, which were then investigated in CM samples obtained from other human breast, canine breast and ovine lung cancer cell lines. The aim was to identify differentially secreted biomarkers that were secreted in response to radiation within 24 h of treatment, and to investigate whether these biomarkers could be found in different cancer types and species. Further investigations were performed using both parental and RR cell lines to assess the expression of candidate biomarkers at gene and intra-cellular protein level, along with their secretion levels up to 24 h following 2 Gy radiation. The aim was to assess the biomarkers potential for use as an indicator of radiosensitivity. To our knowledge, this is the first description of the use of secretomic experiments to identify radiation-induced secreted biomarkers which are released from cancer cells within 24 h of treatment.

5.2 Results

5.2.1 Characterisation of the MCF-7 secretome

The ER^+ MCF-7 cell line was chosen as the initial model system for biomarker discovery as it is an extremely well characterised cell line, with previous studies successfully demonstrating and validating its use in secretomic experiments. Preliminary characterisation of the untreated MCF-7 secretome identified a total of 927 secreted proteins in CM samples up to 24 h post-serum starvation (provided in the appendix). Although at each secretomic analysis time point (1, 2, 4, 8 and 24 h) a unique set of proteins (proteins detected only at one specific time point) were identified, the number of unique proteins remained low up to 8 h post-serum starvation (Figure 5.1a). By 24 h, 160 unique proteins were identified. In total, 239 secreted proteins (provided in the appendix) were common to all time points, and although their secretion levels did vary over time, overall absolute changes in secretion were minimal (only around 2-fold). At later time points lower secretion was seen for proteins functionally enriched for metabolism, including glycolysis and the citrate cycle, whereas higher secretion was found for proteins associated with glycogen biosynthesis and lipid metabolism (Figure 5.1b).

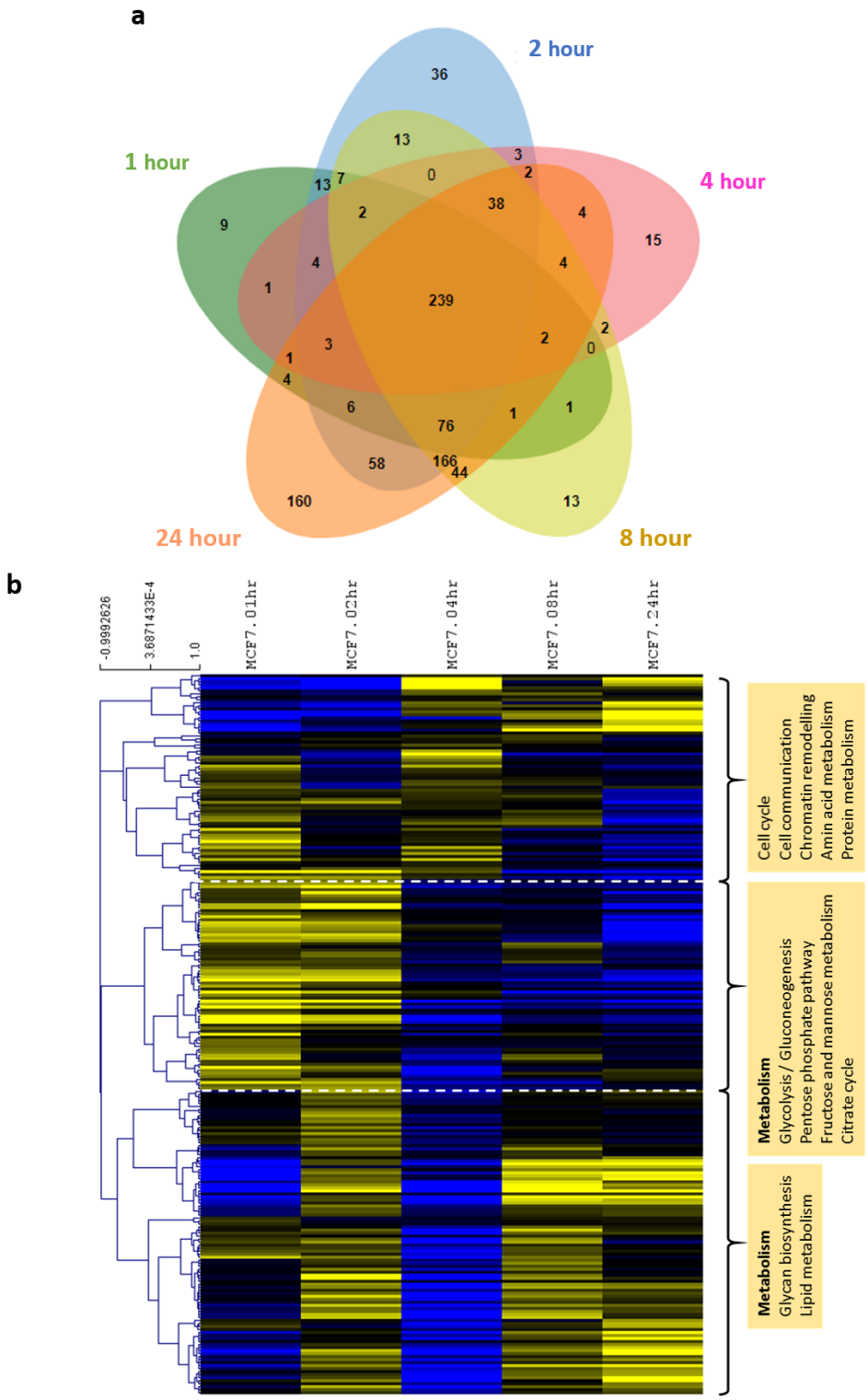

Figure 5.1. Characterisation of the untreated MCF-7 secretome identified 927 unique proteins up to 24 h post-serum starvation. (a) Venn diagram showing the overlap between the total number of detected secreted proteins in the CM of untreated MCF-7 cells at each time point. **(b)** Log2 mean-centered protein heatmap showing secretion levels for the 239 proteins common to all time points (yellow=higher secretion, black=no change, blue=lower secretion, n=1). Heatmap clustering was carried out using Pearson correlation with average linkage.

Following characterisation of the MCF-7 untreated secretome we wished to identify differentially secreted proteins in response to radiation. To achieve this MCF-7 cells were treated with a single dose of radiation (2–10 Gy) and CM samples were obtained up to 24 h post-radiation. To ensure that radiation treatment was not causing significant cell death, cell counts using trypan blue exclusion were performed at the time of the experiments. Although some cell lines did show a statistically significant increase in cell number between untreated samples at 0 h and 24 h, no difference in total cell number or number of dead cells was seen between any of the untreated and radiation treated (up to 10 Gy) groups at 24 h (Figure 5.2) (the proportion of dead cells in each treatment group was less than 5%).

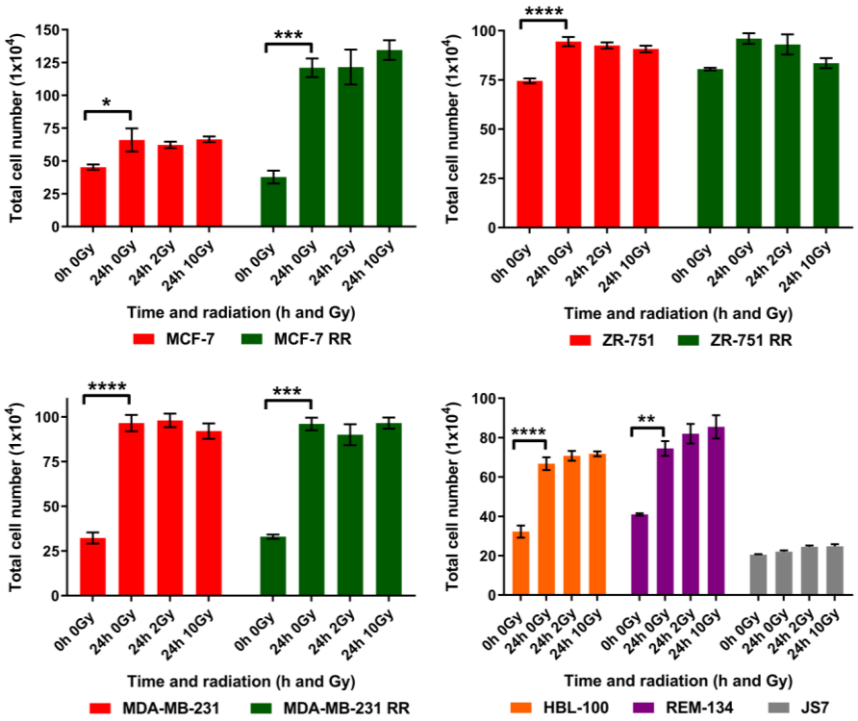

Figure 5.2. Cell numbers were not affected by a single dose of radiation up to 10 Gy at 24 h post-treatment. Cells were seeded at varying numbers to achieve a confluency of 40% at 24 h (MCF-7 and MCF-7 RR $40x10^4$; ZR-751 and ZR-751 RR $60x10^4$; MDA-MB-231, MDA-MB-231 RR, HBL-100 and REM-134 $30x10^4$; JS7 $20x10^4$). After secretome collection, cells were counted routinely using trypan blue exclusion (two-way ANOVA with Holm-Šídák multiple comparisons test; data expressed as mean ± SEM, n=3, ****$p \leq 0.0001$; ***$p \leq 0.001$; **$p \leq 0.01$; *$p \leq 0.05$).

MCF-7 secretomic analysis subsequently focused on CM samples obtained at 24 h post-radiation treatment. This time point was chosen as it was deemed most suitable for use in clinical situations where patients routinely receive daily radiation doses approximately 24 h apart. Characterisation of untreated and radiation treated

CM samples at 24 h identified a total of 765 secreted proteins, of which 530 were common to both the untreated and radiation treated samples (Figure 5.3). Investigation of protein secretion fold changes between untreated and radiation treated samples identified 147 proteins which had a >2-fold increase in secretion levels in radiation treated cells (provided in the appendix).

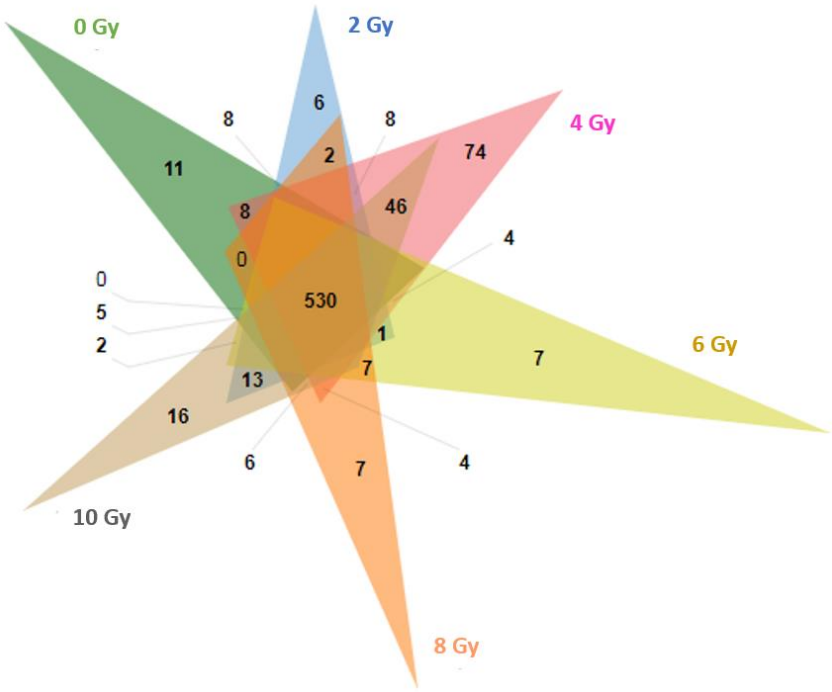

Figure 5.3. Characterisation of the untreated and radiation treated MCF-7 secretome identified 530 common proteins at 24 h. Venn diagram showing the overlap between the total number of detected secreted proteins in the CM of MCF-7 untreated and radiation treated cells (2-10 Gy) at 24 h.

5.2.2 Criteria used for candidate biomarker selection

Using secretomic data initially obtained from the MCF-7 model, several criteria were applied to the biomarkers in order to identify those most appropriate to be taken forward for validation. We had already focused on biomarkers that were released by cells which were detectable at 24 h post-radiation exposure, as this was likely to be the most clinically relevant time point; patients typically receive daily radiation fractions, therefore biomarkers detectable at 24 h post-radiation would allow for ease of monitoring between daily doses. We also wished to identify biomarkers that showed a simple secretion profile whereby levels were low at early time points, then showed a dramatic increase at 24 h, as this would potentially increase the likelihood of successful validation. Selected biomarkers were also

investigated in multiple radiosensitive cancer types from different species. The identification of common biomarkers in several species would give the biomarkers wider application and would allow for large animal model testing, and possible veterinary uses. Following the initial selection based on secretion profiles, final biomarker selection was performed using functional analysis; any biomarkers that played roles in common pathways were preferentially selected.

Although not part of the selection process, further assessment of candidate biomarkers at gene and intra-cellular protein level in parental and RR cell lines was performed to investigate whether a gene/protein expression signature could be obtained to predict radiosensitivity.

5.2.3 MCF-7 preliminary biomarker selection based on increased secretion at 24 hours post-radiation identified 33 candidate biomarkers

Using the 147 biomarkers with >2-fold increase in secretion levels in radiation treated cells, hierarchical clustering with Euclidean distance was performed. A cluster of 33 biomarkers emerged which had higher (up to 12-fold) secretion levels at all radiation doses in treated compared to untreated controls (Figure 5.4) (provided in the appendix). Secretion levels of all 33 biomarkers were then investigated at the earlier time points. Although a small number of the biomarkers had early increased or decreased secretion compared to untreated controls the secretion levels of most of the biomarkers did not change with radiation at the earlier time points (Figure 5.5). A literature search of theses 33 candidates was performed to investigate whether these biomarkers were previously known to be secreted either through the classical or non-classical routes. Cross referencing through Vesiclepaedia[482] identified that all 33 biomarkers have previously been shown to be secreted in microvesicles or exosomes by cancer cells.

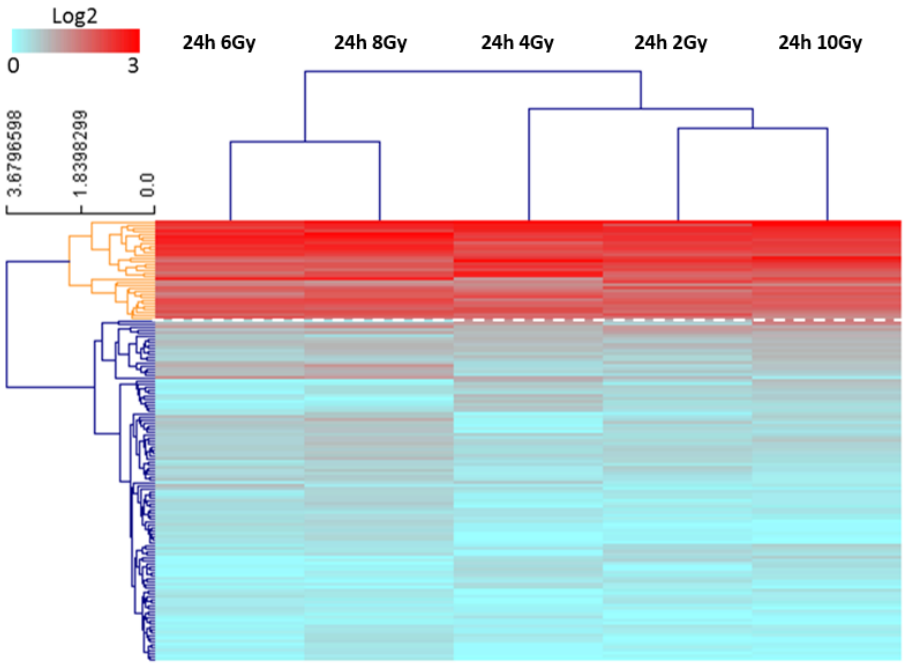

Figure 5.4. Hierarchical clustering identified a cluster of 33 biomarkers with dramatic increase in secretion in response to radiation. Heatmap of log2 fold changes showing the 147 proteins whose increased secretion had fold changes greater than 2 between controls and matched treated samples at 24 h across all doses. Hierarchical clustering identified a cluster of 33 proteins, shown at the top of the heatmap in red, which had increased (up to 12-fold) secretion at all radiation doses in treated compared to untreated controls (red=higher secretion, blue=no change, n=1). Heatmap clustering was carried out using Pearson correlation with average linkage.

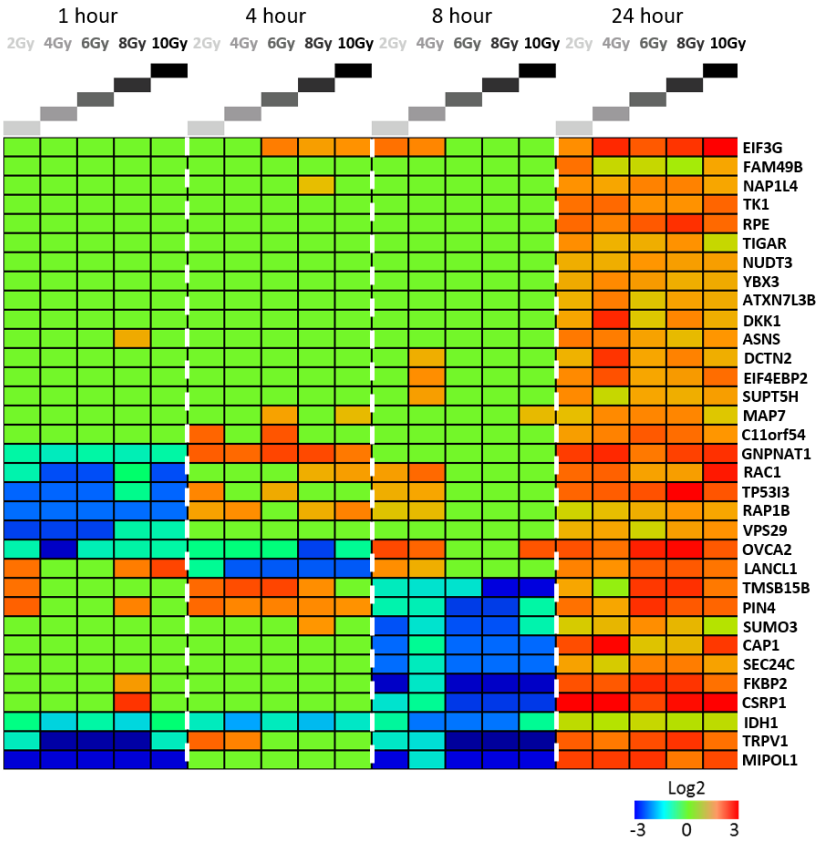

Figure 5.5. MCF-7 secretion patterns of the 33 candidate biomarkers remained stable up to 8 hours post-radiation treatment. Heatmap of log2 fold changes showing secretion levels of the 33 biomarkers compared to untreated controls at each time point up to 24 h post-radiation for each radiation dose (red=higher secretion, green=no change, blue=lower secretion, n=1). Heatmap clustering was carried out using Pearson correlation with average linkage.

5.2.4 No common set of biomarkers were identified between different cancer types

To investigate whether the 33 candidate biomarkers could be found in different cancer types and species, their secretion patterns up to 24 h post-radiation exposure were investigated using secretomic data generated from ER$^-$ human breast (MDA-MB-231 and HBL-100), canine breast (REM-134) and ovine lung (JS7) cancer cell lines. In total across all time points, 20 of the 33 biomarkers were identified in both MDA-MB-231 and HBL-100 cell lines; however, this number reduced to 12 and 6 respectively when including the criteria of increased secretion at the 24 h time point, as was done with the MCF-7 secretomic data. Across all time points only 5 and 4 of the 33 biomarkers were identified in the REM-134 and JS7 cell lines respectively. Most of the biomarkers also had more complicated secretion patterns with increased levels at both 4 and 24 h post-radiation (Figure 5.6).

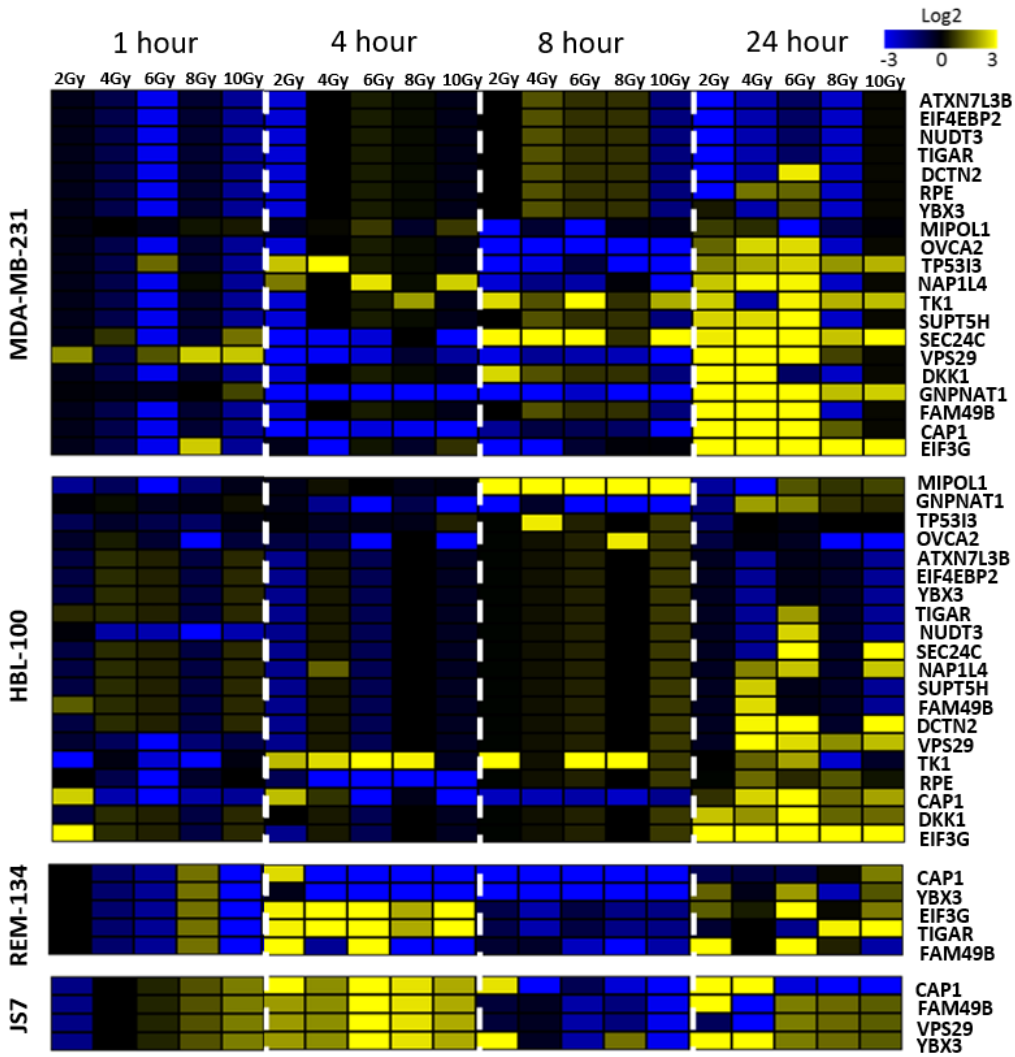

Figure 5.6. Secretion patterns of the 33 candidate biomarkers in multiple cancer cell types and species identified no common set of candidate biomarkers. Heatmap of log2 fold changes showing secretion levels of the 33 biomarkers compared to untreated controls at each time point up to 24 h post-radiation for each radiation dose (yellow=higher secretion, black=no change, blue=lower secretion, n=1). Heatmap clustering was carried out using Pearson correlation with average linkage.

5.2.5 MCF-7 final biomarker selection based on functional analysis of the 33 biomarkers identified 9 candidate biomarkers

Final candidate biomarkers were selected based on secretion profiles and functional analysis. Using the Markov clustering algorithm[382], incorporating the initial 33 candidate biomarkers selected based on secretion profiles, this program identified 3 functionally enriched clusters that included protein transport, transcription and translation (Figure 5.7).

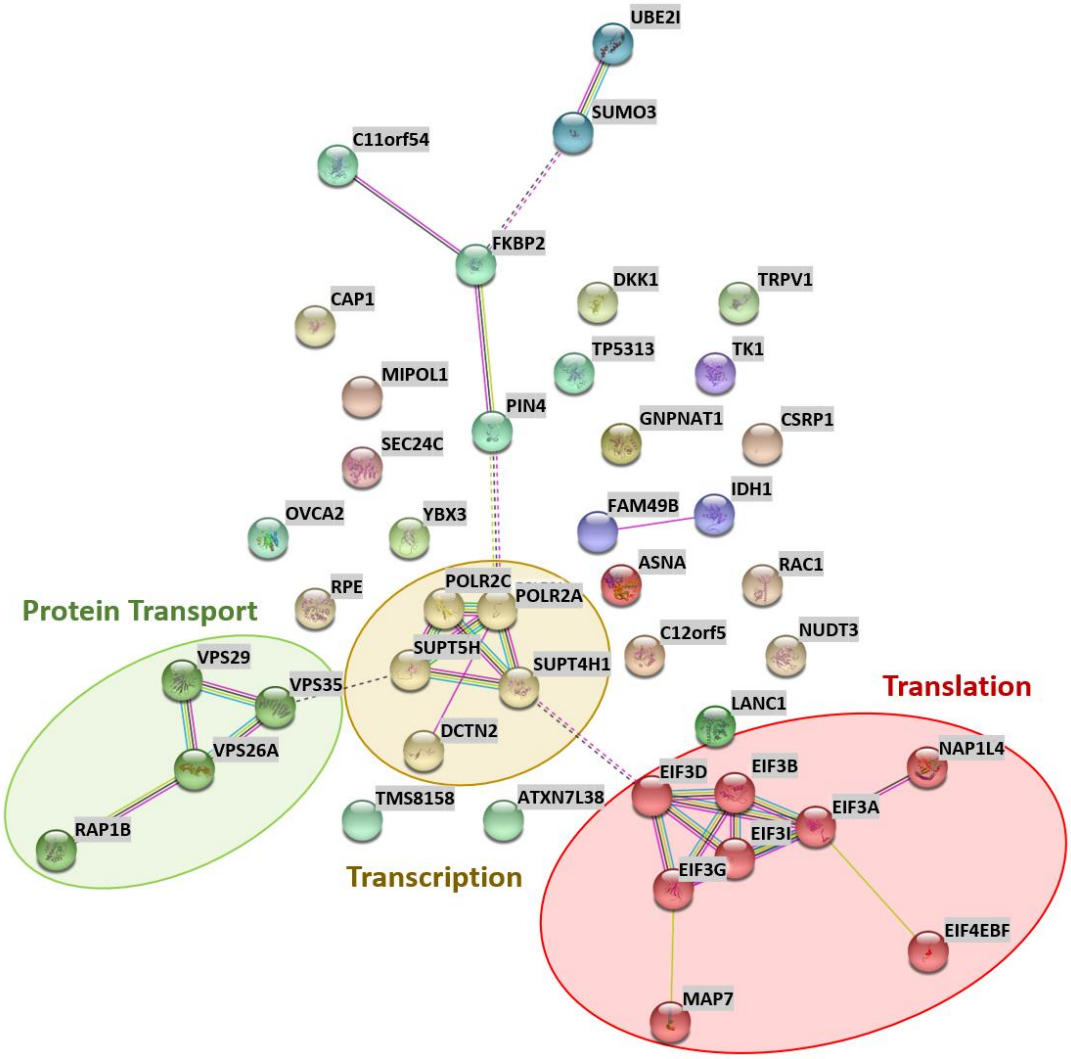

Figure 5.7. Protein interaction networks identified protein transport, transcription and translation as enriched clusters within the 33 candidate biomarkers. Protein interaction network of the 33 candidate biomarkers plus the 10 most closely associated interacting partners using the STRING protein interaction database[381]. Using the Markov clustering algorithm[382], 3 functional clusters were identified: protein transport (green), transcription (yellow) and translation (red).

Any biomarkers identified as playing roles within these 3 functional pathways were selected. Biomarkers involved in signalling pathways that were determined as inherently different between the MCF-7 parental and RR cell lines (described in chapter 4) were also considered as these could potentially be used as biomarkers to determine radiosensitivity; these included UPR, WNT and proliferation. This analysis identified 9 candidate biomarkers that either had excellent secretion profiles (GNPNAT1, YBX3), or played roles in translation (EIF3G,

EIF4EBP2, NAP1L4), proliferation (TK1), protein transport from the ER to the Golgi (SEC24C, VPS29) or WNT signalling (DKK1).

Out of these 9 candidate biomarkers, 4 were selected for initial validation. These were EIF3G, TK1, SEC24C and YBX3. MCF-7 log2 secretion levels were calculated relative to untreated controls at each time point and for each radiation dose (Figure 5.8). The secretion of both TK1 and YBX3 increased 4-fold at 24 h with all doses of radiation, with no detected secretion at the earlier time points. Both EIF3G and SEC24C also had approximately a 4-fold increase in secretion by 24 h. EIF3G had an early secretion peak at 4 h post-radiation at higher doses (6-8 Gy) and increased secretion at 8 h with lower doses (2 and 4 Gy) which was maintained at 24 h. SEC24C had reduced secretion at 8 h compared to the untreated controls prior to a dramatic increase by 24 h post-radiation.

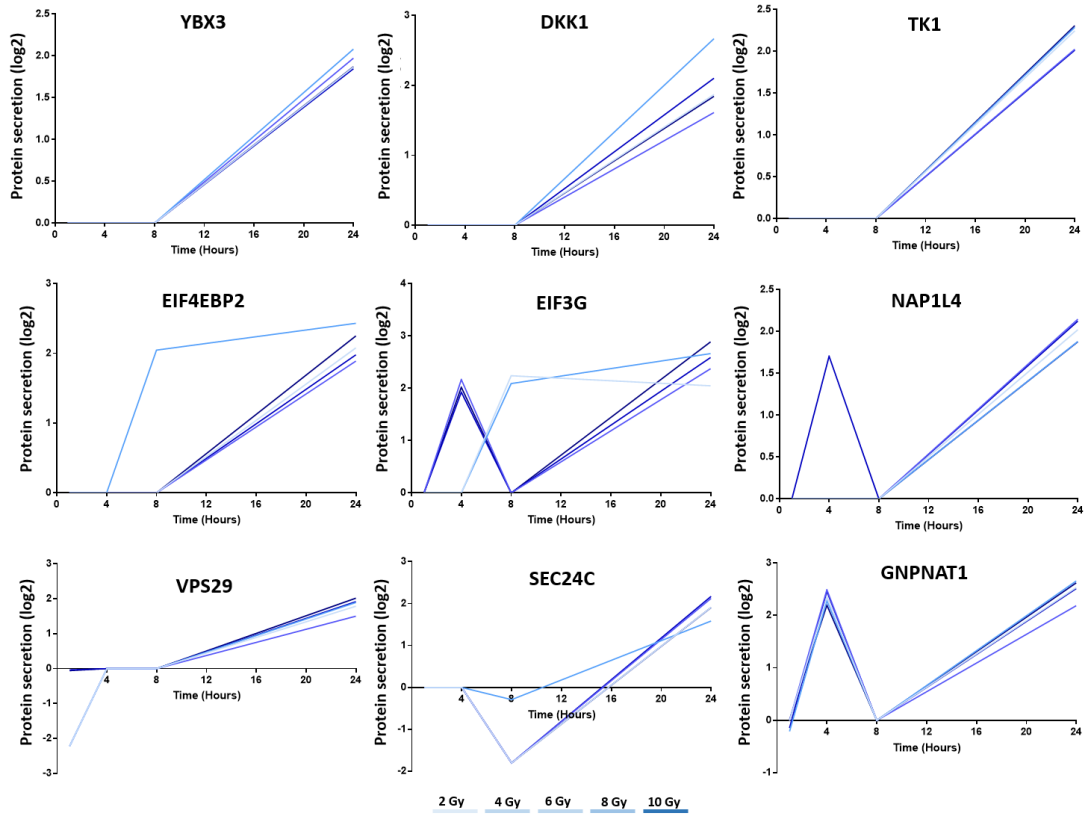

Figure 5.8. The 9 candidate biomarkers show increased secretion levels at all radiation doses at 24 h post-treatment. Graphs of log2 secretion levels of each of the candidate biomarkers relative to untreated controls at each time point and for each radiation dose.

5.2.6 Similarities in secretion patterns of the 4 biomarkers between ER^- and ER^+ cell lines were identified

To specifically investigate the 4 candidate biomarkers in the different cancer types and species their secretion patterns at 8 and 24 h post-radiation were investigated using the secretomic data presented in Figure 5.6. These 4 biomarkers alone are shown in Figure 5.9. Whereas YBX3 was detected in all these cell lines, the other biomarkers were detected only in some of them (Figure 5.9a). In the MDA-MB-231 cell line, except for YBX3, all biomarkers were found to have increased secretion above that of the untreated controls at all doses of radiation at 24 h and at the earlier time point of 8 h for SEC24C and TK1. Only EIF3G was found to have increased secretion in HBL-100 cells at 24 h with all doses of radiation. In the REM-134 cell line only EIF3G and YBX3 were detected, both of which had increased secretion with 3 of the 5 radiation doses. In the JS7 cell line only YBX3 was detected, with increased secretion at 24 h with all doses of radiation. In total 14 members of the EIF family were detected at 24 h in CM samples in the MCF-7, MDA-MB-231 and HBL-100 cell lines, several of which had higher secretion levels in radiation-treated samples compared to untreated controls. Investigation of SEC family members showed that only SEC24C had consistently higher secretion levels at 24 h in the radiation treated samples compared to untreated controls (Figure 5.9b).

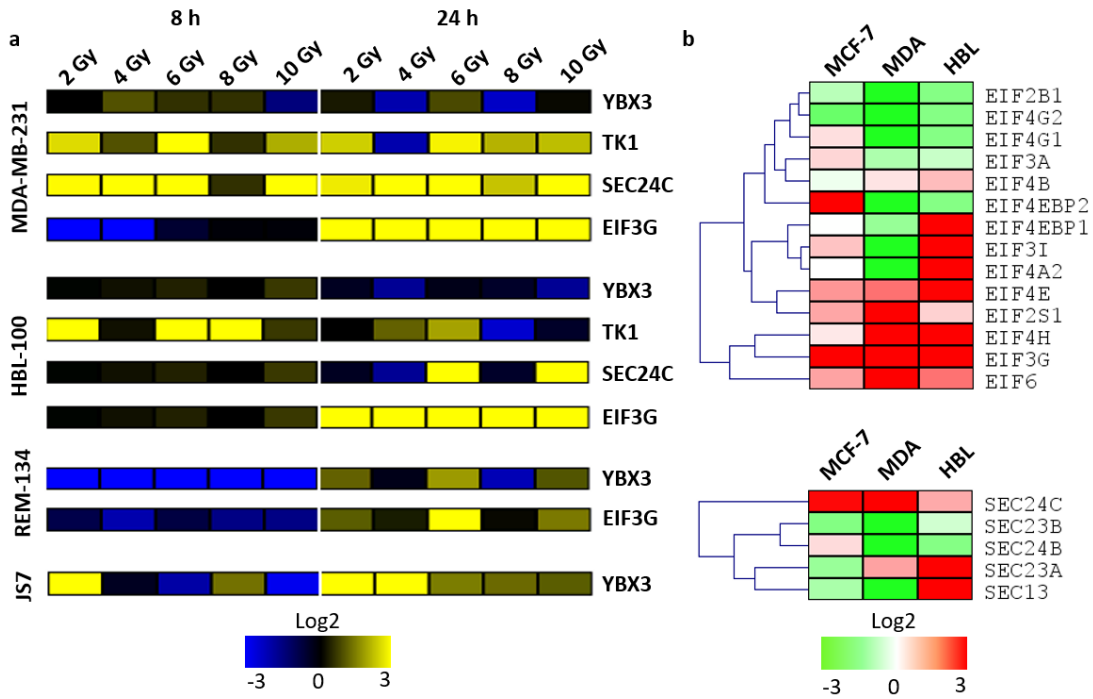

Figure 5.9. Similarities in secretion patterns of the 4 biomarkers at 24 h post-radiation treatment were identified between ER$^-$ and ER$^+$ cell lines. (a) Heatmap of log2 fold changes showing changes in secretion levels of each of the 4 candidate biomarkers compared to untreated controls in MDA-MB-231, HBL-100, REM-134 and JS7 cell lines at 8 and 24 h for all radiation doses (yellow=higher secretion, black=no change, blue=lower secretion, n=1). **(b)** Heatmap of log2 fold changes showing secretion levels compared to untreated controls at 24 h for detected members of the EIF family (upper) and Sec23/24 family (lower) in MCF-7, MDA-MB-231 and HBL-100 cell lines (red=higher secretion, white=no change, and green=lower secretion, n=1). Heatmap clustering was carried out using Pearson correlation with average linkage.

5.2.7 Radioresistant cell lines have lower gene and intra-cellular protein expression of the 4 biomarkers

To investigate the potential of the biomarkers for use as an indicator of radiosensitivity, parental and RR cell lines were used to assess differential expression of candidate biomarkers at gene and intra-cellular protein level. Although these results would not give an indication of secretion, increased gene expression levels may suggest higher amounts of intra-cellular protein, which may lead to increased secretion. As our secretomic results have shown that at least in the MCF-7 model the biomarkers all have increased secretion at 24 h post-radiation, we investigated whether gene changes could be detected up to 8 h post-exposure to 2 Gy.

Analysis of gene expression data investigating the 33 secreted biomarkers from ER$^+$ and ER$^-$ human breast cancer cell lines using both parental and their RR

derivatives identified higher YBX3, EIF3G, EIF4EBP2, TK1, DKK1 NAP1L4 and GNPNAT1 gene expression in the MCF-7 parental cell line compared with the MCF-7 RR cell line; conversely the expression of SEC24C was the opposite with higher levels in the RR cells compared with the parental cells, VPS29 showed little change between the cell lines. These results showed that in total 7 of the 9 candidate biomarkers had higher gene expression levels in the parental cell line. Similar results were seen in the ZR-751 parental and RR cell lines, although higher gene expression levels for both SEC24C and DKK1 were seen in the RR cell line. Gene expression differences between the MDA-MB-231 parental and RR cell lines identified higher YBX3, EIF3G, EIF4EBP2, VPS29, DKK1 and GNPNAT1 expression in the MDA-MB-231 parental cell line. Again, the expression of SEC24C as well as TK1 and NAP1L4 was the opposite with higher levels in the RR cells compared with the parental cell line. A single radiation dose of 2 Gy had little/no effect on gene expression at 2 and 8 h post-treatment in all cell lines (Figure 5.10).

To compare basal intra-cellular protein expression levels of each of the 4 biomarkers in parental and RR cell lines IF was performed using untreated MCF-7 and MCF-7 RR cell lines grown in 2D monolayers. Higher expression levels for all 4 biomarkers were identified in the parental cell line in comparison to the RR derivative (Figure 5.11). To investigate this result further, expression levels were also evaluated using MCF-7, ZR-751 and REM-134 parental and RR MTS (MDA-MB-231 cells failed to form MTS that could withstand IHC processing). Experiments produced similar results to those seen using IF, with higher expression levels identified in the parental cell lines compared to the RR derivatives; the exception was for EIF3G in which the parental MCF-7 cell line had lower expression compared with its RR derivative (Figure 5.12).

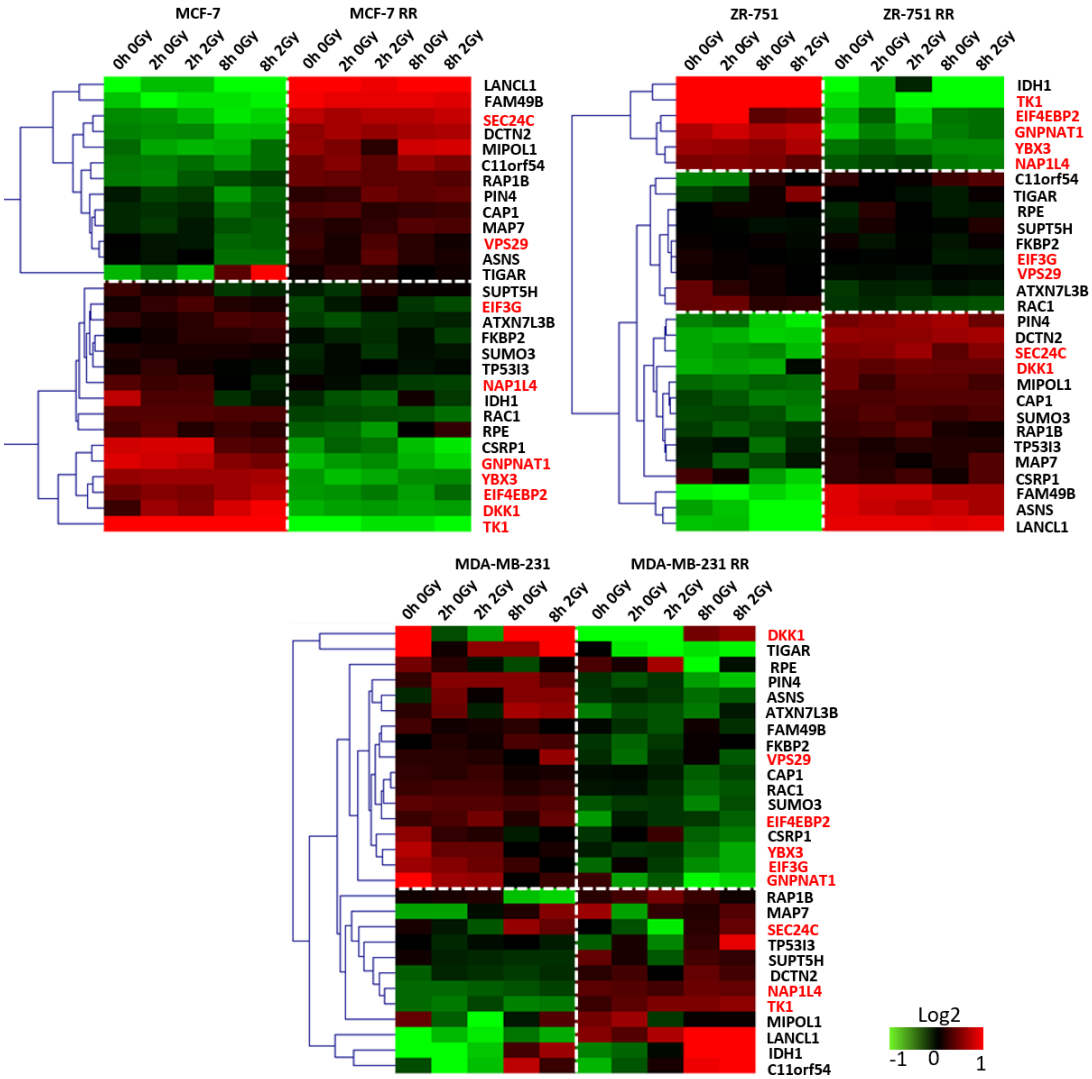

Figure 5.10. MCF-7 and ZR-751 show higher expression of genes encoding 7 of the 9 candidate biomarkers compared with their RR derivatives. Log2 mean-centered gene expression heatmap showing differences in expression of the genes encoding the 33 candidate biomarkers in the human parental and RR breast cancer cell lines at 2 and 8 h post-2 Gy radiation treatment (red=higher expression, black=no change, green=lower expression, n=1). Heatmap clustering was carried out using Pearson correlation with average linkage.

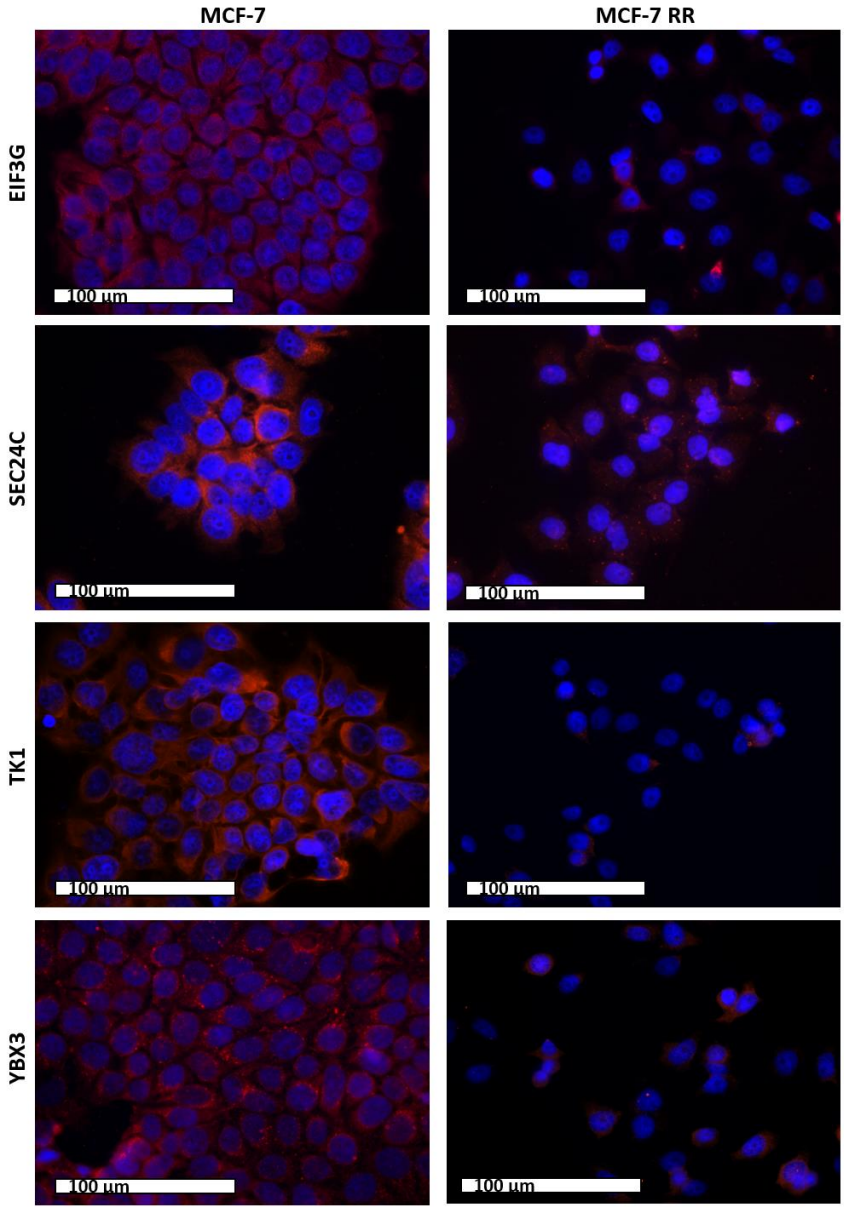

Figure 5.11. MCF-7 cells grown in 2D monolayers show higher intra-cellular expression of EIF3G, SEC24C, TK1 and YBX3 compared with its RR derivative. IF of the 4 candidate biomarkers in MCF-7 and MCF-7 RR cell lines. For each antibody immunofluorescence signal is detected at the expected cellular localisation region: the strongest signal for EIF3G, SEC24C, TK1 and YBX3 is seen predominately in the cytoplasm (representative images, n=3).

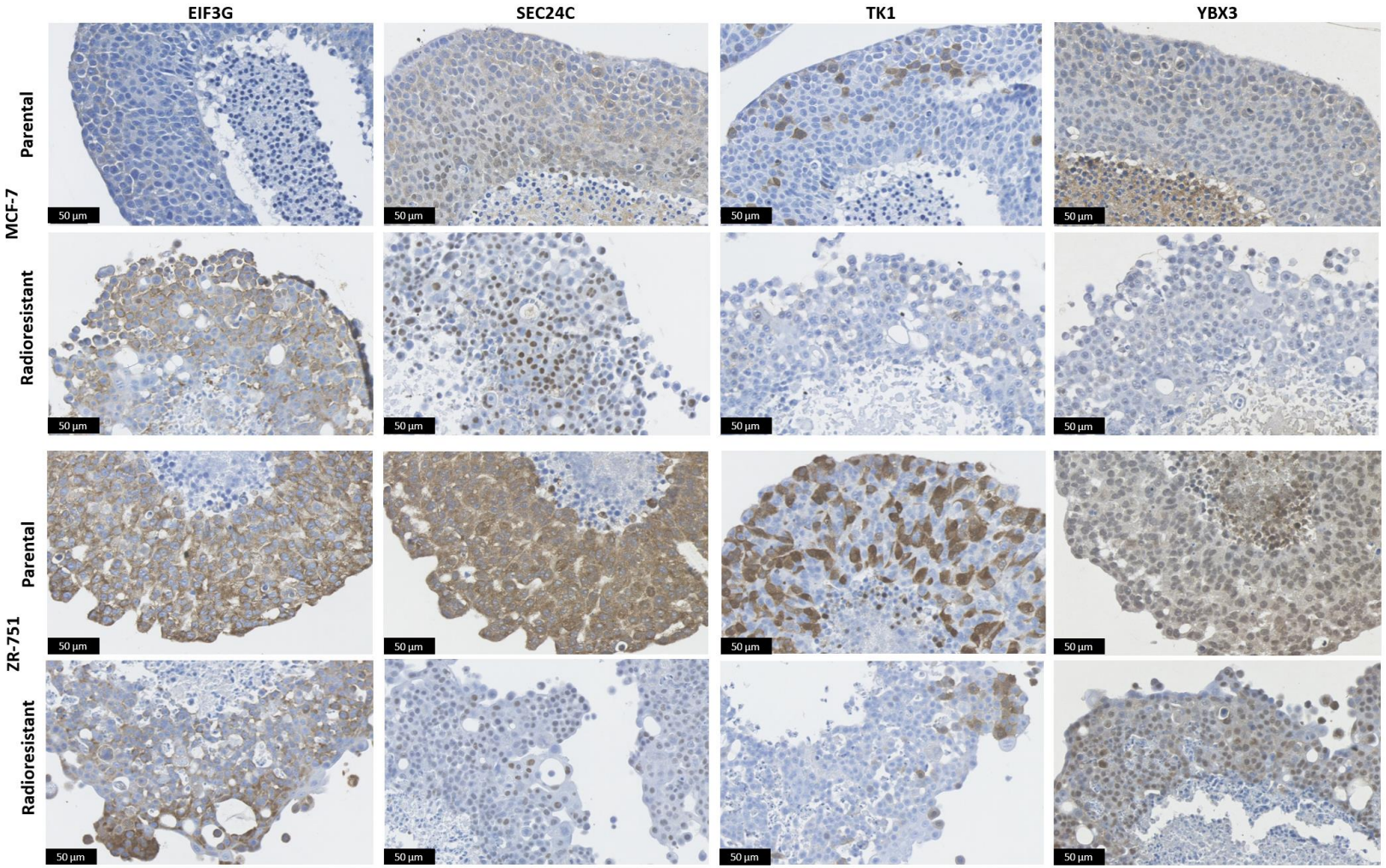

Figure legend on following page.

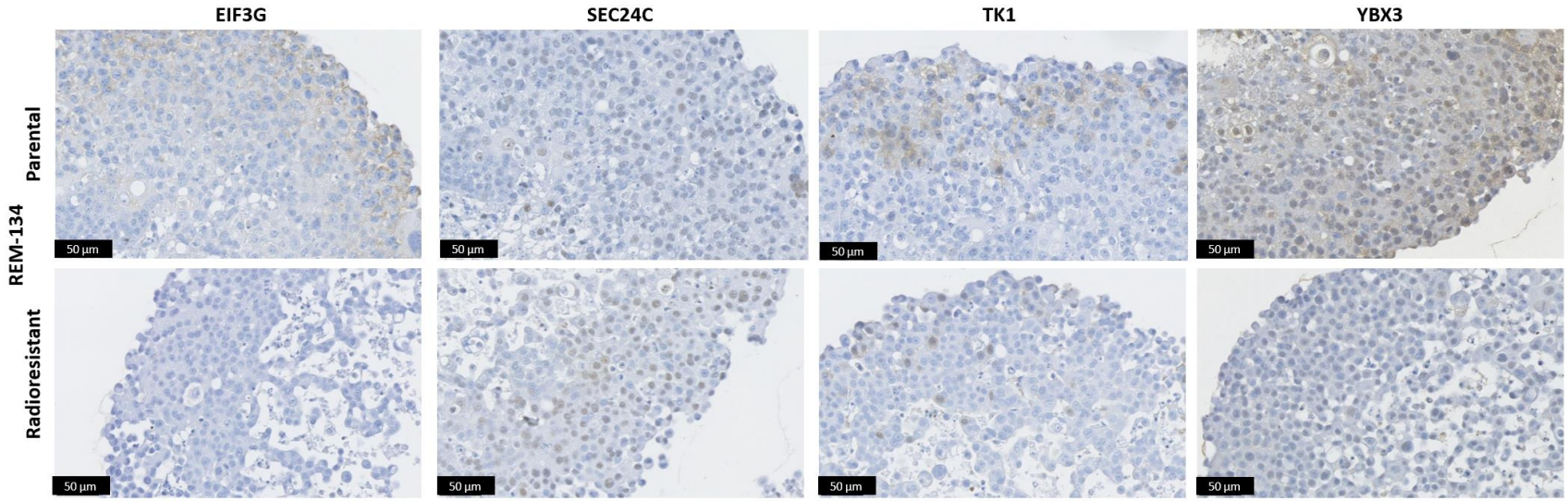

Figure 5.12. MCF-7, ZR-751 and REM-134 MTS show higher intra-cellular expression of SEC24C, TK1 and YBX3 compared with their RR derivatives. IHC of the 4 candidate biomarkers in MCF-7, ZR-751 and REM-134 parental and RR cell lines. Positive DAB staining is seen for each antibody at the expected cellular localisation region: positive EIF3G, SEC24, TK1 and YBX3 staining is seen in the cytoplasm (representative images, n=3).

5.2.8 Differential secretion patterns of the candidate biomarkers occur between sensitive and radioresistant cell lines in multiple species in response to radiation

To validate the secretomic results and to further investigate the potential use of these proteins as biomarkers of radiosensitivity, parental and RR cell lines were used in WB experiments. To achieve this, WB analysis was performed using CM samples to assess the secretion levels obtained from parental and RR cell lines 24 h after the cells had received a single radiation dose of 2 or 4 Gy. Unfortunately, due to time restraints and antibody availability only EIF3G, SEC24C and TK1 validation was performed. GAPDH was used with CM samples to assess for the presence of intra-cellular proteins that could be released into the CM from cell lysis; 2 μg of whole cell lysates were also run in parallel to CM samples to act as positive controls. Revert total protein stain (Li-COR Biotechnology, UK) was used to confirm equal loading of the samples.

Secretion levels of SEC24C, EIF3G and TK1 were found to be significantly increased from MCF-7 cells treated with 2 Gy of radiation at 24 h compared to 24 h untreated controls. Biomarker levels in the CM from radiation-treated and untreated MCF-7 RR cells remained low (Figure 5.13). Similar results were found in ZR-751 parental and RR cell lines with secretion levels of SEC24C and TK1 found to be significantly increased from ZR-751 cells treated with 2 or 4 Gy of radiation at 24 h compared to the 24 h untreated controls. A dose dependent effect was seen for TK1. Biomarker levels in CM from radiation-treated and untreated ZR-751 RR cells remained low. EIF3G was not detected in the CM from the ZR-751 or ZR-751 RR cell lines (Figure 5.14).

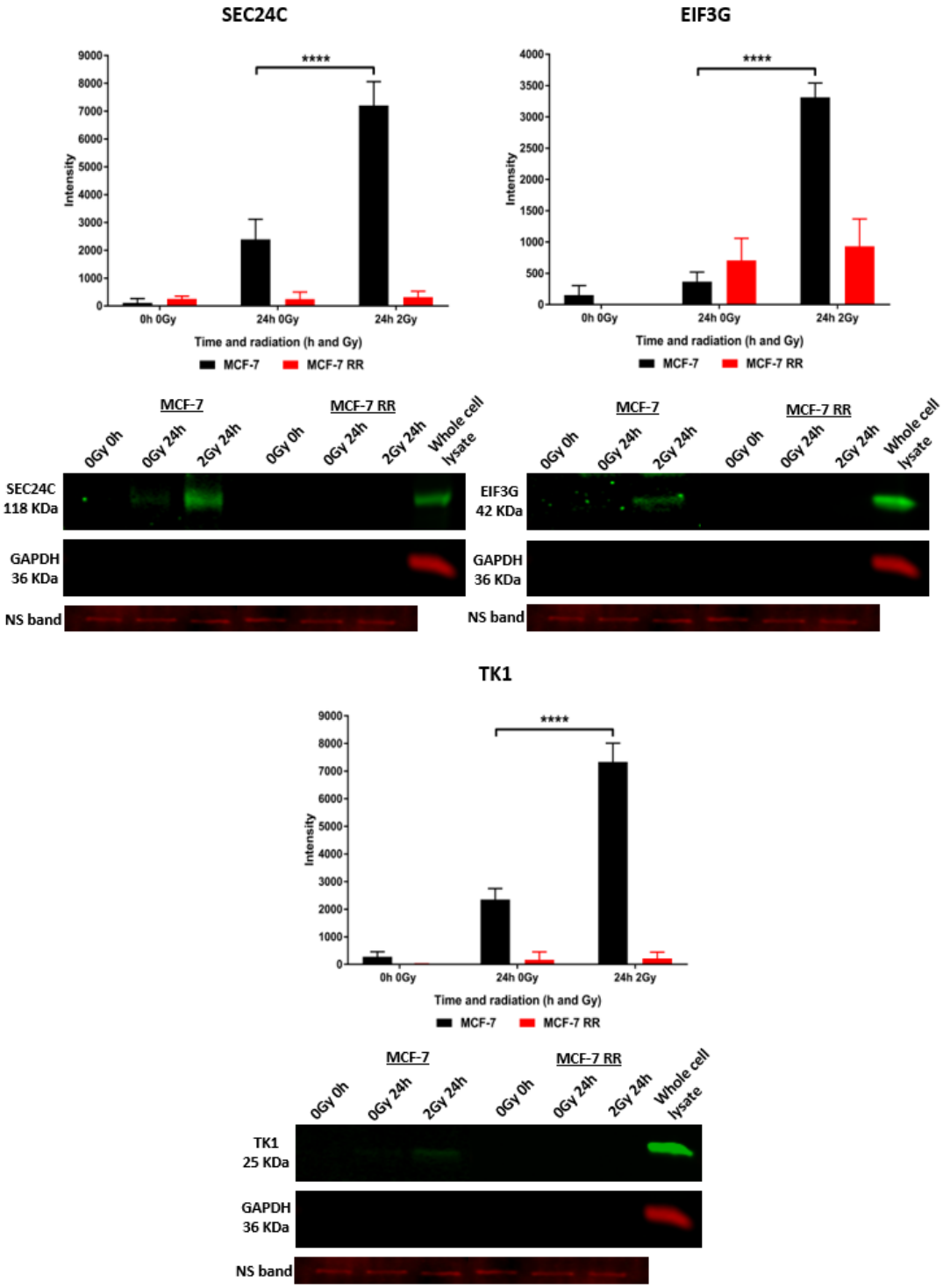

Figure 5.13. MCF-7 secretion levels of SEC24C, EIF3G and TK1 increase in response to radiation. WB analysis of candidate biomarkers in MCF-7 and MCF-7 RR cell lines using CM samples obtained up to 24 h following exposure to a 2 Gy dose of radiation. NS is a non-specific band identified using the total protein stain used to confirm equal loading (two-way ANOVA with Holm-Šídák multiple comparisons test; data expressed as mean ± SEM, n=3, ****$p \leq 0.0001$).

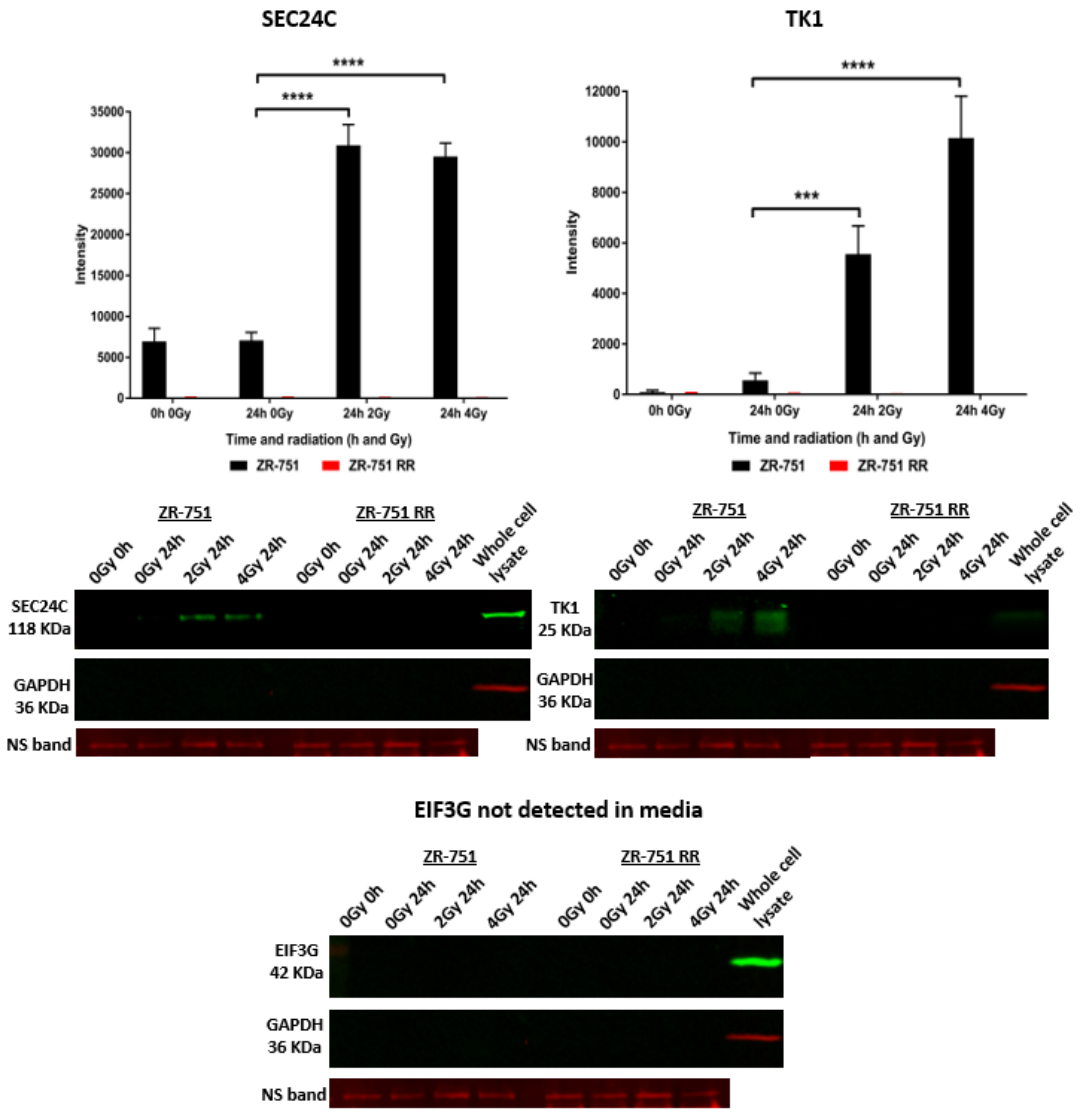

Figure 5.14. ZR-751 secretion levels of SEC24C and TK1 increase in response to radiation. WB analysis of candidate biomarkers in ZR-751 and ZR-751 RR cell lines using CM samples obtained up to 24 h following exposure to a 2 or 4 Gy dose of radiation. NS is a non-specific band identified using the total protein stain used to confirm equal loading (two-way ANOVA with Holm-Šídák multiple comparisons test; data expressed as mean ± SEM, n=3, ****$p \leq 0.0001$; ***$p \leq 0.001$).

Only SEC24C was detected in the CM of MDA-MB-231 and MDA-MB-231 RR cell lines. Although SEC24C secretion in the MDA-MB-231 cell line did occur in response to 2 Gy of radiation at 24 h compared to the 24 h untreated controls, a much larger and statistically significant increase was seen in the MDA-MB-231 RR cell line, demonstrating differences in the results obtained using the ER^+ cell lines (Figure 5.15).

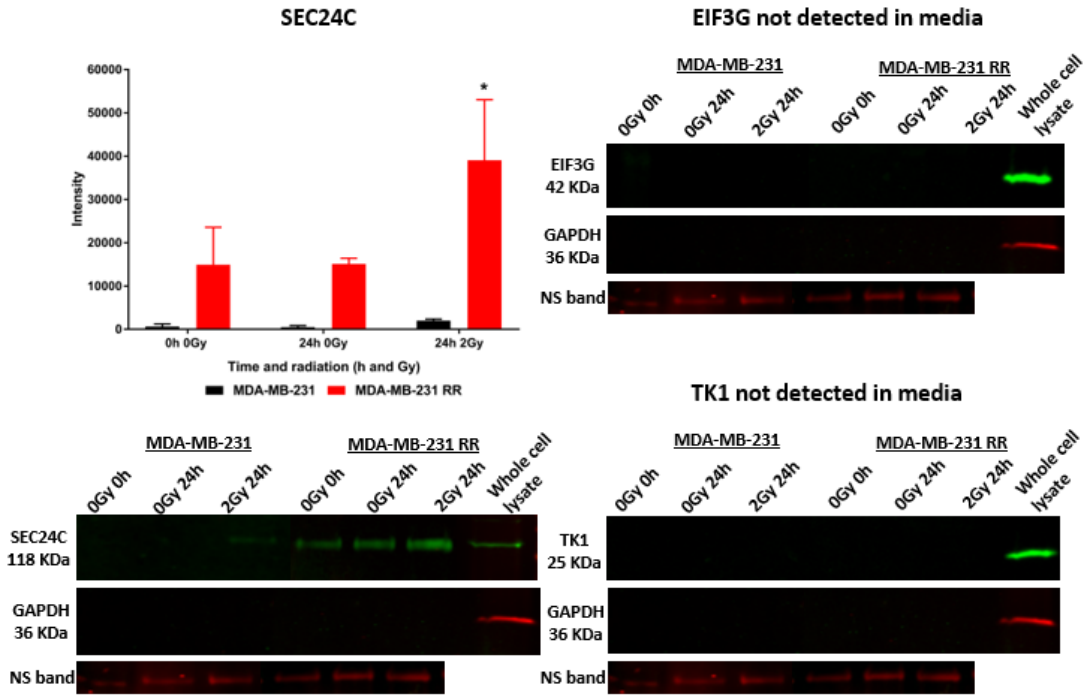

Figure 5.15. MDA-MB-231 RR secretion levels of SEC24C increase in response to radiation. WB analysis of candidate biomarkers in MDA-MB-231 and MDA-MB-231 RR cell lines using CM samples obtained up to 24 h following exposure to a 2 Gy dose of radiation. NS is a non-specific band identified using the total protein stain used to confirm equal loading (two-way ANOVA with Holm-Šídák multiple comparisons test; data expressed as mean ± SEM, n=3, *$p \leq 0.05$).

Secretion levels of SEC24C and EIF3G were found to be significantly increased in the CM of REM-134 cells treated with 2 Gy of radiation at 24 h compared to the 24 h untreated controls. SEC24C and EIF3G levels in CM from radiation treated and untreated REM-134 RR cells remained low. TK1 was not detected in the CM from the REM-134 or REM-134 RR cell lines (Figure 5.16). SEC24C was detected at all time points and treatment groups in both the JS7 and JS7 RR cell lines, however secretion levels were not altered with exposure to radiation. Although EIF3G secretion increased in both the JS7 and JS7 RR cell lines in response to 2 Gy of radiation at 24 h compared to the 24 h untreated controls, a larger and statistically significant increase was seen from the parental JS7 cells. TK1 secretion was also increased in both the JS7 and JS7 RR cell lines in response to 2 Gy of radiation, however these increases were not statistically significant (Figure 5.17). A summary of all validation experiments for all cell lines is provided in Table 5.1 & Table 5.2.

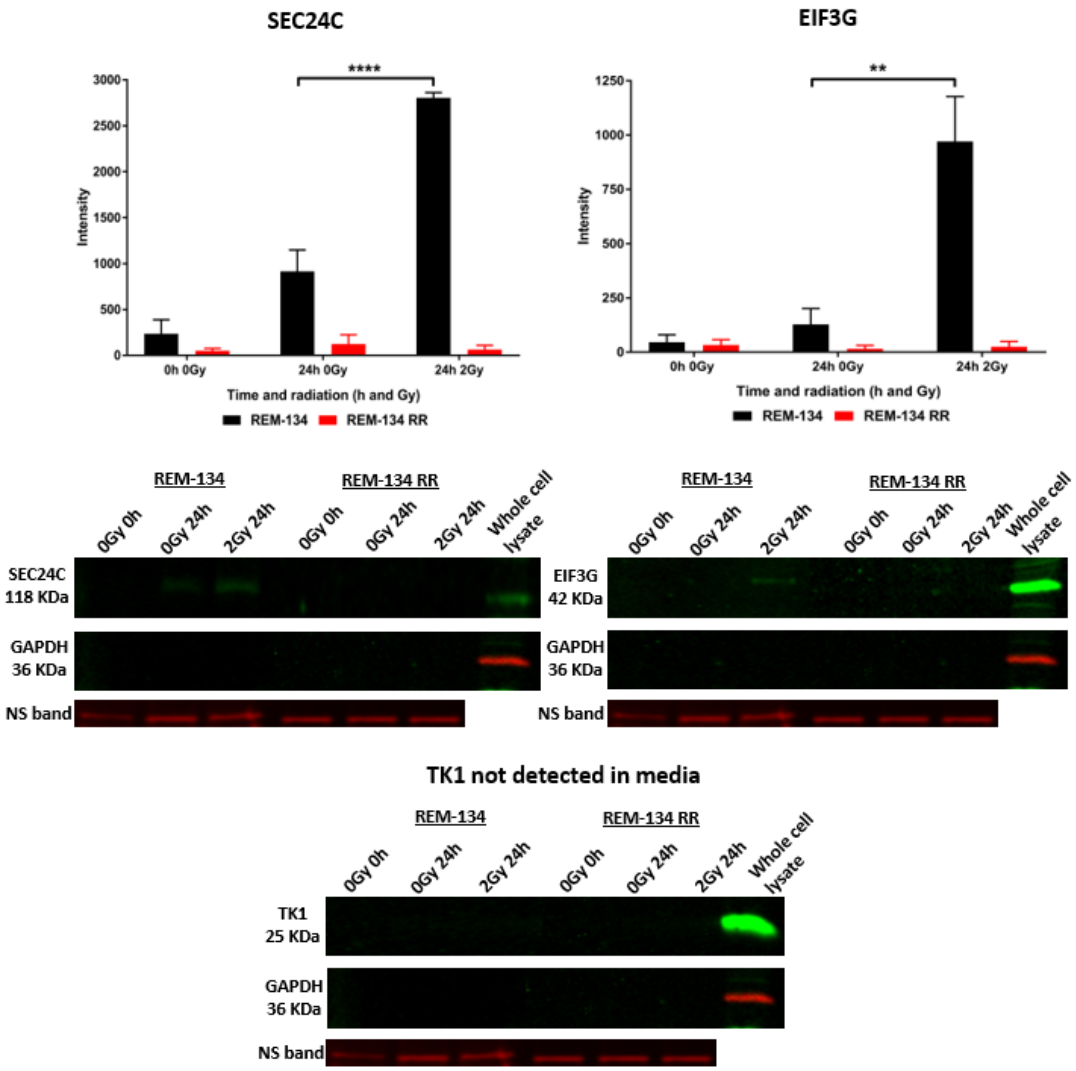

Figure 5.16. REM-134 secretion levels of SEC24C and EIF3G increase in response to radiation. WB analysis of candidate biomarkers in REM-134 and REM-134 RR cell lines using CM samples obtained up to 24 h following exposure to a 2 Gy dose of radiation. NS is a non-specific band identified using the total protein stain used to confirm equal loading (two-way ANOVA with Holm-Šídák multiple comparisons test; data expressed as mean ± SEM, n=3, ****$p \leq 0.0001$; **$p \leq 0.01$).

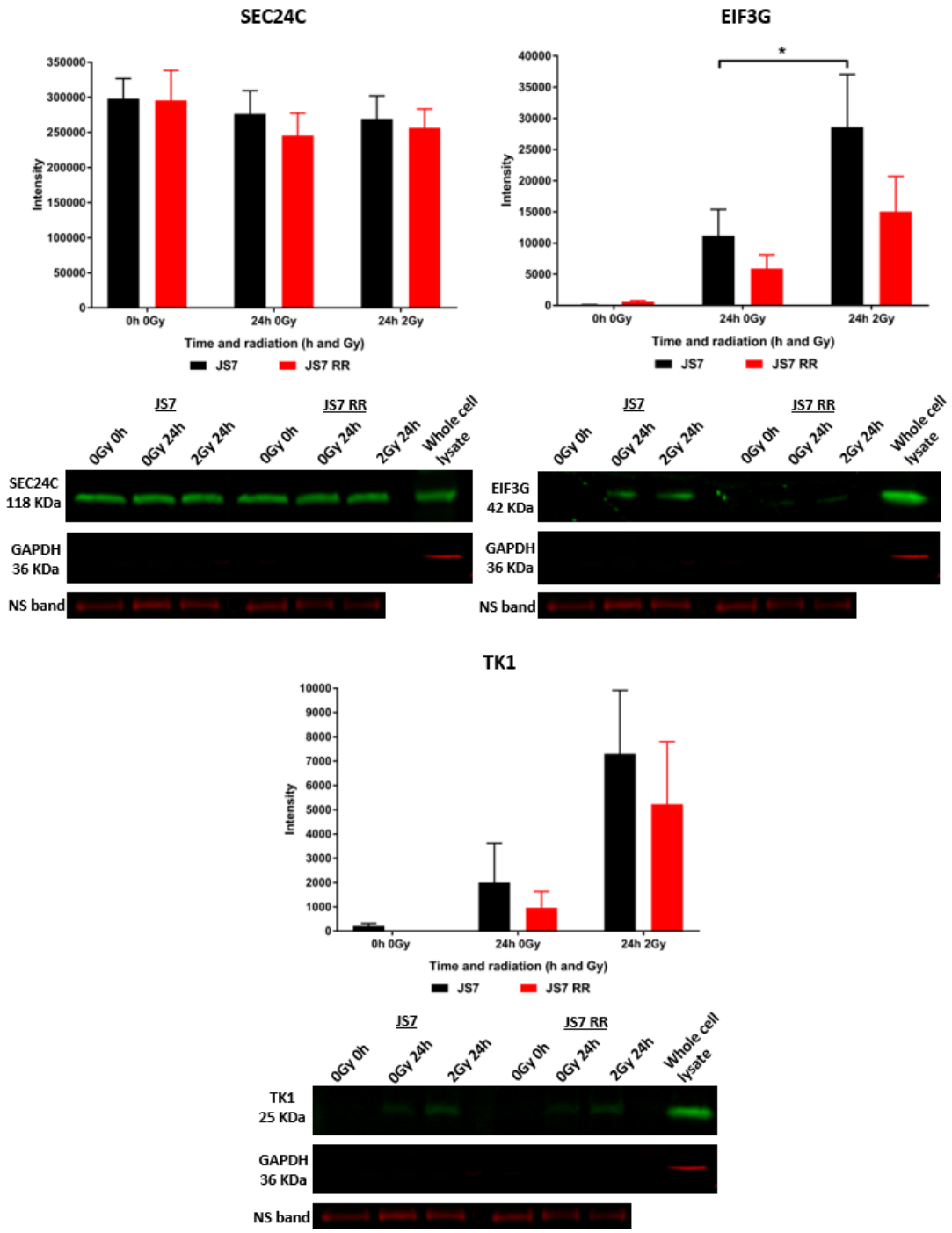

Figure 5.17. JS7 secretion levels of EIF3G increase in response to radiation. WB analysis of candidate biomarkers in JS7 and JS7 RR cell lines using CM samples obtained up to 24 h following exposure to a 2 Gy dose of radiation. NS is a non-specific band identified using the total protein stain used to confirm equal loading (two-way ANOVA with Holm-Šídák multiple comparisons test; data expressed as mean ± SEM, n=3, *$p \leq 0.05$).

Table 5.1. Summary of validation experiments in human breast cancer cell lines. The WB results show whether each biomarker had increased secretion (↑↑), low levels (-) or were not detected in the CM of cells 24 h following a 2 Gy dose of radiation. IF and IHC results show intra-cellular expression levels of each biomarker (results for WB, IF and IHC depict comparisons between each paired parental and RR cell line).

	MCF-7	MCF-7 RR	ZR-751	ZR-751 RR	MDA-MB-231	MDA-MB-231 RR
WB						
SEC24C	↑↑	-	↑↑	-	↑	↑↑
EIF3G	↑↑	-	Not detected	Not detected	Not detected	Not detected
TK1	↑↑	-	↑↑	-	Not detected	Not detected
IF						
SEC24C	↑↑	Lower levels				
EIF3G	↑↑	Lower levels				
TK1	↑↑	Lower levels				
YBX3	↑↑	Lower levels				
IHC						
SEC24C	↑↑	Lower levels	↑↑	Lower levels		
EIF3G	Lower levels	↑↑	↑↑	Lower levels		
TK1	↑↑	Lower levels	↑↑	Lower levels		
YBX3	↑↑	Lower levels	↑↑	Lower levels		

Table 5.2. Summary of validation experiments in canine breast and ovine lung cancer cell lines. The WB results show whether each biomarker had increased secretion (↑↑), low levels (-) or were not detected in the CM of cells 24 h following a 2 Gy dose of radiation. IF and IHC results show intra-cellular expression levels of each biomarker (results for WB, IF and IHC depict comparisons between each paired parental and RR cell line).

	REM-134	REM-134 RR	JS7	JS7 RR
WB				
SEC24C	↑↑	-	↑↑	↑↑
EIF3G	↑↑	-	↑↑	↑
TK1	Not detected	Not detected	↑	↑
IHC				
SEC24C	↑↑	Lower levels		
EIF3G	↑↑	Lower levels		
TK1	↑↑	Lower levels		
YBX3	↑↑	Lower levels		

5.2.9 Increased expression of genes encoding EIF3G, SEC24, YBX3 and those involved in ER stress and the UPR is seen in breast cancer tissue following radiotherapy treatment

Characterisation of the ER^+ parental and RR cell lines previously identified differential activation of UPR pathways, with MCF-7 RR and ZR-751 RR cell lines showing reduced PERK/EIF2α signalling in comparison to their parental cells (described in chapter 4). The UPR is involved in the suspension of translation

following endoplasmic reticulum stress and as we had identified translation components enriched in our candidate biomarkers, we sought to preliminarily investigate any potential relationship between the UPR and our candidate biomarkers. A publicly available data set (GSE59733) was analysed to investigate changes in gene expression that occur following RT. In that study, 9 patients with breast cancer who were at least 55 years old and diagnosed with invasive carcinomas received pre-operative partial breast RT of either 15, 18 or 21 Gy. Surgical resection was performed on patients within 10 days of treatment. As part of the study both pre- and post-radiation biopsy tumour samples were obtained and profiled using Affymetrix whole transcriptome expression analysis with HTA 2.0 arrays. For our analysis, expression of genes encoding the 4 candidate biomarkers and 6 genes involved with ER stress and the UPR were compared in patient samples taken before and after pre-operative RT. Hierarchical cluster analysis using the 4 candidate biomarkers produced 2 clear clusters, 1 enriched for pre-treatment and 1 enriched for post-treatment samples. The post-treatment cluster was characterised by higher expression levels of EIF3G, SEC24 and YBX3, and lower expression levels of TK1 when compared to the pre-treatment cluster. Higher expression of genes involved in ER stress and the UPR was seen in the cluster enriched for post-treatment samples (Figure 5.18).

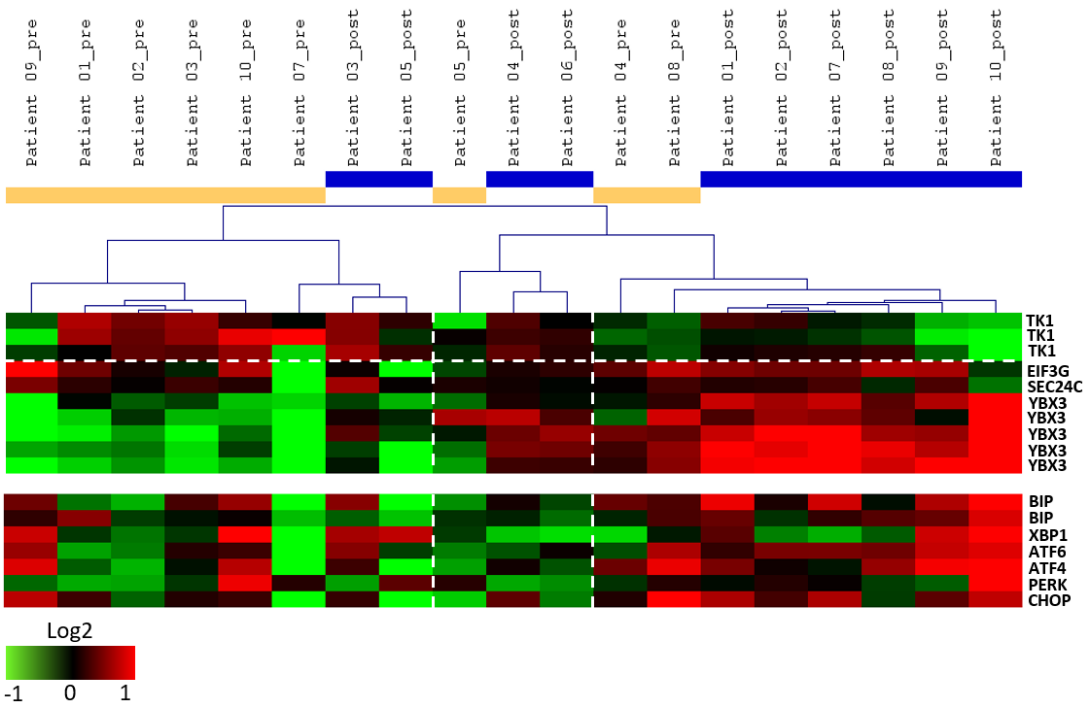

Figure 5.18. Increased expression of genes encoding EIF3G, SEC24 and YBX3 is seen in patient breast cancer tissue following RT. Log2 mean-centered gene expression heatmap showing differential expression of genes encoding the 4 candidate biomarkers and 6 genes involved with ER stress and the UPR using a public gene expression dataset (GSE50811). Gene expression differences are shown from biopsy samples taken before and after pre-operative RT (red=higher expression, black=no change, green=lower expression). Heatmap clustering was carried out using Pearson correlation with average linkage.

5.3 Discussion

The cancer secretome is a potential source of biomarkers suitable for use not only in cancer diagnosis and prognosis but also as a monitoring tool to assess the response of a tumour to treatment. A major advantage of studying the secretome over the cellular proteome is that proteins secreted by tumour cells have the potential to be detected in the blood or locally through the implantation of a sensor into the tumour itself. This chapter describes the characterisation of the cancer secretome using untreated and radiation treated MCF-7 cells and the investigation of selected candidate biomarkers in various other cancer cell lines from multiple species. The aim was to identify biomarkers that were differentially secreted in response to radiation within 24 h of treatment. The incorporation of our novel RR cell lines into validation experiments also allowed the potential of the biomarkers to be used as indicators of radiosensitivity to be assessed.

Several secretomic studies have used CM from breast cancer cell lines as *in vitro* model systems. Most of these studies use non-tumourigenic and tumourigenic cell lines to investigate differentially secreted proteins related to malignancy; results from these studies have shown that secretomic analysis can identify biomarkers related to an aggressive phenotype or predict chemotherapeutic response. One study has investigated secreted biomarkers related to radiation sensitivity by analysing the secretome from various breast cancer cell lines 6 days after exposure to a single radiation dose of 10 Gy[479]. Comparison of the secretomes between untreated cells and those cells that survived radiation identified 17 differentially secreted proteins, including cyclophilin A (CyPA), which was subsequently validated by WB. Further investigation using untreated cell lines with varying radiosensitivities showed that CyPA cellular protein expression was consistent between the cell lines, however higher secretion levels were observed in the most radiosensitive cell lines, demonstrating that CyPA secretion, independent of intra-cellular protein levels, is related to intrinsic radiosensitivity; this led the authors to suggest that secretion levels of CyPA were regulated by post-translation mechanisms. This study provided evidence that protein secretion can be increased following radiation treatment and can relate to radiosensitivity; however, the study did not assess acute changes to the cancer secretome following radiation exposure.

The first step in our experimental design was to obtain CM samples for LC-MS. We chose the technique of using CM from cells grown in serum-free media (SFM). This protocol is simple and can increase the identification of secreted proteins as the presence of serum proteins can mask and dilute the cancer secretome and confound the identification of secreted proteins due to its high abundance or close sequence homology[483]. Although the effect that serum starvation has on cells is under debate[484-487], studies have shown that under correct culture conditions cell death is minimised[477,488] and that serum-free culture does not significantly affect the composition of secreted proteins[489,490]. In order to reduce cytosolic protein contamination from cell death, studies have suggested that optimal cell number and incubation times are required; SFM incubation up to 30 h with cell confluency under 70% are considered optimal cell culture conditions to minimise cell lysis and the release of cytoplasmic proteins[477,488]. These culture conditions were adhered to in our

experiments. An extensive wash step was also performed prior to incubating cells in SFM to remove both cytosolic and serum proteins; this has been shown to reduce CM contamination by serum proteins and increase the number of secreted proteins identified, while not affecting cell growth or viability[491]. As secreted proteins present in the CM are usually at low concentrations they were concentrated before secretomic analysis. All CM samples underwent filtering and centrifugation to reduce contamination by dead cells and debris, with ultrafiltration performed to enrich and concentrate secreted proteins; this method has been successfully used in numerous studies[492,493] despite the potential for column blockade with prolonged centrifugation periods and the loss of low molecular weight proteins[488]. In our experiments control samples were also included at each time point to account for the potential effects from serum starvation. Cell counts, using trypan blue, for each cell line following CM harvesting identified no significant differences in viable cell number between controls and samples treated with up to 10 Gy 24 h post-radiation. This method of assessing cell viability has been used in previous secretomic studies, the results of which are in accordance with our survival data, showing the absence of any significant cell death up to 24 h post 10 Gy radiation[494].

Initial analysis to identify MCF-7 radiation-induced secreted biomarkers involved the 24 h time point. As cancer patients typically receive daily radiation fractions, identification of biomarkers at this time point would be more applicable for use in the clinics; biomarker levels could in theory be measured just prior to daily treatment i.e. 24 h after a patient's previous dose. Using only biomarkers whose levels dramatically rose at 24 h reduced the number of potential biomarkers from 765 to 33. Subsequent investigation of the secretion levels of the 33 biomarkers at earlier time points identified that the majority had low secretion levels up to 8 h post-radiation. Literature searches and cross referencing through Vesiclepaedia[482] identified that all 33 biomarkers have previously been shown to be secreted in microvesicles or exosomes by cancer cells. As our results had previously confirmed that the total number and percentage of dead cells did not change with radiation, and that the total number of unique secreted biomarkers also did not change with radiation, it is unlikely that the identified changes in the secretome up to 24 h post-radiation was related to radiation-induced membrane damage and cell death. Instead,

it is more likely that these biomarkers are either actively secreted or secreted via microvesicles or exosomes, and that the rate of secretion may be increased by radiation treatment. Exosomes (30-150 nm) and microvesicles (100-1000 nm), together with apoptotic bodies (>1 μm), are collectively termed extra-cellular vesicles and are utilised by normal cells for the transmission of proteins, lipids, mRNAs, microRNA and DNA[495,496]. Cancer cells can also use these vesicles to communicate with other cancer and stromal cells through various cytokines and growth factors (VEGF, FGF, TGFβ), enabling then to modify the TME to sustain tumour progression, angiogenesis and promote metastasis[497,498]. Exosome markers and exosome-related proteins have been found in the cancer secretome and in the blood of patients; this exosome cargo is one explanation for the identification of nuclear, cytoplasmic and unconventional secreted biomarkers found in tumour secretomes[499]. Further investigations from our results would be to specifically isolate microvesicles and exosomes and validate the presence of our biomarkers within them; advantages of using the microvesicle/exosome proteome is that it is relatively stable in blood, making it suited for blood-based detection methods.

Although all 33 biomarkers identified from the preliminary MCF-7 characterisation could have been taken forward for validation based on their excellent secretion profiles, we wanted to reduce the numbers further; this was done first by investigating the secretion patterns in other cancer cell types from different species and then through functional analysis. A common set of biomarkers that are released from multiple cancer types and in different species that are sensitive to radiation would allow for wider applications of the biomarkers and would allow for large animal model validation and possible veterinary uses. Unfortunately, from the 33 MCF-7 candidate biomarkers only a small number were identified as having similar secretion patterns in the other cell lines. Using the ER^- human breast cancer cell lines (MDA-MB-231 and HBL-100) only EIF3G, SEC24C, CAP1 and VPS29 shared similar secretion patterns with those found in the MCF-7 secretome. Even fewer similarities in secretion patterns compared with the MCF-7 secretome were seen using the canine breast cancer (REM-134; YBX3 and EIF3G) and ovine lung cancer (JS7; YBX3, VPS29 and FAM49B) cell lines. These results suggest that secretome patterns may be cell line and species specific which is supported by

previous studies that have identified specific secretomes related to aggressive phenotypes. Further investigation of this would require secretome characterisation of untreated and radiation treated samples to be performed from each individual cell line separately, with a subsequent analysis assessing for any biomarker similarities. Unfortunately, time restraints prevented this from being performed, but this analysis may in the future be a means of identifying common biomarkers across cell lines, or at least ones common to specific cancer subtypes i.e. ER^- versus ER^+.

Final candidate biomarker selection was based on those with known roles in the 3 functional pathways identified through Markov clustering. Biomarkers were also selected if they were involved in signalling pathways previously determined as inherently different between the MCF-7 parental and RR cell lines (consisting of proliferation, UPR and WNT pathways). Incorporating these factors into the biomarker selection process could enable the identification of biomarkers that may provide an indication of radiosensitivity. This analysis identified 9 candidate biomarkers that either had excellent secretion profiles (GNPNAT1, YBX3) or had roles in translation (EIF3G, EIF4EBP2, NAP1L4), proliferation (TK1), protein transport from the ER to the Golgi (SEC24C, VPS29) or WNT signalling (DKK1).

Following the selection of lead candidate biomarkers in-lab validation was conducted on 4 of the 9 biomarkers. Validation experiments aimed to confirm that biomarker secretion occurred in response to radiation and to assess whether differential secretion occurred between radiosensitive and radioresistant cell lines. This was achieved predominantly through WB experiments using CM samples and was supported through the investigation of gene and intra-cellular biomarker expression levels. All these validation experiments were performed using paired parental and RR cell lines which had been previously developed and characterised. A brief description of the function of the 4 biomarkers, highlighting their potential roles in cancer and secretion pathways, is discussed in the following sections.

The eukaryotic translation initiation factor 3 (EIF3) complex plays an essential role in RNA transport and protein synthesis through its control of translation initiation[500]. Although essential for normal cellular functions, aberrant EIF3 subunit expression has been shown in several cancer types to be associated with proliferation, invasion, metastasis and prognosis[501-505]. Specifically, increased

EIF3G expression has been shown *in vitro* to enhance the ability of breast cancer cells to proliferate, migrate and invade, whist *in vivo* studies have shown increased expression to correlate with lymph node metastasis and drug resistance[506]. EIF3G has also been found to be secreted via extra-cellular vesicles in numerous cancer types[507-509], breast milk[510] and mesenchymal stem cells[511]. Validation using CM samples identified increased EIF3G secretion levels in response to radiation at 24 h in MCF-7, REM-134 and JS7 parental cell lines, whereas significantly lower or no secretion was observed in the RR cell lines. EIF3G gene expression was also higher in ER^- and ER^+ parental cell lines compared with RR derivatives, which was supported by IHC and IF results. Overall these results provided evidence that EIF3G is secreted in response to radiation, but only in radiosensitive cell lines, and that EIF3G gene expression and intra-cellular protein levels may be related to radiosensitivity.

Protein transport from the endoplasmic reticulum to the Golgi apparatus is an essential component of the classical protein secretion pathway. Transport occurs through the production of Coat Protein Complex II (COPII) vesicles[512], which are composed of 5 proteins (Sar1, Sec23, Sec24, Sec13 and Sec31) that assemble on the cytosolic face of the endoplasmic reticulum membrane[513-515]. Four isoforms of Sec24 exist (A-D) which serve as cargo-binding adaptor molecules in COPII vesicles[516-520]. Cellular kinases may also play a role in post-translational modification of Sec24; AKT has been shown *in vitro* to phosphorylate Sec24C which can decrease its binding affinity with SEC23, thus reducing correct COPII formation and transport ability[521]. This may be an important finding, as our previous characterisation of the MCF-7 RR cell line identified increased AKT pathway activity. The effects of AKT inhibition on SEC24 could warrant further investigation. Increased SEC24C expression has been shown in colorectal cancer[522] and has been found to be secreted via extra-cellular vesicles in numerous cancer types[507,523-526], breast milk[510] and mesenchymal stem cells[511]. Validation using CM samples identified increased SEC24C secretion levels in response to radiation at 24 h in MCF-7, ZR-751, MDA-MB-231 and REM-134 parental cell lines, whereas significantly lower or no secretion was observed in the RR cell lines. The only exception was in the MDA-MB-231 RR cell line, which showed a significant increase in secretion levels. SEC24C gene expression was lower in ER^- and ER^+ parental cell lines compared

with RR derivatives, although this result was not supported by IHC and IF results, which identified higher expression in the parental cell lines. Overall, these results provided evidence that SEC24C is secreted in response to radiation, but secretion may only provide evidence of radiosensitivity in ER^+ cell lines. Differences between SEC24C gene expression and intra-cellular protein levels would require further investigation to determine if levels could relate to radiosensitivity.

Y-box binding protein 3 (YBX3) has been shown to act as a transcription factor, regulating translation[527] and influencing processes such as differentiation, proliferation and survival[528]. YBX3 overexpression and nuclear localisation has been correlated with poor prognosis in hepatocarcinomas[529-531] and is involved with the pathogenesis of gastric cancer through increased invasion and chemoresistance[532]. YBX3 has also been found to be secreted via extra-cellular vesicles in numerous cancer types[507,533,534] and mesenchymal stem cells[535]. Unfortunately, time restraints did not allow for validation using CM samples; however, YBX3 gene expression was higher in ER^- and ER^+ parental cell lines compared with RR derivatives, which was supported by IHC and IF results. Overall these results provided evidence that YBX3 gene expression and intra-cellular protein levels may be related to radiosensitivity.

TK1 is a cell cycle regulator[536] which catalyses the addition of a gamma-phosphate group to thymidine creating thymidine monophosphate, which is the first step in the synthesis of deoxythymidine triphosphate and DNA replication[537]. Intra-cellular TK1 levels vary depending on the stage of the cell cycle, with low concentrations in the G1 phase and higher levels in S/G2 phases. A dramatic fall in concentration is seen in the M-phase as a result of degradation pathways[538]. Increased TK1 expression has been identified in breast tumours and has been shown to correlate with disease stage and grade[539]. TK1 has also been found to be secreted via extra-cellular vesicles in numerous cancer types[507,526,533,534]. Serum TK1 has shown promise as a biomarker of proliferation[540] with diagnostic and prognostic potential in numerous cancer types[536,541]. Serum TK1 has also been investigated for monitoring the response of breast cancer patients to treatment[542] and for predicting the risk of developing distant and/or regional recurrence post-surgery[543]. Validation using CM samples identified increased TK1 secretion levels in response to radiation at 24 h in MCF-7 and ZR-751 parental cell lines, whereas significantly lower or no

secretion was observed in the RR cell lines. Increased secretion levels were seen in both JS7 and JS7 RR cell lines. TK1 gene expression was also higher in the ER^+ parental cell lines compared with RR derivatives, which was supported by IHC and IF results. Gene expression in the ER^- MDA-MB-231 parental and RR cell lines identified higher expression in the RR derivatives. Overall, these results provided evidence that TK1 is secreted in response to radiation but may only provide evidence of radiosensitivity (based on gene analysis) in ER^+ cell lines.

Currently only 4 of the 9 lead biomarkers have undergone preliminary validation and further work will be needed to investigate the remaining candidates. Gene analysis of the REM-134 and JS7 parental and RR cell lines has also not yet been completed; performing this analysis would provide further information of the ability of these biomarkers to be used for predicting radiosensitivity. Another area of future research would involve investigating the mechanisms of biomarker secretion and what roles their secretion plays in terms of radiation response. One speculative mechanistic theory for biomarker secretion that incorporates both protein transport and translation would involve the UPR. From our previous characterisation of the ER^+ parental and RR cell lines we know that there is differential activation in UPR pathways. MCF-7 RR and ZR-751 RR cell lines seemingly lose PERK/EIF2α signalling as opposed to parental cells which show higher expression of total and p-PERK and EIF2α at both gene and protein level. If parental radiosensitive cells block translation in response to radiation, then this could perhaps lead to a build-up of complexes required for translation initiation (EIF3G, EIF4EBP2, NAP1L4) and protein transport from the endoplasmic reticulum to the Golgi (SEC24C, VPS29) within the cytoplasm. While translation is inhibited these biomarkers are no longer required by the cell and so may be preferentially secreted. Although currently there is no direct evidence to support this theory, investigation of UPR associated genes and genes encoding the 4 biomarkers using a publicly available data set (GSE59733) provided preliminary evidence that radiation can increase the expression of UPR response genes and genes encoding EIF3G, SEC24C and YBX3. These results identified a gene signature similar to that seen in MCF-7 and ZR-751 parental cell lines as opposed to their RR derivatives. Further work investigating the UPR would

help to investigate the mechanisms of radioresistance and assess its potential role in radiation-induced secreted biomarkers.

5.4 Conclusion

This chapter has described the preliminary development of an *in vitro* secretomic experiment using CM from cancer cells with the aim of detecting and validating radiation-induced acutely secreted biomarkers. To our knowledge, this is the first description of secretomic experiments being used to identify radiation-induced secreted biomarkers which are released within 24 h of treatment, the results of which were validated using novel RR cell lines. By using these paired parental and RR cell lines we have shown that biomarkers can be released in response to radiation and that differential biomarker secretion profiles can indicate the radiosensitivity of a cancer cell. Furthermore, investigation of differential gene expression and intra-cellular protein levels of the candidate biomarkers also provided an indication of radiosensitivity. In clinical terms, the identification of a panel of biomarkers whose gene expression signature or intra-cellular expression levels predict the likelihood of a tumour responding to RT could be combined with measuring on-treatment secreted levels of the same biomarkers; this may provide a means by which the response of a tumour could both be predicted and also continually assessed. The use of biomarkers for both predicting and monitoring the response to treatment would provide a potential way in which RT could become tailored to an individual patient.

6 Biocompatibility Assessment of Common Implantable Sensor Materials in a Tumour Xenograft Model

This results chapter is an expanded version of a published research article: Gray M, Meehan J, Blair EO, Ward C, Langdon SP, Morrison L, Marland JRK, Tsiamis A, Kunkler IH, Murray A, Argyle D. Biocompatibility of common implantable sensor materials in a tumour xenograft model. Journal of Biomedical Materials Research Part B: Applied Biomaterials 2018; 1-14. This article is open access with the authors retaining copyright to their work with permission to use published figures in this thesis. Sections of text and figures used from this article have been referenced accordingly.

6.1 Abstract

Background: Interest in the use of implantable devices for a wide range of medical conditions is increasing. Unfortunately, following implantation within the body these devices can lose functionality due to biofouling caused by the foreign body response (FBR). To accurately assess the FBR induced by an implanted medical device then biocompatibility evaluation should be performed within tissues where implantation is intended; sensors designed for implantation into solid tumours should be evaluated within a tumour microenvironment. **Methods:** A novel serial sacrifice murine xenograft model was developed to evaluate the potential of 6 biomaterials, used in the construction of the IMPACT O_2 sensor (silicon dioxide, silicon nitride, Parylene-C, Nafion, biocompatible EPOTEK epoxy resin and platinum), to trigger a FBR when implanted into human breast cancer xenograft tumours. Novel protocols were developed to process, and section harvested tumours that allowed identification of the implant site. **Results:** No detrimental effects from implantation of any of the biomaterials on mice body weight or on tumour growth were identified. Immunohistochemistry showed no significant changes in tumour necrosis, hypoxic cell number, proliferation, apoptosis, immune cell infiltration or collagen deposition. **Conclusions:** The lack of biofouling from the implantation of these biomaterials within a solid tumour supports their use in implantable medical devices. To our knowledge, this is the first documented investigation of the effects of modern

biomaterials used in the production of implantable sensors within a tumour microenvironment.

6.2 Introduction

Interest in the development and use of implantable medical devices has increased in recent years due to advances in microfabrication techniques and through the development of novel biocompatible materials. As precision medicine becomes integrated into healthcare practices, the roles of implantable medical devices as diagnostic, therapeutic and monitoring aids will likely become more important in achieving better patient outcomes in a variety of disease conditions. Major challenges in the development of any implantable medical device include the activation of tissue and immune responses that occur post-implantation. These reactions can contribute to device failure or host toxicity and are largely attributed to biofouling and the FBR[165-167]. The extent of these processes can be influenced by the implantation procedure itself as well as the biocompatibility of the device.

Although *in vitro* tests as outlined in the Biological Evaluation of Medical Devices: ISO 10993[161] are excellent screening processes, *in vivo* animal models are required to evaluate tissue reactions, the results of which can influence the selection of materials used in the development of implantable medical devices. *In vivo* models provide a means by which the FBR can be evaluated in a situation similar to that which would occur following implantation into patients. Obtaining tissue or fluid exudates adjacent to the implanted material allows assessment of cellular interactions which occur in the presence of stromal and immune cells; these factors greatly increase the complexity of *in vivo* models compared with *in vitro* testing systems[544].

The cage implant system involves placing candidate materials into stainless-steel cages which are then subcutaneously implanted into an animal. Tissue exudates can be collected from the cage and examined for inflammatory cells, enzymes, fibrous encapsulation and infection[545]. Although no tissue is obtained from this model, it allows for serial exudate samples to be obtained without animal sacrifice. Serial sacrifice models, such as the chamber system, allow for tissue harvesting for histological evaluation of the inflammatory response, fibrous encapsulation and vascularisation. This system utilises a lightweight aluminium or titanium frame fastened to 2 skin folds on the back of a rat or hamster. Candidate materials can then

be implanted into the skin fold. Real-time visualisation can also be achieved with this model by removing a skin section and replacing it with glass[546,547]. The chorioallantoic membrane (CAM) of a developing chick embryo is a simple and cost-effective method of observing tissue responses to materials. Acute and chronic inflammatory responses have been shown to be elicited in a manner similar to that in other animal models. Materials coated in ovalbumin or egg white are placed on top of the CAM, which can become incorporated into it within 7 days. Visualisation of the material is also possible due to the transparent nature of the CAM[548,549].

These models have all been used to evaluate medical devices designed for implantation into normal healthy tissues. However, it has been suggested that biocompatibility is a characteristic of a system rather than of a material and that individual materials may affect different biological systems in different ways. Therefore, materials should undergo biocompatibility testing in the tissue they are designed to be implanted into[166,544,550,551]. This is an important consideration for the IMPACT sensor, designed for implantation into solid tumours, or any device developed for intra or peri-tumoural implantation. For these devices, the FBR must be evaluated within the diseased tissues, rather than relying on published data from implantation studies within healthy tissues. The *in vitro* and *in vivo* biocompatibility of the constituent materials used in the construction of the IMPACT sensor has been previously documented. Various *in vivo* studies have shown that the materials are well tolerated and induce only a minimal FBR. Some of the materials have gained ISO 10993 accreditation, while all have been used in the construction of a variety of medical devices (Table 6.1). However, all these biocompatibility studies used *in vivo* models in which the materials were implanted into healthy, non-diseased tissue; their effects within a tumour have never been evaluated.

This chapter describes the assessment of the intra-tumoural biocompatibility of 6 modern biomaterials that were under consideration for use in the IMPACT sensor. The biomaterials investigated were silicon nitride, silicon dioxide, platinum, Parylene-C, biocompatible EPOTEK epoxy resin and Nafion. Copper was chosen as a positive control implantation material due to its recognised previously published cytotoxic effects[552,553]. Through the development of a novel serial sacrifice murine model, biomaterials were implanted into human breast cancer xenograft tumours and

their biocompatibility assessed up to 14 days post-implantation. Novel protocols were developed to process, and section harvested tumours that allowed identification of the implant site. The effects of the biomaterials were investigated through changes in mean tumour volumes and mouse body weights, while histopathology was used to assess proliferation, apoptosis, hypoxia and necrosis, as well as innate immune responses and collagen deposition occurring within the tumour. To our knowledge, this is the first description of the interaction of modern biomaterials, used in the fabrication of implantable devices within a TME.

Table 6.1. Previously published studies investigating the *in vivo* and *in vitro* biocompatibility testing of IMPACT component biomaterials. (taken from[551]).

Biomaterial	*In vitro* testing	*In vivo* testing	Implantable devices	Regulations
Parylene-C	Haemocompatibility testing[554] Cell culture biocompatibility[555-557] Cytotoxicity, hemocompatibility testing[161]	Systemic toxicity, sensitisation, intracutaneous reactivity testing[161] Neural electrodes biocompatibility: mice[556,558], cat[559], monkey[560], rat[561-563]	Cardiovascular implants[564]	ISO 10993[565]
Platinum	Cell culture biocompatibility[566]		Arterial stents[567,568] Embolization coils[569,570] Pacemaker leads, implantable defibrillators, cochlear implants[571] Brachytherapy devices[572]	
Silicon nitride	Cytotoxicity, haemocompatibility testing[161] Non-toxic, encourage cell adhesion and cellular differentiation[573-577]	Systemic toxicity, sensitisation and intramuscular reactivity testing[161,578] Fracture repair and evaluation of osteoconduction[573,576,579-581] Cage implant biocompatibility testing[582,583]	Orthopaedic and neurosurgical implants[584-586]	ISO 10993[574,578]
Silicon dioxide	Cytotoxicity testing[161] Biocompatibility and antibacterial testing[577,587]	Intramuscular reactivity testing[161,578] Nerve electrodes biocompatibility: rat[588] Cage implant biocompatibility testing[582]	Nanomedicine drug delivery systems and diagnostic probes[589,590]	ISO 10993[578]
Nafion	Biocompatibility and antibacterial testing[591] Non-cytotoxic and allows cellular differentiation[592]	Subcutaneous, intraperitoneal and intravenous biocompatibility: mice[591,593], dogs[594] Intracerebral biocompatibility[145,595-597] Nervous system biocompatibility[592]	Electrochemical sensors and electrodes[598,599]	
EPO-TEK OG116-31 resin	Cytotoxicity, haemocompatibility, genotoxicity testing[161]	Systemic toxicity, sensitisation, intracutaneous and intramuscular reactivity testing[161]	Pacemakers, ophthalmic and neurostimulators, insulin pumps, cochlear implants orthopaedic and neurological implants[600]	ISO 10993[600]

6.3 Results

6.3.1 Development of a percutaneous biomaterial implantation technique

To develop a technique whereby biomaterials could be safely, reliably and quickly implanted into a xenograft tumour, we began to investigate protocols using e*x-vivo* MDA-MB-231 xenograft tumours. A 21G needle was introduced through the skin overlying the tumour but not into the tumour tissue itself. The needle was withdrawn, noting its skin entry position and any blood seeping from the wound. Using needle holders, a length of Cu wire (400 µm in diameter and approximately 7 mm in length) was introduced through the needle-created insertion hole and advanced into tumour tissue until the wire was completely buried under the skin (Figure 6.1). Tumours containing the implanted wires then underwent fixing in formalin, processing and edge embedding in paraffin for IHC.

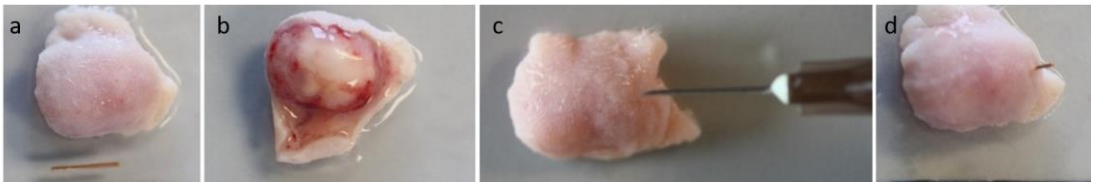

Figure 6.1. Photographs of *ex-vivo* MDA-MB-231 xenograft tumours used in the development of a biomaterial implantation protocol. (a) Dorsal aspect of MDA-MB-231 xenograft tumour, a 1 cm Cu wire is shown for implantation. **(b)** Ventral aspect of MDA-MB-231 xenograft tumour. **(c)** A 21G needle was introduced through the skin overlying the tumour. **(d)** A length of Cu wire was then introduced into the tumour through the insertion hole created by the needle.

6.3.2 Development of an IHC sectioning protocol for xenograft tumours containing implanted biomaterials

Blocks of paraffin-embedded xenograft tumours were sectioned until the tip of the implanted wire was reached. If the wire was flush with the cut surface of the block it was removed, and sectioning continued through the implant site. However, if the trajectory of the wire was directed further into the tumour, sectioning stopped, and the paraffin was melted. The tumour was then trimmed from its sectioned edge as parallel as possible to the path of the wire. The wire was then carefully removed before re-embedding the tumour in paraffin. Once cooled and set, sectioning continued through the block and implant site as previously described (Figure 6.2 & Figure 6.3).

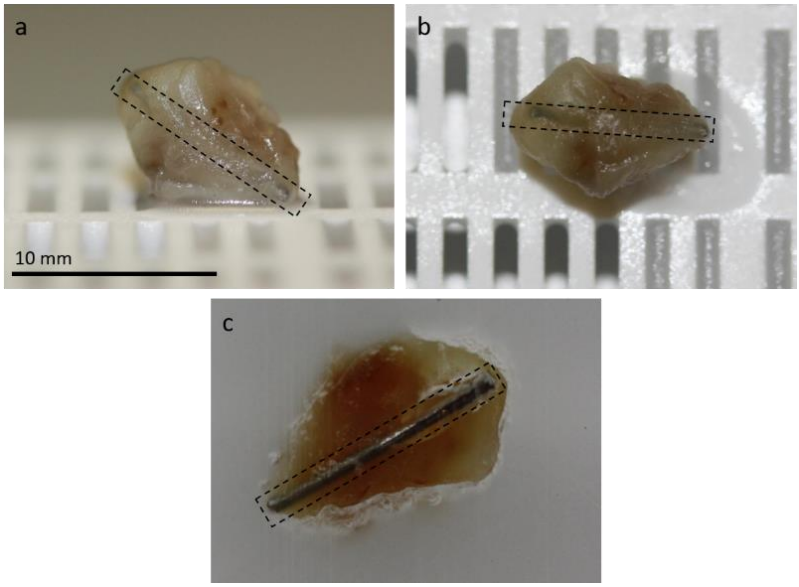

Figure 6.2. Photographs depicting the position of an implanted biomaterial within a xenograft tumour following harvesting and processing for IHC. The dashed box is outlining an OG116-31 resin wire. **(a)** Lateral and **(b)** Dorsal views showing the biomaterial positioned centrally within the tumour; photographs were taken following tumour processing but before paraffin embedding. **(c)** Following edge embedding in paraffin, the tumour was sectioned until the biomaterial was identified. The wire was then removed, and sectioning continued through the implantation site.

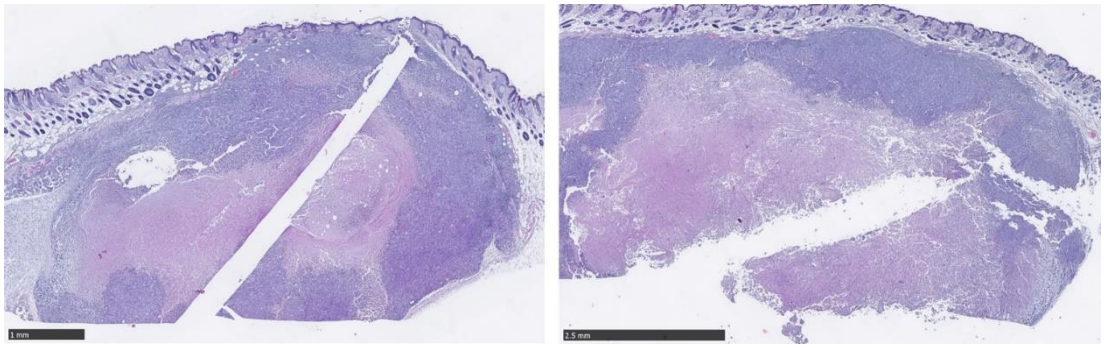

Figure 6.3. Histological appearance of xenograft tumour sections containing the biomaterial implantation site. These H&E stained sections are from 2 xenograft tumours used for development of the sectioning protocol. The implant site can be clearly identified centrally positioned within the tumour.

6.3.3 Refined procedure for biomaterial implantation into xenograft tumours

Following development of the implantation procedure using *ex vivo* xenograft tumours we progressed onto experimental cases. All biomaterials were implanted under general anaesthesia using the same percutaneous technique. MDA-MB-231 human xenograft tumours were generated subcutaneously in CD-1 female nude mice as described in sections 3.2.2 & 3.2.3. Once tumours had developed to an adequate

size (0.7-1.2 mm) mice were randomly assigned into treatment or control groups. Treatment groups consisted of tumours implanted with a single biomaterial, whereas control groups consisted of untreated tumours and those that received a needle tract (NT) injury to mimic the implantation procedure. The generation of bilateral subcutaneous flank xenograft tumours enabled each mouse to act as its own control. This reduced the total number of mice required as 1 tumour received biomaterial implantation or NT injury whilst the contralateral tumour remained untreated.

All mice underwent general anaesthesia as described in section 3.2.4 (defined as day 0). Mice were positioned in dorsal recumbency and the skin immediately surrounding the xenograft tumour was aseptically prepared for surgery using chlorohexidine solution. The biomaterials were implanted using a percutaneous technique based on the developed protocol described in section 6.3.1. A 21G needle was used to penetrate the skin overlying the tumour but not into the tumour parenchyma itself. This entry point was positioned at the caudal aspect of the tumour, so introduction of the biomaterial would be along the long axis. The needle was removed, and a single biomaterial wire was then introduced into the tumour through the pre-made entry point and advanced until the entire length of the wire was within tumour tissue. Tissue adhesive (Vetbond, 3M, Bracknell, UK) was then applied to the skin (Figure 6.4). For NT injury control tumours, a 21G needle was used to penetrate the skin as previously described but was then advanced into the tumour tissue, stopping just short of penetrating the contralateral side of the tumour. The needle was removed, and tissue adhesive was applied to the skin (Figure 6.5). Following surgery all mice were placed into an incubator at 30-35^{o}C until recovered. Anaesthetic duration, including induction and maintenance, aseptic skin preparation, implantation/NT injury and recovery lasted approximately 5 min. No anaesthetic complications were encountered.

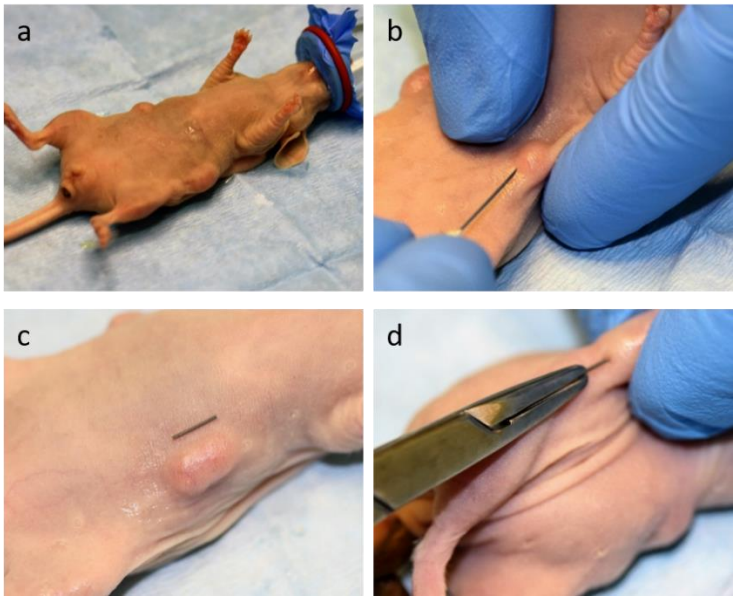

Figure 6.4. Intra-operative photographs depicting percutaneous biomaterial implantation. (a) Under general anaesthesia mice were placed in dorsal recumbency and the skin surrounding the tumour was aseptically prepared. **(b)** A 21G needle was used to make an entry point in the skin overlying the tumour. **(c)** An appropriately sized length of biomaterial was chosen for each tumour. **(d)** Needle holders were used to introduce the biomaterial into the tumour through the pre-prepared hole.

Figure 6.5. Intra-operative photograph depicting needle tract injury. A 21G needle was introduced through the skin overlying the tumour and into the tumour parenchyma itself. The needle was advanced as far as possible through the tumour to ensure the creation of a long NT. The needle stopped short of penetrating the contralateral side of the tumour.

Day 0 mice were euthanised immediately following anaesthesia, whilst the remaining mice were monitored up to 14 days post-implantation. All mice were assessed for signs of ill health with body condition score, body weight and tumour size measured 3 times a week. Relative mouse body weight was calculated by dividing the body weight measured on each day by the weight on day 0. Tumour size (width and length) was measured using Vernier callipers and tumour volume was

calculated as $\pi/6$ x width^2 x length. Relative tumour volume was calculated by dividing the tumour volume on each day by its volume on day 0. Immediately following euthanasia, xenograft tumours were removed and fixed in formalin for subsequent processing and edge embedding in paraffin for IHC.

6.3.4 The percutaneous implantation procedure resulted in a high success rate of biomaterial delivery into xenograft tumours

The mean body weight of each mouse group at day 0 was similar, averaging 26.76 ± 1.2 g. The developed percutaneous implantation procedure resulted in a high success rate of delivering biomaterial wires to the centre of the xenograft tumours. Out of 47 implantations, following harvesting 1 wire was found to have migrated from within the tumour to lie in subcutaneous fat and 1 was found to be peripherally located within the tumour during sectioning; the remainder were all well positioned within central tumour tissue. The method for sectioning biomaterial-containing tumours was also highly successful, with all implant sites identified and every implanted wire successfully recovered (Figure 6.6 & Figure 6.7). The number of mice used in each control and treatment group is provided in Figure 6.8 & Figure 6.9.

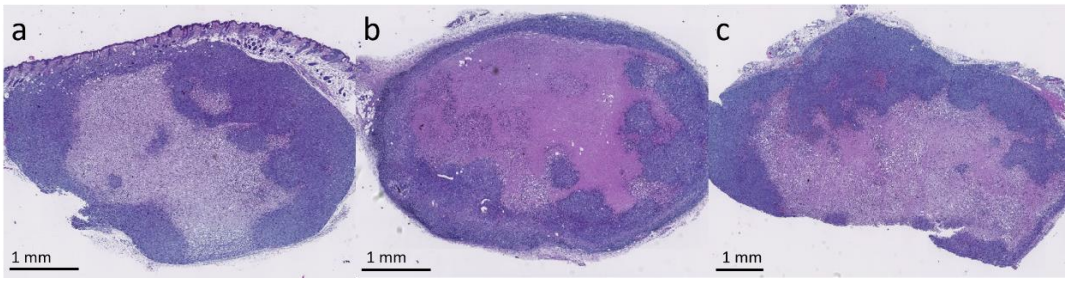

Figure 6.6. Representative H&E stained sections from untreated tumours harvested at day 7.

Figure 6.7. Representative H&E stained sections from biomaterial implanted tumours harvested at day 7 post-implantation. (a) Nafion implanted. **(b)** SiO_2 implanted. **(c)** Pt implanted.

6.3.5 Implanted biomaterials have no effect on mouse body weights and tumour volumes

Body weights of biomaterial (Si_3N_4, SiO_2, Parylene-C, Nafion, Pt and OG116-31 resin) implanted and untreated mice remained stable throughout the 7-day experimental period, with no statistically significant changes in body weight identified within any individual treatment group (Figure 6.8). The body weights of mice whose xenograft tumours were implanted with Cu also remained stable. Furthermore, no statistically significant differences were identified between any of the groups measured at each time point. Mean tumour volumes for untreated, NT injury and all biomaterial implanted and Cu implanted tumours, all showed growth over the 7 days, with no statistically significant differences identified between any group at any time point (Figure 6.8). Similar results were found when Parylene-C was implanted for 14 days; body weights remained stable with no statistically significant changes in body weight observed between implanted and control tumours. Although at day 7 the mean tumour volume of NT injury tumours was statistically lower compared to the untreated control group (p= 0.0211) their volumes increased on subsequent days with differences between the groups becoming non-significant. Tumour volumes for Parylene-C implanted tumours showed no statistical differences between untreated and NT injury tumours at any of the time points up to 14 days post-implantation (Figure 6.9).

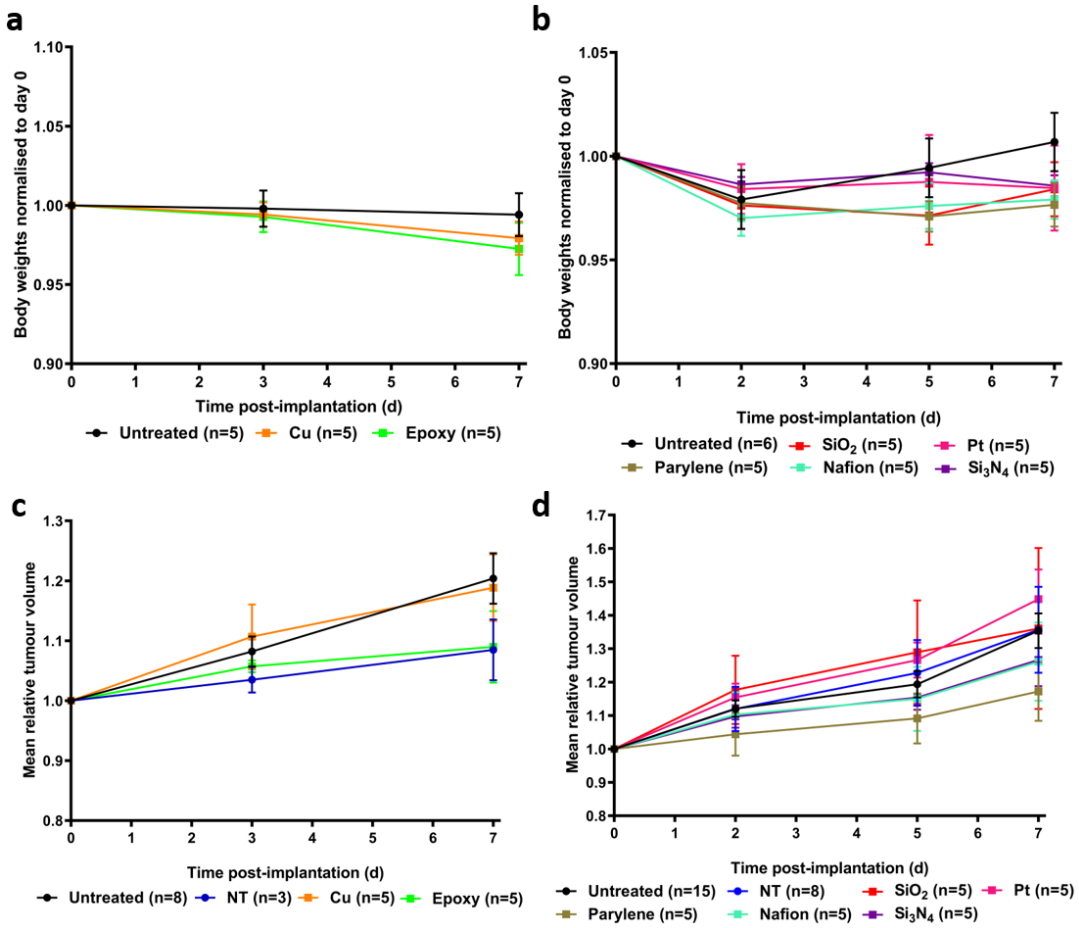

Figure 6.8. Biomaterials have no effect on mice body weights or xenograft tumour growth up to 7 days post-implantation. (a&b) Mice body weights for untreated tumours and Cu, OG116-31 resin, Parylene-C, Nafion, Pt, Si_3N_4 and SiO_2 implanted tumours. Body weights are normalised to the day 0 measurement. **(c&d)** Mean tumour volumes for untreated and NT injury tumours, along with Cu, OG116-31 resin, Parylene-C, Nafion, Pt, Si_3N_4 and SiO_2 implanted tumours. Tumour volumes are normalised to the day 0 measurement. Number of mice in each control and treatment group is provided in each figure legend.

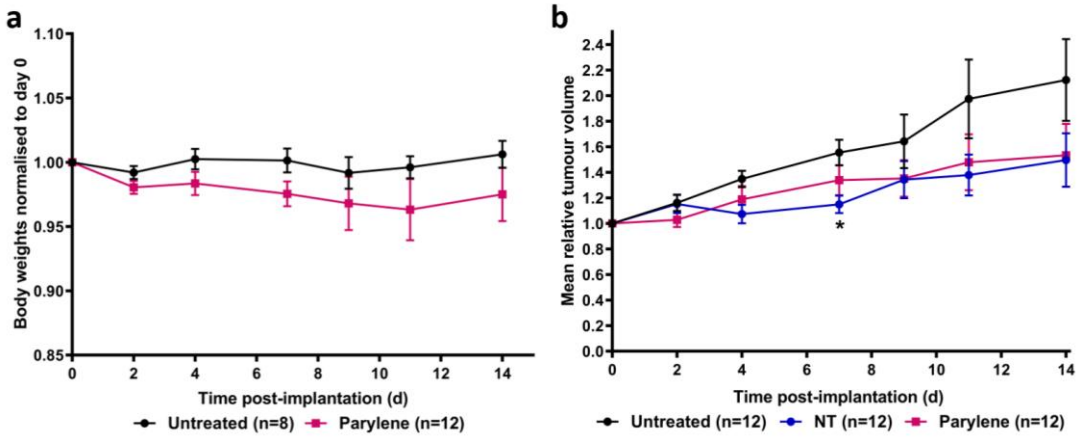

Figure 6.9. Parylene-C has no effect on mice body weights or xenograft tumour growth up to 14 days post-implantation. (a) Mice body weights for untreated tumours and Parylene-C implanted tumours. Body weights are normalised to the day 0 measurement. **(b)** Mean tumour volumes for untreated and NT injury tumours, along with Parylene-C implanted tumours. Tumour volumes are normalised to the day 0 measurement. Number of mice in each control and treatment group is provided in each figure legend (two-way ANOVA with Holm-Šídák multiple comparisons test; data expressed as mean ± SEM, *$p \leq 0.05$).

6.3.6 Implanted biomaterials have no effect on tumour necrosis and CA9 staining

The area of tumour necrosis was calculated as a percentage of the total xenograft tumour area. At 7 days post-implantation xenograft tumours implanted with Cu wires showed a statistically significant increase in the percentage area of necrosis compared to NT injury ($p = 0.0288$) and untreated ($p = 0.0141$) control groups. No significant differences in the area of necrosis were identified between biomaterial implanted xenograft tumours and the control tumours, including Parylene-C up to 14 days post-implantation (Figure 6.10 & Figure 6.11). As a hypoxic marker, CA9 expression was investigated to identify the number of hypoxic cancer cells in each xenograft tumour. No significant differences in the percentage of CA9 positive cells were identified between any of the biomaterial implanted, Cu implanted and control tumours up to 7 days post-implantation (Figure 6.12). CA9 staining was not undertaken in Parylene-C implanted tumours up to 14 days due to limited numbers of available sections.

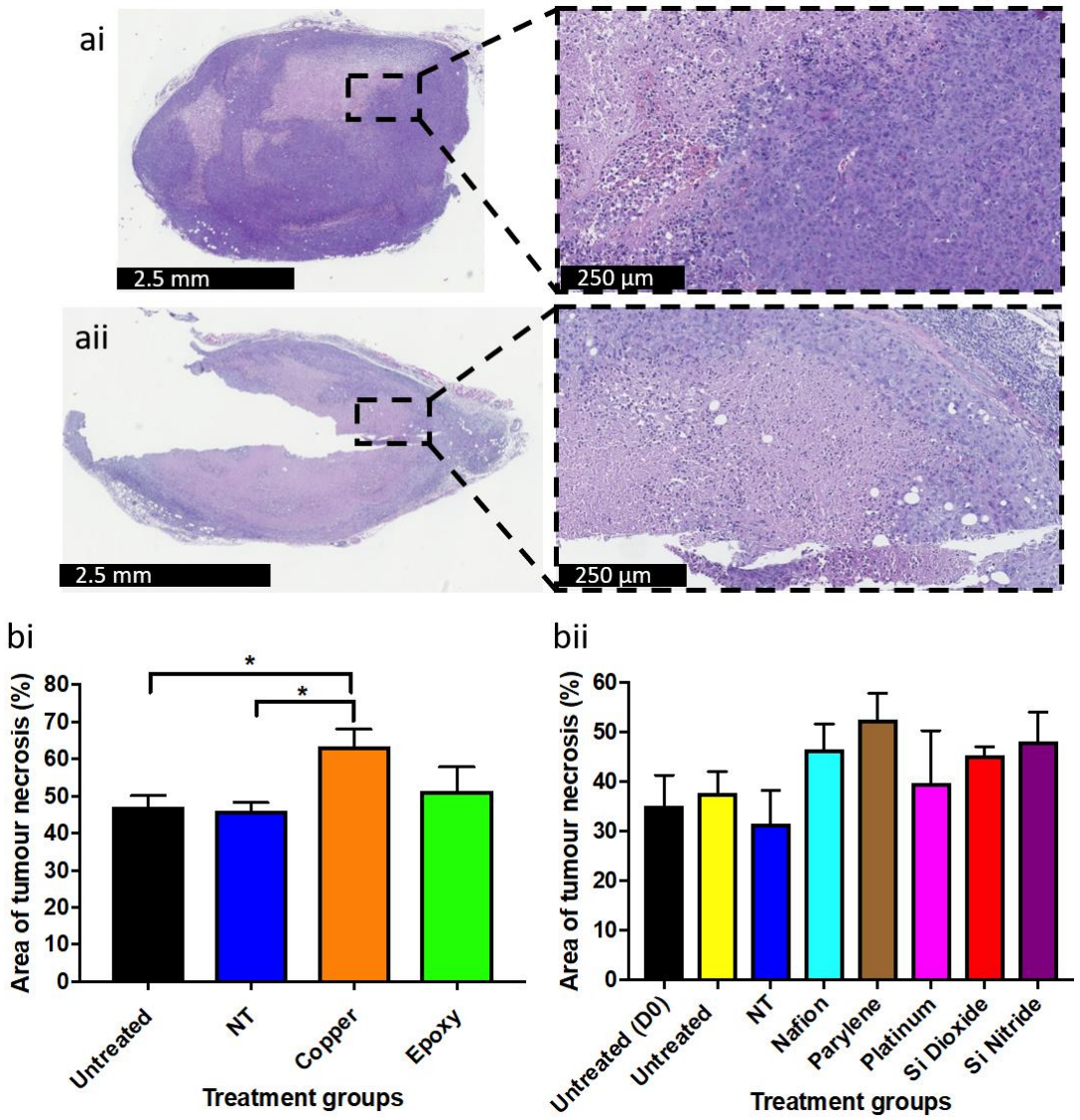

Figure 6.10. Biomaterials have no effect on the percentage area of tumour necrosis up to 7 days post-implantation. (ai&aii) Representative H&E stained sections from tumours harvested at day 7. **(ai)** Untreated. **(aii)** Cu implanted. **(bi&bii)** Percentage area of necrosis for untreated and NT injury tumours, along with Cu, OG116-31 resin, Parylene-C, Nafion, Pt, Si_3N_4 and SiO_2 implanted tumours (one-way ANOVA with Holm-Šídák multiple comparisons test; data expressed as mean ± SEM, *$p \leq 0.05$).

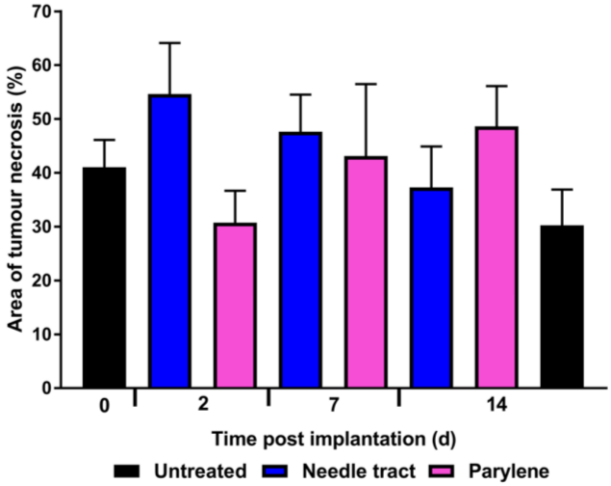

Figure 6.11. Parylene-C has no effect on the percentage area of tumour necrosis up to 14 days post-implantation. Percentage area of necrosis for untreated and NT injury tumours, along with Parylene-C implanted tumours.

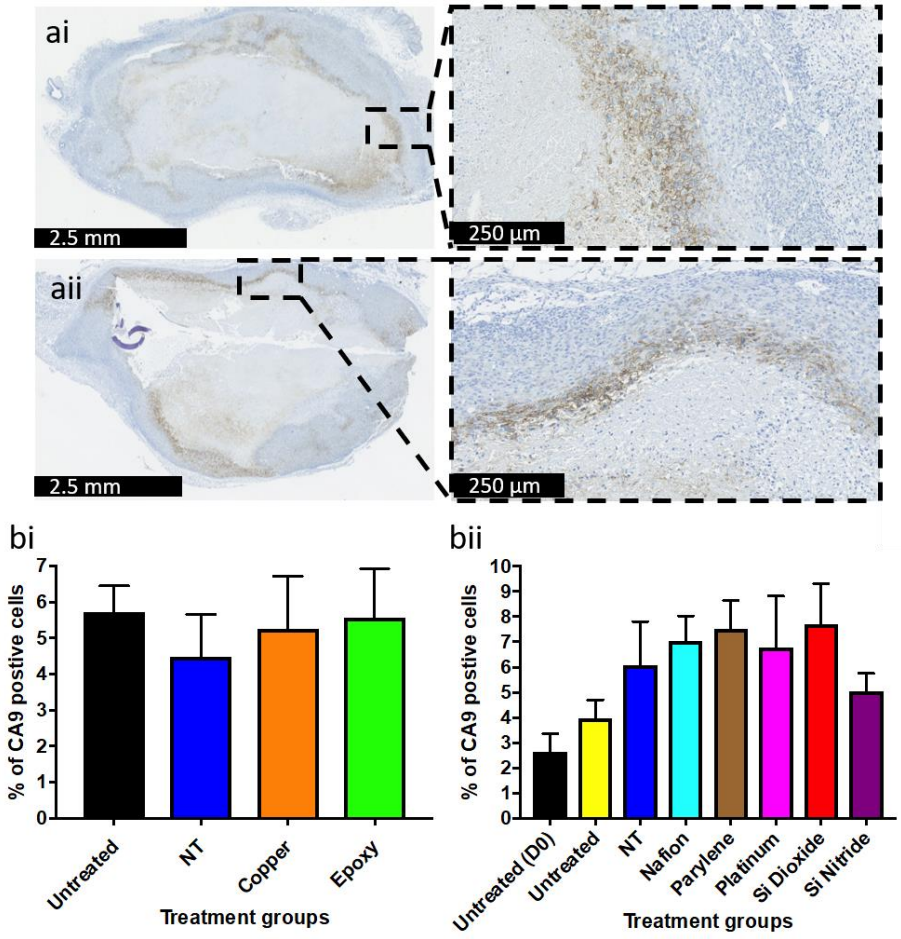

Figure 6.12. Biomaterials have no effect on xenograft cancer cell CA9 staining up to 7 days post-implantation. (ai&aii) Representative CA9 stained sections from tumours harvested at day 7. **(ai)** Untreated. **(aii)** Nafion implanted. **(bi&bii)** Percentage of CA9 positive staining cells for untreated and NT injury xenograft tumours, along with Cu, OG116-31 resin, Parylene-C, Nafion, Pt, Si_3N_4 and SiO_2 implanted tumours.

6.3.7 Implanted biomaterials have no effect on xenograft cancer cell proliferation and apoptosis

As a marker of cells present in active phases of the cell cycle (G1, S, G2) and mitosis, Ki67 expression was investigated to identify the number of proliferating cancer cells in each xenograft tumour. No significant difference in the percentage of Ki67 positive staining cells was identified between any of the biomaterial implanted, Cu implanted and control tumours up to 7 days post-implantation. (Figure 6.13). When Parylene-C implantation was investigated up to 14 days a statistically significant higher percentage of Ki67 positive staining cells was identified in the Parylene-C implanted xenograft tumours compared with NT injury tumours at 2 days post-implantation (p= 0.0037). The numbers of Ki67 positive staining cells increased in the NT injury control group on subsequent days with differences between the groups becoming non-significant (Figure 6.15). As a marker of cells activating death proteases, cleaved caspase 3 expression was investigated to identify the number of apoptotic cancer cells in each xenograft tumour. Only Cu implanted xenograft tumours had a statistically significant increase in the percentage of cleaved caspase 3 positive staining cells compared to untreated (p= 0.0025) and NT (p= 0.0020) control groups at 7 days post-implantation (Figure 6.14). Parylene-C implanted tumours showed no statistical differences in the percentage of caspase 3 positive staining cells between untreated and NT injury tumours at any of the time points up to 14 days post-implantation (Figure 6.15).

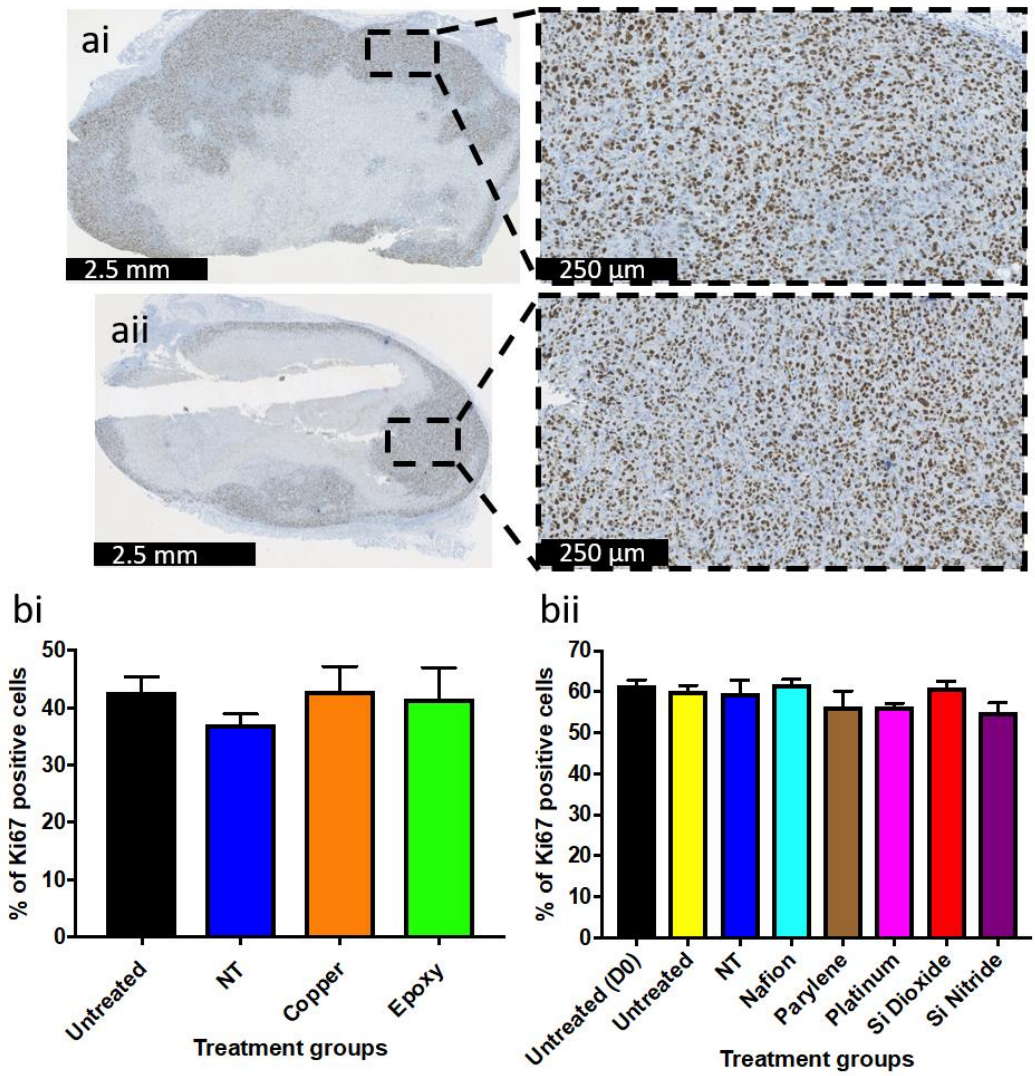

Figure 6.13. Biomaterials have no effect on xenograft cancer cell proliferation up to 7 days post-implantation. (ai&aii) Representative Ki67 stained sections from tumours harvested at day 7. **(ai)** Untreated. **(aii)** SiO_2 implanted. **(bi&bii)** Percentage of Ki67 positive staining cells for untreated and NT injury tumours, along with Cu, OG116-31 resin, Parylene-C, Nafion, Pt, Si_3N_4 and SiO_2 implanted tumours.

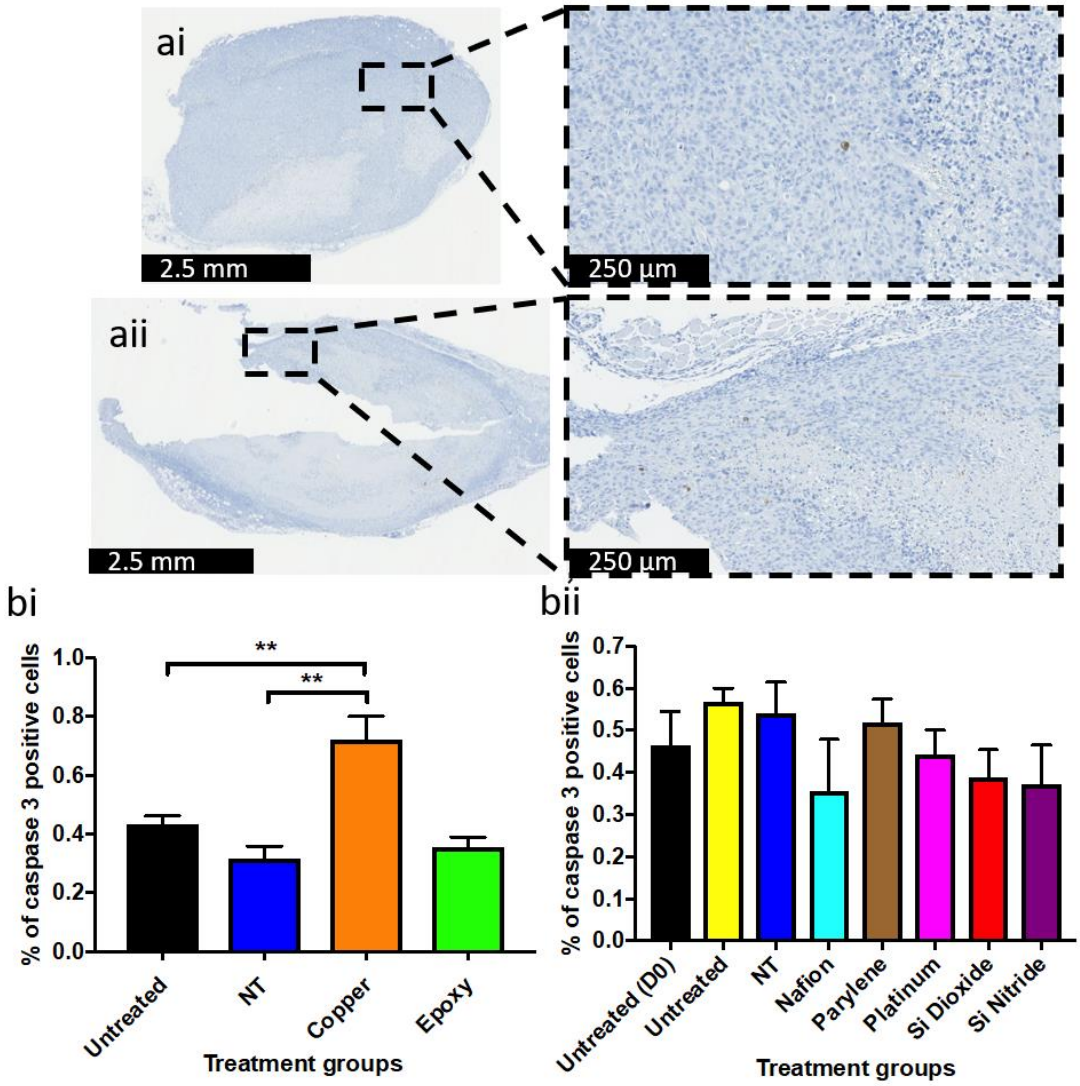

Figure 6.14. Biomaterials have no effect on xenograft cancer cell apoptosis up to 7 days post-implantation. (ai&aii) Representative caspase 3 stained sections from tumours harvested at day 7. **(ai)** Untreated. **(aii)** Cu implanted. **(bi&bii)** Percentage of caspase 3 positive staining cells for untreated and NT injury tumours, along with Cu, OG116-31 resin, Parylene-C, Nafion, Pt, Si_3N_4 and SiO_2 implanted tumours (one-way ANOVA with Holm-Šídák multiple comparisons test; data expressed as mean ± SEM, $^{**}p \leq 0.01$).

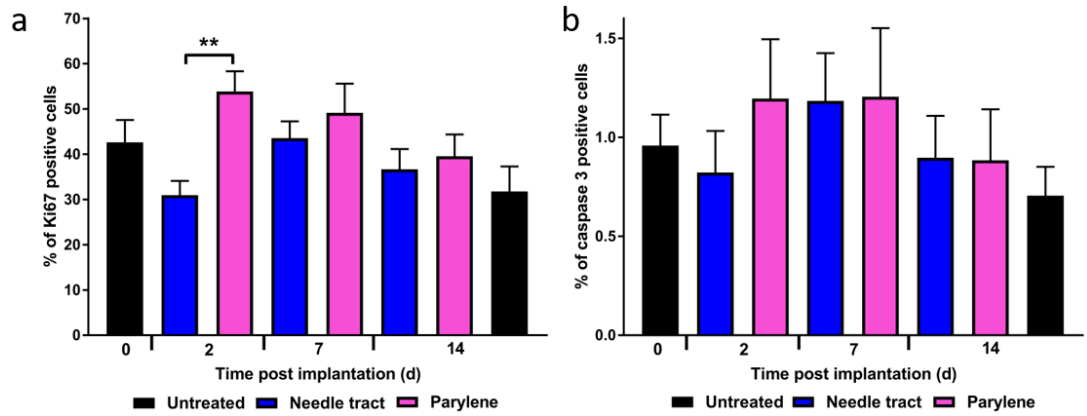

Figure 6.15. Parylene-C has no effect on xenograft cancer cell proliferation and apoptosis up to 14 days post-implantation. (a) Percentage of Ki67 positive staining cells for untreated and NT injury tumours, along with Parylene-C implanted tumours. **(b)** Percentage of caspase 3 positive staining cells for untreated and NT injury tumours, along with Parylene-C implanted tumours (two-way ANOVA with Holm-Šídák multiple comparisons test; data expressed as mean ± SEM, $**p \leq 0.01$).

6.3.8 Implanted biomaterials have no effect on neutrophil and macrophage infiltration within xenograft tumours

Using Ly6G, a glycosylphosphatidylinositol-anchored protein and the glycoprotein F4/80, cellular expression levels of each target was investigated to identify the number of murine neutrophils and macrophages within each xenograft tumour. No significant differences in the percentage of Ly6G or F4/80 positive staining cells were identified between any of the biomaterial implanted, Cu implanted and control tumours up to 7 days post-implantation or up to 14 days with Parylene-C implantation. Only small numbers of Ly6G positive cells were identified in any of the tumours (Figure 6.16, Figure 6.17 & Figure 6.18). Two types of macrophage distribution patterns were identified in implanted and control tumours. In approximately 50% of tumours, a localised region of F4/80 positive stained cells was identified round the periphery of the tumour, whereas the remaining tumours had a more uniform distribution throughout the tumour tissue (Figure 6.19).

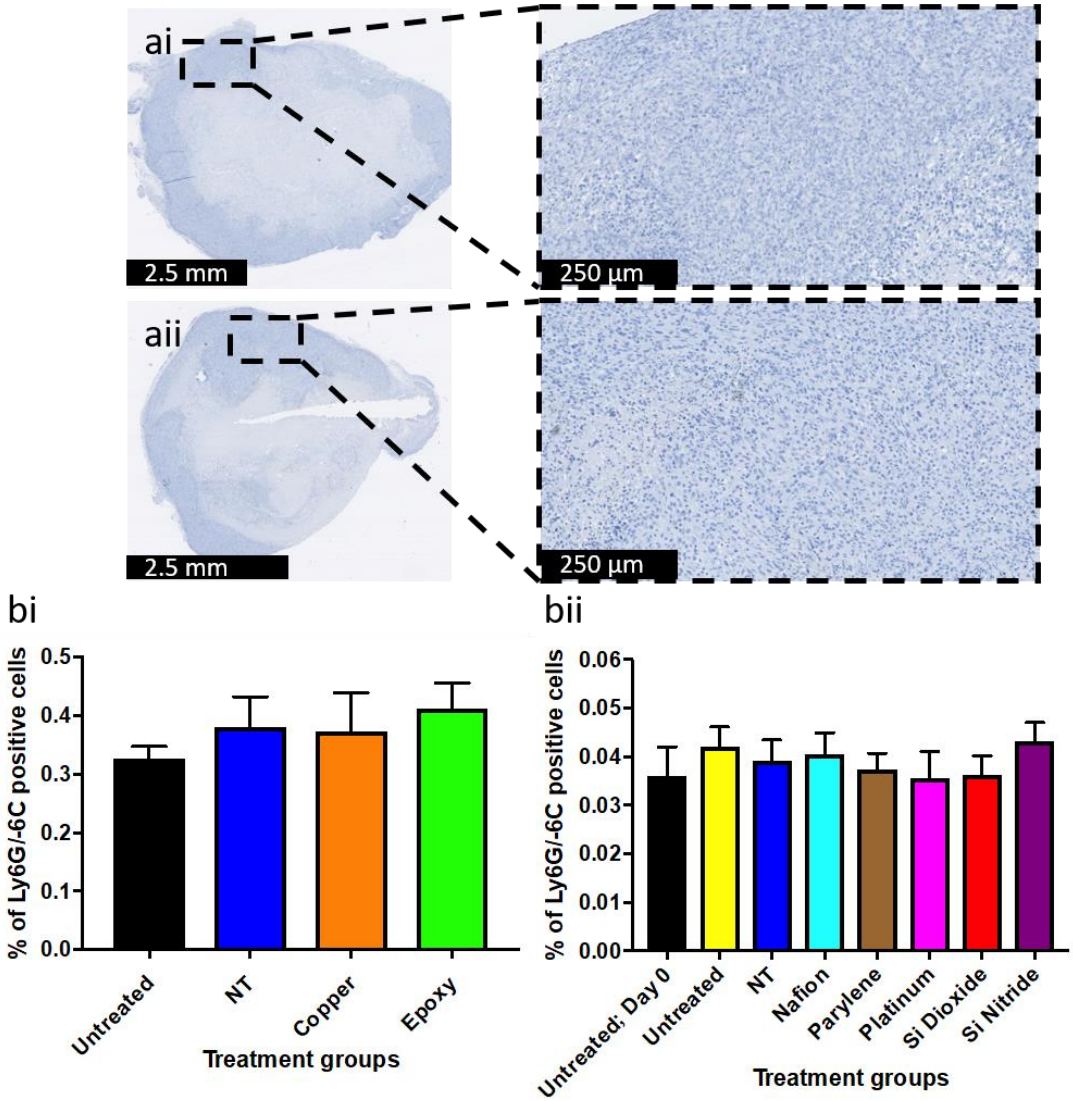

Figure 6.16. Biomaterials have no effect on neutrophil infiltration within tumour tissue up to 7 days post-implantation. (ai&aii) Representative Ly6G stained sections from tumours harvested at day 7. **(ai)** Untreated. **(aii)** Parylene-C implanted. **(bi&bii)** Percentage of Ly6G positive staining cells for untreated and NT injury tumours, along with Cu, OG116-31 resin, Parylene-C, Nafion, Pt, Si_3N_4 and SiO_2 implanted tumours.

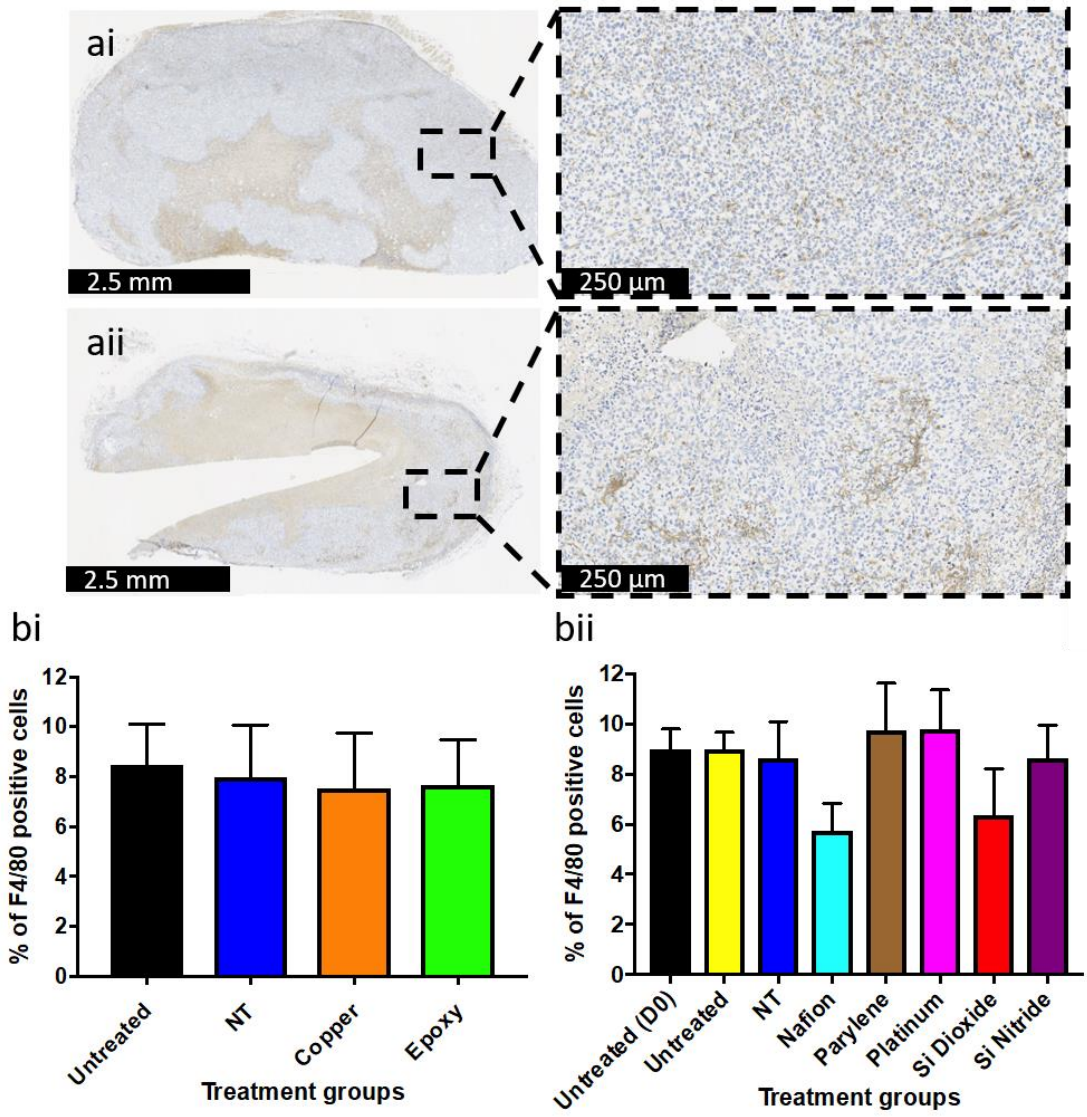

Figure 6.17. Biomaterials have no effect on macrophage infiltration within tumour tissue up to 7 days post-implantation. (ai&aii) Representative F4/80 stained sections from tumours harvested at day 7. **(ai)** Untreated. **(aii)** Si_3N_4 implanted. **(bi&bii)** Percentage of F4/80 positive staining cells for untreated and NT injury tumours, along with Cu, OG116-31 resin, Parylene-C, Nafion, Pt, Si_3N_4 and SiO_2 implanted tumours.

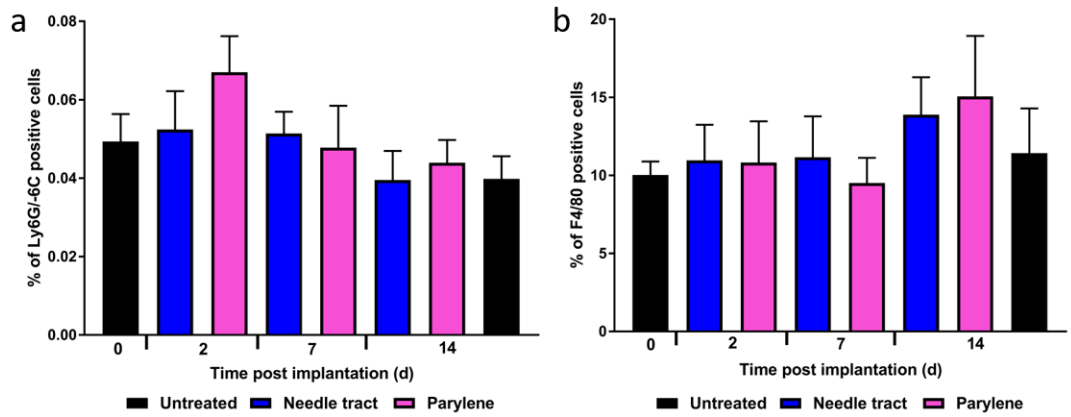

Figure 6.18. Parylene-C has no effect on neutrophil and macrophage infiltration within tumour tissue up to 14 days post-implantation. (a) Percentage of Ly6G positive staining cells for untreated and NT injury tumours, along with Parylene-C implanted tumours. **(b)** Percentage of F4/80 staining cells for untreated and NT injury tumours, along with Parylene-C implanted tumours.

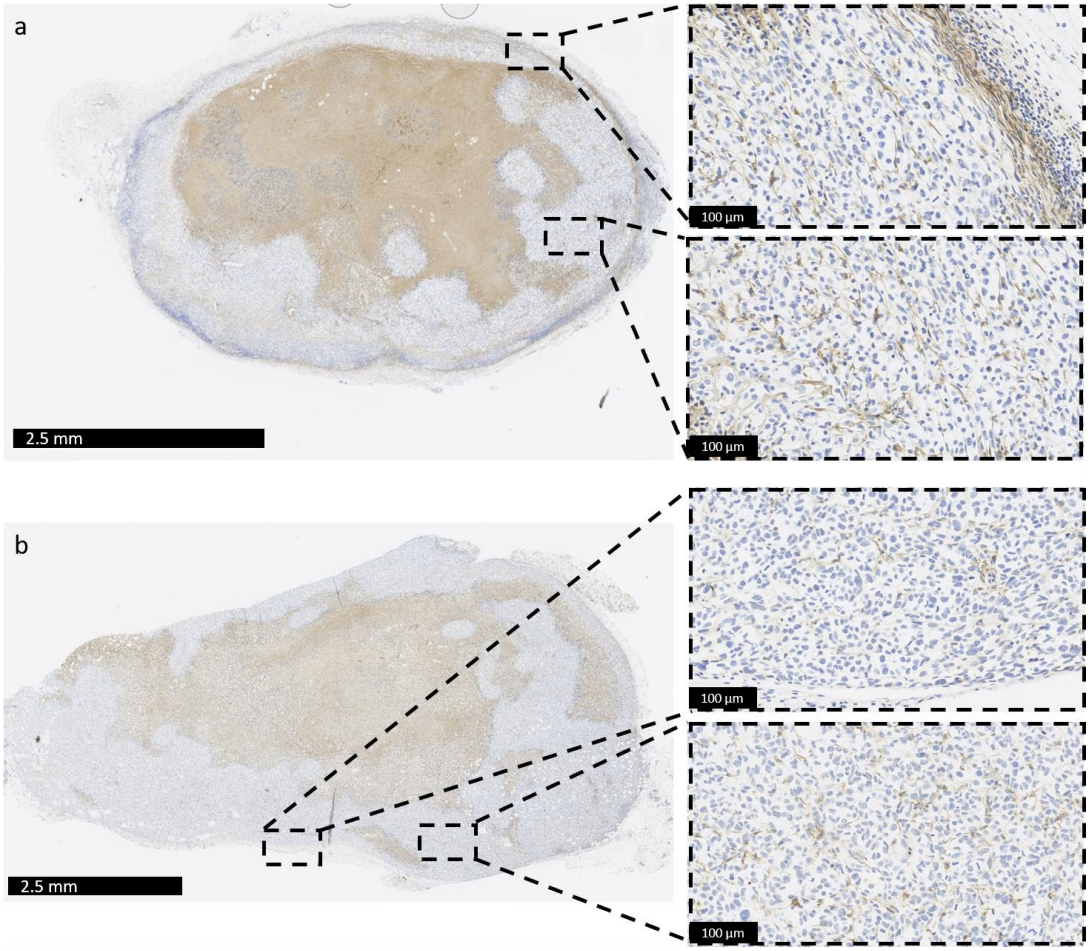

Figure 6.19. Macrophage distribution patterns within untreated xenograft tumours. (a) Macrophages are identified both at the periphery of the tumour and within the tumour tissue. **(b)** Macrophages are uniformly distributed within the tumour tissue.

6.3.9 Implanted biomaterials have no effect on fibroblast infiltration and collagen deposition within xenograft tumours

Using ER-TR7, an antigen expressed in the cytoplasm of fibroblasts, cellular expression levels were investigated to identify the number of murine fibroblasts within each xenograft tumour. Compared to untreated tumours at day 0, there was a significantly higher percentage of ER-TR7 positive staining cells in both untreated (p= 0.0073) and NT injury tumours (p= 0.0445) at day 7. However, no significant differences in the percentage of ER-TR7 positive staining cells were identified between any of the biomaterial implanted, Cu implanted tumours and control tumours at 7 days post-implantation (Figure 6.20) or up to 14 days with Parylene-C implantation (Figure 6.22). Untreated tumours at 7 days post-implantation had a statistically significant higher percentage area of collagen compared to untreated tumours at day 0 (p= 0.0086) (Figure 6.21). However, no significant differences in the percentage area of collagen were identified between any of the biomaterial implanted and control tumours at 7 days post-implantation. Cu implanted tumours, on the other hand, did have a statistically significant increase in collagen compared to untreated (p= 0.0217) and NT (p= 0.0314) control groups at day 7 post-implantation (Figure 6.21). Although a trend for an increase in the percentage area of collagen was noted over the 14-day period for Parylene-C implantation, this was not statistically significant (Figure 6.22).

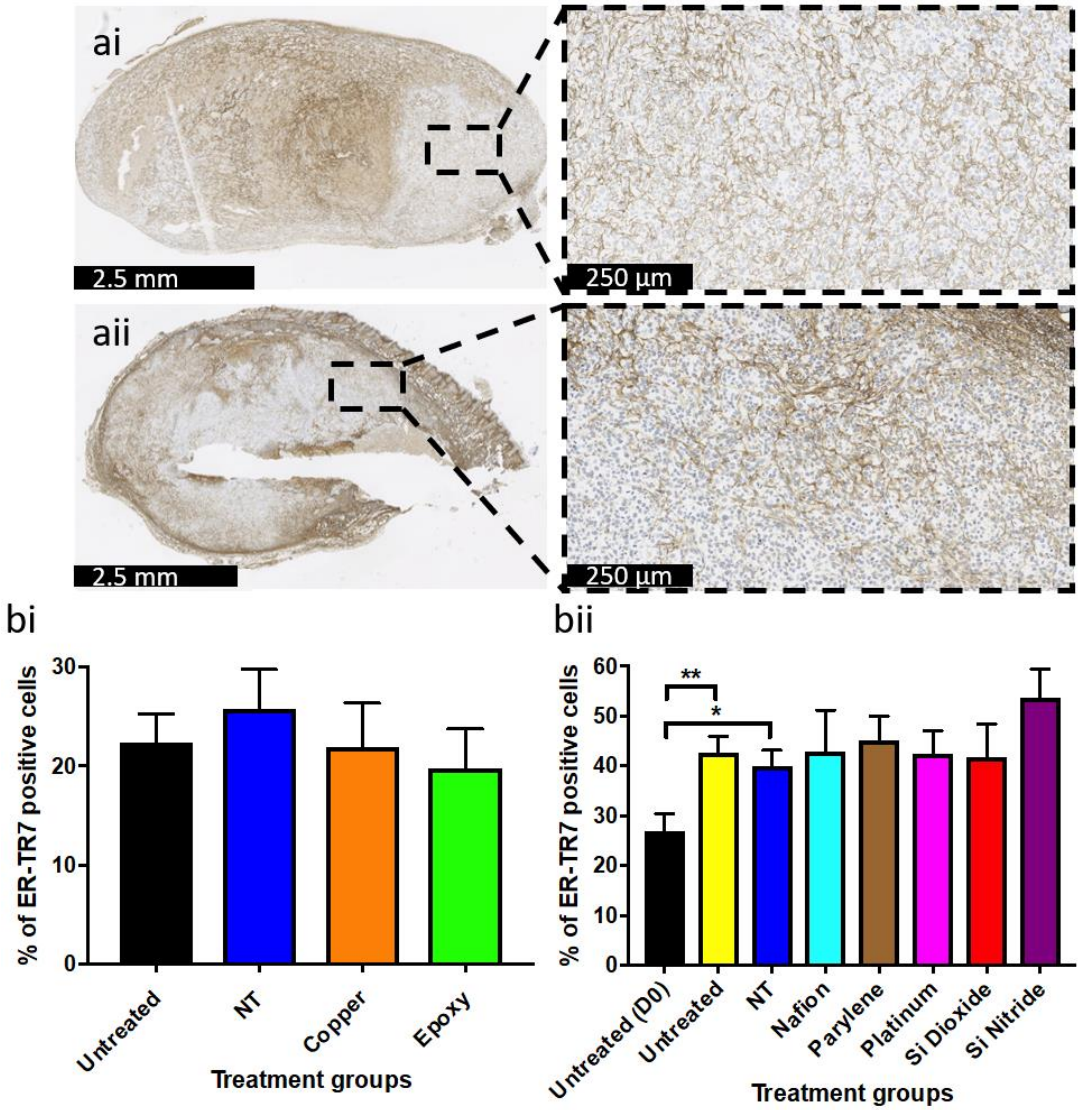

Figure 6.20. Biomaterials have no effect on fibroblast infiltration within xenograft tumour tissue up to 7 days post-implantation. (ai&aii) Representative ER-TR7 stained sections from tumours harvested at day 7. **(ai)** Untreated. **(aii)** Pt implanted. **(bi&bii)** Percentage of ER-TR7 positive staining cells for untreated and NT injury tumours, along with Cu, OG116-31 resin, Parylene-C, Nafion, Pt, Si_3N_4 and SiO_2 implanted tumours (one-way ANOVA with Holm-Šídák multiple comparisons test; data expressed as mean ± SEM, $^{**}p \leq 0.01$; $^{*}p \leq 0.05$).

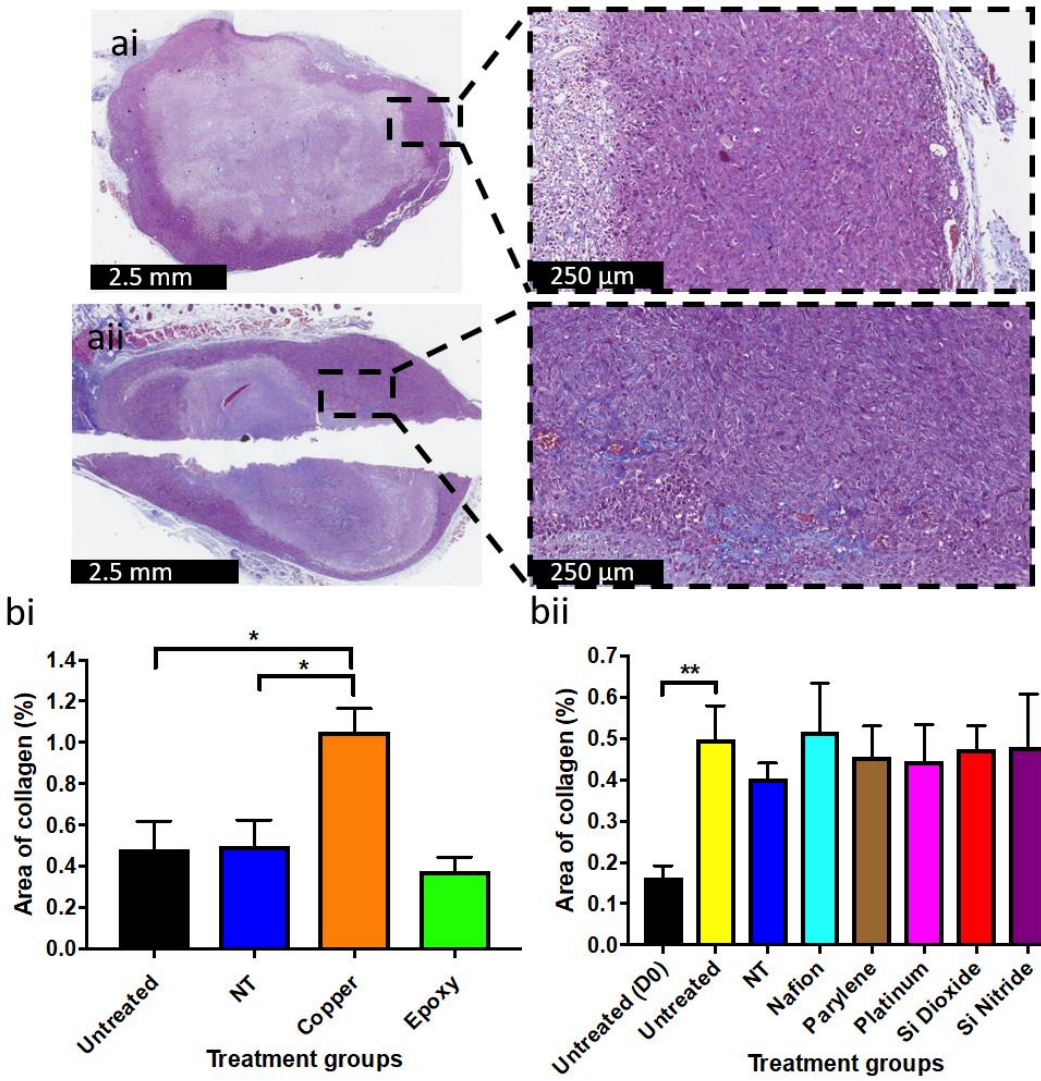

Figure 6.21. Biomaterials have no effect on collagen deposition within xenograft tumour tissue up to 7 days post-implantation. (ai&aii) Representative Masson's trichrome stained sections from tumours harvested at day 7. **(ai)** Untreated. **(aii)** SiO_2 implanted. **(bi&bii)** Percentage area of collagen for untreated and NT injury tumours, along with Cu, OG116-31 resin, Parylene-C, Nafion, Pt, Si_3N_4 and SiO_2 implanted tumours (one-way ANOVA with Holm-Šídák multiple comparisons test; data expressed as mean ± SEM, $^{**}p \leq 0.01$; $^{*}p \leq 0.05$).

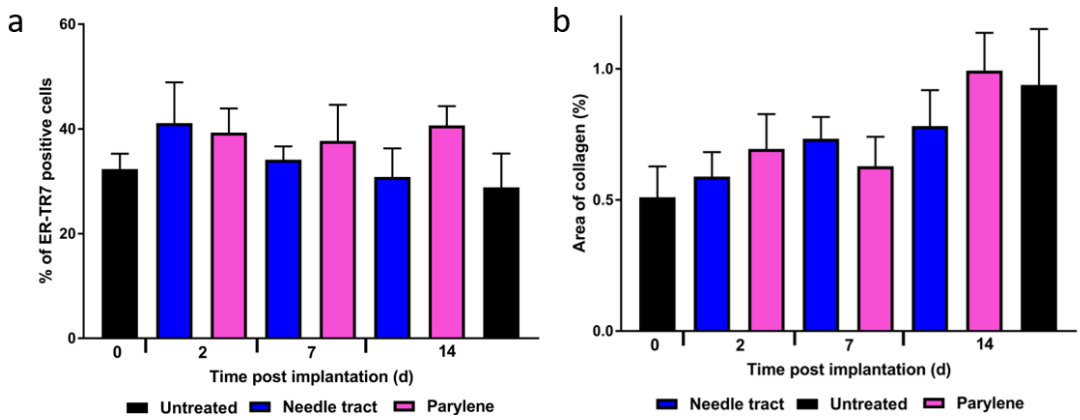

Figure 6.22. Parylene-C has no effect on fibroblast infiltration and collagen deposition within tumour tissue up to 14 days post-implantation. (a) Percentage of ER-TR7 positive staining cells for untreated and NT injury tumours, along with Parylene-C implanted tumours. **(b)** Percentage area of collagen for untreated and NT injury tumours, along with Parylene-C implanted tumours.

6.4 Discussion

Implantable medical devices are becoming increasing used in pre-clinical research for a variety of disease conditions (Table 6.1) including cancer[151]. With the first implantable device for monitoring radiation dose delivery now used in the clinics[157], it is likely more and more devices will become available as their roles in precision medicine become more defined. However, for an implantable device to attain regulatory approval, component materials or, ideally, the complete working device must undergo pre-clinical *in vitro* and *in vivo* biocompatibility testing. Well documented and commonly used biocompatibility models typically implant devices into healthy, non-diseased tissue; to date only limited published information is available regarding biofouling and the FBR that occurs within tumour tissue. Only one historical paper, published in 1962, has investigated the FBR induced following the implantation of cotton into murine tumours. Results showed that following implantation, the FBR seen within the tumours was minimal compared to that of normal tissues, indicating that the induced FBR may be decreased within a TME[601].

This chapter describes the investigation of the effects of selected modern biomaterials within a solid tumour and provides important biocompatibility data. Using human breast cancer xenograft tumours, biocompatibility was assessed up to 14 days following implantation through the development of a novel percutaneous implantation technique and IHC processing and sectioning protocols. The implantation procedure was highly reproducible and minimally invasive.

Approximately 95% of implants were successfully placed within the centre of xenograft tumours with no mice showing signs of inflammation or discomfort around the implantation/NT injury site.

For validation of the results obtained from biomaterial implanted tumours positive control implants were required, Cu wires were used in the experiments for this purpose. Although not previously reported within a TME, Cu has been shown to be cytotoxic[552,553,595], these toxic effects are mediated through a variety of different mechanisms[602,603]. Cu and Cu ions can be involved in the generation of ROS[604], leading to DNA strand breaks, base oxidation and ultimately cell death[605]. Apoptosis induced by Cu^{2+} has also been shown to be mediated through the induction of Bax, NF-ƙB inactivation and ROS formation[606]. In accordance with these results, Cu implanted xenograft tumours in our study had increased percentages of caspase 3 positive staining cells and larger areas of tumour necrosis. Although the mechanisms by which Cu-induced apoptosis were not investigated, the increased levels of caspase 3 expression within Cu implanted tumours agrees with these previously published findings. *In vivo* models have also shown that Cu can generate more severe inflammatory responses and fibrosis compared to non-Cu containing materials[201,607]. Our results demonstrated that, although the absolute percentage of fibroblasts remained the same in Cu implanted tumours, the percentage area of collagen was higher compared to control tumours; increasing to 1.05% in Cu implanted tumours compared with 0.49% in NT injury tumours and 0.48% in untreated tumours. These changes identified in the Cu implanted tumours (apoptosis, necrosis and fibrosis), reflecting the known cytotoxic effects of Cu, provided confidence in the implantation procedure and the method used for quantitative analysis and validated our results seen in the biomaterial implanted xenograft tumours[551].

Potential systemic effects caused by the implanted biomaterials was investigated by monitoring changes in body weight and condition score. No systemic toxicities were identified in mice that underwent biomaterial or Cu implantation, as indicated by maintenance of their body weight and condition score. Localised tumoural effects were investigated by calculating relative mean tumour volumes throughout the experimental period, results showed that all implanted tumours increased in size over 7 or 14 days in accordance with the controls. This result was

further assessed through histopathology by evaluating MDA-MB-231 cancer cell proliferation, apoptosis, necrosis and hypoxia within the xenograft tumours.

Assessment of proliferation and apoptosis was performed through Ki67 and caspase 3 staining respectively. Only Parylene-C implanted tumours had a statistically greater percentage of Ki67 positive cells compared to NT injury tumours at 2 days post-implantation. No further differences in cellular proliferation or apoptosis were observed between the other biomaterials at any of the remaining time points. CA9 is a protein whose expression is induced in hypoxic conditions[117]; expression levels were investigated, as the IMPACT sensor is ultimately designed to monitor intra-tumoural O_2 concentrations. No significant differences in the percentage of CA9 positive staining cells were observed between any of the implanted and control tumours, indicating that the biomaterials did not affect intra-tumoral O_2 levels. MDA-MB-231 xenograft tumours are heterogeneous, containing areas that are normoxic, hypoxic and necrotic[608]. The necrosis that develops can be a result of the tumour outgrowing its blood supply, increased levels of cell death and failure of clearance of these dead cells. Although necrotic areas were identified around the implanted biomaterials, the percentage area of necrosis was not significantly different from that of the control tumours. This suggests that the biomaterials did not increase the levels of necrosis from that seen within untreated xenograft tumours. Together, assessment of these 4 cellular parameters (Ki67, caspase 3, CA9 and necrosis) indicate that the implanted biomaterials did not affect the viability of the MDA-MB-231 cancer cells within the xenograft tumours[551].

Acute inflammation begins immediately after a material has been implanted within the body and can continue for 5 days[168]. The initial trauma caused by the insertion device will largely determine the severity of the acute inflammatory response, whereas the size of the implanted device will have a more significant effect on chronic inflammation and fibrosis[169]. During acute inflammation, polymorphonuclear leukocytes predominate, these cells are typically found in tissues at the implant site immediately following and up to 2 days post-implantation[167]. This component of the acute inflammatory response was investigated through the measurement of murine neutrophil numbers in the xenograft tumours using a primary antibody targeting the Ly6G antigen, a glycosylphosphatidylinositol-anchored

protein (also known as the myeloid differentiation antigen Gr1). Although transiently expressed in eosinophils and bone marrow monocytes[609], Ly6G is predominantly expressed on neutrophils and is a common marker used for murine neutrophil identification[610]. Our study showed that the percentage of Ly6G positive stained cells was considerably lower than that seen using the F4/80 antibody (murine macrophage marker), indicating that cross reactivity between these cell types was unlikely to have occurred. Minimal numbers of neutrophils were identified in both the implanted and control xenograft tumours at day 0 and day 7 post-implantation. Even in the Parylene-C serial sacrifice study at 2 days post-implantation minimal numbers were identified. These results suggest that the acute inflammatory response resolved normally in the presence of the biomaterials.

Chronic inflammation develops following the resolution of acute inflammation because the causative agent (the biomaterial) remains within the tissues at the implantation site. Monocytes, macrophages and fibroblasts are the major cell types present in the first 3 weeks of chronic inflammation, leading to neovascularisation with granulation and fibrous tissue production[167,195]. Macrophages take the lead role in orchestrating events involved with the ongoing immune responses through the formation of FBGCs[185] and production of profibrogenic factors that lead to enhanced fibrogenesis by fibroblasts[200]. The potential of the implanted biomaterials for influencing these chronic immune responses was investigated through the measurement of murine macrophage and fibroblast numbers in the xenograft tumours using primary antibodies targeting the F4/80 and ER-TR7 antigens respectively, while also assessing the area of collagen deposition with Masson's trichrome staining. No significant differences in the percentage of F4/80 positive staining cells were identified between any of the implanted and control tumours up to 7 days post-implantation or up to 14 days with Parylene-C implantation. Both tissue-resident macrophages and tumour-associated macrophages (TAMs) can be present within a tumour. Identification of the separate types can be advantageous, as TAMs have been shown to promote cancer cell invasion, migration, metastasis and angiogenesis; however, differentiating the 2 types of macrophages can be challenging[611]. In our study, macrophage identification was performed using an antibody reactive to murine F4/80, a protein that has been widely used as a pan-

macrophage marker[612,613]; as a result of this, we did not distinguish between the different macrophage types. However, as the percentage of positive staining cells between implanted and control tumours was similar, our results indicated that the biomaterials did not lead to the recruitment of additional macrophages. An association between the percentage number of ER-TR7 positive staining cells and the percentage area of collagen was identified with a statistically significant increase in both parameters occurring between day 0 untreated and day 7 untreated/NT injury tumours, this result was likely due to ongoing tumour growth. Importantly no differences were identified in ER-TR7 positive staining cells and the percentage area of collagen between implanted and control tumours.

When considering the FBR generated by an implanted material, it has been suggested that the physical structure of the material, including its modulus (resistance to elastic (recoverable) deformation), mechanics and stiffness may influence the extent of the inflammatory reactions, with materials of lower moduli producing less fibrosis than more rigid materials[614]. Tissue damage may also be increased in the presence of stiffer materials[615], therefore the use of softer materials with properties more similar to the tissue in which it is implanted may reduce interfacial strain and improve biocompatibility[616]. However, as no significant differences were seen in the FBR between the softest (Nafion, Youngs modulus 600 MPa) and hardest (Pt, Youngs modulus 168 GPa) biomaterials in our study, the results indicate that a material's modulus is not be a major contributing factor to the FBR in this tumour model[551].

Following implantation, a layer of host proteins immediately acquires on the materials surface. The specific types and amounts of these adsorbed proteins is determined by the materials surface charge and hydrophilicity[617]. Adsorbed proteins such as such as albumin, vitronectin, fibronectin, fibrinogen, complement and γ globulin are known influencers of the FBR as they can dictate the adhesion and survival of monocytes, macrophages and FBGCs on the materials surface[167,618,619]. These proteins can also desorb rapidly from the materials surface causing time-dependent fluctuations in protein levels[620]. Various methods could have been used to investigate differences in adsorbed proteins between the materials tested in our study. One method would have been to use the cage implant system whereby exudates

could be examined for these specific proteins. The advantage of using this method would have meant multiple samples could have been obtained without the need for animal sacrifice. Serial samples from the same animal would also mean that levels of specific proteins across time would be directly comparable to each other. A second method would have been to use the serial sacrifice IHC method we developed but harvest mice immediately following implantation and at a greater number of time points within the first 48 h post-implantation. These tumours could then be specifically stained for a range of these adsorbed proteins. These experiments would allow characterisation of the adsorbed proteins for each implanted material which could provide information with regards to the subsequent immune and FBRs that occurred in the surrounding tissues.

Adherent macrophages and FBGC can lead to degradation of materials with subsequent device failure. An important clinical example of this was seen following the replacement of silicon rubber as the insulating material on pacemaker leads for mechanically superior polyether polyurethane (PEU) elastomers[167]. PEU was thought to be biocompatible but following its use in pacemaker leads increased rates of device failure were seen. Initial investigations suggested that environment stress cracking and metal ion oxidation were responsible for these failures with later studies demonstrating that adherent macrophages and FBGC were involved in the mechanisms underlying both these failure mechanisms[621-626]. To investigate the effects of adherent macrophages and FBGC in our model, scanning electron microscopy could have been used on recovered implanted materials. This technique has been previously used to study the progression of the FBR in terms of monocyte adhesion, monocyte-to-macrophage development, macrophage fusion and FBGC formation and so could have been applied to our model[167]. Scanning electron microscopy would also have provided visual information on the presence of any degradation occurring on the materials surface due to the ongoing FBR.

Numerous mouse models (including CD-1 nude mice, SCID and NOD SCID) have been developed specifically to investigate tumourigenesis and pathogenesis of human cancers through the production of xenograft tumours[218,219]. Due to the relative ease, speed and reproducibility of producing human xenograft tumours, CD-1 nude mice were used in our model. Although this model uses athymic nude mice, deficient

in thymus-derived T lymphocytes, they are far from being immunodeficient. T lymphocytes can be produced via thymus-independent pathways (although in diminished numbers), allowing for some T cell-dependent immunity[627]. CD-1 nude mice also demonstrate near-normal responses to T cell-independent antigens, have high, naturally occurring antibody titres that can react with cancer cells[628], have tumouricidal macrophages[629] and have high levels of natural killer (NK) cell activity[630]. As a result of these studies demonstrating the ability of CD-1 nude mice to generate both innate and adapted immune responses, T cell-deficient mice (BALB/c nude mice) have been used in the investigation of the FBR to implanted materials[194]. This study demonstrated that, although the BALB/c nude mice had lower total leukocyte concentrations in the region of the implanted material, FBGC number and morphology were comparable to the control BALB/c mice. This suggests that pathways independent of thymus-matured T lymphocytes can still induce a normal FBR. Using non-immunosuppressed mice models, such as carcinogen-induced or spontaneously occurring tumours, would allow for the generation of tumours in the presence of an intact immune system. However, a significant disadvantage of these models would be the loss of using xenografted human cancer cells; this would mean the FBR induced by the implanted biomaterial would be assessed within murine rather than human cancer cells.

Functional differences between murine and human immune systems need to be considered when evaluating the data presented in this murine study if the results are to be considered comparable to what would be expected to occur in human tissue[551]. Immune system differences in a range of species, including human and CD-1 mice, have been previously investigated which identified significant species differences in circulating leukocyte populations[631]. This study demonstrated that the circulating leukocyte profile in human blood is neutrophilic, composed of approximately 50–70% neutrophils (3500–7000 cells/μl) and 20–40% lymphocytes (1400–4000 cells/μl) in comparison to CD-1 mice which is lymphocytic, composed of approximately 50–70% lymphocytes (1000–7000 cells/μl) and 15–20% neutrophils (300–2000 cells/μl). Neutrophil function and activity can also vary between humans and mice, with differences in mechanisms of leukocyte recruitment and composition of neutrophil granules[632]. As neutrophils are required in the initial

acute inflammatory phase[167] and lymphocytes are transiently present in the chronic phase of the FBR[193], these species differences in circulating leukocyte number and function could potentially result in altered FBR initiation and progression.

The pathological equivalence between human xenografts in nude mice and naturally occurring human tumours needs to be considered, as changes in tumour characteristics such as proliferation rates, histological classification and cell type distribution patterns within the tumour can occur post-transplantation[218,219]. In humans, TAMs are typically distributed uniformly throughout the tumour[633]; while this distribution pattern was identified in approximately 50% of xenograft tumours in our study, the remainder were characterised by macrophages localising towards the periphery of the xenograft tumour. This type of macrophage distribution has been documented previously and may be due to macrophage-associated fibrous capsule formation around the tumour[633]. Whether the distribution of immune cells within human xenograft tumours could influence the FBR is unknown; however, as similar numbers of implanted and control xenograft tumours were observed to present both macrophage distribution types, the effect is likely to be minimal[551].

When developing the percutaneous biomaterial implantation and NT injury techniques, the risks of introducing endogenous cutaneous bacteria or endotoxins into the tumour were considered, as these factors alone could induce an immune reaction within the tumour. The potential for these issues occurring was reduced by the use of aseptic skin preparation and wire sterilisation, along with minimal anaesthesia and surgery time[634]. As all mice remained healthy throughout the experiments, with no visible signs of inflammation occurring at the implant sites, combined with similar levels of inflammation occurring in both implanted and control tumours our results suggest that these potential confounding factors were not an issue. One previous murine study has used a similar percutaneous method to evaluate the FBR to a subcutaneously implanted nylon mesh[613]. This study used a 16G needle as the implantation device and for the creation of a NT injury in control tumours. The advantage of our model over this study is that smaller gauge biomaterial wires and needles were used for implantation and in the creation of NT injuries; this is an important consideration in any model for investigating the FBR, as

the extent of the acute inflammatory response is related to the initial trauma caused by the insertion device[169].

The potential for each biomaterial to induce a FBR was evaluated up to 7 days post-implantation. This length of time is long enough to evaluate the acute inflammatory response and the initial phases of chronic inflammation. Full evaluation of chronic inflammation would require biomaterials to be implanted for a minimum of 3 weeks. This increased experimental time frame is difficult to achieve using murine xenograft models, as continuous tumour growth typically leads to skin ulceration causing localised inflammation and ethical concerns. However, we were able to evaluate Parylene-C up to 14 days post-implantation, providing evidence that the model can be extended for longer periods. Parylene-C was chosen for this extended evaluation as functional sensors were initially designed to be covered with a layer of this material (except for the active sensing area); Parylene-C would therefore be in direct contact with surrounding tumour tissue (subsequent modifications to sensor design finally resulted in the device been encased in biocompatible epoxy resin). Unfortunately, time and resources were not available to evaluate all biomaterials up to 14 days post-implantation. Further investigation of the FBR and biomaterial biocompatibility within a solid tumour, could involve using functional sensors implanted into naturally occurring solid tumours in immunocompetent large animal models. This would enable longer implantation periods to be achieved whilst overcoming the perceived disadvantages of using immunocompromised mice models. These experiments would provide further confidence in the intra-tumoural biocompatibility of these biomaterials.

6.5 Conclusion

This chapter has described the development of a novel *in vivo* murine xenograft biocompatibility model whereby biomaterials can be safely, reliably and quickly implanted into xenograft tumours. IHC protocols were also developed that allowed biomaterial implanted tumours to be sectioned in a way as to identify the implant site. These experiments document, for the first time in the literature, the biocompatibility assessment of SiO_2, Si_3N_4, Parylene-C, Nafion, OG116-31 resin and Pt within a human xenograft tumour. The results demonstrated that these biomaterials had no significant effects on tumour viability and did not trigger a

significant FBR. These results have provided evidence for the use of these biomaterials in the construction of medical devices for implantation within solid tumours and have justified the progression of experiments to use working IMPACT sensors in *in vivo* models to investigate sensor functionality and begin to evaluate their use for clinical applications.

7 Validation of Functionality of the IMPACT Oxygen Sensor to Measure Tissue Oxygen Tension for Clinical Applications

This results chapter is an expanded version of a published research article: Gray M, Marland JRK, Dunare C, Blair EO, Meehan J, Tsiamis A, Kunkler IH, Murray A, Argyle A, Dyson A, Singer M, Potter MA. *In Vivo* Validation of a Miniaturised Electrochemical Oxygen Sensor for Measuring Intestinal Oxygen Tension. American Journal of Physiology - Gastrointestinal and Liver Physiology 2019; 317: 242-252. This article is open access with the authors retaining copyright to their work with permission to use published figures in this thesis. Sections of text and figures used from this article have been referenced accordingly.

7.1 Abstract

Background: An anastomotic leak is a life-threatening complication that can occur following an intestinal resection and anastomosis. Although its aetiology is complex, a leak can occur through tissue hypoxia from compromised anastomotic blood flow. This can impair intestinal healing, resulting in anastomotic dehiscence. Post-operative monitoring of anastomotic oxygenation would provide a means by which intestinal hypoperfusion could be detected allowing the provision of treatments to improve intestinal perfusion and possibly prevent anastomotic breakdown. **Methods:** A novel murine intestinal ischaemic and hypoxic model was developed for validation of the ability of the IMPACT O_2 sensor to provide real-time measurements of intestinal oxygenation. The sensor was placed onto the serosal surface of the small intestine of anaesthetised (non-recovery) rats that underwent ischaemic, hypoxaemic and haemorrhagic insults. **Results:** Sensor readings identified decreased intestinal O_2 tension following occlusion of the superior mesenteric artery and reduction in inspired O_2 concentrations. Sensor readings increased back to baseline levels after reinstating blood flow or increasing inspired O_2 concentrations. **Conclusion:** These results demonstrate *in vivo* validation of the ability of the IMPACT O_2 sensor to detect dynamic changes in intestinal O_2 tension through ischaemia and hypoxaemia and provide evidence for their use as O_2 tension monitoring devices. Sensors placed and left *in situ* at an anastomotic site during surgery would provide a means of

monitoring post-operative intestinal perfusion. This approach, combined with current post-operative monitoring techniques, could allow for early detection of peri-anastomotic tissue hypoxia and enable goal-directed treatments to be provided to restore intestinal oxygenation and prevent anastomotic dehiscence.

7.2 Introduction

Following biocompatibility assessment of sensor materials, *in vivo* functional validation of working IMPACT O_2 sensors was undertaken to assess their suitability for clinical applications. To achieve this, we developed an *in vivo* murine model to investigate the sensor's potential for measuring intestinal and muscular tissue O_2 tension (ptO_2). If successful, these sensors could be developed for use in clinical situations where monitoring tissue perfusion would improve patient outcome. One situation where assessment of tissue perfusion would be advantageous is in the peri-operative management of patients undergoing intestinal surgery.

Intestinal resection and anastomosis is an abdominal procedure used in the treatment of various diseases including diverticulosis, ulcerative colitis, Crohn's disease and cancer. Surgery involves removal (resection) of the diseased segment of intestine followed by re-joining (anastomosis) of the healthy, disease-free intestinal ends, thus restoring intestinal mural and luminal integrity[635]. Surgery can be performed via an open or laparoscopic approach using hand placed sutures or with a stapling device. The procedure is commonly performed, with estimates from the Association of Coloproctology of Great Britain and Ireland (ACPGBI) indicating that every year in the UK and Ireland approximately 20,000 large bowel anastomoses are performed. Regardless of the underlying disease, patient outcomes for those undergoing this procedure have improved through advances in peri-operative management, neoadjuvant and adjuvant radiotherapy and chemotherapy and through refinement of the procedure itself. However, no matter how safe the procedure is regarded to be, surgical complications can still occur.

An anastomotic leak (AL) is a life-threatening complication that occurs as a result of failure of the anastomosis to heal. Anastomotic dehiscence can result in significant increases in morbidity[636-638] and 30-day mortality rates[639] and can result in higher local colorectal cancer recurrence rates and decreased long-term survival for cancer patients[640-643]. Patients that develop an AL are also at an increased risk of

developing post-operative complications such as pneumonia, multi-organ failure, renal and cardiac complications, localised or generalised sepsis, enterocutaneous fistula, wound infections and dehiscence[637]. Revision surgery will be required in approximately 85–95% of patients who develop an AL, of which 50% will need permanent stoma formation[644]. The additional surgery and intensive care needed for the treatment of these patients will increase hospitalisation length[645] and overall treatment costs[646,647].

AL aetiology is complex, with both patient specific and surgical factors being involved (Table 7.1)[643,648]. An important factor involved in AL development is intestinal ptO_2, which is a measure of the partial pressure of O_2 within the interstitial space and is dependent on the balance between O_2 supply and utilisation. If local intestinal O_2 requirements cannot be met due to compromised tissue perfusion from anastomotic tension and disruption of the peri-anastomotic blood supply, then intestinal ischaemia and necrosis can develop[649-652].

Table 7.1. Risk factors associated with the development of an anastomotic leak.

Patient factors		Surgical factors	
Age, gender	Cardiovascular disease	Suboptimal anastomotic blood supply	Intra-operative sepsis
Malnutrition	Chronic obstructive	Concurrent surgical procedures	Peritonitis
Steroid use	pulmonary disease	Poor colonic preparation	Operative time >2 h
Diabetes	Alcohol use	Peri-operative blood transfusion	Pre-operative RT
Hypertension	American Society of	Anastomotic ischaemia or tension	Anastomotic location
Tobacco use	Anaesthesiologists score	Poor surgical technique	Bowel obstruction
Leukocytosis	Diverticulitis	Emergency resection	

Although AL rates can be as high as 24% for surgery performed in the distal rectum, combined rates for surgery performed at any level of the intestinal tract are approximately 6-7%[643,648]. Comprehensive peri-operative patient management is crucial, especially in the early post-operative period, as septic complications following an AL will cause the majority of patients to become clinically ill at 5-8 days post-surgery[653]. Factors that can decrease morbidity and improve patient outcome after abdominal surgery include the preservation of normovolaemia[654], normothermia[655], provision of supplemental O_2[656] and goal-directed fluid therapy[657,658]. These factors, acting largely through improvements in local tissue perfusion and ptO_2, are all applicable to the post-operative care of intestinal resection and anastomosis patients[659]. One major influencer of tissue perfusion is intravenous fluid therapy and although there is debate about the volume and type of peri-

operative fluids that should be administered, intravenous colloid therapy has been shown in a pig model to significantly increase colonic ptO_2 and perfusion in healthy and peri-anastomotic sites[660]. These peri-operative patient management strategies may help promote anastomotic healing and possibly decrease AL rates.

If anastomotic dehiscence does occur, then early diagnosis is critical in improving patient outcomes and decreasing mortality rates[653,661-663]. A delay of 2.5 days for definitive AL treatment can increase mortality rates from 24% to 39%[639] whereas every hour of delay from septic shock onset to the administration of antibiotics is associated with a 7.6% decrease in survival[664]. Research into anastomotic healing and dehiscence has been identified as a priority by the UK NHS National Institute for Health Research, Colorectal Therapies Healthcare Technology Co-operative and the ACPGBI. Unfortunately, no methods are currently available that allow monitoring of post-operative intestinal healing and there is no consensus as to the best approach to diagnose an AL.

AL has no pathognomonic signs and therefore diagnosis cannot be based solely on clinical symptoms. Symptoms range from pyrexia, ileus and cardiorespiratory abnormalities to acute sepsis with multi-organ failure or even faeces draining from the surgical wound. Although blood tests for AL diagnosis based on raised inflammatory markers such as C-reactive protein (CRP) levels may be helpful, these tests are non-specific and can point to a wide range of post-operative complications such as urinary, chest or surgical wound infections. Using a combination of clinically measurable parameters such as temperature, leukocyte count, CRP and creatinine levels as well as systemic inflammatory response syndrome components and urine output has been shown to decrease the delay from the first symptoms of AL to its treatment from 4 to 1.5 days[639]. Current practice for AL diagnosis remains imaging-based, predominantly through contrast-enhanced CT scans. Unfortunately, this technique has variable sensitivity and specificity[665], with false negative rates as high as 47%[666]. These false negative results are likely from CT scans being performed prior to a leak been radiologically visible. Reluctance to perform multiple scans due to cost, logistics and radiation exposure in combination with inherent delays incurred from the time of imaging to the interpretation of results can significantly hinder prompt AL diagnosis[667].

As a result of the deficiencies in the current methods used for AL diagnosis, there is a need for novel monitoring and diagnostic techniques to overcome this unmet clinical issue. A device capable of detecting post-operative peri-anastomotic hypoperfusion could allow early remedial intervention to be instigated to improve tissue perfusion and potentially reduce the risk of an AL from developing. Devices which allow an AL to be diagnosed quicker than current tests allow could also enable repeat surgery to be performed before local sepsis makes surgical revision impossible. The use of an implantable sensor to provide real-time information on spatial and temporal changes in intestinal ptO_2 would be a novel approach to meet these diagnostic needs. Although the principle aim of the IMPACT O_2 sensor is to monitor tissue O_2 levels within a solid tumour, the technology is suitable to multiple applications in which monitoring visceral surface ptO_2 is clinically important and would appear well suited to monitoring peri-anastomotic ptO_2.

This chapter describes the development and use of a murine intestinal ischaemic and hypoxic model for functional validation of the IMPACT O_2 sensor. Following sensor placement onto the serosal surface of a segment of small intestine, we investigated the sensor's ability to detect changes in intestinal ptO_2 following occlusion of the superior mesenteric artery (SMA), manipulation of the inspired fractional oxygen concentration (FiO_2), creation of acute haemorrhage and after euthanasia. This is, to the best of our knowledge, the first time that this developed murine model has been used for validation of a miniaturised Clark O_2 sensor to measure dynamic changes in intestinal ptO_2 which was further evaluated though measuring muscular ptO_2. These results provide robust evidence for further development of the IMPACT O_2 sensor towards clinical applications in man.

7.3 Results

7.3.1 Development of a model to measure intestinal tissue oxygen tension

To develop an *in vivo* model whereby sensor validation for measuring intestinal ptO_2 could be performed, 3 experimental groups were required. One acted as the control group designed to assess sensor longevity and drift, whereas 2 treatment groups were designed to assess the sensor's potential for detecting changes

in intestinal ptO_2 following local (SMA occlusion) or systemic (manipulation of blood O_2 levels and circulating blood volume) insults (Figure 7.1).

All rats underwent general anaesthesia, arterial and venous cannulation and tracheostomy tube placement as described in section 3.3.2. Following a routine ventral midline celiotomy, extending from the manubrium to the pubis, a tube cystotomy was performed. A stab incision was made at the apex of the bladder which was then cannulated with 1.57 mm external diameter polythene tubing (Portex Ltd, Hythe, UK) and sutured in place with a purse string suture. Urine was collected by placing the free end of the tubing into a 1.5 ml Eppendorf tube. To gain access to the abdominal vasculature and to allow sensor placement, the small intestine and caecum were exteriorised and placed to the left-hand side abdominal wall. To reduce evaporative fluid and convective heat loss these exteriorised organs were wrapped in cling film and kept moist via regular topical applications of saline. Using a proximal section of small intestine, the IMPACT O_2 sensor was placed on the antimesenteric serosal surface at the midpoint between small serosal blood vessels (Figure 7.2). Tissue adhesive (Vetbond, 3M, Bracknell, UK) was used to temporarily attach the lead wire to the intestine ensuring close contact between the sensor's central active sensing area and the serosal surface was achieved. Following instrumentation, a stabilisation period of at least 30 min was provided to allow stable baseline physiological variables to be achieved, after which rats were randomly divided into control or treatment groups. Continuous sensor recordings were made throughout each experiment, commencing after the initial stabilisation period and continuing for 15 min following confirmation of death post-euthanasia.

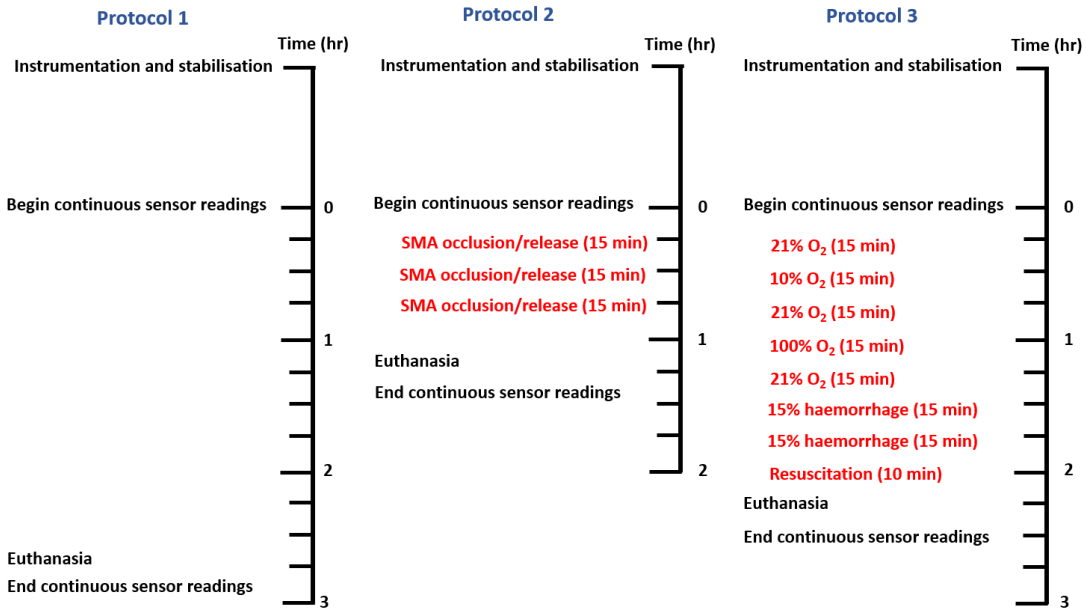

Figure 7.1. Outline of experimental protocols and interventions. Protocol 1: Control animals with no interventions. **Protocol 2:** SMA occlusion. **Protocol 3:** Alterations in FiO_2, haemorrhage and autotransfusion (resuscitation). Instrumentation includes anaesthesia induction, surgical preparation, arterial and venous cannulation, tracheostomy, celiotomy and tube cystotomy.

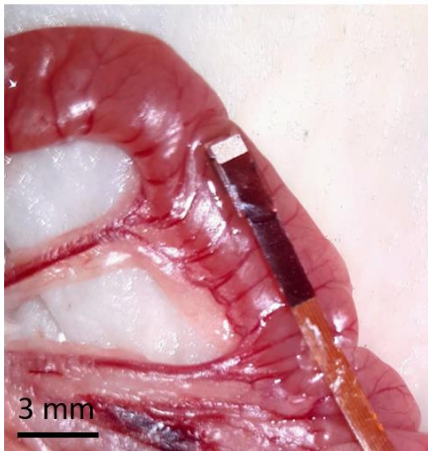

Figure 7.2. Intra-operative photograph depicting intestinal placement of the sensor. Placement of the sensor can be seen on the serosal surface of a section of small intestine.

7.3.2 Protocol 1: Control group

The control group consisted of instrumented rats that received no physiological challenges. Continuous sensor recordings were performed for 165 min. Arterial blood samples were obtained immediately prior to the commencement of sensor recordings, every hour thereafter and then just before euthanasia.

7.3.3 Protocol 2: Intestinal tissue responses to superior mesenteric arterial occlusion

The SMA was identified as a vessel originating from the left side of the aorta at the level of the right renal vein. The artery was isolated, close to the aortic origin, from its associated vein and surrounding soft tissues. A loose suture of 1 metric braided silk (Ethicon, UK) was placed round the artery to aid vessel manipulation and localisation. Following SMA isolation, the vessel was temporarily and reversibly occluded with the use of a haemostatic clamp (Fine Science Tools, Linton, UK). Each occlusion lasted for 5 min with a 10 min reperfusion period between occlusions. Vessel occlusion was confirmed through the development of intestinal pallor with the loss of mesenteric arterial pulsations; these changes were reversible following removal of the haemostatic clamp. The occlusion-reperfusion cycle was performed 3 times. Arterial blood samples were obtained immediately prior to the start of continuous sensor readings and just before euthanasia.

Figure 7.3. Intra-operative photographs depicting SMA isolation, occlusion and release. (a) SMA identification. **(b)** Haemostatic clamp placed across the SMA providing temporary mechanical occlusion. Intestinal pallor was immediately evident upon vessel occlusion. **(c)** Following removal of the haemostatic clamp and re-instigation of blood flow, a hyperaemic intestinal flush was evident.

7.3.4 Protocol 3: Intestinal tissue responses to alterations in inspired oxygen concentrations, progressive haemorrhage and autotransfusion

Alterations in FiO_2 (1.0, 0.21, 0.1) were performed at 15 min intervals with each different O_2 concentration delivered through a flowmeter via the isoflurane vaporiser. The cycle of FiO_2 alterations was: 0.21 for 15 min (baseline), 0.1 for 15 min (inducing hypoxaemia), 0.21 for 15 min, 1.0 for 15 min (inducing

hyperoxaemia) before finally returning to 0.21 for 15 min. Arterial blood samples were taken at the end of each FiO_2 change.

Following completion of FiO_2 alterations, progressive haemorrhage was achieved by removing 15% of the circulating blood volume (estimated as 70 ml/kg) over a period of 5 min. Following a 10 min stabilisation period a further 15% was removed. The exsanguinated blood was collected into a heparinised syringe and maintained at 37^{o}C. Ten min after completion of the second haemorrhage procedure autotransfusion was performed by administering the blood intravenously back to the rat over 10 min. Arterial blood samples were taken at the end of each haemorrhage procedure and just before euthanasia.

7.3.5 Current generated by the sensor remained stable in control rats

To assess the physiological stability of rats throughout the duration of anaesthesia that encompassed the longest experimental protocol, data from blood-gas, biochemical and haematological analysis was combined with variables such as heart rate (HR), respiratory rate (RR), core temperature (CT) and mean arterial blood pressure (MAP). All physiological parameters, blood-gas analysis and electrolytes remained stable throughout anaesthesia. Although blood glucose levels began to decrease towards the end of the procedure this was not statistically significant (p= 0.9304) and was consistent with the fasting state and metabolic demands of the rat during anaesthesia (Figure 7.4a).

To assess stability of sensor measurements over a time period that encompassed the longest experimental protocol, continuous sensor recordings were performed in rats which were not subjected to physiological interventions. Results showed that currents generated in the O_2 sensors were extremely stable over 165 min, with mean currents ranging from -1.14 ± 0.03 nA at 15 min to -1.44 ± 0.15 nA at 135 min. Although a trend towards increasing currents over time was observed, this was not statistically significant (p= 0.7244) (Figure 7.4b).

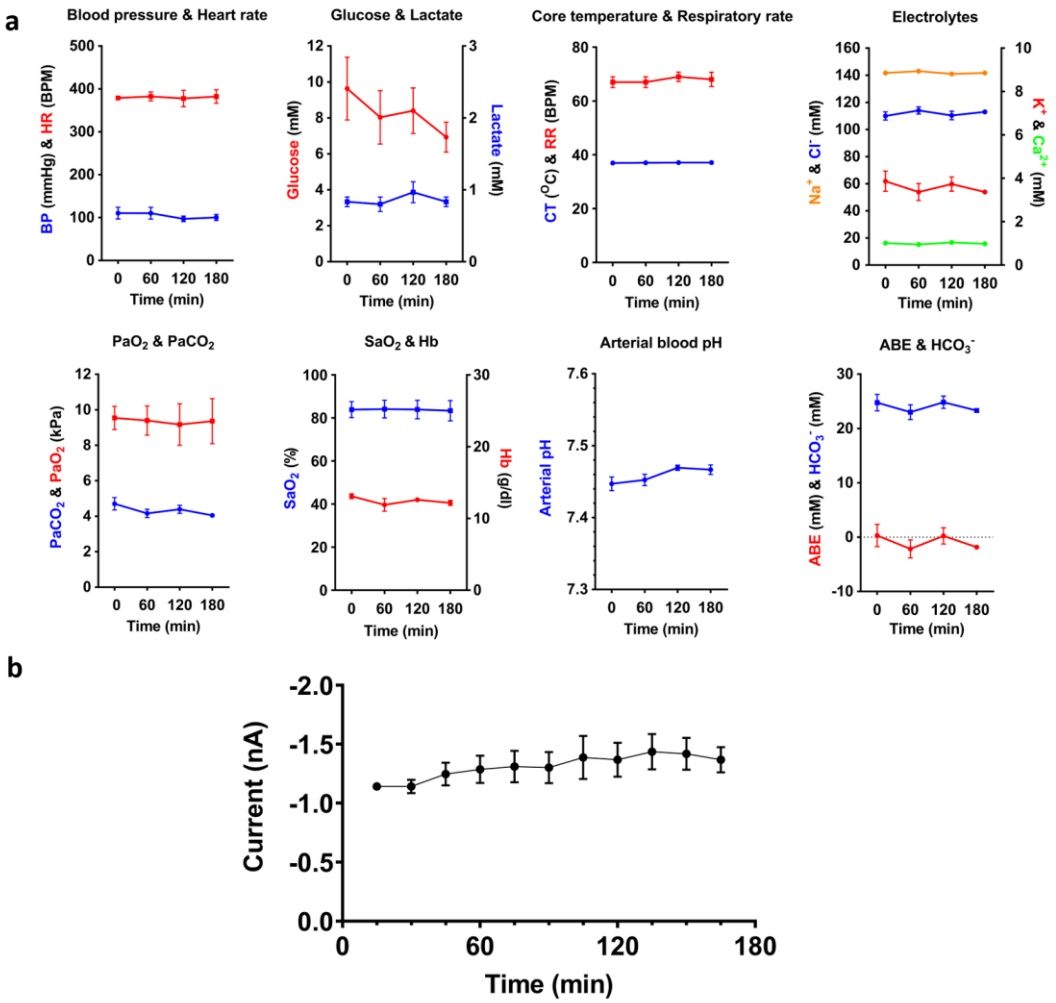

Figure 7.4. Sensor currents and physiological data remain stable in control rats. **(a)** Physiological data (Hb, haemoglobin; ABE, arterial base excess; SaO_2, haemoglobin O_2 saturation; PaO_2, arterial O_2 partial pressure; $PaCO_2$, arterial CO_2 partial pressure; CT, core temperature; RR, respiratory rate; HR, heart rate) (data expressed as mean ± SEM, n=3). **(b)** Current generated at the working electrode of the sensor during continuous sensor readings over a period of 165 min; results show mean current recordings from the final 5 min of each 15 min period (one-way ANOVA with Holm-Šídák multiple comparisons test; data expressed as mean ± SEM, n=3, p= 0.7244).

7.3.6 Current generated by the sensor rapidly decreased following occlusion of the superior mesenteric artery which was reversible upon reinstatement of blood flow

To assess the ability of the sensors to detect changes in intestinal ptO_2 through the generation of temporary and reversible intestinal ischaemia, we performed 3 cycles of SMA occlusion and release. Results showed an almost instantaneous decrease in sensor current after each occlusion, reducing from non-occluded recordings of -1.85 ± 0.05 nA to occluded recordings of -0.27 ± 0.08 nA

(mean current ± SEM) (Figure 7.5a). Changes between the pre- and post-occlusion current measurements for each of the cycles were statistically significant (p= 0.0082). Current reductions were maintained throughout the majority of each occlusion which quickly rose back to non-occluded current values following removal of the haemostatic clamp and re-instigation of blood flow (Figure 7.5b and Table 7.2). Following euthanasia, sensor recordings fell to the lowest recorded current measuring 0.04 ± 0.16 nA, which was statistically significant when compared to non-occluded currents (p= 0.0025).

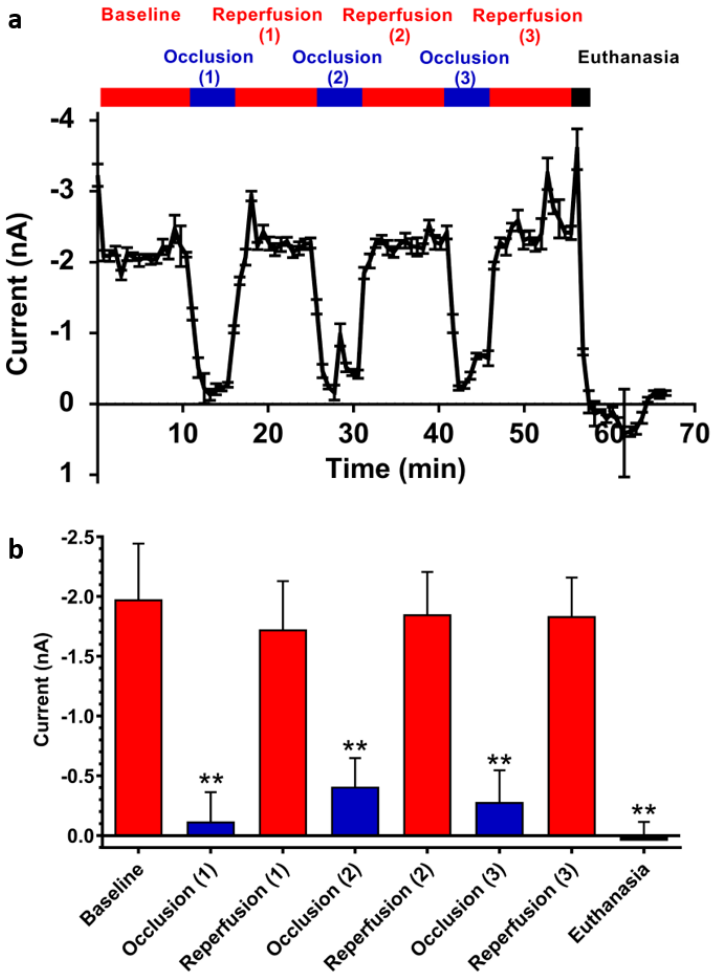

Figure 7.5. Sensor currents rapidly decrease following superior mesenteric artery occlusion. (a) Representative graph showing current generated at the working electrode of the sensor during continuous sensor recordings over a period of 70 min. Three cycles of 5 min occlusion followed by 10 min of reperfusion were performed in each animal before euthanasia. **(b)** Combined analysis comparing current generated at the working electrode of the sensor during periods of SMA occlusion and intestinal reperfusion; results show mean current recordings from the final 5 min of each occlusion and reperfusion period (one-way ANOVA with Holm-Šídák multiple comparisons test; data expressed as mean ± SEM, n=4, **$p \leq 0.01$).

Table 7.2. Current recordings during each SMA occlusion/reperfusion and euthanasia. (n=4; mean ± SEM).

	Baseline	Occlusion (1)	Reperfusion (1)	Occlusion (2)	Reperfusion (2)	Occlusion (3)	Reperfusion (3)	Euthanasia
Current (nA)	-1.98 ± 0.47	-0.12 ± 0.25	-1.73 ± 0.40	-0.41 ± 0.24	-1.85 ± 0.36	-0.28 ± 0.27	-1.84 ± 0.32	0.04 ± 0.16

7.3.7 Current generated by the sensor responded rapidly to alterations in inspired oxygen concentrations

To assess the ability of the sensors to detect changes in intestinal ptO_2 through changes in blood oxygenation we performed sequential alterations in FiO_2 ranging from 0.1-1.0 (Figure 7.6a). Baseline current recordings were first obtained using FiO_2 of 0.21. The mean sensor current during this baseline period was -1.35 ± 0.18 nA. Following a FiO_2 reduction to 0.1, sensor recordings decreased by more than 50%, to -0.60 ± 0.10 nA. This current reduction occurred over a period of 1-2 min, which was maintained throughout the hypoxaemic challenge and was statistically significant when compared to current recordings obtained during baseline measurements (p= 0.0396). Reversal of FiO_2 from 0.1 to 0.21 resulted in an increase in sensor current recordings back to baseline values. Upon increasing FiO_2 to 1.0 sensor currents rapidly increased to -6.53 ± 0.46 nA, which was statistically significant when compared to baseline currents (p< 0.0001). This increase in current was maintained throughout the hyperoxaemic challenge. A final reduction in FiO_2 back to 0.21 resulted in sensor currents returning to baseline levels. Following euthanasia, sensor recordings fell to the lowest recorded current measuring -0.08 ± 0.17 nA, which was statistically significant when compared to baseline currents (p= 0.0006) (Figure 7.6b and Table 7.3). At the end of each FiO_2 alteration arterial blood-gas analysis confirmed the expected physiological changes induced by each challenge. Haemoglobin O_2 saturation (SaO_2) and arterial O_2 partial pressure (PaO_2) both decreased at 0.1, increased at 1.0 (more prominent with PaO_2), and returned to baseline levels at 0.21. Expectedly, total haemoglobin (Hb) concentration remained the same throughout each challenge (Figure 7.6c & d).

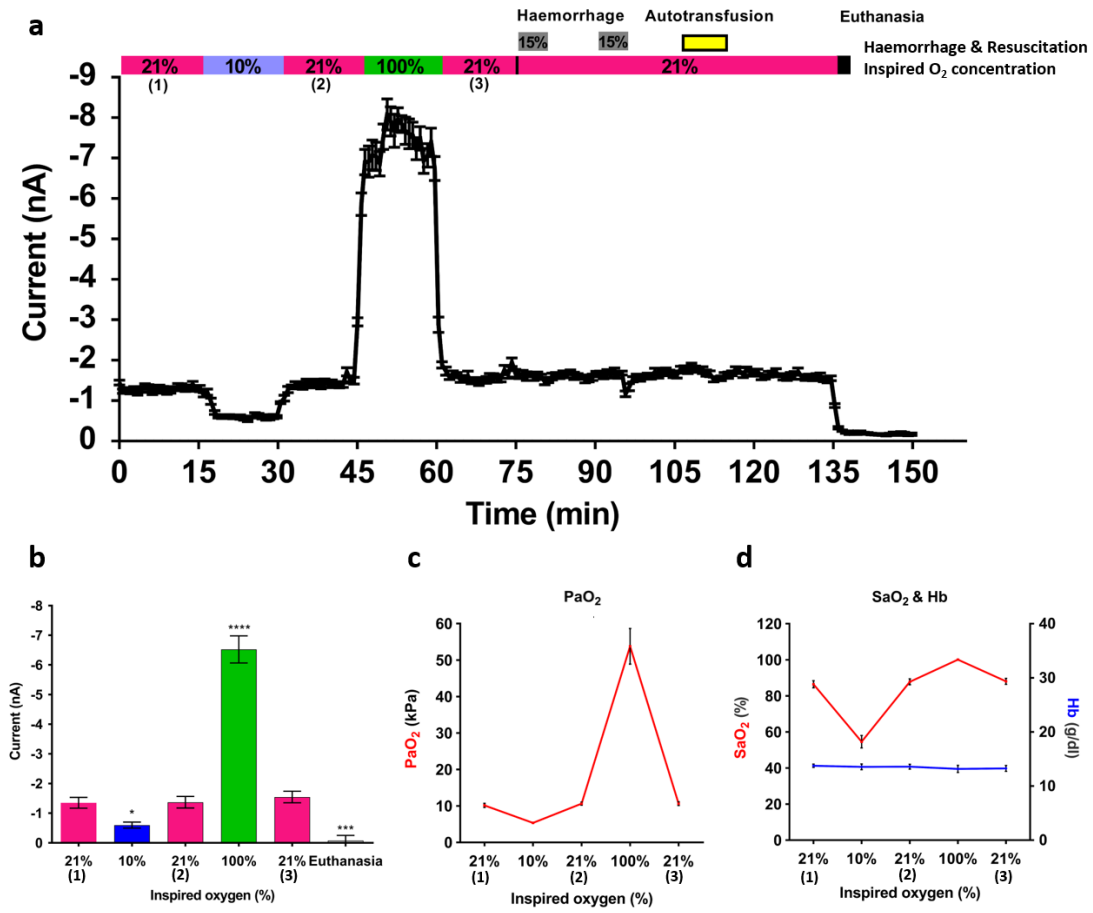

Figure 7.6. Sensor currents change in accordance with alterations in FiO_2. (**a)** Representative graph showing current generated at the working electrode of the sensor during continuous sensor recordings over a period of 150 min. Each FiO_2 challenge was performed in 15 min blocks before removal of 30% of the circulating blood volume. **(b)** Combined analysis comparing current generated at the working electrode of the sensor during each FiO_2 challenge; results show mean current recordings from the final 5 min of each 15 min period (one-way ANOVA with Holm-Šídák multiple comparisons test; data expressed as mean ± SEM, n=5, ****$p \leq 0.0001$; ***$p \leq 0.001$; *$p \leq 0.05$). **(c&d)** Arterial O_2 partial pressure, total haemoglobin and haemoglobin O_2 saturation measured at the end of each FiO_2 challenge.

Table 7.3. Current recordings during each FiO_2 challenge and euthanasia. (n=5; mean ± SEM).

FiO_2	21% (1)	10%	21% (2)	100%	21% (3)	Euthanasia
Current (nA)	-1.35 ± 0.18	-0.60 ± 0.10	-1.37 ± 0.12	-6.53 ± 0.46	-1.55 ± 0.20	-0.08 ± 0.17

7.3.8 Current generated by the sensor remained stable following haemorrhage

Following completion of FiO_2 challenges, the ability of the sensors to detect changes in intestinal ptO_2 through acute haemorrhage was assessed by performing

progressive removal of 30% of the circulating blood volume (performed in 2 x 15% removal periods) (Figure 7.7a). Physiological data and arterial blood-gas analysis obtained 10 min after the end of each haemorrhage procedure confirmed the expected physiological changes induced by acute haemorrhage. Hb concentration, HR and MAP all showed moderate decreases following 15% haemorrhage which became more pronounced after 30% haemorrhage. Baseline values compared to those following 30% haemorrhage showed that Hb concentration decreased from 13.3 ± 0.6 g/dl to 11.4 ± 0.4 g/dl, HR decreased from 405 ± 22 bpm to 348 ± 16 bpm and MAP decreased from 118 ± 12 mmHg to 56 ± 3 mmHg. All these parameters returned to baseline levels following autotransfusion (Figure 7.7b & c). SaO_2 levels remained constant throughout each haemorrhage procedure.

Although physiological responses to acute haemorrhage were induced, only small decreases in sensor current measurements were observed, which were not statistically significant compared with baseline recordings. Baseline measurements at FiO_2 of 0.21 were -1.55 ± 0.20 nA; however, following 15% and 30% haemorrhage currents only decreased to -1.39 ± 0.13 nA and -1.33 ± 0.13 nA respectively. Following autotransfusion, sensor currents failed to increase back to baseline levels, measuring -1.22 ± 0.14 nA at the end of the transfusion (Table 7.4).

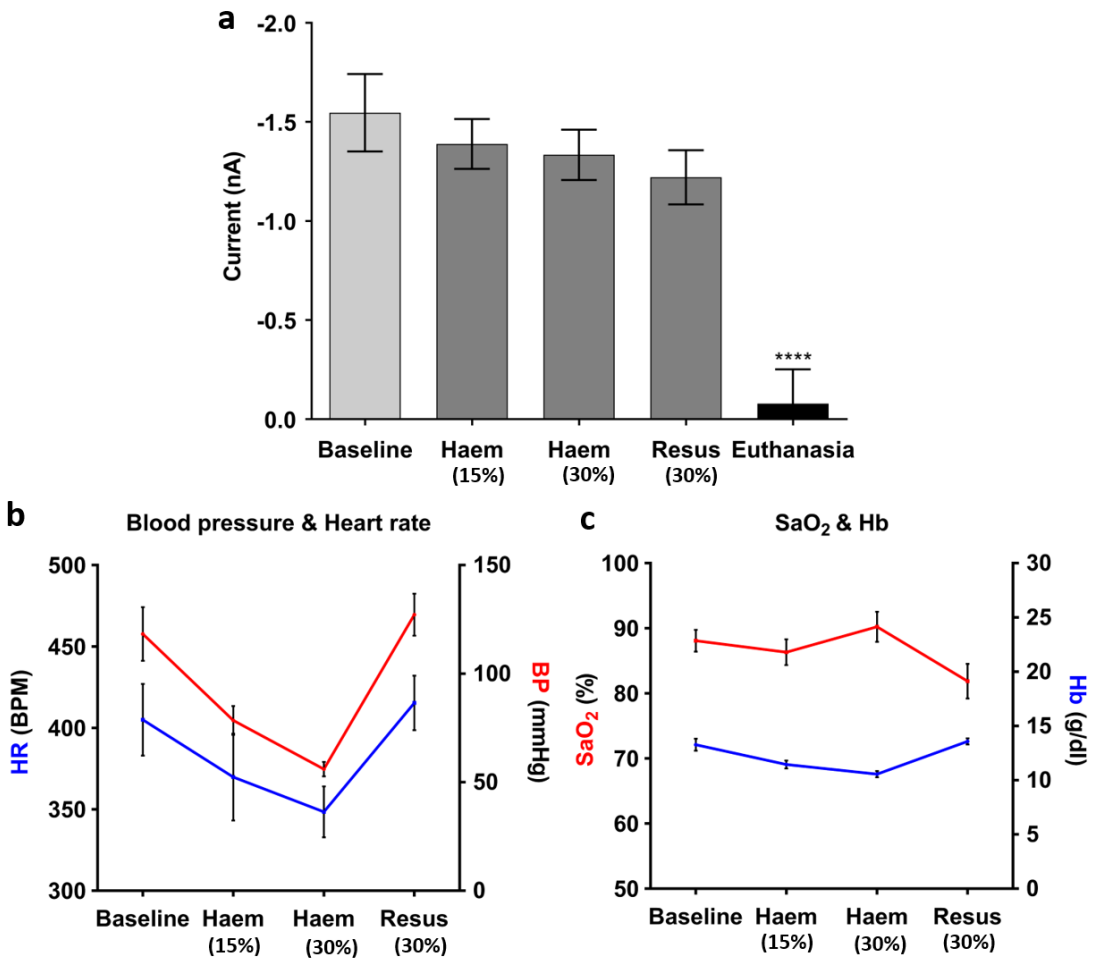

Figure 7.7. Sensor currents remain stable following progressive haemorrhage and autotransfusion. (a) Combined analysis comparing current generated at the working electrode of the sensor during the preceding 15 min baseline period at FiO_2 of 0.21 and 2 subsequent cycles of removal of 15% circulating blood volume followed by autotransfusion; results show mean current recordings from the final 5 min of each period (one-way ANOVA with Holm-Šídák multiple comparisons test; data expressed as mean ± SEM, n=5, ****$p \leq 0.0001$). **(b&c)** Mean arterial blood pressure, heart rate, total haemoglobin and haemoglobin O_2 saturation measured at the end of each of intervention period.

Table 7.4. Current recordings during each haemorrhage procedure and euthanasia. Baseline recordings were made at FiO_2 of 0.21 (n=5; mean ± SEM).

	Baseline	15% haemorrhage	30% haemorrhage	Autotransfusion
Current (nA)	-1.55 ± 0.20	-1.39 ± 0.13	-1.33 ± 0.13	-1.22 ± 0.14

7.3.9 Development of a model to measure muscular tissue oxygen tension

To develop an *in vivo* model whereby sensor validation for measuring muscular ptO_2 could be performed, 1 experimental group was required. The

treatment group was designed to assess the sensor's potential for detecting changes in muscular ptO_2 following systemic insults (manipulation of blood O_2 levels).

All rats underwent general anaesthesia, routine arterial and venous cannulation and tracheostomy tube placement as described in section 3.3.2. An incision was made through the skin and subcutaneous tissues of the lateral aspect of the thigh, mid-way between the patella and greater trochanter of the femur. The vastus lateralis was identified and fascia covering a small area of the muscle was removed. The IMPACT O_2 sensor was placed onto these muscular fibres and the lead wire temporarily attached to the surface of the biceps femoris using tissue adhesive (Figure 7.8), ensuring close contact between the sensor's central active sensing area and the muscular surface was achieved. To reduce evaporative fluid and convective heat loss exposed muscular tissues were covered in cling film and kept moist via regular topical applications of saline. Following instrumentation, a stabilisation period of at least 30 min was provided to allow stable baseline physiological variables to be achieved. Continuous sensor recordings were made throughout each experiment, commencing after the initial stabilisation period and continuing for 15 min following confirmation of death post-euthanasia.

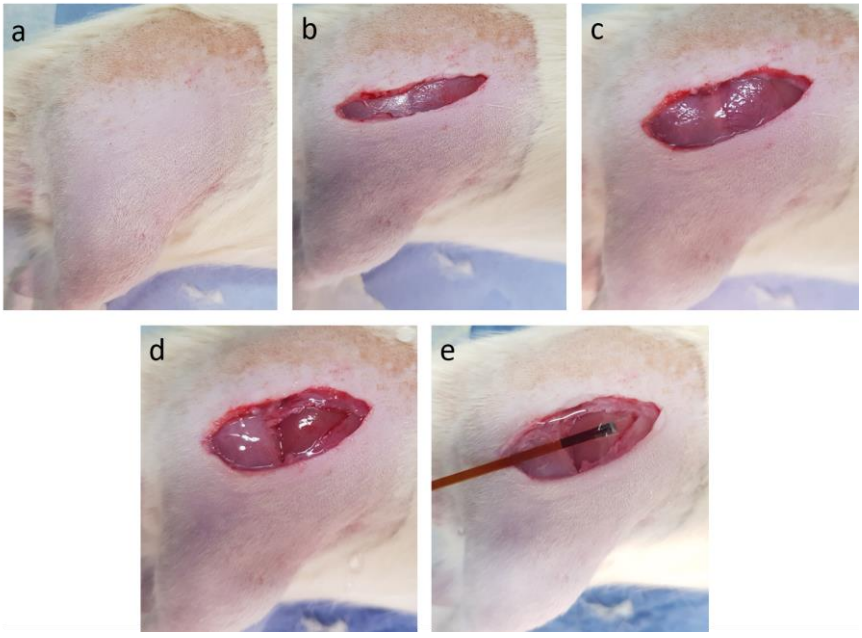

Figure 7.8. Intra-operative photographs depicting muscular placement of the IMPACT sensor. (a-c) A cranial-to-caudal skin incision was made mid-way between the patella and the grater trochanter of the femur. The vastus lateralis (cranial) and biceps femoris (caudal) muscles were identified. **(d)** Fascia was removed from the vastus lateralis exposing the underlying muscular fibres. **(e)** Placement of the sensor on the muscular surface of the vastus lateralis.

7.3.10 Muscular tissue responses to alterations in inspired oxygen concentrations

Alterations in FiO_2 (1.0, 0.21, 0.1) were performed at 15 min intervals with each different O_2 concentration delivered through a flowmeter via the isoflurane vaporiser. The cycle of FiO_2 alterations was: 0.21 for 15 min (baseline), 0.1 for 15 min (inducing hypoxaemia), 0.21 for 15 min, 1.0 for 15 min (inducing hyperoxaemia) before finally returning to 0.21 for 15 min. Arterial blood samples were taken at the end of each FiO_2 challenge.

7.3.11 Current generated by the sensor responded to alterations in inspired oxygen concentrations

To assess the ability of the sensors to detect changes in muscular ptO_2 through changes in blood oxygenation, we performed sequential alterations in FiO_2 ranging from 0.1-1.0 (Figure 7.9a). Baseline current recordings were first obtained using FiO_2 of 0.21. The mean sensor current during this baseline period was -1.46 ± 0.25 nA. Following a FiO_2 reduction to 0.1, sensor current recordings decreased to -1.06 ± 0.18 nA. This current reduction occurred over a period of 5 min but was not statistically significant when compared to current recordings obtained during baseline measurements (p= 0.934). Reversal of FiO_2 from 0.1 to 0.21 resulted in an increase in sensor current recordings back to baseline values, again occurring over a period of 5 min. Upon increasing FiO_2 to 1.0, sensor currents rapidly increased to -3.47 ± 0.71 nA, which was statistically significant when compared to current recordings obtained during baseline measurements (p= 0.0282) and at FiO_2 of 0.1 (p= 0.0075). This increase in current was maintained throughout the hyperoxaemic challenge. A final reduction in FiO_2 back to 0.21 resulted in sensor currents returning to baseline levels of -1.74 ± 0.36 nA, which was statistically significant when compared to current recordings obtained at FiO_2 of 1.0 (p= 0.0393) (Figure 7.9b and Table 7.5). At the end of each FiO_2 alteration, arterial blood-gas analysis confirmed the expected physiological changes induced by each challenge. SaO_2 and PaO_2 both decreased at FiO_2 of 0.1, increased at 1.0 (more prominent with PaO_2) and returned to baseline levels at 0.21. Expectedly, Hb concentration remained the same throughout each challenge (Figure 7.9c & d).

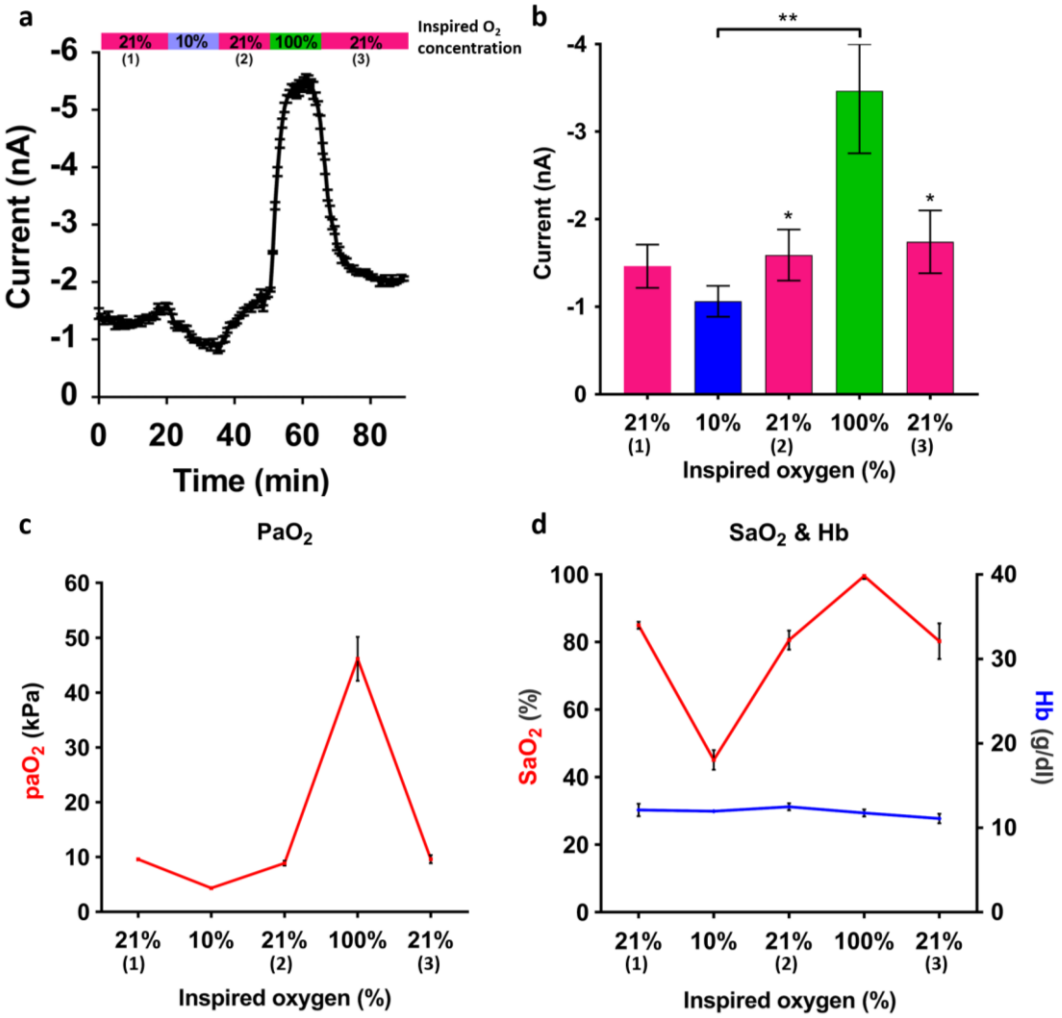

Figure 7.9. Sensor currents change in accordance with alterations in FiO_2. (a) Representative graph showing current generated at the working electrode of the sensor during continuous sensor recordings over a period of 80 min. A 20 min baseline recording at FiO_2 of 0.21was performed prior to 15 min blocks of each FiO_2 challenge. **(b)** Combined analysis comparing current generated at the working electrode of the sensor during each FiO_2 challenge; results show mean current recordings from the final 5 min of each 15 min period (one-way ANOVA with Holm-Šídák multiple comparisons test; data expressed as mean ± SEM, n=4, $^{**}p \leq 0.01$; $^{*}p \leq 0.05$). **(c&d)** Arterial O_2 partial pressure, total haemoglobin and haemoglobin O_2 saturation measured at the end of each FiO_2 challenge.

Table 7.5. Current recordings during each FiO_2 challenge. (n=4; mean ± SEM).

FiO_2	21% (1)	10%	21% (2)	100%	21% (3)
Current (nA)	-1.46 ± 0.25	-1.06 ± 0.18	-1.59 ± 0.29	-3.47 ± 0.71	-1.74 ± 0.36

7.4 Discussion

An AL is a serious complication that can occur following intestinal resection and anastomosis. The condition is life-threatening and can have long-term life

changing consequences. Unfortunately, there is no 'perfect' post-operative diagnostic test for an AL or a device that can monitor anastomotic healing. Although AL aetiology is complex, it has been associated with peri-anastomotic tension and interruption of microvasculature blood flow. This situation can cause peri-anastomotic necrosis and poor intestinal healing through compromised tissue perfusion and decreased ptO_2[668]. In accordance with this, our experiments focused on validating the ability of the IMPACT O_2 sensor to measure intestinal ptO_2 which could be developed as a means of assessing anastomotic healing.

Various intra-operative techniques are available to assess intestinal tissue perfusion (visible light and near infrared spectroscopy and laser fluorescence angiography)[669,670] and O_2 tension (laser Doppler flowmetry and wireless hand held pulse oximeters)[668,671], which have been shown to predict leak occurrence. An ongoing clinical trial is also currently assessing the potential benefits of measuring intra-operative anastomotic perfusion, using intravenous indocyanine green with near-infrared laparoscopy, to minimise leak occurrence compared with conventional white-light laparoscopy[672]. Unfortunately, these techniques are only applicable to intra-operative use and as yet have failed to gain interest with clinicians. Currently, surgeons typically rely on subjective macroscopic tissue appraisal to assess intra-operative intestinal perfusion. Adequate perfusion is deemed present if the intestine has a healthy pink colouration with the presence of intestinal bleeding and palpable mesenteric pulses. Unfortunately, these subjective techniques are only applicable to intra-operative use and are unable to predict the risk of a leak occurring[635].

Clark O_2 electrodes have been previously investigated as a means of measuring intra-operative intestinal ptO_2 using pre-clinical rabbit and dog intestinal devascularisation models[673,674]. These studies created gradual reductions in intestinal perfusion through the sequential ligation of a marginal intestinal artery and demonstrated that intestinal serosal ptO_2 measured immediately before performing an anastomosis could predict leak occurrence. In humans, Clark O_2 electrodes have been used intra-operatively to provide ptO_2 reference ranges for the majority of the gastrointestinal tract (stomach, ileum, caecum and colon)[675] and have been investigated in clinical trials for their ability to predict AL occurrence[676]. This clinical study measured peri-anastomotic colonic ptO_2 before, during and

immediately after performing a resection and anastomosis. The results demonstrated that colonic ptO_2 of less than either 20 mmHg, 50% of the pre-resection values, 15% of the PaO_2 or 40% of the ptO_2 at a control site were all associated with a post-operative AL. Adequate ptO_2 is required for collagen production, with levels lower than 15-20 mmHg associated with impaired synthesis. As submucosal collagen is the major holding layer for sutures/staples in the early stages of anastomotic healing, inadequate collagen synthesis due to low ptO_2 could lead to AL occurrence[676].

Although, these pre-clinical and clinical studies have provided evidence that Clark O_2 electrodes can be used intra-operatively to measure intestinal ptO_2 and predict AL occurrence, they fail to consider their potential post-operative use. The use of novel techniques such as an implantable device that can continuously measure intra- and post-operative peri-anastomotic ptO_2 would not only improve a surgeon's intra-operative ability to identify sites at increased risk of dehiscence[670], but also provide a means for monitoring post-operative anastomotic healing. This concept would be an ideal clinical application for the IMPACT O_2 sensor.

For *in vivo* functional validation and proof-of-concept that the IMPACT O_2 sensor could measure changes in intestinal ptO_2, a rat model was developed. Physiological challenges through either manipulation of intestinal blood flow (through SMA occlusion) to induce ischaemia, alterations in blood oxygenation status (through changes in FiO_2) to cause hypoxaemia and hyperoxaemia and finally creation of a state of acute haemorrhage were developed for use in the model. We suspected that these physiological challenges would cause a change in intestinal ptO_2 that could be detected by the IMPACT O_2 sensor.

Control experiments were first performed to investigate whether the rats could remain physiologically stable for the duration of the longest experimental protocols. Through monitoring physiological variables and evaluating arterial blood-gas, biochemical and haematological data, results demonstrated that the rats could cope with the physiological demands from general anaesthesia for the duration of our experimental protocols; this was in accordance with a previous study[677]. Using the same control group of rats, sensor recordings were performed to evaluate stability of the currents generated by the sensors and investigate any detrimental effects that the tissue environment and anaesthetic gases might have on sensor functionality. These

considerations are important, as halothane anaesthesia has been shown to affect Clark electrode function[678,679]. Our results demonstrated, for the first time in the literature, continuous *in vivo* recordings made using a miniaturised Clark-type electrochemical O_2 sensor for 165 min. No statistically significant changes in measured current were recorded during this period, suggesting that the tissue environment or anaesthetic gases had no effect on sensor function. This result was important in providing confidence that current changes observed in the experimental protocols were due to alterations in intestinal ptO_2 caused by the physiological challenges rather than from sensor drift/inaccuracy. Potential effects of anaesthetic agents and tissue metabolites on the functionality of the IMPACT O_2 sensor are likely to have been minimised/prevented through its design and packaging, predominantly using Nafion as the outer protective coating of the active sensing area. Pore size within Nafion membranes is small enough to exclude proteins that may contaminate the electrode surface, while the presence of charged sulphonate groups causes the electrostatic exclusion of small anions[680].

In all control and experimental groups, intestinal ptO_2 measurements were performed by positioning the sensors on the serosal surface of the small intestine and securing them in place with tissue adhesive. This technique ensured direct contact of the active sensing area with the intestinal serosal surface without the use of excessive pressure which could affect local microvascular blood supply, leading to alterations in ptO_2[675]. The size of the central active sensing area is also an important factor when considering the use of Clark O_2 electrodes for clinical applications, as large sensing areas have the potential to reduce tissue O_2 levels in the process of generating measurable currents. As the sensing area of the IMPACT O_2 sensor is only 50 µm in diameter, its potential for depleting tissue O_2 levels will be minimal. In clinical situations the small sensor size also would allow surgeons to place single or multiple sensors accurately on specific tissue areas. Placement of multiple miniaturised sensors in the case of anastomotic surgery would be particularly advantageous as they could be placed on either side and around the circumference of the anastomosis enabling detailed peri-anastomotic ptO_2 information to be obtained. This could not be achieved with a single sensor with a large sensing area that can only provide mean ptO_2 readings from multiple capillary beds[635].

Initial physiological challenges to validate sensor functionality were performed through intestinal blood flow manipulation to induce ischaemia. To do this, a SMA occlusion and reperfusion technique was developed. The SMA, a direct branch of the aorta, is the principle blood supply to the majority of the gastrointestinal tract, extending from the distal duodenum to the proximal two-thirds of the transverse colon. SMA identification is straightforward due to defined anatomical landmarks; with the small intestine and caecum exteriorised to the left-hand side of the abdomen the artery can be seen originating from the ventral aspect of the aorta at the level of the right renal vein. SMA identification was confirmed by observing small intestinal pallor immediately following vessel occlusion and a hyperaemic flush following vessel release.

SMA occlusion is the most direct way of causing intestinal ischaemia with significant histological changes occurring in the small intestine within 40 min of occlusion[681]. Previous studies have used various SMA occlusion techniques to study ischaemia-reperfusion injuries[682,683], cytokine production and bacteria/endotoxin translocation[684]; however, to our knowledge, this is the first report of the model being used for the validation of a miniaturised Clark O_2 sensor to measure intestinal ptO_2. Our technique of temporary SMA ligation as close to its aortic origin as possible ensured no collateral blood supply to the small intestine could occur from SMA subsidiary branches (inferior pancreaticoduodenal, intestinal, ileocolic, right and middle colic). Our results demonstrated that sensor currents fell to almost 0 nA within 1-2 min of SMA occlusion, indicating a severely hypoxic state as a result of tissue utilisation of the residual available O_2. Upon removal of the SMA occlusion, a rapid increase in sensor current was observed indicating a return of normal intestinal oxygenation as a direct consequence of intestinal reperfusion and flooding of the intestinal capillary beds with oxygenated blood. These results showed that the IMPACT O_2 sensor could quickly, reliably and reproducibly detect changes in intestinal ptO_2 through ischaemic and reperfusion challenges induced by SMA occlusion and release.

Further sensor validation was performed by manipulating intestinal ptO_2 through alterations in blood oxygenation levels, achieved through FiO_2 challenges. Arterial blood-gas analysis was used to confirm the expected physiological responses

to these FiO_2 alterations. Hypoxia caused reductions in both PaO_2 and SaO_2, whereas hyperoxia caused their levels to increase. Changes in sensor currents occurring with FiO_2 challenges matched the same pattern of results obtained using arterial blood-gas analysis with statistically lower and higher currents generated in hypoxaemic and hyperoxaemic conditions respectively. Time taken for sensor currents to change following a FiO_2 alteration was similar to that seen using the SMA model, with typical response times of 1-2 min. These results showed that the sensor could quickly, reliably and reproducibly detect changes in intestinal ptO_2 through hypoxaemic and hyperoxaemic challenges caused by changes in blood oxygenation.

Although significant changes in intestinal ptO_2 were detected through both ischaemic, hypoxaemic and hyperoxaemic challenges, similar results were not demonstrated with acute haemorrhage. Physiological parameters were used to confirm the expected responses caused by acute haemorrhage, which showed significant reductions in HR and MAP following acute removal of 30% of the circulating blood volume. This response is consistent with increased vagal activity and reduced sympathetic input (Bezold–Jarish-like reflex) resulting in a decrease in total peripheral resistance. HR typically only increases during continued and severe circulating blood volume loss in an attempt to maintain tissue perfusion and represents a transition from reversible to irreversible shock[685]. Arterial blood-gas analysis at the end of 30% haemorrhage did identify a slight decrease in Hb concentration. However, SaO_2 levels remained consistent due to the haemorrhage procedures being performed with a FiO_2 of 0.21. It is likely that in our induced model of acute haemorrhage that decreased peripheral resistance combined with stable SaO_2 could have maintained intestinal ptO_2 at normal levels, which is why no changes in sensor current measurements were observed[635].

Although the main aim of these experiments was to investigate the use of the IMPACT O_2 sensor for measuring intestinal ptO_2, we also investigated its potential for measuring ptO_2 in other tissues. Using our developed FiO_2 model we assessed changes in muscular ptO_2 to hypoxaemic and hyperoxaemic challenges. The results showed changes similar to those documented in the intestinal experiments and provided evidence that the sensor may be used for measuring ptO_2 in various tissues.

One significant advantage of our developed *in vivo* model over previous studies using Clark O_2 electrodes is that it allowed not only the assessment of whether the IMPACT sensor could detect changes in intestinal and muscular ptO_2 following the initial physiological challenge, but also whether sensor readings would return to baseline levels upon challenge removal. Previous studies have only reported on Clark O_2 electrodes being used for making individual intestinal ptO_2 measurements at specific time points[673-676]; the continuous recording of data performed in our experiments provided an opportunity to dynamically measure changes in ptO_2 before, during and after each challenge. Our results clearly demonstrated that currents measured by the IMPACT O_2 sensor returned to baseline levels following repeated temporary ischaemic insults and reversible changes in FiO_2. The ability to dynamically measure changes in intestinal ptO_2 could have a significant impact on the peri-operative management of patients undergoing intestinal resection and anastomosis. Miniaturised Clark O_2 sensors placed around the anastomotic site and left *in situ* following surgery could provide post-operative, minimally-invasive, rapid and highly localised continuous real-time data regarding transitory changes in peri-anastomotic intestinal ptO_2. This method of monitoring ptO_2 could detect early peri-anastomotic tissue hypoxia and identify patients that may benefit from treatments aimed at improving local ptO_2 to prevent a leak, or failing that, diagnose a leak earlier than current diagnostic methods allow. The sensor's ability to detect dynamic intestinal ptO_2 changes could also be used to assess treatment responses and, when combined with information gained from conventional monitoring systems, would provide a more accurate assessment of the patient's condition.

7.5 Conclusion

This chapter has described the development of a novel *in vivo* murine ischaemic, hypoxic and haemorrhagic model in which acute and reversible changes in intestinal and muscular ptO_2 were produced. The results demonstrated that the IMPACT O_2 sensor can accurately detect dynamic changes in intestinal ptO_2 through ischaemic insults, alterations in FiO_2 and euthanasia, with similar results also identified in muscular tissues in response to alterations in FiO_2. These results have provided initial functional *in vivo* validation of the IMPACT O_2 sensor and is the

first step in the process of evaluating its potential to be used as an advanced ptO_2 monitoring device. Justification for progressing sensor validation experiments into more complex large animal tumour models has also been successfully achieved.

8 Development of a Pre-Clinical Ovine Pulmonary Adenocarcinoma Model for Human Lung Cancer and Validation of Intra-Tumoural Functionality of the IMPACT Oxygen Sensor

This results chapter is an expanded version of a published research article: Gray M, Sullivan P, Marland JRK, Greenhalgh SN, Meehan J, Gregson R, Clutton RE, Cousens C, Griffiths D, Murray A, Argyle D. A Novel Translational Ovine Pulmonary Adenocarcinoma Model for Human Lung Cancer. Frontiers in Oncology - Molecular and Cellular Oncology 2019; 9(534): 1-17. This article is open access with the authors retaining copyright to their work with permission to use published figures in this thesis. Sections of text and figures used from this article have been referenced accordingly.

8.1 Abstract

Background: Large animal models that accurately reflect human disease are regarded as excellent translational models which can be used in pre-clinical research. Ovine pulmonary adenocarcinoma (OPA) is a naturally occurring lung cancer that has a similar histological classification and oncogenic pathway activation with that of human lung adenocarcinomas; similarities such as these make it a valuable model for studying human lung cancer. **Methods:** A novel OPA model was developed for validation of the ability of the IMPACT O_2 sensor to provide real-time measurements of intra-tumoural O_2 tension. Sensors were implanted into OPA tumours of anaesthetised (non-recovery) sheep using a CT-guided trans-thoracic percutaneous implantation procedure. **Results:** Nine sheep underwent single or double sensor implantations. For single sensor implantations the time taken from initial CT scans to sensor placement was 45 ± 5 min. All implantations resulted in successful sensor delivery into OPA tumours. Post-implantation pneumothorax occurred in 4 sheep. Sensor recordings identified decreased intra-tumoural O_2 tension following a reduction in inspired O_2 concentrations, although these changes were not statistically significant. **Conclusion:** These results demonstrate the *in vivo* validation of the ability of the IMPACT O_2 sensor to detect dynamic changes in intra-tumoural O_2 tension caused by hypoxaemia. Through the integration of techniques used in the

treatment of human lung cancer patients, including ultrasound, general anaesthesia, CT and surgery into the OPA model, we have shown its translational potential. We believe this model can be used for a variety of other pre-clinical applications.

8.2 Introduction

Following initial validation of the ability of the IMPACT O_2 sensor to detect changes in intestinal and muscular ptO_2 in healthy tissues, our aim was to investigate its potential for measuring ptO_2 within a solid tumour. To achieve this, we developed a novel translational large animal ovine model whereby sensors were implanted into naturally occurring OPA tumours. If successful, the aim would be to develop the sensors for use in clinical situations where a patient's cancer treatment could be influenced by the assessment of intra-tumoural ptO_2. Although applicable to many solid tumours, one situation where assessment of intra-tumoural O_2 levels could be advantageous is in the treatment of lung cancer.

Lung cancer is the most commonly diagnosed cancer in the world, with approximately 2 million new cases and 1.8 million cancer-related deaths occurring per year[6]. Historically lung cancer research has largely relied on *in vivo* mouse models. Although these models have increased our molecular understanding of the disease, they have failed to lead to breakthrough advancements in lung cancer treatment. If progress is to be made in improving lung cancer prognosis, then the limitations with current *in vivo* models must be addressed. One solution would be to use complex models that more accurately represent the disease[293]. Similarities in clinical presentation, activated signalling pathways and histological classification between OPA and human lung adenocarcinomas, combined with the availability of several *in vitro and in vivo* OPA model systems, has led to the disease being regarded as a valuable translational model for studying human lung cancer[309].

In vitro OPA models typically use either immortalised cell lines or primary cultures from OPA tumours[331,686,687]. Unfortunately, the lack of an *in vitro* cell line that can support JSRV replication when cells are grown in 2D systems has limited the amount of research that has been performed in this manner. To overcome this limitation, *in vitro* JSRV expression has been shown to be possible by culturing cells using 3D systems[686,688] or by using OPA lung tissue explants[689,690]. These 3D model systems may more accurately recreate the oncogenic events that occur in OPA and

represent transitional models between *in vitro* and *in vivo* systems[273]. *In vivo* small animal OPA models have been developed using immunodeficient[327] and immunocompetent mice[691]. These studies show that intra-nasal administration of adeno-associated virus vectors encoding JSRV Env leads to the formation of lung adenocarcinomas that are comparable to those found in sheep and humans. Although these small animal systems are more widely available than large animal models and do not require specialised animal facilities, they suffer from the same limitations as other *in vitro* cancer mouse models, as described in section 1.9.

To improve complexity and translational ability of OPA models there are 2 *in vivo* ovine models available which use either experimentally induced tumours or naturally occurring disease[273]. The first documented *in vivo* OPA model demonstrated that the formation of lung tumours in healthy sheep could be induced following intra-tracheal injections of either OPA tumour homogenates or JSRV purified from lung fluid[692,693]. Later studies using neonatal lambs improved infection rates and decreased the time required for tumours to develop[351,694]. These improved results are likely due to JSRV preferentially infecting dividing cells, which are more common in younger animals[695]. This model has been constantly refined, most recently through sequencing and cloning of the JSRV genome[322,696] and through the generation of an oncogenic and infectious molecular clone. This has enabled *in vitro* virus production to be achieved through the transfection of cell lines[697], which can be used to infect neonatal lambs. The main advantage of using the *in vivo* lamb model is that it provides the opportunity for studying tumourigenesis and early stage disease. This is an important area of research in human lung cancer as clinical tissue from early cases is generally unavailable. However, while this model is useful for studying tumourigenesis and pathogenesis from infection to the formation of small tumours, for welfare reasons the disease cannot be allowed to reach advanced stages. The use of naturally occurring OPA cases provides the opportunity for studying advanced disease and overcomes the ethical concerns associated with the lamb model.

As OPA is endemic in the UK, this disease population represents a valuable translational research opportunity for assessing human lung cancer treatment strategies. Unfortunately, the lack of reliable ante-mortem, pre-clinical OPA diagnostic tests has limited the use of these naturally occurring cases for research.

Pre-clinical OPA diagnosis is difficult as clinical signs are often lacking. Although JSRV can be detected in blood[347], bronchoalveolar[343] and lung fluid[349] samples through PCR, these tests can suffer from poor sensitivity and are not easily applicable to routine large-scale on-farm testing. To overcome these issues, imaging techniques such as radiography, CT and now ultrasound are being investigated for use in pre-clinical OPA diagnosis[273]. In human thoracic medicine, CT is the imaging modality of choice that allows detailed evaluation of lung tissue which can identify smaller lesions compared to conventional radiography. Its use in OPA models has been demonstrated for monitoring the development and progression of tumours in both naturally occurring[698] and experimentally infected animals[339]. Unfortunately, radiography and CT are cost prohibitive for commercial flocks and require specialised equipment and sedation/general anaesthesia[341].

Trans-thoracic ultrasonography has been proposed as a useful OPA diagnostic technique. One study performed trans-thoracic ultrasound examinations on 100 sheep as part of a series of diagnostic tests for the investigation of weight loss. Based on ultrasound examination alone, 41 sheep were diagnosed as OPA positive, with all cases having the diagnosis confirmed at post-mortem. All remaining sheep had no ultrasonographic changes characteristic of OPA and were diagnosed as OPA negative at post-mortem. These results demonstrated that diagnostic ultrasound was highly specific, producing no false positive or negative results[282]. Trans-thoracic ultrasound can be performed in a sheep in less than 1 minute[699] and can differentiate chronic lung lesions and detect OPA lesions as small as 1-2 cm[282]. As trans-thoracic ultrasound can be performed quickly and in conscious animals the procedure lends itself to routine large-scale on-farm OPA diagnosis programmes[273]. It is also an ideal method for identifying pre-clinical cases for experimental use as individual cases can be selected based on size and location of OPA lesions. These are the reasons why trans-thoracic ultrasound was chosen to select OPA cases for use in our study.

Until now the majority of *in vivo* and *in vitro* OPA models have focused on the investigation of JSRV biology and oncogenesis. One study however has investigated the impact of nutritional selenium on tumourigenesis and progression using naturally occurring OPA cases[698]. Although this study demonstrated the potential for the OPA model to be integrated with techniques such as CT, post-mortem examination, trace

element and liver enzyme activity analysis to provide comprehensive information on tumour pathogenesis, the use of OPA as a pre-clinical model for monitoring the TME, evaluation of chemotherapeutic agents or as a surgical model has yet to be documented.

This chapter describes the development, refinement and use of an anaesthetised OPA model for functional validation of the IMPACT O_2 sensor within a TME. A novel CT-guided trans-thoracic percutaneous implantation procedure was developed for sensor placement into OPA tumours. Following sensor implantation, we investigated the sensors ability to detect changes in intra-tumoural ptO_2 following manipulation of FiO_2. This is, to the best of our knowledge, the first description of the use of naturally occurring OPA cases as a pre-clinical surgical model for the validation of the ability of a miniaturised Clark O_2 sensor to measure dynamic changes in intra-tumoural ptO_2. Through the successful integration of techniques used in the treatment of human lung cancer patients, including ultrasound, general anaesthesia, CT and surgery into the OPA model, we have shown its translational potential. These results provide robust evidence for further development of the IMPACT O_2 sensor towards clinical applications in man.

8.3 Results

8.3.1 Development of a percutaneous technique for sensor implantation into lung tissue

To develop a technique whereby IMPACT O_2 sensors could be safely and reliably implanted into an OPA tumour we began to investigate protocols using sheep carcasses. Although these sheep did not have any lung pathology, we were able to develop the surgical protocol before moving onto experimental animals.

Post-mortem sheep were placed in lateral recumbency and the entire hemithorax was clipped. A 1 cm vertical skin incision was made approximately 1-2 intercostal spaces caudal to the desired site of penetration into the thoracic cavity. Artery forceps were used to develop a subcutaneous tunnel from the skin incision extending cranially to the desired intercostal space. An 8G x 15 cm Jamshidi biopsy needle (Carefusion, France), with its stylet in place, was introduced through the subcutaneous tunnel, then redirected perpendicular to the thoracic wall in the middle of the selected intercostal space. The needle was advanced to enter the thoracic

cavity, with the penetration of the parietal pleura appreciated as the feeling of a ‘pop’. Once the parietal pleura had been penetrated the needle was advanced through the visceral pleura and into lung parenchyma. Following penetration into lung tissue the stylet was removed, and the sensor and lead wire were introduced down the bore of the needle. The obturator was then introduced down the bore of the needle, advancing the sensor past the tip of the needle and positioning it within lung tissue. Once in place, the obturator and implantation needle were withdrawn, leaving the sensor and lead wire *in situ*. A purse string suture of 3 metric braided silk (Ethicon, UK) was placed around the incision, which continued as a Chinese finger trap suture around the lead wire, securing the sensor in place (Figure 8.1). Following sensor insertion, the rib cage was removed to evaluate sensor positioning (Figure 8.2).

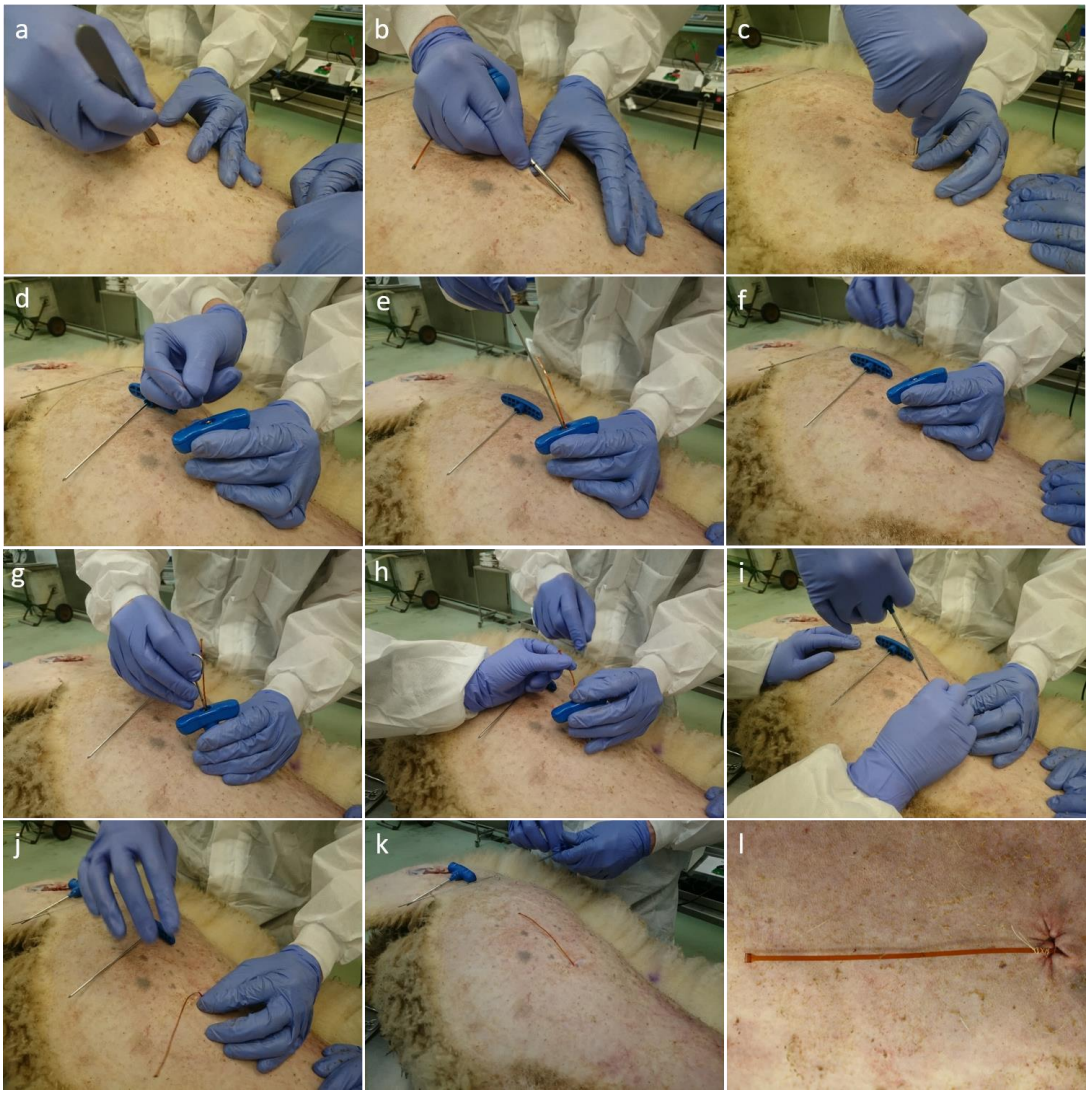

Figure 8.1. Photographs depicting development of a percutaneous implantation technique. (a-c) A skin incision was made through which the Jamshidi needle was introduced. The needle was placed perpendicular to the thoracic wall, introduced into the thoracic cavity and advanced into lung tissue. **(d-g)** The stylet was removed, and the sensor introduced down the bore of the needle. The obturator advances the sensor to position it within the lung tissue. **(h-j)** Removal of the obturator and implantation needle leaves the sensor *in situ*. **(k&l)** The lead wire was sutured in place.

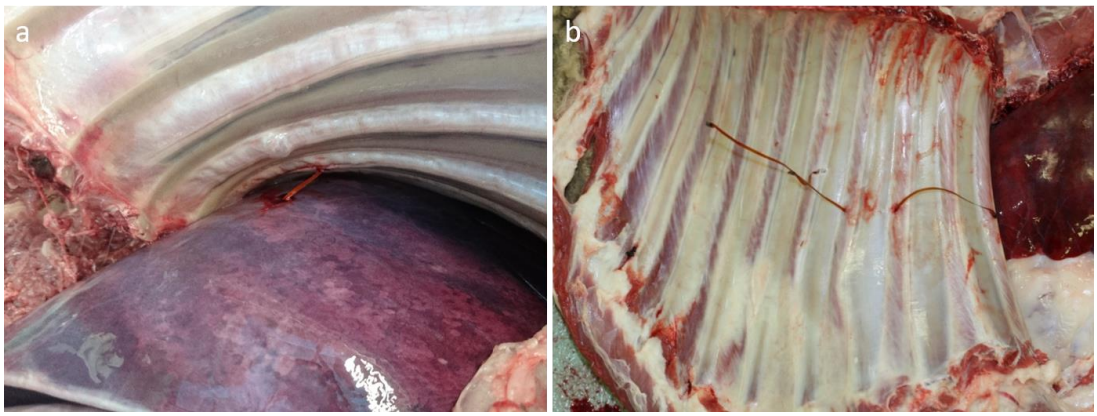

Figure 8.2. Photographs depicting sensor placement through the thoracic wall into lung tissue. The rib cage has been removed to assess sensor position within **(a)** lung tissue and **(b)** within the intercostal space.

8.3.2 Post-mortem cases allowed mapping of accessible regions of the thoracic cavity for sensor implantations

Using post-mortem cases, we performed simulated surgeries on 8 sheep cadavers with multiple implantations in each carcass. These surgeries allowed the development of the implantation procedure and investigation of the potential accessible regions of the thoracic cavity and lung lobes which could be safely implanted into during experimental cases.

The ovine thorax is composed of 13 ribs and 12 intercostal spaces; access to the cranial rib spaces (1-4) was almost entirely prevented by the appendicular skeleton and musculature of the forelimbs, making access to the cranial thoracic cavity impracticable through a lateral approach. Caudally the ovine thoracic cavity does not extend over the whole thorax, and access gained through intercostal spaces caudal to the 8^{th} space resulted in implantation into the costodiaphragmatic recess or penetration through the diaphragm into the abdominal cavity. The 4^{th}-8^{th} intercostal spaces on both sides of the thorax were all used successfully to implant sensors into lung tissue; implants were placed most reliably into the caudal lobes and right middle lung lobe using the 5^{th} and 6^{th} intercostal spaces (Figure 8.3). During implantation the Jamshidi needle caused significant elastic deformation of lung tissue prior to visceral pleural penetration, after which the needle could be advanced through the parenchyma with relative ease, allowing sensor implantation to be performed.

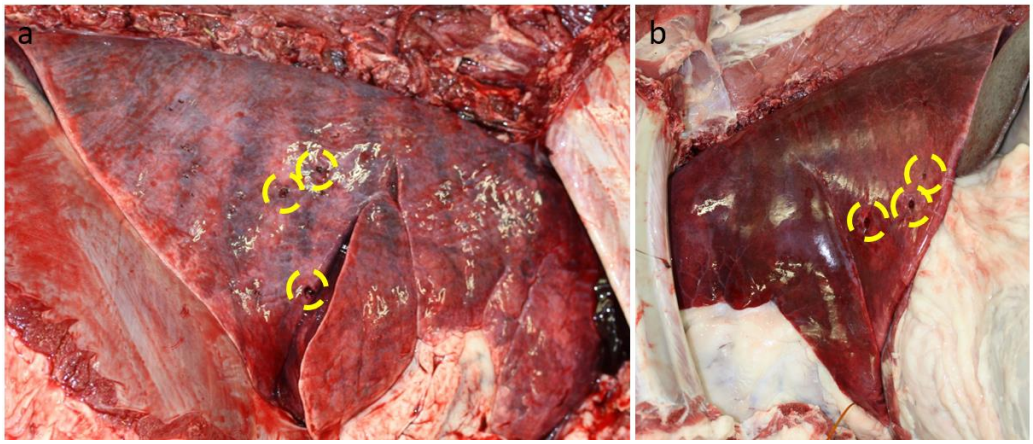

Figure 8.3. Photographs depicting lung lobes which can be accessed through a lateral percutaneous approach for sensor implantations. (a) Right hemithorax. **(b)** Left hemithorax. Yellow circles outline sensor implantation sites.

8.3.3 Development of a CT-guided trans-thoracic percutaneous technique for sensor implantation into OPA tumours

To refine the initial procedure used in post-mortem cases we used 3 sheep diagnosed with OPA (Table 8.1). Following induction of anaesthesia as described in section 3.4.2, the sheep were placed in lateral recumbency with the OPA affected lung uppermost. The thorax was clipped in preparation for surgery; this area extended cranially from just beyond the last rib to the caudal border of the scapula with the dorso-ventral margins extending from the dorsal spinous process of the thoracic vertebrae to the sternum. Following an initial thoracic CT scan, OPA lesion localisation was performed; lesions were localised cranio-caudally based on intercostal spaces and dorso-ventrally based on measurements from the dorsal spinous process of thoracic vertebrae to the OPA lesion. A mark was drawn on the skin to identify the position of thoracic wall penetration for sensor implantation.

Table 8.1. OPA cases used for initial refinement of the CT-guided implantation technique.

Case	Signalment	Weight (kg)	CT lesion localisation	Total anaesthesia time (min)
A	Blackface Female Adult	51	**Left cranial lobe:** entire lobe affected	124
B	Blackface Female Adult	56	**Right caudal lobe:** 2 focal lesions (1 dorsal, 1 ventral), approximately 4-5 cm diameter	142
C	Blackface Female Adult	76	**Right cranial lobe:** entire lobe affected	200

Case A underwent an initial CT scan for lesion localisation, with subsequent sensor implantation performed using the same technique as was developed in the post-mortem cases. The sensor was implanted without CT guidance with one single needle advancement. Although penetration of the parietal and visceral pleura was easily appreciated, this blind technique made it difficult to judge how deep the needle had penetrated into OPA tissue. Post-implantation CT scans identified a severe pneumothorax, and although the sensor was positioned within OPA tissue, it was at the deep margins of the lung lobe (Figure 8.4a). The iatrogenic severe pneumothorax was likely due to the needle passing through a large volume of lung tissue or from air tracking into the thoracic cavity through the subcutaneous tunnel.

To improve accuracy of sensor implantations cases B and C were performed under CT guidance. Following lesion localisation, as performed in case A, repeat CT scans were performed following the initial placement of the needle through the chest wall and following each needle advancement, until the needle was positioned at the desired point within OPA tissue. Post-implantation CT scans of case B identified a small pneumothorax in the region of the implant site, with the sensor positioned in the pneumothorax and not within OPA tissue (Figure 8.4b). Post-implantation CT scans of case C identified the sensor positioned in subcutaneous tissue outside the thoracic cavity (Figure 8.4c). In both cases sensor ‘back out’ was likely due to the sensor not been fully pushed past the tip of the needle into OPA tissue, or the sensor or lead wire catching within the bore of the needle (Table 8.2).

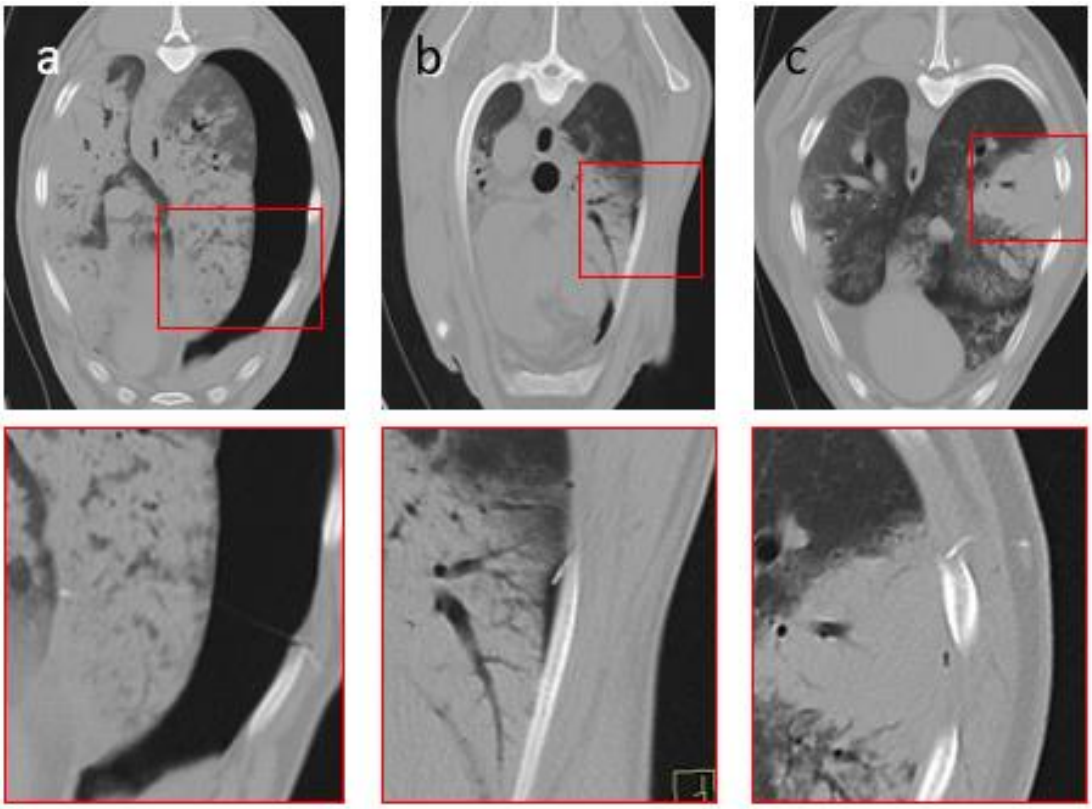

Figure 8.4. Axial CT images documenting surgical complications in the initial 3 OPA cases. CT scans were taken immediately post-sensor implantation. **(a)** Case A. Severe pneumothorax with extensive retraction of the lung lobes away from the chest wall. The sensor is positioned deep within OPA tissue. A small amount of air can be seen in the subcutaneous tissues just proximal to the rib. **(b)** Case B. Mild pneumothorax localised to the implantation site. The sensor and lead wire have 'backed out' during implantation and are positioned within the pneumothorax. **(c)** Case C. The sensor and lead wire have 'backed out' during implantation and are positioned within subcutaneous tissues.

Table 8.2. Results from OPA cases used for initial refinement of the implantation technique. Number of needle advancements, implantation time and complications are provided.

Case	No. of CT scans/needle advancements	Time from initial CT scan to sensor implantation (min)	Sensor placed within OPA tissue (yes/no)	Complications post-implantation
A	1	50	Yes	**Immediate:** Severe pneumothorax
B	2	32	No	**Immediate:** Mild pneumothorax with sensor positioned within pneumothorax
C	4	29	No	**Immediate:** Sensor positioned within thoracic wall musculature

8.3.4 Refined procedure for OPA lesion localisation and CT-guided trans-thoracic percutaneous sensor implantation

Following the initial 3 cases, further refinement of OPA lesion localisation and CT-guided sensor implantation was performed (Table 8.3). Sheep were anaesthetised as described in section 3.4.2, clipped, prepared and positioned for CT scanning and surgery as described in section 8.3.3.

Table 8.3. OPA cases used following refinement of the CT-guided implantation technique. Signalment, CT localisation and total anaesthesia time (time from induction of anaesthesia to euthanasia) are provided.

Case	Signalment	Weight (kg)	CT lesion localisation	Total anaesthesia time (min)
1	Highlander Female Adult	65	**Left caudal lobe:** 1 focal lesion at cranial aspect, approximately 4-5 cm diameter	174
2	Blackface Female Adult	51	**Right caudal lobe:** diffuse area affecting caudal aspect, approximately 4-5 cm diameter	234
3	Blackface Female Adult	39	**Left caudal lobe:** entire lobe affected	161
4	Blackface Female Adult	52	**Left cranial lobe:** entire lobe affected	158
5	Blackface Female Adult	57	**Right cranial lobe:** almost entire lobe affected **Left caudal lobe:** 1 focal lesion at caudal aspect, approximately 10-15 cm diameter	234
6	Blackface Female Adult	39	**Left cranial lobe:** entire lobe affected	247
7	Blackface Female Adult	55	**Right cranial lobe:** entire lobe affected **Left cranial lobe:** entire lobe affected, extending into the cranial aspect of the left caudal lobe	343
8	Blackface Female Adult	58	**Right middle lobe:** entire lobe affected **Left cranial lobe:** entire lobe affected, extending into the cranial aspect of the left caudal lobe	270
9	Mule Female Adult	64	**Right cranial lobe:** almost entire lobe affected	195

To improve the accuracy of OPA lesion localisation and the site for percutaneous sensor implantation a self-adhesive sheet of non-metallic, radiopaque grid lines (GuideLines, Oncology Imaging Systems, UK) was placed on the thoracic wall skin surface in the centre of the clipped area. An initial thoracic CT scan was obtained to assess intra-thoracic pathology and identify OPA lesion(s) (Figure 8.5). OPA lesions for implantation were selected so the needle path would avoid bullae,

fissures, blood vessels and large bronchioles. Peripheral tumours of at least 4 cm in diameter were also preferred to limit the volume of normal aerated lung the needle would pass through and improve sensor implantation into the centre of a lesion. The distance between the skin and pleura was measured at the anticipated penetration site. OPA lesions were localised dorso-ventrally based on the grid lines and cranio-caudally based on intercostal spaces. A mark was drawn on the skin surface to identify the position of thoracic wall penetration for sensor implantation (Figure 8.6). The grid lines were removed, and the skin was aseptically prepared for surgery using chlorohexidine solution before the area was four quarter draped for surgery.

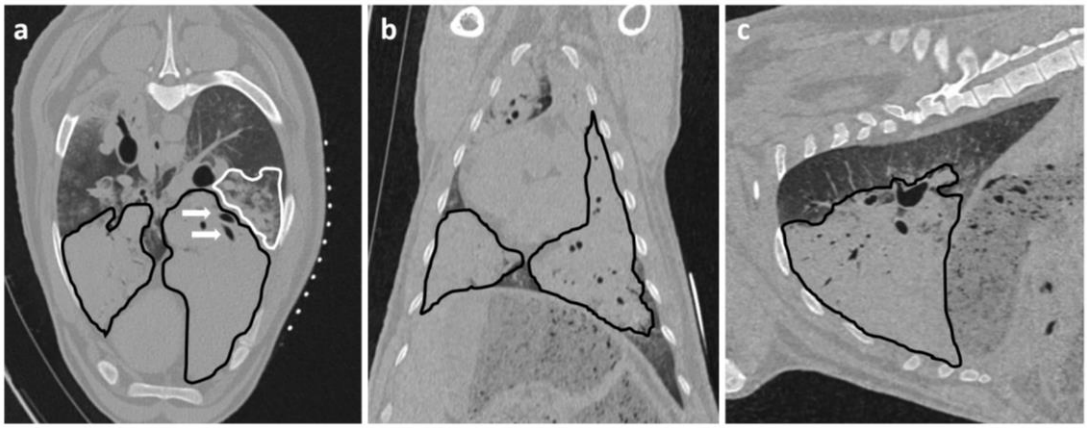

Figure 8.5. Initial CT scan performed to assess intra-thoracic pathology and localise OPA lesions. (a) Axial. **(b)** Coronal. **(c)** Sagittal planes. Large areas of increased radiopacity can be seen affecting the ventral regions of the left cranial and caudal lung lobes and the ventral regions of the right caudal lung lobe (outlined in black). Air bronchograms are visible within this consolidated region (white arrows). A patchy and hazy increased opacity (ground glass appearance) within the dorsal regions of the lung, with preservation of bronchial and vascular margins, suggest the presence of interstitial pneumonia or small foci of neoplastic tissue (outlined in white). The radiopaque circles on the skin surface seen on the axial plane are the grid lines used for OPA lesion localisation.

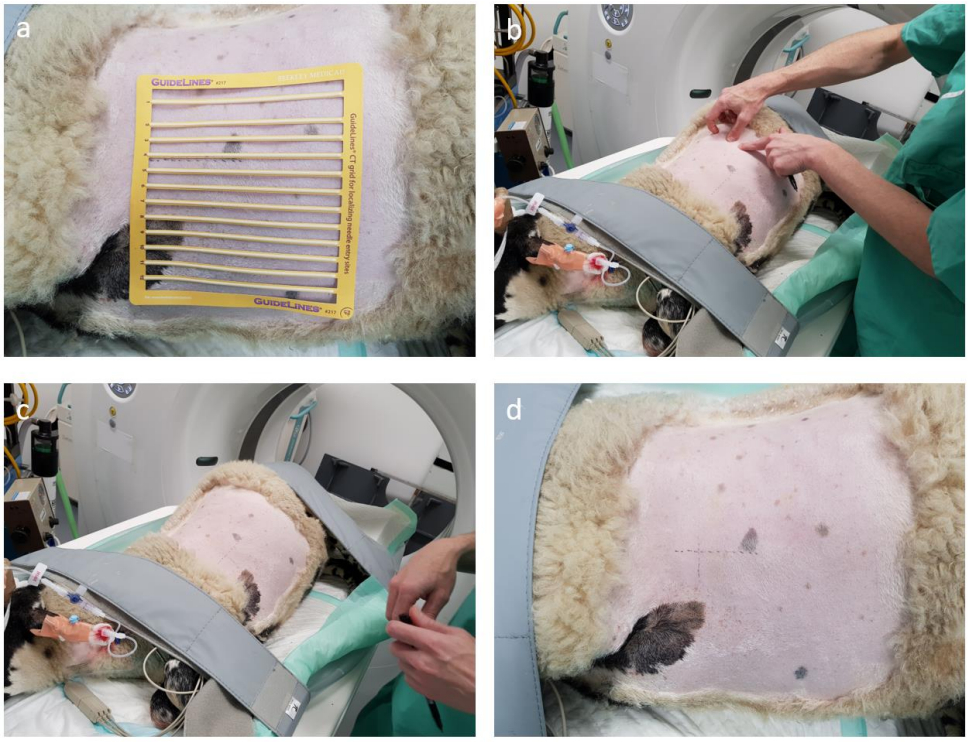

Figure 8.6. OPA lesion localisation. (a) The hemithorax has been clipped for surgery and the radiopaque grid lines placed on the skin surface prior to the initial CT scan. **(b-d)** Following the CT scan the skin was marked both dorso-ventrally and cranio-caudally at the desired point of thoracic wall penetration for sensor implantation.

All sensors were implanted using a trans-thoracic percutaneous technique under CT guidance based on the developed protocol described in section 8.3.1. A skin incision was made 1-2 intercostal spaces caudal to the desired thoracic wall entry point. The Jamshidi biopsy needle, with its stylet in place, was introduced through the skin incision and tunnelled cranially to the desired intercostal space. The tunnel was made long enough to minimise the risk of air entering the thoracic cavity from the external environment following sensor implantation. Once at the desired intercostal space the needle was positioned at 90 degrees to the thoracic wall in the centre of the intercostal space. The needle was then advanced the distance measured from the initial CT scan (approximately 1 cm) through the chest wall so that the needle was just within the thoracic cavity, penetrating the parietal pleura, but not entering lung/OPA tissue. A second CT scan was performed to ensure accurate placement of the needle at the desired position. If the needle position was suboptimal it could be re-positioned with minimal risk of lung damage. Once correctly positioned, the needle was advanced through the visceral pleura into OPA tissue;

repeat CT scans were taken following each needle advancement to ensure correct needle trajectory and accurate localisation of the needle tip. Measurements were taken from each CT scan from the needle tip to the point of desired sensor implantation to make needle advancements more accurate. Once the needle tip was positioned centrally within OPA tissue the stylet was removed, and the sensor and lead wire were introduced down the bore of the needle. The obturator was then introduced to advance the sensor past the tip of the needle into OPA tissue. Once in place, the obturator and implantation needle were withdrawn, leaving the sensor and lead wire *in situ*. Care was taken to ensure the lead wire did not catch on the needle, risking sensor displacement. The lead wire had been previously marked at 1 cm intervals to verify that it was not 'backing out' during needle removal. The lead wire was then sutured in place as described in section 8.3.1 (Figure 8.7 & Figure 8.8).

Following implantation, CT scans were performed to evaluate sensor positioning and assess the presence of any immediate or delayed post-operative complications such as pneumothorax or haemorrhage; these CT scans were performed immediately after implantation and suturing and also following euthanasia (Figure 8.8 & Figure 8.9). If a pneumothorax developed the decision to drain it was made on severity and whether ventilation was compromised. Intermittent percutaneous thoracocentesis was performed if required.

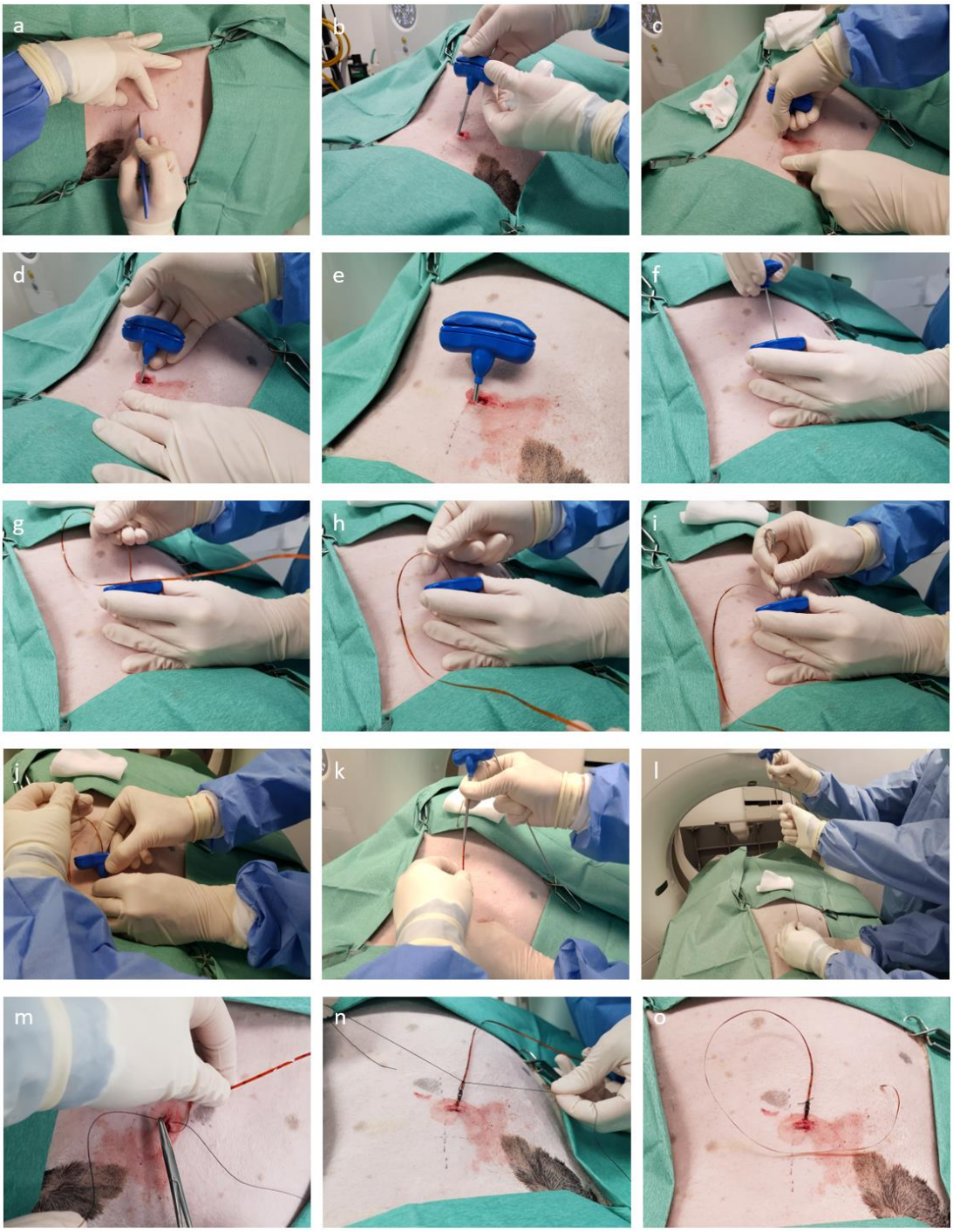

Figure 8.7. Intra-operative photographs depicting trans-thoracic percutaneous sensor implantation. (a&b) A skin incision was made through which the Jamshidi needle was introduced. **(c-e)** Following successive CT scans the needle was progressively advanced into OPA tissue. **(f-h)** Once the needle was in position the stylet was removed and the sensor introduced down the bore of the needle. **(i)** The obturator was used to push the sensor past the tip of the needle into OPA tissue. **(j-l)** The Jamshidi needle was removed, leaving the sensor and lead wire in place. **(m-o)** The skin was closed, and the lead wire secured in place with a purse string and Chinese finger trap suture.

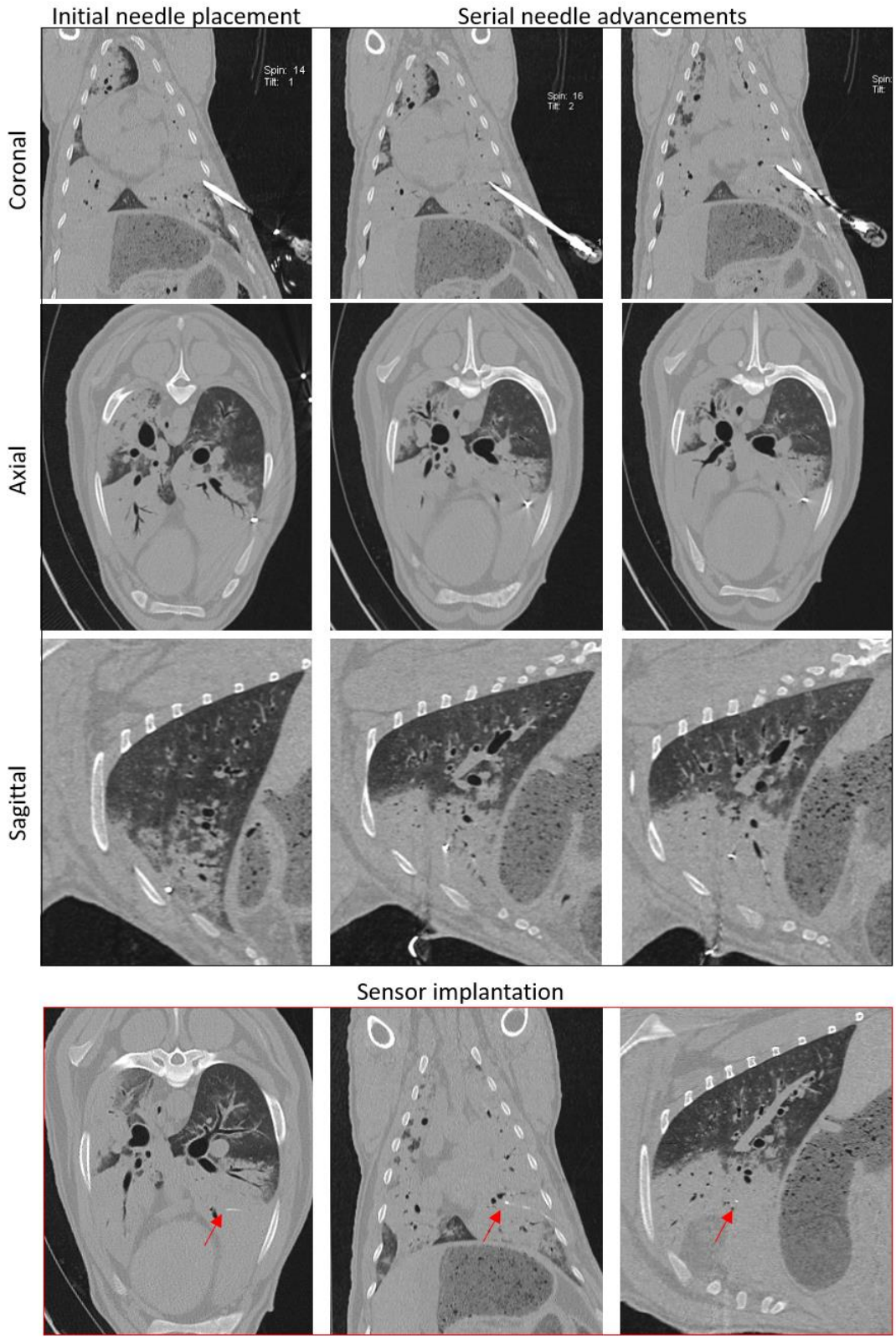

Figure 8.8. Serial CT images taken during sensor implantation. Coronal, axial and sagittal planes are viewed following initial needle placement and after successive needle advancements. The needle was advanced until the tip was at the desired position within the OPA lesion. CT images taken immediately post-implantation demonstrates sensor placement within OPA tissue in all 3 planes (red arrows).

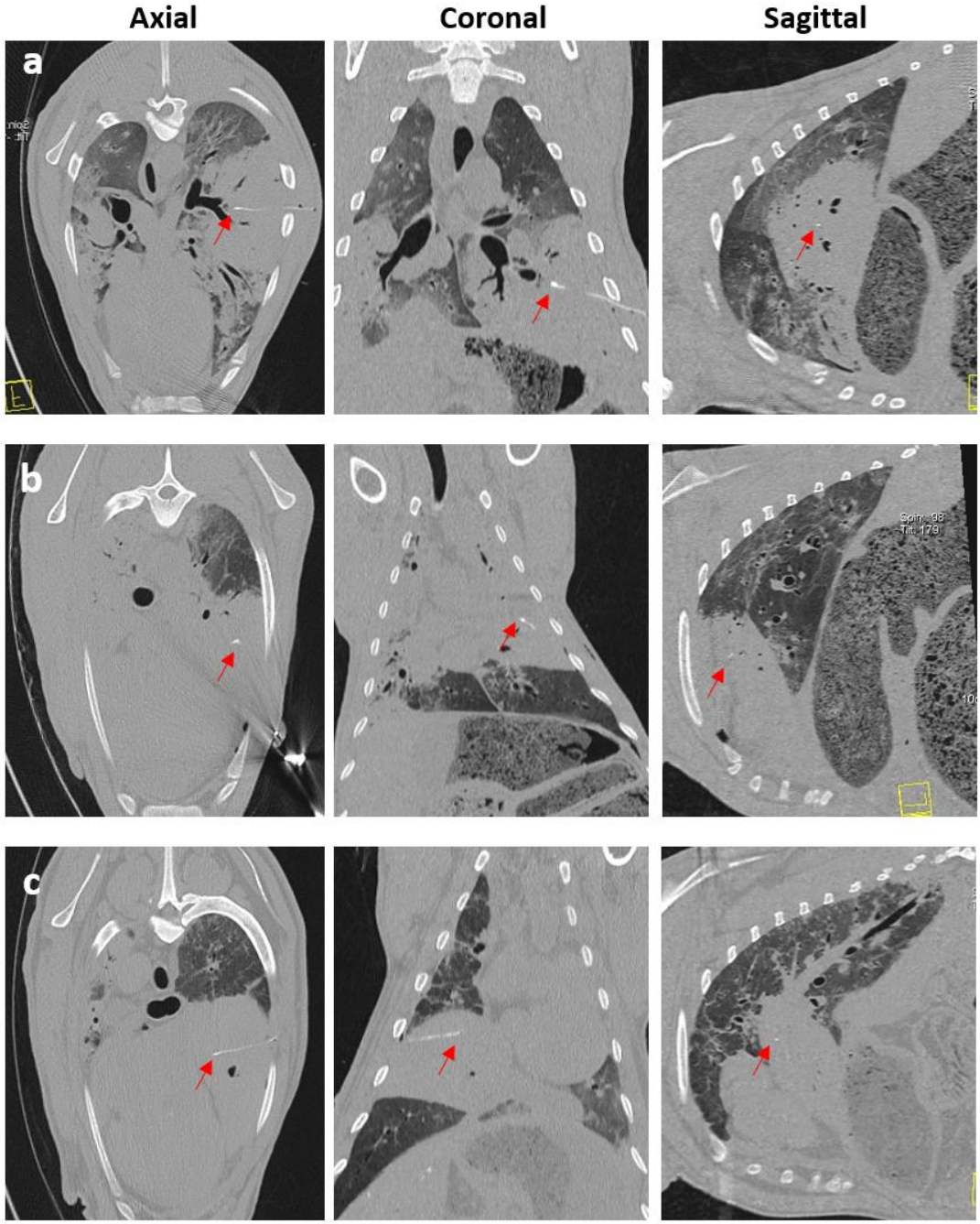

Figure 8.9. CT images taken immediately post-sensor implantation. Images are from 3 separate cases. The sensor and lead wire (red arrows) can be seen within the area of increased radiopacity, consistent with a large consolidated OPA tumour. Repeat CT scans were taken following completion of sensor measurements and euthanasia; these showed no evidence of complications and confirmed the sensor had remained within OPA tissue throughout sensor recordings.

8.3.5 Refined procedure for CT-guided implantation of multiple sensors

Following procedure refinement for single sensor implantations the technique was modified to allow 2 sensors to be implanted into a single lesion. The initial CT

scan verified that the lesion was large enough to accommodate 2 sensors and allowed for sensor implantation planning. Sensors were placed through the same intercostal space 2-3 cm apart. The first needle was placed as previously described, penetrating the parietal pleura. Following CT confirmation of correct needle positioning the needle was advanced into OPA tissue and a second needle was placed, again only penetrating the parietal pleura. A CT scan confirmed placement of the first needle into OPA tissue and the second at the correct position. Both needles were then advanced simultaneously based on sequential CT scans and the sensors implanted as previously described (Figure 8.10).

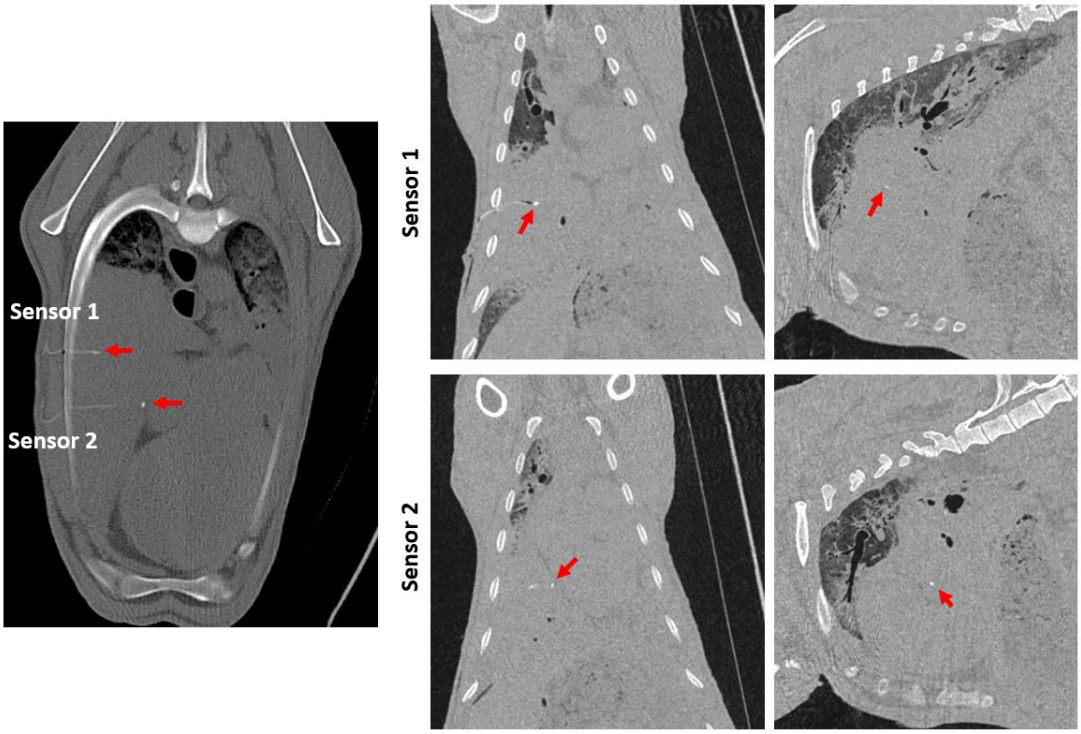

Figure 8.10. CT images taken immediately post-sensor implantation. The sensors and lead wires (red arrows) can be seen within the area of increased radiopacity, consistent with a large consolidated OPA tumour. Sensor 1 is placed centrally within the tumour whereas sensor 2 has been placed further towards the deep margin of the lung lobe. Repeat CT scans were taken following completion of continuous sensor measurements and euthanasia; these documented no evidence of complications and confirmed the sensors had remained within OPA tissue throughout sensor recordings.

8.3.6 CT-guided trans-thoracic percutaneous sensor implantation resulted in a high success rate of delivery of sensors into OPA lesions

A total of 7 OPA sheep underwent CT-guided single sensor implantations (Table 8.4). Time taken from the initial CT scan to sensor placement was 45 ± 5 min

(mean ± SEM). The number of sequential CT scans and needle advancements required from initial needle placement to obtaining the desired position within the OPA lesion ranged from 3–5; however, 4 advancements were required in 5 of the 7 cases. All implantation procedures resulted in sensor placement within OPA tissue. No immediate or delayed complications were identified in 4 of the cases.

Two sheep underwent CT-guided 2 sensor implantations (cases 8 & 9). Time taken from the initial CT scan to sensor placement was 73 and 50 min for each case. The number of sequential CT scans and needle advancements required from the initial placement to correct positioning within OPA tissue was 4 for each needle. In both cases all implantation procedures resulted in sensor placement within OPA tissue. No immediate or delayed complications were identified in 1 of the cases.

Table 8.4. Results from the OPA cases used in CT-guided implantation procedures. Number of needle advancements, implantation time and complications are provided (cases 1-7 are single sensor implantations, cases 8 and 9 are double sensor implantations).

Case	No. of CT scans/needle advancements	Time from initial CT scan to sensor implantation (min)	Sensor placed within OPA tissue	Complications post-sensor placement
1	4	31	Yes	**Immediate:** Mild pneumothorax – not treated
2	3	58	Yes	**Immediate:** Mild pneumothorax – treated successfully with a single thoracocentesis
3	4	46	Yes	**None**
4	4	56	Yes	**None**
5	4	26	Yes	**None**
6	4	60	Yes	**Immediate:** Mild pneumothorax – not treated **Delayed:** Progression of pneumothorax with severe lung lobe collapse and development of subcutaneous emphysema. Final sensor position was within the pneumothorax
7	5	43	Yes	**None**
8	4	73	Yes	**None**
9	4	50	Yes	**Immediate:** Mild pneumothorax – treated successfully with a single thoracocentesis

8.3.7 Iatrogenic pneumothorax is a potential complication following percutaneous sensor implantation

Sensor implantation in 4 cases was associated with iatrogenic pneumothorax. One case (case 1) developed a mild pneumothorax immediately post-sensor implantation; this did not require thoracocentesis and did not progress over the course of the experiment. Two cases (case 2 and 9) also developed a mild pneumothorax immediately post-sensor implantation; each case received a single percutaneous thoracocentesis immediately following pneumothorax detection. CT scans post-thoracocentesis confirmed lung lobe re-expansion with removal of most of the air from within the thoracic cavity. Continuous sensor recordings were performed for approximately 2 h before each sheep was euthanised and a post-mortem CT scan performed. These scans identified no pneumothorax recurrence and confirmed that the sensor had remained within OPA tissue throughout sensor recordings (Figure 8.11).

A final case (case 6) also developed a mild pneumothorax immediately post-sensor implantation, with evidence of a small amount of air surrounding the lead wire in the thoracic wall musculature and subcutaneous tunnel. Thoracocentesis was not performed as only a small volume of air was initially present within the thoracic cavity. Continuous sensor recordings were performed for approximately 4.5 h before the sheep was euthanised and a post-mortem CT scan performed. This CT scan identified pneumothorax progression with further retraction of the lung margins away from the chest wall in the region of the implantation site. Lung lobe retraction was associated with sensor displacement causing both the sensor and lead wire to be situated within the pneumothorax. Significant progression of subcutaneous emphysema had also occurred (Figure 8.12).

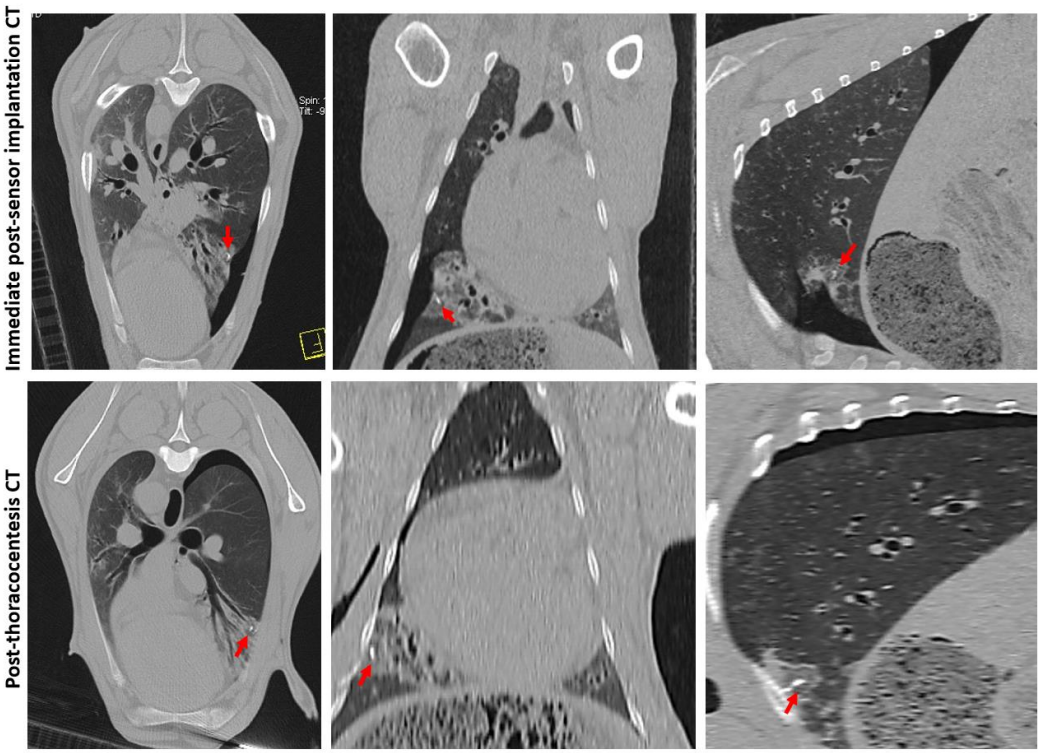

Figure 8.11. CT images documenting iatrogenic pneumothorax. CT images are from case 2. The OPA target lesion is seen as a patchy area of increased radiopacity affecting the ventral region of the right caudal lung lobe. CT scans were taken immediately post-sensor implantation and following euthanasia (2 h post-sensor implantation). A mild pneumothorax was evident immediately post-sensor implantation, predominately localised to the region of the implantation site. The sensor can be seen within OPA tissue (red arrows). Thoracocentesis was performed immediately post-sensor placement, which resulted in lung lobe re-expansion and removal of most of the air from within the thoracic cavity. Following euthanasia, CT scans confirmed successful management of the pneumothorax with reinflation of the collapsed caudal lung lobe and confirmed the sensor had remained within OPA tissue throughout sensor recordings.

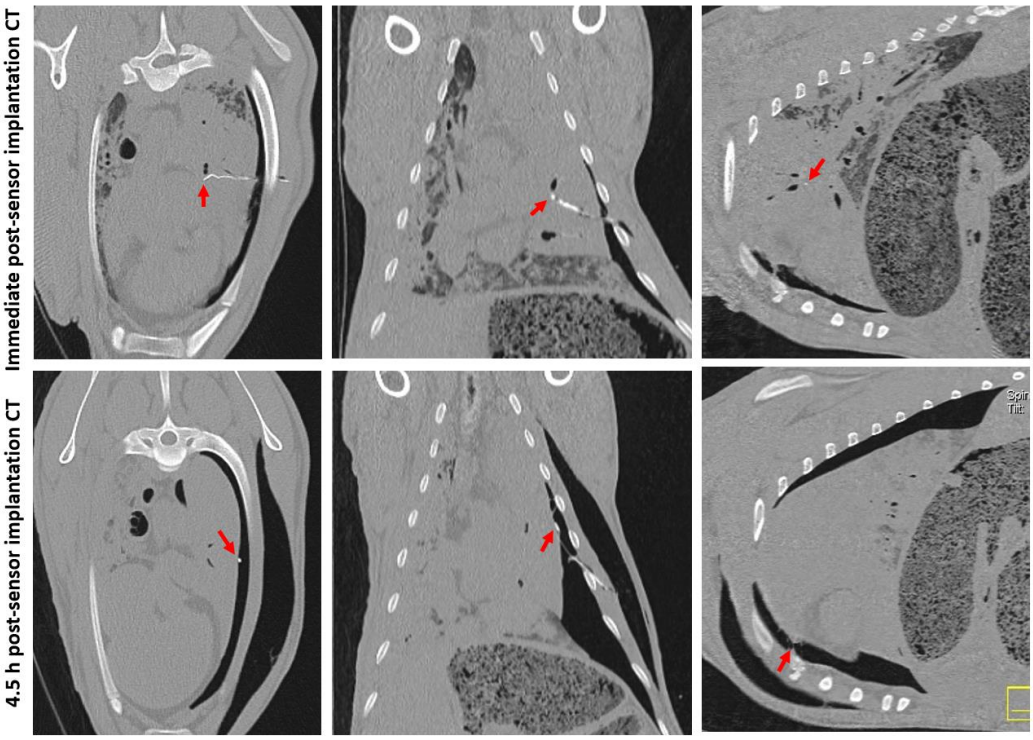

Figure 8.12. CT images documenting iatrogenic pneumothorax. CT images are from case 6. CT scans were taken immediately post-sensor implantation and following euthanasia (4.5 h post-sensor implantation). A mild pneumothorax was evident immediately post-sensor implantation. A small amount of air can be seen in subcutaneous tissues where the lead wire is exiting the thoracic cavity. The sensor can be seen positioned within OPA tissue (red arrows). Thoracocentesis was not performed. Following euthanasia CT scans identified significant progression of the subcutaneous emphysema and pneumothorax. In the axial and coronal planes, the sensor can now be seen positioned on the lung surface within the pneumothorax.

8.3.8 Appropriate anaesthetic protocols enable OPA sheep to remain physiologically stable throughout anaesthesia

To assess physiological stability of OPA sheep throughout anaesthesia, blood-gas, biochemical and haematological data was combined with variables such as HR, RR, CT, and MAP. Results from sheep maintained at FiO_2 of 1.0 showed that physiological and arterial blood variables remained stable with no statistically significant changes occurring over time. Elevated blood lactate levels were identified throughout anaesthesia but showed a tendency to reduce at later time points. Although PaO_2 levels showed marked individual variation and were lower than expected given the FiO_2 of 1.0 (suggesting compromised alveoli O_2 uptake), it was possible to maintain SaO_2 levels above 95%. Peak inspiratory pressure increased throughout anaesthesia, with values at 180 min almost 1.5 times greater than that recorded at 30 min (Figure 8.13).

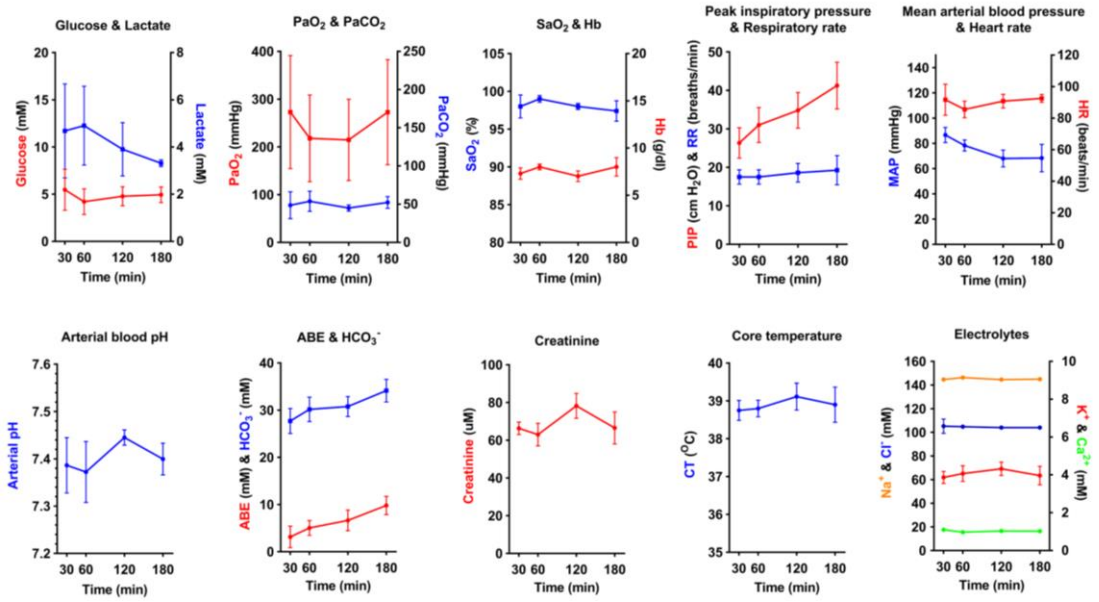

Figure 8.13. Physiological parameters remained stable throughout anaesthesia. Physiological data obtained from OPA cases maintained at FiO_2 of 1.0 throughout anaesthesia (data expressed as mean ± SEM, n=3-5 per time point; times indicate min post-induction of anaesthesia) (Hb, haemoglobin; ABE, arterial base excess; HCO_3^-, bicarbonate; SaO_2, haemoglobin O_2 saturation; PaO_2, arterial O_2 partial pressure; $PaCO_2$, arterial CO_2 partial pressure; CT, core temperature; PIP, peak inspiratory pressure; RR, respiratory rate; HR, heart rate).

8.3.9 Current generated by the sensor responded to alterations in inspired oxygen concentrations

To assess the ability of the sensors to detect changes in intra-tumoural ptO_2 through changes in blood oxygenation we performed sequential alterations in FiO_2, ranging from 0.21-1.0 (Figure 8.14a). Each FiO_2 alteration was performed at 20 min intervals delivered through a flowmeter via the isoflurane vaporiser. The cycle of FiO_2 alterations was: 1.0 for 20 min (baseline), 0.5 for 20 min (inducing mild hypoxaemia), 0.21 for 20 min (inducing moderate hypoxaemia) before finally returning to 1.0 for 20 min. Arterial blood samples were taken at the end of each FiO_2 challenge.

Baseline current recordings were first obtained using FiO_2 of 1.0. The mean sensor current recorded during this baseline period was -1.67 ± 0.80 nA. Following FiO_2 reductions to 0.5 and then to 0.21 sensor recordings decreased to -1.27 ± 0.59 nA and -0.78 ± 0.30 nA respectively. Upon increasing FiO_2 back to 1.0 sensor recordings rose to -1.24 ± 0.69 nA (Figure 8.14b & Table 8.5). Alterations in sensor currents occurred over a period of 10-15 min following each change in FiO_2 and

although trends were identified, these current changes were not statistically significant when compared with baseline recordings. At the end of each FiO_2 challenge arterial blood-gas analysis confirmed the expected physiological changes induced by each challenge. SaO_2 and PaO_2 both decreased at 0.5 and 0.21 and increased back to baseline levels at 1.0. Hb concentration remained the same throughout each challenge, as expected (Figure 8.14c & Figure 8.14d).

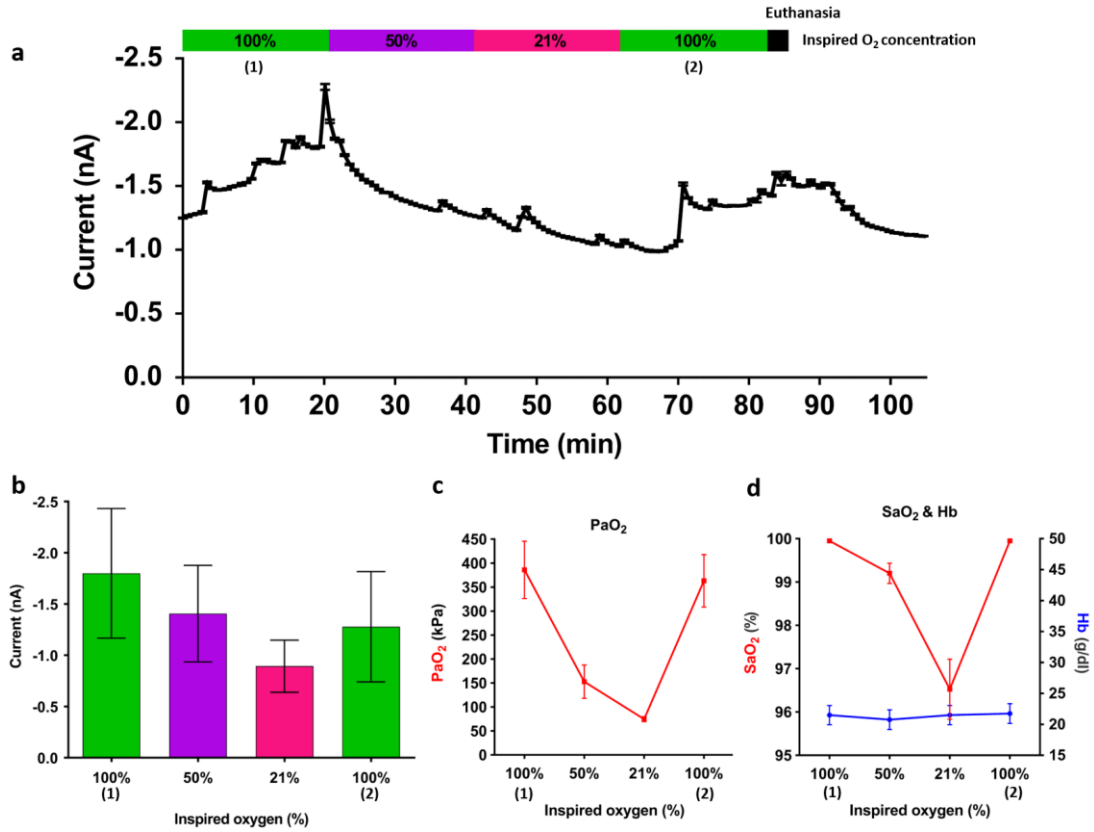

Figure 8.14. Sensor currents change in accordance with alterations in FiO_2. (a) Representative graph showing current generated at the working electrode of the sensor during continuous sensor recordings over a period of 100 min. Each FiO_2 challenge was performed in 20 min blocks. **(b)** Combined analysis comparing current generated at the working electrode of the sensor during each FiO_2 challenge; results show mean current readings from throughout each 20 min period (one-way ANOVA with Holm-Šídák multiple comparisons test; data expressed as mean ± SEM, n=4). **(c&d)** Arterial O_2 partial pressure, total haemoglobin and haemoglobin O_2 saturation measured at the end of each FiO_2 challenge.

Table 8.5. Current recordings generated during each FiO_2 challenge. (n=4; mean ± SEM).

FiO_2	100% (1)	50%	21%	100% (2)
Current (nA)	-1.67 ± 0.80	-1.27 ± 0.59	-0.78 ± 0.30	-1.24 ± 0.69

8.3.10 All implantation sites were identified during post-mortem examination

Following completion of sensor recordings, euthanasia and final CT scans all sheep underwent post-mortem examination. Gross pathology allowed the assessment of lung pathology, identification of the implant site and provided the opportunity to obtain biopsy specimens for histopathological analysis.

Upon entering the thoracic cavity OPA affected regions failed to collapse. Gross pathology identified lesions that were in accordance with those identified on the CT scans in terms of number of lesions, location and size. The majority of tumours were extensive, often involving the majority or entire lung lobe (Figure 8.15a & Figure 8.15b); however occasional multifocal discrete lesions affecting different lung lobes were seen (Figure 8.15c). OPA tumours typically caused distortion of the normal architecture of the affected lung lobe and had a grey colouration, with clear boundaries between tumour tissue and adjacent pink aerated lung. Although the smooth contour of the overlying pleura typically remained intact, several cases had the presence of fibrinous adhesions between the visceral pleura and chest wall. No evidence of intra-thoracic metastasis was identified, with all tracheobronchial and mediastinal lymph nodes appearing grossly normal in all cases. All sensor implantation sites were successfully identified with an entry site seen in the visceral pleura overlying OPA tissue. In 1 case an area of petechial haemorrhage was evident to the lung surface in the region of the implantation site; however, the remaining cases had no gross evidence of parenchymal haemorrhage or haemothorax.

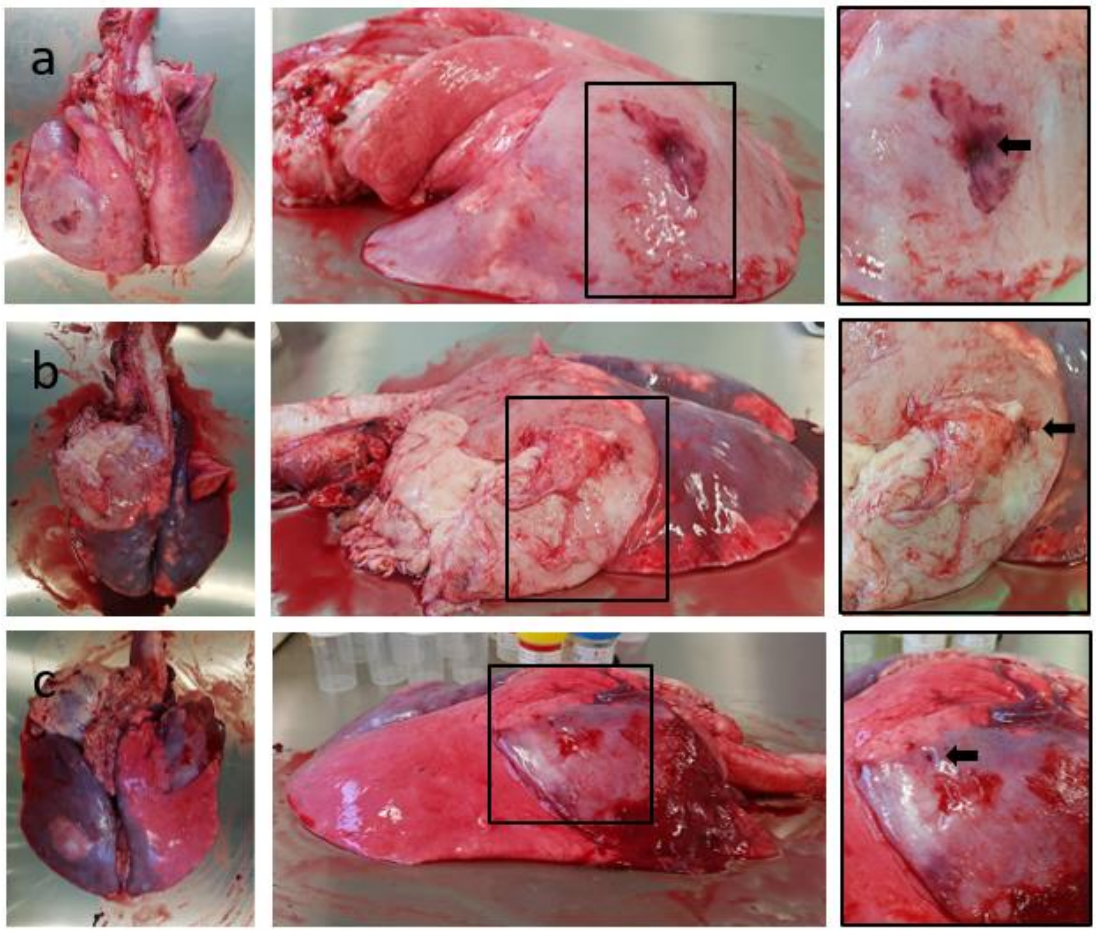

Figure 8.15. Photographs depicting gross pathology seen in typical OPA cases. These photographs are from the implantation cases presented in Figure 8.9. Each implantation site is highlighted with a black arrow. **(a)** Large grey consolidated mass affecting the majority of the left caudal lung lobe. An area of petechial haemorrhage can be seen on the surface of the lung surrounding the needle entry point. **(b)** Large grey consolidated mass affecting the majority of the left cranial lung lobe. Fibrous tissue can be seen adherent to the lung surface just cranial and ventral to the needle entry point. **(c)** One large dark coloured mass affecting the right cranial lung lobe containing the implant site with a further focal lesion within the left caudal lung lobe.

8.3.11 Histopathology of OPA tissue and implant site identified variable amounts of intra-pulmonary haemorrhage

Following gross pathology, the implant site was dissected from OPA tissue. The biopsy specimen was used for both OPA diagnosis and to assess the effects of the implantation procedure on OPA/lung tissue. Histological examination confirmed OPA diagnosis in all cases used for implantations, identifying non-encapsulated neoplastic foci forming acinar and papillary proliferations. In advanced cases separate foci had coalesced into a single large tumour (Figure 8.16a). The extent of inflammation varied considerably between cases and between different tumour areas

in the same case. In all cases large numbers of alveolar macrophages were identified within alveolar spaces (Figure 8.16b). Mononuclear cells including plasma cells and lymphocytes were also common, with some showing prominent lymphofollicular aggregates (Figure 8.16c). Neutrophilic infiltration was also seen, but not to the same extent as lymphocyte numbers. In all tumours, fibrovascular connective tissue was identified surrounding tumour cells (Figure 8.16d).

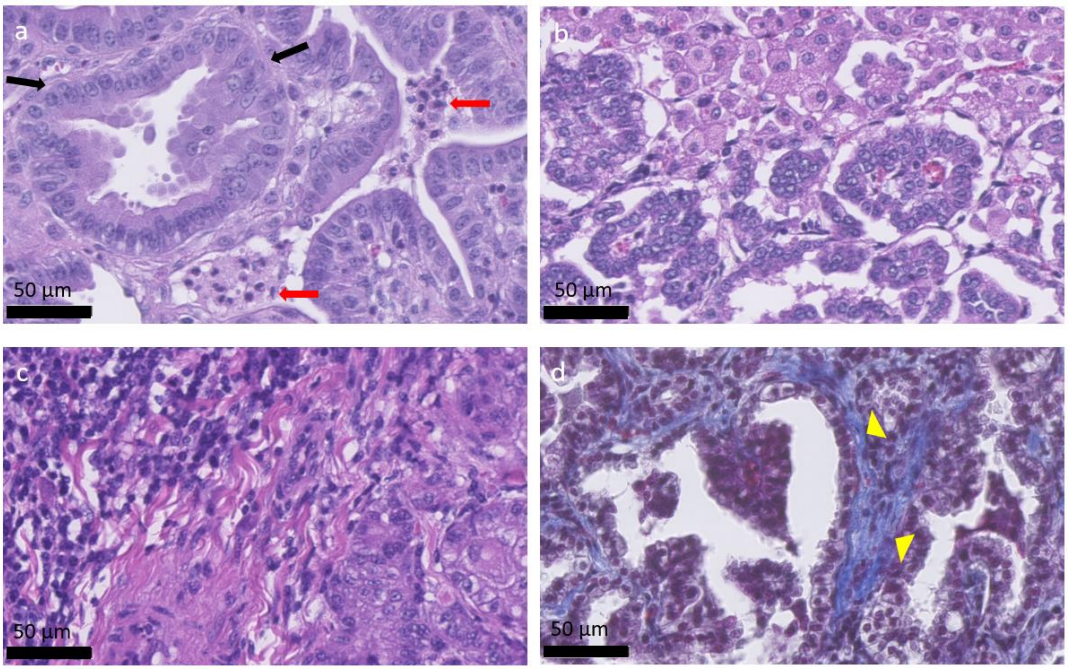

Figure 8.16. Histological appearance of OPA tumours. (a-c) H&E stained sections. **(a)** Columnar tumour cells can be seen lining the alveolar septa (black arrows). Two groups of neutrophils (red arrows) can be seen between the tumour cells. **(b)** Alveolar macrophages are present at the top right-hand side of the image. **(c)** Mononuclear cells, lymphocytes and plasma cells can be observed at the top left-hand side of the image. **(d)** Masson's trichrome stained section. Collagen is stained blue (yellow arrow heads) and can be identified surrounding the tumour cells.

Histopathology identified tumour cells immediately adjacent to the implant site in all cases; however, the percentage area composed of tumour cells varied ranging from 50% in 2 cases up to 80-95% in the remaining 7 cases. Evidence of haemorrhage within the needle tract and implantation site was identified in all cases; however, there was marked variation in the extent of haemorrhage seen between cases. Cases in which the needle passed through areas predominantly composed of tumour cells had evidence of bleeding restricted to within the needle tract itself, whereas cases in which the needle passed through areas of more normal lung showed evidence of intra-alveolar haemorrhage (Figure 8.17 & Figure 8.18).

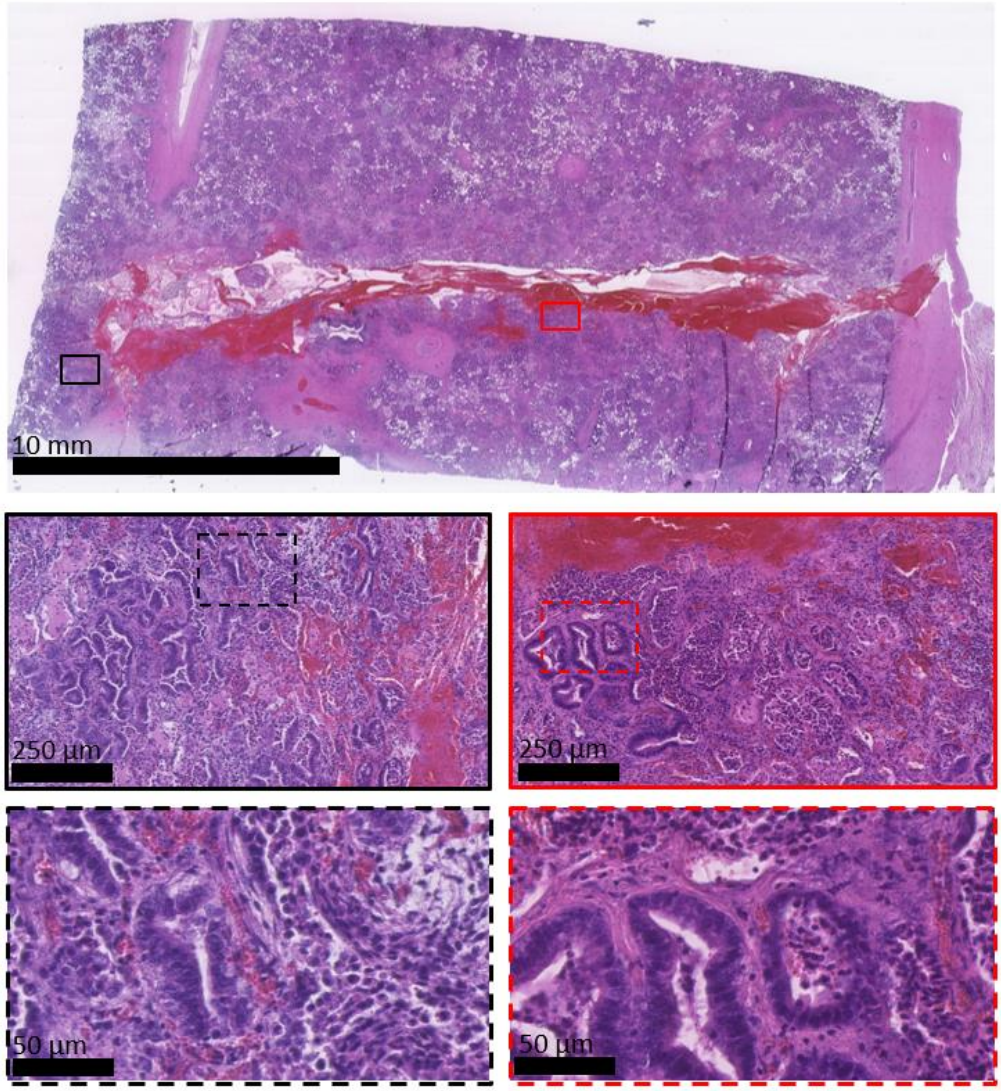

Figure 8.17. Histological appearance of OPA tissue and implantation site. H&E stained sections. The top image shows the needle tract penetrating through the visceral pleura and into OPA tissue. Large numbers of erythrocytes can be seen within the needle tract. Higher magnification images document smaller numbers of erythrocytes extending up to 250 µm from the implant site, predominately located within stromal tissue.

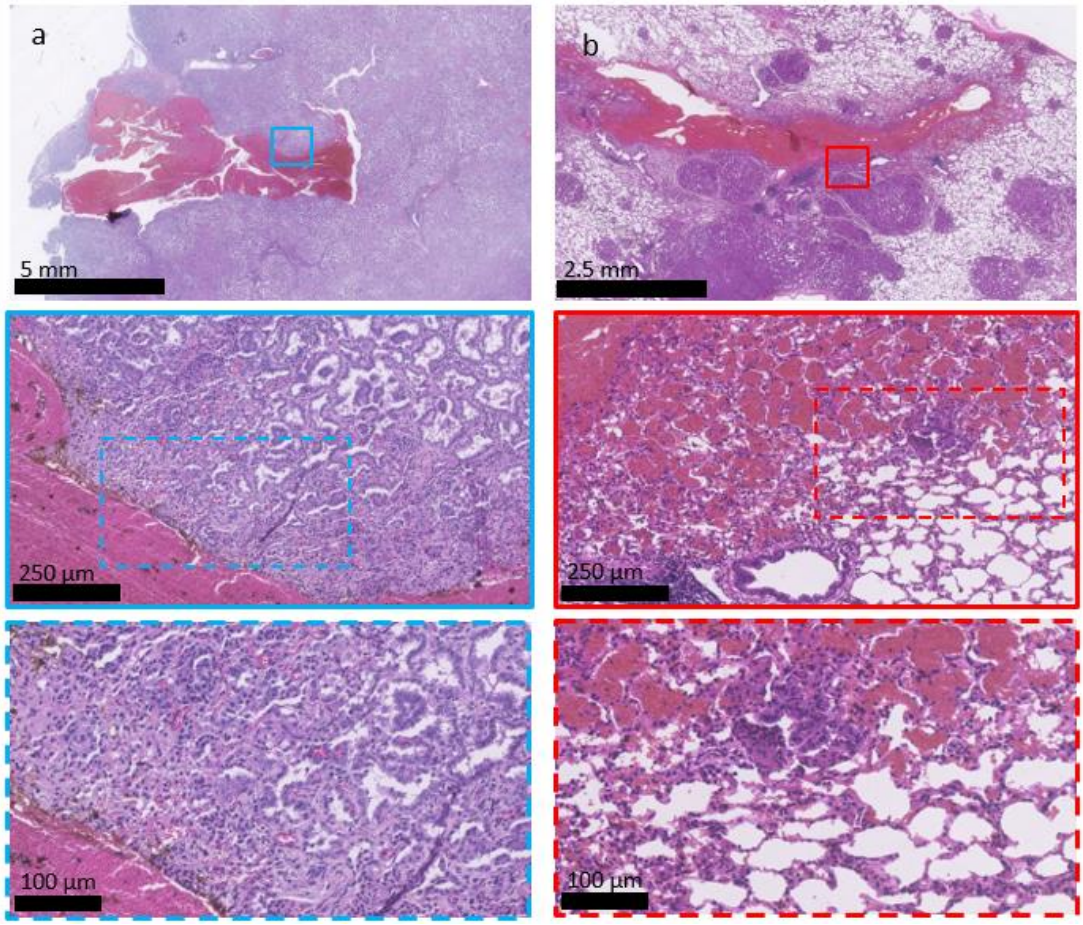

Figure 8.18. Histological appearance of OPA tissue and implant site with minimal and moderate intra-parenchymal haemorrhage. H&E stained sections. **(a)** The implant site is contained within an area consisting predominantly of tumour cells. The needle tract contains large numbers of erythrocytes; however, only small numbers are identified within OPA tissue adjacent to the implant site. **(b)** The implant site is contained within an area consisting of both tumour cells and more normal aerated lung tissue. The needle tract contains large numbers of erythrocytes; however, large numbers of erythrocytes are also identified within alveolar spaces and stromal tissue adjacent to the implant site.

8.4 Discussion

Similarities between OPA and human lung adenocarcinomas, in terms of disease presentation, progression and histological classification, has led to OPA becoming regarded as an excellent model for studying various aspects of human lung cancer biology. *In vitro* and *in vivo* OPA experimental models are well documented and have been used to elicit molecular pathways involved in lung cancer pathogenesis. However, if the disease is to be used as a pre-clinical research tool for human lung cancer, then techniques used in human medicine must be incorporated into the OPA model to demonstrate its translational ability. In order to achieve this,

our novel OPA model, used for validation of the IMPACT O_2 sensors, was developed from protocols currently used in human thoracic medicine[700].

Human lung cancer diagnosis and staging is typically performed from aspirates or biopsy specimens taken using a flexible bronchoscope[701] or via a trans-thoracic approach[702-704]. As both techniques provide an accurate way to obtain a diagnosis[705,706] the choice of which technique to use is largely dependent on lesion location. Central lesions that involve bronchi are readily assessible with a bronchoscope. Peripheral lesions, not visible on endobronchial examination[705], or are less than 3 cm in diameter that do not show a bronchus entering the lesion on CT images, are diagnosed more accurately by minimally invasive trans-thoracic needle biopsy (TTNB)[702,703,707]. Modified techniques of both endoscopic and percutaneous biopsy approaches could have been used in our OPA model for sensor implantations; however, the trans-thoracic percutaneous approach was chosen for several reasons. Initial OPA lesions from naturally occurring cases typically begin at the peripheral regions of the lung lobes. Only as neoplastic foci enlarge and coalesce do the central regions of the lobes become affected. Although bronchioles will frequently be surrounded by tumour tissue the larger bronchi may remain largely unaffected. Although endoscopy can be performed in sheep[275], successful endoscopic sensor implantation would only be possible in tumours which involved bronchi of sufficient diameter that can accommodate the endoscope. This selection criteria would significantly limit the number of cases that could be used and realistically would only be able to be assessed once sheep are anaesthesied and CT images have been obtained. Significant volumes of lung fluid produced by OPA tumours, present in the large and small airways, would also hamper endoscopic airway visualisation and make sensor implantation challenging. The presence of the endoscope within the airway could also hinder the delivery of fresh airflow and hamper attempts to suction away lung fluid. The IMPACT O_2 sensor is also currently wired, and endoscopic delivery would mean that the lead wire would be required to run up through the large airways and out through the larynx; the presence of the endotracheal tube would make this almost impossible. These limitations directed us to develop the trans-thoracic percutaneous approach for sensor implantations[700].

For the development of our OPA model we undertook a staged series of experiments. Each development stage increased the complexity of the model; initially beginning with post-mortem cadavers and finally resulting in a refined protocol used in experimental sheep. Although the cadavers did not have lung pathology, these experiments allowed the initial development and refinement of the surgical procedure and provided information on accessible lung regions through each intercostal space. Using cadavers, we were able to successfully implant sensors into lung tissue using the 4^{th}-8^{th} intercostal spaces on both sides of the thorax. An important consideration is that in live, anaesthetised sheep the positions of accessible regions of the lungs are likely to be slightly different from the results gathered using post-mortem cases. In ruminants the costodiaphragmatic recess can enlarge following death due to atelectasis (causing the caudal border of the lung to move cranially) and from cranial displacement of the diaphragm due to ruminal bloat. These factors are likely to have reduced the implantation window seen using these post-mortem cases. Sensor implantation in these experiments was performed blind, without any image guidance; consequently, assessment of sensor implantation into lung parenchyma was difficult as there was little perceptible tactile feedback from penetration of the visceral pleura. Significant elastic deformation of the lung occurred prior to Jamshidi penetration; this degree of lung deformation could increase the risk of undesirable lung contusions surrounding the implantation site. However, as OPA tumours are likely to be consolidated with areas of fibrosis and adhesions to the parietal pleura, elastic deformation of the visceral pleura as seen using these cadavers was likely to be less of an issue. Following completion of post-mortem experiments, the next stage in model development was identifying an appropriate image guidance technique to aid sensor implantation.

In human medicine TTNB requires the use of image guidance. Fluoroscopy was once the preferred imaging modality of choice as it enabled needle advancements to be visualised in real-time[708]; however, access to deep lesions and avoidance of vascular structures and bullae proved difficult with this method[709]. Ultrasound has the advantage that needle movements can be monitored precisely and extremely quickly during the procedure and can improve the accuracy of obtaining samples from necrotic lesions[710,711] whilst avoiding radiation exposure; however, its

use is restricted to peripheral lesions that produce an acoustic window. CT is now the most commonly used image guidance technique for TTNB. Samples obtained using this procedure have excellent diagnostic accuracy rates ranging from 66–96%[706,712,713]. CT has the advantage over fluoroscopy in that it allows accurate planning of needle path trajectories that avoid aerated lung, bullae, fissures or blood vessels. The procedure can also be used to sample central lesions and those less than 1 cm in diameter[714]. As with ultrasound, CT images can distinguish between necrotic and solid regions of a lesion, allowing for better diagnostic samples to be obtained. CT can be combined with fluoroscopy (CTF) to allow needle adjustments to be made in almost real-time. The technique is primarily used for very small lesions located in difficult to access thoracic regions such as in the costodiaphragmatic recess, or those close to the mediastinum or critical at-risk structures. The procedure can also be performed quickly, which is advantageous in high risk or un-cooperative patients[715].

Although any of these image techniques could have been used in our OPA model, CT was chosen for several reasons. CTF was not considered necessary for our cases and would have required the use of lead aprons and radiation shields for safety purposes. Although ultrasound guidance could have been used for sensor implantations into OPA lesions affecting pleural surfaces, it cannot provide an assessment of pathological lesions occurring throughout the entire thorax. These factors directed us to use CT guidance for sensor implantations[700].

During implantation procedures each CT scan was carefully reviewed. The initial scan allowed for lesion selection for sensor implantation with sequential scans being used to accurately assess needle trajectory and position. Lesion selection and needle path planning was based on risk factors associated with the development of TTNB complications such as pneumothorax and haemorrhage. Risk factors that contribute to TTNB complications include lesion characteristics and underlying disease pathology such as small lesions and the presence of emphysema[716] or chronic obstructive pulmonary disease[717]. Technical factors when performing TTNB including increased amounts of normal aerated lung crossed by the needle[718,719], a small oblique needle angle with the thoracic pleura[720], multiple needle repositionings[721], a greater number of sampling procedures[722], the absence of previous ipsilateral surgery[723], using a trans-fissure approach[719] and damage to

thoracic vasculature can also increase complication rates. In accordance with these known risk factors, lesions were chosen so that the needle path avoided passing through bullae, large vessels, bronchi and interlobar fissures. If possible, a short straight path from the skin to the lesion, that crossed the pleura into the lung at 90 degrees was planned. If more than 1 lesion was present, a peripheral lesion was chosen to decrease the amount of lung tissue that would be traversed[724].

The length of time required to perform CT-guided TTNB in human patients is 1 potential limitation of the procedure, even though procedural length or needle dwell time within the lung has not been associated with increased risk of pneumothorax[722]. In our model single sensor implantations were performed in a time of 45 ± 5 min (mean ± SEM), which is similar to studies in human patients that have documented CT-guided TTNB procedure times of up to 66 min. The radiation risk associated with CT-guided TTNB is a potential concern as the patient effective dose is often greater than standard thoracic CT scans[725]. In our study we did not consider radiation exposure as experiments were performed as non-recovery procedures. However, future studies to investigate if the radiation dose received by these sheep is comparable with that used in human TTNB procedures could be performed.

TTNB in humans is commonly performed under local anaesthesia; however, general anaesthesia was mandatory in our OPA model to ensure sheep and personnel safety. General anaesthesia of OPA sheep can be challenging due to respiratory compromise originating from OPA lesions, lung lobe consolidation, increased respiratory tract secretions, secondary infections and anaesthesia-induced atelectasis. These factors have the potential to lower PaO_2 levels by decreasing the effective movement of inspired O_2 into the blood. In our cases adequate haemoglobin oxygen saturation was achieved by increasing FiO_2 in combination with mechanical ventilation. Although OPA cases may require additional anaesthetic monitoring with respiratory and cardiovascular support, all our cases were successfully managed throughout sensor validation experiments, providing evidence that OPA cases can be used in procedures that require general anaesthesia.

The surgical procedure itself underwent several refinements until the final protocol was defined. From our initial 3 cases the major refinements included the use of radiopaque grid lines for improved accuracy of lesion localisation and performing

serial CT scans to aid needle positioning and sensor implantation. Careful handling of the implantation needle was essential to reduce the risk of iatrogenic lung damage during the surgical procedure, both during its initial insertion and subsequent advancements. One hand placed at the needle tip, near the skin surface, was used to stabilise the needle and prevent excessive needle advancement, while the other hand held the needle hub and provided downward pressure to advance the needle. The needle trajectory was maintained with each advancement as small deviations at the needle hub would produce large deviations at the needle tip. One issue that was encountered was the hub weight of the Jamshidi needle, which had the potential to cause the needle to list/move to one side until it was advanced sufficiently into OPA tissue to support its weight. To reduce the risk of needle movement causing lung damage it was only advanced to the level of the parietal pleura during its initial placement. Only when the needle position was confirmed on CT images was it advanced through the pleura, to the pre-measured depth, seating the needle sufficiently within lung/OPA tissue to prevent listing. Between each subsequent needle advancement, the needle was allowed to move with respiratory motions to prevent damage to lung tissue. Only following CT confirmation of the desired position of the needle tip in the OPA lesion was sensor implantation performed.

Following sensor implantation an immediate CT was performed to evaluate sensor positioning and assess for complications. Known TTNB associated complications are pneumothorax, bleeding (haemoptysis, haemothorax), infection, air embolism, lung lobe torsion and needle tract metastasis. Estimated TTNB mortality rates are very low (approximately 0.02%) and are mainly caused by air embolism or massive haemoptysis[726]. By far the most common complications associated with TTNB are pneumothorax and haemorrhage[700].

Pneumothorax is the most common complication seen following TTNB. Although rates as high as 54% have been documented[727,728], accepted occurrence rates are more likely to be in the region 17–26%, of which only 14% will require treatment through percutaneous aspiration or chest tube insertion[720,723,729,730]. Although most cases will be evident within 60 min following the procedure, serial x-rays up to 3 h post-procedure are usually performed to ensure that a delayed pneumothorax has not occurred[731,732]. In our series of experiments 4 out of 9 cases

(44%) developed an immediate pneumothorax. Three of these cases were classified as mild, with 2 requiring percutaneous needle thoracocentesis. The 2 cases that received thoracocentesis fully resolved and did not show any pneumothorax recurrence; this was likely due to removal of all the excess pleural air from around the implant site, allowing apposition of visceral and parietal pleural surfaces. The remaining case also developed a mild immediate pneumothorax which was not severe enough to warrant drainage. However, following 4.5 h of sensor recordings the post-mortem CT scan identified progression of the pneumothorax with significant subcutaneous emphysema. This case demonstrated the need for repeat CT scans to detect delayed complications. Measures that were taken to reduce the risk of pneumothorax included the use of a coaxial technique to allow the sensor to be placed with a single pleural puncture, and as described above, careful needle path planning. Other techniques which may help reduce pneumothorax occurrence is the technique of obliterating, or 'patching' the needle track by injecting 2–3 ml of blood during withdrawal of the needle[704]. Although this would have been possible to perform it may have interfered with the lead wire and caused the sensor to move whilst the needle was being removed. Following sensor placement, the sheep could also have been repositioned with the puncture site down; however, this would have made connections from the lead wire to recording instrumentation difficult.

Haemorrhage is the second most common TTNB complication occurring in approximately 4-10% of cases[729,733]. Bleeding may be evident as fresh blood passing up through the bore of the needle, or as a ground-glass appearance in CT images in the area of the biopsy or along the needle tract. Fortunately, haemothorax is exceedingly rare, with an incidence of less than 1%[726]. Measures that were taken to reduce the risk of haemorrhage included the avoidance of large pulmonary vessels by the needle path and directing the needle away from the aorta and the heart. Placing the needle through the centre of the intercostal space also reduced the risk of damage to intercostal neurovascular bundles. In our series of experiments no cases were identified as having post-implantation haemorrhage based on CT image evaluation; however, following post-mortem examination and implant site histopathology erythrocytes were identified within the needle tract in all cases. Variable amounts of erythrocytes were also identified in OPA tissue away from the needle tract itself,

possibly to a greater extent in cases where the needle passed through more normal areas of lung tissue. This observation is likely due to OPA affected regions having reduced compliance compared with normal lung tissue, with OPA tissue potentially acting as a tamponade preventing the escape of erythrocytes into the tumour tissue, whereas alveolar spaces would act as reservoir for the erythrocytes. The under reporting of alveolar haemorrhage based on the CT scans is likely due to the appearance of the OPA lesions themselves. All cases had large OPA lesions involving the visceral pleura that were characterised as having increased radiopacity, frequently with the presence of air bronchograms. This OPA CT appearance would have likely obscured any haemorrhage that occurred within the needle path.

One factor that could have contributed to the complication rate seen in our model is the choice of needle that was used for sensor implantations. Needle selection was dictated by the dimensions of the IMPACT sensors; a needle with an internal bore diameter of sufficient size was therefore needed to accommodate the sensor and lead wire. As a result of this an 8G Jamshidi needle was required. This size of needle is considerably larger than the 18-22G needles that would be routinely used in human TTNB procedures. Further development and miniaturisation of the IMPACT O_2 sensor will ultimately allow smaller diameter needles to be used, which will reduce complication rates, especially as bleeding complications are thought to be minimised by using needles smaller than 18G.

Following successful development of the implantation procedure we wished to investigate the functionality of the IMPACT O_2 sensor within the OPA TME. In order to achieve this, we determined if alterations in blood oxygenation levels, through changes in FiO_2, would cause changes in intra-tumoural ptO_2 that could be detected by the sensor. Arterial blood-gas analysis was used to confirm the expected physiological responses to FiO_2 alterations. Hypoxia caused reductions in both PaO_2 and SaO_2, whereas hyperoxia caused their levels to increase. Changes in sensor currents occurring with FiO_2 challenges matched the same pattern of results obtained using arterial blood-gas analysis, with lower and higher currents generated in hypoxaemic and hyperoxaemic conditions respectively. Although, these current changes were not statistically significant when compared to baseline currents generated at FiO_2 of 1.0, they demonstrated that the IMPACT O_2 sensor could detect

changes in intra-tumoural ptO_2. The large variation seen in the results between sheep is likely due to the underlying dynamic nature and heterogeneity of the TME, highlighting the need to spatially map O_2 levels within a tumour. These results document, to the best of our knowledge, the first time that a sensor capable of monitoring intra-tumoural ptO_2 in real-time has been implanted into a solid tumour.

8.5 Conclusion

This chapter has described the use of naturally occurring OPA cases in the development of a novel *in vivo* ovine model for the CT-guided trans-thoracic percutaneous implantation of IMPACT O_2 sensors into lung tumours. This model was further developed to produce acute and reversible changes in intra-tumoural ptO_2 through alterations in FiO_2. These dynamic changes were detectable by the IMPACT O_2 sensors implanted into OPA tumours. Through the integration of techniques such as ultrasound, general anaesthesia, CT and surgery into the OPA model, we have shown the models translational potential and effectiveness as a pre-clinical research tool for human lung cancer. These results have provided evidence for further development of the IMPACT O_2 sensor towards clinical applications in cancer therapy. Our results also demonstrate that the model could be developed further for other pre-clinical uses, such as the procurement of biopsy specimens, the development of medical devices for the local delivery of chemotherapeutic agents, monitoring the TME and to assess the effectiveness of RT or systemic chemotherapeutic agents.

9 Future work

The development and characterisation of our novel human and canine breast and ovine lung cancer radioresistant cell lines in combination with the preliminary data obtained from the secretomic experiments has created numerous opportunities for future research. We envisage these 2 areas of research running both as standalone projects and in combination with each other.

Although genotypic, phenotypic and functional characterisation of the novel human ER^- and ER^+ radioresistant breast cancer cell lines was undertaken, time restrictions prevented analysis of the animal cell lines. Using transcriptomic data from the REM-134 and JS7 parental and RR cell lines, characterisation could be performed using similar analysis criteria as was applied to the human cell line datasets. This could provide important data, as this study is the first to describe the development of radioresistant canine mammary and ovine lung cancer cell lines. This may prove useful in the case of the REM-134 cell line, as canine mammary tumours are seen as excellent models for human mammary tumours and so could represent an excellent comparative model of human disease[734]. In particular, canine mammary tumours show homology to human mammary tumours in the activation of numerous pathways such as PI3K/AKT, KRAS, PTEN, WNT-β-catenin and MAPK[735], some of which were found to be differentially activated in our human parental and RR breast cancer cell lines. Characterisation of the JS7 RR cell line would also investigate the effects that chronic radiation exposure has on *in vitro* JSRV production. Evidence that suggests JS7 RR produces JSRV either in 2D or 3D cultures would provide an exciting and novel model to study virus production and radioresistance.

As stocks of the RR cell lines have been created and stored in liquid nitrogen this will allow future studies to be performed aimed at targeting the differentially activated pathways that we have identified in the RR cell lines. These studies would ultimately focus on radioresistance reversal. Although out-with the scope of this PhD study, these types of experiments are the logical next phase in the use of our radioresistance model. These types of models will likely be instrumental in the development of new therapeutic strategies for patients that either fail to respond to treatment or develop recurrent disease.

One area of research could involve the use of inhibitors against EGFR or its downstream targets. Several phase I and II trials have investigated the use of gefitinib with RT as a means of improving patient outcomes[736]. Although conflicting reports regarding the clinical benefit of using EGFR inhibitors have prevented the routine clinical use of these drugs, some studies have shown they can improve survival rates and quality of life[737,738]. As our results have reported that RR cell lines derived from ER^+ cells showed a shift from ER to EGFR signalling, with a corresponding increase in sensitivity to EGFR inhibition, it would seem logical to investigate inhibition of this pathway, including its downstream targets such as MAPK and PI3K as a means of overcoming radioresistance.

Another area of research would be to investigate WNT signalling, as this pathway was also found to be upregulated in RR cell lines derived from ER^+ cells. WNT and its downstream effectors regulate various processes that are important for tumourigenesis, progression, differentiation and metastasis[739] and further dissection of the pathway may identify targets that can be inhibited to reverse radioresistance. The global approach taken using multiple techniques for characterisation of our radioresistance model identified numerous pathways that were differentially expressed or activated between paired parental and RR cell lines. Although only 2 potential areas of future work have been highlighted here, multiple other pathways could be investigated in order to further characterise the mechanisms of acquired radioresistance and identify possible ways of targeting its development.

The secretomic pilot study has generated a vast amount of data that has yet to be fully analysed. Future work involving the secretomic-based biomarker experiments could be broken down into 4 primary areas: continued biomarker in-lab validation, biomarker detection in blood, mechanisms of biomarker secretion and the development of a potential biomarker signature predictive of RT response. The use of the developed RR cell lines could also continue for the identification of differentially secreted biomarkers as a means of determining radiosensitivity.

Secretome characterisation of untreated and radiation-treated MCF-7 cells identified 9 candidate biomarkers of which we have only started to validate 4. Future in-lab validation would investigate the remaining 5 biomarkers by assessing their secretion levels in CM from parental and RR cell lines 24 h after radiation treatment.

Further secretomic experiments could also be performed using MTS, as we have shown that MCF-7 RR, ZR-751 RR, MDA-MB-231 RR and REM-134 RR all form MTS. Although MTS are a more complex model compared with 2D cultured cells, they still suffer from the same limitations as 2D cultured cells in that they fail to account for the TME and the influence that stromal cells can have on cancer cells and their secretion profiles. Currently, our results are restricted to biomarkers released from cancer cells up to 24 h post-radiation. In order to assess biomarker secretion profiles in response to multiple fractions of radiation, experiments would need to include longer post-radiation time points. In order to overcome some of the aforementioned limitations of 2D and 3D MTS models, further experiments could include not only cancer cell line models, but also tumour explants. Precision cut lung slices of OPA tumours is a well-documented *in vitro* OPA model system[689,690]. This technique could be used in a variety of tissue types such as canine and human breast tumours. These experiments would begin to validate the biomarkers in a more complex model system. Currently, we have no evidence regarding biomarker secretion profiles from cells that have received multiple radiation fractions or how these profiles change beyond 24 h post-radiation. Further experiments continuing this work could begin to answer these questions and help move towards biomarker validation in real cancer tissue. Time course experiments would also allow for fixation of tumour samples after each radiation fraction in order to assess gene expression and intra-cellular protein levels.

Detection of biomarkers in CM of cancer cells or explants could provide robust evidence of their secretion in response to radiation. However, these biomarkers will need to be shown to be detectable in blood before they can be used clinically. Detection protocols and methods would need to be developed for use with either plasma or serum, using techniques such as immunoprecipitation or ELISA. If in-lab detection of biomarkers in blood samples can be achieved, then this could increase the scope of experiments further to include obtaining blood samples from human and veterinary cancer patients undergoing RT. Further *in vivo* validation experiments could be performed using our novel paired sensitive and RR cell lines grown in a xenograft tumour model. Although the generation of xenograft tumours using our RR cell lines has not been attempted before, this would provide an excellent model to

identify differentially secreted biomarkers from known sensitive and RR tumours. Tumours could be radiated and 24 h post-treatment blood samples could be obtained for biomarker analysis.

In order to investigate mechanisms of biomarker secretion, further work could also assess extra-cellular vesicle secretion pathways, as literature searches identified that all 33 candidate biomarkers are known to be secreted in exosomes or microvesicles. Experimental work could include microvesicle and exosome isolation and biomarker detection from the CM following radiation of cells, MTS and explants. The UPR also warrants further investigation, as we showed that the 3 pathways (PERK, IRE1α and ATF6) are differentially activated in ER^+ parental and RR cell lines and that several of our candidate biomarkers are involved with translation or protein trafficking. Using parental and RR cell lines, inhibition of each of the 3 pathways and through inducing ER stress and the UPR would indicate if these pathways play roles in radioresistance development or if they are involved in the secretion of our candidate biomarkers.

As we have shown that there is differential gene and intra-cellular protein expression between parental and RR cell lines, a further area of research would be to investigate whether these biomarkers could be used to produce a predictive signature of RT response. Validation of a panel of biomarkers with a gene signature that can differentiate between our parental and RR cell lines could initially be performed using publicly available datasets of breast cancer cell lines with a range of inherent radiosensitivities and by using clinical samples where follow up data on tumour recurance and survival is known.

Running in parallel to the *in vitro* experiments, the animal work conducted in this PhD project was aimed at producing pre-clinical data on the safety and functionality of the IMPACT O_2 sensor.

The successful validation of the ability of the IMPACT O_2 sensor to accurately detect dynamic changes in intestinal ptO_2 through ischaemic insults and alterations in FiO_2 in our murine model has provided justification for progressing the experiments into more complex translational large animal anastomotic leak models. Pigs are regarded as excellent gastrointestinal translational models, as they are similar to humans in size, anatomy and physiology. A porcine anastomotic leak model using a

low rectal resection and anastomosis, performed with a double-stapled anastomosis without protective ileostoma, has previously been described in the literature[740]. This model shows anastomotic leak rates of up 30% within 9 days following surgery, which is similar to that reported in the human literature. Development of this model could be used in future experiments using the IMPACT O_2 sensors. Initial experiments using a porcine model could involve a staged series of experiments like those used in the development of our ovine model. Experiments would progress from post-mortem cases to develop the surgical technique and assess the feasibility of placing sensors around a low rectal anastomotic site, through to non-recovery and recovery procedures. Porcine non-recovery models could be performed in which sensors are placed on normal bowel, bowel rendered ischaemic by vascular ligation and in proximity to a rectal resection and anastomosis. The resection and anastomosis could also be made to leak through the creation of a full thickness incision through the intestinal wall across the anastomotic site. These experiments would provide data on the ability of the sensors to detect ptO_2 in normal, ischaemic and peri-anastomotic intestine, as well as assessing their suitability for surgical implantation. Clinical, haematological and biochemical data with regards to anastomotic leakage and septic peritonitis could also be obtained. If these initial experiments provide encouraging results, then studies could progress into recovery models providing further evidence of the *in vivo* safety and performance of the IMPACT O_2 sensors.

One question that needs to be answered if the IMPACT O_2 sensor is to be used for resection and anastomotic applications in patients is how these sensors might be placed at the anastomotic site during surgery so that they remain at the site to measure post-operative intestinal ptO_2. Solutions to this issue would include their use akin to a surgical drain or through their incorporation into surgical staples.

Drains are used commonly in anastomotic surgery; although their effectiveness at reducing the occurrence of an anastomotic leak remains open to debate[741-743] they are not associated with any significant complications. Drains are placed in the region of the anastomotic site and exit the body through a skin incision to be connected to external drainage bags. These drains can be easily removed when no longer required, typically several days post-surgery. Drains have been used to obtain post-operative

peritoneal samples from anastomotic sites for measuring bacterial colonisation, cytokines[744] and metabolites[745] that might serve as indicators of early anastomotic leakage. We envisage that designing the IMPACT O_2 sensor in a similar configuration to a surgical drain would allow easy clinical use. The sensors, along with an electrical lead (similar in design to the current IMPACT O_2 sensor and lead wire), could be positioned on the intestine next to the anastomosis site at the time of surgery. The electrical lead would then pass out through the skin in a similar manner to a surgical drain allowing the sensor to be connected to the end-of-bed monitor in the surgical high-dependency unit, providing the surgical team with post-operative, real-time data on peri-anastomotic intestinal ptO_2 levels. The sensors could then be removed in a similar manner to the surgical drains. The advantage of this application would be that the IMPACT O_2 sensor would not require significant further development. Incorporation of IMPACT O_2 sensors into staples would have the advantage that peri-anastomotic ptO_2 could be measured around the entire circumference of the intestine, thus providing detailed spatial information. However, further technological development of the sensor through miniaturisation and the development of wireless technology would be required in order to achieve sensor integration into surgical staples.

The development of our novel OPA model was aimed at validating functionality of the IMPACT O_2 sensor within a solid tumour. However, as the model successfully incorporated techniques commonly used in the management of human lung cancer patients, we have demonstrated the model's translational potential and effectiveness as a pre-clinical model for human lung cancer. The use of the model for sensor implantation was associated with a complication rate similar to that seen in human medicine for TTNB, with pneumothorax being the most commonly encountered complication. We suspect that the size of the sensor and needle required for implantations were major contributing factors related to the complication rate seen. The potential for iatrogenic damage to alveolar spaces and small airways will be increased by using larger diameter implantation devices, which may then promote larger volumes of air to escape from airways within the lung into the pleural space. As the current IMPACT O_2 sensor is also wired, this meant that the lead wire had to run from the sensor (implanted within the tumour) through the chest wall to be

connected to external instrumentation. Although a subcutaneous tunnel was created to reduce the chances of air entering the thoracic cavity from the external environment, we did identify in a couple of cases air within subcutaneous tissues, suggesting that air was able to track within the needle tract created for sensor implantation. Further engineering development of the sensor, rather than modifying the model itself, will be needed to overcome these issues.

Further miniaturisation of the sensor will allow smaller gauge implantation needles to be used, which should reduce the volume of tissue damaged during implantation. Wireless technology would also eliminate the need for the lead wire and subcutaneous tunnel. If these technological advances could be achieved, then they could be utilised in experiments that require sheep to be recovered from anaesthesia following sensor implantation. Although we did investigate the use of wired sensors in recovery procedures by means of connecting the lead wire to a battery pack which was then secured to the sheep using a ram harness, this proved difficult to maintain for long periods of time and was not taken forward. The use of wireless sensors would overcome the need for external devices and make recovery procedures feasible. This would not only advance the OPA model but also provide a means by which new areas of research could be investigated, such as intra-tumoural biocompatibility and modelling of RT treatment programmes.

Our work to date did not investigate the effects of RT on *in vivo* sensor function; this will need to be addressed in the future as the primary aim of the IMPACT O_2 sensor is to monitor intra-tumoural ptO_2 throughout a patient's RT treatment programme. From initial CT scan images, before sensor implantation, RT treatment planning could be carried out in our model as is done in human medicine. Following routine sensor implantation, sheep could be allowed to recover from anaesthesia, and over a period of 2-3 weeks, undergo repeated anaesthetics and external beam RT. Clinically relevant fractionated dose regimes could be delivered to the OPA tumour which would validate the IMPACT O_2 sensor under clinically relevant conditions. Although this type of experiment would not be designed to assess the clinical response of the OPA tumour to RT, if they could be performed on multiple occasions over a period of several weeks then this would provide further evidence for the use of the IMPACT O_2 sensor towards clinical applications in cancer therapy.

Incorporating RT into the OPA model could also enable validation of the biomarkers released from OPA cancer cells in response to radiation. Blood samples taken before and 24 h after a radiation dose could be used to investigate the biomarkers identified through our *in vitro* secretomic experiments.

One of the limitations of the murine biofouling experiments was that the model was unable to be extended for periods that would include the entire chronic inflammatory phase of the FBR. Using OPA recovery procedures would overcome this limitation and would have the advantage of using functional sensors composed of all the biomaterials that were tested individually in the murine model. This would assess for any interactions between the individual biomaterials that could affect the FBR whilst using solid tumours in immunocompetent animals and provide further confidence in the intra-tumoural biocompatibility of the functional sensor and its constituent biomaterials.

The OPA model holds potential to be used for other pre-clinical applications beyond functional validation of the IMPACT O_2 sensor, especially as the disease itself is similar to human lung adenocarcinomas. The model could be adapted for the assessment of either systemically or locally delivered (image-guided injection or implantable drug release device) chemotherapeutic agents, with clinical effectiveness evaluated through a combination of imaging, on-treatment biopsies and post-mortem examination with sample collection.

The *in vivo* work described in this PhD study, ranging from small animal murine models to large animal ovine models, aimed to produce initial pre-clinical data to establish the safety and functionality of an implantable sensor that could be used to monitor *in vivo* environments in human medicine. While not specifically considered in this study, these implantable devices would be equally applicable for use in veterinary patients. Although significant progress has been made towards sensor validation for multiple clinical applications, further engineering development of the sensor with continued large animal validation is required. The ultimate goal of the project would be to apply to the Medicines and Healthcare products Regulatory Agency for approval for use in humans which would allow sensor validation to progress into human clinical trials.

10 References

1. Watson IR, Takahashi K, Futreal PA, Chin L. Emerging patterns of somatic mutations in cancer. Nature Reviews Genetics 2013;14:703-718.
2. Martincorena I, Campbell PJ. Somatic mutation in cancer and normal cells. Science 2015;349(6255):1483-1489.
3. Hanahan D, Weinberg RA. The Hallmarks of Cancer. Cell 2000;100(1):57-70.
4. Cancer_Research_UK. Cancer Statistics for the UK. www.cancerresearchuk.org (Accessed 22th March 2019).
5. Hanahan D, Weinberg RA. Hallmarks of Cancer: The Next Generation. Cell 2011;144(5):646-674.
6. Bray F, Ferlay J, Soerjomataram I, Siegel RL, Torre LA, Jemal A. Global cancer statistics 2018: GLOBOCAN estimates of incidence and mortality worldwide for 36 cancers in 185 countries. CA: A Cancer Journal for Clinicians 2018;68(6):394-424.
7. Bray F, Jemal A, Grey N, Ferlay J, Forman D. Global cancer transitions according to the Human Development Index (2008–2030): a population-based study. Lancet Oncology 2012;13(8):790-801.
8. Biesecker L, Blaser MJ, Wylie Burke, Chute CG, Eddy S, Jaffe E, Kelly BJ, Khosla C, Masys DR, Schwartz SM. The National Academies Collection: Reports funded by National Institutes of Health. Toward Precision Medicine: Building a Knowledge Network for Biomedical Research and a New Taxonomy of Disease. Washington (DC): National Academies Press (US). National Academy of Sciences.; 2011.
9. Alla K. Momentum grows to make personalized medicine more precise. Nature Medicine 2013;19(3):249-250.
10. Ghasemi M, Nabipour I, Omrani A, Alipour Z, Assadi M. Precision medicine and molecular imaging: new targeted approaches toward cancer therapeutic and diagnosis. American journal of nuclear medicine and molecular imaging 2016;6(6):310-327.
11. Penet M-F, Krishnamachary B, Chen Z, Jin J, Bhujwalla ZM. Molecular Imaging of the Tumor Microenvironment for Precision Medicine and Theranostics. Advances in cancer research 2014;124:235-256.
12. Collins FS, Varmus H. A New Initiative on Precision Medicine. New England Journal of Medicine 2015;372(9):793-795.
13. Carrasco-Ramiro F, Peiró-Pastor R, Aguado B. Human genomics projects and precision medicine. Gene Therapy 2017;24(9):551–561.
14. Seoane J, De Mattos-Arruda L. The challenge of intratumour heterogeneity in precision medicine. Journal of Internal Medicine 2014;276(1):41-51.
15. Gray M, Meehan J, Ward C, Langdon SP, Kunkler IH, Murray A, Argyle D. Implantable biosensors and their contribution to the future of precision medicine. The Veterinary Journal 2018;239:21-29.
16. Martinez-Perez C, Turnbull AK, Dixon JM. The evolving role of receptors as predictive biomarkers for metastatic breast cancer. Expert review of anticancer therapy 2019;19(2):121-138.

17. Mangelsdorf DJ, Thummel C, Beato M, Herrlich P, Schütz G, Umesono K, Blumberg B, Kastner P, Mark M, Chambon P. The nuclear receptor superfamily: the second decade. Cell 1995;83(6):835-839.
18. Mohammed H, Russell IA, Stark R, Rueda OM, Hickey TE, Tarulli GA, Serandour AA, Birrell SN, Bruna A, Saadi A. Progesterone receptor modulates ERα action in breast cancer. Nature 2015;523(7560):313-317.
19. Carroll JS, Hickey TE, Tarulli GA, Williams M, Tilley WD. Deciphering the divergent roles of progestogens in breast cancer. Nature Reviews Cancer 2017;17(1):54-64.
20. Viale G, Regan MM, Maiorano E, Mastropasqua MG, Dell'Orto P, Rasmussen BB, Raffoul J, Neven P, Orosz Z, Braye S. Prognostic and predictive value of centrally reviewed expression of estrogen and progesterone receptors in a randomized trial comparing letrozole and tamoxifen adjuvant therapy for postmenopausal early breast cancer: BIG 1-98. Journal of Clinical Oncology 2007;25(25):3846-3852.
21. Nemere I, Pietras RJ, Blackmore PF. Membrane receptors for steroid hormones: signal transduction and physiological significance. Journal of cellular biochemistry 2003;88(3):438-445.
22. Marino M, Galluzzo P, Ascenzi P. Estrogen signaling multiple pathways to impact gene transcription. Current genomics 2006;7(8):497-508.
23. Thomas C, Gustafsson J-Å. The different roles of ER subtypes in cancer biology and therapy. Nature Reviews Cancer 2011;11(8):597-607.
24. Bjornstrom L, Sjoberg M. Mechanisms of estrogen receptor signaling: convergence of genomic and nongenomic actions on target genes. Molecular endocrinology 2005;19(4):833-842.
25. Nicholson RI, Gee JMW. Oestrogen and growth factor cross-talk and endocrine insensitivity and acquired resistance in breast cancer. British journal of cancer 2000;82(3):501-512.
26. Arpino G, Wiechmann L, Osborne CK, Schiff R. Crosstalk between the estrogen receptor and the HER tyrosine kinase receptor family: molecular mechanism and clinical implications for endocrine therapy resistance. Endocrine reviews 2008;29(2):217-233.
27. Arthur LM, Turnbull AK, Khan LR, Dixon JM. Pre-operative Endocrine Therapy. Current breast cancer reports 2017;9(4):202-209.
28. Clarke R, Tyson JJ, Dixon JM. Endocrine resistance in breast cancer–an overview and update. Molecular and cellular endocrinology 2015;418:220-234.
29. Clarke R, Leonessa F, Welch JN, Skaar TC. Cellular and molecular pharmacology of antiestrogen action and resistance. Pharmacological reviews 2001;53(1):25-72.
30. Clarke R, Skaar TC, Bouker KB, Davis N, Lee YR, Welch JN, Leonessa F. Molecular and pharmacological aspects of antiestrogen resistance. The Journal of steroid biochemistry and molecular biology 2001;76(1-5):71-84.
31. Brueggemeier RW. Update on the use of aromatase inhibitors in breast cancer. Expert Opin Pharmacother 2006;7(14):1919-30.
32. McGuire WL. Estrogen receptors in human breast cancer. The Journal of clinical investigation 1973;52(1):73-77.

33. Horowitz K, McGuire WL. Predicting response to endocrine therapy in human breast cancer: a hypothesis. Science 1975;189(4204):726-727.
34. Duffy M, Harbeck N, Nap M, Molina R, Nicolini A, Senkus E, Cardoso F. Clinical use of biomarkers in breast cancer: Updated guidelines from the European Group on Tumor Markers (EGTM). European journal of cancer 2017;75:284-298.
35. Delaney G, Jacob S, Featherstone C, Barton M. The role of radiotherapy in cancer treatment: Estimating optimal utilization from a review of evidence-based clinical guidelines. Cancer 2005;104(6):1129-1137.
36. Denham JW, Steigler A, Lamb DS, Joseph D, Turner S, Matthews J, Atkinson C, North J, Christie D, Spry NA and others. Short-term neoadjuvant androgen deprivation and radiotherapy for locally advanced prostate cancer: 10-year data from the TROG 96.01 randomised trial. The Lancet Oncology 2011;12(5):451-459.
37. Song CH, Wu H-G, Heo DS, Kim KH, Sung M-W, Park CI. Treatment Outcomes for Radiotherapy Alone are Comparable With Neoadjuvant Chemotherapy Followed by Radiotherapy in Early-Stage Nasopharyngeal Carcinoma. The Laryngoscope 2008;118(4):663-670.
38. Sjoquist KM, Burmeister BH, Smithers BM, Zalcberg JR, Simes RJ, Barbour A, Gebski V. Survival after neoadjuvant chemotherapy or chemoradiotherapy for resectable oesophageal carcinoma: an updated meta-analysis. The Lancet Oncology 2011;12(7):681-692.
39. Onitilo AA, Engel JM, Stankowski RV, Doi SA. Survival comparisons for breast conserving surgery and mastectomy revisited: community experience and the role of radiation therapy. Clinical medicine & research 2015;13(2):65-73.
40. Kim J-K, Jeon H-Y, Kim H. The molecular mechanisms underlying the therapeutic resistance of cancer stem cells. Archives of Pharmacal Research 2015;38(3):389-401.
41. Chang L, Graham PH, Ni J, Hao J, Bucci J, Cozzi PJ, Li Y. Targeting PI3K/Akt/mTOR signaling pathway in the treatment of prostate cancer radioresistance. Critical Reviews in Oncology/Hematology 2015;96(3):507-517.
42. Shapiro CL, Recht A. Side effects of adjuvant treatment of breast cancer. New England Journal of Medicine 2001;344(26):1997-2008.
43. Delaney G, Jacob S, Featherstone C, Barton M. The role of radiotherapy in cancer treatment: estimating optimal utilization from a review of evidence‐based clinical guidelines. Cancer: Interdisciplinary International Journal of the American Cancer Society 2005;104(6):1129-1137.
44. Cao J, Olson R, Tyldesley S. Comparison of recurrence and survival rates after breast-conserving therapy and mastectomy in young women with breast cancer. Current Oncology 2013;20(6):593–601.
45. Poortmans P. Evidence based radiation oncology: breast cancer. Radiotherapy and oncology 2007;84(1):84-101.
46. Allemani C, Sant M, Weir HK, Richardson LC, Baili P, Storm H, Siesling S, Torrella‐Ramos A, Voogd AC, Aareleid T. Breast cancer survival in the US and Europe: A CONCORD high‐resolution study. International Journal of Cancer 2013;132(5):1170-1181.

47. Haviland JS, Owen JR, Dewar JA, Agrawal RK, Barrett J, Barrett-Lee PJ, Dobbs HJ, Hopwood P, Lawton PA, Magee BJ and others. The UK Standardisation of Breast Radiotherapy (START) trials of radiotherapy hypofractionation for treatment of early breast cancer: 10-year follow-up results of two randomised controlled trials. The Lancet Oncology 2013;14(11):1086-1094.
48. Nix P, Cawkwell L, Patmore H, Greenman J, Stafford N. Bcl-2 expression predicts radiotherapy failure in laryngeal cancer. British Journal Of Cancer 2005;92:2185–2189.
49. Atkinson Jr AJ, Colburn WA, DeGruttola VG, DeMets DL, Downing GJ, Hoth DF, Oates JA, Peck CC, Schooley RT. Biomarkers and surrogate endpoints: preferred definitions and conceptual framework. Clinical pharmacology & therapeutics 2001;69(3):89-95.
50. Ludwig JA, Weinstein JN. Biomarkers in Cancer Staging, Prognosis and Treatment Selection. Nature Reviews Cancer 2005;5:845–856.
51. Ebeling FG, Stieber P, Untch M, Nagel D, Konecny GE, Schmitt UM, Fateh-Moghadam A, Seidel D. Serum CEA and CA 15-3 as prognostic factors in primary breast cancer. British Journal Of Cancer 2002;86:1217–1222.
52. Duffy MJ, Evoy D, McDermott EW. CA 15-3: Uses and limitation as a biomarker for breast cancer. Clinica Chimica Acta 2010;411(23):1869-1874.
53. Tjalsma H, Bolhuis A, Jongbloed JD, Bron S, van Dijl JM. Signal peptide-dependent protein transport inBacillus subtilis: a genome-based survey of the secretome. Microbiology and Molecular Biology Reviews 2000;64(3):515-547.
54. Paltridge JL, Belle L, Khew-Goodall Y. The secretome in cancer progression. Biochimica et Biophysica Acta (BBA) - Proteins and Proteomics 2013;1834(11):2233-2241.
55. Grønborg M, Kristiansen TZ, Iwahori A, Chang R, Reddy R, Sato N, Molina H, Jensen ON, Hruban RH, Goggins MG. Biomarker discovery from pancreatic cancer secretome using a differential proteomic approach. Molecular & Cellular Proteomics 2006;5(1):157-171.
56. Karagiannis GS, Pavlou MP, Diamandis EP. Cancer secretomics reveal pathophysiological pathways in cancer molecular oncology. Volume 4; 2010. p 496-510.
57. Lee MCS, Miller EA, Goldberg J, Orci L, Schekman R. Bi-diretional protein transport between the ER and Golgi. Annual Review of Cell and Developmental Biology 2004;20(1):87-123.
58. Rabouille C, Malhotra V, Nickel W. Diversity in unconventional protein secretion. Journal of Cell Science 2012;125(22):5251-5255.
59. Vaupel P. Tumor microenvironmental physiology and its implications for radiation oncology. Seminars in Radiation Oncology 2004;14(3):198-206.
60. Vaddiraju S, Tomazos I, Burgess DJ, Jain FC, Papadimitrakopoulos F. Emerging synergy between nanotechnology and implantable biosensors: A review. Biosensors and Bioelectronics 2010;25(7):1553-1565.
61. Bertout JA, Patel SA, Simon MC. The impact of O2 availability on human cancer. Nature Reviews Cancer 2008;8:967-975.

62. Thomlinson RH, Gray LH. The Histological Structure of Some Human Lung Cancers and the Possible Implications for Radiotherapy. British Journal of Cancer 1955;9(4):539-549.
63. Vaupel P, Mayer A. Hypoxia in Tumors: Pathogenesis-Related Classification, Characterization of Hypoxia Subtypes, and Associated Biological and Clinical Implications. In: Swartz HM, Harrison DK, Bruley DF, editors. Oxygen Transport to Tissue XXXVI. New York, NY: Springer New York; 2014. p 19-24.
64. Bayer C, Shi K, Astner ST, Maftei C-A, Vaupel P. Acute Versus Chronic Hypoxia: Why a Simplified Classification is Simply Not Enough. Volume 80; 2011. p 965-968.
65. Brown J. Evidence for acutely hypoxic cells in mouse tumours, and a possible mechanism of reoxygenation. The British journal of radiology 1979;52(620):650-656.
66. Chaplin DJ, Olive PL, Durand RE. Intermittent blood flow in a murine tumor: radiobiological effects. Cancer research 1987;47(2):597-601.
67. Horsman MR, Mortensen LS, Jørgen B, Petersen JB, Busk M, Overgaard J. Imaging hypoxia to improve radiotherapy outcome. Nature Reviews Clinical Oncology 2012;9(12):674-687.
68. Secomb TW, Dewhirst MW, Pries AR. Structural Adaptation of Normal and Tumour Vascular Networks. Basic & Clinical Pharmacology & Toxicology 2012;110(1):63-69.
69. Koch CJ, Jenkins WT, Jenkins KW, Yang XY, Shuman AL, Pickup S, Riehl CR, Paudyal R, Poptani H, Evans SM. Mechanisms of blood flow and hypoxia production in rat 9L-epigastric tumors. Tumor microenvironment and therapy 2013;1:1-13.
70. Dewhirst M, Ong E, Braun R, Smith B, Klitzman B, Evans S, Wilson D. Quantification of longitudinal tissue pO2 gradients in window chamber tumours: impact on tumour hypoxia. British journal of cancer 1999;79(11-12):1717.
71. Trédan O, Galmarini CM, Patel K, Tannock IF. Drug Resistance and the Solid Tumor Microenvironment. JNCI: Journal of the National Cancer Institute 2007;99(19):1441-1454.
72. Bedford JS, Mitchell JB. The effect of hypoxia on the growth and radiation response of mammalian cells in culture. The British Journal of Radiology 1974;47(562):687-696.
73. Yoshiba S, Ito D, Nagumo T, Shirota T, Hatori M, Shintani S. Hypoxia induces resistance to 5-fluorouracil in oral cancer cells via G1 phase cell cycle arrest. Oral oncology 2009;45(2):109-115.
74. Gray LH, Conger AD, Ebert M, Hornsey S, Scott OCA. The Concentration of Oxygen Dissolved in Tissues at the Time of Irradiation as a Factor in Radiotherapy. The British Journal of Radiology 1953;26(312):638-648.
75. Okunieff P, Fenton B, Chen Y. Past, present, and future of oxygen in cancer research. Oxygen Transport to Tissue XXVI: Springer; 2005. p 213-222.
76. Vos O. Role of endogenous thiols in protection. Adv Space Res 1992;12(2-3):201-207.

77. Bhandari V, Hoey C, Liu LY, Lalonde E, Ray J, Livingstone J, Lesurf R, Shiah Y-J, Vujcic T, Huang X. Molecular landmarks of tumor hypoxia across cancer types. Nature genetics 2019:308-318.
78. Leo C, Giaccia AJ, Denko NC. The hypoxic tumor microenvironment and gene expression. Seminars in Radiation Oncology 2004;14(3):207-214.
79. Semenza GL. Targeting HIF-1 for cancer therapy. Nature Reviews Cancer 2003;3(10):721-732.
80. Semenza GL. HIF-1 and tumor progression: pathophysiology and therapeutics. Trends in Molecular Medicine 2002;8(4):62-67.
81. Yan S-F, Lu J, Zou YS, Soh-Won J, Cohen DM, Buttrick PM, Cooper DR, Steinberg SF, Mackman N, Pinsky DJ. Hypoxia-associated induction of early growth response-1 gene expression. Journal of Biological Chemistry 1999;274(21):15030-15040.
82. Koong AC, Chen EY, Mivechi NF, Denko NC, Stambrook P, Giaccia AJ. Hypoxic activation of nuclear factor-κB is mediated by a Ras and Raf signaling pathway and does not involve MAP kinase (ERK1 or ERK2). Cancer Research 1994;54(20):5273-5279.
83. Bandyopadhyay RS, Phelan M, Faller DV. Hypoxia induces AP-1-regulated genes and AP-1 transcription factor binding in human endothelial and other cell types. Biochimica et Biophysica Acta (BBA) - Gene Structure and Expression 1995;1264(1):72-78.
84. Denko NC, Fontana LA, Hudson KM, Sutphin PD, Raychaudhuri S, Altman R, Giaccia AJ. Investigating hypoxic tumor physiology through gene expression patterns. Oncogene 2003;22:5907-5914.
85. Semenza GL. Hypoxia-inducible factor 1: oxygen homeostasis and disease pathophysiology. Trends in molecular medicine 2001;7(8):345-350.
86. Ron D, Walter P. Signal integration in the endoplasmic reticulum unfolded protein response. Nature Reviews Molecular Cell Biology 2007;8:519–529.
87. Blais JD, Addison CL, Edge R, Falls T, Zhao H, Wary K, Koumenis C, Harding HP, Ron D, Holcik M and others. Perk-Dependent Translational Regulation Promotes Tumor Cell Adaptation and Angiogenesis in Response to Hypoxic Stress. Molecular and Cellular Biology 2006;26(24):9517-9532.
88. Zhang B, Wang Y, Pang X, Su Y, Ai G, Wang T. ER stress induced by ionising radiation in IEC-6 cells. International Journal of Radiation Biology 2010;86(6):429-435.
89. Panganiban RAM, Mungunsukh O, Day RM. X-irradiation induces ER stress, apoptosis, and senescence in pulmonary artery endothelial cells. International Journal of Radiation Biology 2013;89(8):656-667.
90. Zhang K, Kaufman RJ. Signaling the unfolded protein response from the endoplasmic reticulum. The Journal of biological chemistry 2004;279(25):25935-25938.
91. Jäger R, Bertrand MJ, Gorman AM, Vandenabeele P, Samali A. The unfolded protein response at the crossroads of cellular life and death during endoplasmic reticulum stress. Biology of the Cell 2012;104(5):259-270.
92. Yoshida H, Matsui T, Yamamoto A, Okada T, Mori K. XBP1 mRNA is induced by ATF6 and spliced by IRE1 in response to ER stress to produce a highly active transcription factor. Cell 2001;107(7):881-891.

93. Schindler AJ, Schekman R. In vitro reconstitution of ER-stress induced ATF6 transport in COPII vesicles. Proceedings of the National Academy of Sciences 2009;106(42):17775-17780.
94. Okada T, Yoshida H, Akazawa R, Negishi M, Mori K. Distinct roles of activating transcription factor 6 (ATF6) and double-stranded RNA-activated protein kinase-like endoplasmic reticulum kinase (PERK) in transcription during the mammalian unfolded protein response. Biochem J 2002;366(2):585-94.
95. Yamamoto K, Sato T, Matsui T, Sato M, Okada T, Yoshida H, Harada A, Mori K. Transcriptional induction of mammalian ER quality control proteins is mediated by single or combined action of ATF6alpha and XBP1. Developmental Cell 2007;13(3):365-376.
96. Yoshida H, Okada T, Haze K, Yanagi H, Yura T, Negishi M, Mori K. ATF6 activated by proteolysis binds in the presence of NF-Y (CBF) directly to the cis-acting element responsible for the mammalian unfolded protein response. Molecular and cellular biology 2000;20(18):6755-6767.
97. Ron D, Walter P. Signal integration in the endoplasmic reticulum unfolded protein response. Nature reviews Molecular cell biology 2007;8(7):519-529.
98. Harding HP, Novoa I, Zhang Y, Zeng H, Wek R, Schapira M, Ron D. Regulated translation initiation controls stress-induced gene expression in mammalian cells. Molecular cell 2000;6(5):1099-1108.
99. Ma Y, Brewer JW, Diehl JA, Hendershot LM. Two distinct stress signaling pathways converge upon the CHOP promoter during the mammalian unfolded protein response. Journal of molecular biology 2002;318(5):1351-1365.
100. Puthalakath H, O'Reilly LA, Gunn P, Lee L, Kelly PN, Huntington ND, Hughes PD, Michalak EM, McKimm-Breschkin J, Motoyama N. ER stress triggers apoptosis by activating BH3-only protein Bim. Cell 2007;129(7):1337-1349.
101. McCullough KD, Martindale JL, Klotz L-O, Aw T-Y, Holbrook NJ. Gadd153 sensitizes cells to endoplasmic reticulum stress by down-regulating Bcl2 and perturbing the cellular redox state. Molecular and cellular biology 2001;21(4):1249-1259.
102. Kim KW, Moretti L, Mitchell LR, Jung DK, Lu B. Endoplasmic reticulum stress mediates radiation-induced autophagy by perk-eIF2α in caspase-3/7-deficient cells. Oncogene 2010;29:3241–3251.
103. Wang M, Kaufman RJ. The impact of the endoplasmic reticulum protein-folding environment on cancer development. Nature Reviews Cancer 2014;14:581-597.
104. Nordsmark M, Bentzen SM, Rudat V, Brizel D, Lartigau E, Stadler P, Becker A, Adam M, Molls M, Dunst J. Prognostic value of tumor oxygenation in 397 head and neck tumors after primary radiation therapy. An international multi-center study. Radiotherapy and Oncology 2005;77(1):18-24.
105. Gatenby RA, Kessler HB, Rosenblum JS, Coia LR, Moldofsky PJ, Hartz WH, Broder GJ. Oxygen distribution in squamous cell carcinoma metastases and its relationship to outcome of radiation therapy. International Journal of Radiation Oncology*Biology*Physics 1988;14(5):831-838.

106. Höckel M, Knoop C, Schlenger K, Vorndran B, Baußnann E, Mitze M, Knapstein PG, Vaupel P. Intratumoral pO2 predicts survival in advanced cancer of the uterine cervix. Radiotherapy and Oncology 1993;26(1):45-50.
107. Höckel M, Schlenger K, Aral B, Mitze M, Schäffer U, Vaupel P. Association between Tumor Hypoxia and Malignant Progression in Advanced Cancer of the Uterine Cervix. Cancer Research 1996;56(19):4509-4515.
108. Nordsmark M, Alsner J, Keller J, Nielsen OS, Jensen OM, Horsman MR, Overgaard J. Hypoxia in human soft tissue sarcomas: Adverse impact on survival and no association with p53 mutations. British Journal Of Cancer 2001;84:1070-1075.
109. Vaupel P, Schlenger K, Knoop C, Höckel M. Oxygenation of human tumors: evaluation of tissue oxygen distribution in breast cancers by computerized O2 tension measurements. Cancer research 1991;51(12):3316-3322.
110. Brizel DM, Sibley GS, Prosnitz LR, Scher RL, Dewhirst MW. Tumor hypoxia adversely affects the prognosis of carcinoma of the head and neck. International Journal of Radiation Oncology* Biology* Physics 1997;38(2):285-289.
111. Okunieff P, Hoeckel M, Dunphy EP, Schlenger K, Knoop C, Vaupel P. Oxygen tension distributions are sufficient to explain the local response of human breast tumors treated with radiation alone. International Journal of Radiation Oncology• Biology• Physics 1993;26(4):631-636.
112. Okunieff P, Hoeckel M, Dunphy EP, Schlenger K, Knoop C, Vaupel P. Oxygen tension distributions are sufficient to explain the local response of human breast tumors treated with radiation alone. International Journal of Radiation Oncology • Biology • Physics 1993;26(4):631-636.
113. Fyles AW, Milosevic M, Pintilie M, Hill RP. Cervix cancer oxygenation measured following external radiation therapy. International Journal of Radiation Oncology* Biology* Physics 1998;42(4):751-753.
114. Varia MA, Calkins-Adams DP, Rinker LH, Kennedy AS, Novotny DB, Fowler WC, Raleigh JA. Pimonidazole: A Novel Hypoxia Marker for Complementary Study of Tumor Hypoxia and Cell Proliferation in Cervical Carcinoma. Gynecologic Oncology 1998;71(2):270-277.
115. Janssens GO, Rademakers SE, Terhaard CH, Doornaert PA, Bijl HP, van den Ende P, Chin A, Marres HA, de Bree R, van der Kogel AJ. Accelerated radiotherapy with carbogen and nicotinamide for laryngeal cancer: results of a phase III randomized trial. Journal of Clinical Oncology 2012;30(15):1777-1783.
116. Le Q-T, Courter D. Clinical biomarkers for hypoxia targeting. Cancer and Metastasis Reviews 2008;27(3):351-361.
117. Meehan J, Ward C, Turnbull A, Bukowski-Wills J, Finch AJ, Jarman EJ, Xintaropoulou C, Martinez-Perez C, Gray M, Pearson M. Inhibition of pH regulation as a therapeutic strategy in hypoxic human breast cancer cells. Oncotarget 2017;8(26):42857–42875.
118. Buffa FM, Harris AL, West CM, Miller CJ. Large meta-analysis of multiple cancers reveals a common, compact and highly prognostic hypoxia metagene. British Journal Of Cancer 2010;102:428-435.
119. Toustrup K, Sørensen BS, Lassen P, Wiuf C, Alsner J, Overgaard J. Gene expression classifier predicts for hypoxic modification of radiotherapy with

nimorazole in squamous cell carcinomas of the head and neck. Radiotherapy and Oncology 2012;102(1):122-129.
120. Overgaard J, Eriksen JG, Nordsmark M, Alsner J, Horsman MR. Plasma osteopontin, hypoxia, and response to the hypoxia sensitiser nimorazole in radiotherapy of head and neck cancer: results from the DAHANCA 5 randomised double-blind placebo-controlled trial. The Lancet Oncology 2005;6(10):757-764.
121. Hammond EM, Asselin MC, Forster D, O'Connor JP, Senra JM, Williams KJ. The meaning, measurement and modification of hypoxia in the laboratory and the clinic. Clinical Oncology 2014;26(5):277-88.
122. Henk JM, Kunkler PB, Smith CW. Radiotherapy and hyperbaric oxygen in head and neck cancer: Final Report of First Controlled Clinical Trial. The Lancet 1977;310(8029):101-103.
123. Janssens GO, Rademakers SE, Terhaard CH, Doornaert PA, Bijl HP, van den Ende P, Chin A, Takes RP, de Bree R, Hoogsteen IJ and others. Improved Recurrence-Free Survival with ARCON for Anemic Patients with Laryngeal Cancer. Clinical Cancer Research 2014;20(5):1345-1354.
124. Bentzen J, Toustrup K, Eriksen JG, Primdahl H, Andersen LJ, Overgaard J. Locally advanced head and neck cancer treated with accelerated radiotherapy, the hypoxic modifier nimorazole and weekly cisplatin. Results from the DAHANCA 18 phase II study. Acta Oncologica 2015;54(7):1001-1007.
125. Nishimura Y, Nakagawa K, Takeda K, Tanaka M, Segawa Y, Tsujino K, Negoro S, Fuwa N, Hida T, Kawahara M and others. Phase I/II Trial of Sequential Chemoradiotherapy Using a Novel Hypoxic Cell Radiosensitizer, Doranidazole (PR-350), in Patients With Locally Advanced Non–Small-Cell Lung Cancer (WJTOG-0002). International Journal of Radiation Oncology*Biology*Physics 2007;69(3):786-792.
126. Overgaard J, Sand Hansen H, Overgaard M, Bastholt L, Berthelsen A, Specht L, Lindeløv B, Jørgensen K. A randomized double-blind phase III study of nimorazole as a hypoxic radiosensitizer of primary radiotherapy in supraglottic larynx and pharynx carcinoma. Results of the Danish Head and Neck Cancer Study (DAHANCA) Protocol 5-85. Radiotherapy and Oncology 1998;46(2):135-146.
127. Hassan Metwally MA, Ali R, Kuddu M, Shouman T, Strojan P, Iqbal K, Prasad R, Grau C, Overgaard J. IAEA-HypoX. A randomized multicenter study of the hypoxic radiosensitizer nimorazole concomitant with accelerated radiotherapy in head and neck squamous cell carcinoma. Radiotherapy and Oncology 2015;116(1):15-20.
128. Horsman MR, Overgaard J. The impact of hypoxia and its modification of the outcome of radiotherapy. Journal of Radiation Research 2016;57(S1):90-98.
129. Wigerup C, Påhlman S, Bexell D. Therapeutic targeting of hypoxia and hypoxia-inducible factors in cancer. Pharmacology & Therapeutics 2016;164:152-169.
130. Rischin D, Peters LJ, O'Sullivan B, Giralt J, Fisher R, Yuen K, Trotti A, Bernier J, Bourhis J, Ringash J. Tirapazamine, cisplatin, and radiation versus cisplatin and radiation for advanced squamous cell carcinoma of the head and neck (TROG 02.02, HeadSTART): a phase III trial of the Trans-Tasman

Radiation Oncology Group. Journal of Clinical Oncology 2008;28(18):2989-2995.
131. DiSilvestro PA, Ali S, Craighead PS, Lucci JA, Lee Y-C, Cohn DE, Spirtos NM, Tewari KS, Muller C, Gajewski WH and others. Phase III randomized trial of weekly cisplatin and irradiation versus cisplatin and tirapazamine and irradiation in stages IB2, IIA, IIB, IIIB, and IVA cervical carcinoma limited to the pelvis: a Gynecologic Oncology Group study. Journal of clinical oncology : official journal of the American Society of Clinical Oncology 2014;32(5):458-464.
132. Borad MJ, Reddy SG, Bahary N, Uronis HE, Sigal D, Cohn AL, Schelman WR, Stephenson J, Jr., Chiorean EG, Rosen PJ and others. Randomized Phase II Trial of Gemcitabine Plus TH-302 Versus Gemcitabine in Patients With Advanced Pancreatic Cancer. Journal of clinical oncology : official journal of the American Society of Clinical Oncology 2015;33(13):1475-1481.
133. Chawla SP, Cranmer LD, Van Tine BA, Reed DR, Okuno SH, Butrynski JE, Adkins DR, Hendifar AE, Kroll S, Ganjoo KN. Phase II study of the safety and antitumor activity of the hypoxia-activated prodrug TH-302 in combination with doxorubicin in patients with advanced soft tissue sarcoma. Journal of clinical oncology : official journal of the American Society of Clinical Oncology 2014;32(29):3299-3306.
134. Toustrup K, Sørensen BS, Nordsmark M, Busk M, Wiuf C, Alsner J, Overgaard J. Development of a hypoxia gene expression classifier with predictive impact for hypoxic modification of radiotherapy in head and neck cancer. Cancer research 2011;71(17):5923-5932.
135. Rischin D, Hicks RJ, Fisher R, Binns D, Corry J, Porceddu S, Peters LJ. Prognostic significance of [F-18]-misonidazole positron emission tomography-detected tumor hypoxia in patients with advanced head and neck cancer randomly assigned to chemoradiation with or without tirapazamine: A substudy of Trans-Tasman Radiation Oncolo. Journal of Clinical Oncology 2006;24(13):2098-2104.
136. Overgaard J. Hypoxic modification of radiotherapy in squamous cell carcinoma of the head and neck – A systematic review and meta-analysis. Radiotherapy and Oncology 2011;100(1):22-32.
137. Baumann M, Krause M, Overgaard J, Debus J, Bentzen SM, Daartz J, Richter C, Zips D, Bortfeld T. Radiation oncology in the era of precision medicine. Nature Reviews Cancer 2016;16:234-249.
138. Hendrickson K, Phillips M, Smith W, Peterson L, Krohn K, Rajendran J. Hypoxia imaging with [F-18] FMISO-PET in head and neck cancer: Potential for guiding intensity modulated radiation therapy in overcoming hypoxia-induced treatment resistance. Radiotherapy and Oncology 2011;101(3):369-375.
139. Søvik Å, Malinen E, Bruland ØS, Bentzen SM, Olsen DR. Optimization of tumour control probability in hypoxic tumours by radiation dose redistribution: a modelling study. Physics in Medicine & Biology 2006;52(2):499-509.

140. Thorwarth D, Eschmann S-M, Paulsen F, Alber M. Hypoxia Dose Painting by Numbers: A Planning Study. International Journal of Radiation Oncology*Biology*Physics 2007;68(1):291-300.
141. Severinghaus JW, Astrup PB. History of blood gas analysis. IV. Leland Clark's oxygen electrode. Journal of Clinical Monitoring 1986;2(2):125-139.
142. Clark LC. Monitor and Control of Blood and Tissue Oxygen Tensions. Transactions - American Society for Artificial Internal Organs 1956;2(1):41-48.
143. Marland JRK, Blair EO, Flynn BW, González-Fernández E, Huang L, Kunkler IH, Smith S, Staderini M, Tsiamis A, Ward C and others. Implantable Microsystems for Personalised Anticancer Therapy. CMOS Circuits for Biological Sensing and Processing: Springer International Publishing; 2018. p 259-286.
144. Crow DR. Principles and applications of electrochemistry. London: Routledge; 2017.
145. Hashemi P, Walsh PL, Guillot TS, Gras-Najjar J, Takmakov P, Crews FT, Wightman RM. Chronically Implanted, Nafion-Coated Ag/AgCl Reference Electrodes for Neurochemical Applications. ACS Chemical Neuroscience 2011;2(11):658-666.
146. McLaughlin GW, Braden K, Franc B, Kovacs GTA. Microfabricated solid-state dissolved oxygen sensor. Sensors & Actuators: B. Chemical 2002;83(1-3):138-148.
147. Chan WP, Narducci M, Gao Y, Cheng M-Y, Cheong JH, George AK, Cheam DD, Leong SC, Damalerio MRB, Lim R. A monolithically integrated pressure/oxygen/temperature sensing SoC for multimodality intracranial neuromonitoring. IEEE Journal of Solid-State Circuits 2014;49(11):2449-2461.
148. Wang P, Liu Y, Abruña HD, Spector JA, Olbricht WL. Micromachined dissolved oxygen sensor based on solid polymer electrolyte. Sensors and Actuators B: Chemical 2011;153(1):145-151.
149. Wu C-C, Yasukawa T, Shiku H, Matsue T. Fabrication of miniature Clark oxygen sensor integrated with microstructure. Sensors and Actuators B: Chemical 2005;110(2):342-349.
150. Park J, Pak YK, Pak JJ. A microfabricated reservoir-type oxygen sensor for measuring the real-time cellular oxygen consumption rate at various conditions. Sensors and Actuators B: Chemical 2010;147(1):263-269.
151. Jonas O, Landry HM, Fuller JE, Santini JT, Baselga J, Tepper RI, Cima MJ, Langer R. An implantable microdevice to perform high-throughput in vivo drug sensitivity testing in tumors. Science Translational Medicine 2015;7(284):257-284.
152. Pardridge WM. The blood-brain barrier: Bottleneck in brain drug development. NeuroRX 2005;2(1):3-14.
153. Masi BC, Tyler BM, Bow H, Wicks RT, Xue Y, Brem H, Langer R, Cima MJ. Intracranial MEMS based temozolomide delivery in a 9L rat gliosarcoma model. Biomaterials 2012;33(23):5768-5775.
154. Farra R, Sheppard NF, McCabe L, Neer RM, Anderson JM, Santini JT, Cima MJ, Langer R. First-in-human testing of a wirelessly controlled drug delivery microchip. Science translational medicine 2012;4(122):1-10.

155. Essers M, Mijnheer B. In vivo dosimetry during external photon beam radiotherapy. International Journal of Radiation Oncology*Biology*Physics 1999;43(2):245-259.
156. Halvorsen PH. Dosimetric evaluation of a new design MOSFET in vivo dosimeter. Medical Physics 2005;32(1):110-117.
157. Beyer GP, Mann GG, Pursley JA, Espenhahn ET, Fraisse C, Godfrey DJ, Oldham M, Carrea TB, Bolick N, Scarantino CW. An Implantable MOSFET Dosimeter for the Measurement of Radiation Dose in Tissue During Cancer Therapy. IEEE Sensors Journal 2008;8(1):38-51.
158. Verma N, Cowperthwaite MC, Burnett MG, Markey MK. Differentiating tumor recurrence from treatment necrosis: a review of neuro-oncologic imaging strategies. Neuro-oncology 2013;15(5):515-534.
159. Daniel KD, Kim GY, Vassiliou CC, Galindo M, Guimaraes AR, Weissleder R, Charest A, Langer R, Cima MJ. Implantable diagnostic device for cancer monitoring. Biosensors and Bioelectronics 2009;24(11):3252-3257.
160. Yibo L, Terrence P, Christophoros CV, Paul LH, Michael JC. Implantable magnetic relaxation sensors measure cumulative exposure to cardiac biomarkers. Nature Biotechnology 2011;29(3):273–277.
161. ISO. Biological evaluation of medical devices - Part 1: Guidence on selection of tests. ISO 10993-1:1992(E) International Organisation for Standardisation (ISO); 1992.
162. Bowers S, Cohen D. How lobbying blocked European safety checks for dangerous medical implants. BMJ 2018;363:1-6.
163. Arshady R. Polymeric biomaterials: chemistry, concepts, criteria. In: Introduction to polymeric biomaterials: the polymeric biomaterials series. London: Citrus Books; 2003.
164. Schoen FR, Anderson JM. Host response to biomaterials and thier evaluation. In: Biomaterials science: an introduction to materials in medicine. San Diego: Elsevier; 2004.
165. Morais J, Papadimitrakopoulos F, Burgess D. Biomaterials/Tissue Interactions: Possible Solutions to Overcome Foreign Body Response. The American Association of Pharmaceutical Scientists 2010;12(2):188-196.
166. Onuki Y, Bhardwaj U, Papadimitrakopoulos F, Burgess DJ. A Review of the Biocompatibility of Implantable Devices: Current Challenges to Overcome Foreign Body Response. Journal of Diabetes Science and Technology 2008;2(6):1003-1015.
167. Anderson JM, Rodriguez A, Chang DT. Foreign body reaction to biomaterials. Seminars in Immunology 2008;20(2):86-100.
168. Anderson JM. Biological responses to materials. Annual Review of Materials Research 2001;31(1):81-110.
169. Wang Y, Vaddiraju S, Gu B, Papadimitrakopoulos F, Burgess DJ. Foreign Body Reaction to Implantable Biosensors: Effects of Tissue Trauma and Implant Size. Journal of Diabetes Science and Technology 2015;9(5):966-977.
170. Gorbet MB, Sefton MV. Biomaterial-associated thrombosis: roles of coagulation factors, complement, platelets and leukocytes. Biomaterials 2004;25(26):5681-5703.

171. McNally AK, Jones JA, MacEwan SR, Colton E, Anderson JM. Vitronectin is a critical protein adhesion substrate for IL-4-induced foreign body giant cell formation. Journal of Biomedical Materials Research Part A 2008;86A(2):535-543.
172. Keselowsky BG, Bridges AW, Burns KL, Tate CC, Babensee JE, LaPlaca MC, García AJ. Role of plasma fibronectin in the foreign body response to biomaterials. Biomaterials 2007;28(25):3626-3631.
173. Jenny CR, Anderson JM. Absorbed serum proteins responsible for surface dependent human macrophage behaviour. Journal of Biomedical Material Research 2000;49(4):435-437.
174. Broughton G, Janis J, Attinger CE. The basic science of wound healing. Plast. Reconstr. Surg. Volume 117; 2006. p 12-34.
175. Tang L, Eaton JW, Jennings TA. Mast cells mediate acute inflammatory responses to implanted biomaterials. Proceedings of the National Academy of Sciences of the United States of America 1998;95(15):8841-8846.
176. Zdolsek J, Eaton JW, Tang L. Histamine release and fibrinogen adsorption mediate acute inflammatory responses to biomaterial implants in humans. Journal of Translational Medicine 2007;5:31-31.
177. Patel JD, Krupka T, Anderson JM. iNOS-mediated generation of reactive oxygen and nitrogen species by biomaterial-adherent neutrophils. Journal of Biomedical Materials Research Part A 2007;80A(2):381-390.
178. Scapini P, Lapinet-Vera JA, Gasperini S, Calzetti F, Bazzoni F, Cassatella MA. The neutrophil as a cellular source of chemokines. Immunological Reviews 2000;177(1):195-203.
179. Park CJ, Gabrielson NP, Pack DW, Jamison RD, Wagoner Johnson AJ. The effect of chitosan on the migration of neutrophil-like HL60 cells, mediated by IL-8. Biomaterials 2009;30(4):436-444.
180. Kobayashi SD, Voyich J, Burlak C, Deleo F. Neutrophils in the innate immune response. Arch. Immunol. Ther. Exp. Volume 53; 2005. p 505-517.
181. Yamashiro S, Kamohara H, Wang J, Yang D, Gong W, Yoshimura T. Phenotypic and functional change of cytokine-activated neutrophils: inflammatory neutrophils are heterogeneous and enhance adaptive immune responses. J. Leukoc. Biol. Volume 69; 2001. p 698-704.
182. Gilroy DW. The endogenous control of acute inflammation – from onset to resolution. Drug Discovery Today: Therapeutic Strategies 2004;1(3):313-319.
183. Castro PR, Marques SM, Viana CTR, Campos PP, Ferreira MAND, Barcelos LS, Andrade SP. Deletion of the chemokine receptor CCR2 attenuates foreign body reaction to implants in mice. Microvascular Research 2014;95:37-45.
184. Xia Z, Triffitt JT. A review on macrophage responses to biomaterials. Biomedical Materials 2006;1:1-9.
185. Zeeshan S, Patricia JB, Oriyah B, Noah F, Michael G. Macrophages, Foreign Body Giant Cells and Their Response to Implantable Biomaterials. Materials 2015;8(9):5671-5701.
186. McNally AK, Anderson JM. Interleukin-4 induces foreign body giant cells from human monocytes/macrophages. Differential lymphokine regulation of

macrophage fusion leads to morphological variants of multinucleated giant cells. The American Journal of Pathology 1995;147(5):1487-1499.
187. Kao WJ, McNally AK, Hiltner A, Anderson JM. Role for interleukin-4 in foreign-body giant cell formation on a poly(etherurethane urea) in vivo. Journal of Biomedical Materials Research 1995;29(10):1267-1275.
188. DeFife KM, Jenney CR, McNally AK, Colton E, Anderson JM. Interleukin-13 induces human monocyte/macrophage fusion and macrophage mannose receptor expression. The Journal of Immunology 1997;158(7):3385-3390.
189. Omid A, Philippe S, Everett M, Mitchell K, Stephane S, Toshinori N, Masaru T, Michael JG, Rosemarie HD, Dale TU. Essential role of NKT cells producing IL-4 and IL-13 in the development of allergen-induced airway hyperreactivity. Nature Medicine 2003;9(5):582-588.
190. Connor GM, Hart OM, Gardiner CM. Putting the natural killer cell in its place. Volume 117. Oxford, UK; 2006. p 1-10.
191. Gessner A, Mohrs K, Mohrs M. Mast Cells, Basophils, and Eosinophils Acquire Constitutive IL-4 and IL-13 Transcripts during Lineage Differentiation That Are Sufficient for Rapid Cytokine Production. The Journal of Immunology 2005;174(2):1063-1072.
192. Yang J, Jao B, McNally AK, Anderson JM. In vivo quantitative and qualitative assessment of foreign body giant cell formation on biomaterials in mice deficient in natural killer lymphocyte subsets, mast cells, or the interleukin‐4 receptor α and in severe combined immunodeficient mice. Journal of Biomedical Materials Research Part A 2014;102(6):2017-2023.
193. Brodbeck WG, MacEwan M, Colton E, Meyerson H, Anderson JM. Lymphocytes and the foreign body response: Lymphocyte enhancement of macrophage adhesion and fusion. Journal of Biomedical Materials Research Part A 2005;74A(2):222-229.
194. Rodriguez A, Macewan SR, Meyerson H, Kirk JT, Anderson JM. The foreign body reaction in T‐cell‐deficient mice. Journal of Biomedical Materials Research Part A 2009;90(1):106-113.
195. Anderson JM. Multinucleated giant cells. Current opinion in hematology 2000;7(1):40-47.
196. Henson PM. The Immunologic Release of Constituents from Neutrophil Leukocytes. I. The Role of Antibody and Complement on Nonphagocytosable Surfaces or Phagocytosable Particles 1971;107(6):1535-1546.
197. Henson PM. The immunologic release of constituents from neutrophil leukocytes. II. Mechanisms of release during phagocytosis, and adherence to nonphagocytosable surfaces. J Immunol 1971;107(6):1547-57.
198. Haas A. The Phagosome: Compartment with a License to Kill. Traffic 2007;8(4):311-330.
199. Kyriakides T, Bornstein P. Matricellular proteins as modulators of wound healing and the foreign body response. Thromb. Haemost. 2003;90(6):986-992.
200. Song E, Ouyang N, Hörbelt M, Antus B, Wang M, Exton MS. Influence of Alternatively and Classically Activated Macrophages on Fibrogenic Activities of Human Fibroblasts. Cellular Immunology 2000;204(1):19-28.

201. Suska F, Emanuelsson L, Johansson A, Tengvall P, Thomsen P. Fibrous capsule formation around titanium and copper. Journal of Biomedical Materials Research Part A 2008;85A(4):888-896.
202. DiMasi JA, Hansen RW, Grabowski HG. The price of innovation: new estimates of drug development costs. Journal of Health Economics 2003;22(2):151-185.
203. Kola I, Landis J. Can the pharmaceutical industry reduce attrition rates? Nature Reviews Drug Discovery 2004;3:711-716.
204. Robert HS. The NCI60 human tumour cell line anticancer drug screen. Nature Reviews Cancer 2006;6(10):813-823.
205. Burdall SE, Hanby AM, Lansdown MR, Speirs V. Breast cancer cell lines: friend or foe? Breast cancer research 2003;5(2):89-97.
206. Kapałczyńska M, Kolenda T, Przybyła W, Zajączkowska M, Teresiak A, Filas V, Ibbs M, Bliźniak R, Łuczewski Ł, Lamperska K. 2D and 3D cell cultures - a comparison of different types of cancer cell cultures. Archives of medical science : AMS 2018;14(4):910-919.
207. Herrmann D, Conway JRW, Vennin C, Magenau A, Hughes WE, Morton JP, Timpson P. Three-dimensional cancer models mimic cell–matrix interactions in the tumour microenvironment. Carcinogenesis 2014;35(8):1671-1679.
208. Kunz-Schughart LA, Freyer JP, Hofstaedter F, Ebner R. The use of 3-D cultures for high-throughput screening: the multicellular spheroid model. Journal of biomolecular screening 2004;9(4):273-285.
209. Ivascu A, Kubbies M. Rapid generation of single-tumor spheroids for high-throughput cell function and toxicity analysis. Journal of biomolecular screening 2006;11(8):922-932.
210. Singh M, Close DA, Mukundan S, Johnston PA, Sant S. Production of uniform 3D microtumors in hydrogel microwell arrays for measurement of viability, morphology, and signaling pathway activation. Assay and drug development technologies 2015;13(9):570-583.
211. Hollingshead M, Plowman J, Alley M, Mayo J, Sausville E. The hollow fiber assay. Relevance of tumor models for anticancer drug development: Karger Publishers; 1999. p 109-120.
212. Richmond A, Su Y. Mouse xenograft models vs GEM models for human cancer therapeutics. The Company of Biologists Ltd; 2008.
213. Sano D, Myers JN. Xenograft models of head and neck cancers. Head & neck oncology 2009;1(1):1-32.
214. Steel GG, Courtenay VD, Peckham MJ. The response to chemotherapy of a variety of human tumour xenografts. British Journal Of Cancer 1983;47:1-13.
215. Kelland LR. “Of mice and men”: values and liabilities of the athymic nude mouse model in anticancer drug development. European Journal of Cancer 2004;40(6):827-836.
216. Johnson JI, Decker S, Zaharevitz D, Rubinstein LV, Venditti JM, Schepartz S, Kalyandrug S, Christian M, Arbuck S, Hollingshead M and others. Relationships between drug activity in NCI preclinical in vitro and in vivo models and early clinical trials. British Journal of Cancer 2001;84(10):1424-1431.

217. Fiebig H-H, Burger AM. Human Tumor Xenografts and Explants. In: Teicher BA, editor. Tumor Models in Cancer Research. Totowa, NJ: Humana Press; 2002. p 113-137.
218. Shimosato Y, Kameya T, Hirohashi S. Growth, morphology, and function of xenotransplanted human tumors. Pathology Annual 1979;14(2):215-57.
219. Sharkey FE, Fogh J. Considerations in the use of nude mice for cancer research. Cancer and Metastasis Reviews 1984;3(4):341-360.
220. Kubota T. Metastatic models of human cancer xenografted in the nude mouse: The importance of orthotopic transplantation. Journal of Cellular Biochemistry 1994;56(1):4-8.
221. Izumchenko E, Meir J, Bedi A, Wysocki P, Hoque M, Sidransky D. Patient-derived xenografts as tools in pharmaceutical development. Clinical Pharmacology & Therapeutics 2016;99(6):612-621.
222. Aston WJ, Hope DE, Nowak AK, Robinson BW, Lake RA, Lesterhuis WJ. A systematic investigation of the maximum tolerated dose of cytotoxic chemotherapy with and without supportive care in mice. BMC cancer 2017;17(1):684-684.
223. Scheerlinck J-PY, Snibson KJ, Bowles VM, Sutton P. Biomedical applications of sheep models: from asthma to vaccines. Trends in Biotechnology 2008;26(5):259-266.
224. Paoloni M, Khanna C. Translation of new cancer treatments from pet dogs to humans. Nature Reviews Cancer 2008;8(2):147-156.
225. Rowell JL, McCarthy DO, Alvarez CE. Dog models of naturally occurring cancer. Trends in molecular medicine 2011;17(7):380-388.
226. Gordon I, Paoloni M, Mazcko C, Khanna C. The Comparative Oncology Trials Consortium: using spontaneously occurring cancers in dogs to inform the cancer drug development pathway. PLoS medicine 2009;6(10):1-5.
227. Pang LY, Argyle DJ. Using naturally occurring tumours in dogs and cats to study telomerase and cancer stem cell biology. Biochimica et Biophysica Acta (BBA) - Molecular Basis of Disease 2009;1792(4):380-391.
228. Lindblad-Toh K, Wade CM, Mikkelsen TS, Karlsson EK, Jaffe DB, Kamal M, Clamp M, Chang JL, Kulbokas EJ, 3rd, Zody MC and others. Genome sequence, comparative analysis and haplotype structure of the domestic dog. Nature 2005;438(7069):803-819.
229. Hoffman MM, Birney E. Estimating the Neutral Rate of Nucleotide Substitution Using Introns. Molecular Biology and Evolution 2006;24(2):522-531.
230. Fenger JM, Rowell JL, Zapata I, Kisseberth WC, London CA, Alvarez CE. Dog models of naturally occurring cancer. Animal Models for Human Cancer: Wiley Online Library; 2016. p 153-221.
231. Moe L. Population-based incidence of mammary tumours in some dog breeds. Journal of reproduction and fertility. Supplement 2001;57:439-443.
232. Pollán M, Pastor-Barriuso R, Ardanaz E, Argüelles M, Martos C, Galcerán J, Sánchez-Pérez M-J, Chirlaque M-D, Larrañaga N, Martínez-Cobo R. Recent changes in breast cancer incidence in Spain, 1980–2004. Journal of the National Cancer Institute 2009;101(22):1584-1591.

233. Dobson JM, Samuel S, Milstein H, Rogers K, Wood JL. Canine neoplasia in the UK: estimates of incidence rates from a population of insured dogs. J Small Anim Pract 2002;43:240-256.
234. Schneider R. Comparison of age, sex, and incidence rates in human and canine breast cancer. Cancer 1970;26(2):419-426.
235. Cohen D, Reif JS, Brodey RS, Keiser H. Epidemiological Analysis of the Most Prevalent Sites and Types of Canine Neoplasia Observed in a Veterinary Hospital. Cancer Research 1974;34(11):2859-2868.
236. Salas Y, Marquez A, Diaz D, Romero L. Epidemiological Study of Mammary Tumors in Female Dogs Diagnosed during the Period 2002-2012: A Growing Animal Health Problem.(Report). 2015;10(5).
237. Schneider R, Dorn CR, Taylor D. Factors Influencing Canine Mammary Cancer Development and Postsurgical Survival. Journal of the National Cancer Institute 1969;43(6):1249-1261.
238. Sonnenschein EG, Glickman LT, Goldschmidt MH, McKee LJ. Body conformation, diet, and risk of breast cancer in pet dogs: a case-control study. American journal of epidemiology 1991;133(7):694-703.
239. Alenza DP, Rutteman GR, Peña L, Beynen AC, Cuesta P. Relation between Habitual Diet and Canine Mammary Tumors in a Case-Control Study. Journal of Veterinary Internal Medicine 1998;12(3):132-139.
240. Greenberg E, Vessey M, McPherson K, Doll R, Yeates D. Body size and survival in premenopausal breast cancer. British journal of cancer 1985;51(5):691-693.
241. Harvie M, Howell A, Vierkant RA, Kumar N, Cerhan JR, Kelemen LE, Folsom AR, Sellers TA. Association of gain and loss of weight before and after menopause with risk of postmenopausal breast cancer in the Iowa women's health study. Cancer Epidemiology and Prevention Biomarkers 2005;14(3):656-661.
242. Gilbertson S, Kurzman I, Zachrau R, Hurvitz A, Black M. Canine mammary epithelial neoplasms: biologic implications of morphologic characteristics assessed in 232 dogs. Veterinary pathology 1983;20(2):127-142.
243. Rosol TJ, Tannehill‐Gregg SH, LeRoy BE, Mandl S, Contag CH. Animal models of bone metastasis. Cancer: Interdisciplinary International Journal of the American Cancer Society 2003;97(S3):748-757.
244. O'Shaughnessy J. Extending Survival with Chemotherapy in Metastatic Breast Cancer. The Oncologist 2005;10(3):20-29.
245. Nguyen F, Peña L, Ibisch C, Loussouarn D, Gama A, Rieder N, Belousov A, Campone M, Abadie J. Canine invasive mammary carcinomas as models of human breast cancer. Part 1: natural history and prognostic factors. Breast cancer research and treatment 2018;167(3):635-648.
246. Sarli G, Preziosi R, Benazzi C, Castellani G, Marcato PS. Prognostic value of histologic stage and proliferative activity in canine malignant mammary tumors. Journal of Veterinary Diagnostic Investigation 2002;14(1):25-34.
247. Klopfleisch R, Lenze D, Hummel M, Gruber AD. Metastatic canine mammary carcinomas can be identified by a gene expression profile that partly overlaps with human breast cancer profiles. BMC Cancer 2010;10(1):618-629.

248. Klopfleisch R, Klose P, Weise C, Bondzio A, Multhaup G, Einspanier R, Gruber AD. Proteome of metastatic canine mammary carcinomas: similarities to and differences from human breast cancer. Journal of proteome research 2010;9(12):6380-6391.
249. MacEwen E, Patnaik A, Harvey H, Panko W. Estrogen receptors in canine mammary tumors. Cancer research 1982;42(6):2255-2259.
250. Rutteman G, Misdorp W, Blankenstein M, Van den Brom W. Oestrogen (ER) and progestin receptors (PR) in mammary tissue of the female dog: different receptor profile in non-malignant and malignant states. British journal of cancer 1988;58(5):594-599.
251. Pichon MF, Broet P, Magdelenat H, Delarue JC, Spyratos F, Basuyau JP, Saez S, Rallet A, Courriere P, Millon R and others. Prognostic value of steroid receptors after long-term follow-up of 2257 operable breast cancers. Br J Cancer 1996;73(12):1545-51.
252. Kim NH, Lim HY, Im KS, Shin JI, Kim HW, Sur JH. Evaluation of Clinicopathological Characteristics and Oestrogen Receptor Gene Expression in Oestrogen Receptor-negative, Progesterone Receptor-positive Canine Mammary Carcinomas. Journal of Comparative Pathology 2014;151(1):42-50.
253. Mainenti M, Rasotto R, Carnier P, Zappulli V. Oestrogen and progesterone receptor expression in subtypes of canine mammary tumours in intact and ovariectomised dogs. The Veterinary Journal 2014;202(1):62-68.
254. Millanta F, Calandrella M, Bari G, Niccolini M, Vannozzi I, Poli A. Comparison of steroid receptor expression in normal, dysplastic, and neoplastic canine and feline mammary tissues. Res Vet Sci 2005;79(3):225-232.
255. Kim NH, Lim HY, Im KS, Shin JI, Kim HW, Sur JH. Evaluation of clinicopathological characteristics and oestrogen receptor gene expression in oestrogen receptor-negative, progesterone receptor-positive canine mammary carcinomas. J Comp Pathol 2014;151(1):42-50.
256. Worzfeld T, Swiercz JM, Looso M, Straub BK, Sivaraj KK, Offermanns S. ErbB-2 signals through Plexin-B1 to promote breast cancer metastasis. J Clin Invest 2012;122(4):1296-1305.
257. Dutra A, Granja N, Schmitt F, Cassali G. c-erbB-2 expression and nuclear pleomorphism in canine mammary tumors. Brazilian Journal of Medical and Biological Research 2004;37(11):1673-1681.
258. Hsu WL, Huang HM, Liao JW, Wong ML, Chang SC. Increased survival in dogs with malignant mammary tumours overexpressing HER-2 protein and detection of a silent single nucleotide polymorphism in the canine HER-2 gene. Vet J 2009;180(1):116-123.
259. Muhammadnejad A, Keyhani E, Mortazavi P, Behjati F, Haghdoost IS. Overexpression of her-2/neu in malignant mammary tumors; translation of clinicopathological features from dog to human. Asian Pac J Cancer Prev 2012;13(12):6415-6421.
260. Silva I, Dias A, Bertagnolli A, Cassali G, Ferreira E. Analysis of EGFR and HER-2 expressions in ductal carcinomas in situ in canine mammary glands. Arquivo Brasileiro de Medicina Veterinária e Zootecnia 2014;66(3):763-768.

261. Kaszak I, Ruszczak A, Kanafa S, Kacprzak K, Król M, Jurka P. Current biomarkers of canine mammary tumors. Acta veterinaria Scandinavica 2018;60(1):66-72.
262. Campos LC, Silva JO, Santos FS, Araujo MR, Lavalle GE, Ferreira E, Cassali GD. Prognostic significance of tissue and serum HER2 and MUC1 in canine mammary cancer. J Vet Diagn Invest 2015;27(4):531-535.
263. Ressel L, Puleio R, Loria GR, Vannozzi I, Millanta F, Caracappa S, Poli A. HER-2 expression in canine morphologically normal, hyperplastic and neoplastic mammary tissues and its correlation with the clinical outcome. Res Vet Sci 2013;94(2):299-305.
264. Masuda H, Zhang D, Bartholomeusz C, Doihara H, Hortobagyi GN, Ueno NT. Role of epidermal growth factor receptor in breast cancer. Breast Cancer Res Treat 2012;136(2):331-345.
265. Carvalho MI, Guimaraes MJ, Pires I, Prada J, Silva-Carvalho R, Lopes C, Queiroga FL. EGFR and microvessel density in canine malignant mammary tumours. Res Vet Sci 2013;95(3):1094-1099.
266. Gama A, Gärtner F, Alves A, Schmitt F. Immunohistochemical expression of Epidermal Growth Factor Receptor (EGFR) in canine mammary tissues. Research in Veterinary Science 2009;87(3):432-437.
267. Guimaraes M, Carvalho M, Pires I, Prada J, Gil AG, Lopes C, Queiroga F. Concurrent expression of cyclo-oxygenase-2 and epidermal growth factor receptor in canine malignant mammary tumours. Journal of comparative pathology 2014;150(1):27-34.
268. Uva P, Aurisicchio L, Watters J, Loboda A, Kulkarni A, Castle J, Palombo F, Viti V, Mesiti G, Zappulli V and others. Comparative expression pathway analysis of human and canine mammary tumors. BMC Genomics 2009;10(1):135-155.
269. Queiroga FL, Raposo T, Carvalho MI, Prada J, Pires I. Canine mammary tumours as a model to study human breast cancer: most recent findings. in vivo 2011;25(3):455-465.
270. Lee C-H, Kim W-H, Lim J-H, Kang M-S, Kim D-Y, Kweon O-K. Mutation and overexpression of p53 as a prognostic factor in canine mammary tumors. Journal of Veterinary Science 2004;5(1):63-70.
271. Lee CH, Kweon OK. Mutations of p53 tumor suppressor gene in spontaneous canine mammary tumors. Journal of veterinary science 2002;3(4):321-326.
272. Wakui S, Muto T, Yokoo K, Yokoo R, Takahashi H, Masaoka T, Hano H, Furusato M. Prognostic status of p53 gene mutation in canine mammary carcinoma. Anticancer research 2001;21(1B):611-616.
273. Gray ME, Meehan J, Sullivan P, Marland JRK, Greenhalgh SN, Gregson R, Clutton RE, Ward C, Cousens C, Griffiths DJ and others. Ovine Pulmonary Adenocarcinoma: A Unique Model to Improve Lung Cancer Research. Frontiers in Oncology 2019;9(335):1-11.
274. Kirschvink N, Reinhold P. Use of alternative animals as asthma models. Current drug targets 2008;9(6):470-484.
275. Meeusen EN, Snibson KJ, Hirst SJ, Bischof RJ. Sheep as a model species for the study and treatment of human asthma and other respiratory diseases. Drug Discovery Today: Disease Models 2009;6(4):101-106.

276. Plopper CG, Mariassy AT, Wilson DW, Alley JL, Nishio SJ, Nettesheim P. Comparison of Nonciliated Tracheal Epithelial Cells in Six Mammalian Species: Ultrastructure and Population Densities. Experimental Lung Research 1983;5(4):281-294.
277. Miller HRP. Mucosal mast cells and the allergic response against nematode parasites. Veterinary Immunology and Immunopathology 1996;54(1):331-336.
278. Collie D, Pyrah I, Watt NJ. Distribution and quantitation of lung parenchymal contractile tissue in ovine lentivirus-induced lymphoid interstitial pneumonia. Do tissue forces limit lung distensibility? Laboratory investigation; a journal of technical methods and pathology 1995;73(3):441-447.
279. Matute-Bello G, Frevert CW, Martin TR. Animal models of acute lung injury. American Journal of Physiology-Lung Cellular and Molecular Physiology 2008;295(3):379-399.
280. Ackermann MR. Lamb Model of Respiratory Syncytial Virus–Associated Lung Disease: Insights to Pathogenesis and Novel Treatments. ILAR Journal 2014;55(1):4-15.
281. Viard R, Tourneux P, Storme L, Girard J-M, Betrouni N, Rousseau J. Magnetic resonance imaging spatial and time study of lung water content in newborn lamb: methods and preliminary results. Investigative radiology 2008;43(6):470-480.
282. Cousens C, Scott PR. Assessment of transthoracic ultrasound diagnosis of ovine pulmonary adenocarcinoma in adult sheep. Veterinary Record 2015;177(14):366-371.
283. Radu DM, Seguin A, Bruneval P, Fialaire Legendre A, Carpentier A, Martinod E. Bronchial Replacement With Arterial Allografts. The Annals of Thoracic Surgery 2010;90(1):252-258.
284. Van der Velden J, Barker D, Barcham G, Koumoundouros E, Snibson K. Assessment of Peripheral Airway Function following Chronic Allergen Challenge in a Sheep Model of Asthma (Small Airway Function in a Sheep Model of Asthma). PLoS ONE 2011;6(12):28740-28746.
285. Abraham WM. Modeling of asthma, COPD and cystic fibrosis in sheep. Pulmonary Pharmacology & Therapeutics 2008;21(5):743-754.
286. Bem RA, Domachowske JB, Rosenberg HF. Animal models of human respiratory syncytial virus disease. American Journal of Physiology-Lung Cellular and Molecular Physiology 2011;301(2):148-156.
287. Youssef G, Wallace WAH, Dagleish MP, Cousens C, Griffiths DJ. Ovine Pulmonary Adenocarcinoma: A Large Animal Model for Human Lung Cancer. Institute for Laboratory Animal Research Journal 2015;56(1):99-115.
288. Travis WD, Brambilla E, Noguchi M, Nicholson AG, Geisinger KR, Yatabe Y, Beer DG, Powell CA, Riely GJ, Van Schil PE and others. International Association for the Study of Lung Cancer/American Thoracic Society/European Respiratory Society International Multidisciplinary Classification of Lung Adenocarcinoma. Journal of Thoracic Oncology 2011;6(2):244-285.
289. Sekido Y, Fong KM, Minna JD. Progress in understanding the molecular pathogenesis of human lung cancer. Biochimica et Biophysica Acta (BBA) - Reviews on Cancer 1998;1378(1):21-59.

290. Carey FA, Wallace WA, Fergusson RJ, Kerr KM, Lamb D. Alveolar atypical hyperplasia in association with primary pulmonary adenocarcinoma: a clinicopathological study of 10 cases. Thorax 1992;47(12):1041-1043.
291. Coggins CR. A review of chronic inhalation studies with mainstream cigarette smoke, in hamsters, dogs, and non-human primates. Toxicologic pathology 2001;29(5):550-557.
292. Liu J, Johnston MR. Animal models for studying lung cancer and evaluating novel intervention strategies. Surgical oncology 2002;11(4):217-227.
293. Pozzi A. Mouse models of lung cancer. Principles and Practice of Lung Cancer, 4th edition. Lippincott Williams and Wilkins, Philadelphia 2010:179-187.
294. Lynch CJ. Studies on the relation between tumor susceptibility and heredity: III. Spontaneous tumors of the lung in mice. Journal of Experimental Medicine 1926;43(3):339-355.
295. Tuveson DA, Jacks T. Modeling human lung cancer in mice: similarities and shortcomings. Oncogene 1999;18:5318–5324.
296. Stoner GD, Adam-Rodwell G, Morse MA. Lung tumors in strain a mice: Application for studies in cancer chemoprevention. Journal of Cellular Biochemistry 1993;53(S17F):95-103.
297. Hoenerhoff MJ, Hong HH, Ton T-v, Lahousse SA, Sills RC. A review of the molecular mechanisms of chemically induced neoplasia in rat and mouse models in National Toxicology Program bioassays and their relevance to human cancer. Toxicologic pathology 2009;37(7):835-848.
298. Szymanska H, Sitarz M, Krysiak E, Piskorowska J, Czarnomska A, Skurzak H, Hart AA, de Jong D, Demant P. Genetics of susceptibility to radiation‐induced lymphomas, leukemias and lung tumors studied in recombinant congenic strains. International journal of cancer 1999;83(5):674-678.
299. Mase K, Iijima T, Nakamura N, Takeuchi T, Onizuka M, Mitsui T, Noguchi M. Intrabronchial orthotopic propagation of human lung adenocarcinoma—characterizations of tumorigenicity, invasion and metastasis. Lung Cancer 2002;36(3):271-276.
300. Kozaki K-i, Miyaishi O, Tsukamoto T, Tatematsu Y, Hida T, Takahashi T, Takahashi T. Establishment and characterization of a human lung cancer cell line NCI-H460-LNM35 with consistent lymphogenous metastasis via both subcutaneous and orthotopic propagation. Cancer Research 2000;60(9):2535-2540.
301. Kuo T-H, Kubota T, Watanabe M, Furukawa T, Kase S, Tanino H, Nishibori H, Saikawa Y, Teramoto T, Ihsibiki K. Orthotopic reconstitution of human small-cell lung carcinoma after intravenous transplantation in SCID mice. Anticancer research 1992;12(5):1407-1410.
302. Manzotti C, Audisio RA, Pratesi G. Importance of orthotopic implantation for human tumors as model systems: relevance to metastasis and invasion. Clinical & experimental metastasis 1993;11(1):5-14.
303. Moorehead RA, Sanchez OH, Baldwin RM, Khokha R. Transgenic overexpression of IGF-II induces spontaneous lung tumors: a model for human lung adenocarcinoma. Oncogene 2003;22(6):853–857.
304. Kohno T, Yokota1 J. How many tumor suppressor genes are involved in human lung carcinogenesis? Carcinogenesis 1999;20(8):1403-1410.

305. Salgia R, Skarin AT. Molecular abnormalities in lung cancer. Journal of Clinical Oncology 1998;16(3):1207-1217.
306. Hoffman RM. Green fluorescent protein imaging of tumour growth, metastasis, and angiogenesis in mouse models. The lancet oncology 2002;3(9):546-556.
307. El Hilali N, Rubio N, Martinez-Villacampa M, Blanco J. Combined noninvasive imaging and luminometric quantification of luciferase-labeled human prostate tumors and metastases. Laboratory investigation 2002;82(11):1563–1571.
308. Mainardi S, Mijimolle N, Francoz S, Vicente-Dueñas C, Sánchez-García I, Barbacid M. Identification of cancer initiating cells in K-Ras driven lung adenocarcinoma. Proceedings of the National Academy of Sciences 2014;111(1):255-260.
309. Palmarini M, Fan H. Retrovirus-induced ovine pulmonary adenocarcinoma, an animal model for lung cancer. Journal of the National Cancer Institute 2001;93(21):1603-1614.
310. DeMartini JC, York DF. Retrovirus-associated neoplasms of the respiratory system of sheep and goats: ovine pulmonary carcinoma and enzootic nasal tumor. Veterinary Clinics: Food Animal Practice 1997;13(1):55-70.
311. Palmarini M, Fan H, Sharp JM. Sheep pulmonary adenomatosis: a unique model of retrovirus associated lung cancer. Trends in microbiology 1997;5(12):478-483.
312. Griffiths DJ, Martineau HM, Cousens C. Pathology and Pathogenesis of Ovine Pulmonary Adenocarcinoma. Journal of Comparative Pathology 2010;142(4):260-283.
313. Leroux C, Girard N, Cottin V, Greenland T, Mornex J-F, Archer F. Jaagsiekte Sheep Retrovirus (JSRV): from virus to lung cancer in sheep. Veterinary research 2007;38(2):211-228.
314. Tustin R. Ovine jaagsiekte. Journal of the South African Veterinary Medical Association 1969;40:3-23.
315. De las Heras M, Gonzalez L, Sharp J. Pathology of ovine pulmonary adenocarcinoma. Jaagsiekte Sheep Retrovirus and Lung Cancer: Springer; 2003. p 25-54.
316. Sanna MP, Sanna E, De Las Heras M, Leoni A, Nieddu A, Pirino S, Sharp J, Palmarini M. Association of jaagsiekte sheep retrovirus with pulmonary carcinoma in Sardinian moufflon (Ovis musimon). Journal of comparative pathology 2001;125(2-3):145-152.
317. Fan H. Jaagsiekte sheep retrovirus and lung cancer: Springer Science & Business Media; 2003.
318. Dungal N, Gislason G, Taylor E. Epizootic adenomatosis in the lungs of sheep—comparisons with jaagsiekte, verminous pneumonia and progressive pneumonia. Journal of Comparative Pathology and Therapeutics 1938;51:46-68.
319. Sharp J, DeMartini J. Natural history of JSRV in sheep. Jaagsiekte Sheep Retrovirus and Lung Cancer: Springer; 2003. p 55-79.
320. Dungal N. Experiments with Jaagsiekte. The American journal of pathology 1946;22(4):737-759.

321. Grego E, De Meneghi D, Álvarez V, Benito AA, Minguijón E, Ortín A, Mattoni M, Moreno B, De Villarreal MP, Alberti A. Colostrum and milk can transmit jaagsiekte retrovirus to lambs. Veterinary microbiology 2008;130(3-4):247-257.
322. York DF, Vigne R, Verwoerd DW, Querat G. Nucleotide sequence of the jaagsiekte retrovirus, an exogenous and endogenous type D and B retrovirus of sheep and goats. Journal of Virology 1992;66(8):4930-4939.
323. Palmarini M, Fan H. Molecular biology of jaagsiekte sheep retrovirus. Jaagsiekte Sheep Retrovirus and Lung Cancer: Springer; 2003. p 81-115.
324. Maeda N, Palmarini M, Murgia C, Fan H. Direct transformation of rodent fibroblasts by jaagsiekte sheep retrovirus DNA. Proceedings of the National Academy of Sciences 2001;98(8):4449-4454.
325. Cousens C, Maeda N, Murgia C, Dagleish MP, Palmarini M, Fan H. In vivo tumorigenesis by Jaagsiekte sheep retrovirus (JSRV) requires Y590 in Env TM, but not full-length orfX open reading frame. Virology 2007;367(2):413-421.
326. Caporale M, Cousens C, Centorame P, Pinoni C, De las Heras M, Palmarini M. Expression of the Jaagsiekte Sheep Retrovirus Envelope Glycoprotein Is Sufficient To Induce Lung Tumors in Sheep. Journal of Virology 2006;80(16):8030-8037.
327. Wootton SK, Halbert CL, Miller AD. Sheep retrovirus structural protein induces lung tumours. Nature 2005;434(7035):904–907.
328. Rai SK, Duh F-M, Vigdorovich V, Danilkovitch-Miagkova A, Lerman MI, Miller AD. Candidate tumor suppressor HYAL2 is a glycosylphosphatidylinositol (GPI)-anchored cell-surface receptor for jaagsiekte sheep retrovirus, the envelope protein of which mediates oncogenic transformation. Proceedings of the National Academy of Sciences 2001;98(8):4443-4448.
329. Hofacre A, Fan H. Jaagsiekte sheep retrovirus biology and oncogenesis. Viruses 2010;2(12):2618-2648.
330. Varela M, Golder M, Archer F, de las Heras M, Leroux C, Palmarini M. A large animal model to evaluate the effects of Hsp90 inhibitors for the treatment of lung adenocarcinoma. Virology 2008;371(1):206-215.
331. Suau F, Cottin V, Archer F, Croze S, Chastang J, Cordier G, Thivolet-Bejui F, Mornex J, Leroux C. Telomerase activation in a model of lung adenocarcinoma. European Respiratory Journal 2006;27(6):1175-1182.
332. Arnaud F, Caporale M, Varela M, Biek R, Chessa B, Alberti A, Golder M, Mura M, Zhang YP, Yu L and others. A paradigm for virus-host coevolution: sequential counter-adaptations between endogenous and exogenous retroviruses. PLoS Pathology 2007;3(11):1716-1729.
333. Cumer T, Pompanon F, Boyer F. Old origin of a protective endogenous retrovirus (enJSRV) in the Ovis genus. Heredity 2018:187–194.
334. Hecht SJ, Carlson JO, Demartini JC. Analysis of a Type D Retroviral Capsid Gene Expressed in Ovine Pulmonary Carcinoma and Present in Both Affected and Unaffected Sheep Genomes. Virology 1994;202(1):480-484.
335. DeMartini J, Carlson J, Leroux C, Spencer T, Palmarini M. Endogenous retroviruses related to jaagsiekte sheep retrovirus. Jaagsiekte Sheep Retrovirus and Lung Cancer: Springer; 2003. p 117-137.

336. Palmarini M, Mura M, Spencer TE. Endogenous betaretroviruses of sheep: teaching new lessons in retroviral interference and adaptation. Journal of General Virology 2004;85(1):1-13.
337. Arnaud F, Murcia PR, Palmarini M. Mechanisms of Late Restriction Induced by an Endogenous Retrovirus. Journal of Virology 2007;81(20):11441-11451.
338. Caporale M, Martineau H, De las Heras M, Murgia C, Huang R, Centorame P, Di Francesco G, Di Gialleonardo L, Spencer TE, Griffiths DJ and others. Host species barriers to Jaagsiekte sheep retrovirus replication and carcinogenesis. Journal of Virology 2013;87(19):10752-10762.
339. Hudachek SF, Kraft SL, Thamm DH, Bielefeldt-Ohmann H, DeMartini JC, Miller AD, Dernell WS. Lung Tumor Development and Spontaneous Regression in Lambs Coinfected With Jaagsiekte Sheep Retrovirus and Ovine Lentivirus. Veterinary Pathology Online 2010;47(1):148-162.
340. Summers C, Norval M, De las Heras M, Gonzalez L, Sharp JM, Woods GM. An influx of macrophages is the predominant local immune response in ovine pulmonary adenocarcinoma. Veterinary Immunology and Immunopathology 2005;106(3):285-294.
341. Scott P, Griffiths D, Cousens C. Diagnosis and control of ovine pulmonary adenocarcinoma (Jaagsiekte). In Practice 2013;35(7):382-397.
342. Scott P, Collie D, McGorum B, Sargison N. Relationship between thoracic auscultation and lung pathology detected by ultrasonography in sheep. The Veterinary Journal 2010;186(1):53-57.
343. Cousens C, Thonur L, Imlach S, Crawford J, Sales J, Griffiths DJ. Jaagsiekte sheep retrovirus is present at high concentration in lung fluid produced by ovine pulmonary adenocarcinoma-affected sheep and can survive for several weeks at ambient temperatures. Research in veterinary science 2009;87(1):154-156.
344. Scott PR, Dagleish MP, Cousens C. Development of superficial lung lesions monitored on farm by serial ultrasonographic examination in sheep with lesions confirmed as ovine pulmonary adenocarcinoma at necropsy. Irish Veterinary Journal 2018;71(1):23-29.
345. Cousens C, Graham M, Sales J, Dagleish MP. Evaluation of the efficacy of clinical diagnosis of ovine pulmonary adenocarcinoma. Veterinary Record 2008;162(3):88-95.
346. Ortín A, Minguijón E, Dewar P, García M, Ferrer LM, Palmarini M, Gonzalez L, Sharp JM, De las Heras M. Lack of a specific immune response against a recombinant capsid protein of Jaagsiekte sheep retrovirus in sheep and goats naturally affected by enzootic nasal tumour or sheep pulmonary adenomatosis. Veterinary Immunology and Immunopathology 1998;61(2):229-237.
347. De las Heras M, Ortín A, Salvatori D, de Villareal MP, Cousens C, Ferrer LM, Cebrián LM, de Jalón JAG, Gonzalez L, Sharp JM. A PCR technique for the detection of Jaagsiekte sheep retrovirus in the blood suitable for the screening of ovine pulmonary adenocarcinoma in field conditions. Research in veterinary science 2005;79(3):259-264.

348. Lewis FI, Brülisauer F, Cousens C, McKendrick IJ, Gunn GJ. Diagnostic accuracy of PCR for Jaagsiekte sheep retrovirus using field data from 125 Scottish sheep flocks. The Veterinary Journal 2011;187(1):104-108.
349. Voigt K, Brügmann M, Huber K, Dewar P, Cousens C, Hall M, Sharp JM, Ganter M. PCR examination of bronchoalveolar lavage samples is a useful tool in pre-clinical diagnosis of ovine pulmonary adenocarcinoma (Jaagsiekte). Research in Veterinary Science 2007;83(3):419-427.
350. Martineau HM, Cousens C, Imlach S, Dagleish MP, Griffiths DJ. Jaagsiekte sheep retrovirus infects multiple cell types in the ovine lung. Journal of virology 2011;85(7):3341-3355.
351. Murgia C, Caporale M, Ceesay O, Di Francesco G, Ferri N, Varasano V, de las Heras M, Palmarini M. Lung adenocarcinoma originates from retrovirus infection of proliferating type 2 pneumocytes during pulmonary post-natal development or tissue repair. PLoS pathogens 2011;7(3):1-12.
352. Platt J, Kraipowich N, Villafane F, DeMartini J. Alveolar type II cells expressing jaagsiekte sheep retrovirus capsid protein and surfactant proteins are the predominant neoplastic cell type in ovine pulmonary adenocarcinoma. Veterinary Pathology 2002;39(3):341-352.
353. De las Heras M, de Martino A, Borobia M, Ortin A, Alvarez R, Borderias L, Gimenez-Mas JA. Solitary tumours associated with Jaagsiekte retrovirus in sheep are heterogeneous and contain cells expressing markers identifying progenitor cells in lung repair. Journal of Comparative Pathology 2014;150(2-3):138-47.
354. Cousens C, Bishop JV, Philbey AW, Gill CA, Palmarini M, Carlson JO, DeMartini JC, Sharp JM. Analysis of integration sites of Jaagsiekte sheep retrovirus in ovine pulmonary adenocarcinoma. Journal of Virology 2004;78:8506-8512.
355. Demartini JC, Rosadio RH, Lairmore MD. The etiology and pathogenesis of ovine pulmonary carcinoma (sheep pulmonary adenomatosis). Veterinary microbiology 1988;17(3):219-236.
356. Rosadio R, Lairmore M, Russell H, DeMartini J. Retrovirus-associated ovine pulmonary carcinoma (sheep pulmonary adenomatosis) and lymphoid interstitial pneumonia. I. Lesion development and age susceptibility. Veterinary pathology 1988;25(6):475-483.
357. Minguijón E, González L, De las Heras M, Gómez N, García-Goti M, Juste RA, Moreno B. Pathological and Aetiological Studies in Sheep Exhibiting Extrathoracic Metastasis of Ovine Pulmonary Adenocarcinoma (Jaagsiekte). Journal of Comparative Pathology 2013;148(2):139-147.
358. Nobel T, Neumann F, Klopfer U. Histological patterns of the metastases in pulmonary adenomatosis of sheep (jaagsiekte). Journal of comparative pathology 1969;79(4):537-545.
359. Soule HD, Vazquez J, Long A, Albert S, Brennan M. A human cell line from a pleural effusion derived from a breast carcinoma. Journal of the National Cancer Institute 1973;51(5):1409-1416.
360. Lee AV, Oesterreich S, Davidson NE. MCF-7 Cells—Changing the Course of Breast Cancer Research and Care for 45 Years. Journal of the National Cancer Institute 2015;107(7):1-4.

361. Engel LW, Young NA, Tralka TS, Lippman ME, O'Brien SJ, Joyce MJ. Establishment and characterization of three new continuous cell lines derived from human breast carcinomas. Cancer research 1978;38(10):3352-3364.
362. Cailleau R, Olivé M, Cruciger Q. Long-term human breast carcinoma cell lines of metastatic origin: Preliminary characterization. In Vitro 1978;14(11):911-915.
363. Gaffney E. A cell line (HBL-100) established from human breast milk. Cell and Tissue Research 1982;227(3):563-568.
364. Else RW, Norval M, Neill WA. The characteristics of a canine mammary carcinoma cell line, REM 134. British Journal of Cancer 1982;46(4):675-681.
365. DeMartini JC, Bishop JV, Allen TE, Jassim F, Sharp JM, de las Heras M, Voelker DR, Carlson JO. Jaagsiekte sheep retrovirus proviral clone JSRVJS7, derived from the JS7 lung tumor cell line, induces ovine pulmonary carcinoma and is integrated into the surfactant protein A gene. Journal of virology 2001;75(9):4239-4246.
366. Weiswald L-B, Bellet D, Dangles-Marie V. Spherical cancer models in tumor biology. Neoplasia 2015;17(1):1-15.
367. Skehan P, Storeng R, Scudiero D, Monks A, McMahon J, Vistica D, Warren JT, Bokesch H, Kenney S, Boyd MR. New colorimetric cytotoxicity assay for anticancer-drug screening. JNCI: Journal of the National Cancer Institute 1990;82(13):1107-1112.
368. Voigt W. Sulforhodamine B assay and chemosensitivity. Chemosensitivity: Springer; 2005. p 39-48.
369. Vichai V, Kirtikara K. Sulforhodamine B colorimetric assay for cytotoxicity screening. Nature protocols 2006;1(3):1112.
370. Liang C-C, Park AY, Guan J-L. In vitro scratch assay: a convenient and inexpensive method for analysis of cell migration in vitro. Nature Protocols 2007;2:329–333.
371. Kramer N, Walzl A, Unger C, Rosner M, Krupitza G, Hengstschläger M, Dolznig H. In vitro cell migration and invasion assays. Mutation Research/Reviews in Mutation Research 2013;752(1):10-24.
372. Dobin A, Davis CA, Schlesinger F, Drenkow J, Zaleski C, Jha S, Batut P, Chaisson M, Gingeras TR. STAR: ultrafast universal RNA-seq aligner. Bioinformatics 2013;29(1):15-21.
373. Gentleman RC, Carey VJ, Bates DM, Bolstad B, Dettling M, Dudoit S, Ellis B, Gautier L, Ge Y, Gentry J. Bioconductor: open software development for computational biology and bioinformatics. Genome biology 2004;5(10):80-96.
374. Howe E, Holton K, Nair S, Schlauch D, Sinha R, Quackenbush J. MeV: MultiExperiment Viewer. In: Ochs MF, Casagrande JT, Davuluri RV, editors. Biomedical Informatics for Cancer Research. Boston, MA: Springer US; 2010. p 267-277.
375. Leek JT, Johnson WE, Parker HS, Jaffe AE, Storey JD. The sva package for removing batch effects and other unwanted variation in high-throughput experiments. Bioinformatics 2012;28(6):882-883.
376. Turnbull AK, Kitchen RR, Larionov AA, Renshaw L, Dixon JM, Sims AH. Direct integration of intensity-level data from Affymetrix and Illumina

microarrays improves statistical power for robust reanalysis. BMC Medical Genomics 2012;5(1):5-35.
377. Sørlie T, Tibshirani R, Parker J, Hastie T, Marron JS, Nobel A, Deng S, Johnsen H, Pesich R, Geisler S. Repeated observation of breast tumor subtypes in independent gene expression data sets. Proceedings of the national academy of sciences 2003;100(14):8418-8423.
378. Gendoo DM, Ratanasirigulchai N, Schröder MS, Paré L, Parker JS, Prat A, Haibe-Kains B. Genefu: an R/Bioconductor package for computation of gene expression-based signatures in breast cancer. Bioinformatics 2015;32(7):1097-1099.
379. Bardou P, Mariette J, Escudié F, Djemiel C, Klopp C. jvenn: an interactive Venn diagram viewer. BMC bioinformatics 2014;15(1):286-293.
380. Edgar R, Domrachev M, Lash AE. Gene Expression Omnibus: NCBI gene expression and hybridization array data repository. Nucleic acids research 2002;30(1):207-210.
381. Szklarczyk D, Morris JH, Cook H, Kuhn M, Wyder S, Simonovic M, Santos A, Doncheva NT, Roth A, Bork P and others. The STRING database in 2017: quality-controlled protein-protein association networks, made broadly accessible. Nucleic Acids Research 2017;45(1):362-368.
382. Vlasblom J, Wodak SJ. Markov clustering versus affinity propagation for the partitioning of protein interaction graphs. BMC bioinformatics 2009;10(1):99-113.
383. Bankhead P, Loughrey MB, Fernandez JA, Dombrowski Y, McArt DG, Dunne PD, McQuaid S, Gray RT, Murray LJ, Coleman HG and others. QuPath: Open source software for digital pathology image analysis. Scientific Reports 2017;7(1):16878-16885.
384. Dowsett M, Nielsen TO, A'hern R, Bartlett J, Coombes RC, Cuzick J, Ellis M, Henry NL, Hugh JC, Lively T. Assessment of Ki67 in breast cancer: recommendations from the International Ki67 in Breast Cancer working group. Journal of the National Cancer Institute 2011;103(22):1656-1664.
385. Pathmanathan N, Balleine RL. Ki67 and proliferation in breast cancer. Journal of clinical pathology 2013;66:512–516.
386. Hu H, Wang Y, Ding X, He Y, Lu Z, Wu P, Tian L, Yuan H, Liu D, Shi G. Long non-coding RNA XLOC_000647 suppresses progression of pancreatic cancer and decreases epithelial-mesenchymal transition-induced cell invasion by down-regulating NLRP3. Molecular cancer 2018;17(1):18.
387. Mosaad E, Chambers K, Futrega K, Clements J, Doran M. The Microwell-mesh: A high-throughput 3D prostate cancer spheroid and drug-testing platform. Scientific reports 2018;8(1):253.
388. Ling B, Watt K, Banerjee S, Newsted D, Truesdell P, Adams J, Sidhu SS, Craig AW. A novel immunotherapy targeting MMP-14 limits hypoxia, immune suppression and metastasis in triple-negative breast cancer models. Oncotarget 2017;8(35):58372–58385.
389. Friedman GK, Nan L, Haas MC, Kelly VM, Moore BP, Langford CP, Xu H, Han X, Beierle EA, Markert JM. γ 1 34.5-deleted HSV-1-expressing human cytomegalovirus IRS1 gene kills human glioblastoma cells as efficiently as wild-type HSV-1 in normoxia or hypoxia. Gene therapy 2015;22(4):348–355.

390. McIlwain DR, Berger T, Mak TW. Caspase functions in cell death and disease. Cold Spring Harbor perspectives in biology 2013;5(4):1-6.
391. Flanagan L, Meyer M, Fay J, Curry S, Bacon O, Duessmann H, John K, Boland K, McNamara D, Kay E. Low levels of Caspase-3 predict favourable response to 5FU-based chemotherapy in advanced colorectal cancer: Caspase-3 inhibition as a therapeutic approach. Cell death & disease 2017;7(2):2087-2098.
392. Xie W, Lu Q, Wang K, Lu J, Gu X, Zhu D, Liu F, Guo Z. miR‐34b‐5p inhibition attenuates lung inflammation and apoptosis in an LPS‐induced acute lung injury mouse model by targeting progranulin. Journal of cellular physiology 2018;233(9):6615-6631.
393. Oak C, Khalifa AO, Isali I, Bhaskaran N, Walker E, Shukla S. Diosmetin suppresses human prostate cancer cell proliferation through the induction of apoptosis and cell cycle arrest. International journal of oncology 2018.
394. Thapa D, Cairns EA, Szczesniak A-M, Toguri JT, Caldwell MD, Kelly ME. The Cannabinoids Δ8THC, CBD, and HU-308 Act via Distinct Receptors to Reduce Corneal Pain and Inflammation. Cannabis and cannabinoid research 2018;3(1):11-20.
395. Li Z, Zhao J, Zhang S, Weinman SA. FOXO3-dependent apoptosis limits alcohol-induced liver inflammation by promoting infiltrating macrophage differentiation. Cell death discovery 2018;4(1):16-30.
396. Erin N, Tanrıöver G, Curry A, Akman M, Duymuş Ö, Gorczynski R. CD200fc enhances anti-tumoral immune response and inhibits visceral metastasis of breast carcinoma. Oncotarget 2018;9(27):19147–19158.
397. De Logu F, Nassini R, Materazzi S, Gonçalves MC, Nosi D, Degl'Innocenti DR, Marone IM, Ferreira J, Puma SL, Benemei S. Schwann cell TRPA1 mediates neuroinflammation that sustains macrophage-dependent neuropathic pain in mice. Nature communications 2017;8(1):1887-1903.
398. Thakur VS, Liang YW, Lingappan K, Jiang W, Wang L, Barrios R, Zhou G, Guntupalli B, Shivanna B, Maturu P. Increased susceptibility to hyperoxic lung injury and alveolar simplification in newborn rats by prenatal administration of benzo [a] pyrene. Toxicology letters 2014;230(2):322-332.
399. Burns KA, Rodriguez KF, Hewitt SC, Janardhan KS, Young SL, Korach KS. Role of estrogen receptor signaling required for endometriosis-like lesion establishment in a mouse model. Endocrinology 2012;153(8):3960-3971.
400. Zaynagetdinov R, Sherrill TP, Kendall PL, Segal BH, Weller KP, Tighe RM, Blackwell TS. Identification of myeloid cell subsets in murine lungs using flow cytometry. American journal of respiratory cell and molecular biology 2013;49(2):180-189.
401. Glass AM, Wolf BJ, Schneider KM, Princiotta MF, Taffet SM. Connexin43 is dispensable for phagocytosis. The Journal of Immunology 2013:1-7.
402. McGee HM, Schmidt BA, Booth CJ, Yancopoulos GD, Valenzuela DM, Murphy AJ, Stevens S, Flavell RA, Horsley V. IL-22 promotes fibroblast-mediated wound repair in the skin. Journal of Investigative Dermatology 2013;133(5):1321-1329.
403. Yin S-Y, Jian F-Y, Chen Y-H, Chien S-C, Hsieh M-C, Hsiao P-W, Lee W-H, Kuo Y-H, Yang N-S. Induction of IL-25 secretion from tumour-associated

fibroblasts suppresses mammary tumour metastasis. Nature communications 2016;7:11311-11325.
404. Treiber N, Maity P, Singh K, Kohn M, Keist AF, Ferchiu F, Sante L, Frese S, Bloch W, Kreppel F. Accelerated aging phenotype in mice with conditional deficiency for mitochondrial superoxide dismutase in the connective tissue. Aging cell 2011;10(2):239-254.
405. Wang X, Cho B, Suzuki K, Xu Y, Green JA, An J, Cyster JG. Follicular dendritic cells help establish follicle identity and promote B cell retention in germinal centers. Journal of Experimental Medicine 2011;208(12):2497-2510.
406. Dyson A, Stidwill R, Taylor V, Singer M. The impact of inspired oxygen concentration on tissue oxygenation during progressive haemorrhage. Intensive Care Medicine 2009;35(10):1783-1791.
407. Barker HE, Paget JTE, Khan AA, Harrington KJ. The tumour microenvironment after radiotherapy: mechanisms of resistance and recurrence. Nature Reviews Cancer 2015;15(7):409-425.
408. Keith B, Simon MC. Hypoxia Inducible Factors, stem cells and cancer. Cell 2007;129(3):465-472.
409. Gray M, Turnbull AK, Ward C, Meehan J, Martinez-Perez C, Bonello M, Pang LY, Langdon SP, Kunkler IH, Murray A and others. Development and characterisation of acquired radioresistant breast cancer cell lines. Radiation Oncology 2019;14(1):64.
410. Smith L, Qutob O, Watson MB, Beavis AW, Potts D, Welham KJ, Garimella V, Lind MJ, Drew PJ, Cawkwell L. Proteomic identification of putative biomarkers of radiotherapy resistance: a possible role for the 26S proteasome? Neoplasia 2009;11(11):1194-1207.
411. Ogata H, Goto S, Sato K, Fujibuchi W, Bono H, Kanehisa M. KEGG: Kyoto Encyclopedia of Genes and Genomes. Nucleic Acids Res 1999;27(1):29-34.
412. Thiery JP, Sleeman JP. Complex networks orchestrate epithelial-mesenchymal transitions. Nature Reviews Molecular Cell Biology 2006;7(2):131-142.
413. Thiery JP. Epithelial–mesenchymal transitions in tumour progression. Nature Reviews Cancer 2002;2(6):442–454.
414. Rokavec M, Kaller M, Horst D, Hermeking H. Pan-cancer EMT-signature identifies RBM47 down-regulation during colorectal cancer progression. Scientific reports 2017;7(1):4687-4702.
415. Theys J, Jutten B, Habets R, Paesmans K, Groot AJ, Lambin P, Wouters BG, Lammering G, Vooijs M. E-Cadherin loss associated with EMT promotes radioresistance in human tumor cells. Radiotherapy and Oncology 2011;99(3):392-397.
416. Perou CM, Sørlie T, Eisen MB, Van De Rijn M, Jeffrey SS, Rees CA, Pollack JR, Ross DT, Johnsen H, Akslen LA. Molecular portraits of human breast tumours. Nature 2000;406(6797):747–752
417. Kyndi M, Sørensen FB, Knudsen H, Overgaard M, Nielsen HM, Overgaard J. Estrogen receptor, progesterone receptor, HER-2, and response to postmastectomy radiotherapy in high-risk breast cancer: the Danish Breast Cancer Cooperative Group. Journal of Clinical Oncology 2008;26(9):1419-1426.

418. Wang Y, Yin Q, Yu Q, Zhang J, Liu Z, Wang S, Lv S, Niu Y. A retrospective study of breast cancer subtypes: the risk of relapse and the relations with treatments. Breast cancer research and treatment 2011;130(2):489-498.
419. Creighton CJ, Hilger AM, Murthy S, Rae JM, Chinnaiyan AM, El-Ashry D. Activation of Mitogen-Activated Protein Kinase in Estrogen Receptor α–Positive Breast Cancer Cells In vitro Induces an In vivo Molecular Phenotype of Estrogen Receptor α–Negative Human Breast Tumors. Cancer Research 2006;66(7):3903-3911.
420. van Ooijen H, Hornsveld M, Dam-de Veen C, Velter R, Dou M, Verhaegh W, Burgering B, van de Stolpe A. Assessment of Functional Phosphatidylinositol 3-Kinase Pathway Activity in Cancer Tissue Using Forkhead Box O Target Gene Expression in a Knowledge-Based Computational Model. The American Journal of Pathology 2018;188:1956-1972.
421. Verhaegh W, van Ooijen H, Inda MA, Hatzis P, Versteeg R, Smid M, Martens J, Foekens J, van de Wiel P, Clevers H and others. Selection of personalized patient therapy through the use of knowledge-based computational models that identify tumor-driving signal transduction pathways. Cancer Research 2014;74(11):2936-2945.
422. Dezső Z, Oestreicher J, Weaver A, Santiago S, Agoulnik S, Chow J, Oda Y, Funahashi Y. Gene expression profiling reveals epithelial mesenchymal transition (EMT) genes can selectively differentiate eribulin sensitive breast cancer cells. PLoS One 2014;9(8):106131-106140.
423. Wang T, Tamae D, LeBon T, Shively JE, Yen Y, Li JJ. The role of peroxiredoxin II in radiation-resistant MCF-7 breast cancer cells. Cancer research 2005;65(22):10338-10346.
424. Li Z, Xia L, Lee LM, Khaletskiy A, Wang J, Wong JY, Li J-J. Effector genes altered in MCF-7 human breast cancer cells after exposure to fractionated ionizing radiation. Radiation research 2001;155(4):543-553.
425. Chang L, Graham PH, Hao J, Ni J, Bucci J, Cozzi PJ, Kearsley JH, Li Y, Chang Y, Graham Y and others. Acquisition of epithelial to mesenchymal transition and cancer stem cell phenotypes is associated with activation of the PI3K/Akt/mTOR pathway in prostate cancer radioresistance. Cell Death and Disease 2013;4(10):875-890.
426. Shimura T, Noma N, Sano Y, Ochiai Y, Oikawa T, Fukumoto M, Kunugita N. AKT-mediated enhanced aerobic glycolysis causes acquired radioresistance by human tumor cells. Radiotherapy and Oncology 2014;112(2):302-307.
427. Jang H, Baek J, Nam K-S, Kim S. Determination of the optimal time for tamoxifen treatment in combination with radiotherapy. International journal of oncology 2016;49(5):2147-2154.
428. Hirschhaeuser F, Menne H, Dittfeld C, West J, Mueller-Klieser W, Kunz-Schughart LA. Multicellular tumor spheroids: an underestimated tool is catching up again. Journal of biotechnology 2010;148(1):3-15.
429. Chang L, Ni J, Beretov J, Wasinger VC, Hao J, Bucci J, Malouf D, Gillatt D, Graham PH, Li Y. Identification of protein biomarkers and signaling pathways associated with prostate cancer radioresistance using label-free LC-MS/MS proteomic approach. Scientific reports 2017;7:41834-41848.

430. Couture C, Raybaud-Diogène H, Têtu B, Bairati I, Murry D, Allard J, Fortin A. p53 and Ki-67 as markers of radioresistance in head and neck carcinoma. Cancer 2002;94(3):713-722.
431. DeSantis C, Siegel R, Bandi P, Jemal A. Breast cancer statistics, 2011. CA: A Cancer Journal for Clinicians 2011;61(6):408-418.
432. Pinto CA, Widodo E, Waltham M, Thompson EW. Breast cancer stem cells and epithelial mesenchymal plasticity – Implications for chemoresistance. Cancer Letters 2013;341(1):56-62.
433. Lee JM, Dedhar S, Kalluri R, Thompson EW. The epithelial–mesenchymal transition: new insights in signaling, development, and disease. J Cell biol 2006;172(7):973-981.
434. Thompson EW, Newgreen DF. Carcinoma invasion and metastasis: a role for epithelial-mesenchymal transition? Cancer research 2005;65(14):5991-5995.
435. Barrallo-Gimeno A, Nieto MA. The Snail genes as inducers of cell movement and survival: implications in development and cancer. Development 2005;132(14):3151-3161.
436. Przybylo JA, Radisky DC. Matrix metalloproteinase-induced epithelial–mesenchymal transition: tumor progression at Snail's pace. The international journal of biochemistry & cell biology 2007;39(6):1082-1088.
437. Marie-Egyptienne DT, Lohse I, Hill RP. Cancer stem cells, the epithelial to mesenchymal transition (EMT) and radioresistance: Potential role of hypoxia. Cancer Letters 2013;341(1):63-72.
438. Shintani Y, Okimura A, Sato K, Nakagiri T, Kadota Y, Inoue M, Sawabata N, Minami M, Ikeda N, Kawahara K and others. Epithelial to Mesenchymal Transition Is a Determinant of Sensitivity to Chemoradiotherapy in Non-Small Cell Lung Cancer. The Annals of Thoracic Surgery 2011;92(5):1794-1804.
439. Sommers CL, Heckford SE, Skerker JM, Worland P, Torri JA, Thompson EW, Byers SW, Gelmann EP. Loss of epithelial markers and acquisition of vimentin expression in adriamycin-and vinblastine-resistant human breast cancer cell lines. Cancer research 1992;52(19):5190-5197.
440. Liu F, Gu LN, Shan BE, Geng CZ, Sang MX. Biomarkers for EMT and MET in breast cancer: An update. Oncology letters 2016;12(6):4869-4876.
441. Yook JI, Li X-Y, Ota I, Fearon ER, Weiss SJ. Wnt-dependent Regulation of the E-cadherin Repressor Snail. Journal of Biological Chemistry 2005;280(12):11740-11748.
442. Thiery JP, Acloque H, Huang RY, Nieto MA. Epithelial-mesenchymal transitions in development and disease. cell 2009;139(5):871-890.
443. Zhou Y-C, Liu J-Y, Li J, Zhang J, Xu Y-Q, Zhang H-W, Qiu L-B, Ding G-R, Su X-M, Mei S and others. Ionizing Radiation Promotes Migration and Invasion of Cancer Cells Through Transforming Growth Factor-Beta–Mediated Epithelial–Mesenchymal Transition. International Journal of Radiation Oncology*Biology*Physics 2011;81(5):1530-1537.
444. Andarawewa KL, Erickson AC, Chou WS, Costes SV, Gascard P, Mott JD, Bissell MJ, Barcellos-Hoff MH. Ionizing radiation predisposes nonmalignant human mammary epithelial cells to undergo transforming growth factor beta induced epithelial to mesenchymal transition. Cancer research 2007;67(18):8662-8678.

445. Sørlie T, Perou CM, Tibshirani R, Aas T, Geisler S, Johnsen H, Hastie T, Eisen MB, Van De Rijn M, Jeffrey SS. Gene expression patterns of breast carcinomas distinguish tumor subclasses with clinical implications. Proceedings of the National Academy of Sciences 2001;98(19):10869-10874.
446. Neve RM, Chin K, Fridlyand J, Yeh J, Baehner FL, Fevr T, Clark L, Bayani N, Coppe J-P, Tong F and others. A collection of breast cancer cell lines for the study of functionally distinct cancer subtypes. Cancer Cell 2006;10(6):515-527.
447. Dai X, Li T, Bai Z, Yang Y, Liu X, Zhan J, Shi B. Breast cancer intrinsic subtype classification, clinical use and future trends. American journal of cancer research 2015;5(10):2929-2943.
448. Sotiriou C, Neo S-Y, McShane LM, Korn EL, Long PM, Jazaeri A, Martiat P, Fox SB, Harris AL, Liu ET. Breast cancer classification and prognosis based on gene expression profiles from a population-based study. Proceedings of the National Academy of Sciences 2003;100(18):10393-10398.
449. Nicholson RI, McClelland RA, Gee JMW, Manning DL, Cannon P, Robertson JFR, Ellis IO, Blamey RW. Epidermal growth factor receptor expression in breast cancer: Association with response to endocrine therapy. Breast Cancer Research and Treatment 1994;29(1):117-125.
450. Nicholson RI, McClelland RA, Finlay P, Eaton CL, Gullick WJ, Dixon AR, Robertson JFR, Blamey RW, Ellis IO. Relationship between EGF-R, c-erbB-2 protein expression and Ki67 immunostaining in breast cancer and hormone sensitivity. European Journal of Cancer 1993;29(7):1018-1023.
451. Wright C, Nicholson S, Angus B, Sainsbury J, Farndon J, Cairns J, Harris A, Horne C. Relationship between c-erbB-2 protein product expression and response to endocrine therapy in advanced breast cancer. British Journal of Cancer 1992;65(1):118–121.
452. Sharma SV, Bell DW, Settleman J, Haber DA. Epidermal growth factor receptor mutations in lung cancer. Nature Reviews Cancer 2007;7(3):169–181.
453. Huang S, Armstrong EA, Benavente S, Chinnaiyan P, Harari PM. Dual-agent molecular targeting of the epidermal growth factor receptor (EGFR): combining anti-EGFR antibody with tyrosine kinase inhibitor. Cancer research 2004;64(15):5355-5362.
454. Erjala K, Raitanen M, Kulmala J, Grénman R. Concurrent use of vinorelbine and gefitinib induces supra-additive effect in head and neck squamous cell carcinoma cell lines. Journal of cancer research and clinical oncology 2007;133(3):169-176.
455. Gutierrez MC, Detre S, Johnston S, Mohsin SK, Shou J, Allred DC, Schiff R, Osborne CK, Dowsett M. Molecular changes in tamoxifen-resistant breast cancer: relationship between estrogen receptor, HER-2, and p38 mitogen-activated protein kinase. Journal of clinical oncology 2005;23(11):2469-2476.
456. Encarnación CA, Ciocca DR, McGuire WL, Clark GM, Fuqua SA, Osborne CK. Measurement of steroid hormone receptors in breast cancer patients on tamoxifen. Breast cancer research and treatment 1993;26(3):237-246.

457. Brünner N, Frandsen TL, Holst-Hansen C, Bei M, Thompson EW, Wakeling AE, Lippman ME, Clarke R. MCF7/LCC2: a 4-hydroxytamoxifen resistant human breast cancer variant that retains sensitivity to the steroidal antiestrogen ICI 182,780. Cancer research 1993;53(14):3229-3232.
458. Long B, McKibben B, Lynch M, Van den Berg H. Changes in epidermal growth factor receptor expression and response to ligand associated with acquired tamoxifen resistance or oestrogen independence in the ZR-75-1 human breast cancer cell line. British journal of cancer 1992;65(6):865–869.
459. Nicholson RI, Gee JMW. Oestrogen and growth factor cross-talk and endocrine insensitivity and acquired resistance in breast cancer. British journal of cancer 2000;82(3):501-513.
460. Fan P, Wang J, Santen RJ, Yue W. Long-term treatment with tamoxifen facilitates translocation of estrogen receptor α out of the nucleus and enhances its interaction with EGFR in MCF-7 breast cancer cells. Cancer research 2007;67(3):1352-1360.
461. McClelland RA, Barrow D, Madden T-A, Dutkowski CM, Pamment J, Knowlden JM, Gee JM, Nicholson RI. Enhanced epidermal growth factor receptor signaling in MCF7 breast cancer cells after long-term culture in the presence of the pure antiestrogen ICI 182,780 (Faslodex). Endocrinology 2001;142(7):2776-2788.
462. Shimura T, Noma N, Oikawa T, Ochiai Y, Kakuda S, Kuwahara Y, Takai Y, Takahashi A, Fukumoto M. Activation of the AKT/cyclin D1/Cdk4 survival signaling pathway in radioresistant cancer stem cells. Oncogenesis 2012;1(6):12-20.
463. Shimura T, Kakuda S, Ochiai Y, Nakagawa H, Kuwahara Y, Takai Y, Kobayashi J, Komatsu K, Fukumoto M. Acquired radioresistance of human tumor cells by DNA-PK/AKT/GSK3β-mediated cyclin D1 overexpression. Oncogene 2010;29(34):4826–4837.
464. Igor V, Charles LS. The phosphatidylinositol 3-Kinase–AKT pathway in human cancer. Nature Reviews Cancer 2002;2(7):489–501.
465. Liang K, Jin W, Knuefermann C, Schmidt M, Mills GB, Ang KK, Milas L, Fan Z. Targeting the phosphatidylinositol 3-kinase/Akt pathway for enhancing breast cancer cells to radiotherapy. Molecular cancer therapeutics 2003;2(4):353-360.
466. Kavanagh BD, Dent P, Schmidt-Ullrich RK, Chen P, Mikkelsen RB. Calcium-dependent stimulation of mitogen-activated protein kinase activity in A431 cells by low doses of ionizing radiation. Radiation research 1998;149(6):579-587.
467. Suy S, Anderson WB, Dent P, Chang E, Kasid U. Association of Grb2 with Sos and Ras with Raf-1 upon gamma irradiation of breast cancer cells. Oncogene 1997;15(1):53–61.
468. Kavanagh BD, Lin P-S, Chen P, Schmidt-Ullrich RK. Radiation-induced enhanced proliferation of human squamous cancer cells in vitro: a release from inhibition by epidermal growth factor. Clinical Cancer Research 1995;1(12):1557-1562.
469. Schmidt-Ullrich RK, Mikkelsen RB, Dent P, Todd DG, Valerie K, Kavanagh BD. Radiation-induced proliferation of the human A431 squamous carcinoma

cells is dependent on EGFR tyrosine phosphorylation. Oncogene 1997;15:1191–1197.
470. Reardon DB, Contessa JN, Mikkelsen RB, Valerie K, Amir C, Dent P, Schmidt-Ullrich RK. Dominant negative EGFR-CD533 and inhibition of MAPK modify JNK1 activation and enhance radiation toxicity of human mammary carcinoma cells. Oncogene 1999;18:4756–4766.
471. Gorman AM, Healy SJM, Jäger R, Samali A. Stress management at the ER: Regulators of ER stress-induced apoptosis. Pharmacology & Therapeutics 2012;134(3):306-316.
472. Oommen D, Prise KM. Down-regulation of PERK enhances resistance to ionizing radiation. Biochemical and Biophysical Research Communications 2013;441(1):31-35.
473. Zheng Z, Wang G, Li L, Tseng J, Sun F, Chen X, Chang L, Heng H, Zhang K. Transcriptional signatures of unfolded protein response implicate the limitation of animal models in pathophysiological studies. Environmental disease 2016;1(1):24-30.
474. Karagiannis GS, Pavlou MP, Diamandis EP. Cancer secretomics reveal pathophysiological pathways in cancer molecular oncology. Molecular Oncology 2010;4(6):496-510.
475. Mbeunkui F, Metge BJ, Shevde LA, Pannell LK. Identification of Differentially Secreted Biomarkers Using LC-MS/MS in Isogenic Cell Lines Representing a Progression of Breast Cancer. Journal of Proteome Research 2007;6(8):2993-3002.
476. Liang X, Huuskonen J, Hajivandi M, Manzanedo R, Predki P, Amshey JR, Pope RM. Identification and quantification of proteins differentially secreted by a pair of normal and malignant breast-cancer cell lines. Proteomics 2009;9(1):182-193.
477. Lai T-C, Chou H-C, Chen Y-W, Lee T-R, Chan H-T, Shen H-H, Lee W-T, Lin S-T, Lu Y-C, Wu C-L and others. Secretomic and Proteomic Analysis of Potential Breast Cancer Markers by Two-Dimensional Differential Gel Electrophoresis. Journal of Proteome Research 2010;9(3):1302-1322.
478. Yao L, Zhang Y, Chen K, Hu X, Xu LX. Discovery of IL-18 As a Novel Secreted Protein Contributing to Doxorubicin Resistance by Comparative Secretome Analysis of MCF-7 and MCF-7/Dox (Secretome Comparison of MCF-7 and MCF-7/Dox). PLoS ONE 2011;6(9):1-13.
479. Chevalier F, Depagne J, Hem S, Chevillard S, Bensimon J, Bertrand P, Lebeau J. Accumulation of cyclophilin A isoforms in conditioned medium of irradiated breast cancer cells. Proteomics 2012;12(11):1756-1766.
480. Kulasingam V, Diamandis EP. Proteomics Analysis of Conditioned Media from Three Breast Cancer Cell Lines. Molecular & Cellular Proteomics 2007;6(11):1997-2011.
481. Kulasingam V, Zheng Y, Soosaipillai A, Leon AE, Gion M, Diamandis EP. Activated leukocyte cell adhesion molecule: A novel biomarker for breast cancer. International Journal of Cancer 2009;125(1):9-14.
482. Kalra H, Simpson RJ, Ji H, Aikawa E, Altevogt P, Askenase P, Bond VC, Borras FE, Breakefield X, Budnik V and others. Vesiclepedia: a compendium for extracellular vesicles with continuous community annotation. PLoS Biol 2012;10(12):1-5.

483. Lin Q, Tan HT, Lim HSR, Chung MC. Sieving through the cancer secretome. Biochimica et Biophysica Acta (BBA)-Proteins and Proteomics 2013;1834(11):2360-2371.
484. Cooper S. Reappraisal of serum starvation, the restriction point, G0, and G1 phase arrest points. The FASEB journal 2003;17(3):333-340.
485. Shin J-S, Hong S-W, Lee S-LO, Kim T-H, Park I-C, An S-K, Lee W-K, Lim J-S, Kim K-I, Yang Y. Serum starvation induces G1 arrest through suppression of Skp2-CDK2 and CDK4 in SK-OV-3 cells. International journal of oncology 2008;32(2):435-439.
486. Hasan NM, Adams GE, Joiner MC. Effect of serum starvation on expression and phosphorylation of PKCα and p53 in V79 cells: Implications for cell death. International journal of cancer 1999;80(3):400-405.
487. Zander L, Bemark M. Identification of genes deregulated during serum‐free medium adaptation of a Burkitt's lymphoma cell line. Cell proliferation 2008;41(1):136-155.
488. Mbeunkui F, Fodstad O, Pannell LK. Secretory protein enrichment and analysis: an optimized approach applied on cancer cell lines using 2D LC− MS/MS. Journal of proteome research 2006;5(4):899-906.
489. Yamaguchi N, Yamamura Y, Koyama K, Ohtsuji E, Imanishi J, Ashihara T. Characterization of new human pancreatic cancer cell lines which propagate in a protein-free chemically defined medium. Cancer research 1990;50(21):7008-7014.
490. Inoue Y, Kawamoto S, Shoji M, Hashizume S, Teruya K, Katakura Y, Shirahata S. Properties of ras-amplified recombinant BHK-21 cells in protein-free culture. Cytotechnology 2000;33(1-3):21-26.
491. Pellitteri-Hahn M, Warren M, Didier D, Winkler E, Mirza S, Greene A, Olivier M. Improved mass spectrometric proteomic profiling of the secretome of rat vascular endothelial cells. Journal of proteome research 2006;5(10):2861-2864.
492. Yamashita R, Fujiwara Y, Ikari K, Hamada K, Otomo A, Yasuda K, Noda M, Kaburagi Y. Extracellular proteome of human hepatoma cell, HepG2 analyzed using two-dimensional liquid chromatography coupled with tandem mass spectrometry. Molecular and Cellular Biochemistry 2007;298(1):83-92.
493. Pardo M, García Á, Antrobus R, Blanco MJ, Dwek RA, Zitzmann N. Biomarker Discovery from Uveal Melanoma Secretomes: Identification of gp100 and Cathepsin D in Patient Serum. Journal of Proteome Research 2007;6(7):2802-2811.
494. Luce A, Courtin A, Levalois C, Altmeyer-Morel S, Romeo P-H, Chevillard S, Lebeau J. Death receptor pathways mediate targeted and non-targeted effects of ionizing radiations in breast cancer cells. Carcinogenesis 2009;30(3):432-439.
495. Wendler F, Favicchio R, Simon T, Alifrangis C, Stebbing J, Giamas G. Extracellular vesicles swarm the cancer microenvironment: from tumor-stroma communication to drug intervention. Oncogene 2017;36(7):877-884.
496. Belting M, Christianson HC. Role of exosomes and microvesicles in hypoxia-associated tumour development and cardiovascular disease. Journal of Internal Medicine 2015;278(3):251-63.

497. Becker A, Thakur BK, Weiss JM, Kim HS, Peinado H, Lyden D. Extracellular Vesicles in Cancer: Cell-to-Cell Mediators of Metastasis. Cancer Cell 2016;30(6):836-848.
498. Kanada M, Bachmann MH, Contag CH. Signaling by Extracellular Vesicles Advances Cancer Hallmarks. Trends Cancer 2016;2(2):84-94.
499. Schaaij-Visser TBM, de Wit M, Lam SW, Jiménez CR. The cancer secretome, current status and opportunities in the lung, breast and colorectal cancer context. Biochimica et Biophysica Acta (BBA) - Proteins and Proteomics 2013;1834(11):2242-2258.
500. Dong Z, Zhang J-T. Initiation factor eIF3 and regulation of mRNA translation, cell growth, and cancer. Critical Reviews in Oncology/Hematology 2006;59(3):169-180.
501. Cappuzzo F, Varella-Garcia M, Rossi E, Gajapathy S, Valente M, Drabkin H, Gemmill R. MYC and EIF3H Coamplification Significantly Improve Response and Survival of Non-small Cell Lung Cancer Patients (NSCLC) Treated with Gefitinib. Journal of Thoracic Oncology 2009;4(4):472-478.
502. Savinainen KJ, Helenius MA, Lehtonen HJ, Visakorpi T. Overexpression of EIF3S3 promotes cancer cell growth. The Prostate 2006;66(11):1144-1150.
503. Zhang L, Pan X, Hershey JW. Individual overexpression of five subunits of human translation initiation factor eIF3 promotes malignant transformation of immortal fibroblast cells. Journal of biological chemistry 2007;282(8):5790-5800.
504. Umar A, Kang H, Timmermans AM, Look MP, Meijer-van Gelder ME, den Bakker MA, Jaitly N, Martens JWM, Luider TM, Foekens JA and others. Identification of a Putative Protein Profile Associated with Tamoxifen Therapy Resistance in Breast Cancer. Molecular & Cellular Proteomics 2009;8(6):1278-1294.
505. Hershey JW. The role of eIF3 and its individual subunits in cancer. Biochim Biophys Acta 2015;1849(7):792-800.
506. Zheng Q, Liu H, Ye J, Zhang H, Jia Z, Cao J. Nuclear distribution of eIF3g and its interacting nuclear proteins in breast cancer cells. Molecular Medicine Reports 2016;13(4):2973-2979.
507. Hurwitz SN, Rider MA, Bundy JL, Liu X, Singh RK, Meckes DG. Proteomic profiling of NCI-60 extracellular vesicles uncovers common protein cargo and cancer type-specific biomarkers. Oncotarget 2016;7(52):86999-87015.
508. He M, Qin H, Poon TC, Sze SC, Ding X, Co NN, Ngai SM, Chan TF, Wong N. Hepatocellular carcinoma-derived exosomes promote motility of immortalized hepatocyte through transfer of oncogenic proteins and RNAs. Carcinogenesis 2015;36(9):1008-1018.
509. Liang B, Peng P, Chen S, Li L, Zhang M, Cao D, Yang J, Li H, Gui T, Li X and others. Characterization and proteomic analysis of ovarian cancer-derived exosomes. Journal of Proteomics 2013;80:171-182.
510. van Herwijnen MJ, Zonneveld MI, Goerdayal S, Nolte-Hoen EN, Garssen J, Stahl B, Maarten Altelaar AF, Redegeld FA, Wauben MH. Comprehensive Proteomic Analysis of Human Milk-derived Extracellular Vesicles Unveils a Novel Functional Proteome Distinct from Other Milk Components. Moleular Cell Proteomics 2016;15(11):3412-3423.

511. Bruno S, Grange C, Deregibus MC, Calogero RA, Saviozzi S, Collino F, Morando L, Busca A, Falda M, Bussolati B and others. Mesenchymal stem cell-derived microvesicles protect against acute tubular injury. Journal of American Society of Nephrology 2009;20(5):1053-1067.
512. D'Arcangelo JG, Stahmer KR, Miller EA. Vesicle-mediated export from the ER: COPII coat function and regulation. Biochimica et Biophysica Acta (BBA) - Molecular Cell Research 2013;1833(11):2464-2472.
513. Barlowe C, Orci L, Yeung T, Hosobuchi M, Hamamoto S, Salama N, Rexach MF, Ravazzola M, Amherdt M, Schekman R. COPII: A membrane coat formed by Sec proteins that drive vesicle budding from the endoplasmic reticulum. Cell 1994;77(6):895-907.
514. Matsuoka K, Orci L, Amherdt M, Bednarek SY, Hamamoto S, Schekman R, Yeung T. COPII-coated vesicle formation reconstituted with purified coat proteins and chemically defined liposomes. Cell 1998;93(2):263-275.
515. Bruno A, David M, Susan H, Lelio O, Randy S. Dynamics of the COPII coat with GTP and stable analogues. Nature Cell Biology 2001;3(6):531-537.
516. Miller E, Antonny B, Hamamoto S, Schekman R. Cargo selection into COPII vesicles is driven by the Sec24p subunit. EMBO Journal 2002;21(22):6105-6113.
517. Miller EA, Beilharz TH, Malkus PN, Lee MCS, Hamamoto S, Orci L, Schekman R. Multiple Cargo Binding Sites on the COPII Subunit Sec24p Ensure Capture of Diverse Membrane Proteins into Transport Vesicles. Cell 2003;114(4):497-509.
518. Mossessova E, Bickford LC, Goldberg J. SNARE Selectivity of the COPII Coat. Cell 2003;114(4):483-495.
519. Mancias J, Goldberg J. The Transport Signal on Sec22 for Packaging into COPII-Coated Vesicles is a Conformational Epitope. Molecular Cell 2007;26(3):403-414.
520. Mancias J, Goldberg J. Structural Basis of Cargo Membrane Protein Discrimination by the Human COPll Coat Machinery. EMBO Journal 2008;27(2008):2918-2928.
521. Sharpe LJ, Luu W, Brown AJ. Akt phosphorylates Sec24: new clues into the regulation of ER-to-Golgi trafficking. Traffic Interchange 2011;12(1):19-27.
522. Quesada-Calvo F, Massot C, Bertrand V, Longuespée R, Blétard N, Somja J, Mazzucchelli G, Smargiasso N, Baiwir D, De Pauw-Gillet M-C and others. OLFM4, KNG1 and Sec24C identified by proteomics and immunohistochemistry as potential markers of early colorectal cancer stages. Clinical Proteomics 2017;14(1):9-22.
523. Silvers CR, Miyamoto H, Messing EM, Netto GJ, Lee YF. Characterization of urinary extracellular vesicle proteins in muscle-invasive bladder cancer. Oncotarget 2017;8(53):91199-91208.
524. Demory Beckler M, Higginbotham JN, Franklin JL, Ham AJ, Halvey PJ, Imasuen IE, Whitwell C, Li M, Liebler DC, Coffey RJ. Proteomic analysis of exosomes from mutant KRAS colon cancer cells identifies intercellular transfer of mutant KRAS. Molecular Cell Proteomics 2013;12(2):343-55.
525. Tauro BJ, Greening DW, Mathias RA, Mathivanan S, Ji H, Simpson RJ. Two distinct populations of exosomes are released from LIM1863 colon

carcinoma cell-derived organoids. Molecular Cell Proteomics 2013;12(3):587-98.
526. Sinha A, Ignatchenko V, Ignatchenko A, Mejia-Guerrero S, Kislinger T. In-depth proteomic analyses of ovarian cancer cell line exosomes reveals differential enrichment of functional categories compared to the NCI 60 proteome. Biochemical and Biophysical Research Communications 2014;445(4):694-701.
527. Matsumoto K, Wolffe AP. Gene regulation by Y-box proteins: coupling control of transcription and translation. Trends in cell biology 1998;8(8):318-323.
528. Dupasquier S, Delmarcelle A-S, Marbaix E, Cosyns J-P, Courtoy PJ, Pierreux CE. Validation of housekeeping gene and impact on normalized gene expression in clear cell Renal Cell Carcinoma: critical reassessment of YBX3/ZONAB/CSDA expression. BMC Molecular Biology 2014;15(1):9-22.
529. Hayashi J, Kajino K, Umeda T, Takano S, Arakawa Y, Kudo M, Hino O. Somatic mutation and SNP in the promoter of dbpA and human hepatocarcinogenesis. International journal of oncology 2002;21(4):847-850.
530. Arakawa Y, Kajino K, Kano S, Tobita H, Hayashi J, Yasen M, Moriyama M, Arakawa Y, Hino O. Transcription of dbpA, a Y box binding protein, is positively regulated by E2F1: implications in hepatocarcinogenesis. Biochemical and Biophysical Research Communications 2004;322(1):297-302.
531. Yasen M, Kajino K, Kano S, Tobita H, Yamamoto J, Uchiumi T, Kon S, Maeda M, Obulhasim G, Arii S and others. The Up-Regulation of Y-Box Binding Proteins (DNA Binding Protein A and Y-Box Binding Protein-1) as Prognostic Markers of Hepatocellular Carcinoma. Clinical Cancer Research 2005;11(20):7354-7361.
532. Wang G, Zheng Y, Che X, Wang X, Zhao J, Wu K, Zeng J, Pan C, He D. Upregulation of human DNA binding protein A (dbpA) in gastric cancer cells. Acta Pharmacologica Sinica 2009;30(10):1436-1442.
533. Hong BS, Cho JH, Kim H, Choi EJ, Rho S, Kim J, Kim JH, Choi DS, Kim YK, Hwang D and others. Colorectal cancer cell-derived microvesicles are enriched in cell cycle-related mRNAs that promote proliferation of endothelial cells. BMC Genomics 2009;10:556-578.
534. Skog J, Wurdinger T, van Rijn S, Meijer DH, Gainche L, Sena-Esteves M, Curry WT, Jr., Carter BS, Krichevsky AM, Breakefield XO. Glioblastoma microvesicles transport RNA and proteins that promote tumour growth and provide diagnostic biomarkers. Nature Cell Biology 2008;10(12):1470-1476.
535. Bruschi M, Santucci L, Ravera S, Bartolucci M, Petretto A, Calzia D, Ghiggeri GM, Ramenghi LA, Candiano G, Panfoli I. Metabolic Signature of Microvesicles from Umbilical Cord Mesenchymal Stem Cells of Preterm and Term Infants. Proteomics Clinical Applications 2018;12(3):1-11.
536. Aufderklamm S, Todenhöfer T, Gakis G, Kruck S, Hennenlotter J, Stenzl A, Schwentner C. Thymidine kinase and cancer monitoring. Cancer Letters 2012;316(1):6-10.

537. Eriksson S, Munch-Petersen B, Johansson K, Ecklund H. Structure and function of cellular deoxyribonucleoside kinases. Cellular and Molecular Life Sciences CMLS 2002;59(8):1327-1346.
538. Ke P-Y, Chang Z-F. Mitotic degradation of human thymidine kinase 1 is dependent on the anaphase-promoting complex/cyclosome-CDH1-mediated pathway. Molecular and Cellular Biology 2004;24(2):514-526.
539. Mao Y, Wu J, Wang N, He L, Wu C, He Q, Skog S. A Comparative Study: Immunohistochemical Detection of Cytosolic Thymidine Kinase and Proliferating Cell Nuclear Antigen in Breast Cancer. Cancer Investigation 2002;20(7-8):922-931.
540. Topolcan O, Holubec Jr L. The role of thymidine kinase in cancer diseases. Expert opinion on medical diagnostics 2008;2(2):129-141.
541. Li H, Lei D, Wang X, Skog S, He Q. Serum thymidine kinase 1 is a prognostic and monitoring factor in patients with non-small cell lung cancer. Oncology reports 2005;13(1):145-149.
542. He Q, Zou L, Zhang P, Lui J, Skog S, Fornander T. The clinical significance of thymidine kinase 1 measurement in serum of breast cancer patients using anti-TK1 antibody. The International journal of biological markers 2000;15(2):139-146.
543. He Q, Fornander T, Johansson H, Johansson U, Hu GZ, Rutqvist L-E, Skog S. Thymidine kinase 1 in serum predicts increased risk of distant or loco-regional recurrence following surgery in patients with early breast cancer. Anticancer research 2006;26(6C):4753-4759.
544. Anderson JM, Langone JJ. Issues and perspectives on the biocompatibility and immunotoxicity evaluation of implanted controlled release systems: Based on the plenary lecture of J. Anderson, given on June 22, 1998 at the 25th International Symposium Controlled Release of Bioactive Materials, Las Vagas, NV, USA. Journal of Controlled Release 1999;57(2):107-113.
545. Koschwanez HE, Reichert WM. In vitro, in vivo and post explantation testing of glucose-detecting biosensors: Current methods and recommendations. Biomaterials 2007;28(25):3687-3703.
546. Papenfuss HD, Gross JF, Intaglietta M, Treese FA. A transparent access chamber for the rat dorsal skin fold. Microvascular Research 1979;18(3):311-318.
547. Ertefai S, Gough DA. Physiological preparation for studying the response of subcutaneously implanted glucose and oxygen sensors. Journal of Biomedical Engineering 1989;11(5):362-368.
548. Valdes TI, Klueh U, Kreutzer D, Moussy F. Ex ova chick chorioallantoic membrane as a novel in vivo model for testing biosensors. Journal of Biomedical Materials Research Part A 2003;67(1):215-223.
549. Valdes TI, Kreutzer D, Moussy F. The chick chorioallantoic membrane as a novel in vivo model for the testing of biomaterials. Journal of Biomedical Materials Research 2002;62(2):273-282.
550. Williams DF. There is no such thing as a biocompatible material. Biomaterials 2014;35(38):10009-10014.
551. Gray ME, Meehan J, Blair EO, Ward C, Langdon SP, Morrison LR, Marland JR, Tsiamis A, Kunkler IH, Murray A. Biocompatibility of common

implantable sensor materials in a tumor xenograft model. Journal of Biomedical Materials Research Part B: Applied Biomaterials 2018:1-14.
552. Cao B, Zheng Y, Xi T, Zhang C, Song W, Burugapalli K, Yang H, Ma Y. Concentration-dependent cytotoxicity of copper ions on mouse fibroblasts in vitro : effects of copper ion release from TCu380A vs TCu220C intra-uterine devices. BioMEMS and Biomedical Nanotechnology 2012;14(4):709-720.
553. Lin CH, Chen CH, Huang YS, Huang CH, Huang JC, Jang JSC, Lin YS. In-vivo investigations and cytotoxicity tests on Ti/Zr-based metallic glasses with various Cu contents. Materials Science & Engineering C 2017;77:308-317.
554. Weisenberg BA, Mooradian DL. Hemocompatibility of materials used in microelectromechanical systems: Platelet adhesion and morphology in vitro. Journal of Biomedical Materials Research 2002;60(2):283-291.
555. Wright D, Rajalingam B, Karp JM, Selvarasah S, Ling Y, Yeh J, Langer R, Dokmeci MR, Khademhosseini A. Reusable, reversibly sealable parylene membranes for cell and protein patterning. Journal of biomedical materials research Part A 2008;85(2):530-538.
556. Castagnola V, Descamps E, Lecestre A, Dahan L, Remaud J, Nowak LG, Bergaud C. Parylene-based flexible neural probes with PEDOT coated surface for brain stimulation and recording. Biosensors and Bioelectronics 2015;67:450-457.
557. Wright D, Rajalingam B, Selvarasah S, Dokmeci MR, Khademhosseini A. Generation of static and dynamic patterned co-cultures using microfabricated parylene-C stencils. Lab on a Chip 2007;7(10):1272-1279.
558. Lecomte A, Degache A, Descamps E, Dahan L, Bergaud C. In vitro and in vivo biostability assessment of chronically-implanted Parylene C neural sensors. Sensors & Actuators: B. Chemical 2017;251:1001-1008.
559. Yuen TGH, Agnew WF, Bullara LA. Tissue response to potential neuroprosthetic materials implanted subdurally. Biomaterials 1987;8(2):138-141.
560. Schmidt EM, McIntosh JS, Bak MJ. Long-term implants of Parylene-C coated microelectrodes. Med Biol Eng Comput 1988;26(1):96-101.
561. Winslow BD, Christensen MB, Yang W-K, Solzbacher F, Tresco PA. A comparison of the tissue response to chronically implanted Parylene-C-coated and uncoated planar silicon microelectrode arrays in rat cortex. Biomaterials 2010;31(35):9163-9172.
562. Pellinen DS, Moon T, Vetter RJ, Miriani R, Kipke DR. Multifunctional Flexible Parylene-Based Intracortical Microelectrodes. 2005 17-18 Jan. 2006. p 5272-5275.
563. Schendel AA, Thongpang S, Brodnick SK, Richner TJ, Lindevig BD, Krugner-Higby L, Williams JC. A cranial window imaging method for monitoring vascular growth around chronically implanted micro-ECoG devices. Journal of neuroscience methods 2013;218(1):121-130.
564. Fontaine AB, Koelling K, Passos SD, Cearlock J, Hoffman R, Spigos DG. Polymeric surface modifications of tantalum stents. Journal of Endovascular Therapy 1996;3(3):276-283.
565. Stark N. Literature review: biological safety of parylene C. Medical Plastic and Biomaterials 1996;3:30-35.

566. Geninatti T, Bruno G, Barile B, Hood RL, Farina M, Schmulen J, Canavese G, Grattoni A. Impedance characterization, degradation, and in vitro biocompatibility for platinum electrodes on BioMEMS. Biomedical microdevices 2015;17(1):24.
567. O'Brien BJ, Stinson JS, Larsen SR, Eppihimer MJ, Carroll WM. A platinum–chromium steel for cardiovascular stents. Biomaterials 2010;31(14):3755-3761.
568. Tzifa A, Ewert P, Brzezinska-Rajszys G, Peters B, Zubrzycka M, Rosenthal E, Berger F, Qureshi SA. Covered cheatham-platinum stents for aortic coarctation: Early and intermediate-term results. Journal of the American College of Cardiology 2006;47(7):1457-1463.
569. Guglielmi G, Vinuela F, Sepetka I, Macellari V, Strother CM. Electrothrombosis of saccular aneurysms via endovascular approach Part 1: Electrochemical basis, technique, and experimental results. American Journal of Neuroradiology 2001;22(5):1010-1012.
570. Yuki I, Spitzer D, Guglielmi G, Duckwiler G, Fujimoto M, Takao H, Jahan R, Tateshima S, Murayama Y, Vinuela F. Immunohistochemical analysis of a ruptured basilar top aneurysm autopsied 22 years after embolization with Guglielmi detachable coils. Journal of Neurointerventional Surgery 2014.
571. Stöver T, Lenarz T. Biomaterials in cochlear implants. GMS current topics in otorhinolaryngology, head and neck surgery 2009;8:1-22.
572. Daly NJ, De Lafontan B, Combes PF. Results of the treatment of 165 lid carcinomas by iridium wire implant. International Journal of Radiation Oncology, Biology, Physics 1984;10(4):455-459.
573. Neumann A, Unkel C, Werry C, Herborn CU, Maier HR, Ragoß C, Jahnke K. Prototype of a silicon nitride ceramic-based miniplate osteofixation system for the midface. Otolaryngology—Head and Neck Surgery 2006;134(6):923-930.
574. Kue R, Sohrabi A, Nagle D, Frondoza C, Hungerford D. Enhanced proliferation and osteocalcin production by human osteoblast-like MG63 cells on silicon nitride ceramic discs. Biomaterials 1999;20(13):1195-1201.
575. Cappi B, Neuss S, Salber J, Telle R, Knüchel R, Fischer H. Cytocompatibility of high strength non‐oxide ceramics. Journal of Biomedical Materials Research Part A 2010;93(1):67-76.
576. Howlett C, McCartney E, Ching W. The effect of silicon nitride ceramic on rabbit skeletal cells and tissue. An in vitro and in vivo investigation. Clinical orthopaedics and related research 1989(244):293-304.
577. Kristensen BW, Noraberg J, Thiébaud P, Koudelka-Hep M, Zimmer J. Biocompatibility of silicon-based arrays of electrodes coupled to organotypic hippocampal brain slice cultures. Brain Research 2001;896(1):1-17.
578. Kotzar G, Freas M, Abel P, Fleischman A, Roy S, Zorman C, Moran JM, Melzak J. Evaluation of MEMS materials of construction for implantable medical devices. Biomaterials 2002;23(13):2737-2750.
579. Anderson MC, Olsen R. Bone ingrowth into porous silicon nitride. Journal of Biomedical Materials Research Part A 2010;92A(4):1598-1605.
580. Guedes e Silva CC, König B, Carbonari MJ, Yoshimoto M, Allegrini S, Bressiani JC. Bone growth around silicon nitride implants—An evaluation by

scanning electron microscopy. Materials Characterization 2008;59(9):1339-1341.
581. Guedes e Silva CC, König B, Carbonari MJ, Yoshimoto M, Allegrini S, Bressiani JC. Tissue response around silicon nitride implants in rabbits. Journal of Biomedical Materials Research Part A 2008;84(2):337-343.
582. Voskerician G, Shive MS, Shawgo RS, Von Recum H, Anderson JM, Cima MJ, Langer R. Biocompatibility and biofouling of MEMS drug delivery devices. Biomaterials 2003;24(11):1959-1967.
583. Hernandez P, Taboada C, Leija L, Tsutsumi V, Vazquez B, Valdes-Perezgasga F, Reyes J. Evaluation of biocompatibility of pH-ISFET materials during long-term subcutaneous implantation. Sensors and Actuators B: Chemical 1998;46(2):133-138.
584. Gorth DJ, Puckett S, Ercan B, Webster TJ, Rahaman M, Bal BS. Decreased bacteria activity on Si_3N_4 surfaces compared with PEEK or titanium. International journal of nanomedicine 2012;7:4829-4836.
585. Webster TJ, Patel AA, Rahaman MN, Sonny Bal B. Anti-infective and osteointegration properties of silicon nitride, poly(ether ether ketone), and titanium implants. Acta Biomaterialia 2012;8(12):4447-4454.
586. Bal BS, Rahaman M. Orthopedic applications of silicon nitride ceramics. Acta biomaterialia 2012;8(8):2889-2898.
587. Mediaswanti K, Wen C, Ivanova EP, Berndt CC, Pham VT, Malherbe F, Wang J. Investigation of bacterial attachment on hydroxyapatite-coated titanium and tantalum. International Journal of Surface Science and Engineering 15 2014;8(2-3):255-263.
588. Edell DJ, Churchill JN, Gourley IM. Biocompatibility of a silicon based peripheral nerve electrode. Biomaterials, medical devices, and artificial organs 1982;10(2):103-122.
589. Campbell PK, Jones KE, Huber RJ, Horch KW, Normann RA. A silicon-based, three-dimensional neural interface: manufacturing processes for an intracortical electrode array. IEEE Transactions on Biomedical Engineering 1991;38(8):758-768.
590. Benezra M, Penate-Medina O, Zanzonico PB, Schaer D, Ow H, Burns A, DeStanchina E, Longo V, Herz E, Iyer S. Multimodal silica nanoparticles are effective cancer-targeted probes in a model of human melanoma. The Journal of clinical investigation 2011;121(7):2768-2780.
591. Kim G, Kim H, Kim I, Kim J, Lee J, Ree M. Bacterial adhesion, cell adhesion and biocompatibility of Nafion films. Journal of Biomaterials Science, Polymer Edition 2009;20(12):1687-1707.
592. Lee YJ, Kim HJ, Kang JY, Do SH, Lee SH. Biofunctionalization of Nerve Interface via Biocompatible Polymer‐Roughened Pt Black on Cuff Electrode for Chronic Recording. Advanced Healthcare Materials 2017;6(6):1601022.
593. Turner RF, Harrison DJ, Rajotte RV. Preliminary in vivo biocompatibility studies on perfluorosulphonic acid polymer membranes for biosensor applications. Biomaterials 1991;12(4):361-8.
594. Moussy F, Harrison D, Rajotte R. A miniaturized Nafion-based glucose sensor: in vitro and in vivo evaluation in dogs. The International Journal of Artificial Organs 1994;17(2):88-94.

595. Park Y-J, Song Y-H, An J-H, Song H-J, Anusavice KJ. Cytocompatibility of pure metals and experimental binary titanium alloys for implant materials. Journal of Dentistry 2013;41(12):1251-1258.
596. Brown FO, Finnerty NJ, Lowry JP. Nitric oxide monitoring in brain extracellular fluid: characterisation of Nafion®-modified Pt electrodes in vitro and in vivo. Analyst 2009;134(10):2012-2020.
597. Vreeland RF, Atcherley CW, Russell WS, Xie JY, Lu D, Laude ND, Porreca F, Heien ML. Biocompatible PEDOT: Nafion composite electrode coatings for selective detection of neurotransmitters in vivo. Analytical chemistry 2015;87(5):2600-2607.
598. Wisniewski N, Reichert M. Methods for reducing biosensor membrane biofouling. Colloids Surf B Biointerfaces 2000;18(3-4):197-219.
599. Moatti-Sirat D, Poitout V, Thome V, Gangnerau M, Zhang Y, Hu Y, Wilson G, Lemonnier F, Klein J, Reach G. Reduction of acetaminophen interference in glucose sensors by a composite Nafion membrane: demonstration in rats and man. Diabetologia 1994;37(6):610-616.
600. www.epotek.com. Epoxy Technology. Volume 2018; 2018.
601. Mahoney MJ, Leighton J. The Inflammatory Response to a Foreign Body within Transplantable Tumors. Cancer Research 1962;22(3):334-338.
602. Kawakami M, Inagawa R, Hosokawa T, Saito T, Kurasaki M. Mechanism of apoptosis induced by copper in PC12 cells. Food and Chemical Toxicology 2008;46(6):2157-2164.
603. VanLandingham JW, Tassabehji NM, Somers RC, Levenson CW. Expression profiling of p53-target genes in copper-mediated neuronal apoptosis. Neuromolecular medicine 2005;7(4):311-324.
604. Franco R, Sanchez-Olea R, Reyes-Reyes EM, Panayiotidis MI. Environmental toxicity, oxidative stress and apoptosis: menage a trois. Mutation Research/Genetic Toxicology and Environmental Mutagenesis 2009;674(1-2):3-22.
605. Valko M, Morris H, Cronin M. Metals, toxicity and oxidative stress. Current medicinal chemistry 2005;12(10):1161-1208.
606. Zhai Q, Ji H, Zheng Z, Yu X, Sun L, Liu X. Copper induces apoptosis in BA/F3β cells: Bax, reactive oxygen species, and NFκB are involved. Journal of cellular physiology 2000;184(2):161-170.
607. Hoene A, Prinz C, Walschus U, Lucke S, Patrzyk M, Wilhelm L, Neumann H-G, Schlosser M. In vivo evaluation of copper release and acute local tissue reactions after implantation of copper-coated titanium implants in rats. Biomedical Materials 2013;8(3):1-7.
608. Ameri K, Luong R, Zhang H, Powell AA, Montgomery KD, Espinosa I, Bouley DM, Harris AL, Jeffrey SS. Circulating tumour cells demonstrate an altered response to hypoxia and an aggressive phenotype. British Journal Of Cancer 2010;102:561–569.
609. Rose S, Misharin A, Perlman H. A novel Ly6C/Ly6G‐based strategy to analyze the mouse splenic myeloid compartment. Cytometry Part A 2012;81(4):343-350.
610. Miura M, Fu X, Zhang Q-W, Remick DG, Fairchild RL. Neutralization of Groα and Macrophage Inflammatory Protein-2 Attenuates Renal

Ischemia/Reperfusion Injury. The American Journal of Pathology 2001;159(6):2137-2145.
611. Cassetta L, Noy R, Swierczak A, Sugano G, Smith H, Wiechmann L, Pollard JW. Isolation of mouse and human tumor-associated macrophages. Tumor Microenvironment: Springer; 2016. p 211-229.
612. Austyn JM, Gordon S. F4/80, a monoclonal antibody directed specifically against the mouse macrophage. European Journal of Immunology 1981;11(10):805-815.
613. Higgins DM, Basaraba RJ, Hohnbaum AC, Lee EJ, Grainger DW, Gonzalez-Juarrero M. Localized Immunosuppressive Environment in the Foreign Body Response to Implanted Biomaterials. The American Journal of Pathology 2009;175(1):161-170.
614. Sanders JE, Bale SD, Neumann T. Tissue response to microfibers of different polymers: Polyester, polyethylene, polylactic acid, and polyurethane. Journal of Biomedical Materials Research 2002;62(2):222-227.
615. Subbaroyan J, Martin DC, Kipke DR. A finite-element model of the mechanical effects of implantable microelectrodes in the cerebral cortex. Journal of neural engineering 2005;2(4):103-113.
616. Helton KL, Ratner BD, Wisniewski NA. Biomechanics of the sensor-tissue interface - Effects of motion, pressure, and design on sensor performance and the foreign body response - Part I: Theoretical framework. Volume 5; 2011. p 632-646.
617. Wilson CJ, Clegg RE, Leavesley DI, Pearcy MJ. Mediation of biomaterial–cell interactions by adsorbed proteins: a review. Tissue engineering 2005;11(1-2):1-18.
618. Jenney CR, Anderson JM. Adsorbed serum proteins responsible for surface dependent human macrophage behavior. Journal of Biomedical Materials Research: An Official Journal of The Society for Biomaterials and The Japanese Society for Biomaterials 2000;49(4):435-447.
619. Brodbeck WG, Colton E, Anderson JM. Effects of adsorbed heat labile serum proteins and fibrinogen on adhesion and apoptosis of monocytes/macrophages on biomaterials. Journal of Materials Science: Materials in Medicine 2003;14(8):671-675.
620. Xu L-C, Siedlecki CA. Effects of surface wettability and contact time on protein adhesion to biomaterial surfaces. Biomaterials 2007;28(22):3273-3283.
621. Zhao QH, McNally AK, Rubin KR, Renier M, Wu Y, Rose-Caprara V, Anderson JM, Hiltner A, Urbanski P, Stokes K. Human plasma α2-macroglobulin promotes in vitro oxidative stress cracking of pellethane 2363-80A: In vivo and in vitro correlations. Journal of Biomedical Materials Research 1993;27(3):379-388.
622. Kao WJ, Zhao QH, Hiltner A, Anderson JM. Theoretical analysis of in vivo macrophage adhesion and foreign body gaint cell formation on polydimethylsiloxane, low density polyethylene, and polyetherurethanes. Journal of biomedical materials research 1994;28(1):73-79.
623. Christenson EM, Anderson JM, Hiltner A. Oxidative mechanisms of poly (carbonate urethane) and poly (ether urethane) biodegradation: in vivo and in

vitro correlations. Journal of Biomedical Materials Research Part A 2004;70(2):245-255.
624. Wiggins MJ, Wilkoff B, Anderson JM, Hiltner A. Biodegradation of polyether polyurethane inner insulation in bipolar pacemaker leads. Journal of Biomedical Materials Research 2001;58(3):302-307.
625. Labow RS, Meek E, Matheson LA, Santerre JP. Human macrophage-mediated biodegradation of polyurethanes: assessment of candidate enzyme activities. Biomaterials 2002;23(19):3969-3975.
626. Santerre J, Woodhouse K, Laroche G, Labow R. Understanding the biodegradation of polyurethanes: from classical implants to tissue engineering materials. Biomaterials 2005;26(35):7457-7470.
627. Pardoll D. Cancer and the Immune System: Basic Concepts and Targets for Intervention. Semin Oncol 2015;42(4):523-38.
628. Manning JK, Reed ND, Jutila JW. Antibody response to Escherichia coli lipopolysaccharide and type III pneumococcal polysaccharide by congenitally thymusless (nude) mice. The Journal of Immunology 1972;108(5):1470-1472.
629. Johnson W, Balish E. Macrophage function in germ-free, athymic (nu/nu), and conventional-flora (nu/+) mice. Journal of the Reticuloendothelial Society 1980;28(1):55-66.
630. Hanna N. Role of natural killer cells in control of cancer metastasis. Cancer and Metastasis Reviews 1982;1(1):45-64.
631. Haley PJ. Species differences in the structure and function of the immune system. Toxicology 2003;188(1):49-71.
632. Zschaler J, Schlorke D, Arnhold J. Differences in innate immune response between man and mouse. Critical Reviews in Immunology 2014;34(5):433-454.
633. Bucana CD, Fabra A, Sanchez R, Fidler IJ. Different patterns of macrophage infiltration into allogeneic-murine and xenogeneic-human neoplasms growing in nude mice. The American journal of pathology 1992;141(5):1225-1236.
634. Alfonso-Sanchez JL, Martinez IM, Martín-Moreno JM, González RS, Botía F. Analyzing the risk factors influencing surgical site infections: the site of environmental factors. Canadian Journal of Surgery 2017;60(3):155-161.
635. Gray ME, Marland JRK, Dunare C, Blair EO, Meehan J, Tsiamis A, Kunkler IH, Murray AF, Argyle D, Dyson A and others. In vivo validation of a miniaturized electrochemical oxygen sensor for measuring intestinal oxygen tension. American Journal of Physiology-Gastrointestinal and Liver Physiology 2019;317(2):242-252.
636. Hallböök O, Sjödahl R. Anastomotic leakage and functional outcome after anterior resection of the rectum. British journal of surgery 1996;83(1):60-62.
637. Kube R, Mroczkowski P, Granowski D, Benedix F, Sahm M, Schmidt U, Gastinger I, Lippert H. Anastomotic leakage after colon cancer surgery: A predictor of significant morbidity and hospital mortality, and diminished tumour-free survival. European Journal of Surgical Oncology (EJSO) 2010;36(2):120-124.
638. Marra F, Steffen T, Kalak N, Warschkow R, Tarantino I, Lange J, Zünd M. Anastomotic leakage as a risk factor for the long-term outcome after curative

resection of colon cancer. European Journal of Surgical Oncology 2009;35(10):1060-1064.
639. den Dulk M, Noter SL, Hendriks ER, Brouwers MA, van der Vlies CH, Oostenbroek RJ, Menon AG, Steup W-H, van de Velde CJ. Improved diagnosis and treatment of anastomotic leakage after colorectal surgery. European journal of surgical oncology 2009;35(4):420-426.
640. Bell SW, Walker KG, Rickard MJFX, Sinclair G, Dent OF, Chapuis PH, Bokey EL. Anastomotic leakage after curative anterior resection results in a higher prevalence of local recurrence. British Journal of Surgery 2003;90(10):1261-1266.
641. Petersen S, Freitag M, Hellmich G, Ludwig K. Anastomotic leakage: impact on local recurrence and survival in surgery of colorectal cancer. International Journal of Colorectal Disease 1998;13(4):160-163.
642. Branagan G, Finnis D. Prognosis After Anastomotic Leakage in Colorectal Surgery. Diseases of the Colon & Rectum 2005;48(5):1021-1026.
643. Boccola MA, Buettner PG, Rozen WM, Siu SK, Stevenson ARL, Stitz R, Ho Y-H. Risk Factors and Outcomes for Anastomotic Leakage in Colorectal Surgery: A Single-Institution Analysis of 1576 Patients. World Journal of Surgery 2011;35(1):186-195.
644. Lindgren R, Hallböök O, Rutegård J, Sjödahl R, Matthiessen P. What is the risk for a permanent stoma after low anterior resection of the rectum for cancer? A six-year follow-up of a multicenter trial. Diseases of the Colon & Rectum 2011;54(1):41-47.
645. Choi H-K, Law W-L, Ho JW. Leakage after resection and intraperitoneal anastomosis for colorectal malignancy: analysis of risk factors. Diseases of the colon & rectum 2006;49(11):1719-1725.
646. Brisinda G, Vanella S, Cadeddu F, Civello IM, Brandara F, Nigro C, Mazzeo P, Marniga G, Maria G. End‐to‐end versus end‐to‐side stapled anastomoses after anterior resection for rectal cancer. Journal of surgical oncology 2009;99(1):75-79.
647. Koperna T. Cost-effectiveness of defunctioning stomas in low anterior resections for rectal cancer: a call for benchmarking. Archives of Surgery 2003;138(12):1334-1338.
648. Kingham TP, Pachter HL. Colonic anastomotic leak: risk factors, diagnosis, and treatment. Journal of the American College of Surgeons 2009;208(2):269-278.
649. Fujiwata H, Kuga T, Esato K. High submucosal blood flow and low anastomotic tension prevent anastomotic leakage in rabbits. Surgery Today 1997;27(10):924-929.
650. Attard J-AP, Raval MJ, Martin GR, Kolb J, Afrouzian M, Buie WD, Sigalet DL. The Effects of Systemic Hypoxia on Colon Anastomotic Healing: An Animal Model. Diseases of the Colon & Rectum 2005;48(7):1460-1470.
651. Enestvedt CK, Thompson SK, Chang EY, Jobe BA. Clinical review: healing in gastrointestinal anastomoses, part II. Microsurgery 2006;26(3):137-143.
652. Thompson SK, Chang EY, Jobe BA. Clinical review: healing in gastrointestinal anastomoses, part I. Microsurgery 2006;26(3):131-136.

653. Hyman N, Manchester TL, Osler T, Burns B, Cataldo PA. Anastomotic Leaks After Intestinal Anastomosis: It's Later Than You Think. Annals of Surgery 2007;245(2):254-258.
654. Brandstrup B, Tønnesen H, Beier-Holgersen R, Hjortsø E, Ørding H, Lindorff-Larsen K, Rasmussen MS, Lanng C, Wallin L, Iversen LH. Effects of intravenous fluid restriction on postoperative complications: comparison of two perioperative fluid regimens: a randomized assessor-blinded multicenter trial. Annals of surgery 2003;238(5):641-648.
655. Kurz A, Sessler DI, Lenhardt R. Perioperative normothermia to reduce the incidence of surgical-wound infection and shorten hospitalization. New England Journal of Medicine 1996;334(19):1209-1216.
656. Belda FJ, Aguilera L, De La Asunción JG, Alberti J, Vicente R, Ferrándiz L, Rodríguez R, Sessler DI, Aguilar G, Botello SG. Supplemental perioperative oxygen and the risk of surgical wound infection: a randomized controlled trial. Jama 2005;294(16):2035-2042.
657. Gan TJ, Soppitt A, Maroof M, El-Moalem H, Robertson KM, Moretti E, Dwane P, Glass PS. Goal-directed intraoperative fluid administration reduces length of hospital stay after major surgery. The Journal of the American Society of Anesthesiologists 2002;97(4):820-826.
658. Donati A, Loggi S, Preiser J-C, Orsetti G, Münch C, Gabbanelli V, Pelaia P, Pietropaoli P. Goal-Directed Intraoperative Therapy Reduces Morbidity and Length of Hospital Stay in High-Risk Surgical Patients. Chest 2007;132(6):1817-1824.
659. Foster ME, Laycock JRD, Silver IA, Leaper DJ. Hypovolaemia and healing in colonic anastomoses. BJS 1985;72(10):831-834.
660. Kimberger MDO, Arnberger MDM, Brandt MDS, Plock MDJ, Sigurdsson MDPDGisli H, Kurz MDA, Hiltebrand MDL. Goal-directed Colloid Administration Improves the Microcirculation of Healthy and Perianastomotic Colon. Anesthesiology 2009;110(3):496-504.
661. Murrell ZA, Stamos MJ. Reoperation for anastomotic failure. Clinics in colon and rectal surgery 2006;19(4):213-216.
662. Macarthur DC, Nixon SJ, Aitken RJ. Avoidable deaths still occur after large bowel surgery. British Journal of Surgery 1998;85(1):80-83.
663. Alves A, Panis Y, Pocard M, Regimbeau J-M, Valleur P. Management of anastomotic leakage after nondiverted large bowel resection. Journal of the American College of Surgeons 1999;189(6):554-559.
664. Dellinger RP, Levy MM, Rhodes A, Annane D, Gerlach H, Opal SM, Sevransky JE, Sprung CL, Douglas IS, Jaeschke R. Surviving Sepsis Campaign: international guidelines for management of severe sepsis and septic shock, 2012. Intensive care medicine 2013;39(2):165-228.
665. Power N, Atri M, Ryan S, Haddad R, Smith A. CT assessment of anastomotic bowel leak. Clinical Radiology 2007;62(1):37-42.
666. Hirst N, Tiernan J, Millner P, Jayne D. Systematic review of methods to predict and detect anastomotic leakage in colorectal surgery. Colorectal Disease 2014;16(2):95-109.
667. Komen N, De Bruin RWF, Kleinrensink GJ, Jeekel J, Lange JF. Anastomotic leakage, the search for a reliable biomarker. A review of the literature. Colorectal Disease 2008;10(2):109-115.

668. Servais EL, Rizk NP, Oliveira L, Rusch VW, Bikson M, Adusumilli PS. Real-time intraoperative detection of tissue hypoxia in gastrointestinal surgery by wireless pulse oximetry. Surgical endoscopy 2011;25(5):1383-1389.
669. Karliczek A, Benaron D, Baas P, Zeebregts C, Wiggers T, Van Dam G. Intraoperative assessment of microperfusion with visible light spectroscopy for prediction of anastomotic leakage in colorectal anastomoses. Colorectal Disease 2010;12(10):1018-1025.
670. Kudszus S, Roesel C, Schachtrupp A, Höer JJ. Intraoperative laser fluorescence angiography in colorectal surgery: a noninvasive analysis to reduce the rate of anastomotic leakage. Langenbeck's archives of surgery 2010;395(8):1025-1030.
671. Boyle N, Manifold D, Jordan M, Mason R. Intraoperative assessment of colonic perfusion using scanning laser doppler flowmetry during colonic resection1. Journal of the American College of Surgeons 2000;191(5):504-510.
672. Armstrong G, Croft J, Corrigan N, Brown JM, Goh V, Quirke P, Hulme C, Tolan D, Kirby A, Cahill R and others. IntAct: intra-operative fluorescence angiography to prevent anastomotic leak in rectal cancer surgery: a randomized controlled trial. Colorectal Disease 2018;20(8):226-234.
673. Shandall A, Lowndes R, Young HL. Colonic anastomotic healing and oxygen tension. British Journal of Surgery 1985;72(8):606-609.
674. Locke R, Hauser CJ, Shoemaker WC. The use of surface oximetry to assess bowel viability. Archives of Surgery 1984;119(11):1252-1256.
675. Sheridan WG, Lowndes RH, Young HL. Intraoperative tissue oximetry in the human gastrointestinal tract. The American Journal of Surgery 1990;159(3):314-319.
676. Sheridan WG, Lowndes RH, Young HL. Tissue oxygen tension as a predictor of colonic anastomotic healing. Diseases of the colon & rectum 1987;30(11):867-871.
677. Dyson A, Stidwill R, Taylor V, Singer M. Tissue oxygen monitoring in rodent models of shock. American Journal of Physiology-Heart and Circulatory Physiology 2007;293(1):526-533.
678. Severinghaus JW, Weiskopf RB, Nishimura M, Bradley AF. Oxygen electrode errors due to polarographic reduction of halothane. Journal of applied physiology 1971;31(4):640-642.
679. Bates ML, Feingold A, Gold MI. The Effects of Anesthetics on an In-vivo Oxygen Electrode. American Journal of Clinical Pathology 1975;64(4):448-451.
680. Rocchitta G, Spanu A, Babudieri S, Latte G, Madeddu G, Galleri G, Nuvoli S, Bagella P, Demartis MI, Fiore V. Enzyme biosensors for biomedical applications: Strategies for safeguarding analytical performances in biological fluids. Sensors 2016;16(6):780-801.
681. Puglisi RN, Whalen TV, Doolin EJ. Computer analyzed histology of ischemic injury to the gut. Journal of Pediatric Surgery 1995;30(6):839-844.
682. Kozar RA, Holcomb JB, Hassoun HT, Macaitis J, DeSoignie R, Moore FA. Superior mesenteric artery occlusion models shock-induced gut ischemia-reperfusion. Journal of Surgical Research 2004;116(1):145-150.

683. Gordeeva AE, Temnov AA, Charnagalov AA, Sharapov MG, Fesenko EE, Novoselov VI. Protective Effect of Peroxiredoxin 6 in Ischemia/Reperfusion-Induced Damage of Small Intestine. Digestive Diseases and Sciences 2015;60(12):3610-3619.
684. Grotz MR, Ding J, Guo W, Huang Q, Deitch EA. Comparison of plasma cytokine levels in rats subjected to superior mesenteric artery occlusion or hemorrhagic shock. Shock 1995;3(5):362-368.
685. Secher NH, Van Lieshout JJ. Heart rate during haemorrhage: time for reappraisal. The Journal of Physiology 2010;588(1):19-23.
686. Archer F, Jacquier E, Lyon M, Chastang J, Cottin V, Mornex J-f, Leroux C. Alveolar type II cells isolated from pulmonary adenocarcinoma: a model for JSRV expression in vitro. American journal of respiratory cell and molecular biology 2007;36(5):534-540.
687. Jassim F, Sharp J, Marinello P. Three-step procedure for isolation of epithelial cells from the lungs of sheep with jaagsiekte. Research in veterinary science 1987;43(3):407-409.
688. Johnson C, Fan H. Three-dimensional culture of an ovine pulmonary adenocarcinoma-derived cell line results in re-expression of surfactant proteins and Jaagsiekte sheep retrovirus. Virology 2011;414(1):91-96.
689. Cousens C, Alleaume C, Bijsmans E, Martineau HM, Finlayson J, Dagleish MP, Griffiths DJ. Jaagsiekte sheep retrovirus infection of lung slice cultures. Retrovirology 2015;12(1):31-47.
690. Sanderson MJ. Exploring lung physiology in health and disease with lung slices. Pulmonary pharmacology & therapeutics 2011;24(5):452-465.
691. Linnerth-Petrik NM, Santry LA, Darrick LY, Wootton SK. Adeno-associated virus vector mediated expression of an oncogenic retroviral envelope protein induces lung adenocarcinomas in immunocompetent mice. PLoS One 2012;7(12):51400-51415.
692. Martin WB, Scott FM, Sharp JM, Angus KW, Norval M. Experimental production of sheep pulmonary adenomatosis (Jaagsiekte). Nature 1976;264(5582):183-187.
693. Sharp J, Angus K, Gray E, Scott F. Rapid transmission of sheep pulmonary adenomatosis (jaagsiekte) in young lambs. Archives of virology 1983;78(1-2):89-95.
694. Salvatori D, Gonzalez L, Dewar P, Cousens C, de las Heras M, Dalziel RG, Sharp JM. Successful induction of ovine pulmonary adenocarcinoma in lambs of different ages and detection of viraemia during the preclinical period. Journal of general virology 2004;85(11):3319-3324.
695. Lewis PF, Emerman M. Passage through mitosis is required for oncoretroviruses but not for the human immunodeficiency virus. Journal of virology 1994;68(1):510-516.
696. York DF, Vigne R, Verwoerd D, Querat G. Isolation, identification, and partial cDNA cloning of genomic RNA of jaagsiekte retrovirus, the etiological agent of sheep pulmonary adenomatosis. Journal of virology 1991;65(9):5061-5067.
697. Palmarini M, Sharp JM, De Las Heras M, Fan H. Jaagsiekte sheep retrovirus is necessary and sufficient to induce a contagious lung cancer in sheep. Journal of virology 1999;73(8):6964-6972.

698. Humann-Ziehank E, Renko K, Bruegmann ML, Devi VR, Hewicker-Trautwein M, Andreae A, Ganter M. Long-term study of ovine pulmonary adenocarcinogenesis in sheep with marginal vs. sufficient nutritional selenium supply: Results from computed tomography, pathology, immunohistochemistry, JSRV-PCR and lung biochemistry. Journal of Trace Elements in Medicine and Biology 2013;27(4):391-399.
699. Scott P, Cousens C. Ultrasonography of ovine pulmonary adenocarcinoma. In Practice 2018;40(7):291-300.
700. Gray ME, Sullivan P, Marland JRK, Greenhalgh SN, Meehan J, Gregson R, Clutton RE, Cousens C, Griffiths DJ, Murray A and others. A Novel Translational Ovine Pulmonary Adenocarcinoma Model for Human Lung Cancer. Frontiers in Oncology 2019;9(534):1-17.
701. Wallace JM, Deutsch AL. Flexible Fiberoptic Bronchoscopy and Percutaneous Needle Lung Aspiration for Evaluating the Solitary Pulmonary Nodule. Chest 1982;81(6):665-671.
702. Aristizabal JF, Young KR, Nath H. Can chest CT decrease the use of preoperative bronchoscopy in the evaluation of suspected bronchogenic carcinoma? Chest 1998;113(5):1244-1249.
703. Mazzone P, Jain P, Arroliga AC, Matthay RA. Bronchoscopy and needle biopsy techniques for diagnosis and staging of lung cancer. Clinics in Chest Medicine 2002;23(1):137-158.
704. Laurent F, Montaudon M, Latrabe V, Bégueret H. Percutaneous biopsy in lung cancer. European Journal of Radiology 2003;45(1):60-68.
705. Schreiber G, McCrory DC. Performance characteristics of different modalities for diagnosis of suspected lung cancer: summary of published evidence. Chest 2003;123(1):115-128.
706. Swischuk JL, Castaneda F, Patel JC, Li R, Fraser KW, Brady TM, Bertino RE. Percutaneous transthoracic needle biopsy of the lung: review of 612 lesions. Journal of vascular and interventional radiology 1998;9(2):347-352.
707. Gaeta M, Pandolfo I, Volta S, Russi EG, Bartiromo G, Girone G, La Spada F, Barone M, Casablanca G, Minutoli A. Bronchus sign on CT in peripheral carcinoma of the lung: value in predicting results of transbronchial biopsy. American journal of roentgenology 1991;157(6):1181-1185.
708. House AJ, Thomson KR. Evaluation of a new transthoracic needle for biopsy of benign and malignant lung lesions. American Journal of Roentgenology 1977;129(2):215-20.
709. Klein JS, Zarka MA. Transthoracic needle biopsy. Radiologic Clinics of North America 2000;38(2):235-266.
710. Liao W-Y, Chen M-Z, Chang Y-L, Wu H-D, Yu C-J, Kuo P-H, Yang P-C. US-guided transthoracic cutting biopsy for peripheral thoracic lesions less than 3 cm in diameter. Radiology 2000;217(3):685-691.
711. Pan J-F, Yang P-C, Chang D-B, Lee Y-C, Kuo S-H, Luh K-T. Needle aspiration biopsy of malignant lung masses with necrotic centers: improved sensitivity with ultrasonic guidance. Chest 1993;103(5):1452-1456.
712. Li H, Boiselle PM, Shepard JO, Trotman-Dickenson B, McLoud TC. Diagnostic accuracy and safety of CT-guided percutaneous needle aspiration biopsy of the lung: comparison of small and large pulmonary nodules. American journal of roentgenology 1996;167(1):105-109.

713. Connor S, Dyer J, Guest P. Image-guided automated needle biopsy of 106 thoracic lesions: a retrospective review of diagnostic accuracy and complication rates. European Radiology 2000;10(3):490-494.
714. Mueller PR, vanSonnenberg E. Interventional radiology in the chest and abdomen. New England Journal of Medicine 1990;322(19):1364-1374.
715. Daly B, Templeton PA. Real-time CT fluoroscopy: evolution of an interventional tool. Radiology 1999;211(2):309-315.
716. Cox JE, Chiles C, McManus CM, Aquino SL, Choplin RH. Transthoracic needle aspiration biopsy: variables that affect risk of pneumothorax. Radiology 1999;212(1):165-168.
717. Fish GD, Stanley JH, Miller KS, Schabel SI, Sutherland SE. Postbiopsy pneumothorax: estimating the risk by chest radiography and pulmonary function tests. American Journal of Roentgenology 1988;150(1):71-74.
718. Haramati LB, Austin J. Complications after CT-guided needle biopsy through aerated versus nonaerated lung. Radiology 1991;181(3):778-778.
719. Lim C-S, Tan L-E, Wang J-Y, Lee C-H, Chang H-C, Lan C-C, Yang M-C, Tsao TC-Y, Wu Y-K. Risk factors of pneumothorax after CT-guided coaxial cutting needle lung biopsy through aerated versus nonaerated lung. Journal of Vascular and Interventional Radiology 2014;25(8):1209-1217.
720. Saji H, Nakamura H, Tsuchida T, Tsuboi M, Kawate N, Konaka C, Kato H. The Incidence and the Risk of Pneumothorax and Chest Tube Placement After Percutaneous CT-Guided Lung Biopsy: The Angle of the Needle Trajectory Is a Novel Predictor: The Angle of the Needle Trajectory Is a Novel Predictor. Chest 2002;121(5):1521-1526.
721. Moore EH, Shepard JA, McLoud TC, Templeton PA, Kosiuk JP. Positional precautions in needle aspiration lung biopsy. Radiology 1990;175(3):733-735.
722. Ko JP, Shepard J-AO, Drucker EA, Aquino SL, Sharma A, Sabloff B, Halpern E, McLoud TC. Factors influencing pneumothorax rate at lung biopsy: are dwell time and angle of pleural puncture contributing factors? Radiology 2001;218(2):491-496.
723. Covey AM, Gandhi R, Brody LA, Getrajdman G, Thaler HT, Brown KT. Factors associated with pneumothorax and pneumothorax requiring treatment after percutaneous lung biopsy in 443 consecutive patients. Journal of vascular and interventional radiology 2004;15(5):479-483.
724. Kazerooni EA, Lim FT, Mikhail A, Martinez FJ. Risk of pneumothorax in CT-guided transthoracic needle aspiration biopsy of the lung. Radiology 1996;198(2):371-375.
725. Tsalafoutas IA, Tsapaki V, Triantopoulou C, Gorantonaki A, Papailiou J. CT-guided interventional procedures without CT fluoroscopy assistance: patient effective dose and absorbed dose considerations. American Journal of Roentgenology 2007;188(6):1479-1484.
726. Tomiyama N, Yasuhara Y, Nakajima Y, Adachi S, Arai Y, Kusumoto M, Eguchi K, Kuriyama K, Sakai F, Noguchi M. CT-guided needle biopsy of lung lesions: a survey of severe complication based on 9783 biopsies in Japan. European journal of radiology 2006;59(1):60-64.

727. Klein JS, Salomon G, Stewart EA. Transthoracic needle biopsy with a coaxially placed 20-gauge automated cutting needle: results in 122 patients. Radiology 1996;198(3):715-720.
728. Ng YL, Patsios D, Roberts H, Walsham A, Paul NS, Chung T, Herman S, Weisbrod G. CT-guided percutaneous fine-needle aspiration biopsy of pulmonary nodules measuring 10 mm or less. Clinical Radiology 2008;63(3):272-277.
729. Yeow K-M, See L-C, Lui K-W, Lin M-C, Tsao TC-Y, Ng K-F, Liu H-P. Risk factors for pneumothorax and bleeding after CT-guided percutaneous coaxial cutting needle biopsy of lung lesions. Journal of Vascular and Interventional Radiology 2001;12(11):1305-1312.
730. Khan MF, Straub R, Moghaddam SR, Maataoui A, Gurung J, Wagner TO, Ackermann H, Thalhammer A, Vogl TJ, Jacobi V. Variables affecting the risk of pneumothorax and intrapulmonal hemorrhage in CT-guided transthoracic biopsy. European Radiology 2008;18(7):1356-1363.
731. Taleb S, Jalaeian H, Frank N, Golzarian J, D'Souza D. Is a Routine Chest X-ray Necessary in Every Patient After Percutaneous CT-Guided Lung Biopsy? A Retrospective Review of 278 Cases. Cardiovascular Interventional Radiology 2017;40(9):1415-1420.
732. Choi CM, Um SW, Yoo CG, Kim YW, Han SK, Shim YS, Lee CT. Incidence and risk factors of delayed pneumothorax after transthoracic needle biopsy of the lung. Chest 2004;126(5):1516-1521.
733. Heyer CM, Reichelt S, Peters SA, Walther JW, Muller KM, Nicolas V. Computed tomography-navigated transthoracic core biopsy of pulmonary lesions: which factors affect diagnostic yield and complication rates? Academic Radiology 2008;15(8):1017-1026.
734. Pinho SS, Carvalho S, Cabral J, Reis CA, Gärtner F. Canine tumors: a spontaneous animal model of human carcinogenesis. Translational Research 2012;159(3):165-172.
735. Uva P, Aurisicchio L, Watters J, Loboda A, Kulkarni A, Castle J, Palombo F, Viti V, Mesiti G, Zappulli V. Comparative expression pathway analysis of human and canine mammary tumors. BMC genomics 2009;10(1):135-155.
736. Searle EJ, Illidge TM, Stratford IJ. Emerging Opportunities for the Combination of Molecularly Targeted Drugs with Radiotherapy. Clinical Oncology 2014;26(5):266-276.
737. Ma S, Xu Y, Deng Q, Yu X. Treatment of brain metastasis from non-small cell lung cancer with whole brain radiotherapy and Gefitinib in a Chinese population. Lung Cancer 2009;65(2):198-203.
738. Rodriguez CP, Adelstein DJ, Rice TW, Rybicki LA, Videtic GMM, Saxton JP, Murthy SC, Mason DP, Ives DI. A Phase II Study of Perioperative Concurrent Chemotherapy, Gefitinib, and Hyperfractionated Radiation Followed by Maintenance Gefitinib in Locoregionally Advanced Esophagus and Gastroesophageal Junction Cancer. Journal of Thoracic Oncology 2010;5(2):229-235.
739. Anastas JN, Moon RT. WNT signalling pathways as therapeutic targets in cancer. Nature Reviews Cancer 2012;13:11-26.
740. Wenger FA, Szucsik E, Hoinoiu BF, Ionac M, Walz MK, Schmid KW, Reis H. A new anastomotic leakage model in circular double stapled colorectal

anastomosis after low anterior rectum resection in pigs. Journal of Investigative Surgery 2013;26(6):364-72.
741. Karliczek A, Jesus E, Matos D, Castro A, Atallah A, Wiggers T. Drainage or nondrainage in elective colorectal anastomosis: a systematic review and meta-analysis. Colorectal Disease 2006;8(4):259-265.
742. Petrowsky H, Demartines N, Rousson V, Clavien P-A. Evidence-based value of prophylactic drainage in gastrointestinal surgery: a systematic review and meta-analyses. Annals of surgery 2004;240(6):1074-1085.
743. Rondelli F, Bugiantella W, Vedovati M, Balzarotti R, Avenia N, Mariani E, Agnelli G, Becattini C. To drain or not to drain extraperitoneal colorectal anastomosis? A systematic review and meta‐analysis. Colorectal Disease 2014;16(2):35-42.
744. Fouda E, El Nakeeb A, Magdy A, Hammad EA, Othman G, Farid M. Early detection of anastomotic leakage after elective low anterior resection. Journal of Gastrointestinal Surgery 2011;15(1):137-144.
745. Pedersen ME, Qvist N, Bisgaard C, Kelly U, Bernhard A, Pedersen SM. Peritoneal Microdialysis. Earlydiagnosis of Anastomotic Leakage after Low Anterior Resection for Rectosigmoid Cancer. Scandinavian Journal of Surgery 2009;98(3):148-154.

11 Appendix

11.1 Gene lists used in chapter 4 for characterisation of the parental and radioresistant cell lines

Table 11.1. Epithelial and mesenchymal gene lists. Epithelial and mesenchymal genes are taken from a pan-cancer EMT-associated gene expression signature[345].

Epithelial				Mesenchymal	
AFTPH	ELMO3	LOC440335	SH3YL1	ACOT9	LGALS1
AIM1L	ELOVL7	LPAR2	SLC15A2	ANXA5	LOC100505634
ANKRD5	EPCAM	LSR	SLC22A23	AP1M1	MAP7D3
ANXA9	EPN3	MAL2	SLC29A2	AP1S2	MRC2
AP1M2	ESRP1	MAP7	SLC39A9	ASAP1	MSN
ARHGEF16	ESRP2	MAPK13	SLC44A1	C14orf149	MSRB3
ARHGEF5	EXPH5	MARVELD2	SPINT1	C17orf51	NMT2
ATP2C2	F11R	MARVELD3	SPINT2	C6orf225	OSTM1
ATXN7L3B	FA2H	MKL2	SPPL3	C9orf21	P4HA3
BLCAP	FAAH	MYH14	SSH3	CCDC88A	PDLIM4
BSPRY	FAAH2	MYLIP	ST14	CCDC99	PGBD1
C17orf28	FAM108C1	MYO1D	SYNGR2	CFL2	PPM1F
C1orf172	FAM83H	MYO5B	TLCD1	CHST10	PTRF
C1orf210	FUCA1	MYO5C	TM9SF2	CTGF	RAB11FIP5
C2orf15	FUK	OVOL1	TMC4	DBN1	RAB32
C6orf132	FXYD3	OVOL2	TMEM125	DENND5A	RRAS
CAMSAP3	GALNT3	PKP3	TMEM184A	EIF5A2	RWDD1
CBLC	GGCT	PLEKHG6	TMEM30B	EMP3	SACS
CCDC64B	GRHL1	PPL	TMEM79	ETS1	SCARF2
CDH1	GRHL2	PROM2	TNK1	FAM101B	SGCB
CDH3	HOOK1	PRR15L	TSPAN13	FAM127A	SH2B3
CDS1	HOOK2	PRRG2	TSTD1	FERMT2	ST3GAL2
CLDN7	ICA1	PRRG4	WIBG	FEZ2	STX2
CMTM4	IDH1	PRSS8	XBP1	FGFR1	SYDE1
CNKSR1	IGSF9	PTPN6	ZFP62	FMNL3	TGFB1I1
CRB3	ILDR1	PVRL4	ZNF552	GLIPR1	TMEM158
CTSH	INADL	RAB11FIP4		GNAI2	TTC7B
CYB561	IRF6	RASEF		GNG11	TTL
DDR1	ITPKC	RBM47		GSTO1	TTL
DENND2D	JUP	REL		HABP4	TWF2
DSP	LENG9	ROD1		IKBIP	UROD
DTX4	LIMK2	RREB1		KATNAL1	VIM
EFNA1	LLGL2	S100A14		KIAA1949	WTIP
ELF1	LNX1	SDR42E1		LATS2	WWC2
ELF3	LNX2	SH2D3A		LEPRE1	ZEB1

Table 11.2. WNT signalling and WNT target gene lists. WNT signalling pathway members and their down-stream targets were taken from the KEGG database[342].

WNT Signalling		WNT Targets	
DVL2	LEF1	PLAUR	SOX9
DKK3	PRICKLE1	CD44	SIX1
RHOA	WNT9A	CDH1	FST
LRP6	SKP2	CDON	MYC
FBXW11	TCF7L1	BIRC5	LEF1
GSK3B	FZD7	EFNB1	WNT9A
NLK	FZD1	NRP1	EGFR
EP300	CTBP1	JAG1	GJA1
DAAM1	LRP5	MET	FZD7
PORCN	FZD5	AHR	PPAP2B
AXIN1	FZD6	DKK1	BTRC
FZD3	FRAT1	CCND1	ANGPTL4
DVL1	BTRC	PPARD	AXIN2
MAPK8	CTNNB1	VEGFA	IRS1
DKK1	AXIN2	WNT5A	ANTXR1
CCND1	FZD4	FN1	FOSL1
WNT5B	FOSL1	ID2	SOX2
PPARD	RUVBL1	CTGF	PTCH1
CSNK1A1	FZD8	EGR1	TLE1
WNT5A	JUN	TWIST1	
NFATC1	CTNNBIP1	LRP1	
APC	FZD2	RUNX2	
MYC	WNT7B	BMP4	

11.2 Protein lists generated in chapter 5 for characterisation of MCF-7 secretome

Table 11.3. The total 927 secreted proteins identified in the conditioned media of untreated MCF-7 cells up to 24 h post-serum starvation.

CON P02769	HSPA4	HIST1H4A	CNDP2	NPEPL1
PPIA	TXNDC17	YWHAQ	G6PD	PTMA
ENO1	GDI1	MTPN	AKR1A1	TMA7
ALDOA	RPL11	FANCD2	CON__P02668	HMGN1
HSPA8	GLO1	CON P00978	PPP1CA	FAHD1
TPI1	YWHAG	UBE2I	CKAP4	RRM2
CFL1	EIF5A	CS	HSPH1	NUDT2
GAPDH	CON Q3SZR3	YWHAH	CON P02663	DDT
HSPA1B	ADH5	ALDH9A1	ADK	GMFB
KRT8	DPP3	NUTF2	TTN	HSPB11
PGK1	PGLS	RNPEP	LRRCC1	GLUD1
ACTB	KRT1	PGP	KARS	CON 24466
FBP1	ATIC	FABP5	NEDD8 MDP1	UBE2L3
PEBP1	PDIA3	C1orf123	HPRT1	ACO2
CALM1	APEX1	PGD	SHMT1	TFF1
MIF	PA2G4	PEPD	DLD	LSM2
MDH2	NPEPPS	LXN	PCNA	CON P06868
GPI	HMGN2	DNPEP	NLN	GNPDA1
TMSB4X	HSPA6	ERH	CON REFSEQ	OTUB1
PGAM1	SORD	CON P02662	DDAH2	CBS
YWHAZ	TALDO1	SH3BGRL3	GCLC	TRPV1
LDHA	COTL1	ESD	DCTPP1	TFRC
MDH1	PNP	CON Q95121	CKMT1A	TATDN1
CON P00761	SUMO2	HIST1H2AJ	LSM3	PPP1CC
SOD1	CON Q2KJF1	KRT19	GSTM3	BOLA2
CON Q3SZ57	GGCT	PRDX6	PGM2	SHMT2
YWHAE	DDB1	WDR1	HIST2H3A	MAT2B
TKT	GLOD4	GOT2	PHPT1	PDLIM1
CON Q0IIK2	CON P02754	RBBP4	TARS	MYH9
PFN1	CBR1	PKM	ENO2	PCBD1
UBA52	TXNRD1	THOP1	MAT2A	GYG1
NAPA	TPT1	ASS1	RAB11A	CON 18229
CLIC1	CON P12763	NME2	IDH1	EIF4H
KRT18	LAP3	AIMP1	GCSH	NUDT1
GNB2L1	KRT10	APEH	S100A11	TXN
PPIB	FBP2	CON Q58D62	MYDGF	TBCA
DUT	GSR	RCC2	GNPNAT1	DDAH1
GDI2	KRT9	CSTB	CON P41361	TSN
RAN	DSTN	LTA4H	CON P28800	ACTG1
TMSB10	HIST1H2BM	DBI	EIF6	PPIF
CON Q3MHN5	CON Q3SZV7	SFN	ACLY	DYNC1LI2
CON P34955	GSS	Streptavidin	PPIL3	ME1
ALDOC	YWHAB	FH	CMPK1	TXNL1
PARK7	SELENBP1	SCRN1	MT2A	HMCN1
TSTA3	DNASE2	PDAP1	EEF1A1P5	SPTAN1
CON P21752	PSMA7	RAC1	FLNB	PPP2R1A
HN1	DPYSL2	GORASP2	ALB	UGP2
WDR5	NT5DC1	PLS3	F11	FKBP2

TRIM28	GSTO1	REXO2	PRDX1	ABCE1
MSN	ADSS	ANXA5	ACTN1	RANBP1
ECI1	COX17	PTRHD1	VCP	GABARAPL2
OLA1	ANXA3	CSDE1	CANX	UFM1
PFAS	NANS	TCEB2	CLTC	AARS
CON P50448	HN1L	LMAN2	RCN1	VAPA
CPPED1	YTHDF2	ABAT	HSPE1	RAB21
FLNA	FKBP4	HSPB1	SGTA	CRYZ
OAT	MAPRE1	RPSA	RAB7A	NQO1
ARHGDIA	PPIH	CON P17690	RABIF	ARMT1
HSPA4L	ISOC1	CON Q3Y5Z3	TUBA1B	TAGLN2
EIF2A	ENOPH1	COX4I1	AHCY	FSCN1
FDPS	HIF1A	ACTN4	CYCS	PPA1
NIF3L1	SERF2	SH3BGRL	HSPA9	CDH1
PPP1CB	DTD2	MAGOHB	EEF2	SLC9A3R1
APRT	MVD	HNRNPA1	HNRNPA2B1	ACAA2
CON P02672	IDI1	CON Q3KUS7	NME1	UBA1
OVCA2	CON Q1RMN8	LGALS3BP	P4HB	S100A16
PROSC	POLR2H	NIT2	TPM4	PYCARD
FAH	PIR	RAB6B	HNRNPAB	PLOD3
CON 38329	VCL	CTSB	QSOX1	PSMB2
BLMH	WDR12	KRT2	ECH1	PSPH
CBR3	CALU	PSMB1	EIF5	ACTA1
VAPB	EIF2S2	CON Q9TRI1	ARPC4	PSMA1
MAP4	GRPEL1	HSPA5	OXCT1	PIN4
BASP1	BPNT1	DTD1	ERP29	CNBP
S100A13	GLRX	CTSD	CON 15497	A0A0U1RRE5
PPP2R4	ZNF300	PCMT1	HPDL	VPS26A
UFC1	HEBP2	PLEC	BANF1	CORO1B
PFN2	VPS29	UBE2V1	AIFM1	PSMA2
LAMB1	ANXA2	TP53I3	C21orf33	SPARC
EPPK1	AAMP	UBE2V2	MAPK1IP1L	ARPC2
CON Q2UVX4	HSPD1	PSAT1	PSAP	ACTR3
ACYP1	NAGK	CMBL	MANF	IGHA2
MIPOL1	NRBP1	PROCR	PSMA6	RAD23B
RBBP9	ADI1	CON Q9QWL7	WARS	KRT5
IMPA1	DENR	RAP1B	PARS2	APOA1BP
FKBP1A	PPIL1	CTTN	HDGF	CTSL
FASN	HRSP12	LMNB1	PRDX2	RAB1A
VIM	EML2	TPD52L2	STARD10	TXNDC12
NR2C2AP	GART	SPINT2	DSG2	PSMA4
CLIC4	NUP37	PRRC2C	PDXK	RNH1
BLVRB	SUMO1	EIF4A1	PAFAH1B3	ACP1
RPL19	CNPY2	B2M	TUBB	RSU1
EEF1G	CON Q9TT36	CST3	LDLR	IGHG1
PRKCSH	CSTF1	AP1G1	EEF1A2	FKBP3
PSMB5	DYNLL2	C11orf54	GGH	KRT16
PAICS	ZNF706	NBEA	UCHL1	EIF4EBP1
KPNA2	BAG3	NUDT14	COPB2	GCLM
ATP5B	TAX1BP3	MCAM	MB	GLA
PSMA5	EZR	RBMX	CCT3	LRRC59
SLC7A5	CON Q2KIT0	ALAD	NUDT3	PCNP
MTDH	PAFAH1B1	C1QBP	NASP	TWF1
LAMC1	DCPS	PDCD5	TCP1	CD44
CKS1B	CLEC3B	ASNS	RNASET2	VBP1

RBM8A	PVRL4	ETF1	PMM2	GFRA1
PPP1R14B	UBE2A	TPM3	CON 2777	CIRBP
SCIN	CON 735	PRTFDC1	HEXB	RPS3
PKIB	CON P19001	HMGN3	MCM4	ABHD14B
PGM1	DHX38	PLIN3	XRCC6	UBE2N
SERPINB1	CAPN1	CFL2	RUVBL2	NLE1
ARPC5	CCT8	TMSB15B	SUPT5H	UBAP2L
UCHL3	MYL6	PTPRK	IQGAP1	GOLM1
GRB2	Sep-02	ARFIP1	HIST1H1B	KRT7
PPP2CA	PVRL1	KRT6A	HPX	MAVS
CUTA	WDR92	NUP107	GARS	TLN1
RARS	EEF1B2	HNRNPM	EPRS	EFNA1
KIAA1279	CAPZA1	EIF3G	CON 81644	EIF3A
LANCL1	CDV3	EPCAM	GSN	TMPO
ARCN1	RPIA	CARHSP1	CCT5	RPL27A
CON 3SZH5	RAB14	BTD	CORO1C	PABPC1
DAG1	PSME1	LACTB2	GNS	LDHB
EIF1AX	SUMO3	PPP5C	SKP1	DSP
HIST1H1C	KATNAL2	HAGH	STMN1	PITHD1
BCAT2	ESYT1	SHROOM2	HSP90AA1	MARCKSL1
GMPS	EIF4B	CAPRIN1	FREM2	ACACA
EDF1	AK2	PIN1	RPL10A	PC
ISG15	AK1	CTSC	GLRX3	CCT6A
CALR	SFPQ	LMNA	SLC3A2	PCCB
ITPA	COPG1	PUF60	EIF4G2	KRT6B
CRK	SRP9	LCP1	MAP7	PCCA
DDX39B	CRABP2	SEC23B	SART3	KRT14
PSMA3	RPS28	TOP1	SRRM2	SDC1
TXN2	PAWR	PCBP1	EIF2B1	CON 8VED5
CLSTN1	GOT1	PSMB7	HTATSF1	TWSG1
PCK2	CON 7350	YBX1	DDR1	S100A6
PREPL	CBX3	CAP1	LSM6	FUCA2
RPE	CON V8M9	MYOD1	GALNS	ZBTB8OS
PSMB6	ADPRHL2	ALCAM	DLST	GNB4
XPNPEP1	HARS	CON Q2KJ62	HIST1H1D	KRT74
TXNDC5	STIP1	FKBP15	CRKL	CON 1252647
LGALS1	CON 7665	MSRA	COL5A1	KRT6C
MYH15	UBE2K	CAST	ENSA	CON Q95M1
HMGN4	USP8	RPL5	MARCKS	CSNK1A1
MT1E	STMN2	PTK7	DBN1	RABEP1
TPP2	SEC24C	PCBP2	NPW	S100A8
AMY1A	MYO1C	XRCC5	PPP2R5E	TOR1AIP1
DYNC1H1	CON Q32PI4	SCAMP3	SNRPD3	SUCLG1
CON P01966	HNRNPU	SLC25A5	AP2B1	SF3B4
COX7C	KIF5A	CAPZB	CCT7	SNRPC
THBS1	F11R	CON Q3SX09	EIF4G1	PSMD6
RBBP7	BID	SF3B3	DARS	SNRPA
CON P08730-1	IGFBP4	PRPF19	PITPNB	LASP1
HNRNPD	CAD	PTBP1	AP1B1	RPS10
PSMB3	CLEC3A	ILF3	SEC13	CCDC124
SORT1	THUMPD1	LGMN	AREG	NRP1
SERBP1	KHDRBS1	TNFRSF12A	IARS	DDX17
NAGLU	SERPINB9	DDX21	CON 3ZBS7	EFHD1
ALYREF	HSP90AB1	HK1	SEC23A	BROX
TSNAX	NUCB1	PSMC2	PCSK1N	PHGDH

CANT1	SPINT1	AIMP2	PSMD9	CARS
CA12	CLU	HMGA1	CCT2	TIMP2
CSRP1	SDC4	PDIA6	VAMP8	HMGB3
UBE2D3	TUBB4B	NAP1L2	CON 16046	PSMD14
FUCA1	BCAM	IMPDH2	AKAP1	ACTR2
GRN	CTSA	ANXA1	KHSRP	DCXR
PDE6D	ILF2	CON 01045-1	SERPINH1	FN1
SHISA5	EWSR1	CALML5	ITPK1	AHNAK
HNRNPK	DDX6	PRMT1	LRRN2	L1CAM
CAT	LSR	TIMP1	POLDIP2	UBLCP1
PPIC	PFDN2	TUBA1C	SF3B2	GCN1L1
VASN	SYNCRIP	PDIA4	PSMB4	RRBP1
RUVBL1	RPL12	TMOD3	USP14	FUBP1
CON Q3T052	RAB5C	PSMD11	FAM107B	AGRN
CON P05784	CAPNS1	TRAP1	SND1	ADRM1
LSM8	RBM3	Sep-09	NUDC	
COL1A1	RPS12	HSP90AB2P	TPD52	
FUS	NCAM2	PABPN1	GAA	
HNRNPH1	RCN2	CRIP2	HSP90B1	
NUDT9	RAB2A	COMT	SEC31A	
PFDN4	M0QZD8	NPC2	RPS11	
NUDT5	MDK	HEXA	PSME3	
PPT1	ANP32A	ARPP19	ATRN	
PPP6R3	LRRFIP1	TMEM132A	CXCL12	
COA3	TAF15	IGF2	LAMTOR5	
CDC37	CHORDC1	HDLBP	MGMT	
PLOD1	COX6B1	CTH	LGALS7	
PRDX3	FLNC	PAK2	GNAS	
IGFBP2	COA4	PPP4C	SPTBN1	
FAM129B	HNRNPL	CIAPIN1	CCT4	

Table 11.4. The 239 secreted proteins common to all time points in the conditioned media of untreated MCF-7 cells up to 24 h post-serum starvation.

CON 2769	LDHA	ALDOC	SORD	HIST1H2BM
PPIA	MDH1	PARK7	TALDO1	CON Q3SZV7
ENO1	CON P00761	HSPA4	COTL1	GSS
ALDOA	SOD1	TXNDC17	PNP	YWHAB
HSPA8	CON Q3SZ57	GDI1	SUMO2	SELENBP1
TPI1	YWHAE	RPL11	CON Q2KJF1	HIST1H4A
CFL1	TKT	GLO1	GGCT	YWHAQ
GAPDH	CON Q0IIK2	YWHAG	DDB1	MTPN
HSPA1B	PFN1	EIF5A	GLOD4	FANCD2
KRT8	UBA52	CON Q3SZR3	CON P02754	CON P00978
PGK1	NAPA	ADH5	CBR1	UBE2I
ACTB	CLIC1	DPP3	TXNRD1	CS
FBP1	KRT18	PGLS	TPT1	YWHAH
PEBP1	GNB2L1	KRT1	CON P12763	ALDH9A1
CALM1	PPIB	ATIC	LAP3	NUTF2
MIF	DUT	PDIA3	KRT10	RNPEP
MDH2	GDI2	APEX1	FBP2	PGP
GPI	RAN	PA2G4	GSR	FABP5
TMSB4X	TMSB10	NPEPPS	CON 24146	C1orf123
PGAM1	CON Q3MHN5	HMGN2	KRT9	PGD
YWHAZ	CON P34955	HSPA6	DSTN	PEPD
LXN	G6PD	CON 28800	EIF4H	ADSS
DNPEP	AKR1A1	EIF6	TXN	COX17
ERH	CON P02668	ACLY	DDAH1	YTHDF2
CON 02662	PPP1CA	PPIL3	TSN	FKBP4
SH3BGRL3	CKAP4	CMPK1	PPIF	SERF2
CON 95121	HSPH1	MT2A	ME1	IDI1
HIST1H2AJ	CON P02663	NPEPL1	TSTA3	CON 1RMN8
KRT19	TTN	PTMA	CON P21752	POLR2H
PRDX6	LRRCC1	TMA7	HN1	HEBP2
GOT2	KARS	HMGN1	WDR5	ADI1
RBBP4	NEDD8-MDP1	FAHD1	OLA1	PPIL1
PKM	HPRT1	NUDT2	CON P50448	SUMO1
THOP1	DLD	DDT	ARHGDIA	REXO2
ASS1	NLN	GLUD1	FDPS	HSPB1
NME2	CON 585019	CON 24466	NIF3L1	COX4I1
AIMP1	DDAH2	UBE2L3	CON P02672	ACTN4
APEH	GCLC	TFF1	PROSC	MAGOHB
CON 58D62	DCTPP1	CON P06868	FAH	HNRNPA1
RCC2	CKMT1A	GNPDA1	BLMH	LGALS3BP
CSTB	PGM2	OTUB1	CBR3	CTSB
LTA4H	PHPT1	CBS	VAPB	KRT2
DBI	ENO2	TFRC	BASP1	HSPA5
SFN	RAB11A	TATDN1	EPPK1	CTSD
Streptavidin	IDH1	BOLA2	CON Q2UVX4	UBE2V1
FH	GCSH	MYH9	FKBP1A	B2M
SCRN1	S100A11	PCBD1	DNASE2	EEF1A1P5
CNDP2	CON 41361	CON 18229	PSMA7	

Table 11.5. The 147 secreted proteins which had greater than 2-fold increase in secretion levels in radiation treated MCF-7 cells compared to untreated controls at 24 h post-treatment.

CSRP1	C11orf54	SUMO3	FSCN1	DDAH2
EIF3G	ASNS	BLVRB	GNB2L1	ISG15
RAC1;RAC3;RAC2	SUPT5H	NIT2	KARS	CBR3
GNPNAT1	NUDT3	GAPDH	HNRNPA1	ADH5
CAP1	SEC24C	EIF2A	MGMT	TALDO1
MIPOL1	FAM49B	PGD	GSTM3	CCDC124
TP53I3	RAP1B;RAP1A	EIF6	PGK1	CBR1
OVCA2	NAP1L4	WDR1	CRIP2	TMPO
PIN4	YBX3	PA2G4	PKIB	PDCD5
TK1	ATXN7L3B	CLIC1	RPIA	SORD
RPE;RPEL1	DKK1	ESD	TMA7	EIF4G1
EIF4EBP2	DCTN2	RAN	ARMT1	HNRNPAB
TRPV1;SHPK	MAP7	AHCY	CFL1	RBMX;RBMXL1
FKBP2	CON 2777	ASS1	PPIA	RNPEP
LANCL1	FUBP1	NUTF2	ACP1	PHPT1
TMSB15B	TIGAR	AKR1A1	ALDH9A1	GART
VPS29	IDH1	YWHAH	PKM	ATIC
CORO1B	OLA1	S100A11	MAPRE1	SUMO2
GSTO1	RAD23B	HMGN3	HMGN1	VAPA
PIN1	FABP5	EDF1	ENO1	CAT
VAPB	ALDOC	IDI1	GSR	AIMP1
ANXA2;ANXA2P2	ERH	DTD1	NUDT1	HRSP12
NAGK	COTL1	RBBP9	POLR2H	MTDH
CDV3	PARK7	BASP1	LTA4H	TPI1
DSTN	DDT;DDTL	OTUB1	ESYT1	CDH1
FAM107B	CLIC4	PGP	SUMO1	EFHD1
EPPK1	SH3BGRL3	HMGN2	TCEB2	ABHD14B
ENSA	MAP4	ITPA	EIF4H	
HNRNPM	NT5DC1	CTTN	TSTA3	
ALDOA	CMBL	SERBP1	PPP2R4	

Table 11.6. The 33 secreted proteins which had up to 12-fold increase in secretion levels in radiation treated MCF-7 cells compared to untreated controls at 24 h post-treatment.

CSRP1	PIN4	TK1	IDH1	NUDT3
EIF3G	RPE	EIF4EBP2	SUPT5H	YBX3
GNPNAT1	TRPV1	ASNS	RAP1B	MAP7
MIPOL1	LANCL1	DKK1	VPS29	TIGAR
TP53I3	C11orf54	DCTN2	ATXN7L3B	SUMO3
OVCA2	RAC1	TMSB15B	SEC24C	
FKBP2	CAP1	FAM49B	NAP1L4	

11.3 Journal articles

11.3.1 Published articles

Gray M, Meehan J, Ward C, Langdon SP, Kunkler IH, Murray A, Argyle D. Implantable biosensors and their contribution to the future of precision medicine. The Veterinary Journal 2018; 239: 21-29.

Gray M, Turnbull AK, Ward C, Meehan J, Martínez-Pérez C, Bonello M, Pang LP, Langdon SP, Kunkler IH, Murray A, Argyle D. Development and characterisation of acquired radioresistant breast cancer cell lines. Radiation Oncology 2019; 14(64): 1-19.

Gray M, Meehan J, Blair EO, Ward C, Langdon SP, Morrison L, Marland JRK, Tsiamis A, Kunkler IH, Murray A, Argyle D. Biocompatibility of common implantable sensor materials in a tumor xenograft model. Journal of Biomedical Materials Research Part B: Applied Biomaterials 2018; 1-14.

Gray M, Marland JRK, Dunare C, Blair EO, Meehan J, Tsiamis A, Kunkler IH, Murray A, Argyle A, Dyson A, Singer M, Potter MA. *In Vivo* Validation of a Miniaturised Electrochemical Oxygen Sensor for Measuring Intestinal Oxygen Tension. American Journal of Physiology - Gastrointestinal and Liver Physiology 2019; 317: 242-252.

Gray M, Meehan J, Sullivan P, Marland JRK, Greenhalgh SN, Gregson R, Clutton RE, Ward C, Cousens C, Griffiths D, Murray A, Argyle D. Ovine Pulmonary Adenocarcinoma: A Unique Model to Improve Lung Cancer Research. Frontiers in Oncology - Molecular and Cellular Oncology 2019; 9(335): 1-11.

Gray M, Sullivan P, Marland JRK, Greenhalgh SN, Meehan J, Gregson R, Clutton RE, Cousens C, Griffiths D, Murray A, Argyle D. A Novel Translational Ovine Pulmonary Adenocarcinoma Model for Human Lung Cancer. Frontiers in Oncology - Molecular and Cellular Oncology 2019; 9(534): 1-17.

11.3.2 Submitted articles

Marland JRK, Gray M, Dunare C, Blair EO, Tsiamis A, Sullivan P, González-Fernández E, Greenhalgh SN, Gregson R, Clutton RE, Parys MM, Dyson A, Singer M, Kunkler IH, Potter MA, Mitra S, Terry JG, Smith S, Mount AR, Underwood I, Walton AJ, Argyle D, Murray A. Real-time Measurement of Tumour Hypoxia Using An Implantable Microfabricated Oxygen Sensor. Sensors & Actuators B.

Blair EO, Buchoux A, Tsiamis A, Dunare C, Marland JRK, Gray M, Terry JG, Smith S, Walton AJ. Test Structures for Developing Packaging for Implantable Sensors. Transactions on Semiconductor Manufacturing.